SEISMIC PERFORMANCE OF HIGH-STRENGTH SELF-COMPACTING CONCRETE IN REINFORCED CONCRETE STRUCTURES

A thesis submitted in partial fulfilment of the requirements for the degree of

Doctor of Philosophy in Structural Engineering

By

MOHAMMAD SOLEYMANI ASHTIANI

Supervised by

Professor Rajesh Dhakal

Dr Allan Scott

DEPARTMENT OF CIVIL AND NATURAL RESOURCES ENGINEERING

UNIVERSITY OF CANTERBURY

CHRISTCHURCH, NEW ZEALAND

NOVEMBER 2013

ABSTRACT

Self-compacting concrete (SCC) was first developed in Japan about two decades ago. Since then, it has been offered as a solution to various challenges inherently associated with traditional concrete construction; i.e. quality and speed of construction, impact of unskilled labour force and noise pollution etc. SCC flows into a uniform level under its own weight and fills in all recesses and corners of the formwork even in highly congested reinforcement areas. In recent years the interest in using SCC in structural members has increased manifold; therefore many researchers have started investigating its characteristics. Nevertheless, before this special concrete is widely accepted and globally used in structures, its structural performance under different conditions should be investigated.

This research focuses on investigating the behaviour of high-strength self-compacting concrete (HSSCC) in reinforced concrete (RC) structures through a systematic approach in order to bridge part of an existing gap in the available literature. The dissertation is comprised of four main stages; namely, mix design development and mechanical properties of HSSCC, bond performance of deformed bars in HSSCC, experimental investigation on interior RC beam-column joints (BCJs) cast with HSSCC under reversed cyclic excitations, and finally finite element (FE) modelling and analysis of interior BCJs.

First, a HSSCC mix proportion yielding compressive strength greater than 100 MPa was developed in the laboratory using locally available materials in New Zealand. Two benchmark concrete mixes of conventionally-vibrated high-strength concrete (CVHSC) and normal-strength conventionally vibrated concrete (CVC) were also designed for comparison purposes. Material characteristics (such as compressive, splitting tensile and flexural strengths as well as modulus of elasticity, shrinkage and microstructural properties) of all mixes were evaluated. It was found that, once the lower quality of material in normal strength concrete is offset by achieving a denser mix in high-strength concrete, mechanical properties of HSSCC are equivalent to or higher than those in CVHSC.

Given that the performance of RC structures (and in specific BCJs) is highly dependent on bond between reinforcement and concrete, understanding the bond behaviour in HSSCC was an imperative link between the first and third phases of this research. Therefore, the second phase focused on scrutinizing bond properties of deformed bars in HSSCC using monotonic pull-out and innovative cyclic beam tests. Processing of the pull-out results revealed that a shorter development length may be utilized in HSSCC. In addition, the grade (or ductility) of reinforcing steel was found to substantially influence the post-yield bond performance. Important modifications to the bond model used in the CEB-FIP model code and Maekawa's bond-slip-strain relationship were suggested from the results of this phase. An innovative cyclic beam specimen and test setup were also designed such that a more realistic bond performance could be observed in the laboratory tests compared to that in real RC structures. Deleterious impact of cyclic loading and buckling of reinforcement on bond performance were investigated using this testing protocol.

The third phase of this research focused on the design, fabrication and testing of seven full-size BCJs. BCJs are one of the most critical parts in RC frame structures and their response substantially affects the overall behaviour of the structure. In seismically active regions like New Zealand, the criticality of BCJs is exacerbated with the complexities involved in seismic resistance. The already congested intersection of RC beam and column looks more like a solid steel connection after consideration of earthquake requirements, and placement of concrete becomes problematic in such areas. At the same time, in many of the high-rise structures, normal strength concrete does not meet the capacity requirements; this requires the usage of high-strength concrete. Therefore, once the seismic performance of HSSCC is guaranteed, it can possibly be a solution to both the capacity and compaction problems. Variables such as axial load, concrete type, steel grade, casting direction, and joint shear reinforcement were considered variable in the experimental investigations. It was found that HSSCC has similar seismic performance to that of CVHSC and it can also be incorporated in the joint area of CVC for an enhanced performance.

Finally, DIANA (a nonlinear FE program) was used to simulate the experimental results obtained in the third phase of this research. All BCJs were successfully modelled using their relevant attributes (such as the mechanical properties of HSSCC, steel stress-strain response, test setup and loading protocol) and nonlinear FE analyses (FEA) were performed on each model. FE results were compared to those obtained in the laboratory

which showed a reasonable agreement between the two. The capabilities of the FEA were scrutinized with respect to the hysteresis loops, energy dissipation, joint shear deformations, stress development in the concrete and steel, and drift components.

Integrating the results of all stages of this research provided better understanding of the performance of HSSCC both at the material and structural levels. Not only were none of the seismically important features compromised by using HSSCC in BCJs, but also many other associated benefits were added to their performance. Therefore, HSSCC can be confidently implemented in design of RC structures even in seismically active regions of the world.

UNIVERSITY OF CANTERBURY
Te Whare Wānanga o Waitaha
CHRISTCHURCH NEW ZEALAND

Deputy Vice-Chancellor's Office
Postgraduate Office

CO-AUTHORSHIP FORM

This form is to accompany the submission of any thesis that contains research reported in co-authored work that has been published, accepted for publication, or submitted for publication. A copy of this form should be included for each co-authored work that is included in the thesis. Completed forms should be included at the front (after the thesis abstract) of each copy of the thesis submitted for examination and library deposit.

Please indicate the chapter/section/pages of this thesis that are extracted from co-authored work and provide details of the publication or submission from the extract comes:

Chapter 2:

Soleymani Ashtiani, M, Scott, AN & Dhakal, RP 2013, 'Mechanical and Fresh Properties of High-Strength Self-Compacting Concrete Containing Class C Fly Ash', *Construction and Building Materials*, vol. 47, pp. 1217-1224.

Soleymani Ashtiani, M, Scott, AN & Dhakal, RP 2010, 'Mechanical properties of high-strength self-compacting concrete', in *Proceedings of the 21st Australasian Conference on the Mechanics of Structures and Materials*, Melbourne, Australia, pp. 827-832.

Chapter 3:

Soleymani Ashtiani, M, Dhakal, RP & Scott, AN 2013, 'Post-yield bond behaviour of deformed bars in high-strength self-compacting concrete', *Construction and Building Materials*, vol. 44, no. 0, pp. 236-248.

Soleymani Ashtiani, M, Dhakal, RP & Scott, AN 2011, 'Bond properties of reinforcement in high-strength self-compacting concrete', in *Proceedings of the 9th Symposium on High Performance Concrete Design, Verification and Utilization*, Rotorua, New Zealand.

Chapter 4:

Soleymani Ashtiani, M, Dhakal, RP, Scott, AN & Bull, DK 2013, 'Cyclic beam bending test for assessment of bond–slip behaviour', *Engineering Structures*, vol. 56, no. 0, pp. 1684-1697.

Soleymani Ashtiani, M, Dhakal, RP & Scott, AN 2012, 'Cyclic Beam Bending Test for Assessment of Bond-Slip Behaviour', in *15th World Conference on Earthquake Engineering*, Lisbon, Portugal.

Soleymani Ashtiani, M, Dhakal, RP, Scott, AN & Bull, DK 2013, 'Experimental investigations on cyclic bond-slip behaviour of reinforced concrete members', in *New Zealand Concrete Industry Conference*, Queenstown, New Zealand.

Chapter 5:

Soleymani Ashtiani, M, Dhakal, RP & Scott, AN 2013, 'Seismic Performance of High-Strength Self-Compacting Concrete in Reinforced Concrete Beam-Column Joints', journal of structural Engineering, DOI: 10.1061/(ASCE)ST.1943-541X.0000973 (Published)

Soleymani Ashtiani, M, Dhakal, RP & Scott, AN 2012, 'Seismic Performance of High-Strength Self-Compacting Concrete in Reinforced Concrete Beam-Column Joints', in *15th World Conference on Earthquake Engineering*, Lisbon, Portugal.

Soleymani Ashtiani, M, Dhakal, RP & Scott, AN 2012, 'Combining high-strength self-compacting and normal-strength concretes in reinforced concrete frame structures', in *22nd Australasian Conference on the Mechanics of Structures and Materials, ACMSM22, December, 2012*, Sydney, Australia.

Soleymani Ashtiani, M, Dhakal, RP & Scott, AN 2013, 'Using High-Strength Self-Compacting Concrete in Reinforced Concrete Beam-Column Joints', in *New Zealand Society for Earthquake Engineering*, Wellington, New Zealand.

Soleymani Ashtiani, M, Dhakal, RP & Scott, AN 2013, 'Shear behavior of high-strength self-compacting concrete beam-column joint panels', in *Fifth North American Conference on the Design and Use of Self-Consolidating Concrete*, Chicago, Illinois, USA.

Chapter 6:

Soleymani Ashtiani, M, Dhakal, RP & Scott, AN 2014, 'Analytical Investigation on Seismic Performance of a High-Strength Self-Compacting Concrete Beam-Column Joint', in *Tenth U.S. National Conference on Earthquake Engineering*, Anchorage, Alaska.

Please detail the nature and extent (%) of contribution by the candidate:

The candidate did all the work (100%) under our supervision.

Certification by Co-authors:

If there is more than one co-author then a single co-author can sign on behalf of all

The undersigned certifys that:

- The above statement correctly reflects the nature and extent of the PhD candidate's contribution to this co-authored work
- In cases where the candidate was the lead author of the co-authored work he or she wrote the text

Name: Rajesh P. Dhakal Signature: Rajesh P. Dhakal Date: 25/Nov/2013

ACKNOWLEDGMENTS

The research undertaken and the work presented in this dissertation were supervised by Associate Professor Rajesh Dhakal and Senior Lecturer Allan Scott to whom I am deeply grateful. Without their continuous support and encouragement throughout this project, achievement of the set goals would have been very difficult. They helped flourish my critical mind into what's required to become a professional independent researcher.

Completion of this research would have not been feasible without the financial support provided by the University of Canterbury; the Department of Civil and Natural Resources Engineering; the Earthquake Commission New Zealand; and the New Zealand Concrete Society. Also the fruitful discussions and critical thinking supports provided by James Mackechnie and Professor Des Bull were absolutely providential for the research work. The contributions of all organisations and colleagues are immensely acknowledged.

I would like to thank all of the supportive technicians in the structural laboratory who have helped to accomplish the experimental phases of this research by their valuable inputs and technical expertise. Special thanks go to Tim Perigo who was directly involved throughout the experimental stage of this project. Without his diligent efforts accomplishment of such delicate tests would have not been possible. I am also grateful for the supports provided by David MacPherson, John Maley, Peter Coursey, Stuart Toase, Mosese Fifita, Russell McConchie, Gavin Keats, Kevin Wines, and Bob Wilsea-Smith.

I am indebted to all my fellow postgraduate friends for their support and friendship which made these four years of my life memorable. In particular Joe Byrne, Amir Khanlou, Vinod Sadashiva, Jose Chanchi Golonrdino, Colin Whittaker, Jawad Arefi, Farhad Dashti, Milad Ghorban Ebrahimi, Atefeh Pourali Bejarbaneh, Melanie Liu, and Merrick Taylor.

Finally, I wish to express my deepest gratitude to my family. To my parents Mohammadtaghi and Fatemeh; my wife Sheila; and my sisters Sudeh and Nafiseh for all their love, understanding and encouragements during the past few years.

LIST OF PUBLICATIONS

The following papers have been published based on the work reported in this thesis.

JOURNAL PAPERS

Soleymani Ashtiani, M, Dhakal, RP & Scott, AN 2013, 'Post-yield bond behaviour of deformed bars in high-strength self-compacting concrete', *Construction and Building Materials*, vol. 44, no. 0, pp. 236-248.

Soleymani Ashtiani, M, Scott, AN & Dhakal, RP 2013, 'Mechanical and Fresh Properties of High-Strength Self-Compacting Concrete Containing Class C Fly Ash', *Construction and Building Materials*, vol. 47, pp. 1217-1224.

Soleymani Ashtiani, M, Dhakal, RP, Scott, AN & Bull, DK 2013, 'Cyclic beam bending test for assessment of bond–slip behaviour', *Engineering Structures*, vol. 56, no. 0, pp. 1684-1697.

Soleymani Ashtiani, M, Dhakal, RP & Scott, AN 2013, 'Seismic Performance of High-Strength Self-Compacting Concrete in Reinforced Concrete Beam-Column Joints', *journal of structural Engineering*, DOI: 10.1061/(ASCE)ST.1943-541X.0000973 (Published)

CONFERENCE PAPERS

Soleymani Ashtiani, M, Scott, AN & Dhakal, RP 2010, 'Mechanical properties of high-strength self-compacting concrete', in *Proceedings of the 21st Australasian Conference on the Mechanics of Structures and Materials*, Melbourne, Australia, pp. 827-832.

Soleymani Ashtiani, M, Dhakal, RP & Scott, AN 2011, 'Bond properties of reinforcement in high-strength self-compacting concrete', in *Proceedings of the 9th Symposium on High Performance Concrete Design, Verification and Utilization*, Rotorua, New Zealand.

Soleymani Ashtiani, M, Dhakal, RP & Scott, AN 2012, 'Seismic Performance of High-Strength Self-Compacting Concrete in Reinforced Concrete Beam-Column Joints', in *15th World Conference on Earthquake Engineering*, Lisbon, Portugal.

Soleymani Ashtiani, M, Dhakal, RP & Scott, AN 2012, 'Cyclic Beam Bending Test for Assessment of Bond-Slip Behaviour', in *15th World Conference on Earthquake Engineering*, Lisbon, Portugal.

Soleymani Ashtiani, M, Dhakal, RP & Scott, AN 2012, 'Combining high-strength self-compacting and normal-strength concretes in reinforced concrete frame structures', in *22nd Australasian Conference on the Mechanics of Structures and Materials, ACMSM22, December, 2012*, Sydney, Australia.

Soleymani Ashtiani, M, Dhakal, RP & Scott, AN 2013, 'Using High-Strength Self-Compacting Concrete in Reinforced Concrete Beam-Column Joints', in *New Zealand Society for Earthquake Engineering*, Wellington, New Zealand.

Soleymani Ashtiani, M, Dhakal, RP & Scott, AN 2013, 'Shear behavior of high-strength self-compacting concrete beam-column joint panels', in *Fifth North American Conference on the Design and Use of Self-Consolidating Concrete*, Chicago, Illinois, USA.

Soleymani Ashtiani, M, Dhakal, RP, Scott, AN & Bull, DK 2013, 'Experimental investigations on cyclic bond-slip behaviour of reinforced concrete members', in *New Zealand Concrete Industry Conference*, Queenstown, New Zealand.

Soleymani Ashtiani, M, Dhakal, RP & Scott, AN 2014, 'Analytical Investigation on Seismic Performance of a High-Strength Self-Compacting Concrete Beam-Column Joint', in *Tenth U.S. National Conference on Earthquake Engineering*, Anchorage, Alaska.

TABLE OF CONTENTS

1 INTRODUCTION

Self-compacting concrete (SCC) represents one of the most outstanding advances in concrete technology during the past two decades. Concept of SCC was first proposed by Hajime Okamura (Ozawa et al., 1989) of Kochi University of Technology, Japan, in 1986 as a solution to concrete durability concerns. Inadequate concrete consolidation and unskilled labour were the main causes for poor durability performance of Japanese structures. Development of a concrete that self-consolidates would eliminate, from the construction process, the factors driving poor durability performance of concrete. The prototype was finally developed in 1988 by Ozawa at the University of Tokyo (Maekawa et al., 1999; Okamura et al., 1993).

SCC describes a concrete which flows to a virtually uniform level under the influence of gravity with the ability to compact itself only by means of its own weight without the requirement of vibration. It fills all recesses, reinforcement spaces, and voids even in highly congested concrete members and flows free of segregation. While flowing in the formwork SCC is able to de-aerate from large unnecessary voids, forming a good air-void system required for being a durable concrete.

SCC is a high-performance concrete with special properties. Like other high-performance concretes (e.g. high-strength concrete, acid-resistant concrete), its special properties are achieved only by systematic optimization of both individual constituents and composition. The flowability and mix stability of SCC are determined primarily by the interactions between powder, water, and super-plasticizer. SCC is defined as a fresh concrete possessing superior flowability while maintaining stability; hence, it should have the following characteristics:

- Flowing ability – filling all areas and reaching nooks and corners into which it is placed.
- Passing ability – passing through congested reinforcement without segregation of the constituents or blocking.
- Resistance to segregation – retain coarse components of the mix in suspension in order to maintain a homogenous material.

1.1 LITERATURE REVIEW

1.1.1 CONSTITUENT MATERIALS AND MIX DESIGNS

SCC has the same main ingredients as normal concrete except for the requirement of using Super-Plasticizer (SP) and Viscosity Modifying Agent (VMA) in order to satisfy the necessary fresh properties for self-compactibility. Although in normal concrete it is not necessary to use SP, flowability of SCC relies on the presence of super-plasticizers; other properties will be ensured by providing large amount of powder. In addition, various types of supplementary cementitios materials (SCM) such as fly ash, silica fume, ground granulated blast furnace slag, and limestone filler can be used in SCC just like conventionally vibrated concrete (CVC).

There are various mix design methods for SCC such as Japanese (Okamura, 1997), Chinese (Su et al., 2001; Su et al., 2003), and European (EFNARC, 2002,2005), as well as other methods proposed by different researchers. However, Su et al. (2001) developed one of the most practical and acceptable mix proportioning methods for SCC which works based on packing factor of coarse and fine aggregates.

1.1.2 FRESH PROPERTIES

The unique fresh properties of SCC are achieved by balancing the constituent materials. However, physical interaction between SP and cementitious materials in mix design is of crucial importance. It is essential to mention that not all cement types are compatible with different SPs. Therefore, choosing appropriate SP for the available cement type is important before finalizing the actual SCC mix design. In addition, the compatibility of any other admixtures (VMA, Air Entraining Admixtures) with each other and cement should also be checked (Bedard et al., 2005,2006). As mentioned earlier, SCC develops the required air-void system; however, it is acceptable to use AEA in order to enhance durability characteristics such as freeze-thaw resistance and expansion (Bassuoni et al., 2009). Once again, consistency of the admixture should be checked with the incorporated SP and VMA.

During the previous years, a number of testing methods have been developed and standardized in order to measure flowing and passing abilities as well as resistance to segregation of self-compacting concrete. These methods are now accepted by both European and American standards (ACI237, 2007; ASTM, 2002; EFNARC, 2005). A brief definition of different testing methods for fresh properties of SCC is given below.

- Slump Flow: to assess filling ability, suitable for laboratory and site use
- J-Ring: to assess passing ability, suitable for laboratory and site use
- U-Box: to assess passing and filling ability, suitable for laboratory use
- L-Box: to assess passing ability, suitable for laboratory use
- V-Funnel: indicates filling ability and blocking, suitable for laboratory and site use
- Orimet: indicates filling ability and blocking, suitable for laboratory and site use
- Sieve Stability: to assess segregation resistance, suitable for laboratory and site use
- Penetration: to assess segregation, used in combination with the sieve stability test

The above mentioned fresh properties of SCC should be within specific ranges in order to be accepted as a SCC (Table 1.1).

Table 1.1: Typical Values for Fresh Properties of SCC

Method	Unit	Typical Ranges of Values	
		Minimum	Maximum
Slump Flow	mm	600	800
T_{50} Slump Flow	Sec	2	5
J-Ring	mm	0	10
V-Funnel	Sec	4	12
V-funnel at T_5	Sec	0	+3
L-Box	H_2/H_1	0.8	1.0
U-Box	(H_2-H_1), mm	0	30
Orimet	Sec	0	5

Detailed testing procedures for the fresh properties of SCC are explained in the European and American standards. In addition, fresh properties of various SCC mixes are reported extensively by different researchers (Abou-Zeid et al., 2005; Bonen et al., 2005; Boukendakdji et al., 2009; Dinakar et al., 2008; Felekoglu et al., 2007; Leemann et al.,

2005; Torrijos et al., 2008; Yun Wang et al., 2006). Detailed discussion of these is out of the scope of this thesis

1.1.3 MECHANICAL PROPERTIES

Majority of the literature agrees that if the compressive strength of SCC and CVC is in the same range, both concrete types would develop comparable mechanical properties (Domone, 2007; Felekoglu et al., 2007; Persson, 2001; Suksawang et al., 2006). To concisely understand the differences between the mechanical characteristics of SCC and CVC, dedicated research efforts are required on the mechanical properties, bond between reinforcement and concrete, structural performance and other characteristics of SCC of different strength grades. This way, the possible advantages and disadvantages of SCC compared to CVC would be identified and specific design codes can be developed so that any possible benefits of SCC can be fully utilized.

Generally, compressive strength of SCC and CVC of similar composition does not differ significantly in the majority of the published test results (Domone, 2006). Isolated cases however, showed that SCC develops slightly higher compressive strength compared to CVC when both concrete types have similar water/binder (w/b) ratios. The main reason is because SCC does not require vibration, the interface between aggregate and hardened paste improves (Domone, 2007; Persson, 2001). The ratio of cylinder to cube compressive strength of SCC is also reported to be different than that of CVC (0.9 to 1.0 and 0.8 to 1.0 for CVC and SCC, respectively). A possible explanation of this difference in the behaviour of the two concrete types may come from the contribution of aggregate interlock to the shear strength of the cracked sections which is reported to be lower by about 10% in SCC. This is attributed to the smoother crack surface in SCC as a result of lower coarse aggregate content (Domone, 2007).

Tensile strength of SCC with different compressive strengths may safely be assumed to be the same as that of CVC because the volume of the paste (cement + fines + water) is believed to have no significant effect on the tensile strength of concrete (EFNARC, 2005). However, some studies (Suksawang et al., 2006) showed that SCC has slightly higher splitting tensile strength than CVC for a given compressive strength. Having a better

microstructure, especially lower total porosity and more even pore-size distribution within the interfacial transition zone (ITZ), better quality of the ITZ, denser cement matrix due to the higher content of ultra-fines, better packing factor (proportion of coarse and fine aggregates), and lack of segregation are considered possible reasons (Dinakar et al., 2008; Domone, 2007; Persson, 2001). Due to the fact that the direct tensile test is somewhat delicate and complicated to perform and the scatter of the obtained result is substantial, the indirect tensile strength tests were included in many of the studies (Domone, 2007; Felekoglu et al., 2007). Figure 1.1 shows the typical relationships between cylinder splitting strengths and modulus of rupture values with compressive cube strength for both SCC and CVC mixes. Modulus of rupture results show higher scatter, with the mean being close to the relationship given in the CEB-FIP model code 1990 (1993) as below:

$$f_r = 0.40 \times (f_{ck})^{2/3} \qquad 1.1$$

where, 'f_r' is the modulus of rupture of the concrete (MPa) and 'f_{ck}' is the compressive strength of the cube specimens (MPa)

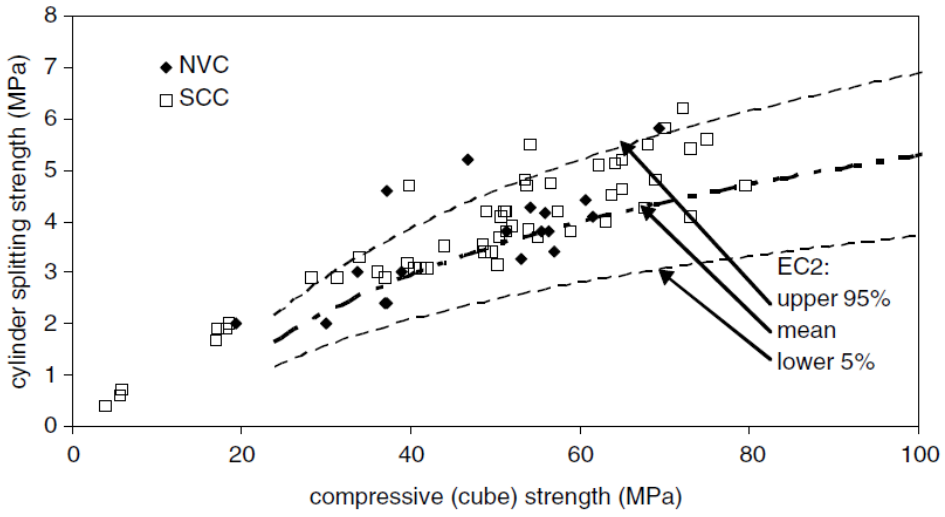

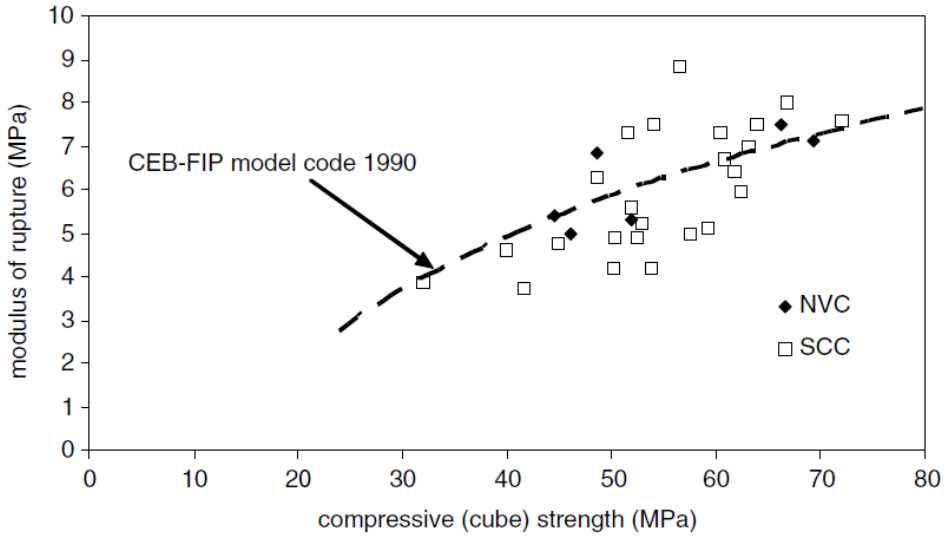

Figure 1.1: Cylinder splitting and modulus of rupture vs. compressive strength

Modulus of elasticity (the ratio between stress and strain – 'E') is used in calculation of elastic deflection which is one of the controlling parameters in flexural design of RC members. Due to the fact that the bulk volume of concrete consists of coarse aggregate, type, amount and modulus of elasticity of coarse aggregate are more influential in determining the elastic modulus of the mix. Therefore, selecting an aggregate with a high modulus of elasticity will increase the modulus of elasticity of concrete. On the other hand, paste (water+binder) and fine aggregate (sand) generally have lower modulus of elasticity; therefore, increasing their quantities in the mix could in turn decrease the value of 'E'. Because SCC often has higher paste and fine aggregate content than CVC, some differences can be expected between their elastic modulus and the value of 'E' may be somewhat lower in case of the former. It is shown that for similar compressive strengths, the modulus of elasticity of SCC can be up to 20 % lower than that of CVC (Felekoglu et al., 2007). Persson (2001) proposed an equation for the modulus of elasticity of SCC as follows:

$$E_c = 3750 \times \sqrt{f_{ck}} \qquad 1.2$$

Where, 'E_c' is the modulus of elasticity of SCC (MPa) and 'f_{ck}' is the compressive strength of the cube specimens (MPa). The 'R^2' in equation 1.2 is 0.78 as determined by Persson (2001).

1.1.4 MONOTONIC BOND BEHAVIOUR OF DEFORMED BARS IN HSSCC

Bond between steel and concrete is an important phenomenon which allows the RC section to function as a structural member. Forces are transferred between the two materials through adhesion, friction and bearing actions. Basic analysis theories of RC members (beams, columns, walls, piles, etc.) are developed based on a perfect bond between steel bars and concrete such a way that compatibility of strains between both materials is valid at all times. However, due to a number of different reasons bond between steel bars and concrete may not always be perfect.

Effectiveness of bond is mainly controlled by factors such as the steel grade, bar diameter, bar ductility, geometry of the ribs, steel corrosion, position of the embedded bar, bond length, quality of concrete and interfacial transition zone (ITZ), concrete cover, confinement (active and passive), and loading type. Generally, bond failure happens due to a combination of the mentioned factors and the failure mechanism is usually complex. Therefore, investigating bond properties between steel bars and concrete has become the focus of many investigations. In order to facilitate more accurate testing of the bond between reinforcement and concrete under monotonic and cyclic loads, different test setups have been developed (namely, direct tension, direct pullout, beam-end test, and beam test).

In case of CVC, poor bond often results from the failure of concrete in fully encapsulating the bar during placing or bleeding and segregation of concrete before hardening which arises from inadequate or excessive vibration, respectively. This can reduce the quality of contact between steel and concrete in the ITZ which is especially pronounced for top bars in deep sections (known as the top bar effect). However, superior quality of the material and homogeneity and consistency of the mix for SCC is reported to increase the quality of the ITZ (Castel et al., 2006; Zhu et al., 2004). In addition, experimental investigations have showed that the effect of top bar phenomenon (segregation and bleeding) is also reduced in SCC which in turn increases the bond between concrete and reinforcing steel (Castel et al., 2006; De Almeida Filho et al., 2008; Esfahani et al., 2008; Valcuende et al., 2009).

Although there is a range of opinion, the majority of the literature agrees that SCC possesses stronger bond properties than CVC (ranging from less than 4% to as much as

70%). Nevertheless in some investigations, steel-to-concrete bond of CVC is reported to be up to 15% higher than SCC (Valcuende et al., 2009). There is still a wide scatter and disagreement among the reported results on bond performance of SCC and CVC. Amongst the mentioned tests for evaluating bond properties of steel and concrete, RILEM-FIP-CEB (1973) direct pullout and beam tests are more popular among researchers (Figure 1.2). the direct pull out test is the most preferred method due to its relative simplicity in casting and testing specimens. However, while testing, the reinforcement is under tension whereas the concrete is under compression. This contradicts the actual RC member behaviour in which both surrounding concrete and the embedded steel are under similar stresses at a given time. Beam test on the other hand gained attraction because of its capability in representing the actual behaviour of bond in structural elements under more realistic conditions; nevertheless, this test method involves considerable time and effort.

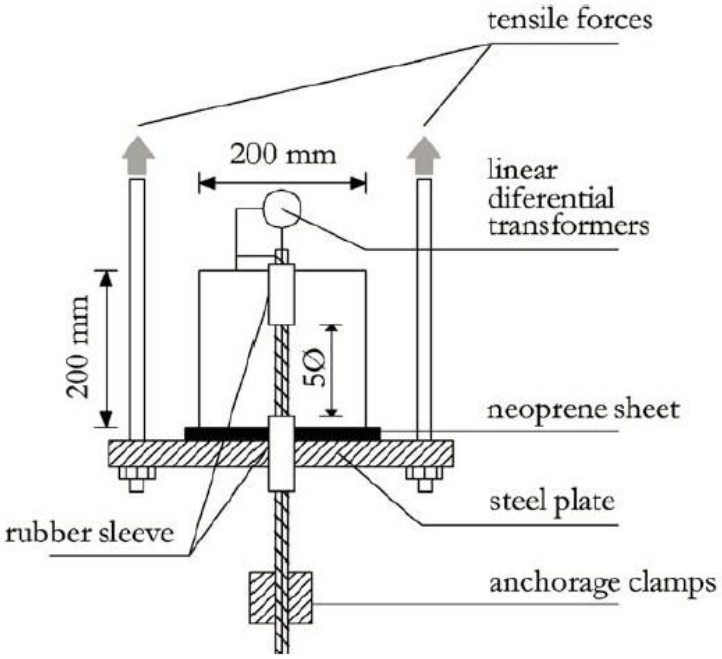

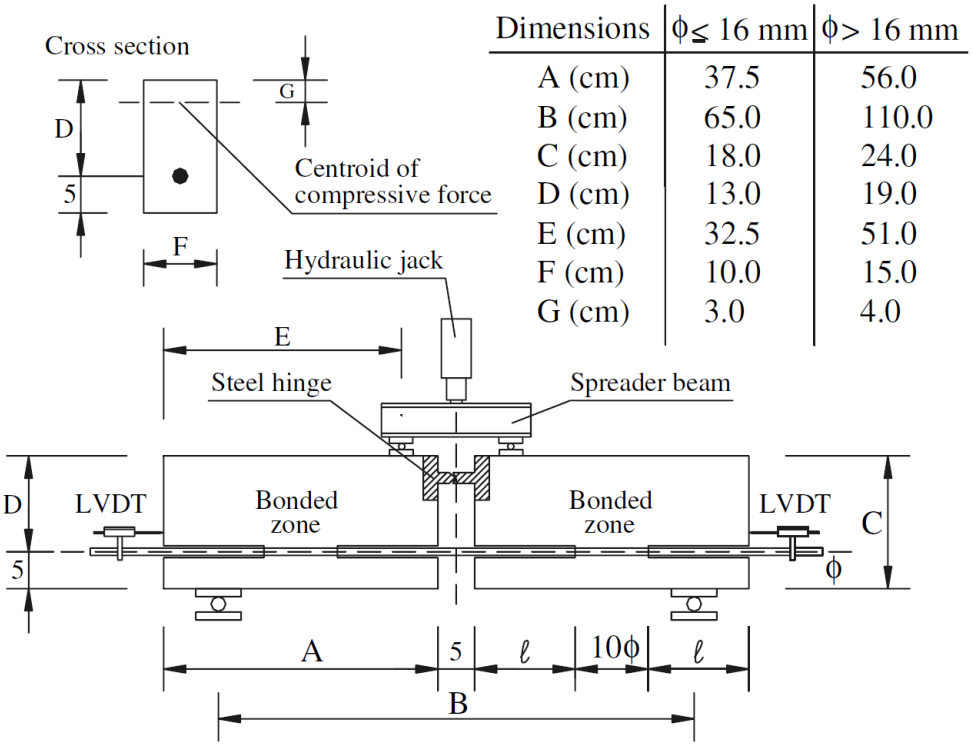

Dimensions	ϕ≤ 16 mm	ϕ> 16 mm
A (cm)	37.5	56.0
B (cm)	65.0	110.0
C (cm)	18.0	24.0
D (cm)	13.0	19.0
E (cm)	32.5	51.0
F (cm)	10.0	15.0
G (cm)	3.0	4.0

Figure 1.2: RILEM specimen and test setup details for the pull-out (top) and beam tests (bottom)

Valcuende et al. (2009) investigated bond properties of deformed bars and CVC and SCC of different mix proportions using direct pullout tests. The concrete compressive strength ranged from around 30 to 70 MPa (at the age of 28 and 90 days) and the corresponding mean and ultimate bond stresses varied from about 8 to 22 MPa and 15 to 40 MPa, respectively. It should be noted that the mean bond stress is defined as the arithmetic mean of the stresses at slip levels of 0.01 mm, 0.1 mm and 1 mm. It is reported that for the concrete strength of 30 MPa, SCC showed 30% higher mean bond stress than CVC. However, as the quality and strength of the concrete increased, the difference decreased to less than 10%. The variation in bond properties between SCC and CVC is attributed to the greater filling capacity and less bleeding in the former. In addition, lower slip quantities were reported for SCC at identical bond stress levels. Nevertheless, when the bond behaviour was looked at under failure conditions, the relatively large differences reported for the mean bond stress tend to disappear. Consolidation of the steel-concrete interface (Figure 1.3) and slightly lower tensile strength of SCC was reported to be the possible reasons for this change.

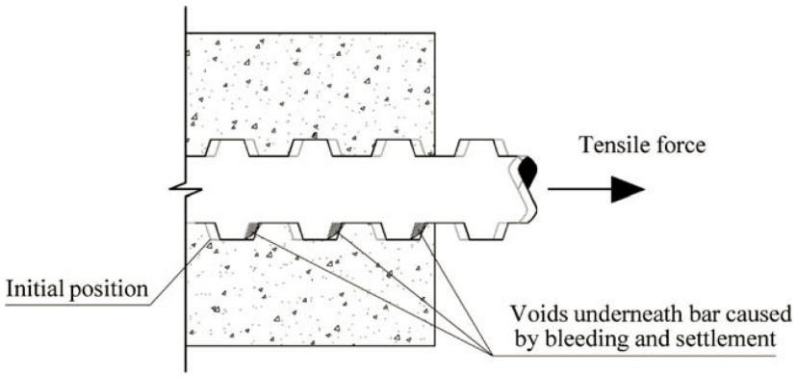

Figure 1.3: Consolidation of voids under the reinforcement during the pullout test

Chan et al. (2003a) studied the development of bond strength of reinforcement in SCC using direct pullout tests arranged in a large RC block of dimensions 1100 mm x 1500 mm. The reinforcement was used to ensure the integrity of the specimen, provide proper confinement and avoid premature de-bonding due to splitting of concrete block. They argued that the critical bond strength (bond stress corresponding to a slip value of 0.25 mm) is a more suitable criterion for design purposes than ultimate bond strength (bond stress pertaining to the peak point of pullout load versus slip curve). The reason is that in terms of structural behavior, bond strength is equivalent to the crack width of a loaded member. In case of the ultimate bond strength, the structural member should experience a large crack width which means considerable deflection. Therefore, the member may be close to its ultimate stage which makes the adoption of ultimate bond strength for the purpose of structural analysis or design unconservative. Experimental results of Chan et al. (2003a) research showed that the normalized bond strength of SCC ranged from 1.72 to 1.97, while that of CVC ranged between 1.18 and 1.59. This indicates that, SCC exhibits significantly higher bond strength and less significant top bar effect compared to CVC.

Most of the available literature on bond properties between SCC (even more generally, CVC) and deformed bars focused on assessing bond performance while reinforcement is in its elastic range. Main reasons for such an inclination amongst different researchers were found to be the difficulties involved in designing the required test setup as well as the complexity of analysing the results. For simplicity, the usual procedure for connecting the testing bar and loading system in the pullout test is to thread the end of the bar and attach it to the hydraulic jack using a coupler, another threaded bar and a nut. By nature, this mechanism prevents the bar from entering its actual post-yield phase; because the bar

would break at its weak point where threading starts before it actually completes its strain hardening and reaches its ultimate strength. Some researchers used different gripping mechanisms to prevent the mentioned drawback; however, they did not investigate bond properties in the post-yield phase of the steel bar. The reason is that when reinforcement is in its post-yield stage, nonlinearity of the bond phenomenon and that of steel tends to blend with each other which make the explanation of the results complex. Most of the researchers did not directly report the stress levels in the reinforcement while testing the pull-out specimens; although steel levels can be calculated using the bond stress. This shows that the focus of such studies were mostly on the concrete bond strength without evaluating possible effects of steel stress-strain profile.

Desnerck et al. (2010) investigated the bond behaviour of SCC and high-strength deformed bars (yield strength of around 600 N/mm^2) using beam test as recommended by RILEM (1973). They considered the concrete type (CVC or SCC), compressive strength of concrete (50 and 60 MPa) and diameter of reinforcement (12, 20, 25, 32, and 40 mm) as variables. Because the concrete strength was higher than what was mentioned in the RILEM standards, Desnerck et al changed the bond length in the beam specimens from 10 to 5 times the bar diameter in order to avoid yielding and in some cases rupture of the bar. For the larger bar sizes (32 and 40 mm ones), they produced a larger beam specimen so as to prevent a brittle failure by splitting of the concrete cover. After analysing the experimental results of their research it was concluded that for larger bar diameters the bond strength of SCC and CVC is comparable. However, when smaller bar diameters were used, SCC showed higher bond strength than CVC. They also suggested that for an equal water/cement ratio the compressive strength of the powder-type SCC is considerably more than that of CVC. Compared to the experimental results of the bond-slip behaviour in other researches, there is a peculiarity in some of the bond-slip curves reported in this research. A clear plateau is recognizable after the linear branch of the bond-slip curves which shows occurrence of a certain mechanism; unfortunately, Desnerck et al did not emphasis possible reasons of the mentioned phenomenon. Presence of the mentioned plateau after yield is also mentioned by Chan et al. (2003a) and FIB Bulletin 10 (2000) without explaining clearly what possible reasons could result such behaviour. Further research is required to investigate in more details and explain the nonlinear mechanics of such phenomenon.

De Almeida Filho et al. (2008) performed a series of bond tests on both CVC and SCC using pullout and beam tests as prescribed by RILEM (1973) in order to evaluate the advantages and disadvantages of each testing method. They explained that if auxiliary reinforcement is used in the pullout specimen, it can hide the effect of compressive strength and bar diameter on bond performance and this is why most of the researchers prefer to used unreinforced prisms for doing this test. Moreover in the case of high-strength concrete the behaviour of the specimen can be affected by the concrete cover splitting. Varying parameters in the investigation conducted by De Almeida Filho et al. (2008) were the concrete type (SCC and CVC), concrete compressive strength (30 and 60 MPa) and bar diameter (10 and 16 mm). The experimental results of this study proved that in case of normal strength concrete, the behaviour of bond stress and slip (even in the post-peak range) were similar between the pullout and beam tests. Therefore considering the ease of construction of pullout specimens and the difficulty involved in making beam specimens, it is suggested to use the former for evaluating the bond properties of normal strength concrete. Nevertheless, pullout and beam specimens did not show such close similarity when high-strength concrete was used. Pullout specimens illustrated a linear branch until failure and a sudden splitting in the concrete block was followed; whereas, beam specimens reached a ductile branch after the initial linear one. It is believed that the ductile portion of bond-slip curves in the beam specimens happened due to yielding of the steel bar.

The available literature on bond properties of reinforcement and SCC seems to be limited and experimental results fluctuate considerably among different studies. The term high strength self-compacting concrete (HSSCC) is defined differently by various researchers; the compressive strength usually ranges from 50 to 70 MPa. Most of the researchers chose to investigate the bond properties of deformed bars and concrete when the reinforcement is in its elastic range (or slightly passed its yield point). Although in some cases (De Almeida Filho et al., 2008; Desnerck et al., 2010) rupture of the bar happened in pullout or beam tests, results were not sufficiently investigated to differentiate possible differences between elastic and post-yield phases. In fact, in most of such studies, tests were repeated by either reducing the bond length or by using high-strength steel so that the bar remains below its yield when slip failure happens. More focused research is required to assess the bond properties of deformed bars and SCC (including HSSCC) such that the effect of nonlinearity of the concrete and steel stress-strain profile can be accounted for.

In addition, bond between deformed bars and concrete plays an important role when it comes to the cyclic performance of reinforced concrete (RC) beam-column joints (BCJs). Slippage of the beam bars through column and their local slip in plastic hinge zone of BCJs is one of the common failure mechanisms of the joint area in RC structures. As a result, most of the concrete standards set limiting constraints on the minimum required depth of column. This limitation is a function of the diameter of beam bars, concrete compressive strength and steel yield strength; otherwise known as the most important parameters in defining bond strength between the reinforcement and concrete. Note that these criteria are based on an extensive database of test results of mostly normal strength concrete. Therefore as long as the column remains elastic (which is in line with the strong-column weak-beam philosophy), high-strength concrete might require a shorter bond development length.

At the same time due to different proportioning of the coarse and fine aggregates in SCC compared to that in CVC, a general notion of a weaker bond in SCC exists amongst the practitioners. As a result, investigating bond performance of deformed bars in HSSCC is a crucial link not only to bridge the current gap in the literature; but also to connect the material characteristic and the structural performance of HSSCC in BCJs. Furthermore, it is felt essential to develop an appropriate test methodology to investigate the effect of cyclic loading on bond performance for SCC more realistically through which the laboratory results may be able to be correlated to the actual seismic behaviour of the structural members.

1.1.5 CYCLIC BOND BEHAVIOUR OF DEFORMED BARS IN HSSCC

Bond between reinforcement and concrete is one of the most important aspects in structural response of RC members. Basic RC theories assume compatibility of strains between concrete and reinforcing bars which is valid only if a perfect bond exists between the two materials. Therefore investigating bond between concrete and reinforcing bars under different loading conditions is of great importance and it has been the focus of many investigations in the past. Several researchers have explored bond between steel and concrete using different test setups and specimens such as direct pull-out, beam anchorage and beam-column joint tests (Alavi-Fard et al., 2002; Desnerck et al., 2010; El-Hacha et

al., 2006; Popov, 1984). Nevertheless, direct pull-out tests with different arrangements appear to be the most commonly preferred approach for investigating bond properties of reinforcement and concrete under both monotonic and cyclic loads (Alavi-Fard et al., 2002; Campione et al., 2005; Cattaneo et al., 2009; Chan et al., 2003a; Fang et al., 2006). The main reasons of choosing pull-out tests over the other methods are the simplicity in producing specimens and the ability of isolating the effects of different parameters on the overall bond performance. However in most of the available pull-out test setups, concrete and steel work under different stress states; i.e. at the same time when the latter experiences tension, the former is in compression and vice versa. This is not a real condition in structural members where either both concrete and steel are in tension or in compression. Especially, in the case of high strength concrete, direct pull-out tests may not necessarily represent the actual behaviour (De Almeida Filho et al., 2008). Other test setups and specimens have also been developed to more accurately replicate the actual state of stress in real structures.

In addition to the common pull-out test, RILEM-FIP-CEB (1973) provides a test setup and specimen specifications for a beam bending test to investigate bond between reinforcing bar and concrete under monotonic two-point flexural loading. Figure 1.4 shows details of the beam bending test recommended by RILEM. The beam specimen comprises of two half-beams connected to each other at the centre with a steel hinge (on the top) and a deformed bar (at the bottom). This way when the specimen is loaded, the bending moment at the centre of the beam is taken care of by the steel hinge (in compression) and the deformed bar (in tension) only. Therefore in the section analysis, the effect of concrete is eliminated which in turn reduces the complexity of dealing with concrete compression block. In addition to the main reinforcing steel in which the bond is assessed, there exists other reinforcement (auxiliary steel) in each half of the beam as shown in Figure 1.4. This extra reinforcement is required to account for the shear and bending forces as well as to represent the effect of confinement provided by transverse reinforcement (which does exist in real structural members) on the bond performance.

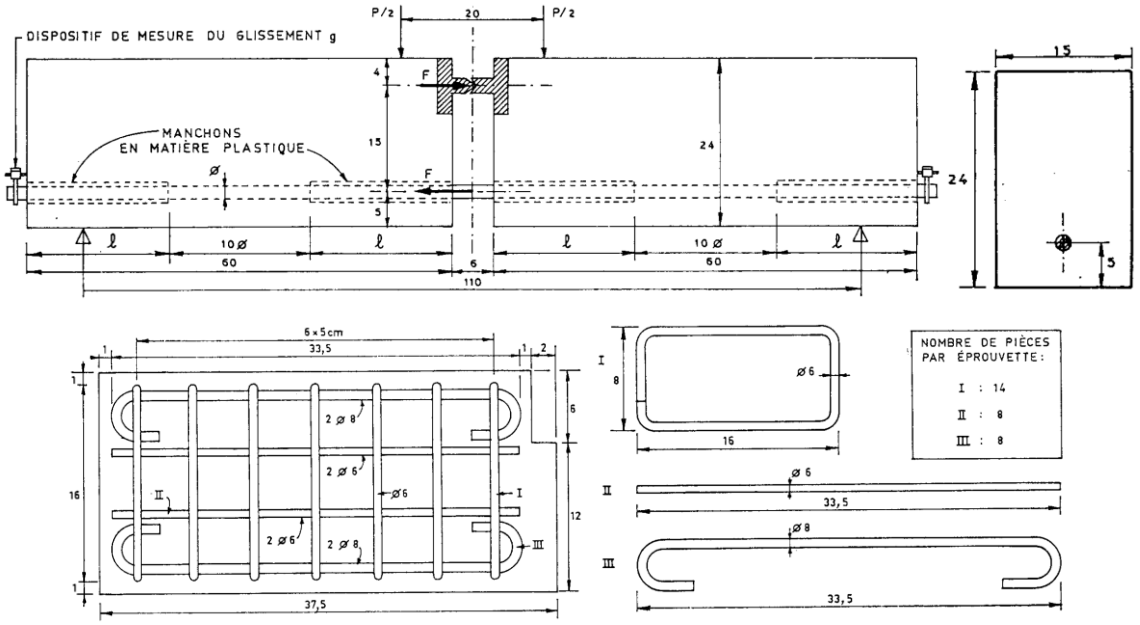

Figure 1.4: Details of the RILEM beam specimen for two-point monotonic loading

RILEM pull-out and beam bending test setups and specimens were originally designed for assessing bond under monotonic loading. It should be noted that although the beam test has some advantages over the direct pull-out test, due to the complexities involved in both test setup and specimen fabrication, fewer studies have been performed using the RILEM beam test (Dancygier et al., 2010; De Almeida Filho et al., 2008; Desnerck et al., 2010; El-Hacha et al., 2006). While some modifications have been suggested for the RILEM beam test setup and specimen, all of the reported studies were performed using monotonic loading. Although researchers have extensively explored bond-slip relationships for different concrete and steel types under monotonic loading using different test setups, less is reported on bond properties under reversed cyclic loading. As real structures are subjected to load reversals (earthquake, wind and live load) during their life-span, it is important to investigate their behaviour under cyclic loads.

Modified pullout tests have previously been used to investigate cyclic bond-slip relationships (Alavi-Fard et al., 2002; Campione et al., 2005; Fang et al., 2006). Details of a typical test setup for assessing bond under cyclic loading using pullout specimens (cyclic pullout) are shown in Figure 1.5. The two steel plates adjacent to the concrete specimen faces (one at the top and the other at the bottom) have circular holes of two times the bar diameter as recommended by RILEM. A steel frame which comprises of a combination of two steel plates, 4 bolts and 8 nuts is assembled (as seen in Figure 1.5) in such a way that it

holds the concrete specimen and the two steel plates together. The nuts provided at the top and bottom of the steel plates should be properly tightened so that any slack between different parts is eliminated. A slip gauge (usually an LVDT) is fixed on the top steel plate which reads the slip at the free end of the deformed bar; the other end is placed into a griping mechanism located at the fixed end of the testing apparatus. Four steel rods are attached to the top steel plate and are connected to another steel plate just below the reciprocating head of the testing machine. A steel rod connects the top most steel plate and the griping mechanism. The desired loading sequence is applied to the specimen through the reciprocating head of the testing apparatus which can exert both tensile and compressive forces. If a displacement controlled loading regime is used, it can either be controlled by the displacement at the loaded end of the bar or the slip at the free end. For this test a specific type of testing machine capable of applying load reversals is required; the gripping mechanisms also need to be specially designed so that the bars do not slip under cyclic loading. It is obvious that the cyclic pullout test setup is much more demanding than the monotonic pullout test.

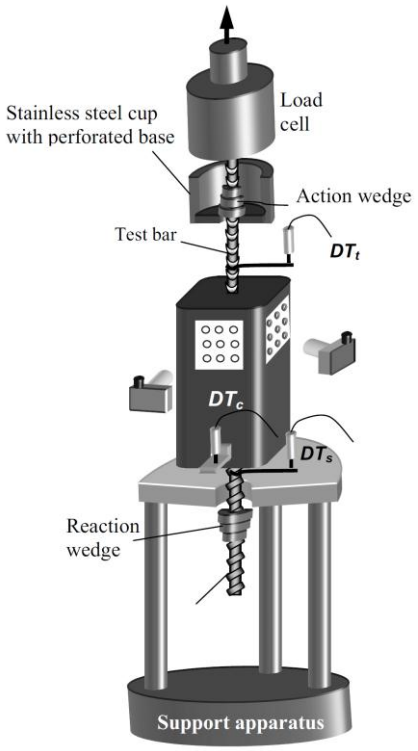

Figure 1.5: Details of a typical cyclic pullout test setup (Tastani et al., 2010)

Nevertheless as mentioned previously, the pullout based bond tests do not represent the actual state of stresses inside RC members subjected to flexural actions. For this purpose,

in this study an attempt has been made to modify the beam specimen for the monotonic bond test suggested by RILEM and develop a suitable test setup capable of applying load reversals to the modified specimen. Although the alteration of the RILEM monotonic test setup and specimen bring more intricacy to the system, special attention is paid to keep the details as simple, repeatable and applicable as possible.

1.1.6 SCC IN STRUCTURAL MEMBERS

1.1.6.1 FLEXURAL BEHAVIOUR OF SCC BEAMS

Structural performance of RC originates from a combination of factors such as its mechanical properties, durability aspects, concrete-rebar bond, ductility, deformation and cracking behaviours, flexural and shear capacities, and finally the loading characteristics. As opposed to numerous investigations on the fundamental behaviours of SCC, there are not many studies available on SCC structural elements and their responses under various loading conditions. Verifying the structural performance of SCC members is equally important and crucially significant when it comes to structural applications of this special concrete. However, there are only a handful of technical papers on the structural performance of elements cast with SCC including beams, columns, beam-column joints, and frames which are discussed in more detail below.

Sonebi et al. (2003) conducted an investigation on the performance and cracking behaviour of SCC beams. Two different SCC grades of compressive strength 35 and 60 MPa were used to fabricate RC beams of 200 x 300 x 3800 mm $200 \times 300 \times 3800\text{mm}$ size. Moment vs. deflection and crack width vs. maximum moment curves were derived and the performances of CVC and SCC elements were compared. Results were also compared with available expressions in various standards. It was concluded that, the moment carrying capacity of SCC beams is comparable to CVC ones and the ultimate deflection is slightly higher for SCC compared to the reference beams.

Peter et al. (2004) investigated the flexural behaviour of reinforced SCC beams by casting four beams of dimensions 150 x 400 x 3000 mm $150 \times 400 \times 3000\text{mm}$ which included two SCC and two CVC beams having different steel ratios. It was concluded from the

results that, SCC beams had higher ductility up to the peak load and lower afterwards compared to that of the CVC beams. It is to be noticed that, a lower ductility of SCC beams compared to CVC ones is in contradiction with the result of a previous pull-out test (Valcuende et al., 2009). Crack spacing and width of cracks were comparable in both SCC and CVC beam specimens. Load vs. deformation behaviour of both concrete types was similar up to the peak load stage. However, after the peak load the load carrying capacity of SCC beams reduced significantly compared to that of CVC ones.

Ganesan et al. (2006) performed an investigation on ultimate strength of steel fibre reinforced (SFR) SCC flexural elements which was a new attempt in assessing structural capabilities of SFRSCC. Twenty beams of size 100 x 150 x 1200 mm were cast and tested under four-point bending out of which two were without fibre and the rest were categorized using volumetric fraction and aspect ratio of steel fibres. It was concluded that by addition of fibres the first crack load, ultimate load carrying capacity and ductility of SCC beams improved substantially.

1.1.6.2 SHEAR BEHAVIOUR OF SCC BEAMS

Many researchers have focused on the shear behaviour of SCC, fibre reinforced SCC (FRSCC), and Pre-stressed beams cast with SCC. Lachemi et al. (2005) tested eighteen beams of constant width and length of 100 and 900 mm respectively, and varying heights of 150, 200 and 300 mm. Beams were designed to withstand flexure; but totally devoid of shear reinforcement in order to ensure shear failure. Two different sizes of coarse aggregate were used in order to assess the influence of aggregate size on shear capacity. Although, SCC had lower coarse aggregate amount by 30%, it was found that the shear capacity of SCC beams was comparable to CVC ones.

Hassan et al. (2008) investigated 20 beams of constant span to total depth ratio of 2.5 and width of 400 mm with no shear stirrups in order to guarantee the shear failure. Although SCC beams had lower ultimate shear capacity than CVC ones, the difference was not significant. Shear capacity difference between SCC and CVC beams increased by up to about 15% as the depth increased and the reinforcement amount decreased. However, for shallow beams, influence of concrete type and reinforcement ratio on shear strength

seemed to be negligible. The lower shear strength of SCC beams compared to that of CVC ones was attributed to lesser coarse aggregate interlock.

Greenough et al. (2008) assessed the shear behaviour of FRSCC slender beams. Thirteen beams of size 200 x 300 x 2400 mm $200 \times 300 \times 2400\text{mm}$ and varying fibre content and type were cast and tested. Based on the outcome, shear capacity, flexural toughness (the area below the load-deflection curve) and ductility of FRSCC beams increased along with fibre content. In addition, suitability of using fibres as a replacement of minimum required shear reinforcement in beams was suggested. It was also reported that FRSCC beams (without stirrups) have slightly higher shear capacity compared to FRC ones; especially in higher fibre contents.

1.1.6.3 FLEXURAL BEHAVIOUR OF SCC COLUMNS

Structural performance of SCC columns has also been investigated by different researchers. Khayat et al. (2001) investigated the structural performance and mechanical properties of SCC used for casting highly reinforced columns. Two SCC and their counterpart CVC columns of size 235 x 235 x 1400 mm were cast and tested under monotonic concentric axial loading until failure. In addition, four unreinforced columns of the same size were cast and used to obtain the mechanical properties of both SCC and CVC in actual specimens rather than auxiliary ones. It was concluded from the results that, adequately proportioned SCC can be used to cast highly confined columns. SCC columns can develop comparable maximum load carrying capacity with considerably greater ductility than CVC ones. Greater homogeneity of compressive strength distribution can be obtained using SCC; however, in spite of SCC's high deformability, it can develop lower in-place compressive strength by up to 10% than the strength determined by the control cylinders.

Paultre et al. (2005) evaluated the structural performance of SCC used in confined concrete columns which seems to be a continuation of the work done by Khayat et al. (2001). Nine SCC concrete columns of various compressive strengths (40 to 80 MPa) and two of CVC having a compressive strength of 40 MPa were cast and tested under monotonic concentric axial loading. In order to enable a full comparison between SCC and CVC columns, results

of previous investigations on confined normal concrete columns were used (Paultre et al., 2005). In addition to the mentioned 11 reinforced columns, 5 unreinforced columns were cast in order to assess the in-place concrete compressive strength under concentric loading and distribution. Similar conclusions were made as in the previous study with some additions regarding the confinement performance of SCC and CVC with ordinary and high strength steel bars.

Chien-Hung et al. (2008) investigated SCC columns under concentric compression by casting 16 SCC and 16 CVC columns of size 300 x 300 x 1400 mm with three different tie arrangements. The experimental results of this investigation were compared with a previous investigation performed by the same group of researchers on the high-workability concrete (HWC) columns under concentric compression (Lin et al., 2004). It was concluded that, the SCC columns of this study had more stiffness than CVC ones with better ductility. Whereas, columns cast by HWC had better stiffness and ductility than SCC ones which can be attributed to the larger amount of coarse aggregates contained in HWC. Crack width of SCC columns was less than that of both CVC and HWC ones which could be due to the better flowability and higher amount of supplementary cementitious materials of SCC.

1.1.6.4 BEHAVIOUR OF SCC BEAM-COLUMN JOINTS

Luo et al. (2004) and Said et al. (2007) performed investigations on static and cyclic behaviour of SCC frames, respectively. Unfortunately, the original publication language of the former is Chinese which restricts reporting on the work carried out by Luo et al. (2004).

However, Said et al. (2007) are the first group of researchers who investigated the behaviour of SCC structural elements under cyclic loading. Besides discussing the use of SCC in structural frames, behaviour of SCC beam-column joints (BCJs) under reversed cyclic loading was investigated and compared with that of CVC in terms of load–displacement envelope, cumulative dissipated energy, steel and concrete contribution to beam and joint shear resistance, and secant stiffness. One standard BCJ of each concrete type (SCC and CVC) was considered in order to represent part of a structural concrete frame and to assess quasi-static cyclic response of concrete structures. Loading pattern was

intentionally selected to cause forces which simulate high levels of inelastic deformations that may be experienced by frame during a severe earthquake. Therefore, the loading sequense was consisted of two phases: load-controlled and displacement-controlled. It was concluded that SCC BCJs have comparable load carrying capacity to that of CVC up to a certain ductility level, and at higher ductility levels SCC specimens may not maintain the same load carrying capacity as CVC ones. While this could be attributed to the fact that the lower coarse aggregate content in SCC reduced the contribution of the aggregate interlock to the total shear resistance mechanism, further research is required in order to fully understand this behaviour. Performance of SCC under shear stress in the joint panel was comparable to that of CVC in terms of cracking and deformation. SCC beam–column joint specimen performed adequately in terms of the mode of failure and ductility requirements. Contribution of concrete to shear resistance in the beam section of CVC beam–column specimen was higher than that of SCC specimen, especially at high drifts. In case of the joint section, concrete contribution to shear resistance remained significant until the end of the test for both specimens. Main difference in both cases was attributed to smaller slippage along cracks in joint area compared with that of beam hinging zone. Further studies are needed to investigate the behaviour of SCC under cyclic loading in hinging zones and to quantify aggregate interlock contribution mechanisms for different coarse aggregate contents and maximum aggregate size along with the effect of other mixture design parameters.

1.1.7 SUMMARY AND RESEARCH MOTIVATIONS

Although SCC was introduced to the field of civil engineering about twenty years ago, its suitability for being applied in the field is still ambiguous for structural engineers. This is not surprising given that even the exact behaviour of normal concrete, which has been around for more than 150 years, has not yet been completely understood. Likewise, it is expected to take a long time before SCC can be thoroughly researched, acknowledged, and standardized for being incorporated in future structures safely and confidently. Based on the above information regarding the current status of literature on different aspects of SCC, it is apparent that a wide range of topics is still exposed to uncertainties. Specifically, SCC performance needs to undergo various investigations before being introduced into structural applications with behavioural complexities. High rise buildings, towers, dams,

and offshore structures are some examples of such intricate situations. Although the nature of the proposed study is to concentrate on the seismic behaviour of structural elements cast with HSSCC, it is worthwhile discussing the other possible areas of investigation which can be brought up into the picture as a part of initial phases of the project in more detail.

One of the very initial stages of SCC performance in structures is based on how well it gets compacted while pouring into the formworks of various shapes. Being capable of flowing through reinforcement and filling in all corners and recesses, SCC enables fabricating structural elements from a single casting point. In most of the available investigations on structural members, casting was done from one end of the formwork in order to show passing ability of SCC as well as its compactability. It is worthwhile noticing that although SCC is capable of being poured into the formwork from a single point, this may be deleterious for its mechanical properties. For instance in a recent investigation by Hassan et al. (2009) on corrosion resistance of SCC, it is suggested that while casting structural members with SCC it is better to move the casting point along the formwork in order to ensure uniform compaction especially at corners. To make the point clearer, consider CVC and its casting procedure in slabs where plane dimensions are large compared to the thickness. Concrete is first poured at various locations and compacted afterwards; in addition, each concrete layer is compacted separately. In case of SCC as the name suggests, compaction is meant to happen under SCC's self-weight also promoted by the concrete flowability. Therefore, the flowability of SCC is required to complete the compaction and not merely reaching all parts of the formwork.

Another possible area of research is comparison of the compaction levels of CVC and SCC. As it has always been an issue, compaction of normal concrete remains one of the challenging tasks in practice. Obtaining all of the other characteristics of concrete; thus, its structural performance depends highly on whether or not compaction can be performed well. Vibrating CVC has been considered one of the most delicate and demanding tasks; yet it is very difficult to reach a perfect level of compaction. Chan et al. (2003b) attempted to investigate the effect of compaction on bond properties of reinforcement and concrete. Nevertheless, other engineering properties of concrete are also affected by different compaction levels. Therefore, another appealing topic of investigation could be to compare the fundamental properties of SCC with that of CVC having considered various levels of compaction and evaluating its effects on the physical properties.

One of the other important aspects of understanding concrete behaviour is to characterize its performance under tension and compression. Wustholz et al. (2007) investigated the deformation of SCC under tensile loading (short term and long term). However, there is no report regarding the behaviour of compression stress-block for SCC which can be quite interesting owing to the fact that the amount of fine aggregate is more than coarse aggregate in SCC.

SCC tends to behave differently than CVC in terms of bond between reinforcement and concrete. Previous researchers tend not to suggest any specific expressions or models explaining this behavioural variation, rather they assessed the applicability of the available codal expressions (developed for CVC) to SCC. Based on the fact that bond-slip behaviour is a crucial factor in evaluating concrete capacity under different loading situations, it is necessary to conduct experiments in order to develop specific expressions and models to predict the bond-slip characteristic. Such models can later be used in calibrating analysis programs in order to predict the structural response of SCC elements more accurately.

As explained earlier, basic laboratory experiments had been performed to investigate the behaviour of SCC elements including beams and columns; however, slabs cast with SCC have not yet been investigated. Because in a majority of concrete structures, floors are cast using concrete slabs, conducting laboratory tests for evaluating and assessing SCC slabs and their behaviour under various loadings can be one of the other areas of investigation. Besides, behaviour of SCC beams and columns under torsion is another intricate behaviour of these structural elements which has not yet been scrutinized and needs to undergo detailed experimental investigations in order to understand probable differences compared to CVC.

Having considered the above non-seismic research possibilities; in the next section, an effort has been made towards proposing possible seismic topics of investigations which are of more interest in seismically active regions like New Zealand. One of the most interesting and delicate parts of a building is the intersection of columns and beams. There have always been major concerns towards analysing, designing, and executing these sections as their behaviour and performance affect the overall functionality of the structure. On one hand, beam-column joints (BCJ) of RC buildings are considered one of the main

areas of reinforcement congestion where placing concrete becomes difficult. On the other, their response under major earthquake events is of crucial significance for structural engineers. In case of CVC, numerous laboratory investigations have been performed in order to understand different mechanisms in BCJs. Based on the available literature, there are a couple of factors pertinent to the strength and behaviour of BCJs under seismic excitations; such as axial load, ratio of shear reinforcement in joint, amount and diameter of beam bars passing through the joint, middle layers of beam reinforcement, etc. Besides, different arrangements of struts and shear reinforcements in joints have considerable impact on final resistance of beam-column joints. At the same time, one of the major mechanisms which should be assessed and controlled when analysing the behaviour of BCJs is the formation of plastic hinges. Design of beam-column intersections in RC frames is conducted in a way that the plastic hinges occur in the beam rather than the column.

It is therefore clear that performing parametric analysis on the effect of each individual parameter on overall behaviour of BCJs is extremely difficult by conducting laboratory experiments. That is when performing a numerical simulation (such as finite element analysis) gains importance in connecting and improving various outcomes. However, it is first essential to validate the finite element (FE) models with respect to the available experimental results and check the consistency of final outcomes. Afterwards, it becomes practical to expand the created models in order to further understand the behaviour of such intricate elements. Nevertheless, as mentioned before there have not been many dedicated studies towards evaluating structural performance of SCC elements under seismic excitations. Because, SCC is different from CVC in some of the physical characteristics (modulus of elasticity, bond-slip behaviour, creep, and shrinkage), appropriate models and elements should first be selected and calibrated in order to increase the accuracy of the results.

1.2 RESEARCH OBJECTIVES

The main focus of this research is to address the suitability, applicability and performance of high-strength self-compacting concrete (HSSCC) in RC beam-column joints subjected to reversed cyclic loading. In order to achieve the main research goal, a systematic approach is set out by fulfilling the following main objectives:

- ✓ Developing a high-strength self-compacting concrete (HSSCC) mix using the locally available materials and capable of being reproduced in a commercial concrete plant. Also developing benchmark mixes of conventionally vibrated high-strength concrete (CVHSC) for comparison purpose. Investigation of the material characteristics (microstructural and physical properties) of the developed mixes.
- ✓ Scrutinizing the bond between high-strength concrete and deformed reinforcements under monotonic type loading and address possible difference compared with the normal strength concrete.
- ✓ Developing a test method and specimen for investigating the bond properties under reversed cyclic loading and also establishing a database using different parameters such as the concrete type and strength, steel grade, bar diameter, and bond length.
- ✓ Experimental investigation on cyclic performance of full-scale RC beam-column joints cast with HSSCC and considering different variables such as the concrete type and strength, amount of joint shear reinforcement, percentage of axial load, casting direction, and steel grade.
- ✓ Numerical simulations of the experimentally tested beam-column joints using the finite element (FE) software "DIANA", calibration of the material models, performing the nonlinear analysis, and comparing the FE predictions with the experimental results of the seismically important features; namely the hysteresis response, damping, stiffness, contribution of steel and concrete in the joint shear force, joint shear deformations, elongation of the beam plastic hinge zone, and strain development in the reinforcement.

1.3 ORGANISATION OF THESIS

This research work is divided into four main parts:

- ✓ Concrete mix design development and material characterization
- ✓ Investigations on bond properties of deformed bars and concrete under monotonic loads
- ✓ Development of a test setup and beam specimen for scrutinizing bond under cyclic loads

- ✓ Seismic performance of RC BCJs under quasi-static type excitations
- ✓ Finite element simulations and nonlinear analysis of the BCJ experimental investigations

The thesis consists of seven chapters including the "Introduction", "Conclusions" and five core chapters. Each of the five core chapters are either an exact representation or expanded version of one or more journal and/or conference papers; this is indicated at the top of each chapter. Therefore in many places, additional information necessary to fully understand the materials provided in the chapters is moved to the appendices. A brief outline of each chapter is given below.

Chapter 2 describes the procedure of developing a high-strength self-compacting concrete (HSSCC) mix as well as two comparable conventionally vibrated high-strength concrete (CVHSC) mixes using the locally available materials in New Zealand. Physical and some of the chemical properties of all mix designs are also investigated using various standard laboratory test methods such as the compressive, split tensile and flexural strength as well as the modulus of elasticity, shrinkage, scanning electron microscopy, and resistivity tests.

Chapter 3 aims at investigating the bond properties of reinforcement and the developed concrete mixes under monotonic loading. Two main series of pullout specimens were designed, fabricated and tested using slightly different test setups. Factors such as the concrete type and strength, steel grade, bar diameter, and bond length were considered as variables among the specimens. Bond properties were investigated in both pre and post-yield phases of reinforcement and a thorough scrutiny of the post-yield bond performance is performed in this chapter.

Chapter 4 deals with the design, modification and development of a unique test setup and beam specimen to enable exploring bond properties under reversed cyclic excitations. The beam specimen proposed by RILEM is modified in such a way that it can withstand load reversals. A special test setup incorporating some of the fundamental structural analysis concepts is designed and fabricated to allow cyclic testing of the modified beam specimen. The suitability and validity of the devised test setup is checked using a sample beam specimen. Further, a total of eighteen beam specimens incorporating different variables were tested using the proposed setup and results were compared with the pullout tests. In

addition, an attempt is made towards modelling the sample beam specimen using DIANA (a nonlinear finite element 'FE' software) and FE analysis and experimental results are compared.

Chapter 5 provides the details of the seven beam-column joint (BCJ) specimens tested in this study and explains the testing procedure, setup, loading protocol, and other important features. Out of the seven fabricated BCJs, four were cast using HSSCC, one with CVHSC, one with normal-strength conventionally vibrated concrete (CVC) and one with CVC incorporating HSSCC only in its joint area. Concrete type and strength, axial load ratio, amount of joint shear reinforcement, steel grade, and casting direction were considered variable among the tested BCJs. Seismically important features such as the hysteresis response, crack pattern and width, damping, stiffness, strain development in the joint stirrups, contribution of concrete and steel in taking joint shear force, drift components, and beam plastic hinge elongation were investigated.

Chapter 6 describes the numerical simulation of BCJs with a focus on finite element modelling and analysis. Constitutive material models selected for the concrete (total-strain rotating crack model) and steel (Menegotto Pinto model) are explained and calibrated using the BCJ experimental investigations and the available literature. Selection of a suitable bond property for the modelled specimens is also described. Appropriate elements for discretization of the BCJs are investigated and mesh sensitivity is checked in both pushover and cyclic analyses. Finally, the seismically important features are extracted from the FE predictions and compared with the experimental results.

1.4 REFERENCES

Abou-Zeid, MN & Roushdy, MS 2005, 'Performance and uniformity of self-compacting concrete', *Transportation Research Record*, no. 1914, pp. 71-80.

ACI237 2007, 'Self-Consolidating Concrete (ACI 237R-07)'. ACI Committee 237.

Alavi-Fard, M & Marzouk, H 2002, 'Bond behavior of high strength concrete under reversed pull-out cyclic loading', *Canadian Journal of Civil Engineering*, vol. 29, no. 2, pp. 191-200.

ASTM 2002, 'American Society for Testing and Materials'.

Bassuoni, MT & Nehdi, ML 2009, 'Durability of self-consolidating concrete to sulfate attack under combined cyclic environments and flexural loading', *Cement and Concrete Research*, vol. 39, no. 3, pp. 206-226.

Bedard, C & Mailvaganam, NP 2005, 'The use of chemical admixtures in concrete. Part I: Admixture-cement compatibility', *Journal of Performance of Constructed Facilities*, vol. 19, no. 4, pp. 263-266.

Bedard, C & Mailvaganam, NP 2006, 'The use of chemical admixtures in concrete. Part II: Admixture-admixture compatibility and practical problems', *Journal of Performance of Constructed Facilities*, vol. 20, no. 1, pp. 2-5.

Bonen, D & Shah, SP 2005, 'Fresh and hardened properties of self-consolidating concrete', *Progress in Structural Engineering and Materials*, vol. 7, no. 1, pp. 14-26.

Boukendakdji, O, Kenai, S, Kadri, EH & Rouis, F 2009, 'Effect of slag on the rheology of fresh self-compacted concrete', *Construction and Building Materials*, vol. 23, no. 7, pp. 2593-2598.

Campione, G, Cucchiara, C, La Mendola, L & Papia, A 2005, 'Steel-concrete bond in lightweight fiber reinforced concrete under monotonic and cyclic actions', *Engineering Structures*, vol. 27, no. 6, pp. 881-890.

Castel, A, Vidal, T, Viriyametanont, K & Francois, R 2006, 'Effect of reinforcing bar orientation and location on bond with self-consolidating concrete', *ACI Structural Journal*, vol. 103, no. 4, pp. 559-567.

Cattaneo, S & Rosati, G 2009, 'Bond between Steel and Self-Consolidating Concrete: Experiments and Modeling', *ACI Structural Journal*, vol. 106, no. 4, pp. 540-550.

CEB-FIP-MC 1993, 'Model Code 1990: Design Code'. T. Telford, London.

Chan, Y-W, Chen, Y-S & Liu, Y-S 2003a, 'Development of bond strength of reinforcement steel in self-consolidating concrete', *ACI Structural Journal*, vol. 100, no. 4, pp. 490-498.

Chan, YW, Chen, YG & Liu, YS 2003b, 'Effect of consolidation on bond of reinforcement in concrete of different workabilities', *ACI Materials Journal*, vol. 100, no. 4, pp. 294-301.

Chien-Hung, L, Chao-Lung, H, Shih-Ping, L & Chih-Hsiuan, L 2008, 'Self-consolidating concrete columns under concentric compression', *ACI Structural Journal*, vol. 105, no. 4, pp. 425-432.

Dancygier, AN, Katz, A & Wexler, U 2010, 'Bond between deformed reinforcement and normal and high-strength concrete with and without fibers', *Materials and Structures/Materiaux et Constructions*, vol. 43, pp. 839-856.

De Almeida Filho, FM, El Debs, MK & El Debs, ALHC 2008, 'Bond-slip behavior of self-compacting concrete and vibrated concrete using pull-out and beam tests', *Materials and Structures/Materiaux et Constructions*, vol. 41, no. 6, pp. 1073-1089.

Desnerck, P, De Schutter, G & Taerwe, L 2010, 'Bond behaviour of reinforcing bars in self-compacting concrete: Experimental determination by using beam tests', *Materials and Structures/Materiaux et Constructions*, vol. 43, pp. 53-62.

Dinakar, P, Babu, KG & Santhanam, M 2008, 'Mechanical properties of high-volume fly ash self-compacting concrete mixtures', *Structural Concrete*, vol. 9, no. 2, pp. 109-116.

Domone, PL 2006, 'Self-compacting concrete: An analysis of 11 years of case studies', *Cement and Concrete Composites*, vol. 28, no. 2, pp. 197-208.

Domone, PL 2007, 'A review of the hardened mechanical properties of self-compacting concrete', *Cement and Concrete Composites*, vol. 29, no. 1, pp. 1-12.

EFNARC 2002, *Specification and Guidelines for Self-Compacting Concrete*, European Federation of Procedures and Applicators of Specialist Products for Structures

EFNARC 2005, *The European Guidelines for Self-Compacting Concrete Specification, Production and Use*, European Federation of Procedures and Applicators of Specialist Products for Structures

El-Hacha, R, El-Agroudy, H & Rizkalla, SH 2006, 'Bond characteristics of high-strength steel reinforcement', *ACI Structural Journal*, vol. 103, no. 6, pp. 771-782.

Esfahani, MR, Lachemi, M & Kianoush, MR 2008, 'Top-bar effect of steel bars in self-consolidating concrete (SCC)', *Cement and Concrete Composites*, vol. 30, no. 1, pp. 52-60.

Fang, CQ, Gylltoft, K, Lundgren, K & Plos, M 2006, 'Effect of corrosion on bond in reinforced concrete under cyclic loading', *Cement and Concrete Research*, vol. 36, no. 3, pp. 548-555.

Felekoglu, B, Turkel, S & Baradan, B 2007, 'Effect of water/cement ratio on the fresh and hardened properties of self-compacting concrete', *Building and Environment*, vol. 42, no. 4, pp. 1795-1802.

Fib-Bulletin-10 2000, 'Fib (CEB-FIP) Bulletin 10, Bond of reinforcement in concrete: state-of-art report', vol. 10., no. Book, Whole

Ganesan, N, Indira, PV & Santhosh Kumar, PT 2006, 'Ultimate strength of steel fibre reinforced self compacting concrete flexural elements', *Indian Concrete Journal,* vol. 80, no. 12, pp. 8-15.

Greenough, T & Nehdi, M 2008, 'Shear behavior of fiber-reinforced self-consolidating concrete slender beams', *ACI Materials Journal,* vol. 105, no. 5, pp. 468-477.

Hassan, AAA, Hossain, KMA & Lachemi, M 2008, 'Behavior of full-scale self-consolidating concrete beams in shear', *Cement and Concrete Composites,* vol. 30, no. 7, pp. 588-596.

Hassan, AAA, Hossain, KMA & Lachemi, M 2009, 'Corrosion resistance of self-consolidating concrete in full-scale reinforced beams', *Cement and Concrete Composites,* vol. 31, no. 1, pp. 29-38.

Khayat, KH, Paultre, P & Tremblay, S 2001, 'Structural performance and in-place properties of self-consolidating concrete used for casting highly reinforced columns', *ACI Materials Journal,* vol. 98, no. 5, pp. 371-378.

Lachemi, M, Hossain, KMA & Lambros, V 2005, 'Shear resistance of self-consolidating concrete beams - Experimental investigations', *Canadian Journal of Civil Engineering,* vol. 32, no. 6, pp. 1103-1113.

Leemann, A & Hoffmann, C 2005, 'Properties of self-compacting and conventional concrete - Differences and similarities', *Magazine of Concrete Research,* vol. 57, no. 6, pp. 315-319.

Lin, C-H, Lin, S-P & Tseng, C-H 2004, 'High-Workability Concrete Columns Under Concentric Compression', *ACI Structural Journal,* vol. 101, no. 1, pp. 85-93.

Luo, S-R, Wang, X-F & Zheng, J-L 2004, 'Experimental study of the aseismic behavior of self-compacting high strength concrete frames', *Gongcheng Lixue/Engineering Mechanics,* vol. 21, no. 6, pp. 144-148.

Maekawa, K & Ozawa, K 1999, 'Developmen of SCC's prototype', *Self-Compacting High-Performance Concrete (Social System Institute),* pp. 20-32.

Okamura, H 1997, 'Self-compacting high-performance concrete', *Concrete International,* vol. 19, no. 7, pp. 50-54.

Okamura, H, Maekawa, K & Ozawa, K 1993, 'High performance concrete. Tokyo, Gihido'

Ozawa, K, Maekawa, K, Kunishima, M & Okamura, H 1989, 'Development of high performance concrete based on the durability design of concrete structures', in *Proceedings of the 2nd East-Asia and Pacific Conference on Structural Engineering and Construction (EASEC-2),* vol. 1, pp. 445-450.

Paultre, P, Khayat, KH, Cusson, D & Tremblay, S 2005, 'Structural performance of self-consolidating concrete used in confined concrete columns', *ACI Structural Journal*, vol. 102, no. 4, pp. 560-568.

Persson, B 2001, 'A comparison between mechanical properties of self-compacting concrete and the corresponding properties of normal concrete', *Cement and Concrete Research*, vol. 31, pp. 193-198.

Peter, JA, Lakshmann, N, Manoharan, PD, Rajamane, NP & Gopalakrishnan, S 2004, 'Flexural behaviour of RC beams using selfcompacting concrete', *Indian Concrete Journal*, vol. 78, no. 6, pp. 66-72.

Popov, EP 1984, 'Bond and Anchorage of Reinforcing Bars Under Cyclic Loading', *Journal of the American Concrete Institute*, vol. 81, no. 4, pp. 340-349.

RILEM-FIP-CEB 1973, 'Tentative recommendations, recommendations for reinforcing steel, bond test for reinforcing steel: 1- Beam test (7-II-28 D) 2- Pull-out test (7-II-128)', *Materials and Structures*, vol. 6, no. 2, pp. 79-118.

Said, A & Nehdi, M 2007, 'Behaviour of reinforced self-consolidating concrete frames', *Proceedings of the Institution of Civil Engineers: Structures and Buildings*, vol. 160, no. 2, pp. 95-104.

Sonebi, M, Tamimi, AK & Bartos, PJM 2003, 'Performance and Cracking Behavior of Reinforced Beams Cast with Self-Consolidating Concrete', *ACI Materials Journal*, vol. 100, no. 6, pp. 492-500.

Su, N, Hsu, K-C & Chai, H-W 2001, 'A simple mix design method for self-compacting concrete', *Cement and Concrete Research*, vol. 31, no. 12, pp. 1799-1807.

Su, N & Miao, B 2003, 'A new method for the mix design of medium strength flowing concrete with low cement content', *Cement and Concrete Composites*, vol. 25, no. 2, pp. 215-222.

Suksawang, N, Nassif, HH & Najm, HS 2006, 'Evaluation of mechanical properties for self-consolidating, normal, and high-performance concrete', *Transportation Research Record*, no. 1979, pp. 36-45.

Tastani, SP & Pantazopoulou, SJ 2010, 'Direct tension pullout bond test: Experimental results', *Journal of Structural Engineering*, vol. 136, no. Compendex, pp. 731-743.

Torrijos, MC, Barragan, BE & Zerbino, RL 2008, 'Physical-mechanical properties, and mesostructure of plain and fibre reinforced self-compacting concrete', *Construction and Building Materials*, vol. 22, no. 8, pp. 1780-1788.

Valcuende, M & Parra, C 2009, 'Bond behaviour of reinforcement in self-compacting concretes', *Construction and Building Materials*, vol. 23, no. 1, pp. 162-170.

Wustholz, T & Reinhardt, H-W 2007, 'Deformation behaviour of self-compacting concrete under tensile loading', *Materials and Structures/Materiaux et Constructions*, vol. 40, no. 9, pp. 965-977.

Yun Wang, C, Yong Jic, K, Hwa Cheol, S & Han Young, M 2006, 'An experimental research on the fluidity and mechanical properties of high-strength lightweight self-compacting concrete', *Cement and Concrete Research*, vol. 36, no. 9, pp. 1595-1602.

Zhu, W, Sonebi, M & Bartos, PJM 2004, 'Bond and interfacial properties of reinforcement in self-compacting concrete', *Materials and Structures/Materiaux et Constructions*, vol. 37, no. 271, pp. 442-448.

2 DEVELOPMENT AND PROPERTIES OF HIGH-STRENGTH SELF-COMPACTING CONCRETE (HSSCC)

Soleymani Ashtiani, M, Scott, AN & Dhakal, RP 2013, 'Mechanical and Fresh Properties of High-Strength Self-Compacting Concrete Containing Class C Fly Ash', *Construction and Building Materials*, vol. 47, pp. 1217-1224.

Soleymani Ashtiani, M, Scott, AN & Dhakal, RP 2010, 'Mechanical properties of high-strength self-compacting concrete', in *Proceedings of the 21st Australasian Conference on the Mechanics of Structures and Materials*, Melbourne, Australia, pp. 827-832.

2.1 ABSTRACT

In the present study, using the locally available materials in Christchurch, New Zealand, a commercially reproducible high-strength self-compacting concrete (HSSCC) mix of 100 MPa compressive strength was designed following the available guidelines for normal-strength self-compacting concrete (NSSCC). Benchmark mixes of conventionally vibrated high-strength concrete (CVHSC) were also designed considering the most important parameters in producing comparable concrete mixes; i.e. similar water-to-binder (w/b) ratio and comparable concrete compressive strength. It was found that with an equivalent w/b ratio, HSSCC develops considerably higher compressive strength (more than 15 MPa) compared to that of CVHSC. Therefore, a lower w/b ratio was chosen to reproduce CVHSC mix with strength comparable to the HSSCC mix.

Fresh properties (slump cone, slump flow, J-ring, L-box and V-funnel) and mechanical properties (compressive, splitting tensile and flexural strengths as well as modulus of elasticity and shrinkage) of all concrete types were evaluated at 3, 7, 28, and 90 days. The microstructure of the mixes was assessed by means of resistivity, porosity and SEM imaging. New expressions were developed to predict different characteristics of HSSCC and suggestions were made to modify the existing equations where applicable. Finally,

experimental results of this study were compared with some of the available codal provisions in order to assess the applicability of the existing criterion to HSSCC.

2.2 INTRODUCTION

The concept of self-compacting concrete (SCC) was first proposed by Hajime Okamura in 1986 as a solution to concrete durability concerns; however the first SCC prototype was developed in 1988 (Maekawa et al., 1999; Okamura et al., 1993; Ozawa et al., 1989). SCC represents one of the most important advances in concrete technology during the past two decades. Because of its superior fresh properties, it flows into a uniform level under the influence of gravity with the ability to compact itself by means of its own weight without the requirement of vibration. Even in the most highly congested reinforced concrete (RC) members, SCC is able to flow free of segregation and de-aerate from large voids.

Due to its unique specifications, SCC may contribute significantly towards improving the quality of concrete structures. Use of SCC offers several benefits to construction practice such as elimination of compaction, shortening of construction time, noise reduction, improved homogeneity, and excellent surface quality. Since the advent of SCC, researchers have investigated its mix designs (Su et al., 2001), fresh and hardened properties (Persson, 2001) and structural performance in RC members (Hassan et al., 2008). In cases where the available expressions developed for conventionally vibrated concrete (CVC) were unable to predict the behavior of SCC accurately, suitable modifications have been made and new expressions have been proposed by different researchers (Felekoglu et al., 2007; Persson, 2001).

In an attempt to produce low cost SCC, Akram et al (Akram et al., 2009) incorporated various percentages of bagasse ash as replacement for cement. They found some of the fresh properties of the modified SCC not conforming to the guidelines. Therefore, adjustments of mix proportions as well as the percentage of superplasticizer were necessary. Overall, out of the twenty five mixes generated in the laboratory, only five satisfied the fresh property criterion set by the EFNARC (EFNARC, 2002,2005). Thus Akram et al (Akram et al., 2009) suggested that the fresh properties of the bagasse ash SCC should be checked to arrive at a proper mix. The compressive strength of the

modified concrete is reported to be comparable to that of the control mix after 28 days. The cost comparison of the two concrete mixes showed around 35% lesser expenses in producing one meter cube of CVC compared to SCC with the compressive strength of both concrete types above 34 MPa. In an experimental study, Wu et al (Wu et al., 2009) investigated the workability of self-compacting lightweight concrete (SCLC) using the overall calculation method with fixed fine and course aggregate contents and incorporating low weight aggregates (LWA). The workability and uniformity of the SCLC and SCC mixes were validated using fresh property tests, column segregations test and cross-section images. The shear flow velocity is reported to increase but the resistance to segregation decreases along with an increase in the binder content.

The material investigations on SCC has gone so far that researchers have even started scrutinizing the effects of inclusion of nanoparticles of different types in SCC (Nazari et al., 2010,2011,2012). In a recent study, Nazari et al (Nazari et al., 2011) investigated the role of SiO2 nanoparticles and ground granulated blast furnace slag (GGBFS) on the properties of SCC ranging in compressive strength between 15 MPa and 82 MPa after 7 and 90 days. They found that the increased GGBFS content of up to 45% (by weight) could potentially improve the splitting tensile strength and the pore structure of concrete. However, this would increase the weight loss of the specimens in thermogravimetric analysis. In addition they reported that the addition of SiO2 nanoparticles of up to 3% (by weight) could improve the compressive, split tensile and flexural strengths of concrete due to formation of more hydrated products. Presence of SiO2 nanoparticles could also improve the water permeability of concrete as it acts as a nanofiller for the mix.

While most of the available literature has focused on normal-strength self-compacting concrete (NSSCC) with compressive strengths ranging between 30 to 80 MPa, little has been reported on the production and properties of high-strength self-compacting concrete (HSSCC) with compressive strengths in excess of 80 MPa (Dinakar et al., 2008; El-Dieb, 2009; Persson, 2001). Persson (2001) briefly reported some of the current applications of SCC with their mix designs and investigated the concrete compressive strengths in excess of 100, 130, 150 and 170 MPa at 7, 28, 90 and 180 days, respectively. However the relevant mix designs and fresh properties of these mixes were not reported. Persson (2001) also suggested new expressions to predict the compressive strength, modulus of elasticity and shrinkage of SCC.

Dinakar et al. (2008) investigated the mechanical properties of high-volume fly ash SCC mixtures with compressive strengths ranging from as low as 8 MPa at 3 days to as high as 103 MPa at 180 days. They reported the properties of the constituent materials, pertinent mix designs and fresh properties (slump flow, J-ring and V-funnel), as well as the hardened properties (compressive and splitting tensile strengths and modulus of elasticity) of the investigated SCC mixes. Dinakar et al proposed empirical expressions to correlate the splitting tensile strength and modulus of elasticity of SCC to its compressive strength. Unfortunately for the higher strength SCC mixes reported by Dinakar et al, some of the fresh properties were out of the acceptable ranges prescribed by different standards for SCC (Hwang et al., 2006). El-Dieb (2009) assessed the mechanical properties of ultra-high-strength self-compacting concrete (UHSSCC) incorporating steel fibers (0.08% to 0.12% and 0.52% volume fraction) with 90-day cube compressive strength ranging between 100 MPa to 150 MPa. The durability and microstructural characteristics of UHSSCC were also investigated. El-Dieb concluded that all of the assessed mechanical properties were improved by inclusion of steel fibers. Except for the slump flow values of the investigated mixes which were stated sporadically, none of the other fresh properties were reported.

For a concrete mix to satisfy the self-compactibility characteristics, its fresh properties should be within appropriate ranges (Hwang et al., 2006). However, it can be seen in the available literature on HSSCC that, either the fresh properties have not been investigated or they have not been sufficiently reported. Furthermore the terms “high-strength” and sometimes “ultra-high-strength” have been used differently by different researchers for a wide range of concrete compressive strengths. Only limited researches have been conducted on handling and properties of HSSCC. Considering the increasing interest in using SCC during the recent years and its various advantages especially in highly congested RC members, high-rise buildings could possibly be one of its future targets. However due to the higher demands in the capacity of structural members in high-rise buildings (especially in the lower stories), incorporating SCC of normal strength may not be a preferred option. Nevertheless before a HSSCC mix can be widely used, more research is required to establish its fresh and mechanical properties so that the users have confidence in its performance.

In the present study, a HSSCC mix was developed in the laboratory following the guidelines given for NSSCC (Su et al., 2001); the same mix was later proved to be commercially reproducible and used for casting beam-column joints (Soleymani Ashtiani et al., 2012). For comparison, benchmark mixes of conventionally vibrated high-strength concrete (CVHSC) were also designed considering the two most important parameters used in comparing concrete mix designs; i.e. similar water/binder (w/b) ratio and comparable concrete compressive strength. The fresh and hardened properties of all concrete types were assessed in detail and new expressions were proposed to predict different characteristics of HSSCC. The microstructure of each mix was characterized by resistivity, porosity and some SEM imaging. Finally, experimental results of this study were compared with the available expressions proposed by different researchers and codal provisions originally developed for CVC and CVHSC in order to assess their applicability to HSSCC; where necessary, modifications were suggested to the available expressions.

2.3 MATERIALS

Locally available materials in Christchurch, New Zealand were used in order to design HSSCC and CVHSC mixes. General Purpose (GP) Cement, Fly ash (Class C), and a polycarboxylic ether polymer based superplasticizer (SP) were used. Chemical composition, physical properties of the cement and fly ash are given in Table 2.1 and Table 2.2. The particle size distribution (PSD) of cement and fly ash are provided in Figure 2.1. An X-Ray diffraction (XRD) diagram for major cement components is provided in Figure 2.2. Locally available semi-crushed coarse aggregate (maximum size of 13 mm) and fine aggregate (natural river sand) were used in all concrete mixes. Physical properties and grading of aggregates are given in Table 2.3 and Table 2.4. Potable water was used in all concrete mixes.

Table 2.1: Chemical composition of cement and fly ash

Chemical composition	Cement (% by mass)	Fly ash (% by mass)
SiO_2	20.2	40.1
Al_2O_3	4.35	19.8
Fe_2O_3	2.22	12.2
CaO	63.8	14.9
MgO	-	3.68
SO_3	2.87	0.68
Na_2O	-	1.57
K_2O	-	0.56
TiO_2	-	1.37
P_2O_5	-	0.32
Loss on ignition	-	0.1
Total chloride content	-	0.002

Table 2.2: Physical properties of cement and fly ash

Property	Cement	Fly ash
Specific gravity (g/cm^3)	3.11	2.55
Mean diameter (μm)	45.0	20.5
Specific surface area (m^2/kg)	367	270

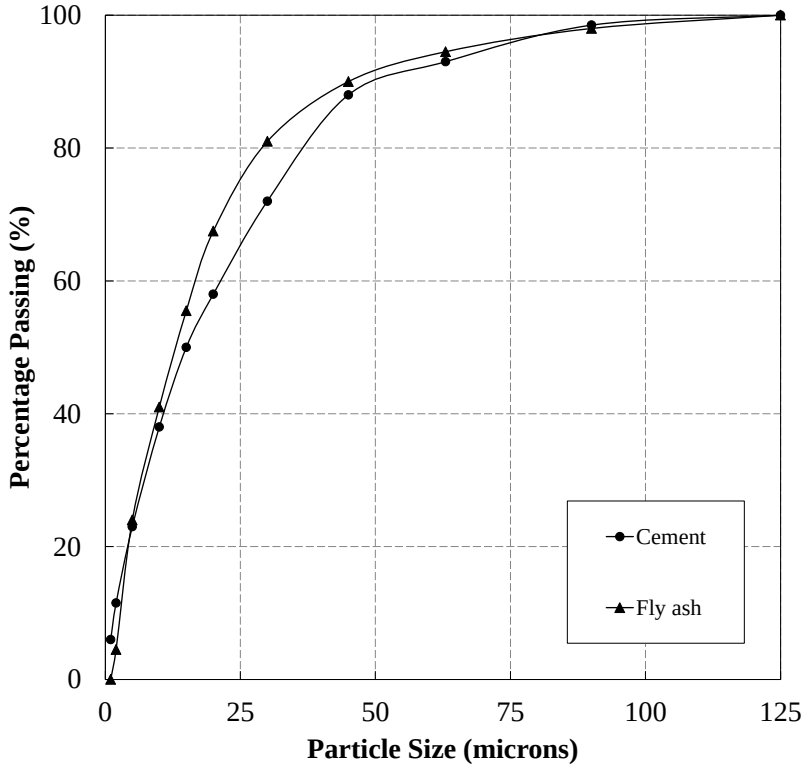

Figure 2.1: PSD of cement and fly ash (Sedigraph 5100 (Sedigraph-5100) were used in determining the PSD)

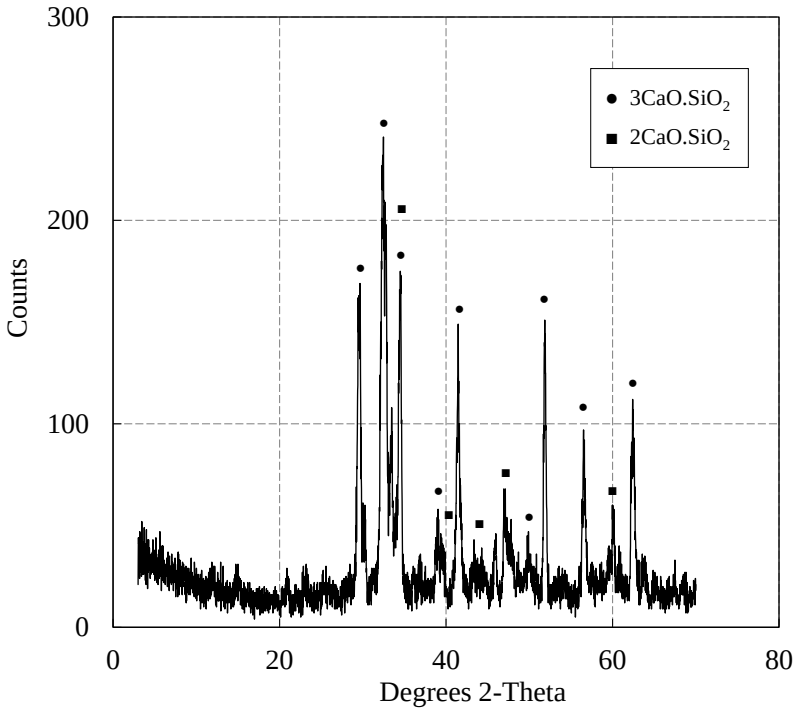

Figure 2.2: XRD results for cement

Table 2.3: Physical properties of aggregates

Property	River sand	13 mm
Specific gravity (g/cm^3)	2.61	2.67
Bulk density (kg/m^3)	1550	1530
Void ratio	0.54	0.72
Water absorption (%)	0.8	0.8

Table 2.4: Aggregates grading

Sieve size (mm)	River sand (% passing)	13 mm (% passing)
13.20	-	96.1
9.50	-	42.7
4.75	99.3	0.3
2.36	74.9	-
1.18	62.5	-
0.60	55.4	-
0.30	37.2	-
0.15	8.8	-
Pan	0.0	0.0

The grading distribution of aggregates was performed based on the NZS3111 (1986)

2.4 EXPERIMENTAL INVESTIGATIONS

Mix design method proposed by Su et al. (2001) and guidelines provided by EFNARC (2002,2005) were used in order to reach an initial mix proportioning for HSSCC and a finalized mix was obtained through a series of laboratory trials. A brief explanation of the steps involved in the mix design procedure is given below.

The principal consideration of the Su et al. (2001) method is based on filling the paste of binders into the voids between the loosely piled aggregates. The workability of the concrete is provided by the binding paste in its fresh state; while the concrete compressive strength is governed by the aggregates being bonded with the paste in its hardened stage. The Su et al. (2001) mix design consists of nine main steps briefed here; detailed explanation of these steps as well as relevant formulation are presented elsewhere (Su et al., 2001). In the first step, quantities of the fine and coarse aggregates are determined. Packing factor (the ratio of mass of tightly packed aggregate to that of loosely packed) plays an important role in the calculation of the coarse and fine aggregates. The density of aggregates and ratio of fine to total amount of aggregates are also considered in the design.

The cement content is calculated in the second step. An empirical expression based on unit MPa of produced strength per kilogram of cement is utilized for this calculation. In the third step, water content is calculated based on an assumed w/c ratio. Calculation of the pozzolanic material contents (such as fly ash) follows in the fourth step; which is based on the specific gravity of the materials and air content in the mix. The required water for the added fillers are also calculated in this step. In step five, the total water content required by the mix is determined simply by adding the water required for cement and other supplementary cementitious materials. Amount of superplasticizer is evaluated in the sixth step. Based on the moisture content, relevant adjustments to the free water required for the mix is performed in step seven. Concrete mix trials, their fresh properties and adjustments of the mix proportions are performed in steps eight and nine.

Having fixed the HSSCC mix design and considering the fact that the same water/binder (w/b) ratio should produce comparable compressive strengths, the mix proportion for CVHSC-1 was reached at by changing the proportions of coarse and fine aggregates

(keeping their total quantity the same as in the HSSCC mix). This way, a comparable mix design with respect to material quantities and w/b ratio was achieved. Nevertheless, as the strength development was considerably higher in the HSSCC mix, another mix (CVHSC-2) was designed with a lower w/b ratio in order to produce comparable concrete compressive strength. Table 2.5 shows the finalized mix designs for all three concrete types.

Table 2.5: Mix proportions for HSSCC, CVHSC-1 and CVHSC-2

Material	HSSCC (kg/m^3)	CVHSC-1 (kg/m^3)	CVHSC-2 (kg/m^3)
Coarse aggregate	880	1145	1145
Fine aggregate	870	605	695
Cement	385	385	385
Fly ash	165	165	165
Water	165	165	148.5
Super-plasticizer	3.58 (0.65%)	1.1 (0.2%)	1.93 (0.35%)

Aggregates were used in saturated surface dried (SSD) condition.

A pan mixer of 90 liters capacity was used to make the concrete mixes. Initially, materials were dry-mixed for about a minute before introducing water and SP to the mix. 80% of the required water was added in several stages while mixing, and an additional 1 minute of mixing followed. The remaining 20% of water (which was premixed with the required SP) was introduced to the mixer and another minute of mixing followed. At this stage, concrete was left for about a minute in the mixer (without mixing); after which the entire mixing procedure was concluded with a final minute of mixing.

For CVHSC mixes, the only fresh property measured was the slump using the standard slump cone test which led to a slump value of 120 mm for both CVHSC-1 and CVHSC-2 mixes. Fresh properties of HSSCC were assessed using the slump-flow, J-ring, L-box, and V-funnel tests (see Appendix A). The results of these tests as well as their typical acceptable ranges (Hwang et al., 2006) are shown in Table 2.6.

Table 2.6: Fresh properties of HSSCC and accepted values

Test type	Experiment	Acceptable Range
Slump-flow diameter (mm)	750	600 – 800
Slump-flow T_{500} (second)	4.2	2 – 7
J-Ring flow diameter (mm)	720	580 – 780
J-Ring height H_{in} - H_{out} (mm)	6	0 – 15
L-Box ratio	0.92	0.75 – 1.0
V-Funnel T_0 (second)	8	6 – 12
V-Funnel T_5 (second)*	9.16	$T_0 – (T_0+3)$

* Same test was repeated after concrete settlement for 5 minutes.

In order to assess the mechanical properties of the concrete mixes, cylindrical specimens of 200 mm height and 100 mm diameter were cast to assess the compressive and splitting tensile strengths and the modulus of elasticity. Beams of 120×120 mm cross section and 470 mm length were used to investigate the flexural strength. In addition, prisms of 75×75 mm cross section and 280 mm height were prepared to study the drying shrinkage (see Appendix A for more details). The CVHSC-1 and CVHSC-2 specimens were cast in 3 layers and each layer was compacted using a vibrating table operated at 2500 rpm for 15 seconds; whereas the HSSCC specimens were cast without using any internal or external vibration. After casting, all specimens were covered using suitable materials (steel caps for cylinders and wet burlaps for the beams) to avoid excessive water evaporation. Specimens were de-moulded 24 hours after casting and cured in lime water with a temperature of approximately 20°C until the day of the test. For shrinkage, six standard prisms were cast for each concrete mix, de-moulded after 24 hours from casting and kept for 7 days in the curing tank under water. The prisms were then taken out of the curing tank, surface-dried and first readings for the drying shrinkage were taken which made the datum for future readings. Prisms were kept in a standard shrinkage chamber with a relative humidity (RH) range of 48% to 52% and a constant temperature of 23°C. Subsequent readings were taken after 14, 21, 28, 42, 56, 70, and 90 days (measured from the casting date).

The microstructure of three mixes was assessed primarily through resistivity measurements made from approximately 25 mm thick disks cut from the cylinders after 28 days of curing. The specimens were vacuum saturated with tap water and an AC current was applied across the specimens and voltage measured.

There is relatively little apparent difference in microstructure between the two CVHSC and one HSSCC mixes. Scanning electron microscope (SEM) images provided in Figure 2.3 show very similar structure at both the mm and μm level. Some small macro-scale differences are however evident when comparing the average resistivity test results of 38, 47 and 40 kOhm.cm for CVHSC-1, CVHSC-2 and HSSCC respectively. The two mixes at a w/b ratio of 0.3 showed nearly identical resistivity values while the 0.27 w/b mix had a resistivity of approximately 8 kOhm.cm greater. The generally similar microstructural performance is to be expected given the w/b ratio of 0.3 for CVHSC-1 and HSSCC were identical and CVHSC-2 had at w/b ratio of 0.27. The Fly Ash – GP binder system was the same for all three mixes.

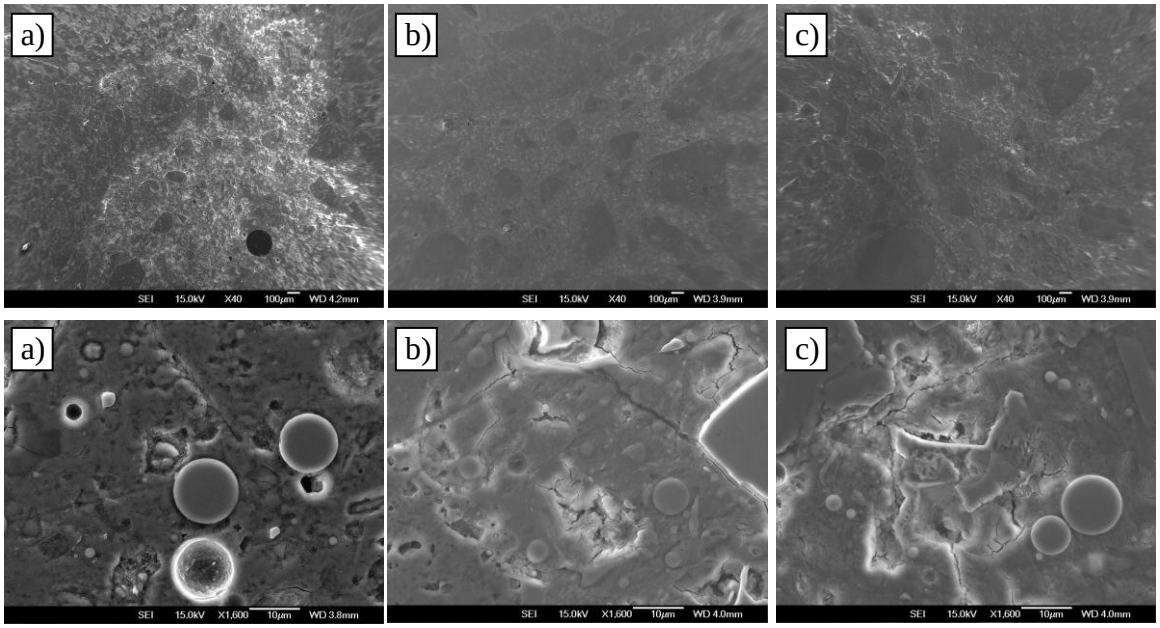

Figure 2.3: SEM images for the a) CVHSC-1 (w/b = 0.3), b) CVHSC-2 (w/b = 0.27), and c) HSSCC (w/b = 0.3)

2.5 RESULTS AND DISCUSSIONS

Specimens were tested following relevant ASTM standards after 3, 7, 28, and 90 days of curing for evaluation of compressive (C39/C39M-99, 2002), splitting tensile (C496-96, 2002), and flexural strengths (C78-94, 2002) as well as modulus of elasticity (C469-94, 2002). In addition, Australian Standard (AS1012.13, 1992) guidelines were used for measuring drying shrinkage of all concrete samples. As evaluating the compressive, splitting tensile and flexural strength tests needed crushing individual samples, three

specimens were tested at each specific age (3, 7, 28, 90 days). However, because of the non-destructive nature of assessing the modulus of elasticity and drying shrinkage, the same 3 cylinders and 6 small prisms were repeatedly used throughout the test. After each test at a specific age, samples were returned to the curing tank or climate chamber. Table 2.7 shows the experimental results of the measured mechanical properties for all concrete types. Density of the concrete mixes was found to be 2470.1, 2466.6 and 2489.2 kg/m^3 for HSSCC, CVHSC-1 and CVHSC-2, respectively.

Table 2.7: Mechanical properties all concrete mixes

Age (day)	Compressive strength (MPa)			Splitting tensile strength (MPa)			Flexural strength (MPa)			Modulus of elasticity (GPa)		
	HSSCC	CVHSC		HSSCC	CVHSC		HSSCC	CVHSC		HSSCC	CVHSC	
		1	2		1	2		1	2		1	2
3	49.4	40.7	50.8	5.1	3.8	5.9	6.5	6.3	7.3	34.8	37.5	36.8
7	70.1	60.4	69.2	6.1	4.8	6.5	8.7	7.5	9.1	40.2	41.6	40.7
28	88.7	69.4	86.2	6.7	6.2	7.3	8.8	9.4	11.1	42.8	42.4	44.7
90	101.6	85.7	104.5	8.1	6.2	7.5	11.7	10.1	11.6	44.7	46.2	48.5

The development of the concrete compressive strength vs. time is shown in Figure 2.4 for all concrete types. Although the HSSCC and CVHSC-1 mix proportions were identical even in terms of water/binder (w/b) ratios (except for the proportions of coarse and fine aggregates), the former developed considerably higher compressive strength at identical concrete ages. In order to achieve the same global compressive strength, CVHSC required a lower w/b ratio to offset issues such as compaction and segregation. Therefore, in the case of CVHSC-2 and HSSCC, despite having water/binder ratios of 0.27 and 0.3 respectively, the strengths were very similar. There are a number of factors which may have contributed to this behaviour. The use of vibration when producing CVHSC may have resulted in some degree of partial segregation; however, properly designed HSSCC is manufactured without any vibration; thus segregation is not an issue. Hence, reduced segregation of HSSCC results in better performance which is demonstrated by the increased strength at each age for a given w/b ratio.

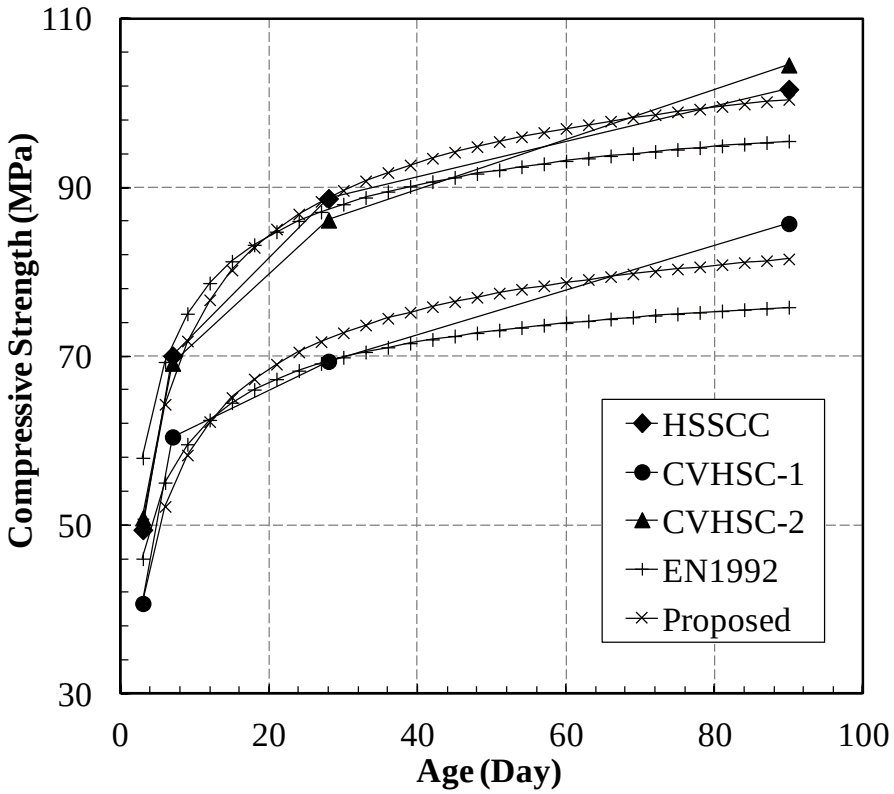

Figure 2.4: Strength development vs. time

Another important issue is the packing factor (Su et al., 2001) which affects both the final strength and strength gain rate. Packing factor is mainly controlled by the proportioning of coarse and fine aggregate in a mix which defines how well different particles come in contact and adhere to each other using the available paste (cementitious material, sand and water). Higher packing factor means better grading of the coarse and fine aggregates which results in better compaction and consequently a higher compressive strength. Given the fact that HSSCC had more fine aggregate compared to CVHSC, its packing factor was higher than the latter.

The use of super-plasticizer (SP) has been shown to have a positive effect on strength development (Meddah et al., 2010). However, the increase in strength requires that no segregation occurs after adding SP. In this study the amount of SP used in HSSCC was 3.3 and 1.9 times of that provided in CVHSC-1 and CVHSC-2, respectively.

Persson (2001) suggested an expression for predicting the concrete compressive strength development vs. time based on the w/b ratio. However as explained before, similar w/b ratio did not result in comparable compressive strengths between HSSCC and CVHSC-1;

therefore the proposed expression by Persson could not be applied to predict the experimental results of this study. For comparison, the experimental results were compared with the model given by the EN1992-2 (2005) model (Equation 2.1).

$$f_c'(t) = f_{c,28}' e^{s\left(1-\sqrt{28/t}\right)} \quad 2.1$$

In Equation 1, "$f'_c(t)$" is the compressive strength (MPa) at the age of t (days), "$f'_{c,28}$" is the 28-day compressive strength of concrete (MPa), "s" is the coefficient depending on type of cement, and "t" is the age of concrete (days). It should be noted that, the strength gain trend was similar in all cases and the Eurocode model seemed to provide reasonable prediction of concrete strength gain vs. time. However it appeared that,

- As a class C fly ash was used in this study, an "s" factor of 0.33 provided the best estimation for the experimental results. Note that this "s" factor lied between the "normal and rapid hardening cements" and "slowly hardening cements" (0.25 and 0.38, respectively) categories suggested by Eurocode. However, both the start and end points of the graph seemed to deviate from matching the experimental results. It is expected that such a divergence between the model and experimental results was introduced because of the fly ash usage in the mix which results in "low-early" and "high-late" strength gain.

- As the expression given by EN1992-2 (2005) was based on the 28-day compressive strength of concrete, prediction of results was possible after determining the 28-day strength. This meant that the formula required an input from the actual experimental data which needed about a month time; this is a disadvantage when early age predictions are required.

Therefore, a new empirical expression was developed (Equation 2.2) to model the experimental results of this study more accurately. This expression has the advantage of being based on the 3-day compressive strength of concrete rather than the 28-day strength.

$$f_c'(t) = f_{c,3}' e^{as\left(1-\sqrt{3/t}\right)} \quad 2.2$$

In Equation 2 "$f'_c(t)$" is the compressive strength (MPa) at the age of t (days), "$f'_{c,3}$" is the 3-day compressive strength of concrete (MPa), "t" is the age of concrete (days), "a" is the correcting factor for HSSCC (2.65 in this study), and "s" is the coefficient depending on type of cement (0.32 using Equation 2.2).

Although tensile strength of concrete is an important characteristic which is used for designing and analysing strength and serviceability of concrete structures, it is relatively difficult to be measured due to the problems associated with gripping the specimen. Therefore, the splitting tensile and flexural strengths (indirect tensile strength) are often used instead of the direct tensile strength test. In the present study the splitting tensile and flexural strengths of all concrete types were assessed using the appropriate specimens mentioned previously and results are shown in (Figure 2.5).

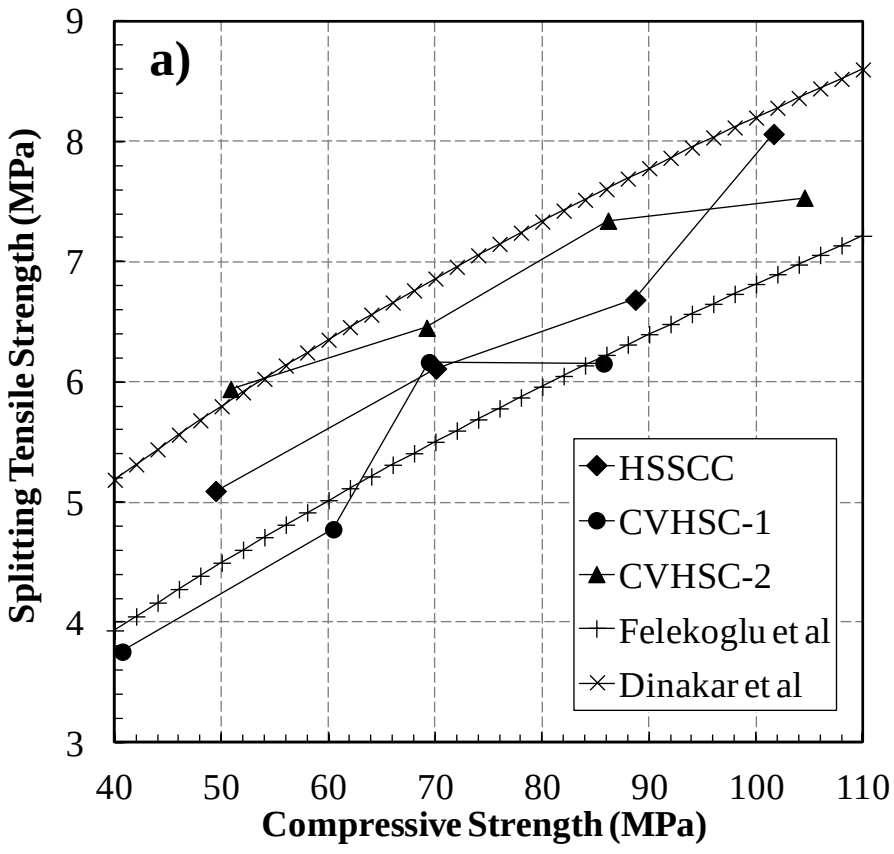

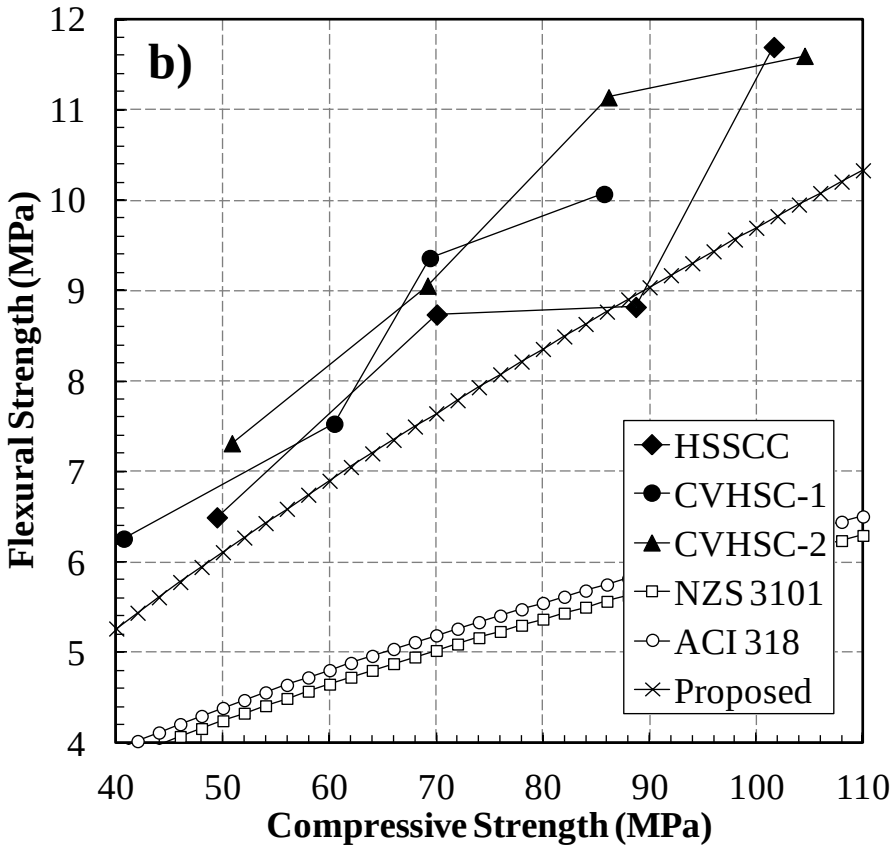

Figure 2.5: Variation of a) splitting tensile strength and b) flexural strength versus the concrete compressive strength

According to Figure 2.5a, when the compressive strength was comparable between concrete mixes (HSSCC and CVHSC-2), for a given strength the splitting tensile strength of CVHSC-2 was slightly higher than that of HSSCC. One possible explanation for this behaviour was that the CVHSC-2 had higher coarse aggregate content which helped holding individual sections together. Another explanation relates to the quality of paste which was believed to have a greater impact on tensile strength. As the CVHSC-2 mix had a better paste (lower w/b ratio), it should also have a higher tensile strength for any given compressive strength. However, it seemed by the time when the 90-day strength (compressive strength in excess of 100 MPa) was reached, the paste was virtually fully hydrated and the HSSCC developed higher splitting tensile strength. The improvement of the paste was then offset by the slightly weakened global structure of the CVHSC-2 (possible segregation associated with vibration). The quality of the aggregate and its interface then had a much more important role resulting in an improved matrix in HSSCC. In addition, a higher autogenous shrinkage in HSSCC compared to that of CVHSC generates internal micro cracks which in turn makes HSSCC weaker in tension. More

focused testing is required to determine the exact cause of the variation in tensile strength between HSSCC and CVHSC-2. However, the improved packing factor and homogeneity of HSSCC (compared to CVHSC-2) resulted in a more uniform material (superior compaction without vibration) over the full length of the HSSCC specimens, and the possibility of a weaker section was lower in HSSCC compared to that of CVHSC-2. Although the latter should develop higher splitting tensile strength at a given age, lower homogeneity and material quality could have prevented full strength development. Splitting tensile test results are compared with the models for HSSCC and SCC proposed by Dinakar et al. (2008) and Felekoglu et al. (2007); Equations 2.3 and 2.4, respectively (Figure 2.5).

$$f_{sp} = 0.82\sqrt{f'_c} \qquad 2.3$$

$$f_{sp} = 0.43 f_c'^{0.6} \qquad 2.4$$

In these equations, "f_{sp}" is the splitting tensile strength (MPa) and "f'_c" is the compressive strength (MPa). Both models seemed to reasonably predict the variations of splitting tensile strength vs. concrete compressive strength for the HSSCC and CVHSC mixes.

In Figure 2.5-b, it is evident that at most values of compressive strength, flexural strength of both CVHSC-1 and CVHSC-2 was more than that of HSSCC. This was consistent with the relative values of splitting tensile strengths of the three concrete mixes and can be explained considering the higher quantity of coarse aggregate in both CVHSC mixes.

However compared to the CVHSC mixes, the HSSCC mix developed higher flexural strength between 28 and 90 days of age. This can also be attributed to the same mechanism as explained earlier for the splitting tensile strength development pattern. In the available literature, no expressions could be found to specifically predict the flexural behaviour of HSSCC; therefore the experimental results were compared to the analytical models given by NZS3101 (2006) and ACI-318 (2005); Equations 2.5 and 2.6, respectively.

$$f_r = 0.6\sqrt{f'_c} \qquad 2.5$$

$$f_r = 0.62\sqrt{f_c'} \quad 2.6$$

In these equations, "f_r" is the flexural strength or modulus of rupture (MPa) and "f'_c" is the compressive strength (MPa). According to Figure 2.5-b, neither NZS3101 (2006) nor ACI-318 (2005) were able to predict the flexural strengths of any of the concrete mixes; in fact they underestimated the flexural strengths by a large margin. Therefore, a new expression (Equation 2.7) was proposed by the authors to predict the flexural strength of HSC which gives a conservative prediction of the experimental results (Figure 2.5-b).

$$f_r = 0.45(f_c')^{2/3} \quad 2.7$$

Modulus of elasticity was also investigated for all concrete types and compared with the proposed expressions for HSSCC and normal concrete available in the literature such as Gardner (Suksawang et al., 2006), Dinakar et al. (2008) and Persson (2001) (Equations 2.8, 2.9 and 2.10, respectively). An illustration of this comparison is given in Figure 2.6-a.

$$E_c = 4300\sqrt{f_c'} + 3500 \quad 2.8$$

$$E_c = 4180\sqrt{f_c'} \quad 2.9$$

$$E_c = 3750\sqrt{f_c'} \quad 2.10$$

In Equations 2.8 to 2.10, "E_c" is the modulus of elasticity (MPa) and "f'_c" is the compressive strength (MPa). According to Figure 2.6-a, the modulus of elasticity of HSSCC is slightly lower than that of both CVHSC-1 and CVHSC-2 which agrees with the available literature (Domone, 2006). The lower modulus of elasticity was attributed to the higher volume of fine materials in HSSCC compared to both CVHSC mixes; i.e. 49.7%, 34.6% and 37.8% of the total aggregate content was natural sand in HSSCC, CVHSC-1 and CVHSC-2 respectively. It is known that the modulus of elasticity of a mix directly correlates to the characteristics of the constituent materials. Since there was a higher proportion of coarse aggregate in the CVHSC mixes, the accompanying modulus of elasticity was also greater than the HSSCC. The effect of mix proportion on the modulus of

elasticity was even evident when comparing the elastic modulus of CVHSC-1 with a higher proportion of coarse aggregate and CVHSC-2. Despite an increased quality of the cement paste, the modulus of elasticity of CVHSC-2 (with w/b ratio 0.27) was lower than that of CVHSC-2 (with w/b ratio 0.3). Nevertheless, the higher compressive strength started to offset this difference after the CVHSC-2 reached its 28-day strength. Amongst the selected models only the Gardner's model (Suksawang et al., 2006) was capable of reasonably predicting the modulus of elasticity of the concrete mixes used in this research. Although the expressions proposed by Dinakar et al. (2008) and Persson (2001) were developed to predict the elastic modulus of HSSCC, they significantly underestimated this property of all concrete mixes.

Finally, shrinkage of the designed concrete mixes was also investigated following the Australian standard (AS1012.13, 1992) and experimental results were compared with the available shrinkage models provided in ACI209 (2008) and EN1992-2 (2005) (Equations 2.11 and 2.12, respectively). Averaged shrinkage results for all concrete types as well as their comparison with the mentioned models are presented in Figure 2.6-b.

$$(\varepsilon_{sh})_t = \frac{t}{\eta + t} 780\gamma_{sh} \qquad 2.11$$

$$\varepsilon_{cd}(t) = \frac{(30 - 0.21 f_c')(72e^{-0.046 f_c'} + 75 - RH)(t - t_s)}{t - t_s + \beta_{cd}(\frac{2A_c}{U})^2} \qquad 2.12$$

Where, "$(\varepsilon_{sh})t$" is the shrinkage strain at any age (micro strains), "t" is the concrete age (day), "η" is 35 for shrinkage after 7 days for moist-cured concrete, "γ_{sh}" is the product of applicable correction factors that are associated with relative humidity, specimen size, slump, FA percentage, cement content, and air content (1.35 for this study), "$\varepsilon_{cd}(t)$" is the shrinkage strain at any age (micro strains), "f'_c" is the 28-day compressive strength of concrete (MPa), "RH" is the relative humidity (%), "t_s" is the curing time (day), "β_{cd}" is 0.007, "A_c" is the cross-sectional area (mm^2), and "U" is the perimeter of the member exposed to atmosphere (mm).

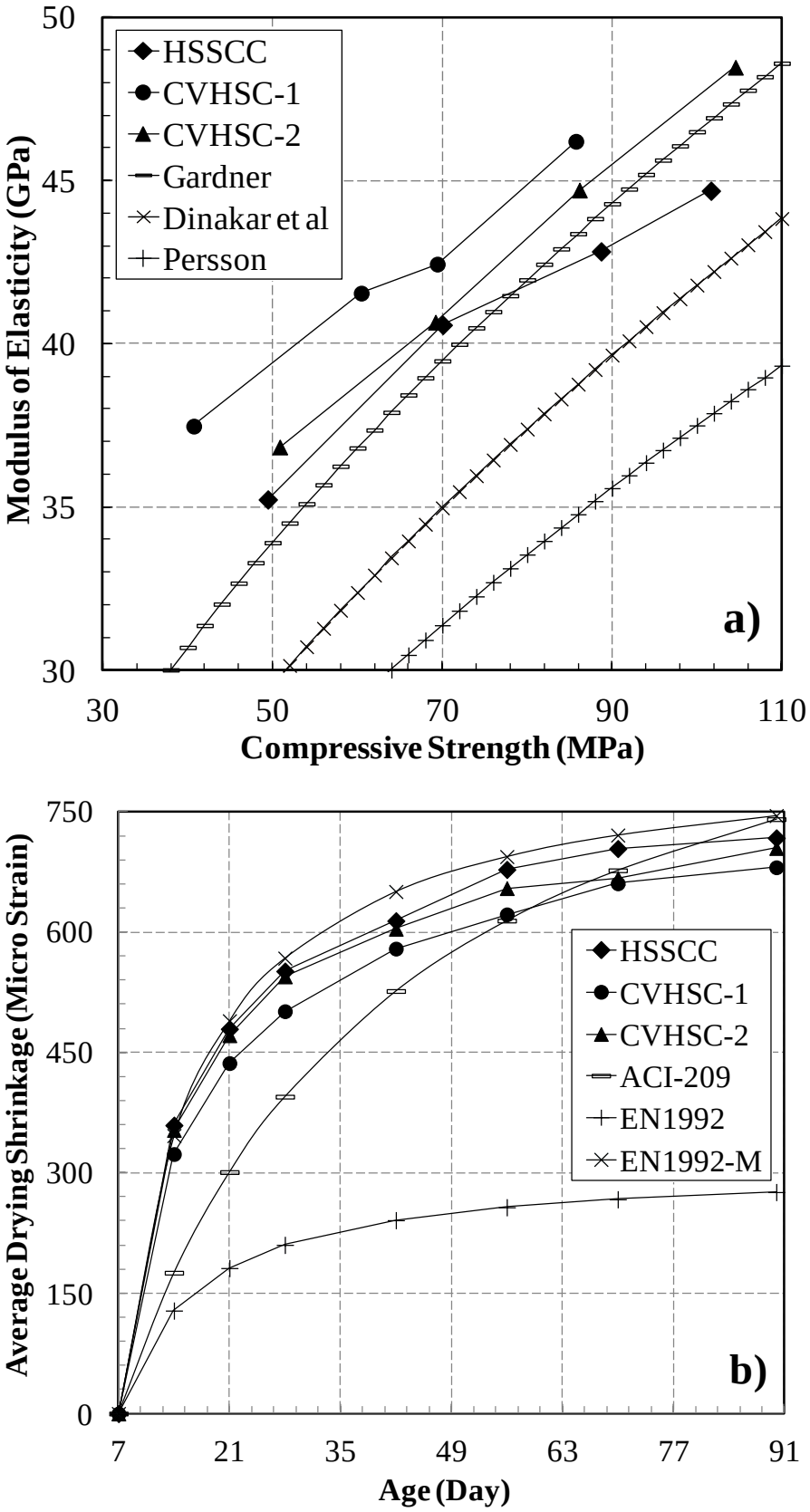

Figure 2.6: a) modulus of elasticity vs. concrete compressive strength and b) averaged drying shrinkage vs. time

According to Figure 2.6-b the drying shrinkage of CVHSC mixes was slightly less than that of HSSCC; the reason for which was the higher paste content of the latter. Even between CVHSC-1 and CVHSC-2 mixes, the former showed less shrinkage which can be attributed to its lower sand content. ACI209 (2008) model seemed to provide an acceptable prediction of the experimental shrinkage results as it provided a correction factor which was adjusted to suit the designed mixes. This factor takes into account the effect of relative humidity, specimen size, slump, FA percentage, cement content, and air content. In spite of a close prediction of the final shrinkage (at 90 days), ACI209 (2008) model underestimated the early-age shrinkage of all mixes. EN1992-2 (2005) model had more input parameters to accommodate different variables of shrinkage test, but it significantly underestimated the experimental results of this study. It should however be noted that should the EN1992-2 (2005) model have a correction factor like the one in the ACI209 (2008) model, it would have given a much closer prediction of the results. Therefore, authors would like to present a modification to the EN1992-2 (2005) expression (Equation 2.13) in the form of a correcting factor which takes into account the effect of slump, FA percentage, cement content, and air content (Figure 2.4, Proposed).

$$\varepsilon_{cd,\mathrm{modified}}(t) = \varepsilon_{cd}(t)\gamma_{sh} \qquad 2.13$$

Where "$\varepsilon_{cd,modified}(t)$" is the modified shrinkage at any age (micro strain), "$\varepsilon_{cd}(t)$" is the calculated shrinkage from the EN1992 model at any age (micro strain) and "γ_{sh}" is the proposed correction factor (2.7 in this study).

2.6 CONCLUSIONS

The following conclusions and remarks are made based on the experimental results of the present study:

CVHSC-1 mix was designed with identical material proportions and w/b ratio to that of HSSCC; except for the proportions of coarse and fine aggregates (even the total amount of aggregates was identical between the two mixes). Although HSSCC and CVHSC-1 had similar w/b ratios, the former developed considerably more compressive strength due to its higher material quality. CVHSC-2 mix was designed by reducing the w/b ratio and

adjusting the coarse and fine aggregates contents in such a way that comparable concrete compressive strengths were achieved. In spite of the lower w/b ratio (0.27) in CVHSC-2, it developed virtually the same compressive strength compared to that of HSSCC (with 0.3 w/b ratio). The higher strength in HSSCC was attributed to the improved homogeneity and lower possibility of partial segregation resulting from vibration. A better packing factor in HSSCC also contributed to the higher strength development. The use of higher quantities of super-plasticizer in HSSCC was also believed to partially take part in its higher compressive strength compared to CVHSC-2.

EN1992 model was used to predict the rate of strength-gain vs. time for all mixes and the model was found inefficient for two main reasons: a) the 28-day strength is an essential input for the EN1992 model which unfavourably delays the strength prediction procedure and b) due to the usage of fly-ash the EN1992 model was unable to predict the low-early-high-late strength-gain behaviour of the mixes. A new model was proposed based on the 3-day strength of the mixes to predict more accurately the rate of strength development in the designed mixes. Note that in the suggested model, the effect of using fly ash in the concrete mixes was also accounted for by devising appropriate correcting factors. These factors can be calibrated to predict the strength development behaviour of other concrete mixes.

At comparable compressive strengths the splitting tensile strength of both CVHSC mixes proved to be slightly higher than that of HSSCC before the age of 28 days. This was attributed to the higher coarse content of the former compared to the latter. However the HSSCC developed more splitting tensile strength between the age of 28 and 90 days in such a way that at the age of 90 days it reached a higher splitting tensile strength than that of CVHSC-2. Better material quality, higher homogeneity and lesser void in self-compacting concrete were seemed to be the possible reasons for such phenomenon. Except for slight differences, the selected models for SCC and HSSCC were capable of predicting the splitting tensile strength of all concrete types.

The flexural strengths of all three concrete mixes followed almost the same trend as their splitting tensile strength; i.e. both CVHSC mixes maintained higher flexural strength up to the age of 28 after which HSSCC overtook and reached a higher flexural strength. As the

selected models underestimated the flexural strength of all concrete mixes, a new model was proposed and proved to accurately predict the experimental results of this study.

At a given compressive strength, the modulus of elasticity of HSSCC was lower compared to that of CVHSC. This happened because the HSSCC had lower coarse aggregate content compared to that of both CVHSC mixes. The selected models for HSSCC, underestimated the elastic modulus of all three concrete types. However, Gardner proposed an expression which showed a very close correlation with the experimental results of this study.

Finally, HSSCC seemed to result in a slightly higher drying shrinkage compared to that of both CVHSC mixes. This was believed to come from the higher volume of paste in HSSCC. The ACI-209 and EN1992 models were used to predict the experimental results; however the former provided better match for the results of this research. Nevertheless before the concrete age of 60 days, the ACI209 model could not predict the shrinkage results accurately. As the EN1992 model was more flexible with respect to its input variable, a correcting factor was suggested for the original EN1992 model such a way that the modified model was capable of accurately predicting the drying shrinkage results of all three concrete mixes.

The above conclusions are based on laboratory experiments on a reasonable number of samples (to cater for sample-to-sample randomness) made of three different concrete mixes including HSSCC. Considering that HSSCC may gain greater attention and use in the near future due to its exceptional fresh and hardened properties, more detailed and focused investigations are required in order to provide further confidence-boosting evidences for designers to implement HSSCC in RC structures. As the available literature shows very limited investigations reported on HSSCC, this study provides a very useful database to plan further investigation on this special concrete type.

2.7 REFERENCES

ACI209 2008, 'Guide for Modeling and Calculating Shrinkage and Creep in Hardened Concrete (ACI 209.2R-08)'. ACI Committee 209, p. 45.

ACI-318 2005, Building code requirements for structural concrete and commentary (ACI 318M-05), American Concrete Institute, Farmington Hills, Mich.

Akram, T, Memon, SA & Obaid, H 2009, 'Production of low cost self compacting concrete using bagasse ash', Construction and Building Materials, vol. 23, no. 2, pp. 703-712.

AS1012.13 1992, 'AS1012.13 Methods of testing concrete - Determination of the drying shrinkage of concrete for samples prepared in the field or in the laboratory'. Standards Australia, p. 12.

C39/C39M-99, A 2002, 'ASTM C39/C39M-99 Standard test method for compressive strength of cylindrical concrete specimens'. Annual Book of ASTM Standards.

C78-94, A 2002, 'ASTM C78-94 Standard test method for flexural strength of concrete (using simple beam with third-point loading)'. Annual Book of ASTM Standards.

C469-94, A 2002, 'ASTM C469-94 Standard test method for static modulus of elasticity and poisson's ratio of concrete in copression'. Annual Book of ASTM Standards.

C496-96, A 2002, 'ASTM C496-96 Standard test method for splitting tensile strength of cylindrical concrete specimens'. Annual Book of ASTM Standards.

Dinakar, P, Babu, KG & Santhanam, M 2008, 'Mechanical properties of high-volume fly ash self-compacting concrete mixtures', Structural Concrete, vol. 9, no. 2, pp. 109-116.

Domone, PL 2006, 'Self-compacting concrete: An analysis of 11 years of case studies', Cement and Concrete Composites, vol. 28, no. 2, pp. 197-208.

EFNARC 2002, Specification and Guidelines for Self-Compacting Concrete, European Federation of Procedures and Applicators of Specialist Products for Structures

EFNARC 2005, The European Guidelines for Self-Compacting Concrete Specification, Production and Use, European Federation of Procedures and Applicators of Specialist Products for Structures

El-Dieb, AS 2009, 'Mechanical, durability and microstructural characteristics of ultra-high-strength self-compacting concrete incorporating steel fibers', Materials and Design, vol. 30, no. 10, pp. 4286-4292.

EN1992-2 2005, 'EN1992-2 Design of concrete structures'. Comite Europeen de Normalisation (CEN), Brussels, Belgium.

Felekoglu, B, Turkel, S & Baradan, B 2007, 'Effect of water/cement ratio on the fresh and hardened properties of self-compacting concrete', Building and Environment, vol. 42, no. 4, pp. 1795-1802.

Hassan, AAA, Hossain, KMA & Lachemi, M 2008, 'Behavior of full-scale self-consolidating concrete beams in shear', Cement and Concrete Composites, vol. 30, no. 7, pp. 588-596.

Hwang, S-D, Khayat, KH & Bonneau, O 2006, 'Performance-based specifications of self-consolidating concrete used in structural applications', ACI Materials Journal, vol. 103, no. 2, pp. 121-129.

Maekawa, K & Ozawa, K 1999, 'Developmen of SCC's prototype', Self-Compacting High-Performance Concrete (Social System Institute), pp. 20-32.

Meddah, MS, Zitouni, S & Belaabes, S 2010, 'Effect of content and particle size distribution of coarse aggregate on the compressive strength of concrete', Construction & Building Materials, vol. 24, no. Copyright 2010, The Institution of Engineering and Technology, pp. 505-512.

Nazari, A & Riahi, S 2010, 'Microstructural, thermal, physical and mechanical behavior of the self compacting concrete containing SiO2 nanoparticles', Materials Science and Engineering A, vol. 527, no. 29-30, pp. 7663-7672.

Nazari, A & Riahi, S 2011, 'The role of SiO2 nanoparticles and ground granulated blast furnace slag admixtures on physical, thermal and mechanical properties of self compacting concrete', Materials Science and Engineering A, vol. 528, no. 4-5, pp. 2149-2157.

Nazari, A & Riahi, S 2012, 'The effect of aluminium oxide nanoparticles on the compressive strength and structure of self-compacting concrete', Magazine of Concrete Research, vol. 64, no. 1, pp. 71-82.

NZS3101 2006, 'NZS3101 Concrete structures standard Parts 1 & 2: The Desing of Concrete Structures and Commentary'. Standards New Zealand, Wellington, New Zealand, p. 698.

NZS3111 1986, 'NZS3111 Methods of test for water and aggregate for concrete'. Standards Association of New Zealand, Wellington, NZ.

Okamura, H, Maekawa, K & Ozawa, K 1993, 'High performance concrete. Tokyo, Gihido'

Ozawa, K, Maekawa, K, Kunishima, M & Okamura, H 1989, 'Development of high performance concrete based on the durability design of concrete structures', in Proceedings of the 2nd East-Asia and Pacific Conference on Structural Engineering and Construction (EASEC-2), vol. 1, pp. 445-450.

Persson, B 2001, 'A comparison between mechanical properties of self-compacting concrete and the corresponding properties of normal concrete', Cement and Concrete Research, vol. 31, pp. 193-198.

Sedigraph-5100, 'Sedigraph 5100 Particle Size Analyzer'. Mircromeritics, p. 6.

Soleymani Ashtiani, M, Dhakal, RP & Scott, AN 2012, 'Seismic Performance of High-Strength Self-Compacting Concrete in Reinforced Concrete Beam-Column Joints', in 15th World Conference on Earthquake Engineering, Lisbon, Portugal.

Su, N, Hsu, K-C & Chai, H-W 2001, 'A simple mix design method for self-compacting concrete', Cement and Concrete Research, vol. 31, no. 12, pp. 1799-1807.

Suksawang, N, Nassif, HH & Najm, HS 2006, 'Evaluation of mechanical properties for self-consolidating, normal, and high-performance concrete', Transportation Research Record, no. 1979, pp. 36-45.

Wu, Z, Zhang, Y, Zheng, J & Ding, Y 2009, 'An experimental study on the workability of self-compacting lightweight concrete', Construction and Building Materials, vol. 23, no. 5, pp. 2087-2092.

3 EXPERIMENTAL EVALUATION OF MONOTONIC BOND BETWEEN DEFORMED BARS AND HSSCC

Soleymani Ashtiani, M, Dhakal, RP & Scott, AN 2013, 'Post-yield bond behaviour of deformed bars in high-strength self-compacting concrete', *Construction and Building Materials*, vol. 44, no. 0, pp. 236-248.

Soleymani Ashtiani, M, Dhakal, RP & Scott, AN 2011, 'Bond properties of reinforcement in high-strength self-compacting concrete', in *Proceedings of the 9th Symposium on High Performance Concrete Design, Verification and Utilization*, Rotorua, New Zealand.

3.1 BOND PERFORMANCE OF HSSCC

3.1.1 ABSTRACT

Self-Compacting Concrete (SCC) has gained substantial attention since its advent for its ability to compact without the need for either internal or external vibration even in areas of highly congested reinforcement such as beam-column joints. During the past two decades, extensive research has been conducted on both the fresh and hardened properties of normal strength SCC; however, only recently has interest in high-strength self-compacting concrete (HSSCC) gained momentum.

This paper focuses on determining bond properties between reinforcement and HSSCC. An appropriate HSSCC mix was first developed to achieve a concrete grade of 90 MPa. The effects of bar grade, diameter, and bond length in HSSCC were determined by means of pullout tests.

3.1.2 INTRODUCTION

Self-Compacting Concrete (SCC) was first developed in Japan by Prof. Hajime Okamura and his research team from the University of Tokyo in 1986 as a solution to concrete durability and unskilled labour force. It is one of the prominent advances in concrete

technology during the past twenty years. SCC is a special concrete which flows to a uniform level and compacts itself under the effect of gravitational forces without the need for vibration. SCC is capable of flowing free of segregation and filling all recesses, reinforcement spaces, and voids even in highly congested concrete members.

SCC is a high-performance concrete with special properties which are achieved only by systematic optimization of both individual constituents and composition. The flowability and mix stability of SCC are determined primarily by the interactions between powder, water, super-plasticizer, and viscosity modifying admixture (VMA) where applicable. Therefore, SCC is defined as a fresh concrete possessing superior flowability while maintaining stability. In order to perform suitably under various circumstances, SCC should possess the following characteristics in fresh state: flowing ability, passing ability, and resistance to segregation. Due to its unique features, SCC may contribute to significant quality improvements of concrete structures and open up new fields for concrete applications. Use of SCC offers several benefits to construction practice such as elimination of compaction, shortening of construction time, noise reduction, improved homogeneity, and excellent surface quality.

Performance of reinforced concrete (RC) elements is dependent on various factors, among which bond strength between reinforcement and concrete plays an important role in overall behaviour of structures. Since the advent of SCC, various researchers (Castel et al., 2006; Cattaneo et al., 2009; Chan et al., 2003; De Almeida Filho et al., 2008; Desnerck et al., 2010; Hassan et al., 2010; Lachemi et al., 2009; Valcuende et al., 2009; Zhu et al., 2004) have worked on bond properties of reinforcing bars in self-compacting concrete. However, bond properties of bars in high strength self-compacting concrete (HSSCC) have not yet been investigated. The present study experimentally investigates bond properties of steel and HSSCC considering bond length, bar diameter, and steel grade as variables. An effort has been made to differentiate between the post-yield slip behaviour of different steel grades.

3.1.3 EXPERIMENTAL INVESTIGATION

3.1.3.1 MATERIAL PROPERTIES AND MIX DESIGN DETAILS

Locally available materials in Christchurch, New Zealand were used in order to design a HSSCC mix. General Purpose Cement (GPC) (equivalent to ASTM "Type I" cement), fly ash (Class C), and a third generation polycarboxylic ether polymer based superplasticizer (SP) were used. Locally available coarse aggregate (semi-crushed of maximum size 13mm), fine aggregate (natural river sand), and potable water were used in the mix. Details of physical properties of the cement, fly ash, and aggregates used in the mix are described in another paper (Soleymani Ashtiani et al., 2011b).

The mix design method proposed by Su et al. (2001) and guidelines provided by EFNARC (2002,2005) were used in order to reach an initial mix proportioning for HSSCC and a finalized mix was obtained through a series of laboratory trials. Table 3.1 shows the finalized mix design for HSSCC.

Table 3.1: Mix proportions of HSSCC

Material	HSSCC (kg/m^3)
Coarse aggregate	880
Fine aggregate	870
Cement	385
Fly ash	165
Water	165
Superplasticizer	3.3

A 150-liter capacity drum mixer was used. The mixing procedure adopted in this study is as follows. Initially, materials were dry-mixed for about one minute before introducing water and SP to the mix. Afterwards, 80% of the required water was added in several stages while mixing and an additional 1 minute of mixing followed. The remaining 20% of water (which was premixed with required SP) was introduced to the mixer and another minute of mixing followed. At this stage, concrete was left for about a minute in the mixer (without mixing); after which, the entire mixing procedure was concluded with a final minute of mixing. Fresh properties of HSSCC were assessed using Slump-flow, J-ring, L-box, and V-funnel tests. The results of these tests as well as their typical acceptable ranges are shown in Table 3.2.

Table 3.2: Fresh properties of HSSCC (Hwang et al., 2006)

Test type	Experiment	Accepted range
Slump-flow diameter (mm)	750	600 – 800
Slump-flow t_{500} (s)	4.2	2 – 7
J-ring flow diameter (mm)	720	580 – 780
J-ring height H_{in} - H_{out} (mm)	6	0 – 15
L-box ratio	0.92	0.75 – 1.0
V-funnel T_0 (s)	8	6 – 12
V-funnel T_5 (s)*	9.16	0 – 3 (+T_0)**

* Same test is performed after letting concrete settle for 5 minutes.

** This time range should be added to that of T0.

3.1.3.2 DETAILS OF PULL-OUT SPECIMENS AND TEST SETUP

In the experimental investigations of bond characteristics between concrete and reinforcement, various parameters can be considered as variables. In the present study, bar diameter, steel grade, and bond length were varied among different specimens; whereas, concrete mix was kept constant throughout. In total, 18 specimens with 16 mm diameter (Φ16) and 3 specimens with 25 mm diameter (Φ25) deformed bars were cast. All specimens were cast in a single day; however, two concrete batches were used due to the mixing capacity limitation. The first batch consisted of pull-out specimens series 1 and 3 and the second one was used to produce specimens for series 2 and 4 (Table 3.3). Along with each concrete batch, 6 standard cylinders, of 100 mm diameter and 200 mm length, were cast in order to evaluate the compressive and splitting tensile strengths of the mix at the day of testing. Both pull-out specimens and auxiliary specimens were wet cured (everyday) for 14 days and covered with plastic wrap (until the test day) in order to hold the moisture inside. RILEM (1973) recommendations were used in order to prepare and test the pull-out specimens; however, minor modifications were made in order to suite the available test facilities. Details of the pull-out specimens and test set-up are presented in Table 3.3 and Figure 3.1. A hollow-core hand operated hydraulic jack of 300 kN capacity and a slip gauge of 5 mm traverse with an accuracy of 0.001 mm were used in order to measure the load and end-slip of pull-out specimens, respectively (see Appendix B for more details).

Table 3.3: Properties of pull-out specimens

Series No.	Bond Length L (mm)	H (mm)	No. of Samples	Bar Dia (Φ) (mm)	Steel Grade (MPa)	Specimen ID
1	80 mm (5Φ)	200	3	16	300	Φ16-5Φ-300G
			3	16	500	Φ16-5Φ-500G
2	120 mm (7.5Φ)	200	3	16	300	Φ16-7.5Φ-300G
			3	16	500	Φ16-7.5Φ-500G
3	160 mm (10Φ)	200	3	16	300	Φ16-10Φ-300G
			3	16	500	Φ16-10Φ-500G
4	125 mm (5Φ)	250	3	25	300	Φ25-10Φ-300G

Along with each concrete batch, pertaining cylindrical specimens were also tested. Table 3.4 shows the compressive and splitting tensile strengths for both concrete batches which were practically identical. Individual deformed bars (Φ16, Φ25) of different steel grades (300G and 500G) were tested in order to obtain their stress-strain pattern and yielding and ultimate stresses (Figure 3.1); see also Appendix B. It should be noted that for an identical bar diameter, rib dimensions and pattern of both bar grades were the same.

Table 3.4: Compressive and splitting tensile strength of HSSCC mixes

Series No.	Compressive Strength (MPa)	Splitting Tensile Strength (MPa)
1, 3	94.60	5.60
2, 4	94.80	5.90

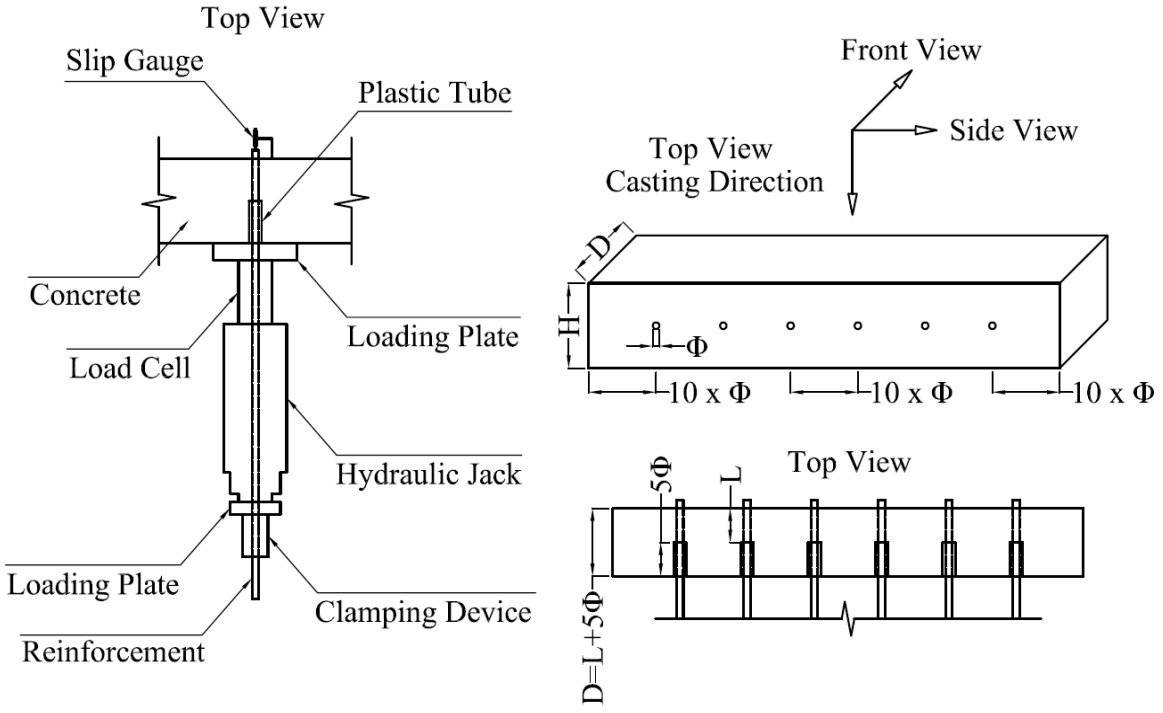

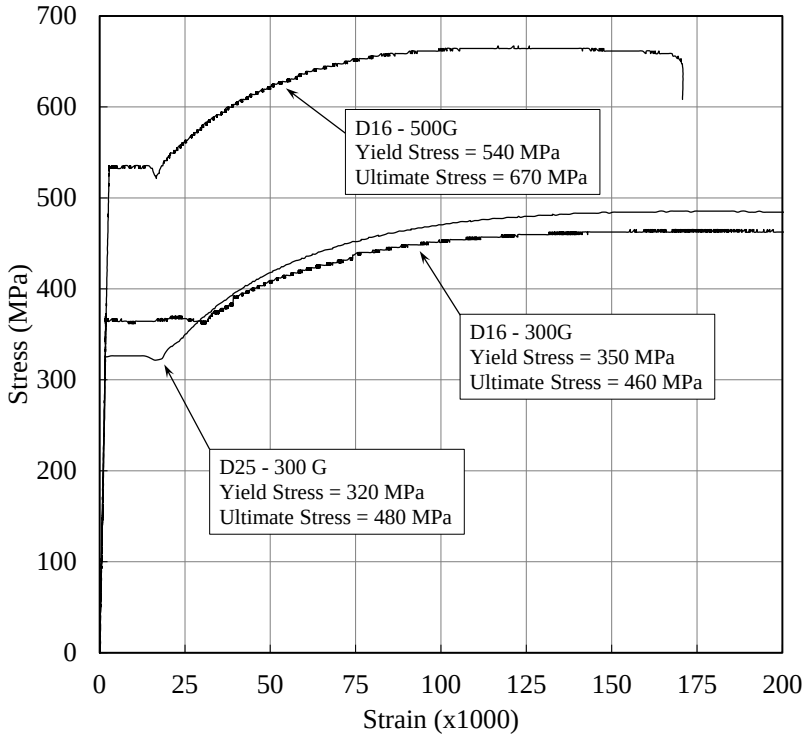

Figure 3.1: Details of test setup and pull-out specimens and average stress-strain curves of bars

3.1.4 RESULTS AND DISCUSSIONS

Pull-out specimens were tested 28 days after the casting date. The averaged bond-stress vs. slip behaviour of the pull-out specimens is shown in Figure 3.2. The slip was measured directly at the unloaded end of the bars and the bond stress was calculated by dividing the axial load by the surface area of the bar in the bonded length.

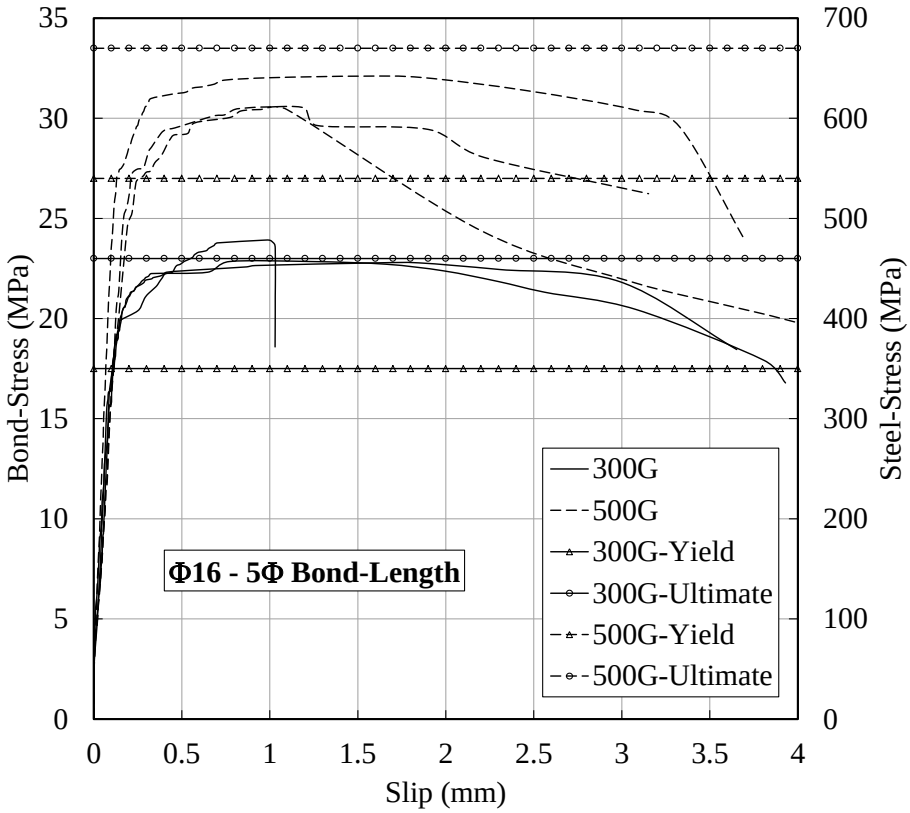
Bond-Stress (MPa)
Steel-Stress (MPa)
Slip (mm)
Φ16 - 5Φ Bond-Length
300G
500G
300G-Yield
300G-Ultimate
500G-Yield
500G-Ultimate

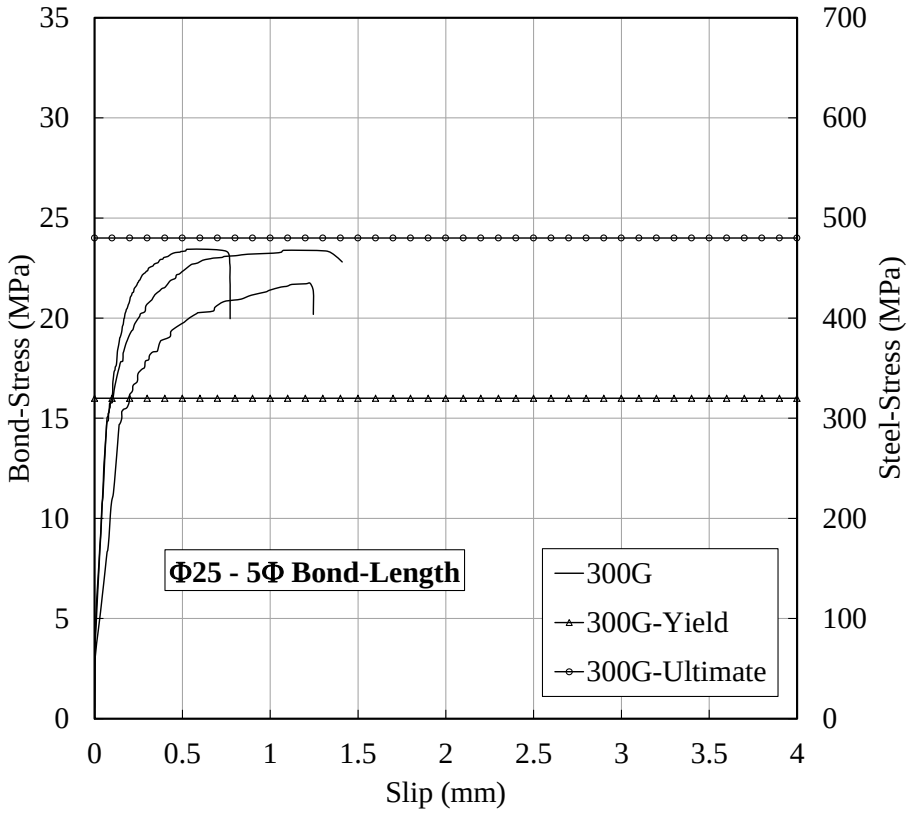
Bond-Stress (MPa)
Steel-Stress (MPa)
Slip (mm)
Φ25 - 5Φ Bond-Length
300G
300G-Yield
300G-Ultimate

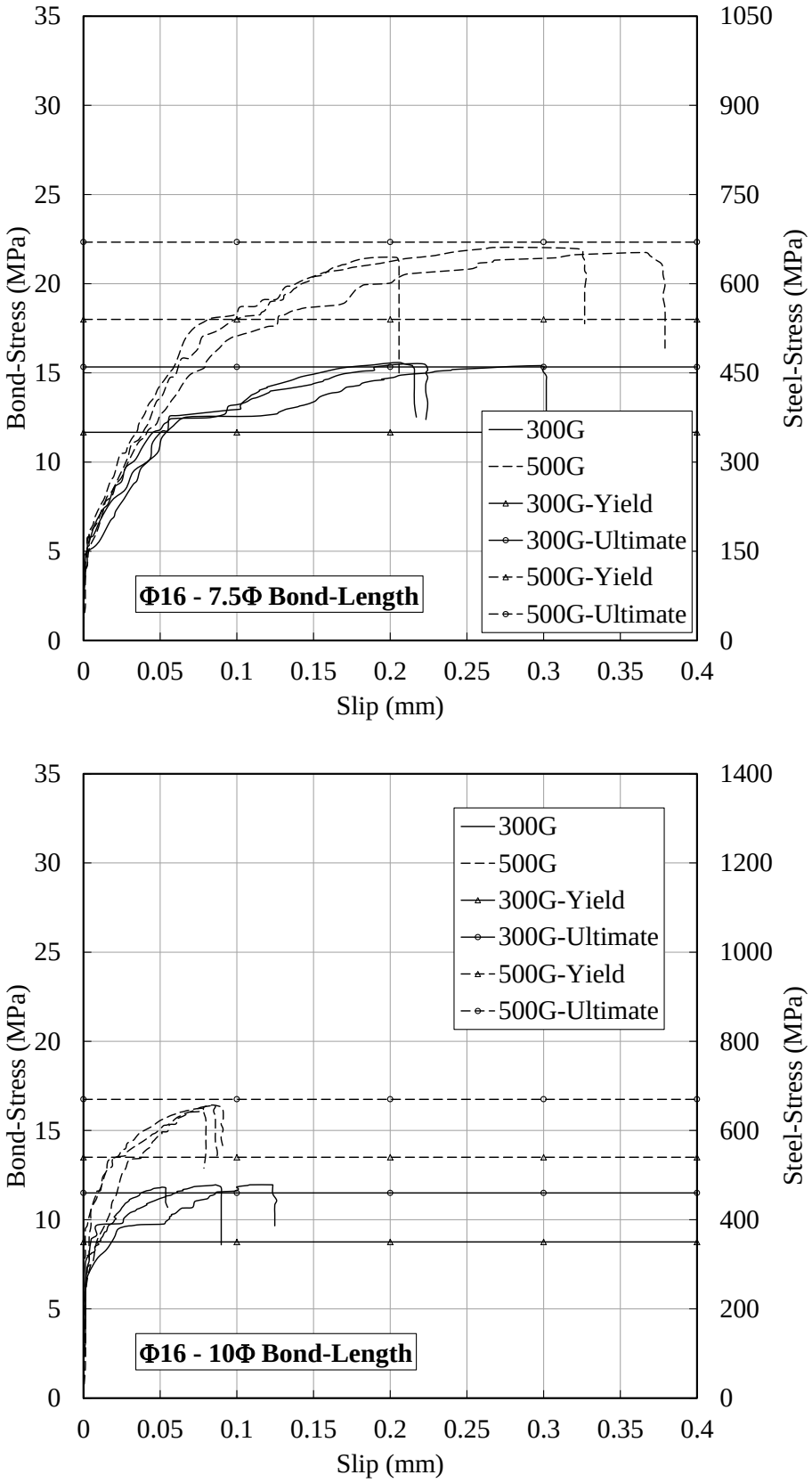

Figure 3.2: Average bond stress – sleep for different bar diameters, bond lengths, and bar grades

As mentioned earlier, two different bar diameters were used in this study; however, only the Φ16 bar types had both steel grades of 300 MPa and 500 MPa; deformed Φ25 bars were of grade 300 MPa. In Figure 3.2 (except for Φ25 bars), the three lines at the top represent the bond-slip behaviour of grade 500 steel; whereas, the three bottom ones show that of grade 300 bars. The horizontal lines plotted in the curves represent average yield and ultimate stress levels for different steel grades.

All specimens with Φ16 deformed bars and 5Φ bond length were pulled out of the concrete (except for one in which the bar failed before pull-out happened). However, different bond-strengths were observed at failure (namely 23 and 31 MPa for 300G and 500G bars, respectively); the reason for which was not obvious given that both bar grades had the same (Figure 3.3) rib pattern. The specimens were cut open to check for possible rib erosion especially for 300G bars; however, no signs of rib deformation or erosion were found in either of the specimens (Figure 3.3). Referring to the stress-strain curves of individual bars (Figure 3.1), it is understood that the strain ductility of 300G steel bars is considerably more than that of 500G ones. This means that the reduction in diameter under post-yield tension for 300G bars should be more than that for 500G. The difference between bar diameter both before and after the test was measured (the details of which are beyond the scope of this paper), and it was found that the diameter reduction was approximately 4% (0.6 mm) throughout the bar length. Considering that both bond and bar failures happened well after the yield point (refer to the horizontal lines in Figure 3.2), the reduction in diameter is permanent. This decrease in bar diameter after yielding starts progressing its way through to the sections of the bar until it reaches the faces of the clamp in one end and the concrete in the other end. It then starts penetrating inside the clamp and concrete. As the diameter reduces in the clamped section of the bar, jaws continue to hold by grasping the perimeter of the bar. On the contrary though, concrete is unable to continue to hold the other end; therefore the bar gradually starts to pull out of the concrete. As a result, bond failure happens far before the actual capacity of the bond between concrete and steel develops.

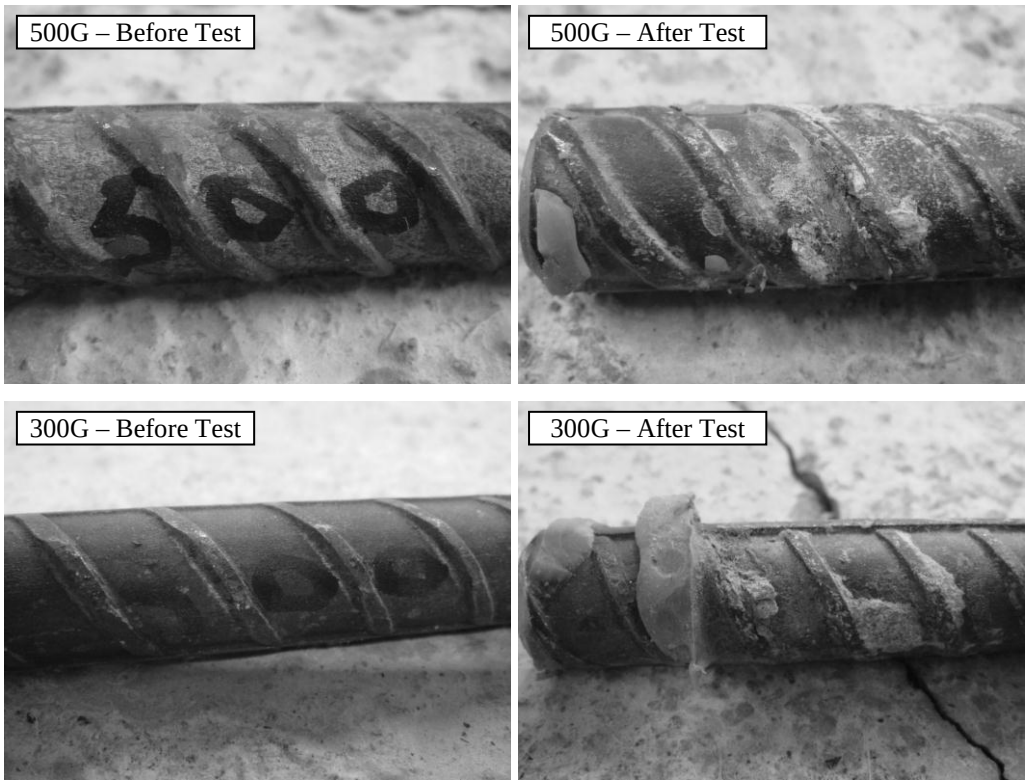

Figure 3.3: Rib patterns for both 300G and 500G bars before and after test

This phenomenon happened for both 300G and 500G bars; however, since the 300G bars are more ductile than the 500G ones and their diameter reduces more between yield and failure, the effect of this mechanism is significantly more prominent for the 300G steel bars. As a case in point, 300G-Φ16 bars developed an ultimate average bond stress of about 23 MPa; whereas, 500G-Φ16 ones built up around 31 MPa bond stress before failure. The critical bond length should be chosen in such a way that it supports both bar grades against pull-out until after the yield and well into the strain hardening region; so that the elongation and diameter reduction of the bars become substantial and the effect of such behaviour becomes clearly evident. It is worthwhile mentioning that this difference in bond performance of various grade steel bars in high-strength concrete has not previously been addressed in the available literature (based on authors' knowledge).

In case of Φ16 bars having 7.5Φ and 10Φ bond length, pull-out did not happen for any of the 300G or 500G bars. Nevertheless, similar bond behaviour can be noticed by comparing slips and bond stress levels between 300G and 500G bars. Considering an identical slip (for example 0.2 mm and 0.08 mm in Φ16 bars with 7.5Φ and 10Φ bond length, respectively), it can easily be seen that the corresponding bond-stress level for 500G steel

bars is higher than that of 300G ones by about 5 to 7 MPa. As both bar grades had the same rib pattern, it is generally expected that an identical level of slip happens for a similar stress level (irrespective of steel grade). Therefore, the above mentioned phenomenon of the effect of bar diameter reduction on bond performance remains valid even in cases where complete pullout failure didn't happen.

For the specimens with Φ25 bars, the ratio of concrete block dimension to bar diameter was reduced by 2.5 in order to investigate the effect of concrete cover on bond performance in the absence of transverse reinforcement. It was observed that the propagation of splitting tensile cracks led to concrete block breakage (Figure 3.4) before either de-bonding or bar failure happened (except for one specimen). Nevertheless, as the final bond-strengths of Φ16-5Φ-300G bars and that of Φ25-5Φ-300G ones were equal (about 23 MPa), it can be assumed that the concrete cover was just insufficient for the latter.

Figure 3.4: Concrete block breakage

3.1.5 CONCLUSIONS

Through a systematic mix design method for SCC and laboratory trials, a high-strength self-compacting concrete (HSSCC) mix was developed. Pullout specimens consisting of different bar diameter, steel grades, and bond lengths were cast from the HSSCC mix and tested under monotonic loading. Measurements of load and slip at the unloaded end were made throughout the test until either bond failure, reinforcement breakage, or concrete block breakage occurred.

After analysing the experimental results of Φ16 pullout specimens with 5Φ bond length, different bond mechanisms were observed between 300G and 500G steel bars which were difficult to comprehend since both steel grade bars had the same rib pattern. An explanation for this behaviour was found through a series of further investigations. It was found that the reduction of bar diameter (which is inevitable; especially in the post-yielding phase) has a considerable impact on bond performance. Even for the specimens with longer bond lengths (7.5Φ and 10Φ) in which bar failure happened before de-bonding, the same phenomenon was noticed which resulted in identical slips at different bond stress levels.

In case of Φ25 bars, only one steel grade (300 MPa) was used; however, the ratio of concrete block dimensions to bar diameter was reduced intentionally in order to investigate the effect of concrete confinement on bond performance of HSSCC. Through analysis of the results it was found that the new ratio was insufficient to force the bar to fail in either tension or bond failure; hence it failed by cracking of the concrete block. Thus, it was concluded that in the absence of transverse reinforcement a minimum concrete cover of 12.5 times the bar diameter should be applied for HSSCC.

In the current research, authors focused on bond properties of HSSCC and different steel grade reinforcement from which a new parameter (effect of reduction in bar diameter after yield) is found to affect the bond between the concrete and rebar (when steel grade/ductility changes). Future research should focus on a more detailed assessment of this phenomenon and its effect on the bond properties of reinforcement and concrete in different concrete types and strengths. In addition, introducing this parameter into relevant computer programs, which are used to numerically model the concrete bond, is also desirable in the long run.

3.2 POST-YIELD BOND PERFORMANCE OF HSSCC

3.2.1 ABSTRACT

Self-compacting concrete (SCC) has gained substantial attention since its advent for its ability to compact without the need for either internal or external vibration even in areas of highly congested reinforcement such as beam-column joints. During the past two decades, extensive research has been conducted on both the fresh and hardened properties of normal strength SCC; however, only recently has interest in high-strength self-compacting concrete (HSSCC) gained momentum.

This study investigates bond properties between reinforcement and HSSCC as well as conventionally vibrated high-strength concrete (CVHSC). Appropriate mix designs for both HSSCC and CVHSC were first developed to achieve comparable concrete compressive strength of about 90 MPa. The effects of bar grade, diameter, bond length, and concrete type were investigated by means of pull-out tests for both concrete types; where, special attention was paid to the post-yield slip behaviour of different steel grades. It was found that the difference in ductility of bars with different grades results in different rate of diameter reduction due to axial tensile stress which consequently affects their bond performance; especially in the post-yield range. Available bond models were applied to the experimental outcomes of this study and modifications and/or new expressions are suggested where possible.

3.2.2 INTRODUCTION

Self-compacting concrete (SCC) was first developed in Japan by Prof. Hajime Okamura and his research team at the University of Tokyo in 1986 (Ozawa et al., 1989) as a solution to problems related to concrete durability and unskilled labour force. It is one of the prominent advances in concrete technology during the past twenty years. SCC is a special high-performance concrete which compacts itself under the effect of gravitational forces without any external/internal vibration. SCC is capable of flowing to a uniform level free of segregation and filling all recesses, reinforcement spaces and voids even in highly congested areas.

The unique properties of SCC are achieved only by systematic optimization of both individual constituents and composition. The flowability and mix stability of SCC are determined primarily by the interactions between powder, water, super-plasticizer, and viscosity modifying admixture (VMA). SCC possesses the following characteristics in fresh state: flowing ability, passing ability, and resistance to segregation (EFNARC, 2002,2005). Due to its unique features, SCC may contribute to significant quality improvements of concrete structures and open up new fields for concrete applications. Use of SCC offers several benefits to construction practice such as elimination of compaction, shortening of construction time, noise reduction, improved homogeneity, and excellent surface quality (Khayat, 1999).

Performance of reinforced concrete (RC) elements is dependent on various factors, among which bond strength between reinforcement and concrete plays an important role in enabling RC to function as a composite structural material. Since the advent of SCC, various researchers have investigated the bond properties of reinforcing bars in SCC. Valcuende et al. (2009) provided a brief state-of-the-art on a number of previous studies performed on the bond behaviour of reinforcement and SCC and pointed out various factors and reasons for the discrepancies of the results. In addition to the physicochemical (adhesion) and mechanical (friction and bearing) properties, there are other factors affecting the bond behaviour of reinforcement and concrete. Factors such as concrete quality (flowability and stability), changes in the mix design (fluidity and fine content), placement (excessive or insufficient vibration), casting direction (bleeding and porosity of the interface), location of the bar (top-bar effect), and concrete cover can affect the bond performance. Looking into the material behaviour from a microstructural level reveals that the interfacial transition zone (ITZ) around reinforcement (which directly affects the bond strength) is denser, stronger, stiffer, wider, and more uniform in SCC compared to that in conventionally vibrated concrete (CVC) of the same water to cement (w/c) ratio (Valcuende et al., 2009). The top-bar effect has also been investigated by different researchers but the results are inconsistent due to differences in the specimen attributes (height, concrete strength and cover). Some studies indicated that the bond strength does not change with the location of the bar along the height of the member (when lower heights are used) while others found that the effect of bar location is less pronounced in SCC compared to CVC in deeper RC members (Castel et al., 2006; Khayat et al., 1997).

Esfahani et al. (2008) reported that the loss of bond strength for a top bar can be up to 20% more in SCC compared to CVC when smaller concrete cover is provided and splitting (rather than pullout) is the governing mode of failure. Valcuende et al. (2009) found that the higher the concrete compressive strength the lower is the difference in bond strength between SCC and CVC. This difference was attributed to the greater filling capacity and less bleeding in SCC; because it is highly viscous, the flow of water to the surface is small even when the w/c ratios are high. In their experiment, they found that the loss of mean bond strength between the top and bottom of a 1500 mm high column varied between 40% to 61% and 79% to 86% for SCC and CVC, respectively; lesser bleeding and higher homogeneity of SCC being the possible reasons for such a behaviour.

Hassan et al. (2010) investigated the bond between 40 MPA strength SCC and 20 mm diameter deformed bars in heavily reinforced large concrete members and compared the experimental results with its CVC counterpart. The main focus of their study was to examine the effect of concrete age and depth on bond performance. The rate of bond strength development along the height of the specimens was found to be fast before 7 days and then very slow up to 28 days. Further, it was shown that the bond stress was not necessarily proportional to the compressive strength at early ages. The development of bond stress with age (especially at early ages) was faster than the development of compressive strength in both SCC and CVC mixes, which was in agreement with the findings of other researchers. Although the difference between the normalized bond stress in SCC and CVC was hardly noticeable, the ratio of normalized bond stress of SCC to CVC was higher in the top bars compared to the bottom bars and in aged concrete compared to early age concrete. It was found that the normalized bond stress of the top bars was slightly higher in SCC compared to that of CVC; however, in case of the bottom bars bond stresses were similar. Other researchers (Cattaneo et al., 2009; Chan et al., 2003; De Almeida Filho et al., 2008; Hossain et al., 2008; Zhu et al., 2004) adopted different test setups, specimens, concrete and bar types, and other variables (such as bar diameter and bond length) to investigate the bond performance of SCC in reinforced concrete structures and obtained results which were not in complete agreement or disagreement with each other. Nevertheless, the majority of the literature agrees that, SCC provides a stiffer bond compared to CVC, with its bond strength reported being up to 70% higher than that in CVC (but mostly in the range of 10-40%). In very few cases, the bond strength of CVC is reported to be greater than that of SCC by up to 15%. The main reasons for these

discrepancies in the results were mentioned to be the concrete compressive strength (the higher the strength the lower the difference between SCC and CVC) and quality of the materials and mixes (Valcuende et al., 2009).

Although in some of the mentioned investigations (Cattaneo et al., 2009; Esfahani et al., 2008; Hossain et al., 2008; Valcuende et al., 2009; Zhu et al., 2004) SCC mixes with relatively higher compressive-strength (60 to 80 MPa) were adopted, bond properties of bars in high strength self-compacting concrete (HSSCC) is not yet fully understood. In addition, most of the available literature focused on investigating the bond behaviour of steel and concrete while the former remained in elastic range. Nevertheless, the bond performance of deformed bars and concrete in the post-yield range of steel bars is of greater relevance to the modern seismic design approaches which are based on ductility and capacity design principles. In case of RC framed structures, capacity design ensures that under lateral reversing loads plastic hinges form close to the column face where the beams undergo inelastic rotation and plastic strains in reinforcement at these locations are inevitable. Therefore, the present study mainly investigates post-yield bond properties of deformed steel bars in HSSCC through a series of pull-out specimens. For comparison purposes, benchmark specimens of conventionally vibrated high-strength concrete (CVHSC) were also cast and tested under similar conditions. In this study bar grade was also chosen as a variable, in addition to bond length, concrete type, concrete strength, and bar diameter. Experimental results of this study show that the bar grade has considerable impact on bond between deformed bars and concrete; especially in the post-yield range.

3.2.3 EXPERIMENTAL INVESTIGATION

3.2.3.1 MATERIAL PROPERTIES AND MIX DESIGN DETAILS

In the present investigation, locally available materials in Christchurch, New Zealand were used in order to design both HSSCC and CVHSC mixes. General Purpose Cement (GPC), fly ash (Class C), and a third generation polycarboxylic ether polymer based superplasticizer (SP) were used. Locally available semi-crushed coarse aggregate (maximum size 13 mm), fine aggregate (natural river sand), and potable water were used in both concrete mixes. Details of physical properties of the cement, fly ash, and aggregates

used in the mix have been described elsewhere by the authors (Soleymani Ashtiani et al., 2011b).

The mix design method proposed by Su et al. (2001) and guidelines provided by EFNARC (2002,2005) were used in order to reach an initial mix proportioning for HSSCC and a finalized mix was obtained through a series of laboratory trials. CVHSC mix was then achieved by varying proportions of coarse and fine aggregates, water/binder ratio and percentage of superplasticizer. Table 3.5 shows the finalized mix design for HSSCC and CVHSC.

Table 3.5: Mix proportions of HSSCC and CVHSC

Material	HSSCC (kg/m^3)	CVHSC (kg/m^3)
Coarse aggregate	880	1145
Fine aggregate	870	695
Cement	385	385
Fly ash	165	165
Water	165	148.5
Super-plasticizer (SP)	3.575 (0.65%*)	1.925 (0.35%*)
28-day compressive strength	88.7 MPa	86.2 MPa
Standard deviation	0.35	2.65

*The percentage of SP is determined on the sum of cement and fly ash

A 150-liter capacity drum mixer was used for mixing both the HSSCC and CVHSC batches. The mixing procedure adopted in this study was the same for both concrete types. Initially, materials were dry-mixed for about one minute before introducing water and SP to the mix. Afterwards, 80% of the required water was added in several stages while mixing and an additional 1 minute of mixing followed. The remaining 20% of water (which was premixed with required SP) was introduced to the mixer and another minute of mixing followed. At this stage, concrete was left for about a minute in the mixer (without mixing); after which, the entire mixing procedure was concluded with a final minute of mixing. For CVHSC, the only fresh property measured was slump using the standard slump cone test which led to a slump value of approximately 120 mm. Fresh properties of HSSCC were assessed using Slump-flow, J-ring, L-box, and V-funnel tests. The results of these tests as well as their typical acceptable ranges (Hwang et al., 2006) are shown in Table 3.6.

Table 3.6: Fresh properties of HSSCC

Test type	Experiment	Accepted range
Slump flow diameter (mm)	750	600-800
Slump flow T_{500} (second)	4.2	2-7
J-Ring flow diameter (mm)	720	580-780
J-Ring height H_{in} - H_{out} (mm)	6	0-15
L-Box ratio	0.92	0.75-1.0
V-Funnel T_0 (second)	8	6-12
V-Funnel T_5 (second)*	9.16	0-3 (+T_0)**

* Same test was performed after allowing concrete to settle for 5 minutes.

** This time range should be added to that of T_0.

3.2.3.2 DETAILS OF PULL-OUT SPECIMENS, TEST SETUP AND TESTING PROCEDURE

In an experimental investigation of bond characteristics between concrete and reinforcement, various parameters can be considered as variables. In the present study, bar diameter, steel grade, bond-length, and concrete type were varied between different specimens. In total, 30 pull-out specimens were cast in different concrete batches. Along with each concrete batch, 6 standard cylinders of 100 mm diameter and 200 mm height were cast in order to evaluate the compressive and splitting tensile strengths of the mix at the day of test. Pull-out and cylinder specimens were wet cured for 14 days and covered with plastic wrap until the test day in order to hold the moisture inside (Appendix B).

RILEM (1973) recommendations were used to prepare and test the pull-out specimens; however, minor modifications were made in order to suite the available test facilities. According to RILEM, an un-bonded length of 5 times bar diameter was provided in the loading face of each specimen using a plastic tube. It should be noted that no extra allowance was made for bond deterioration zone. The test setup of a typically instrumented specimen is shown in Figure 3.5. A force controlled universal testing machine with a maximum capacity of 1000 kN was used to axially load the pullout specimens. Cubic concrete blocks of 200 mm and 300 mm dimension were used for Φ16 and Φ25 bars, respectively. The concrete block was held to the bottom of the stationary head of the Avery using a steel frame fixed to the loading plate. A neoprene pad (5 mm thick) was used to reduce the friction between the concrete block and the loading plate. A slip gauge of 10 mm traverse (0.001 mm least count) was fixed to the bottom of the concrete block in order to measure the free-end displacement of the bar. Additionally, elongation of the bar was

measured using a 200 mm traverse displacement gauge (with an accuracy of 0.01 mm) fixed to the face of loading device (Figure 3.5).

It should be mentioned that the concrete casting direction was chosen perpendicular to the direction of the loading in order to magnify the negative effects of bleeding and concentration of air-bubbles underneath the reinforcement. This way, the obtained results will be on the safe side compared to when the casting direction is parallel to the bar direction (or loading direction in this case) and the accumulation of water particles underneath the bar is minimal.

Lack of confinement has been found to be a reason for premature failure of pull-out specimens in previous tests (Soleymani Ashtiani et al., 2011a). Hence, dimensions of the cubic concrete blocks were increased in order to provide enough confinement in the pull-out specimens without the use of other constraints (active or passive).

Pull-out specimens were named with a 5 component ID according to their variables. For example in "CVHSC-D16-300G-5D-S2" the first part represents the concrete type (HSSCC or CVHSC), second is the bar diameter (16 mm or 25 mm), third component illustrates the steel grade (300 or 500 MPa), fourth one shows the bond length (2.5, 5, or 7.5 times the bar diameter), and the last indicates the sample number (1, 2, or 3). The chart below identifies and distinguishes all 30 pull-out specimens with their variables.

$$HSSCC \rightarrow \begin{cases} D16 \begin{cases} 300G \begin{cases} 2.5D/S1 \rightarrow S3 \\ 5D/S1 \rightarrow S3 \end{cases} \\ 500G \begin{cases} 2.5D/S1 \rightarrow S3 \\ 5D/S1 \rightarrow S3 \end{cases} \end{cases} \\ D25 \begin{cases} 300G/5D/S1 \rightarrow S3 \\ 500G/5D/S1 \rightarrow S3 \end{cases} \end{cases} \qquad CVHSC \rightarrow D16 \begin{cases} 300G \begin{cases} 5D/S1 \rightarrow S3 \\ 7.5D/S1 \rightarrow S3 \end{cases} \\ 500G \begin{cases} 5D/S1 \rightarrow S3 \\ 7.5D/S1 \rightarrow S3 \end{cases} \end{cases}$$

Strain gauges were installed on all bars in order to investigate the strain penetration in the bonded zone at various stages of the test. However, special attention was paid in choosing the strain gauge type, length and their locations on the bar in order to minimize any deleterious effects on bond performance. Strain gauges of 1 mm gauge-length were chosen in order to facilitate their placement between the reinforcement ribs without the necessity

of removing ribs. Two different arrangements were adopted for installation of strain gauges based on the bar diameter and length of the bonded area (Figure 3.5). Despite acknowledging that the bond stress is not constant within the bonded region, no effort was made in this study to measure local strains inside the bonded region as investigating the local bond stress profile was outside the scope of this study. Instead, it was decided to compare the bond performance in terms of average bond stress within the bonded zone in line with the RILEM approach. Note that the "average bond stress" reported here does not account for the variation of local bond stress within the bonded zone; which can be substantial specially in the specimens with longer bond length.

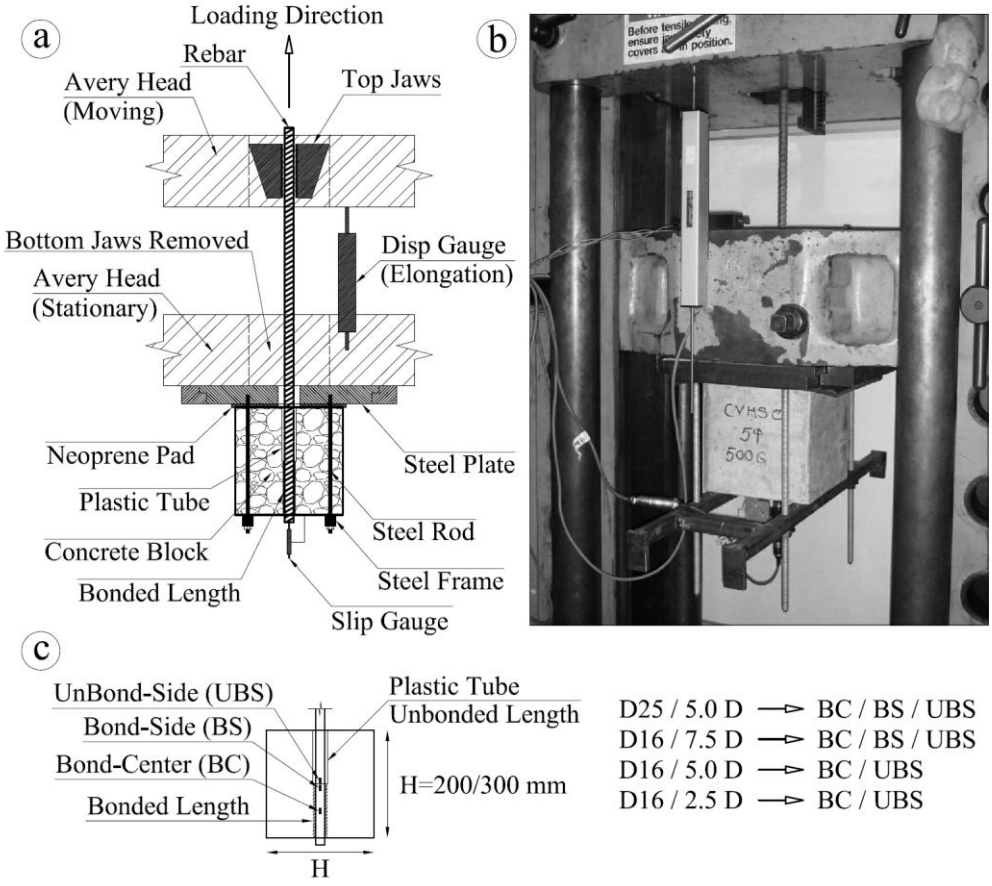

Figure 3.5: Details of test setup (a), pull-out specimens (b) and strain gauge detailing (c)

3.2.4 RESULTS AND DISCUSSIONS

The pull-out specimens were tested 90 days after the casting date along with their auxiliary cylinders. The average compressive and splitting tensile strengths of the different concrete batches at the day of test are shown in Table 3.7.

Table 3.7: Average compressive and splitting tensile strength at the day of test

Batch No.	Concrete type	Bar diameter (mm)	Ave comp. strength (MPa)	SD	Ave split tensile strength (MPa)	SD
1	CVHSC	16	101.4	5.74	6.7	0.25
2	HSSCC	16	103.1	7.57	6.4	0.33
3	HSSCC	25	114.4	5.72	6.8	0.45

Individual deformed bars of different diameters (16 and 25 mm) and steel grades (300 and 500 MPa) were tested in order to obtain their stress-strain relationship and yielding and ultimate stresses (Figure 3.6). It should be noted that the rib pattern and dimensions of both bar grades were the same for an identical bar diameter. The bar specifications followed the Australian/New Zealand Standards - AS/NZS 4671 (2001); i.e. all ribs were run at 60° to the axis of the bar and rose off the bar at 45° angle to the surface. The rib specific projected area was 0.11, 0.1, 0.098, and 0.087 and the rib height was 1.29, 1.2, 1.84, 1.63 mm for the D16-300G, D16-500G, D25-300G, and D25-500G, respectively.

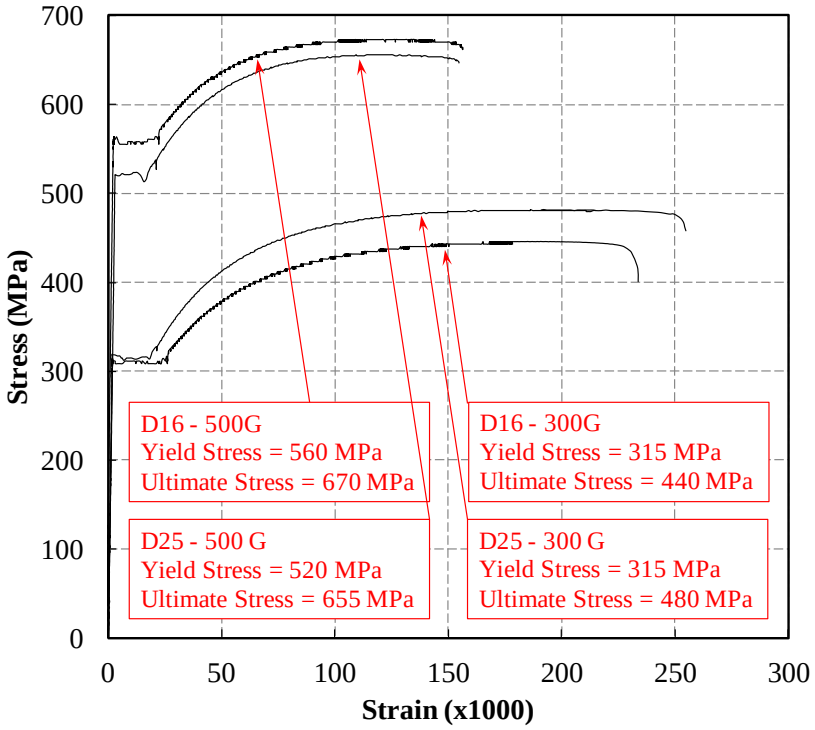

Figure 3.6: Averaged stress strain curves of different diameter and grade bars

The averaged bond-stress vs. end-slip curves for the pull-out specimens are shown in Figure 3.7 where the solid and dashed lines represent bond-slip behaviour of 300 and 500

grade steel bars, respectively. The slip was measured directly at the unloaded end of the bars and the average bond stress was calculated by dividing the pulling force by the bonded surface area of the bar. It should be noted that in Figure 3.7, the second vertical axis shows the average tensile stress level in steel from which (comparing with Figure 3.6) it can easily be confirmed if the bars yielded and what stress range they experienced.

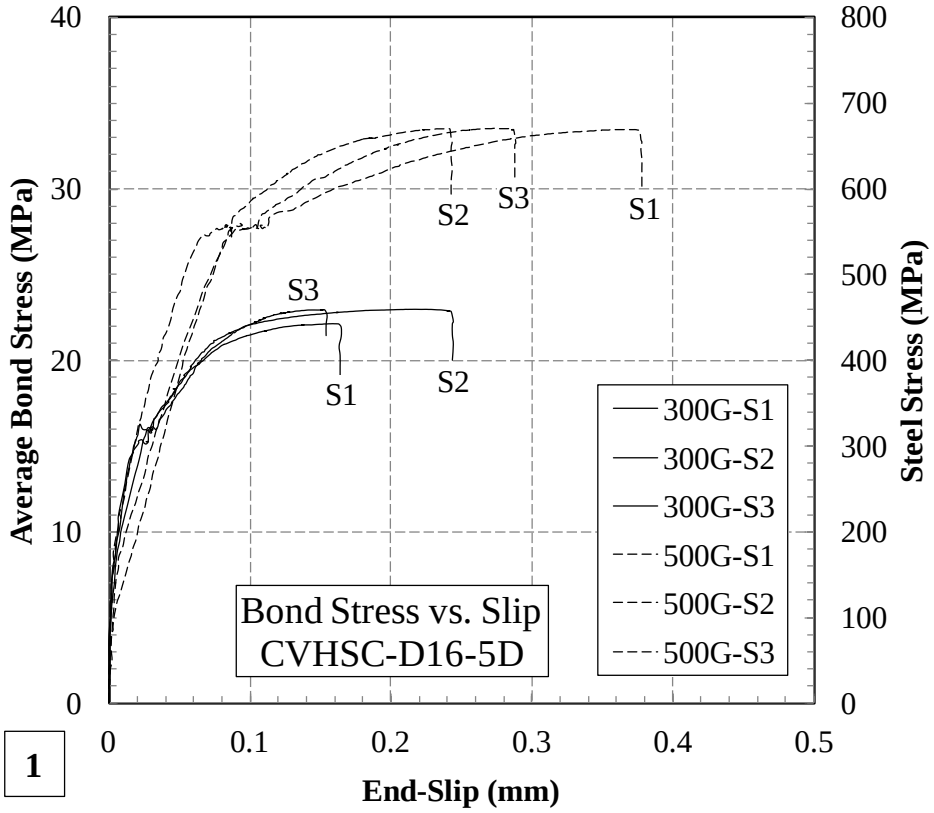

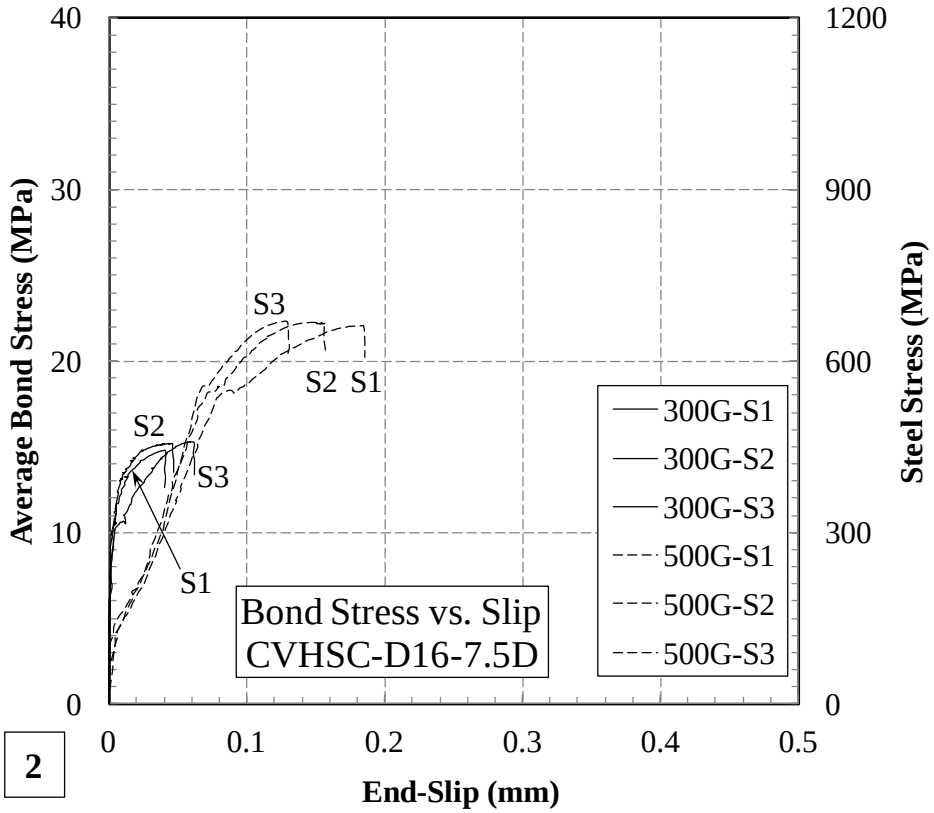
Average Bond Stress (MPa)
Steel Stress (MPa)
End-Slip (mm)
Bond Stress vs. Slip
CVHSC-D16-7.5D
300G-S1
300G-S2
300G-S3
500G-S1
500G-S2
500G-S3
S1
S2
S3
0
10
20
30
40
0
300
600
900
1200
0
0.1
0.2
0.3
0.4
0.5

2

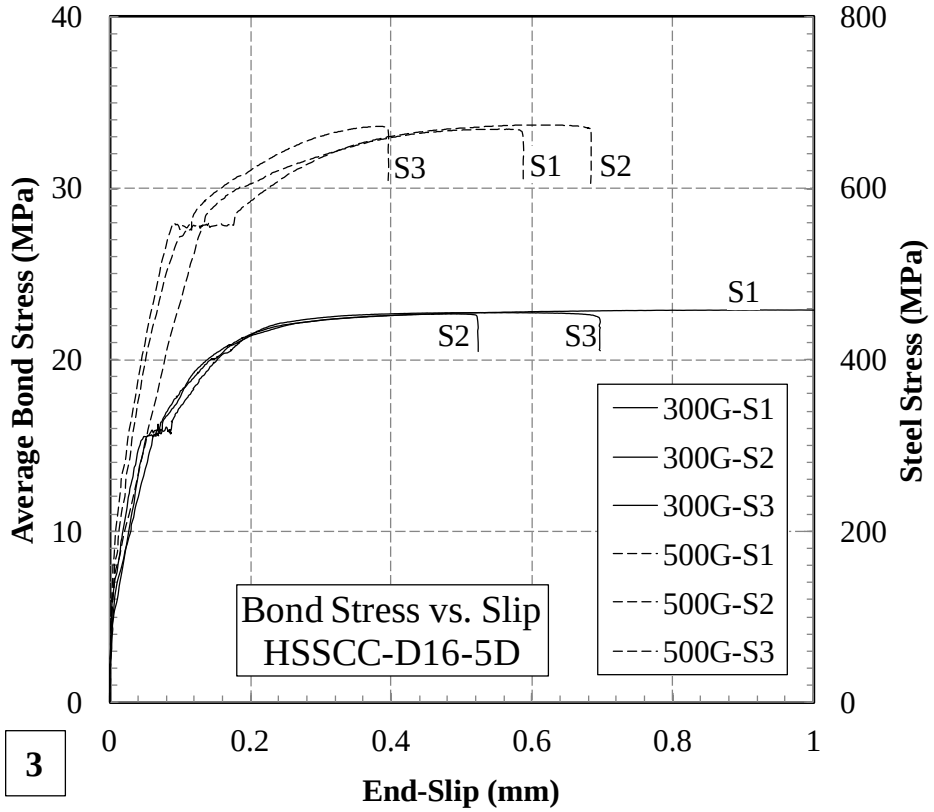
Average Bond Stress (MPa)
Steel Stress (MPa)
End-Slip (mm)
Bond Stress vs. Slip
HSSCC-D16-5D
300G-S1
300G-S2
300G-S3
500G-S1
500G-S2
500G-S3
S1
S2
S3
0
10
20
30
40
0
200
400
600
800
0
0.2
0.4
0.6
0.8
1

3

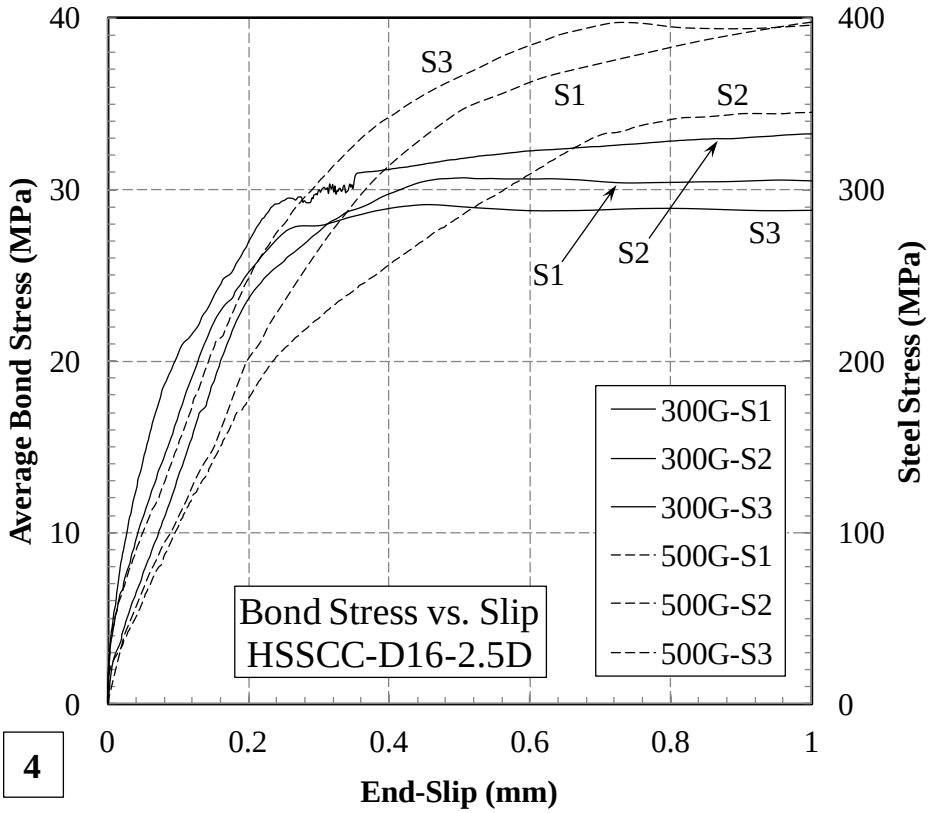
Average Bond Stress (MPa)
Steel Stress (MPa)
End-Slip (mm)
Bond Stress vs. Slip
HSSCC-D16-2.5D
300G-S1
300G-S2
300G-S3
500G-S1
500G-S2
500G-S3
S1
S2
S3
0
10
20
30
40
100
200
300
400
0.2
0.4
0.6
0.8
1

4

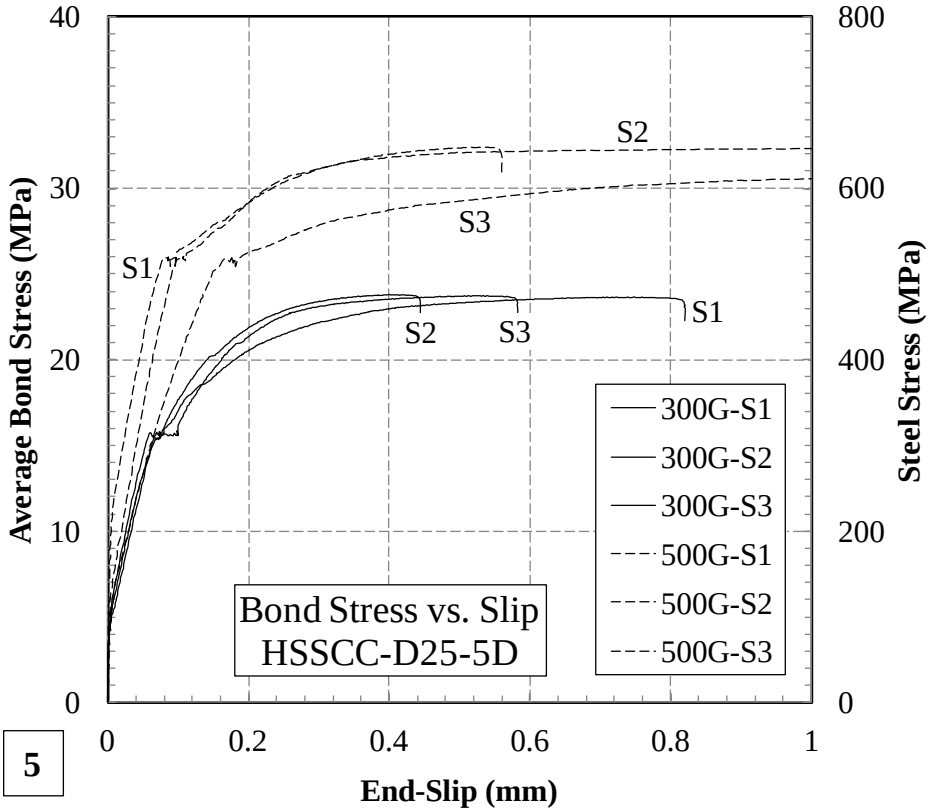
Average Bond Stress (MPa)
Steel Stress (MPa)
End-Slip (mm)
Bond Stress vs. Slip
HSSCC-D25-5D
300G-S1
300G-S2
300G-S3
500G-S1
500G-S2
500G-S3
S1
S2
S3
0
10
20
30
40
200
400
600
800
0.2
0.4
0.6
0.8
1

5

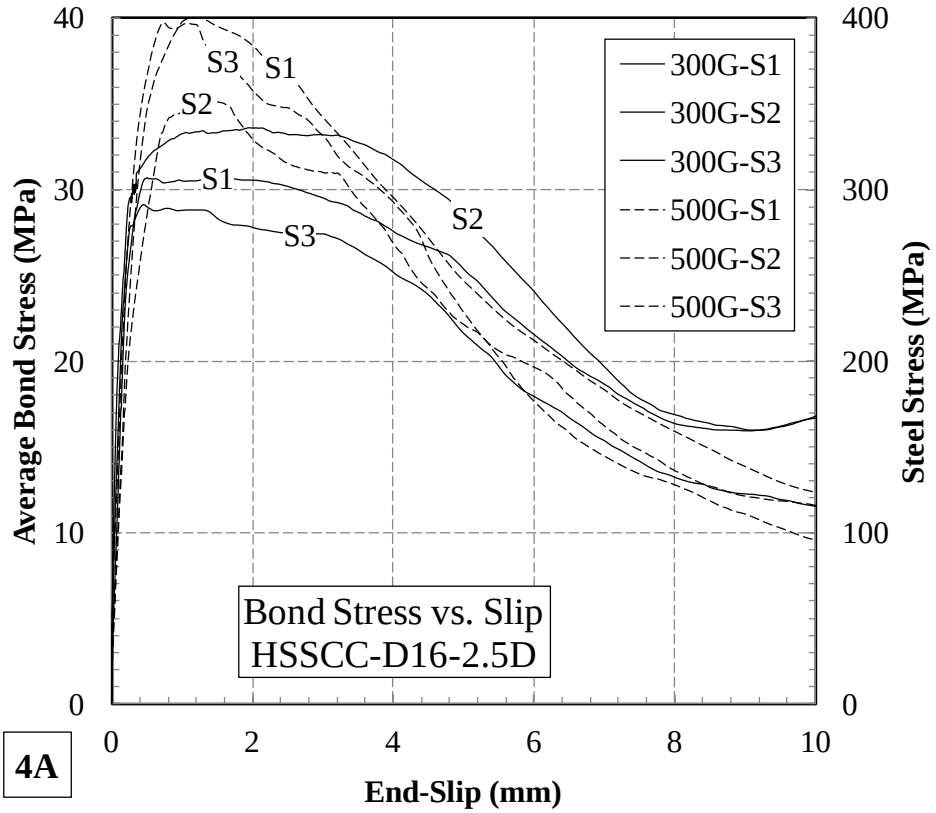

Figure 3.7: Average bond-stress vs. end-slip for different concrete types, bar diameters, bond lengths, and bar grades

Although considerable amount of slip occurred in most of the specimens, it is obvious from Figure 3.7 that the rupture of steel bar outside of concrete was the final mode of failure in all specimens (with the exception of the specimens with bond-length of 2.5D). For ease of comparison, bond-slip behaviour of the specimens with 2.5D bond-length is shown in two different slip scales (Figure 3.7 graphs 4&4A). The final mode of failure for these specimens was pull-out of the steel bars due to shearing of the concrete between the ribs without any apparent split-tensile cracking in the surrounding concrete block. This shows that the ratio of concrete block dimension to bar diameter (i.e. confinement ratio) was sufficient to confine the bar embedded in the concrete. Only in the HSSCC-D25-500G-5D-S3 specimen, splitting cracks did appear on the surface of the concrete block and the final failure mode was the splitting of concrete block after about 2.5 mm of slip. Considering a confinement ratio of 12.5 and 12 for 16 mm and 25 mm bars, the mentioned failure mode was not unexpected. In fact, this confirms that a confinement ratio of at least 12 is essential in order to prevent splitting tensile cracks in high strength concrete when no other means of confinement are used. It is worthwhile noting that RILEM (1973)

recommends a confinement ratio of 10 for direct pull-out test in concrete with compressive strength between 27 to 33 MPa.

Unlike normal strength SCC for which a better bond performance is reported compared to that of CVC, when the quality of material increases and a less porous matrix is achieved by implementing denser and higher strength concrete, the ultimate bond stress did not vary considerably between HSSCC and CVHSC. This is evident by comparing graphs 1 and 3 in Figure 3.7. However, higher slips were observed in HSSCC compared to that of CVHSC (1.95 and 4.79 times for 500 and 300 grade steel bars, respectively) which is attributed to the less amount of coarse aggregate (i.e. higher paste content) in HSSCC.

The HSSCC 2.5D series were the only specimens which failed in pullout mode and gave a precise value of the bond strength. With the advantage of hindsight, a CVHSC specimen with 2.5D bond length would have facilitated a more direct comparison of the bond strength; but it is important mentioning that the selection of bond length for this study was based on the information in the available literature on bond of deformed bars and concrete. In most cases, literature agrees that bond length of 5 times the bar diameter is small enough to cause a complete pullout failure before yielding; let alone the occurrence of bar breakage. Considering the fact that the concrete used in this study was of higher strength (compared to the ones available in the literature) and post-yield bond-slip behaviour was the main focus of this research, the authors decided to limit the bond length to 5D for the HSSCC specimens. However, the results have proven that even such a short bond length could avoid complete pullout and divert the failure mode from pullout to the bar breakage.

However, the test results of other specimens can also be used to deduce bond strength. Note that the horizontal axis in these plots is slip (not strain) and the bond-slip curves of all 5D specimens are well into the nonlinear plateau region; which means that the bars in these specimens ruptured very close to their pullout limit, which is also supported by a considerable amount of slip observed in these specimens (close to 0.4 mm in CVHSC and 1 mm in HSSCC) before the bars ruptured. The stable plateau in the bond-slip curve also indicated that the bond strength could not be significantly greater than the maximum bond stress seen in these specimens. Comparing the HSSCC and CVHSC bond-slip curves of the 5D bond length series (Figure 3.7-1, 3, 5), as all three series sustained similar maximum bond stress before failure, it is expected that they have comparable bond strength as well.

Figure 3.7 shows two major phenomena in bond-slip behaviour of both HSSCC and CVHSC: 1- Significant difference between stress levels of 300 and 500 grade bars at identical slip values despite similar bar diameter and surface geometry. 2- A distinct yield plateau in the bond-slip curves. Although these phenomena have indirectly been referred to for normal strength concrete by Maekawa et al. (2003) and Fib-Bulletin-10 (2000), they have mostly been overlooked in the available bond literature mainly because of the following reasons:

- Experimental investigations on bond normally include specimens with short bond lengths to ensure the occurrence of pull-out in the elastic range; and the yield point of steel bars is not reached in most cases.
- Studies on bond commonly focus on normal strength concrete in which even comparatively long bond lengths do not require the steel bar to enter the post-yield range.
- In order to avoid complexities of bond behaviour in the post-yield range, researchers often intentionally choose to investigate only the elastic response range where numerical modelling becomes less laborious.
- As confinement is an important parameter in bond performance, the focus of some studies available in the literature was to test partially confined specimens to investigate the effect of confinement on the overall bond behaviour. Understandably, these studies did not pay much attention to the effect of bar grade.
- Different bar grades (different ductility) having same rib geometry are not commonly used in bond investigations.
- More importantly, a specific combination of the above factors (bond-length, bar grade, similar geometry, concrete strength, and confinement) is required to substantiate the occurrence of such phenomenon.

The following sections provide qualitative and quantitative evidences and reasons to explain the occurrence of these phenomena.

3.2.4.1 DISSIMILARITY IN PULLOUT STRENGTH OF DIFFERENT BAR GRADES

Maekawa et al. (2003) compared the bond-slip behaviour of steel and aluminium bars and different grade steel bars of same geometry. In case of aluminium bars they correlated the lower bond-stress with lower Young's modulus. They further explained that the difference in bond-slip behaviour may be caused by the difference in tensile strain or stress in the bar assuming that the bond stress is lower for larger strain values at the same slip. Maekawa et al. (2003) suggested that the difference in bond-slip relations of steel bars in short pull-out specimens and axial tension specimens is caused by this strain difference. They further explained that all differences between the experimental results can uniquely be expressed by defining a bond-slip-strain relationship (details of which are explained in the following sections).

In addition, there is some limited though variable information contained in the Fib-Bulletin-10 (2000) with regard to the post-yield bond-slip behaviour in concrete. It is explained that for deformed bars even when the stresses in steel bars are higher (post-yield range), the effect of transverse deformation (Poisson effect) coupled with the longitudinal steel stresses is small in comparison with the rib height. It is pointed out that the effect of steel yielding on bond-slip performance is not yet well understood. Nevertheless, it is described that due to the contraction of the steel bar at and beyond yielding, the outward component of the pressure may decrease, resulting in a reduced contribution of macro friction. Fib-Bulletin-10 (2000) also explains that yielding affects the geometry of the ribs by reducing the area of the projection and the relative rib area (bond index). It is mentioned that, CEB-FIP-MC (1993) implicitly takes the effect of bar contraction into account by assuming the variable bond-slip relation along the transfer length. In another section, it is described how the role of Poisson effect tends to increase in a deformed bar after the concrete key between the ribs is sheared off.

According to the discussions by both Maekawa et al and Fib bulletin 10, it can be inferred that although post-yield behaviour of the steel reinforcement is expected to affect its bond performance in concrete, there is a level of uncertainty in its actual mechanism and occurrence. Therefore, in the following sections the authors provide further evidence and discussions on how this phenomenon occurs.

In all of the specimens tested (except for the CVHSC-D16-7.5D series where excessive bond-length was provided and slip values were low), there was a significant difference

between the ultimate bond-stress of grade 300 and 500 bars at identical slip levels. Given that the bar geometry (rib height, spacing, surface area, etc.) was the same for both steel grades, pull-out could be expected to take place at similar bond-stress levels. Nevertheless, experimental results of this study proved otherwise. As a case in point consider graph 3 of Figure 3.7: for a slip value of 0.5 mm bond stress reached approximately 23 and 33 MPa for 300 and 500 grade bars, respectively. Similar trend can be traced in graphs 1, 5 and even 4 (4A). This consistency between different specimens shows that the mentioned phenomenon has not randomly occurred and needs to be explained.

Because of the fact that high strength concrete with proper confinement was used in preparing these specimens, one possible explanation to this mechanism could be the likelihood of 300 grade bar-ribs being degraded. Therefore after the test, all specimens were cut open to check for evidence of such incident. Not surprisingly though, there were absolutely no evidence supporting this hypothesis; and for both bar grades, ribs were intact after the test. Figure 3.8 shows the surface condition of the bars before and after the test for two typical specimens.

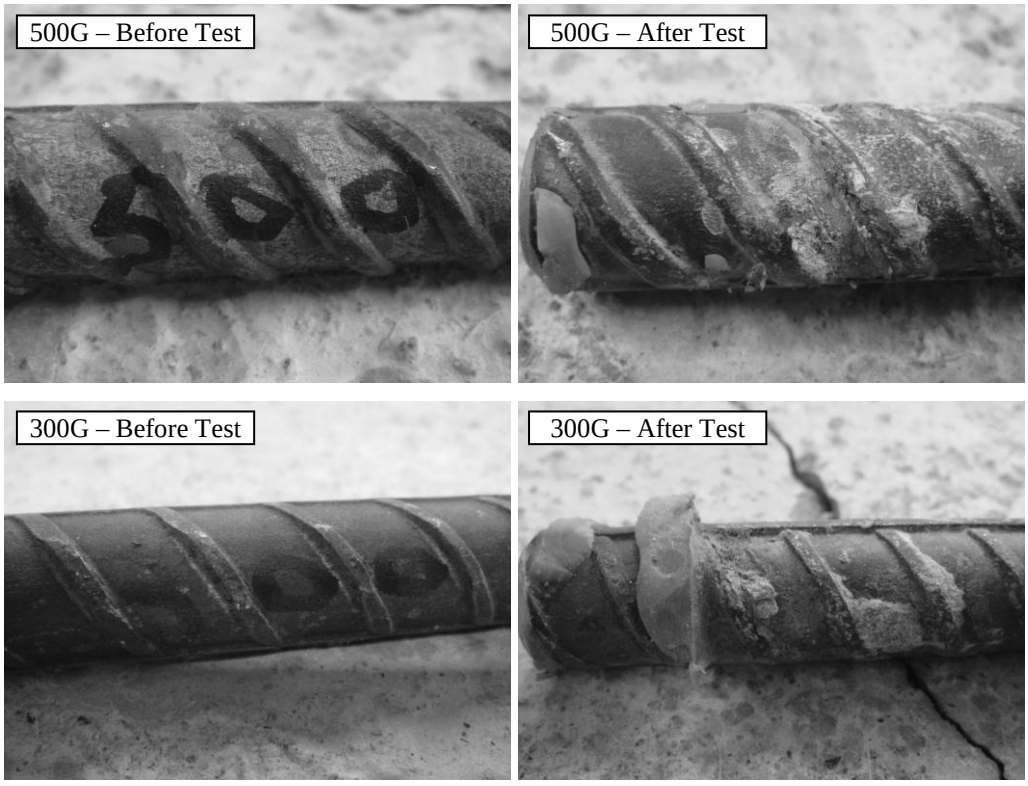

Figure 3.8: Rib patterns for both 300G and 500G bars before and after test

Although the geometry of bars was the same, 300 grade bars were more ductile than the 500 grade ones as shown in Figure 3.6 where ultimate strain of 300 and 500 grade bars at the onset of failure was 240 mε and 150 mε respectively. This means that the 300 grade bars should have experienced a greater reduction of diameter before failure. In order to prove the dissimilarity of reduction in diameter between different grade bars, measurements of the bar diameter (outside the concrete) for all specimens were performed before and after the test (Table 3.8). It should be noted that the bar diameter was measured at three locations (first measurement was taken very close to the bonded zone and the consecutive ones at 100 and 200 mm from the first) on outer perimeter of the ribs using a calliper of 0.01 mm accuracy. Therefore the values in Table 3.8 should not be considered as the actual diameter of the steel core for stress calculation purposes. The reduction of bar diameter was then calculated by dividing the difference between the measurement before and after the test by the measured diameter before the test and multiplying by 100 to obtain the percentage. As mentioned earlier, HSSCC-D25-500G-5D-S3 failed in a different mode than others; therefore its results are not included in Table 3.8.

Table 3.8: Average bar diameter outside concrete before and after the test

Series No.	Series name	Dia (mm) before	SD before	Dia (mm) after	SD after	Dia reduction (%)
1	HSSCC-D16-300G-2.5D	17.10	0.17	16.87	0.21	1.36
2	HSSCC-D16-300G-5D	16.97	0.15	15.45	0.15	8.94
3	HSSCC-D25-300G-5D	26.47	0.12	24.03	0.15	9.19
4	CVHSC-D16-300G-5D	16.95	0.18	15.42	0.16	9.05
5	CVHSC-D16-300G-7.5D	17.05	0.09	15.45	0.10	9.38
6	HSSCC-D16-500G-2.5D	17.20	0.09	17.20	0.09	0.00
7	HSSCC-D16-500G-5D	17.23	0.08	16.32	0.08	5.32
8	HSSCC-D25-500G-5D	26.20	0.12	24.70	0.53	5.73
9	CVHSC-D16-500G-5D	17.23	0.08	16.25	0.05	5.71
10	CVHSC-D16-500G-7.5D	17.23	0.12	16.30	0.13	5.42

Please note that all of the strain and diameter measurements are averaged and performed outside of the bond-length unless mentioned otherwise. Referring to Table 3.8 and comparing the results with Figure 3.7 the following points can be deduced:

Specimens of all categories (except for 2.5D bond-length) ruptured after experiencing their complete strain profile. Obviously the reinforcing bars entered their post-yield phase which resulted in significant reduction in diameter. 300 grade bars showed an average reduction

of 9.14% in diameter; whereas 500 grade ones shrank by 5.55% only. This means a reduction in the area of 17.44% and 10.79% for 300 and 500 grade bars (before failure) respectively. The significance of such reduction can be clearly understood when comparing the rib-height of the bars with the amount of contraction in bar diameter. Consider that for 16 mm diameter bars of 300 grade steel, a 9.14% reduction in bar diameter means 1.46 mm. In deformed bars, the bond between steel and concrete relies mostly on the bearing capacity of the ribs and splitting tensile strength of concrete. As mentioned in the previous sections, identical slip values were generated at different stress levels for specimens of same series (see Figure 3.7). This means that greater reduction of diameter in 300 grade bars resulted in a higher deterioration of bearing capacity (loss of grip between bar ribs and concrete keys) compared to that of 500 grade ones. This explains the discrepancy of bond-stress levels between the specimens of different steel grade.

As seen in Figure 3.7 – graph 4A, at the ultimate bond stress (onset of pull-out) the 300 grade bars just reached/passed their yielding point (more details in Figure 3.7, graph 4) of about 300 MPa. Whereas, the 500 grade bars reached a maximum stress levels of around 350 to 400 MPa (far below their yield-stress of around 500 MPa). Therefore, it is expected that the reduction in bar diameter for both bar grades is minimal. This has also been proved through diameter measurement (Table 3.8 series No. 1 and 6). Due to the fact that 300 grade bars reached/passed their yielding point the reduction of diameter was measured to be 1.36%; whereas, no reduction in diameter was observed for 500 grade bars.

Although 2.5D bond-length specimens had such a small contact area with concrete, only the 500 grade bars failed in bond in their elastic region. However, 300 grade specimens of 2.5D bond-length seemed to be on the verge of their yielding plateau in such a way that S3 failed just below the plateau, S1 failed on the plateau and S2 failed just above the plateau (this will later be seen clearly in the slip-strain curves). This explains the slight inconsistency of bond stress levels even in graph 4 and 4A. In other words if the bond failure happens once bar enters its post-yield range, the ultimate bond stress will be lower compared to a bond failure occurrence in the elastic range (compare 300 and 500 grade bars in Figure 3.7 – graph 4A). The further the bar continues into its post-yield range, the more reduction in bond capacity would result.

As mentioned earlier, available literature provides an impression that the effect of bar contraction compared to the rib height can be neglected even in higher stress levels. On the contrary, the experimental results presented herein prove that this is not the case and the Poisson effect should not be underestimated especially where high-ductility deformed bars are used. In addition, not only the bar diameter reduction affects the friction between the bar surface and concrete, more importantly it also reduces the bearing capacity of the ribs on concrete keys which in turn lowers the bond capacity particularly after yielding. A schematic view of what is explained above is shown in Figure 3.9.

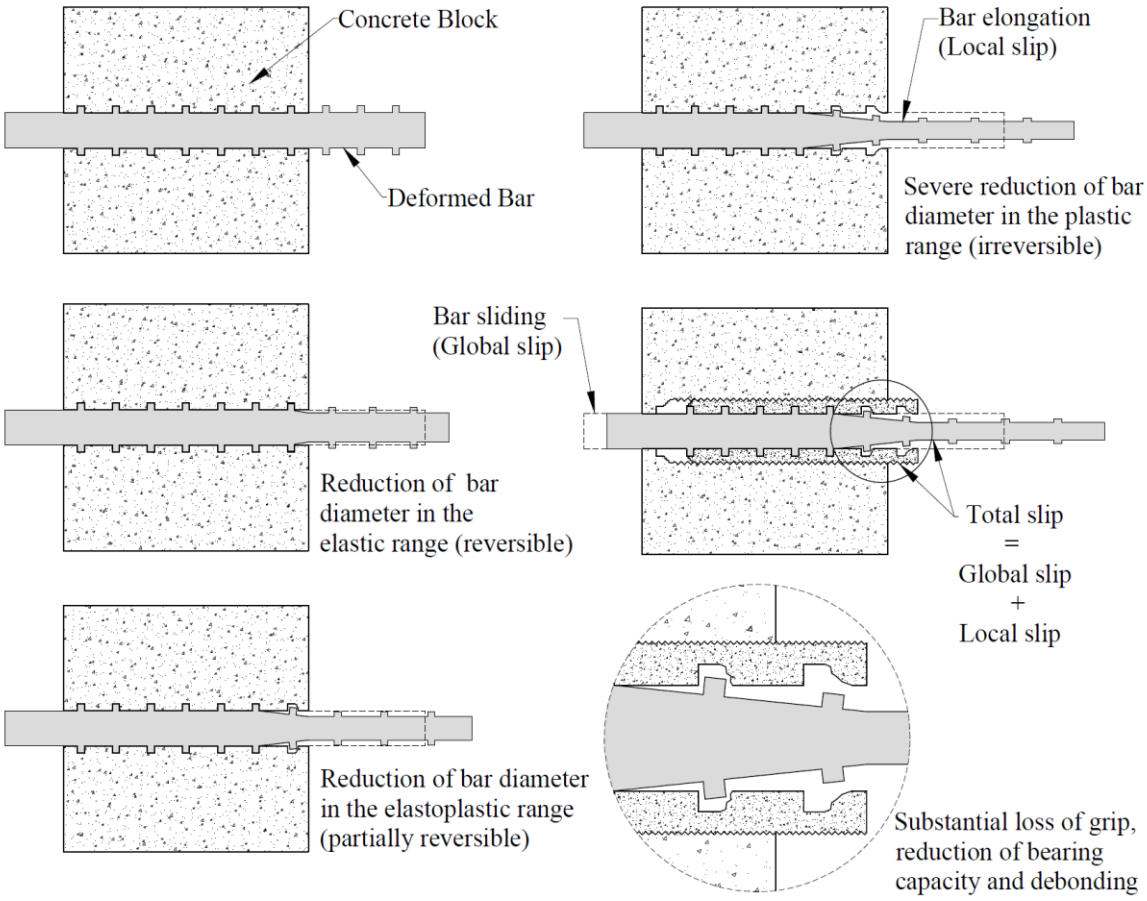

Figure 3.9: A schematic view of bar elongation and loss of grip

3.2.4.2 YIELD PLATEAU IN BOND-SLIP CURVES

In the stress vs. strain behaviour of bare steel reinforcement there usually is a plateau between the yielding point and the initiation of strain hardening over which stress remains constant. As this plateau happens after steel reaches its yield point, it is commonly called the yield plateau. Available literature (Fib-Bulletin-10, 2000; Maekawa et al., 2003) agrees

that the yield plateau disappears in the RC member response (in this case pull-out). However, experimental results presented in this study indicate otherwise.

Figure 3.7 plots the bond stress vs. end-slip relationships for the specimens; nevertheless, it is interesting to note that they are similar to Figure 3.6 (i.e. stress-strain curves of bare steel bars in tension). There is a visible yield-plateau in the bond-stress vs. slip curves (Figure 3.7) which can be found in the response of almost all specimens when they pass their yield point. Even for the 2.5D bond-length specimens (Figure 3.7, graph 4), HSSCC-D16-300G-2.5D-S2 shows a distinguishable yield plateau (this can be seen clearly in Figure 3.10, graphs 4 and 4A). In other words, the bond-slip curves follow the trend of stress-strain curves of the bar which suggests the existence of an interrelationship between strain and slip.

The mechanism of the yield plateau formation in the bond stress vs. end-slip response can be explained by the following potential hypothesis. When the concrete is cast around deformed bars, the transition zone between concrete and ribs is weaker by nature which is conceptually similar to the interfacial transition zone (ITZ) between paste and aggregates in concrete. This weakness is introduced by the formation of voids and concrete paste around the surface of the ribs. The initial slip in the elastic region is mainly due to the crushing of the weak concrete around the ribs which continues up to the yield plateau. As mentioned before the effect of diameter reduction is minimal in the elastic region; however, along with the initiation of the yield plateau (elastoplastic region), part of deformations (both axial and transverse) tend to become permanent. At this stage (yield plateau) although the force tends to remain constant, the effect of diameter reduction increases on the first few ribs (closer to the concrete face at the loading side) which intensifies the stress concentration on the surrounding weak area. As a result, slip continues even when the force is constant which creates the bond-stress vs. slip yield plateau.

As mentioned earlier, during the pull-out tests elongation of the bars outside the concrete was measured by means of a linear potentiometer attached to the face of the loading device (see Figure 3.5). The spacing between the two faces (namely the stationary and moving heads) was kept the same for all tests; therefore, initial length of the bars was taken as the length between the loading plate and the beginning of the bonded zone. It should be

mentioned that the measured elongation was a relative entity and absolute elongation of the bars was calculated by deducting the slip at the free end from the measured elongation. Knowing the absolute elongation and original length, average strain of the bars (outside the concrete) was calculated during the pull out test. For better understanding of the discussions in the following sections, the average strain in steel (outside the concrete) vs. end-slip is shown in Figure 3.10.

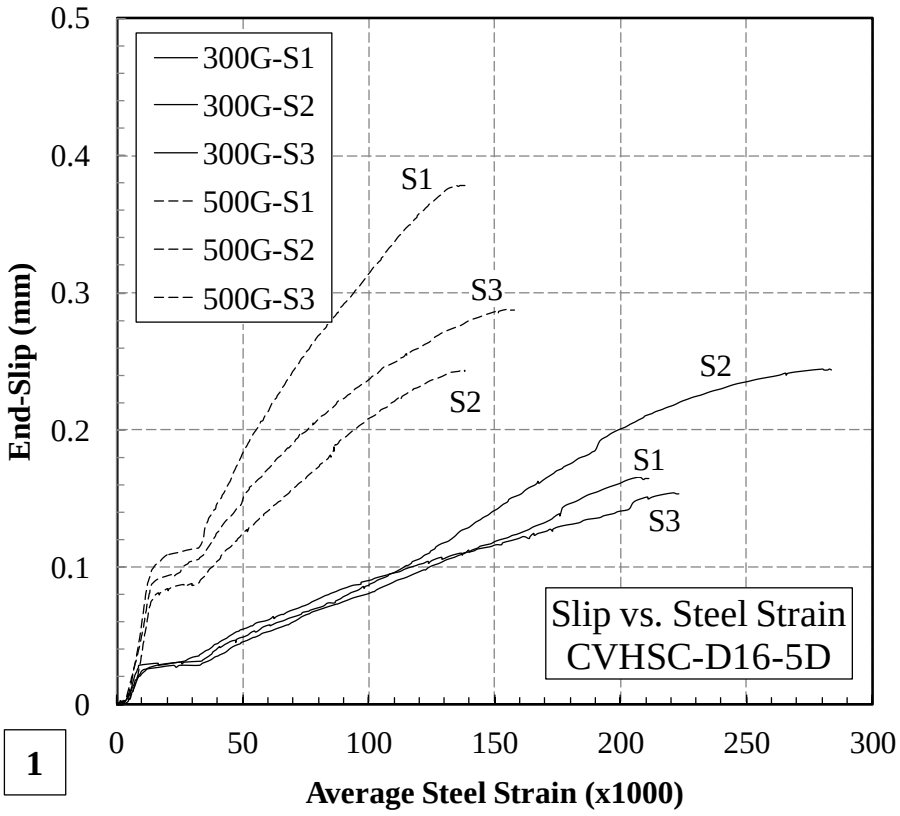

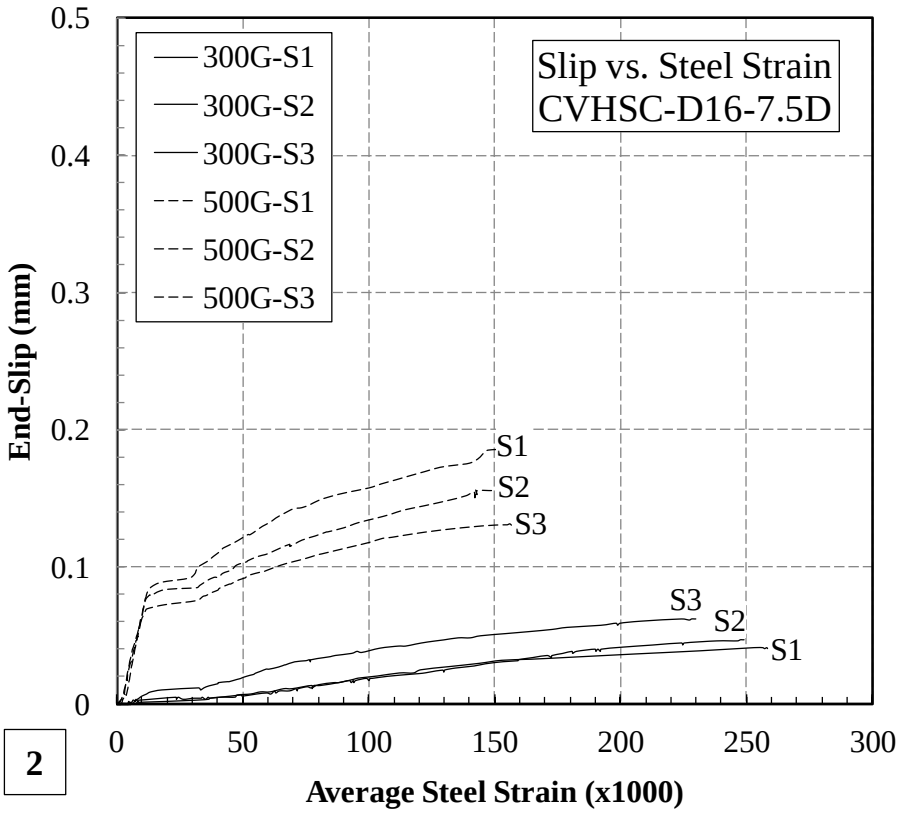
Slip vs. Steel Strain
CVHSC-D16-7.5D
300G-S1
300G-S2
300G-S3
500G-S1
500G-S2
500G-S3
S1
S2
S3
S3
S2
S1
End-Slip (mm)
Average Steel Strain (x1000)
0
0.1
0.2
0.3
0.4
0.5
0
50
100
150
200
250
300

2

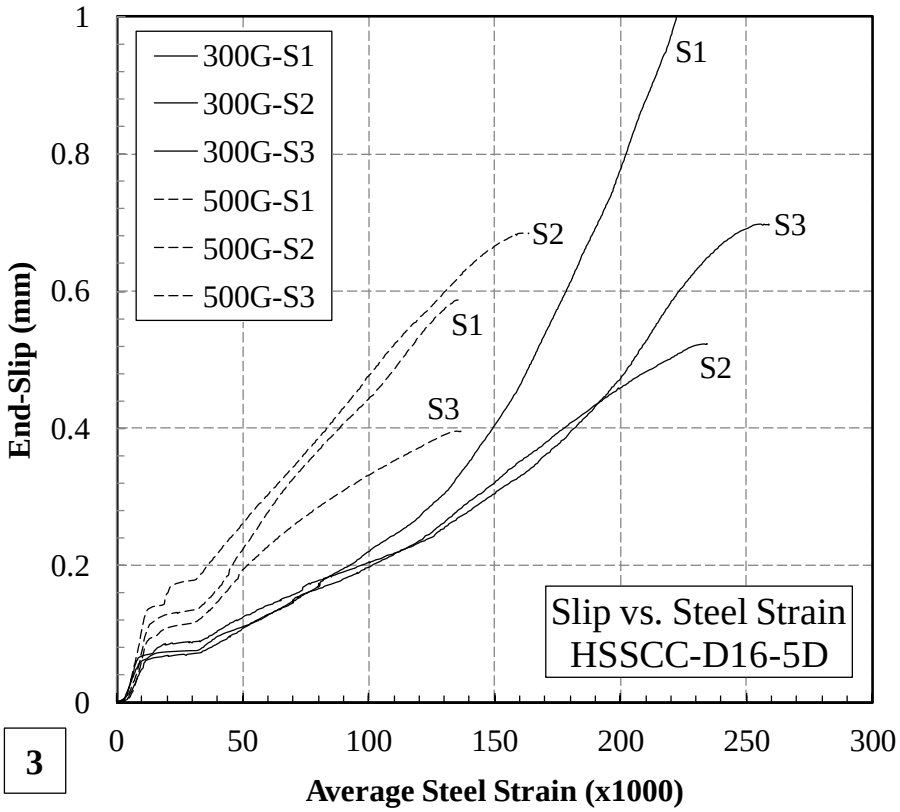
Slip vs. Steel Strain
HSSCC-D16-5D
300G-S1
300G-S2
300G-S3
500G-S1
500G-S2
500G-S3
S1
S2
S3
S1
S2
S3
End-Slip (mm)
Average Steel Strain (x1000)
0
0.2
0.4
0.6
0.8
1
0
50
100
150
200
250
300

3

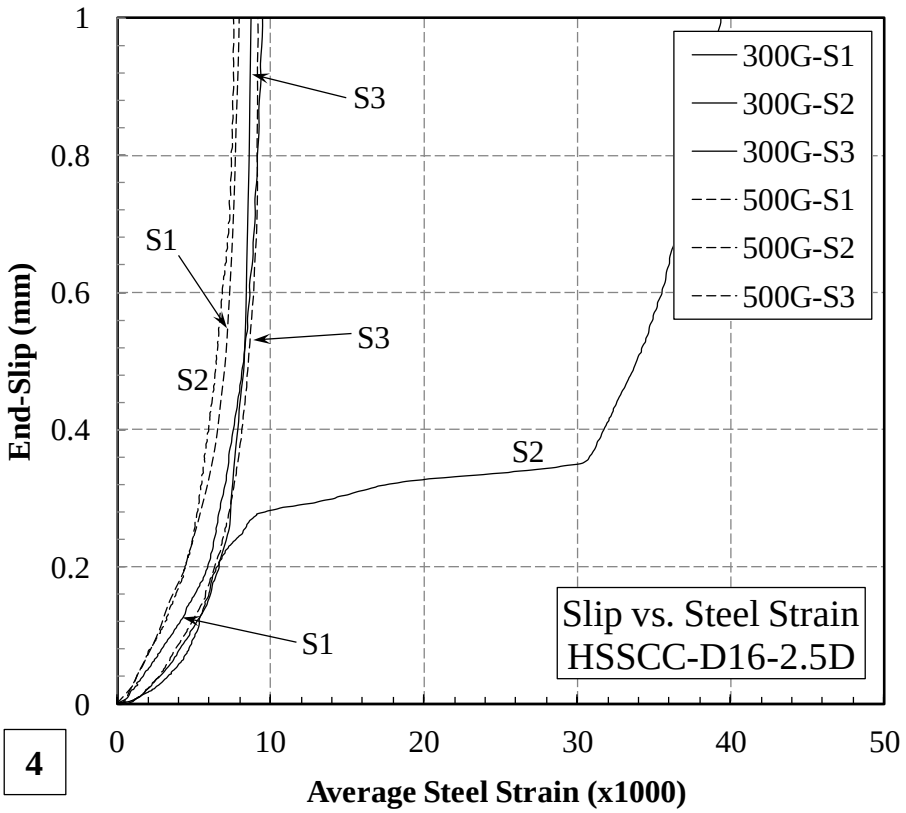
End-Slip (mm)
Average Steel Strain (x1000)
300G-S1
300G-S2
300G-S3
500G-S1
500G-S2
500G-S3
S1
S2
S3
Slip vs. Steel Strain
HSSCC-D16-2.5D

4

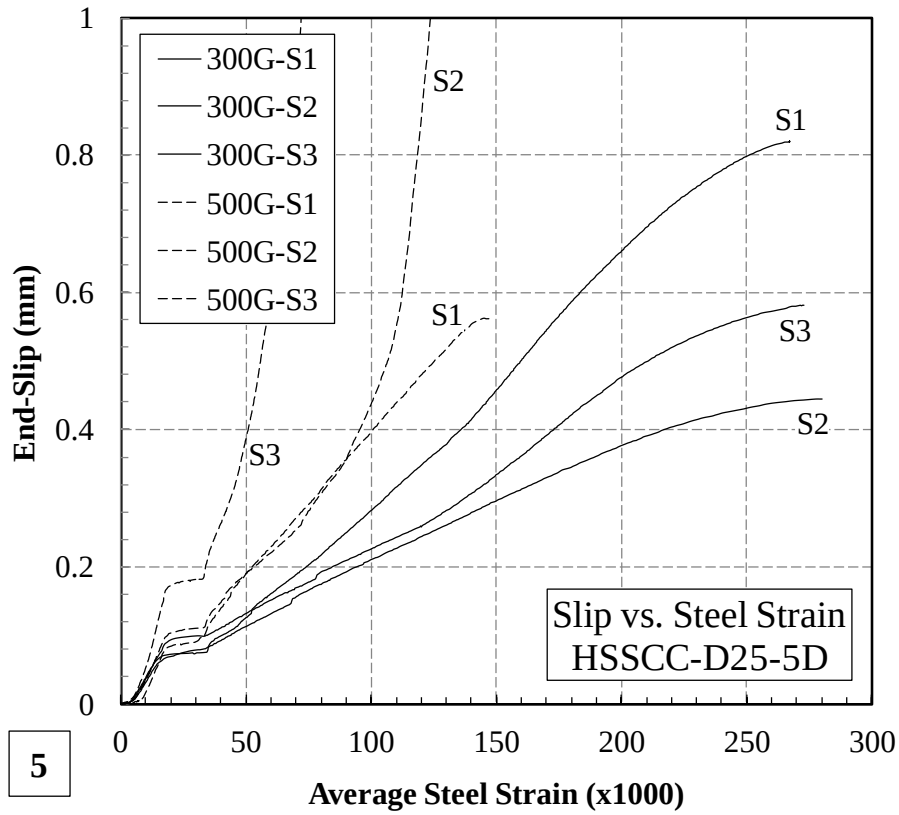
End-Slip (mm)
Average Steel Strain (x1000)
300G-S1
300G-S2
300G-S3
500G-S1
500G-S2
500G-S3
S1
S2
S3
Slip vs. Steel Strain
HSSCC-D25-5D

5

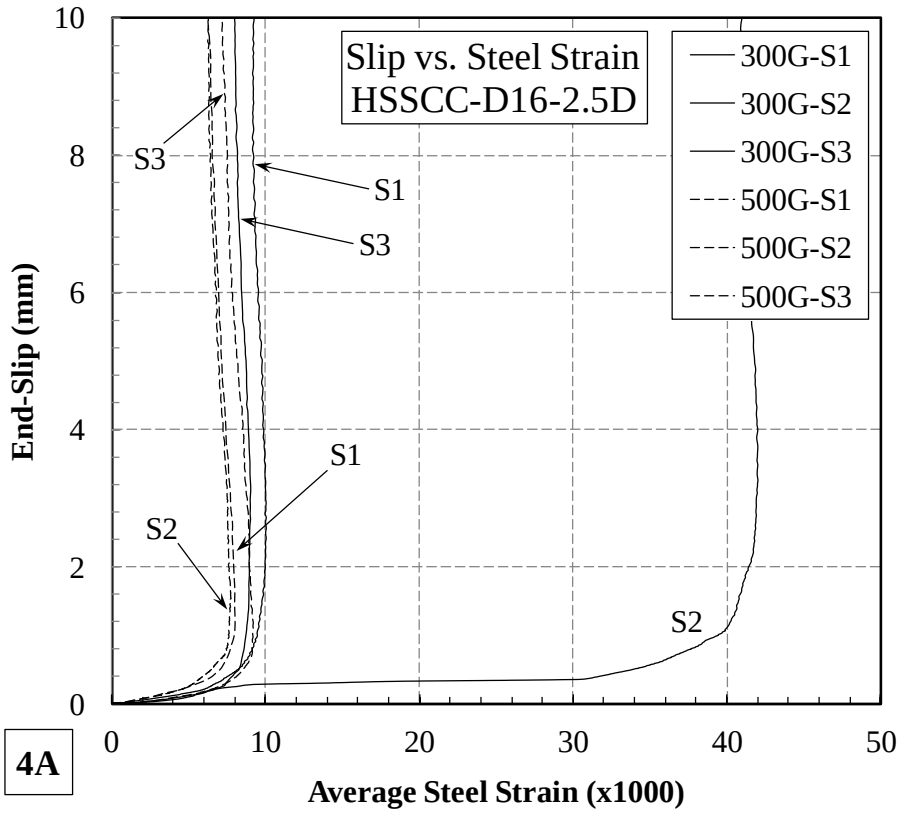

Figure 3.10: Average strain in steel vs. end-slip for different concrete types, bar diameters, bond lengths, and bar grades

The correlation between slip and strain was previously studied by Maekawa et al. (2003) in the form of bond-stress vs. slip vs. strain relationships. In order to investigate the post-yield bond performance, they designed pull-out specimens with very long bond-lengths (50 times bar diameter) and different steel grades (300, 500 and 700 MPa); so that, even in the post yield range there was no free-end slip. Strain gauges of 5 mm gauge-length were installed at different locations on the steel bar (inside the concrete) and slip was measured in the load-end. In addition, the measured local strain profile between a point and the zero strain/slip point was integrated to obtain the local-slip of the bar at that point relative to the concrete. Maekawa et al discussed that there exists a unique relationship between bond-stress, slip and strain which is independent of bar diameter and concrete strength; given as:

$$s = \frac{S}{D} \times K_{fc} \qquad 3.1$$

$$K_{fc} = \left(\frac{f'_c}{20} \right)^{2/3} \tag{3.2}$$

$$s = \varepsilon_s \times (2 + 3500 \times \varepsilon_s) \qquad \varepsilon_s \leq \varepsilon_y \tag{3.3}$$

$$s = s_y \qquad \varepsilon_y < \varepsilon_s \leq \varepsilon_{sh} \tag{3.4}$$

$$s = s_y + 0.047 \times (f_u - f_y) \times (\varepsilon_s - \varepsilon_{sh}) \qquad \varepsilon_s > \varepsilon_{sh} \tag{3.5}$$

where,

's' = non-dimensional local-slip normalized with respect to the bar diameter and multiplied by a factor (K_{fc}) to account for the variations in concrete strength

'S' = local-slip in concrete (mm)

'D' = bar diameter (mm)

'f'_c' = compressive strength of concrete (MPa)

'ε_s' = local-strain in the bar

'sy' = local-slip at yield (mm) obtained by using 'ε_y' in equation 3.3

'f_u' = ultimate strength of the bar (MPa)

'f_y' = yield strength of the bar (MPa)

'ε_{sh}' = local-strain in the bar at the onset of hardening.

Maekawa et al. (2003) also developed an equation to calculate the bond-stress from the local strains at each point inside the bond length (discussion of which is not in the scope of this study). Figure 3.11 shows typical experimental and analytical results for slip-strain relationships in both elastic and post-yield range as presented by Maekawa et al. (2003).

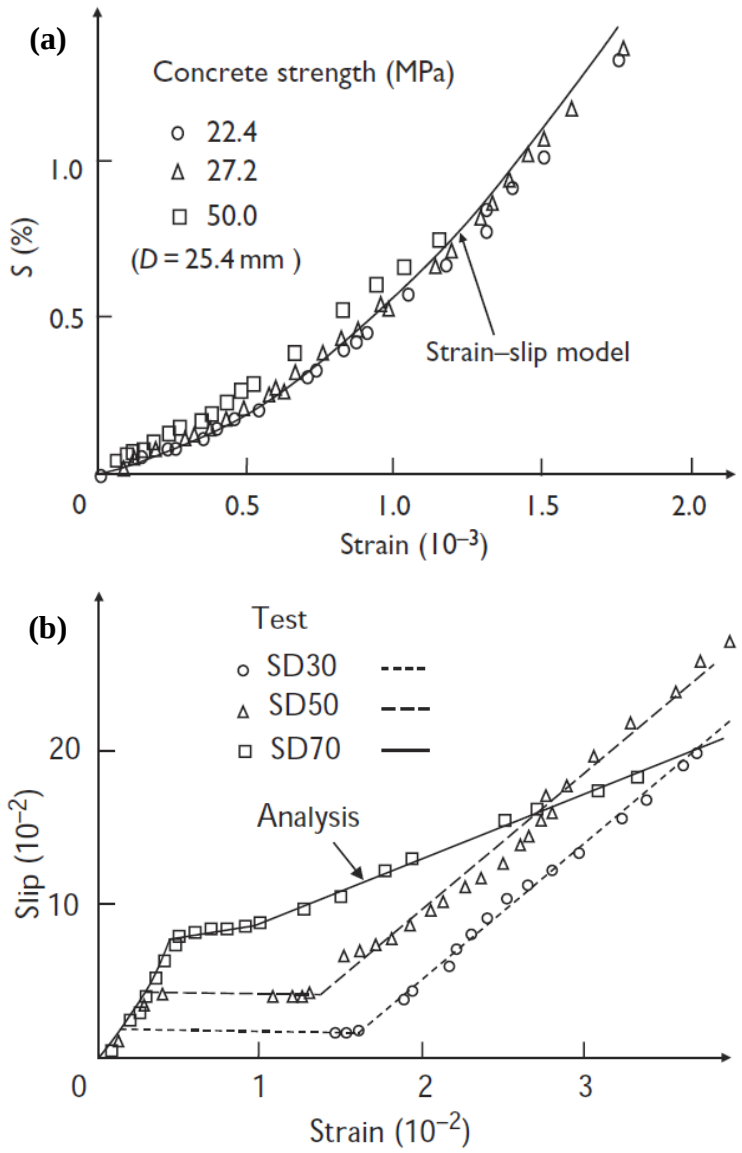

Figure 3.11: Local slip-strain response of steel bars in elastic (a) and post-yield (b) range (Maekawa et al., 2003)

Similar pattern is recognizable by comparing Figure 3.10 graphs 1-3, 5 and 7. Note that in graphs 4 and 4A of Figure 3.10 the bars experienced pull-out in the elastic range (except for S2). Therefore, the elastic response in Figure 3.11-a provides a proper match for the specimens of this series. The mentioned yield plateau in Figure 3.7 is clearly visible in the slip-strain behaviour of all specimens in which steel bar passed its yield point (Figure 3.10). It is worthwhile reminding that Maekawa et al. (2003) model was calibrated using the loaded-end slip (with zero slip at the free end) and local steel strain inside the concrete (using strain gauges). In other words, the calculated slip at a point was due to the elongation of the bar up to that point from the point of zero strain. On the contrary, the

experimental results of this research are based on the free-end slip and steel average-strain (elongation of the bar) outside the bond-length. At a given loading level, the average-strain outside the bond-length is far greater than the local-strain inside the concrete. Hence, the values of average strains in the horizontal axis of Figure 3.10 are much larger than the strains in Figure 3.6 and Figure 3.11.

Although overall recorded patterns were similar in both cases (Maekawa's model and experimental results of this study), calibration and/or modification of the original bond-slip model seems necessary in order to predict the experimental results of this study. For comparison purposes, Figure 3.12-a shows Maekawa's model against experimental results of HSSCC-D16-5D series (Figure 3.10, graph 3). Because the basis of the original model is the local-slip and local-strain inside the concrete, it is obvious that the model does not match the experimental results of this study which are based on free-end slip and average-strain outside the concrete. Therefore, some modifications are suggested to the original formulation and results are shown in Figure 3.12-b. Table 3.9 shows conceptual differences between the original model and the modified one with respect to the major calibrating parameters.

Table 3.9: Conceptual differences between main parameters of original and modified models

Parameter	Maekawa et al Model	Modified Model
Steel strain	Local-strain inside the bond length	Average-strain outside the bond length
Slip	Local-slip integrated from the local strains	Free-end slip measured at the unloaded end of the specimen

$$s = \frac{S}{D} \times K_{fc} \tag{3.6}$$

$$K_{fc} = \left(\frac{f'_c}{20} \right)^{2/3} \tag{3.7}$$

$$s = \alpha \times \varepsilon_s \times \left(2 + 3500 \times \varepsilon_s\right) \qquad \varepsilon_s \le \varepsilon_{y,m} \tag{3.8}$$

$$s = s_{y,m} \qquad \varepsilon_{y,m} < \varepsilon_s \le \varepsilon_{sh,m} \tag{3.9}$$

$$s = s_{y,m} + \beta \times \left(f_u - f_y\right) \times \left(\varepsilon_s - \varepsilon_{sh,m}\right) \qquad \varepsilon_s > \varepsilon_{sh,m} \qquad 3.10$$

Where,

α = elastic modification factor (0.025 and 0.04 for 300 and 500 steel grades)

β = post-yield modification factor (0.003 and 0.006 for 300 and 500 steel grades)

ε_y = steel average-strain at yield

$\varepsilon_{y,m}$ = modified steel average-strain (outside the concrete) at yield (equals 6 times ε_y)

ε_s = steel average-strain

ε_{sh} = steel average-strain at the onset of hardening

$\varepsilon_{sh,m}$ = modified steel average-strain (outside the concrete) at the onset of hardening (equals 1.7 times ε_{sh})

D = bar diameter (mm)

f'_c = compressive strength of concrete

f_u = ultimate strength of steel (MPa)

f_y = yield strength of steel (MPa)

s = non-dimensional free-end slip

S = free-end slip (mm)

$s_{y,m}$ = modified non-dimensional free-end slip (calculated using $\varepsilon_{y,m}$ in equation 3.8)

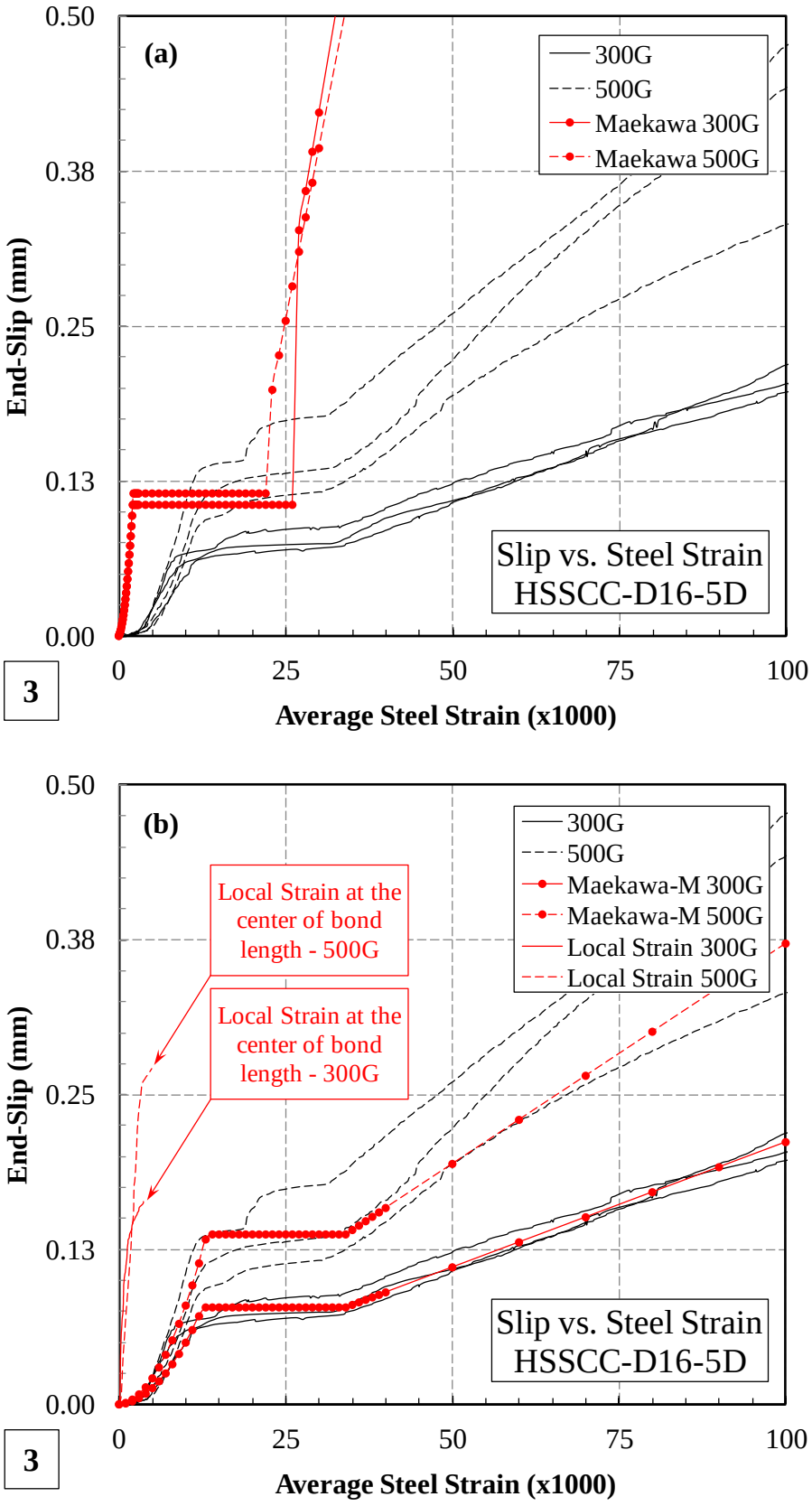

Figure 3.12: Comparison of Maekawa's and modified models with experimental results

As mentioned earlier, in this study local-strains were also measured at specific locations inside the bond-length up to the yield point using strain gauges. For comparison purpose, Figure 3.12-b shows the averaged local-strains for 300 and 500 grade bars measured at the center of the bond-length together with the average-strain outside the concrete. This clearly shows that at an identical end-slip the local-strain in steel inside the concrete is far smaller than the steel average-strain outside the bond-length. Note that the measured local-strain has approximately the same value as that represented by Maekawa et al model (compare Figure 3.12-a, b).

Although the modified model is now capable of predicting the experimental slip-strain behaviour; because the original model was developed using specific specimens (as previously explained), its validity is dependent on the following conditions: 1- free-end slip values are small (maximum 0.3 mm) 2- concrete confinement is enough to avoid splitting failure. Therefore, the developed model loses its uniqueness once pull-out happens and the predicted results deviate significantly from the actual test results. The authors believe that calibrating finite element analysis programs which can cover most (if not all) of the variables would probably provide better representation of the test results compared to closed-form solutions.

3.2.4.3 CEB-FIP MODEL CODE 1990 (MC90) BOND-SLIP MODEL

CEB-FIP-MC (1993) provides a generalized model for bond-slip behaviour of reinforcement in concrete considering different variables (Figure 3.13-a). The model is calibrated using the experimental results of direct pull-out specimens where free-end slip is measured at the unloaded end of the specimen and average bond stress is calculated by dividing the pulling force by the contact surface area of the concrete and steel. In order to accurately predict the bond-slip behaviour, a set of parameters need to be defined and calibrated using the experimental results of previously tested specimens of the same concrete and steel characteristics. It should be mentioned that the CEB-FIP-MC (1993) model is not as accurate as the model proposed by Maekawa et al. (2003) and the interrelationship of bond stress and slip with strain is not explicitly considered. In Fib-Bulletin-10 (2000), a group of researchers modified the CEB-FIP-MC (1993) model by using a different set of parameters in order to replicate the bond-slip behaviour of high-strength concrete more accurately (Figure 3.13-b). In high-strength concrete bond model,

the solid line shows the behaviour of the bar in its elastic range; whereas the dashed line models the bond-slip when the reinforcement enters its post-yield response. It is explained in Fib-Bulletin-10 (2000) that when yielding occurs, the bond stress decreases abruptly before reaching the otherwise full bond capacity.

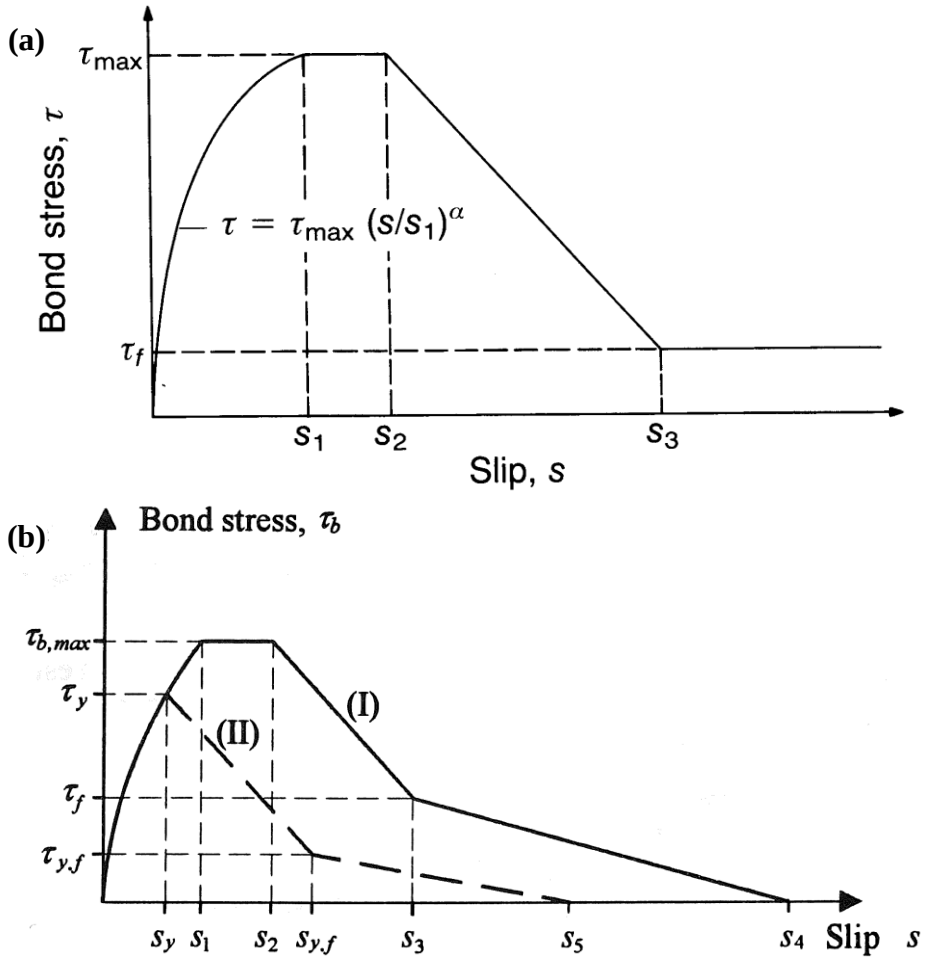

Figure 3.13: Generalized bond-slip models for normal and high-strength concretes

If pull-out happens while reinforcement is still in its elastic response range, both of the above models are capable of predicting the pattern (Figure 3.7, graph 4A) quite accurately. However as soon as the steel bar enters its post-yield range, bond-slip follows the same pattern as that of stress-strain curves of the bare bar. This particularly means that if a yield plateau exists in the response of steel bar, the same plateau shows up even in the bond-slip curves (Figure 3.7, graphs 1, 2, 3, and 5). According to the results of this study and based on the CEB-FIP-MC (1993) bond model (Figure 3.13-a), a new model is proposed in order to predict and match the actual bond-slip response of the steel bars in their post-yield range more accurately. Figure 3.14 depicts the proposed model described by equations 3.11 to

3.16 and Table 3.10 shows the recommended values of the model parameters calibrated based on the experimental results.

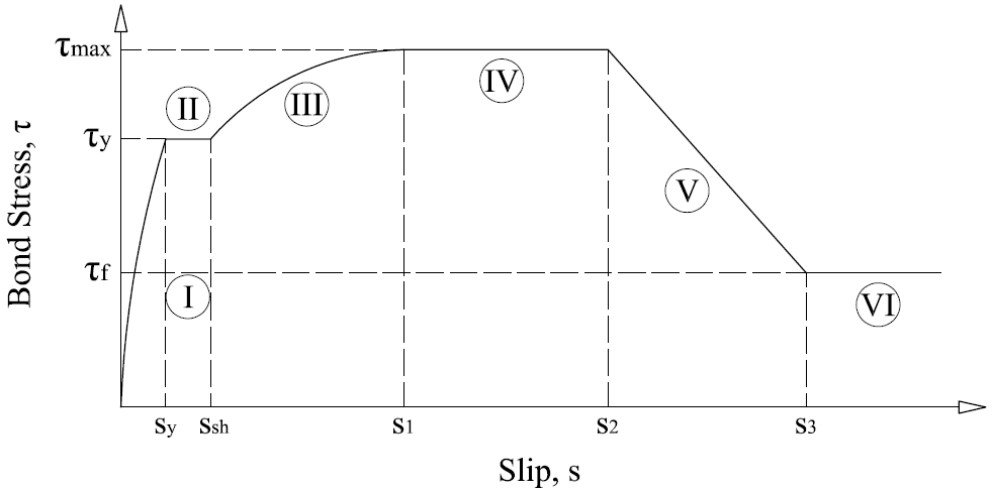

Figure 3.14: Proposed bond-slip model for predicting post-yield behaviour of deformed bars

$$\tau = \tau_y \times \left(\frac{s}{s_y}\right)^{\alpha} \qquad o \le s \le s_y \qquad 3.11$$

$$\tau = \tau_y \qquad s_y < s \le s_{sh} \qquad 3.12$$

$$\tau = \left(\tau_{\max} - \tau_y\right) \times \left(\frac{s - s_{sh}}{s_1 - s_{sh}}\right)^{\beta} + \tau_y \qquad s_{sh} < s \le s_1 \qquad 3.13$$

$$\tau = \tau_{\max} \qquad s_1 < s \le s_2 \qquad 3.14$$

$$\tau = \tau_{\max} - \left(\tau_{\max} - \tau_f\right) \times \left(\frac{s - s_2}{s_3 - s_2}\right) \qquad s_2 < s \le s_3 \qquad 3.15$$

$$\tau = \tau_f \qquad s_3 < s \qquad 3.16$$

where,

τ = Bond stress (MPa)

τ_f = Residual bond stress (MPa)

τ_{max} = Maximum bond stress (MPa)

τ_y = Bond stress at yield point (MPa)

s = Slip (mm)

s_{sh} = Slip at strain hardening point (mm)

s_y = Slip at yield point (mm)

Table 3.10: Typical choice of parameters required for the proposed bond-slip model

Parameters	Values for high-strength concrete
α	0.5 for both steel grades
β	0.3 for 300 and 0.4 for 500 steel grade
τ_f	0.4 τ_{max}
τ_{max}	1.5 τ_y for 300 and 1.2 τ_y for 500 steel grade
τ_y	Calculated using f_y for each steel grade and considering bond area
s_1	0.5 mm for both steel grades
s_2	3.0 mm for both steel grades
s_3	Clear rib spacing
s_{sh}	0.10 mm for 300 and 0.15 mm for 500 steel grade
s_y	0.05 mm for 300 and 0.10 mm for 500 steel grade

Based on the experimental results, in addition to a decrease of about 15% in bond capacity after yield, there is a reduction of about 70% and 85% in bond stiffness (the slope of the bond-slip curve just before and after the yield plateau) of 300 and 500 grade bars. Although the increment of slip over the yield plateau is small (0.05 mm in this case) it plays an important role and should not be neglected. The plateau (branch II) in the bond-slip response divides the ascending branch of the model into two parts of different stiffness (branches I and III). One should always notice that in the proposed bond model, the value of 's_1' is highly sensitive to the bond length. It is important noticing that the proposed model is capable of being calibrated for different test conditions and variables in order to predict bond-slip behaviour of different concrete and steel types. For example if pull-out happens in the elastic range of the steel bar, the value of "τ_y" and "s_{sh}" should simply be equated to zero and all equations remain valid. Figure 3.15 compares the modified bond-slip model with the experimental results of this study, which shows a close agreement between the two.

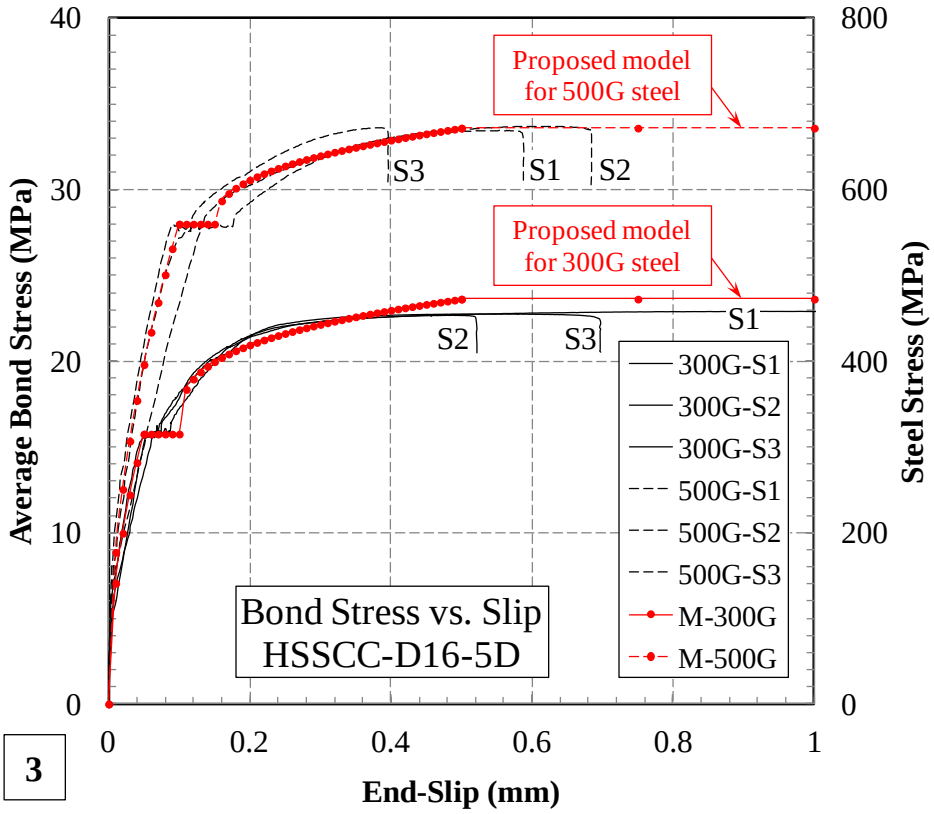

Figure 3.15: Proposed bond-slip model versus the experimental results

3.2.5 CONCLUSIONS AND RECOMMENDATIONS

Through a systematic mix design method and laboratory trials, a high-strength self-compacting concrete (HSSCC) and a conventionally vibrated high-strength concrete (CVHSC) mix were developed. Pullout specimens consisting of different bar diameter, steel grades, and bond lengths were cast from both concrete types and tested under monotonic loading. The load, steel strain, slip at the unloaded end, and change in bar diameter were measured until the specimen failed either by bond, reinforcement rupture, or concrete block splitting. Proper confinement was provided to avoid concrete splitting failure and different specimens were designed in such a way that pull-out occured in elastic (2.5D specimens) as well as post-yield (5D and 7.5D specimens) phases of the steel bars.

After analysing the experimental results of pullout specimens with the same bond length, significant difference was observed between the ultimate bond-stress of specimens with 300G and 500G steel bars. Given that the geometry of different grade bars (rib height and area) was identical, the same bond-stress level was expected at the initiation of pull-out;

this made the observed difference difficult to be comprehended. Nevertheless, an explanation for this behaviour was found through a series of further investigations. A relationship was established between end-slip and average strain which was compared with the bond-strain-slip model developed by Maekawa et al. (2003). A modification was proposed to the original slip-strain model and it was shown that once pull-out (including free-end slip) starts, the relationship between slip and strain is no longer unique.

It was also found that the reduction of bar diameter has a considerable effect on bond performance in the post-yield phase compared to when pull-out happens in the elastic response range of the steel bars. Reduction of bar diameter affects the bond performance even more when high-ductility bars (300 grade) are used; because, their diameter reduces more before failure. Therefore, overall bond performance of grade 500 bars was generally better than 300 grade ones. In the available bond literature, the effect of bar ductility/grade on bond performance has never been investigated in detail. Experimental results of this research showed that in the post-yield range, 500 grade bars can provide ultimate bond-stress levels of up to 1.4 times higher than 300 grade ones. In other words, 300 grade bars showed a diameter reduction of about 50% more than 500 grade ones before failure which in turn deteriorated the bearing capacity of ribs on concrete keys.

In specimens with 2.5D bond-length, pull-out happened in elastic range for 500 grade bars. Nevertheless, the 300 grade bars just exceeded their yield point at the ultimate bond stress; hence, they had a lower ultimate bond stress compared to that of 500 grade ones. In case of 7.5D bond length specimens, excessive bond length resulted in very small slip values (maximum of 0.07 and 0.18 mm for 300 and 500 grade bars respectively); therefore, different bond-slip mechanisms between the two grade bars could not be noticed. It should be noted that in this case, the slight difference between the ultimate bond strength of 300 and 500 grade bars was only due to higher load capacity of the latter.

It is explained in Fib-Bulletin-10 (2000) that the yield plateau of the bare bar stress-strain response vanishes in the member response. On the contrary, in the specimens in which pull-out happened in the post-yield range of bars, a visible yield plateau could be observed in the bond-slip and slip-strain curves. This plateau divides the ascending branch of the bond-slip curves into two parts of different bond stiffness. Based on the experimental results of this study and using the CEB-FIP-MC (1993) bond model, a modified model has

been proposed for the bond of deformed bars of different grade in the post-yield range. The proposed model is capable of predicting the experimental results more accurately and can be calibrated to represent different experiments.

In the current research, the authors focused on bond properties of HSSCC and CVHSC and rebars of different steel grades. This introduced a new parameter (effect of reduction in bar diameter and ductility after yield) which was found to affect the bond between concrete and reinforcement of different steel grades. In addition, the yield plateau was found even in the member response and a modified bond model was proposed to capture this behaviour. A future research should focus on a more detailed assessment of this phenomenon and its effects on bond properties of reinforcement and concrete in different concrete types and strengths. Precise measurements of the bar diameter at different locations along the bar and throughout the test (rather than just before and after) is suggested in future research. In addition, introducing this parameter into relevant computer programs, which are used to numerically model bond, is also desirable in the long run.

3.3 REFERENCES

AS/NZS-4671 2001, 'AS/NZS 4671 Steel Reinforcing Materials'. Australian/New Zealand Standards, p. 49.

Castel, A, Vidal, T, Viriyametanont, K & Francois, R 2006, 'Effect of reinforcing bar orientation and location on bond with self-consolidating concrete', ACI Structural Journal, vol. 103, no. 4, pp. 559-567.

Cattaneo, S & Rosati, G 2009, 'Bond between Steel and Self-Consolidating Concrete: Experiments and Modeling', ACI Structural Journal, vol. 106, no. 4, pp. 540-550.

CEB-FIP-MC 1993, 'Model Code 1990: Design Code'. T. Telford, London.

Chan, Y-W, Chen, Y-S & Liu, Y-S 2003, 'Development of bond strength of reinforcement steel in self-consolidating concrete', ACI Structural Journal, vol. 100, no. 4, pp. 490-498.

De Almeida Filho, FM, El Debs, MK & El Debs, ALHC 2008, 'Bond-slip behavior of self-compacting concrete and vibrated concrete using pull-out and beam tests', Materials and Structures/Materiaux et Constructions, vol. 41, no. 6, pp. 1073-1089.

Desnerck, P, De Schutter, G & Taerwe, L 2010, 'Bond behaviour of reinforcing bars in self-compacting concrete: Experimental determination by using beam tests', Materials and Structures/Materiaux et Constructions, vol. 43, pp. 53-62.

EFNARC 2002, Specification and Guidelines for Self-Compacting Concrete, European Federation of Procedures and Applicators of Specialist Products for Structures

EFNARC 2005, The European Guidelines for Self-Compacting Concrete Specification, Production and Use, European Federation of Procedures and Applicators of Specialist Products for Structures

Esfahani, MR, Lachemi, M & Kianoush, MR 2008, 'Top-bar effect of steel bars in self-consolidating concrete (SCC)', Cement and Concrete Composites, vol. 30, no. 1, pp. 52-60.

Fib-Bulletin-10 2000, 'Fib (CEB-FIP) Bulletin 10, Bond of reinforcement in concrete: state-of-art report', vol. 10., no. Book, Whole

Hassan, AAA, Hossain, KMA & Lachemi, M 2010, 'Bond strength of deformed bars in large reinforced concrete members cast with industrial self-consolidating concrete mixture', Construction and Building Materials, vol. 24, no. 4, pp. 520-530.

Hossain, KMA & Lachemi, M 2008, 'Bond behavior of self-consolidating concrete with mineral and chemical admixtures', Journal of Materials in Civil Engineering, vol. 20, no. 9, pp. 608-616.

Hwang, S-D, Khayat, KH & Bonneau, O 2006, 'Performance-based specifications of self-consolidating concrete used in structural applications', ACI Materials Journal, vol. 103, no. 2, pp. 121-129.

Khayat, KH 1999, 'Workability, testing, and performance of self-consolidating concrete', ACI Materials Journal, vol. 96, no. 3, pp. 346-353.

Khayat, KH, Manai, K & Trudel, A 1997, 'In situ mechanical properties of wall elements cast using self-consolidating concrete', ACI Materials Journal, vol. 94, no. 6, pp. 491-500.

Lachemi, M, Bae, S, Hossain, KMA & Sahmaran, M 2009, 'Steel-concrete bond strength of lightweight self-consolidating concrete', Materials and Structures/Materiaux et Constructions, vol. 42, no. 7, pp. 1015-1023.

Maekawa, K, Pimanmas, A & Okamura, H 2003, Nonlinear mechanics of reinforced concrete, Spon Press, New York.

Ozawa, K, Maekawa, K, Kunishima, M & Okamura, H 1989, 'Development of high performance concrete based on the durability design of concrete structures', in

Proceedings of the 2nd East-Asia and Pacific Conference on Structural Engineering and Construction (EASEC-2), vol. 1, pp. 445-450.

RILEM-FIP-CEB 1973, 'Tentative recommendations, recommendations for reinforcing steel, bond test for reinforcing steel: 1- Beam test (7-II-28 D) 2- Pull-out test (7-II-128)', Materials and Structures, vol. 6, no. 2, pp. 79-118.

Soleymani Ashtiani, M, Dhakal, RP & Scott, AN 2011a, 'Bond properties of reinforcement in high-strength self-compacting concrete', in Proceedings of the 9th Symposium on High Performance Concrete Design, Verification and Utilization, Rotorua, New Zealand.

Soleymani Ashtiani, M, Scott, AN & Dhakal, RP 2011b, 'Mechanical properties of high-strength self-compacting concrete', 21st Australasian Conference on the Mechanics of Structures and Materials, ACMSM21, December 7, 2010 - December 10, 2010, CRC Press, Melbourne, VIC, Australia, pp. 827-832

Su, N, Hsu, K-C & Chai, H-W 2001, 'A simple mix design method for self-compacting concrete', Cement and Concrete Research, vol. 31, no. 12, pp. 1799-1807.

Valcuende, M & Parra, C 2009, 'Bond behaviour of reinforcement in self-compacting concretes', Construction and Building Materials, vol. 23, no. 1, pp. 162-170.

Zhu, W, Sonebi, M & Bartos, PJM 2004, 'Bond and interfacial properties of reinforcement in self-compacting concrete', Materials and Structures/Materiaux et Constructions, vol. 37, no. 271, pp. 442-448.

4 CYCLIC BOND BEHAVIOUR OF DEFORMED BARS IN HSSCC

Soleymani Ashtiani, M, Dhakal, RP, Scott, AN & Bull, DK 2013, 'Cyclic beam bending test for assessment of bond–slip behaviour', *Engineering Structures*, vol. 56, no. 0, pp. 1684-1697.

Soleymani Ashtiani, M, Dhakal, RP & Scott, AN 2012, 'Cyclic Beam Bending Test for Assessment of Bond-Slip Behaviour', in *15th World Conference on Earthquake Engineering*, Lisbon, Portugal.

Soleymani Ashtiani, M, Dhakal, RP, Scott, AN & Bull, DK 2013, 'Experimental investigations on cyclic bond-slip behaviour of reinforced concrete members', in *New Zealand Concrete Industry Conference*, Queenstown, New Zealand.

4.1 ABSTRACT

This paper presents the details of a novel cyclic beam testing method to assess the bond performance of steel bars in reinforced concrete members under reversed cyclic bending actions. The beam specimen originally proposed by RILEM for assessment of bond properties under monotonic flexural loading is modified to sustain displacement reversals without premature buckling of the bar. RILEM suggests a two-point loading (four-point bending) setup for testing beam specimens which would work only under monotonic loading. Hence, a new test setup is designed in such a way that the application of reversed cyclic loading becomes feasible to obtain the cyclic bond-slip relationship. Special attention is paid to ensure the stability of the proposed test setup and to ascertain that no unwanted forces are generated in the system during the course of the test. Performance of the devised cyclic test setup and modified specimen is scrutinised and remedial measures are discussed for the potential issues that may affect the functionality of the proposed testing method. Finally, the cyclic bond test results are compared with the results of the most commonly used pullout tests to validate that the bond stress and slip obtained from the proposed test are reliable.

4.2 INTRODUCTION

Bond between reinforcement and concrete is one of the most important aspects in structural response of reinforced concrete (RC) members. Basic RC theories assume compatibility of strains between concrete and steel which is valid only if a perfect bond exists between the two materials. Therefore investigating bond between concrete and reinforcing bars under different loading conditions is of great importance and it has been the focus of many investigations in the past. Several researchers have explored bond between steel and concrete using different test setups and specimens such as direct pull-out, beam anchorage and beam-column joint tests (Alavi-Fard et al., 2002; Desnerck et al., 2010; El-Hacha et al., 2006; Popov, 1984). Nevertheless, direct pull-out tests with different arrangements appear to be the most commonly preferred approach for investigating bond properties of reinforcement and concrete under both monotonic and cyclic loads (Alavi-Fard et al., 2002; Campione et al., 2005; Cattaneo et al., 2009; Chan et al., 2003; Fang et al., 2006). The main reasons of choosing pull-out tests over the other methods are the simplicity in producing specimens and the ability of isolating the effects of different parameters on the overall bond performance. However in most of the available pull-out test setups, concrete and steel work under different stress states; i.e. at the same time when the latter experiences tension, the former is in compression and vice versa. This is not a real condition in structural members where either both concrete and steel are in tension or in compression. Especially, in the case of high strength concrete, direct pull-out tests may not necessarily represent the actual behaviour (De Almeida Filho et al., 2008). Other test setups and specimens have also been developed to more accurately replicate the actual state of stress in real structures.

In addition to the common pull-out test, RILEM-FIP-CEB (1973) provides a test setup and specimen specifications for a beam bending test to investigate bond between reinforcing bar and concrete under monotonic two-point flexural loading. Figure 1.4 shows details of the beam bending test recommended by RILEM. The beam specimen comprises of two half-beams connected to each other at the centre with a steel hinge (on the top) and a deformed bar (at the bottom). This way when the specimen is loaded, the bending moment at the centre of the beam is taken care of by the steel hinge (in compression) and the deformed bar (in tension) only. Therefore in the section analysis, the effect of concrete is

eliminated which in turn reduces the complexity of dealing with concrete compression block. In addition to the main reinforcing steel in which the bond is assessed, there exists other reinforcement (auxiliary steel) in each half of the beam as shown in Figure 1.4. This extra reinforcement is required to account for the shear and bending forces as well as to represent the effect of confinement provided by transverse reinforcement (which does exist in real structural members) on the bond performance.

Figure 4.1: Details of the RILEM beam specimen for two-point monotonic loading (all dimensions are in “mm”)

RILEM pull-out and beam bending test setups and specimens were originally designed for assessing bond under monotonic loading. It should be noted that although the beam test has some advantages over the direct pull-out test, due to the complexities involved in both test setup and specimen fabrication, fewer studies have been performed using the RILEM beam test (Dancygier et al., 2010; De Almeida Filho et al., 2008; Desnerck et al., 2010; El-Hacha et al., 2006). While some modifications have been suggested for the RILEM beam test setup and specimen, all of the reported studies were performed using monotonic loading.

Although researchers have extensively explored bond-slip relationships for different concrete and steel types under monotonic loading using different test setups, less is reported on bond properties under reversed cyclic loading. As real structures are subjected to load reversals (earthquake, wind and live load) during their life-span, it is important to investigate their behaviour under cyclic loads.

Modified pullout tests have previously been used to investigate cyclic bond-slip relationships (Alavi-Fard et al., 2002; Campione et al., 2005; Fang et al., 2006). Details of a typical test setup for assessing bond under cyclic loading using pullout specimens (cyclic pullout) are shown in Figure 1.5. The two steel plates adjacent to the concrete specimen faces (one at the top and the other at the bottom) have circular holes of two times the bar diameter as recommended by RILEM. A steel frame which comprises of a combination of two steel plates, 4 bolts and 8 nuts is assembled (as seen in Figure 1.5) in such a way that it holds the concrete specimen and the two steel plates together. The nuts provided at the top and bottom of the steel plates should be properly tightened so that any slack between different parts is eliminated. A slip gauge (usually an LVDT) is fixed on the top steel plate which reads the slip at the free end of the deformed bar; the other end is placed into a griping mechanism located at the fixed end of the testing apparatus. Four steel rods are attached to the top steel plate and are connected to another steel plate just below the reciprocating head of the testing machine. A steel rod connects the top most steel plate and the griping mechanism. The desired loading sequence is applied to the specimen through the reciprocating head of the testing apparatus which can exert both tensile and compressive forces. If a displacement controlled loading regime is used, it can either be controlled by the displacement at the loaded end of the bar or the slip at the free end. For this test a specific type of testing machine capable of applying load reversals is required; the gripping mechanisms also need to be specially designed so that the bars do not slip under cyclic loading. It is obvious that the cyclic pullout test setup is much more demanding than the monotonic pullout test.

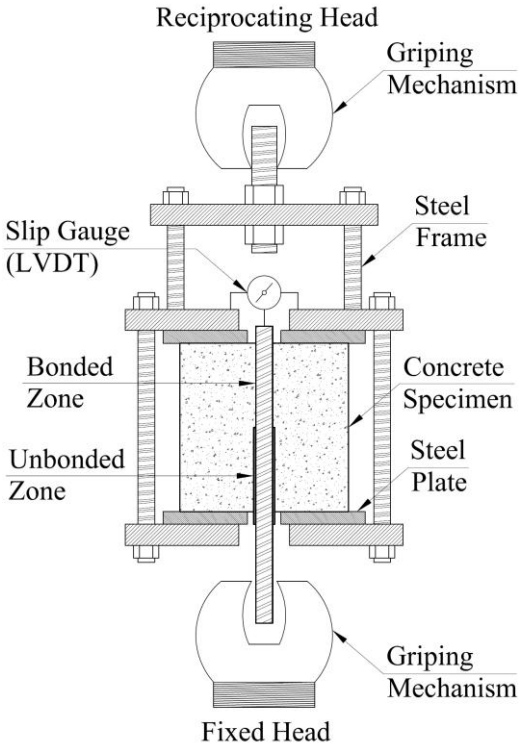

Figure 4.2: Details of a typical cyclic pullout test setup

Nevertheless as mentioned previously, the pullout based bond tests do not represent the actual state of stresses inside RC members subjected to flexural actions. For this purpose, in this study an attempt has been made to modify the beam specimen for the monotonic bond test suggested by RILEM and develop a suitable test setup capable of applying load reversals to the modified specimen. Although the alteration of the RILEM monotonic test setup and specimen bring more intricacy to the system, special attention is paid to keep the details as simple, repeatable and applicable as possible.

4.3 EXPERIMENTAL INVESTIGATIONS

4.3.1 DETAILS OF THE MODIFIED RILEM BEAM SPECIMEN

Most details of the main and auxiliary reinforcement in the modified specimen were unchanged from the original RILEM-FIP-CEB (1973) specifications. However, some modifications were required in order to test the beams under cyclic loading. First, because high-strength concrete with higher splitting tensile strength (thus higher bond stress) was used, the bond-length between concrete and steel was reduced from 10 to 5 times bar

diameter (80 mm in this case). The decision on appropriate bond-length was made based on the outcome of previous experimental studies on bond performance of deformed bars and concrete (Soleymani Ashtiani et al., 2011a). Second, the position of bond-length was relocated from the centre of each half-beam towards the centre of the beam specimen. This alteration was adopted in order to reduce the unbonded length of the bar between the two bonded regions. This effectively reduces the potential buckling length, which in turn delays the bar buckling during the course of the test (Dhakal et al., 2002). It should be noted that in the present study, only the specimen type B (larger specimen as stated in RILEM) was used (see Figure 4.3).

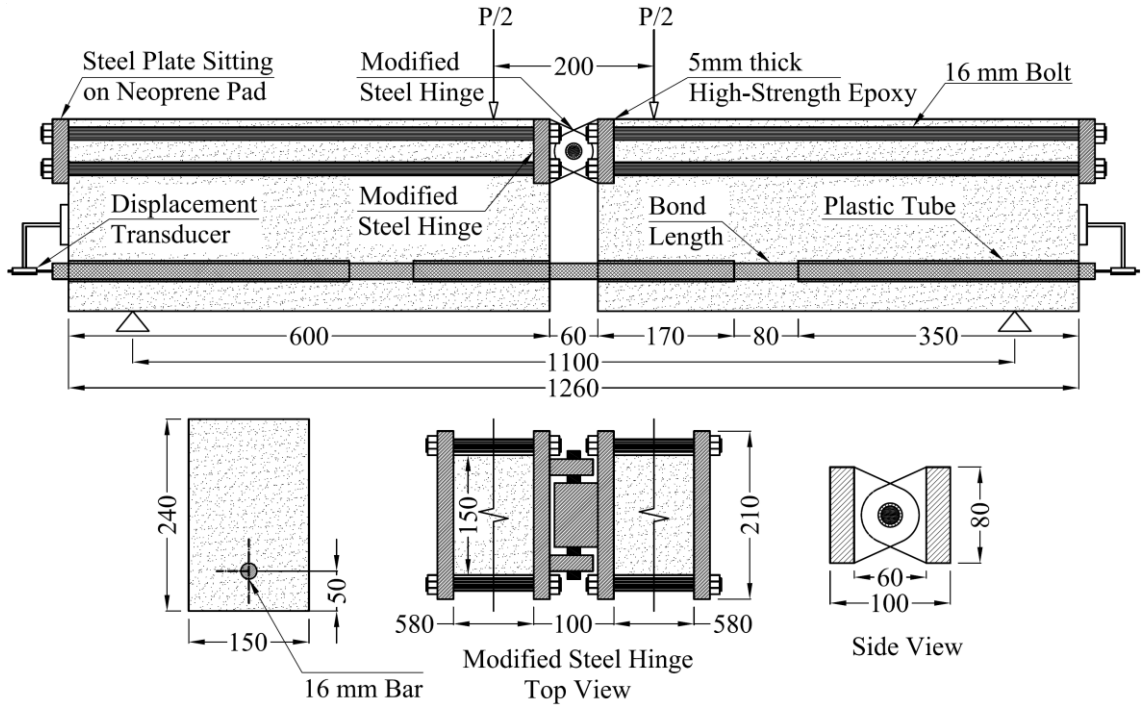

Figure 4.3: Details of the modified RILEM beam specimen for cyclic loading (all dimensions are in "mm")

Being designed for a monotonic test, the RILEM original beam was unable to take cyclic load; because the steel hinge at the top could only take compressive forces. Should any load reversals happen, the steel hinge starts tearing apart as soon as the compressive force reaches zero and tensile force tends to develop at the top of the beam. Therefore, a replacement for the original steel hinge recommended by RILEM was required to suit the cyclic nature of the test. For this purpose a modified steel hinge was designed and fabricated with a high-strength pin of 1100 MPa tensile strength (precision machine made) and a bearing mechanism which made it capable of taking both compressive and tensile

forces with little friction involved. Figure 4.3 shows the modified steel hinge; both in detail, and as installed on the specimen. Using steel plates, neoprene pads and steel bolts and nuts, a locking mechanism was designed (as shown in Figure 4.3) in order to install the hinge on the beam specimen. It is important noting that the mentioned mechanism was devised externally; so that, the same hinge could be utilized for testing different specimens. A 5 mm gap was provided between the faces of the steel hinge and the beam which was later filled with a high strength epoxy (left for 12 hours for strength development) before locking the steel hinge to the specimen.

4.3.2 DETAILS OF THE PROPOSED CYCLIC TEST SETUP

As mentioned earlier, the original test setup recommended by RILEM-FIP-CEB (1973) was a simple two-point loading (four-point bending) arrangement which sufficed the purpose of monotonic testing. In a monotonic setup, additional internal forces affecting the behaviour of the element can easily be taken care of by using steel rollers at supports and loading points. The usual practice is to employ two different arrangements for the steel rollers: 1- free rotation and translation (roller support) 2- free rotation and restrained translation (pin support) (Figure 4.4). It is important to notice that as the steel plates sitting on the face of concrete are not clamped to the specimen (as in the cyclic version) and the loading is on the side opposite to the supports, having two pins (one at support and the other at loading point) does not bring indeterminacy to the system (it is different in case of cyclic test which is explained in the following sections). This way the length of beam element can freely increase/decrease under flexure avoiding generation of unwanted internal constraints. Note that the specimen and test setup together should act as a stable yet determinate rigid body at all times to make sure that the behaviour is not complicated by extra constraints.

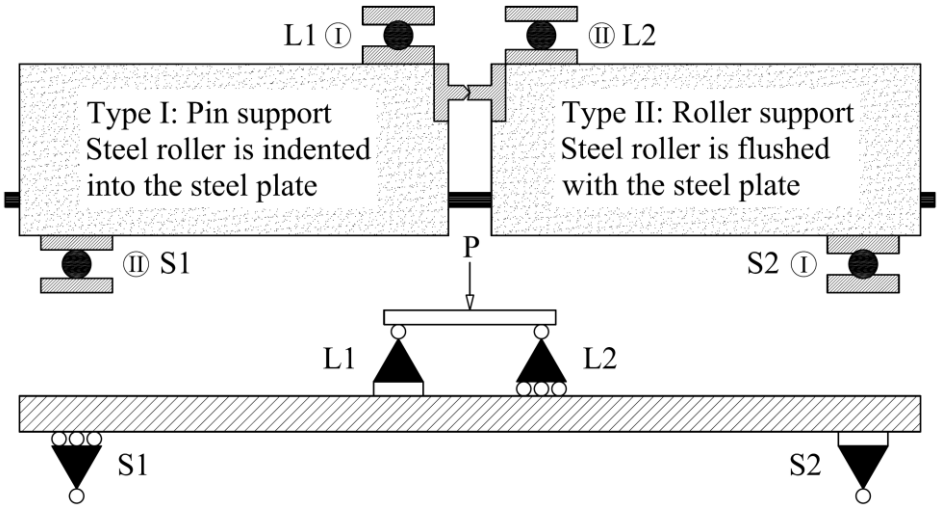

Figure 4.4: Schematic view and details of supports and loading points in monotonic test

Nevertheless, the generation of both tensile and compressive forces in a cyclic test makes the monotonic test setup inapplicable, and a different test setup is required. Here too, the basic requirements are the same; i.e. the system should be stable and determinate at all time during the test without having extra internal or external constraints. It is obvious that a clamping mechanism is necessary in order to hold the beam at both supports and loading points so that the load can be reversed in a stable manner. Hence, the support clamping mechanism and the connection between the loading point and the specimen (as shown in Figure 4.4) needed to be redesigned to enable cyclic loading. Unlike in the monotonic test setup, all points (namely L1, L2, S1, and S2 in Figure 4.4) should be clamped to the specimen in the cyclic test setup. In the case of the former, this ideally requires 2 pins (one at a support and the other at a loading point); however the same arrangement in the latter adds an undesirable constraint to the setup. Therefore, one of the pins is replaced with a roller to maintain a determinate structure; thus three rollers and one pin makes the cyclic test setup stable and determinate. Figure 4.5 shows a schematic view and details of the mentioned concept and requirements. In order to maintain uniform distribution of loads from the setup to the specimen, all steel plates sit on neoprene pads which in turn rest on the specimen surface.

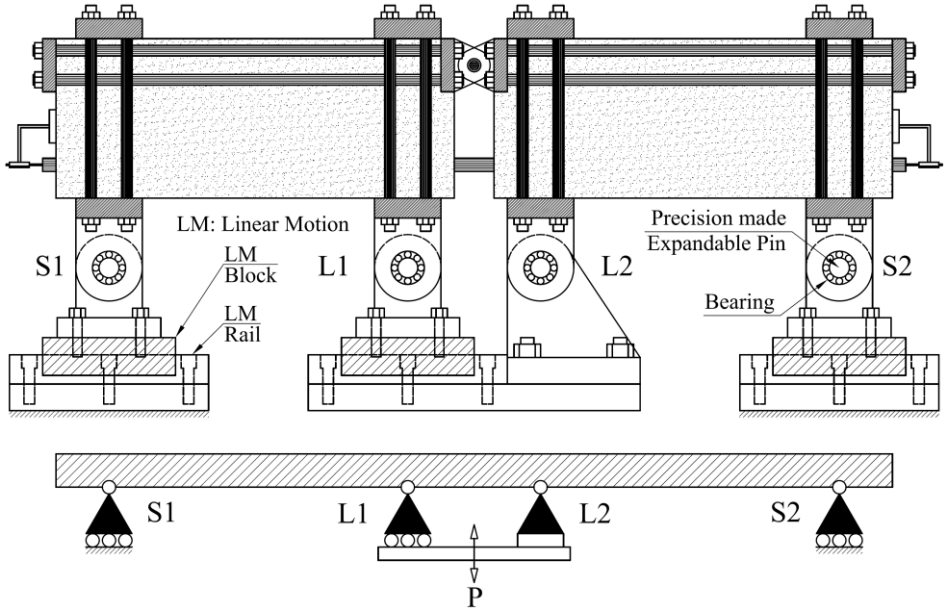

Figure 4.5: Schematic view and details of supports and loading points in cyclic test

In order to achieve the explained set of requirements for the supports and loading points of the cyclic test, special rollers (linear motion – LM) and precision made expandable pins are used (Figure 4.5). The LM roller is a specially made unit which possesses a very high accuracy with high load and moment carrying capacity. Only the movement in the direction of LM rail is possible and all other translations and rotations are restricted. In other words, the LM roller is a fixed-roller support which provides a virtually slack-free and friction-less rolling movement even under high axial and bending forces (Figure 4.6).

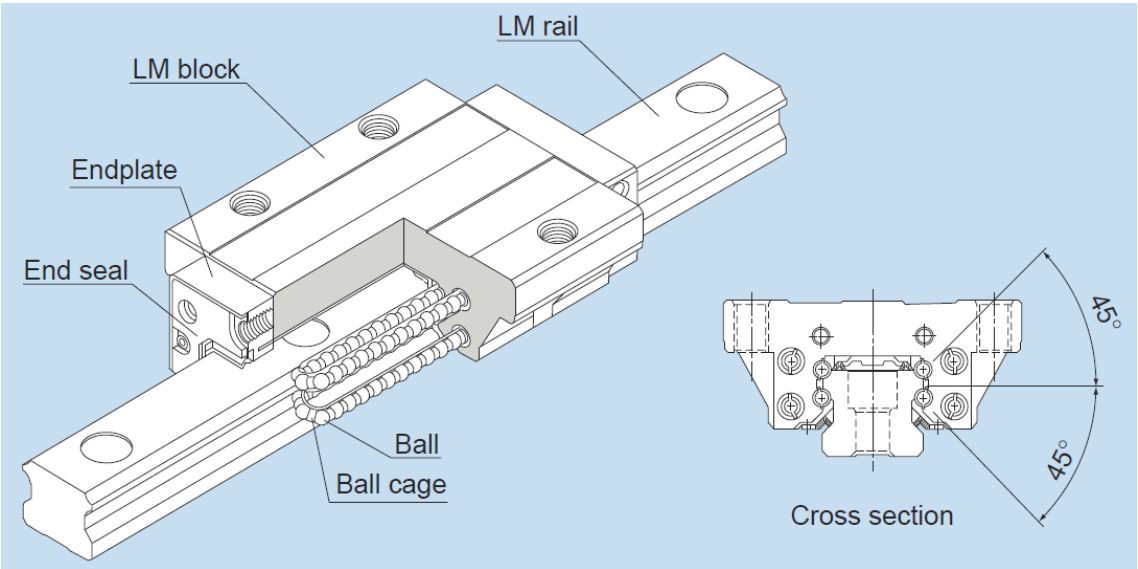

Figure 4.6: Details of the Linear Motion (LM) rollers used in the cyclic test setup

The pins shown in Figure 4.5 were specially-made expandable precision pins which were combined with spherical plain (SP) bearings to take up practically all of the slack in the system and form a friction-less pin support. Each pin consisted of a central 16 mm high tensile bolt and nut, 2 steel washers at the ends, 3 cone-shaped steel pieces symmetrically placed at the ends and the centre, and 2 expandable notched steel bushes (Figure 4.7). Tightening the bolt and nut forces the cone-shaped parts into the notched bushes which result in expansion of the pin. Note that the combination of LM rollers, steel plates, expandable pins, and SP bearings renders the roller supports suitable for the cyclic test (Figure 4.5). Finally, Figure 4.8 shows a modified beam specimen together with the proposed cyclic test setup as described in the previous sections.

Figure 4.7: Details of the expandable pins used in the cyclic test setup

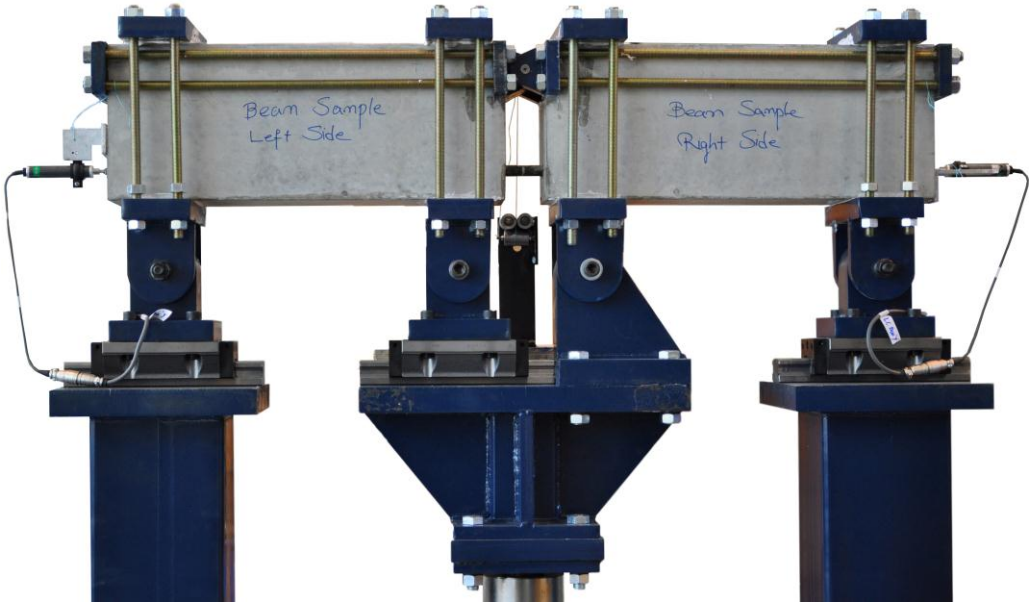

Figure 4.8: Details of the proposed cyclic test setup and modified RILEM beam specimen

4.3.3 MATERIAL PROPERTIES AND MIX DESIGN DETAILS

A high-strength self-compacting concrete (HSSCC) mix was developed using general purpose cement (GPC), fly ash (Class C), and a third generation polycarboxylic ether polymer based superplasticizer. Locally available coarse aggregate (semi-crushed of maximum size 13mm), fine aggregate (natural river sand), and potable water were used in both concrete mixes. Details of physical properties of the cement, fly ash, and aggregates used in the mix are described in a previous study by the authors (Soleymani Ashtiani et al., 2011b; Soleymani Ashtiani et al., 2013). The mix design method proposed by Su et al. (2001) and guidelines provided by EFNARC (2002,2005) were used in order to reach an initial mix proportioning for HSSCC and a finalized mix was obtained through a series of laboratory trials. Table 4.1 shows the finalized mix design for HSSCC.

Table 4.1: Mix proportions of HSSCC

Material	HSSCC (kg/m^3)
Coarse aggregate	880
Fine aggregate	870
Cement	385
Fly ash	165
Water	165
Super-plasticizer	3.575 (0.65%)

Compressive and splitting tensile strengths of the HSSCC were measured (using standard cylinders) to be 97.5 MPa and 7.7 MPa respectively on the day of test (28 days after casting). Deformed 16 mm diameter steel reinforcement of grade 500 having yield and ultimate strengths of 560 MPa and 670 MPa respectively was used as the main deformed bar. Round 10 and 12 mm mild-steel bars of grade 300 were used as auxiliary reinforcement to replicate the confinement effects and take care of the shear and bending forces in each half of the beam specimen as explained before.

4.3.4 LOADING PROTOCOL AND MEASUREMENTS

The displacement pattern shown in Figure 4.9-a was fed to the hydraulic actuator through a computerized controller program. A total of six different cycles (measuring ±1, ±2, ±4, ±8, ±16, and ±32 mm) were applied to the specimen with displacement increments of 0.5 mm in each step.

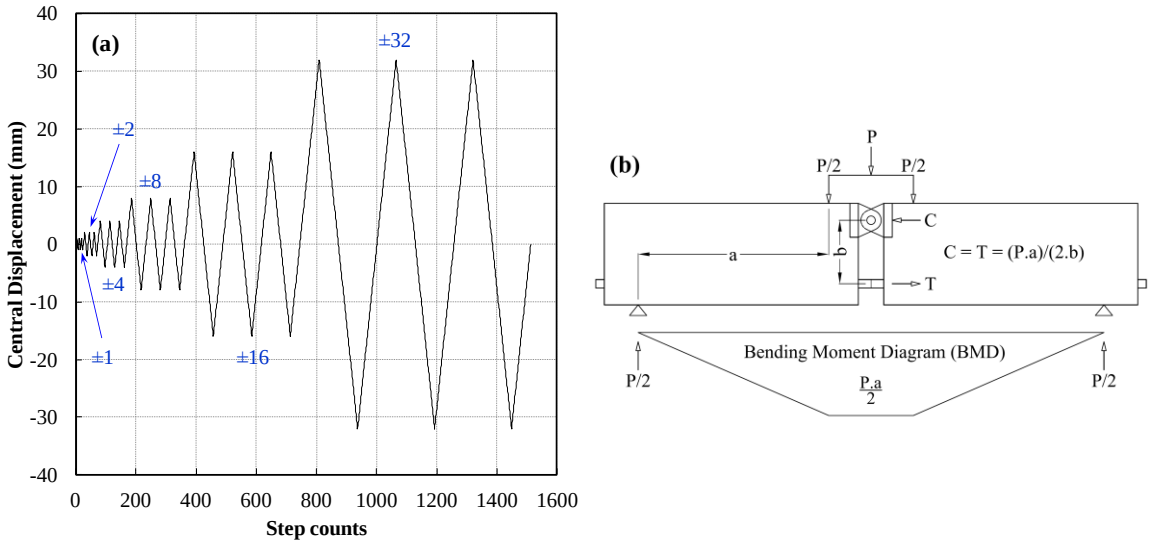

Figure 4.9: Displacement protocol applied to the centre of the beam specimen (a) and the force calculation concept of RILEM in the deformed bar (b)

Each cycle was repeated three times in order to replicate the effects of loading reversals on bond. Positive (+) and negative (-) displacement values account for the upward and downward movement of the centre of the beam specimen, respectively. The cyclic loading was applied through a displacement controlled actuator of 400 kN capacity connected to

the centre of the beam specimen through L1 and L2 (Figure 4.5). The generated loads were measured using a load-cell located between the actuator and the loading points. Central displacement of the specimen was measured using a rotary potentiometer of 200 mm traverse connected to the centre of the steel hinge (located at the top-centre of the beam). In addition, the slip of the bar was recorded throughout the test using two linear variable displacement transducers (LVDTs) of 10 mm traverse and 0.001 mm least count, one at each end of the beam. Lateral movement of the actuator was monitored (using a linear potentiometer of 20 mm traverse) during the test in order to make sure that no internal forces were generated in either the specimen or the test setup. Measurements showed that there was no lateral movement in the actuator meaning that the whole system was in a balanced condition throughout the test. Using the guidelines provided in RILEM-FIP-CEB (1973), the geometry of loading and the distance between the steel hinge and the deformed bar (Figure 4.9-b), the load measured in the loadcell (central load) was converted into the tension and compression force in the deformed bar at the bottom of the specimen.

4.4 RESULTS AND DISCUSSIONS

The relationship between the applied total vertical load as well as the corresponding axial force induced in the bar and the central displacement of the beam is plotted in Figure 4.10a. It is important mentioning that due to the physical constraints imposed by the movement of the sliding supports; especially the one at the centre of the specimen (L1 in Figure 4.5), the displacement reversals of the test set up were limited to 45 mm and 105 mm in the positive (upward) and negative (downward) directions, respectively. In other words, when the centre of the beam is pushed upwards (positive cycles), the central roller (L1) moves towards L2 (Figure 4.5) and the provided gap of 50 mm between L1 and L2 will be filled by the time a maximum of +45 mm central displacement is applied. Likewise, in negative cycles when the centre of the specimen is pulled downwards, the roller (L1) moves away from L2. By the time a maximum of -105 mm central displacement is applied, L1 reaches halfway out of the rail (i.e., 150 mm movement from its original location) and it would not be safe to pull the specimen further in the negative (downward) direction. If the displacements are expected to exceed these limits, the gap between the supports L1 and L2 and/or the allowance of the sliding support L1 should be increased proportionally. However, these displacement limits did not pose any problem in the test conducted in this

study. As it is evident from Figure 4.10-a, the onset of bond failure happened when the central displacement of the specimen was only about 8 mm. The central displacement had reached a maximum of 32 mm only by the time the specimen failed by excessive bond deterioration.

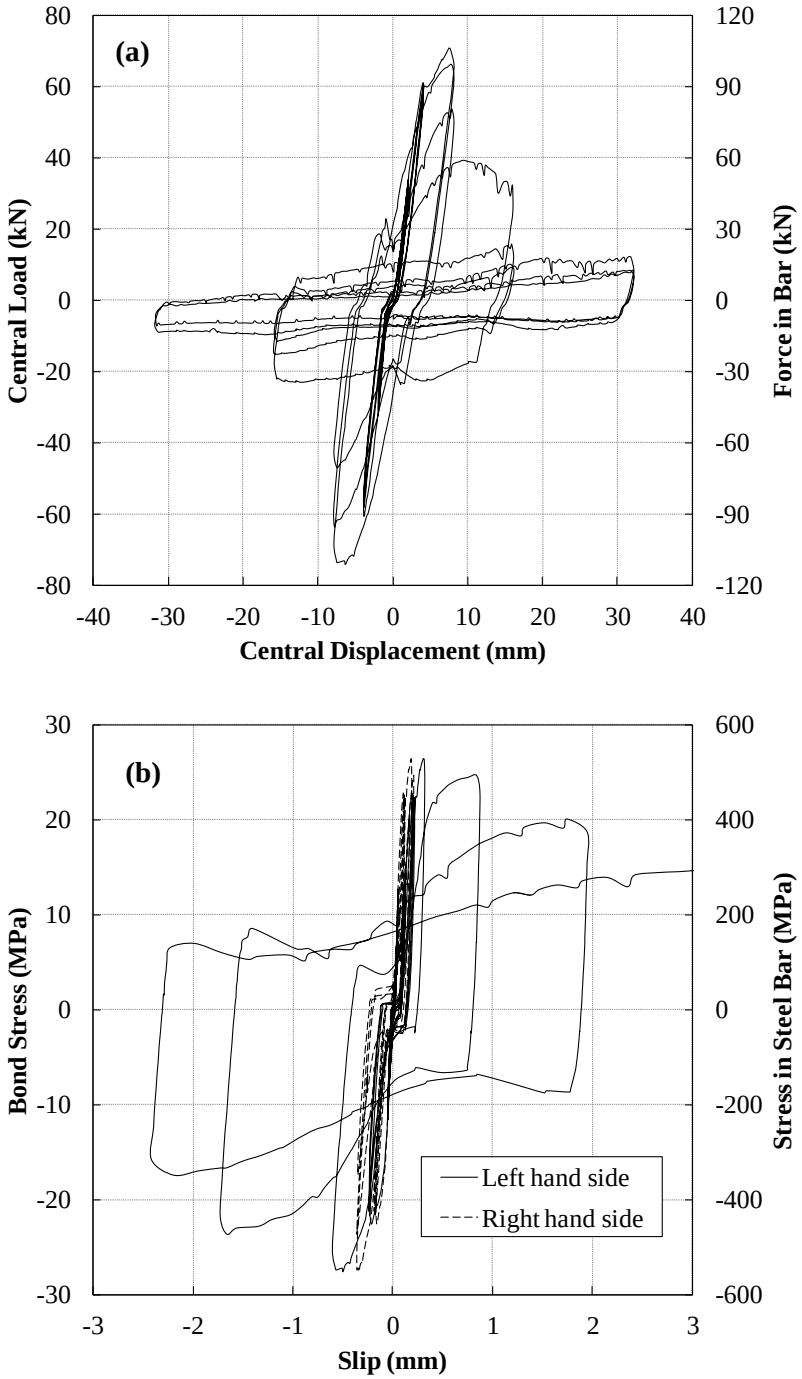

Figure 4.10: (a) Load vs. displacement and (b) averaged bond-stress vs. slip for the sample beam specimen

Figure 4.10-b plots the bond stress as well as the axial stress in the steel bar (shown in the second vertical axis) against the slip. The averaged bond stress was calculated by dividing the tension/compression force in the bar by the contact surface area between the steel bar and concrete. Similarly, the axial stress in the steel bar was calculated by dividing the force in the bar (related to the applied load as shown in Figure 4.9-b) by the cross-sectional area of the deformed bar. In addition, the end-slip of the deformed bar was obtained from the readings provided by the two LVDTs installed at the left and right ends of the beam. It should be noted that the positive (+) and negative (-) load and stress values accounted for compressive (upward movement of the specimen) and tensile (downward movement of the specimen) stresses in the bar, respectively. Although the ±5 mm traverse of the LVDTs (or a total of 10 mm as mentioned previously) was a limiting factor in measuring the end-slip values, it was sufficient to measure 3 mm of slip which represents an acceptable limit for the bond failure (Campione et al., 2005; Cattaneo et al., 2009; De Almeida Filho et al., 2008; Desnerck et al., 2010). Note that the test setup and specimen were not perfectly symmetrical (as opposed to the theoretical assumption); hence, only one side of the beam specimen (either left or right) will fail in pull-out after the ultimate bond stress is reached. In this case, the de-bonding of the deformed bar in the left side caused the final failure of the specimen.

Considering the unsupported distance of 400 mm between the two bonded regions and the cyclic nature of the test with complete displacement reversals, buckling of the bar in the mentioned region could possibly be an issue of this testing arrangement (see Figure 4.3). Nevertheless, no evidence of such phenomenon was observed whatsoever and the deformed bar remained straight throughout the course of the test (Figure 4.11). However, it should be noted that some combination of bonded zone length, steel grade and the concrete compressive strength could avoid (or substantially delay) the bond failure. In such cases, buckling of the bar could well be the failure mode as was observed by the authors in some tests (as reported later) with higher concrete compressive strength and lower steel grade. In the test used herein to describe the nuances of the proposed test method, the bonded length of 5 times bar diameter was chosen based on the results of monotonic pullout tests conducted by the authors in a previous study (Soleymani Ashtiani et al., 2011a).

If cyclic testing is to be conducted on specimens with longer bond length, higher concrete compressive strength or lower steel grade using the proposed test setup, appropriate

adjustments to the loading protocol should be made to limit the displacement reversals in the upward direction so that the bar does not buckle. Another important factor to be considered in designing the proposed test setup is the diameter of the steel pin (located at the centre of the hinge) which takes both the tension and compression forces in different cycles. In this study, a 15 mm diameter steel pin of grade 1100 MPa was used in the steel hinge which sufficed tolerating the imposed forces from a grade 500 MPa 16 mm diameter deformed bar. However, should a larger size reinforcement and/or higher grade steel be used, the diameter of the pin needs to be increased.

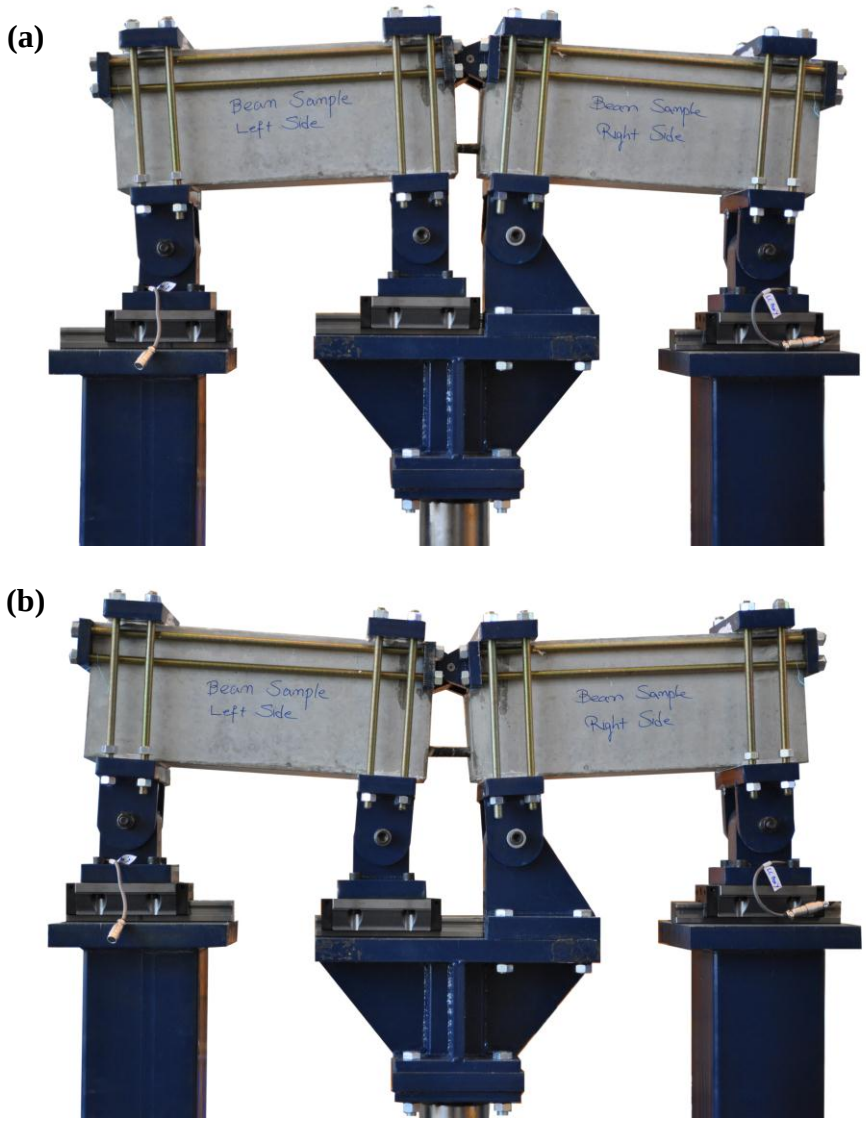

Figure 4.11: Typical pictures of the beam test setup and specimen in positive (a) and negative (b) cycles

Figure 4.10-a, b clearly show a linear phase as well as a nonlinear one in the central load vs. deflection relationship of the beam specimen. In the first three cycles (namely ±1, ±2 and ±4 mm) the specimen responded linearly, and the response deviated towards nonlinearity afterwards. For a better illustration of the transition from the linear to the nonlinear phase, Figure 4.12 shows the central displacement versus slip relationships in two different scales including a closer view. Apparent deterioration of the bond started at the beginning of the ±8 mm displacement cycle in the left side of the specimen (Figure 4.12-a). By the time when the third ±8 mm cycle finished, bond had deteriorated significantly with a slip of about 2 mm (Figure 4.12-b).

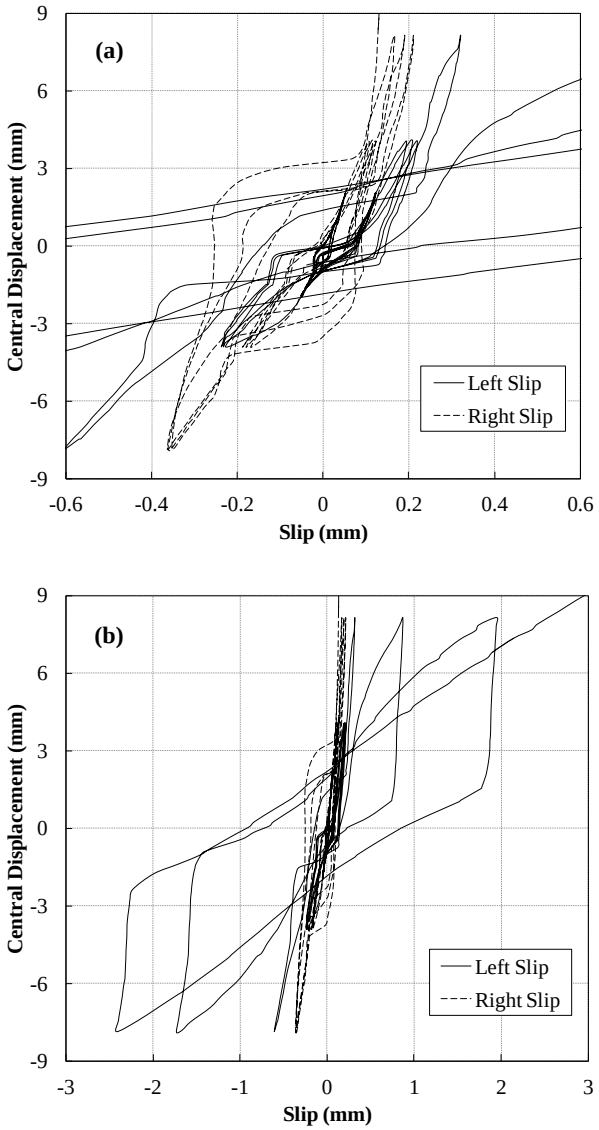

Figure 4.12: Central deflection of the beam specimen against left and right slip for limited values

4.5 COMPARISON WITH PULLOUT TEST RESULTS

Experimental results of the described cyclic test are compared with three equivalent monotonic bond-slip tests (commonly known as the pullout test) performed by the authors in a previous study (Soleymani Ashtiani et al., 2011a). The pullout specimens were cast using a comparable HSSCC of 94.6 MPa compressive strength and 500 grade 16 mm diameter deformed bars of yield and ultimate stresses of 540 MPa and 670 MPa, respectively. The bond length between the deformed bar and concrete was 5 times the bar diameter in all pullout specimens which was the same as in the cyclic beam specimen reported in the previous section. The load was applied to the deformed bar through a hollow-core hydraulic jack of 300 kN capacity and the slip was measured at the unloaded end of the deformed bar using the same LVDT as used in the present study. A schematic view of the pullout test setup and specimens is shown in Figure 4.13.

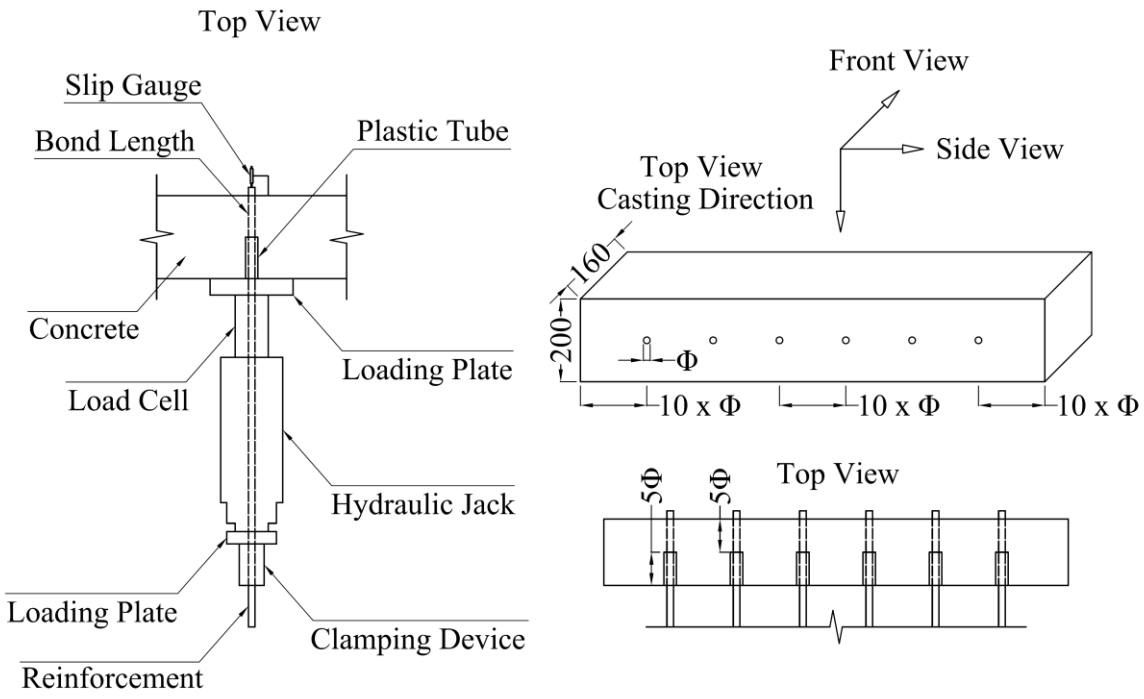

Figure 4.13: Schematic view of the pullout test setup and specimen

Figure 4.14-a shows the bond-slip behaviour of the cyclic beam test in comparison with the monotonic pullout tests. In both monotonic and cyclic tests, bond-slip relationship followed almost the same path as long as the response was in the linear phase. In the nonlinear phase the bond stress continued to increase in the monotonic pullout tests and it

peaked at around 31 MPa at a slip of about 1 mm after which the bond started to deteriorate. However, in the cyclic test the effect of load reversals started deteriorating the bond between steel and concrete after the first cycle of +8 mm displacement, when the bond stress reached its maximum value of about 27 MPa and the slip was about 0.3 mm. In the subsequent cycles, the average cyclic bond stress reduced to just below 24 MPa by the time when the slip reached 1 mm. Overall, the ultimate bond stress levels were slightly higher in the monotonic pullout tests; mainly because of more bond deterioration in the cyclic test.

Figure 4.14-b shows a typical bond-slip performance obtained from cyclic pullout test (Fang et al., 2006), which is used for qualitative comparison with the overall bond-slip behaviour obtained from the proposed cyclic beam test. Details of the test setup and specimens used in this experiment can be found elsewhere (Fang et al., 2006); however, some of the important parameters are reported here. Prismatic concrete specimens of 180 mm length and 140x140 mm cross-section were cast using concrete of 56.2 MPa cube compressive strength (100x100x100 mm) and a 20 mm deformed rebar (of 350.9 MPa yield strength and 521.2 MPa ultimate strength). A bond length of 4 times the bar diameter was provided and displacement cycles of ±0.1, ±0.3, ±0.6 mm amplitude were applied to the bar. Note that 6 mm diameter round bars were used to passively confine the pullout specimens. In the presented graph (Figure 4.14-b) the horizontal axis represents the displacement of the loaded end of the deformed bar rather than the slip at its unloaded end. Although no specific values were provided, it was reported that the slip values were either smaller than or close to the applied displacement. The exact bond-slip behaviour cannot be compared between the two cyclic tests due to the differences in the loading protocols and the measured parameters. It is however obvious that the bond stress versus slip relationship features gradual increase of bond stress until the bond strength is reached followed by a faster reduction of the bond stress in the post-pullout phase (see Figure 4.14). Hence, the overall cyclic bond-slip behaviour obtained from the proposed cyclic beam test does not appear to be inconsistent with the results obtained from traditional pullout-based cyclic tests. The only distinguishable difference is the existence of a constant bond stress plateau in the pullout-based cyclic test (Figure 4.14-b). Whereas in the proposed cyclic beam test method, the bond stress keeps decreasing once the maximum bond strength is reached. Further experimental investigations are required to compare the two cyclic tests (namely the pullout and beam tests) in order to quantify possible variations in the effect of testing

method on the measured bond performance. Effect of other variables such as the loading protocol and the extent of confinement should also be considered in future researches.

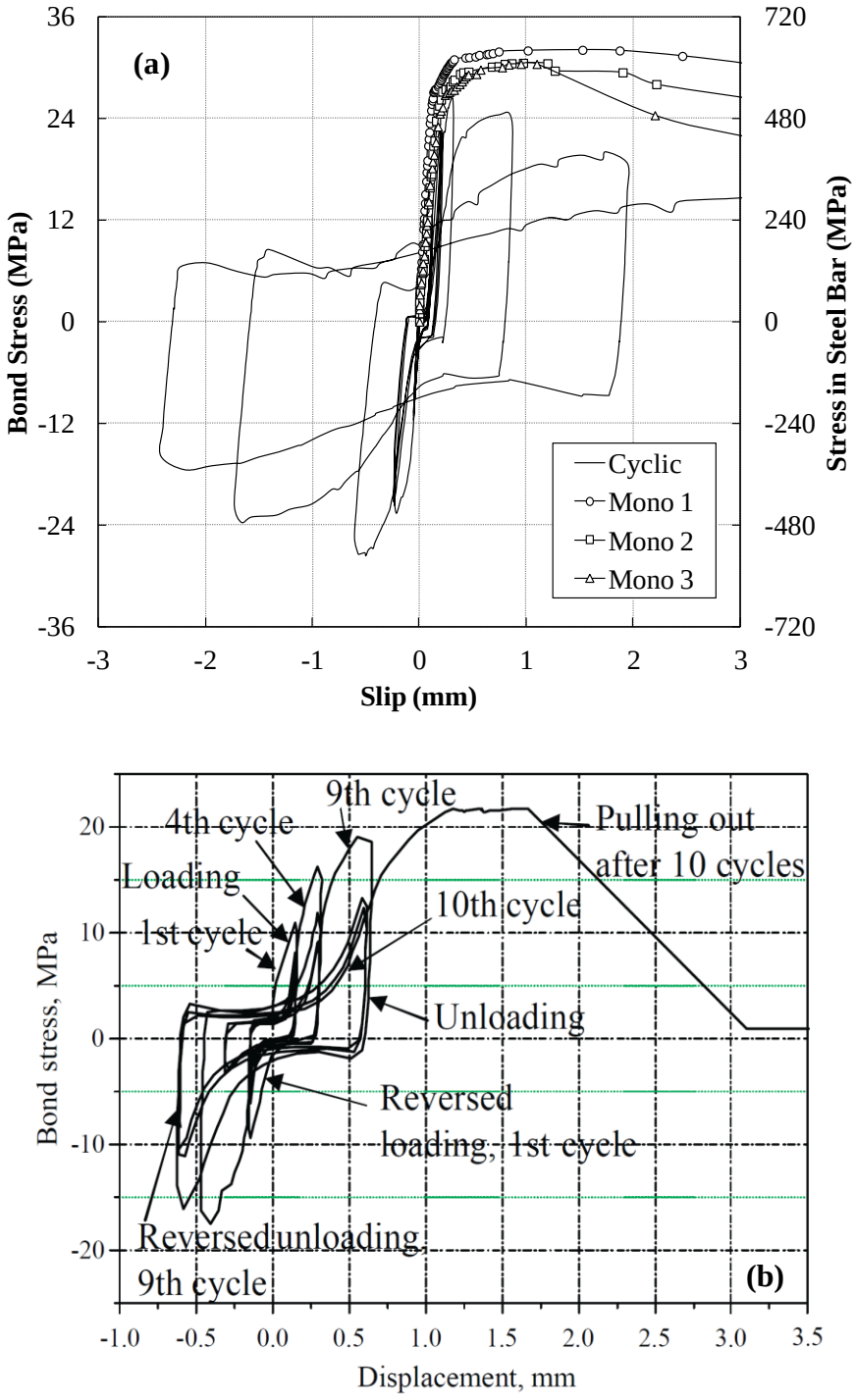

Figure 4.14: (a) Bond under cyclic and monotonic loads and (b) typical pullout-based cyclic test results

4.6 FURTHER VALIDATION OF THE TEST SETUP

In order to further examine the repeatability, validity and stability of the proposed test setup, further laboratory tests were devised and performed on beam specimens considering the loading protocol, concrete type, steel grade and bond length as variables. In addition to the HSSCC used before, a conventionally vibrated high-strength concrete (CVHSC) was also designed for comparison purposes (Table 4.2). The beams were tested around 90 days after casting which provided more time for strength development given the presence of fly ash in both concrete mixes. Deformed bars of 16 mm diameter (300 grade) having yield and ultimate strengths of 315 MPa and 440 MPa respectively were used as the main reinforcement.

Table 4.2: Mix proportions and mechanical properties of HSSCC and CVHSC

Material	HSSCC (kg/m^3)	CVHSC (kg/m^3)
Coarse aggregate	880	1145
Fine aggregate	870	695
Cement	385	385
Fly ash	165	165
Water	165	148.5
Super-plasticizer	3.575 (0.65%)	1.925 (0.35%)
Compressive. Strength*	114.1 MPa	114 MPa
Split tensile strength*	6.4 MPa	7.1 MPa

* These were measured at the day of test (about 90 days after pouring)

In total, eighteen beam specimens were cast; namely CVHSC-D16-300G-5D-S1 to S3, HSSCC-D16-300G-5D-S1 to S3, HSSCC-D16-300G-2.5D-S1 to S3, HSSCC-D16-500G-5D-S1 to S3, HSSCC-D25-300G-5D-S1 to S3, and HSSCC-D16-300G-5D-Mono-S1 to S3. A five or six term coding fashion was chosen to identify these specimens. These terms determined the concrete type, bar diameter, steel grade, bond length, and specimen number, respectively. Note that all specimens were tested under cyclic loading except for one where the term "Mono" precedes the specimen number (in the six-term code specimen) which was tested under monotonic loading.

As the CVHSC-D16-300G-5D-S1 specimen had the same bond length, higher concrete strength and lower grade steel compared to the specimen reported in the previous section, it was expected that pullout would not be the mode of failure. Nevertheless, the loading

protocol was kept unchanged from the previous test (Figure 4.9-a) to investigate possible effects of buckling at the center of the specimen. Figure 4.15 shows the central load vs. displacement as well as the bond stress vs. slip for this specimen.

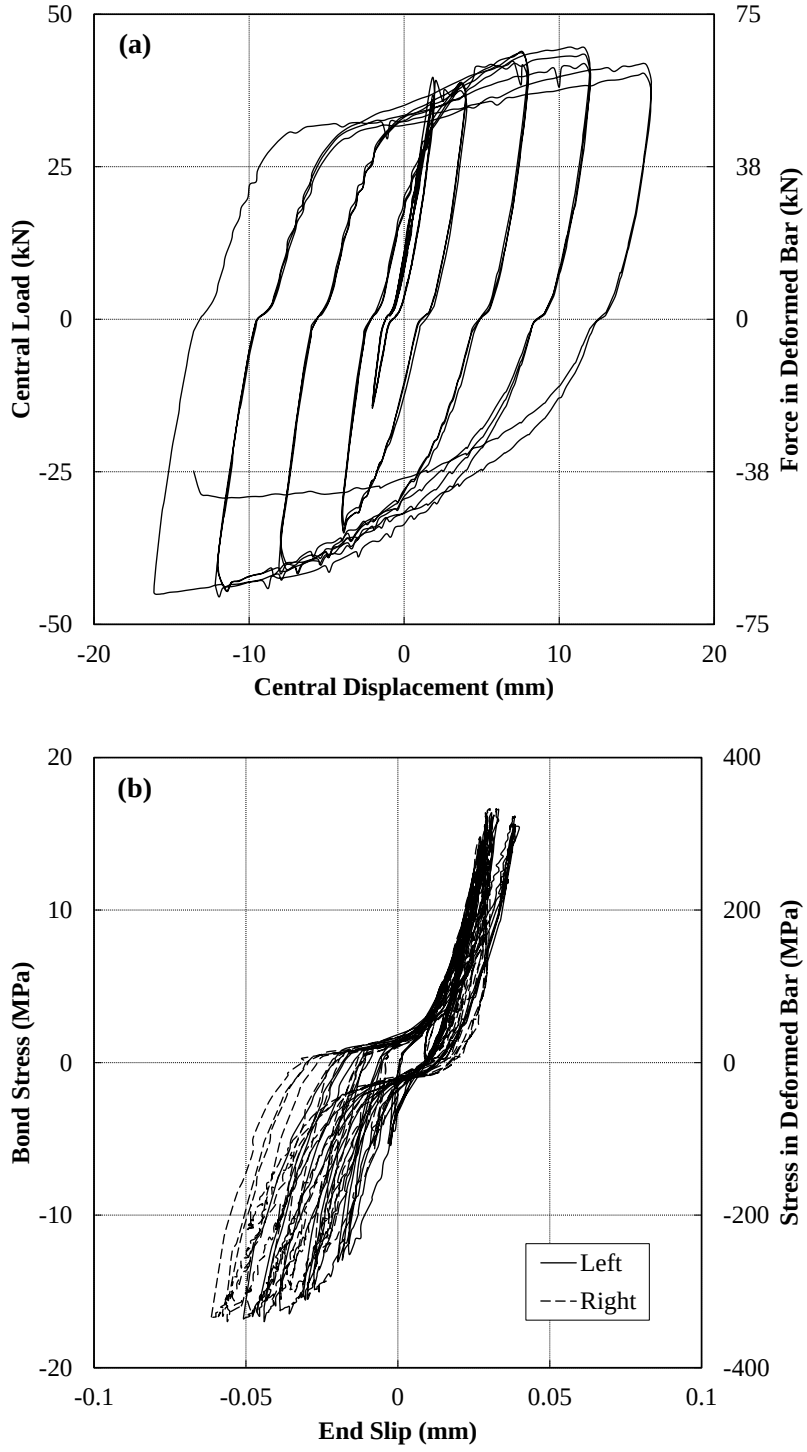

Figure 4.15: (a) Load vs. displacement and (b) averaged bond-stress vs. slip for CVHSC-D16-300G-5D-S1

By the end of the first three displacement steps (i.e. ±1, ±2 and ±4 mm), evidence of buckling was noticeable at the center of the bar during the positive (upward) cycles. This also showed up in the load-displacement graph (Figure 4.15-a) in the form of a reduction in capacity in the positive cycles. Buckling was more prominent in the following larger displacement cycles and finally resulted in a premature buckling failure of the bar during the ±16 mm displacement cycles when the slip was only about 0.05 mm (Figure 4.16).

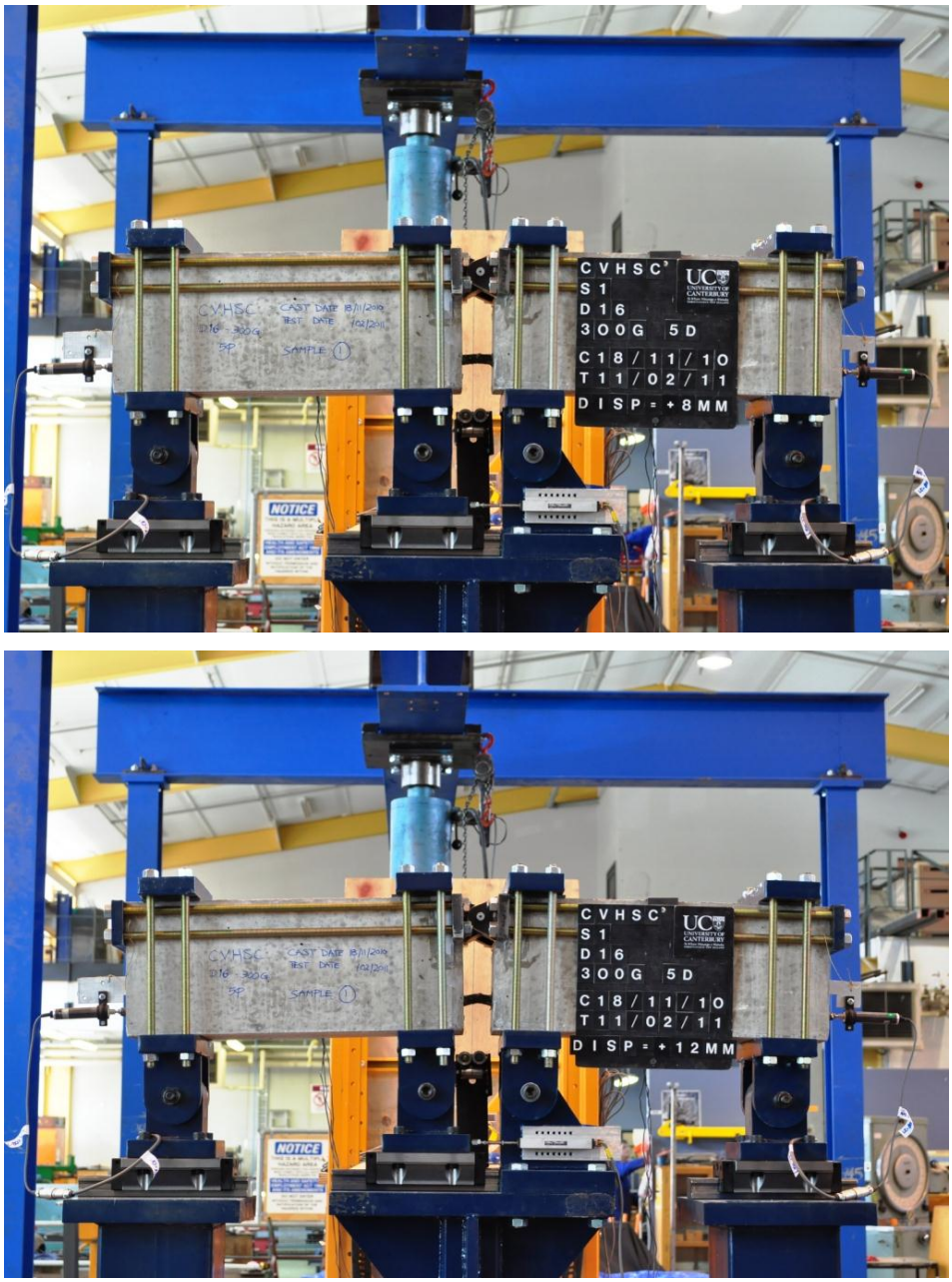

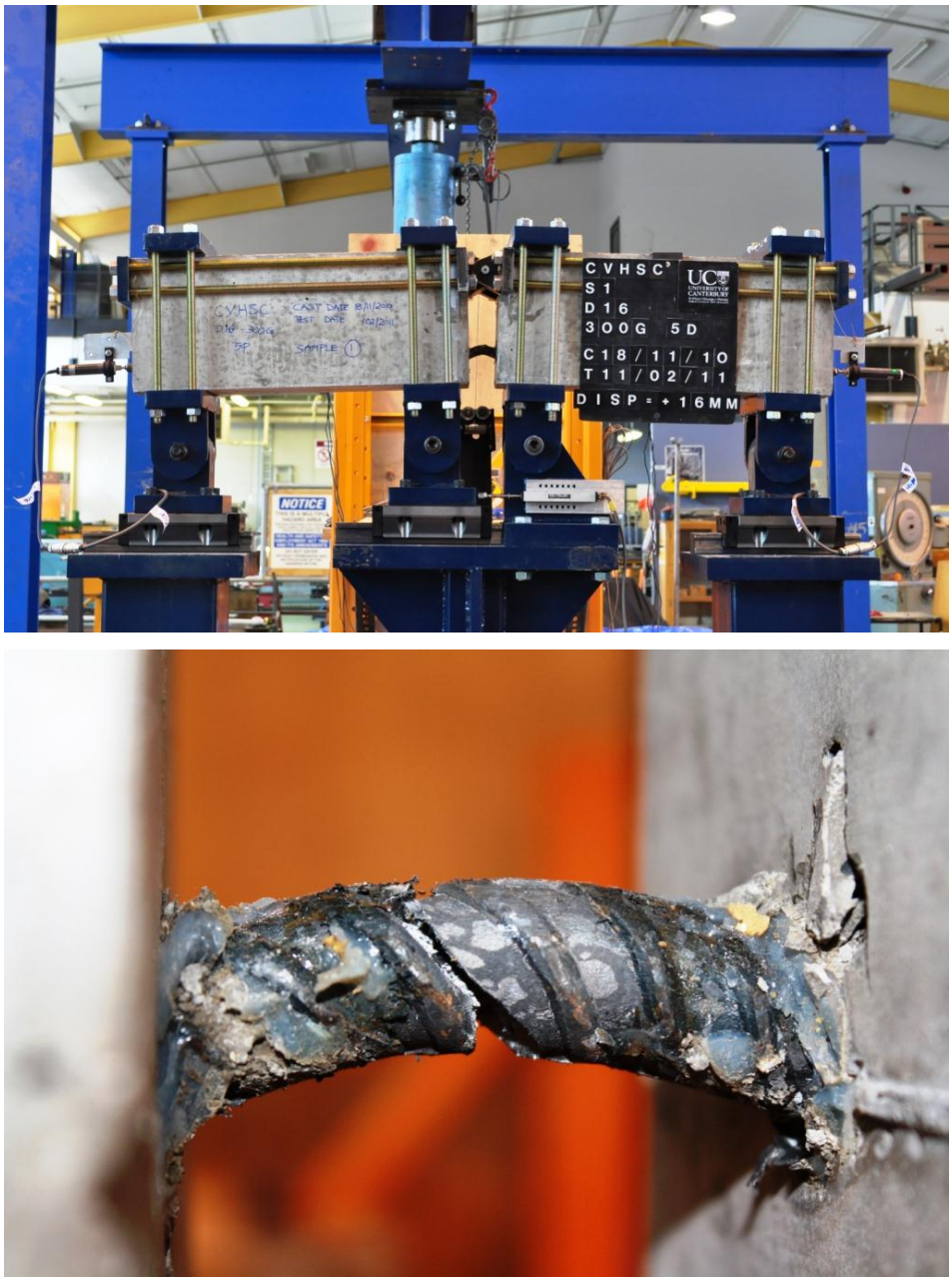

Figure 4.16: Premature buckling of the bar in positive cycles at the center of beam specimen

In other tests, the loading protocol was adjusted in order to minimize or completely avoid the bar buckling in such a way that the stress reversals still occurred and the cyclic nature of the test was preserved. This was done through a procedure of trial and error to arrive at an optimized loading protocol; i.e. for each new loading protocol one specimen was tested and based on the experimental results the next change (if needed) was decided. Given that the positive displacements (which caused compressive strength in the bar) were responsible for causing buckling of the bar, they were omitted in the adjusted loading

protocol. However, this did not necessarily mean the omission of compressive stresses as due to the prior elongation of the bar in the negative (tensile) direction, compressive stresses could develop during the reversed direction (upward) even when the absolute displacement is negative. Figure 4.17 illustrates the procedure of adjusting the cyclic loading protocols as well as the adopted equivalent monotonic one. Table 4.3 shows the relevant parameters of all loading protocols. In the first few cycles of the adjusted cyclic loading protocols, the displacement was reversed back to zero. However in the further cycles when the bar went into the inelastic response range, the displacement was not reversed back to zero in order to avoid possible initiation of buckling. In the first adjustment of the loading protocol, the maximum applied displacement was also limited to 44 mm in order to limit the plastic elongation of the bar. However, results showed that applying this constraint in turn limited the maximum force and slip as well. Therefore in further adjustments, the maximum displacement was increased as much as possible within the constraints of the test setup (about 100 mm).

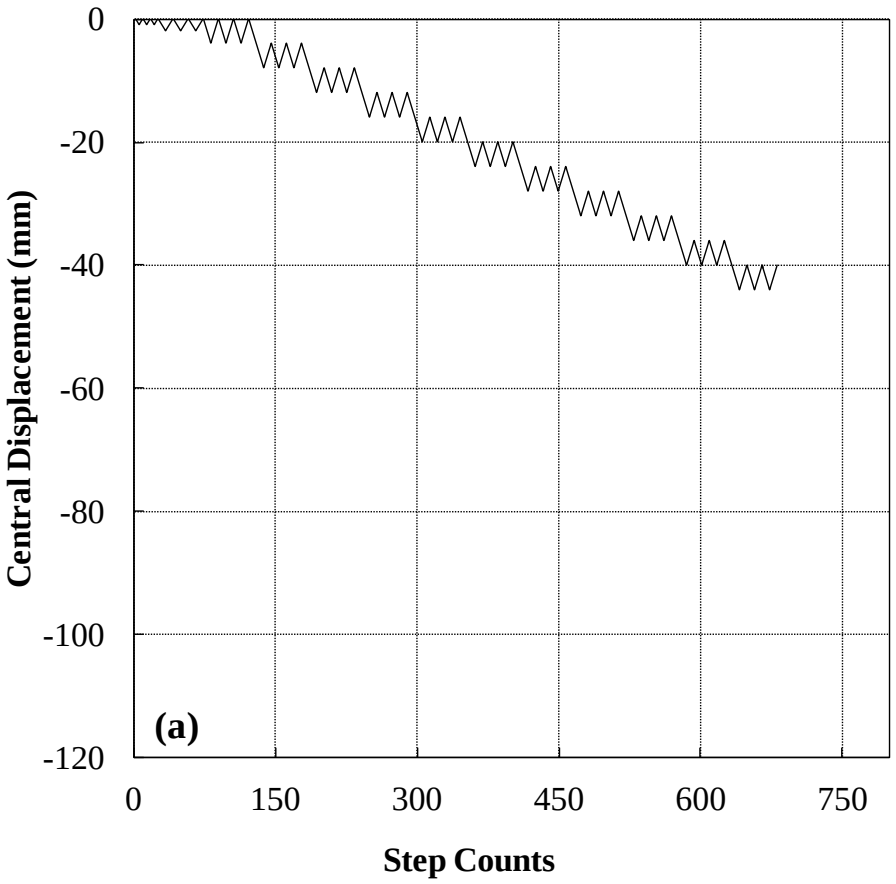

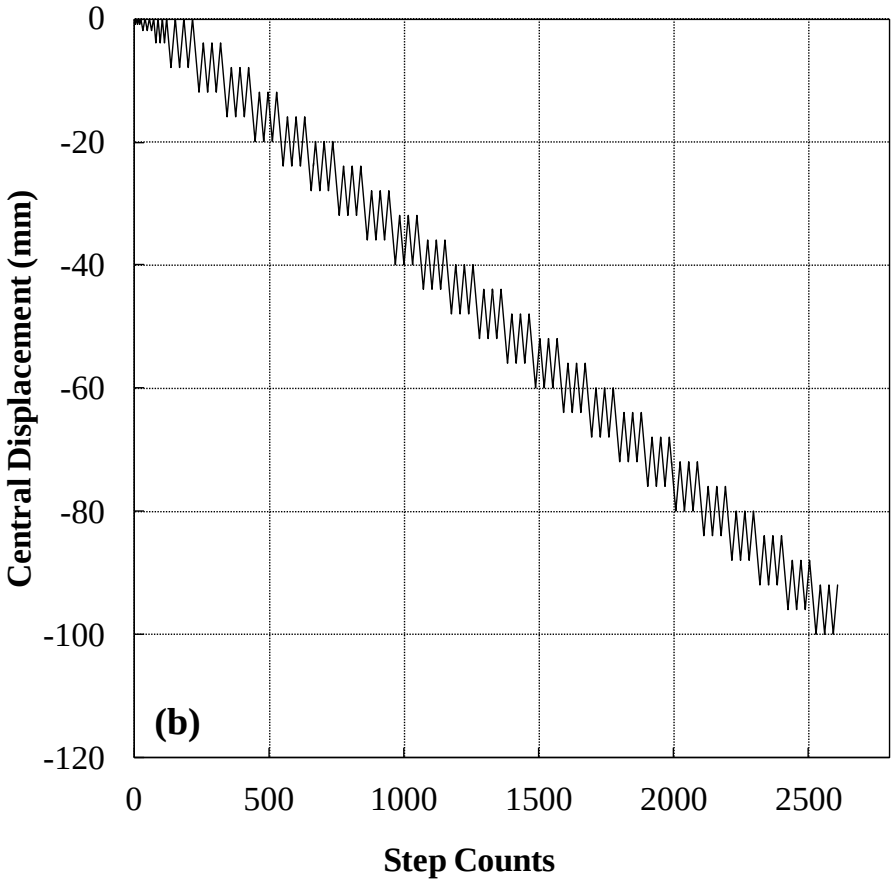
0
-20
-40
-60
-80
-100
-120
Central Displacement (mm)
(b)
0
500
1000
1500
2000
2500
Step Counts

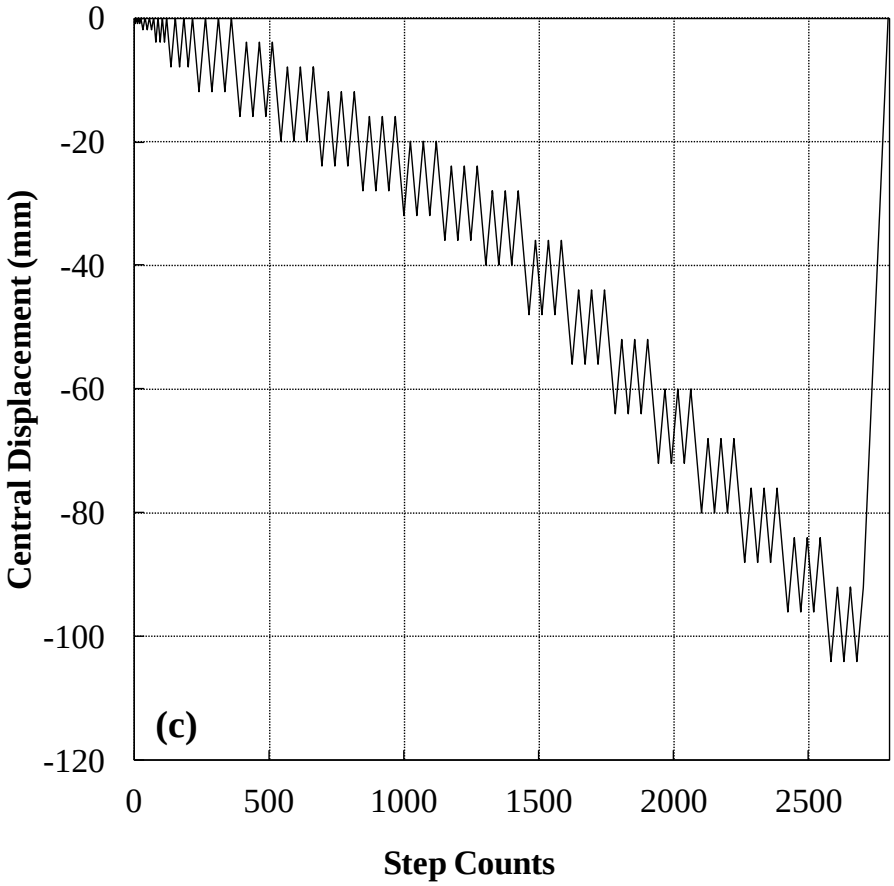
0
-20
-40
-60
-80
-100
-120
Central Displacement (mm)
(c)
0
500
1000
1500
2000
2500
Step Counts

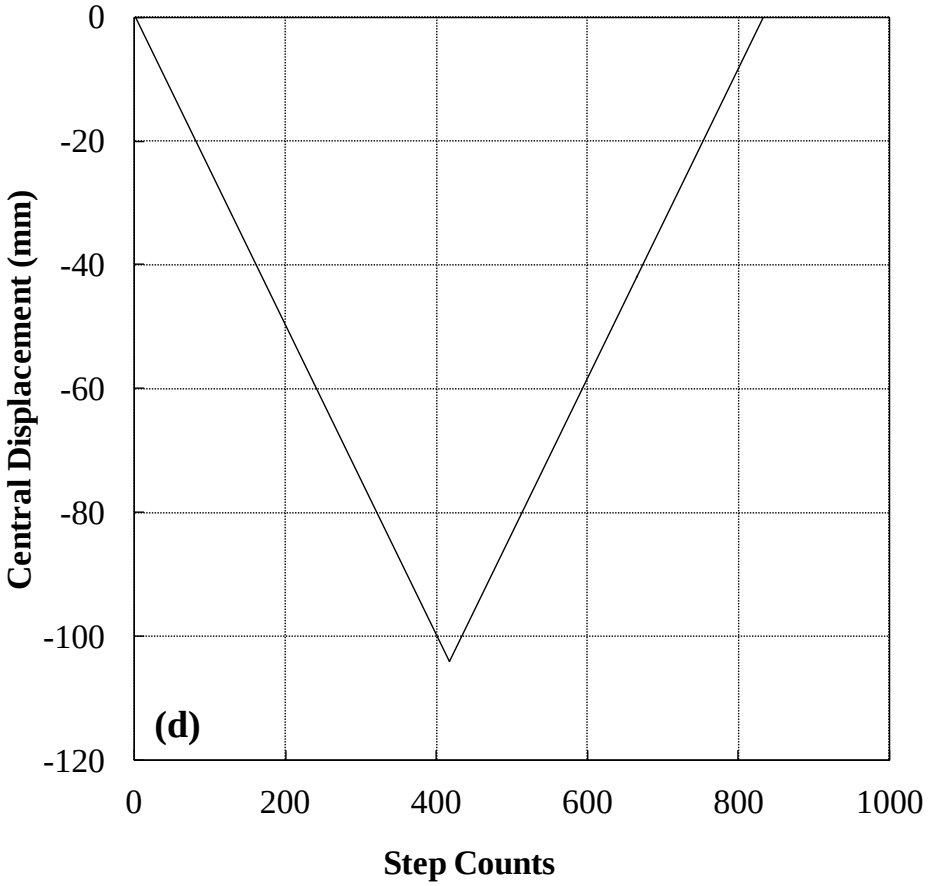

Figure 4.17: a-c) Procedure of adjusting the cyclic load protocols and d) monotonic load protocol

Table 4.3: Specifications of different load protocols

Protocol	No. of steps	Steps reversing back to zero	Loading increment (mm)	Increase in disp. amplitude between the steps	Oscillation in each cycle
a	13	1,2,4 mm	0.5	4 mm after the 3rd step	4 mm after the 3rd step
b	27	1,2,4,8 mm	0.5	4 mm after the 3rd step	8 mm after the 4th step
c	20	1,2,4,8,12 mm	0.5	4 mm after the 3rd step 8 mm after the 12th step	12 mm after the 5th step
d	-	104 mm	0.25	-	-

The first adjusted loading protocol (Figure 4.17-a) was applied to the HSSCC-D16-300G-5D-S1 specimen and the results are shown in Figure 4.18. It is clear from the figure that the amount of compressive force (positive) in the bar was very small (only about 10 kN) when the displacement reversal happened. Accordingly, the amount of bond stress, steel

stress and slip were also limited. This time no evidence of buckling was observed in the tested bar; therefore, the loading protocol was further modified (Figure 4.17-b) and applied to CVHSC-D16-300G-5D-S2 specimen (Figure 4.19). The compressive force in the bar reached to a peak of about 60 kN in the first few displacement cycles with no evidence of buckling in any cycle. Although the slip values were still small (0.2 mm) the cyclic bond-slip behaviour could easily be distinguished (Figure 4.19-b). The cyclic nature of the test was preserved; however the compressive force in the bar started to reduce especially over the last 10 cycle series. As a result, a small modification was made in the next loading protocol (Figure 4.17-c) and applied to the CVHSC-D16-300G-5D-S3 specimen (Figure 4.20). This was the optimized loading protocol (which had a return-to-zero branch at the end) and was used in the rest of the cyclic tests. For validation and comparison purposes, the rest of the specimens (except for the monotonic ones) were also tested using the last loading protocol (Figure 4.17-c) and the results are shown in Figure 4.21 to Figure 4.31. In addition, the equivalent monotonic loading (Figure 4.17-d) was applied to the HSSCC-D16-300G-5D-Mono-S1 to S3 specimens and the results are illustrated in Figure 4.32 to Figure 4.34.

Figure 4.20-a shows that the compressive force in the bar (plotted on the positive side in the graph) reached a maximum of 60 kN; only in the last 4 loading steps did it reduce below 20 kN. Maximum bond stresses of about 20 MPa and 15 MPa resulting in end-slips of about 0.2 mm and 0.1 mm in the tensile and compressive (downward and upward) cycles were achieved, respectively. Although the loading protocols were slightly different between the CVHSC-D16-300G-5D-S2 and S3 specimens, repeatability of the results could be proved by comparing Figure 4.19 and Figure 4.20. After all displacement cycles were applied, the displaced center of the beam was returned to its original position (i.e. zero displacement). During the return-to-zero branch of the loading protocol, the elongated bar buckled severely (Figure 4.35).

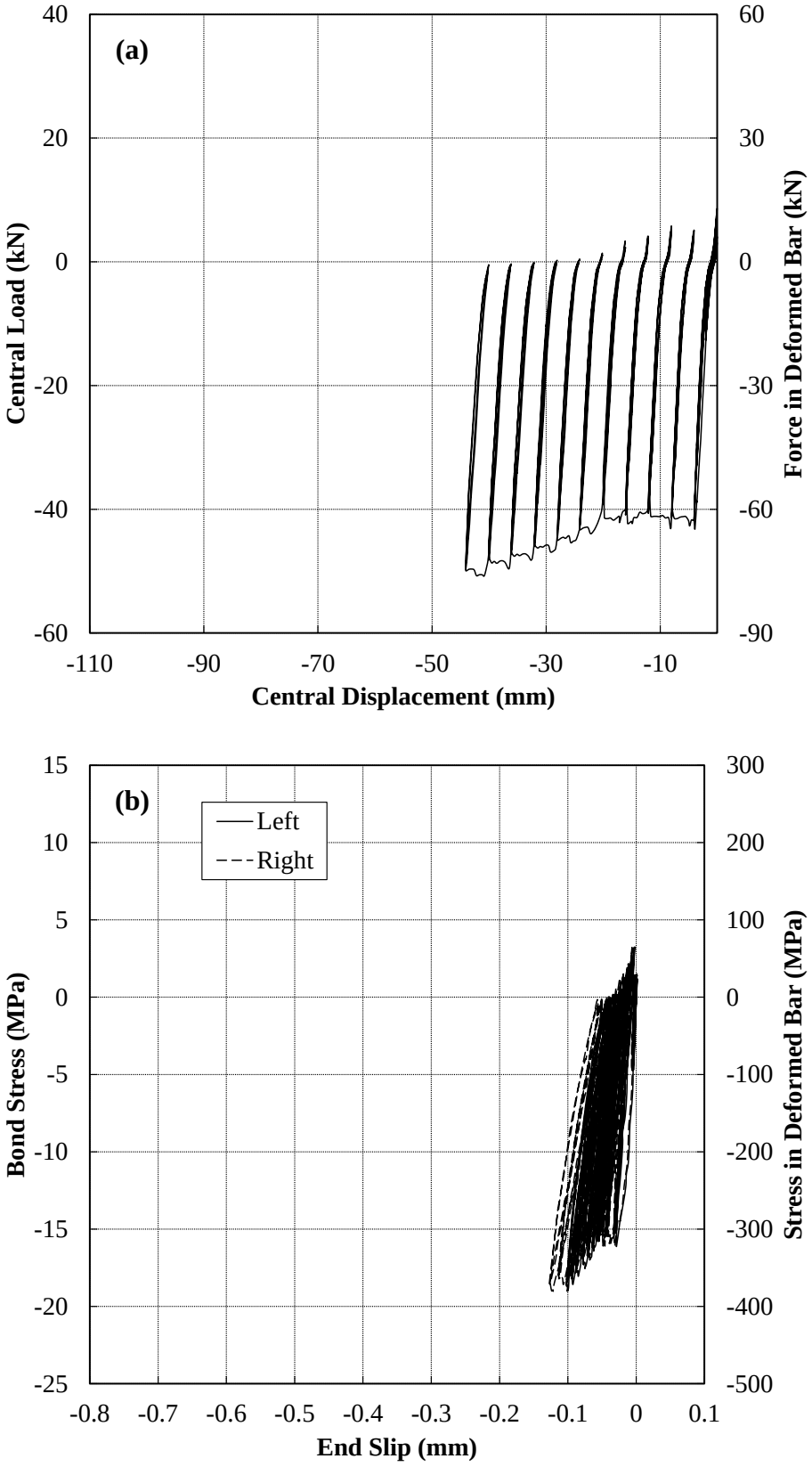

Figure 4.18: (a) Load vs. displacement and (b) averaged bond-stress vs. slip for HSSCC-D16-300G-5D-S1

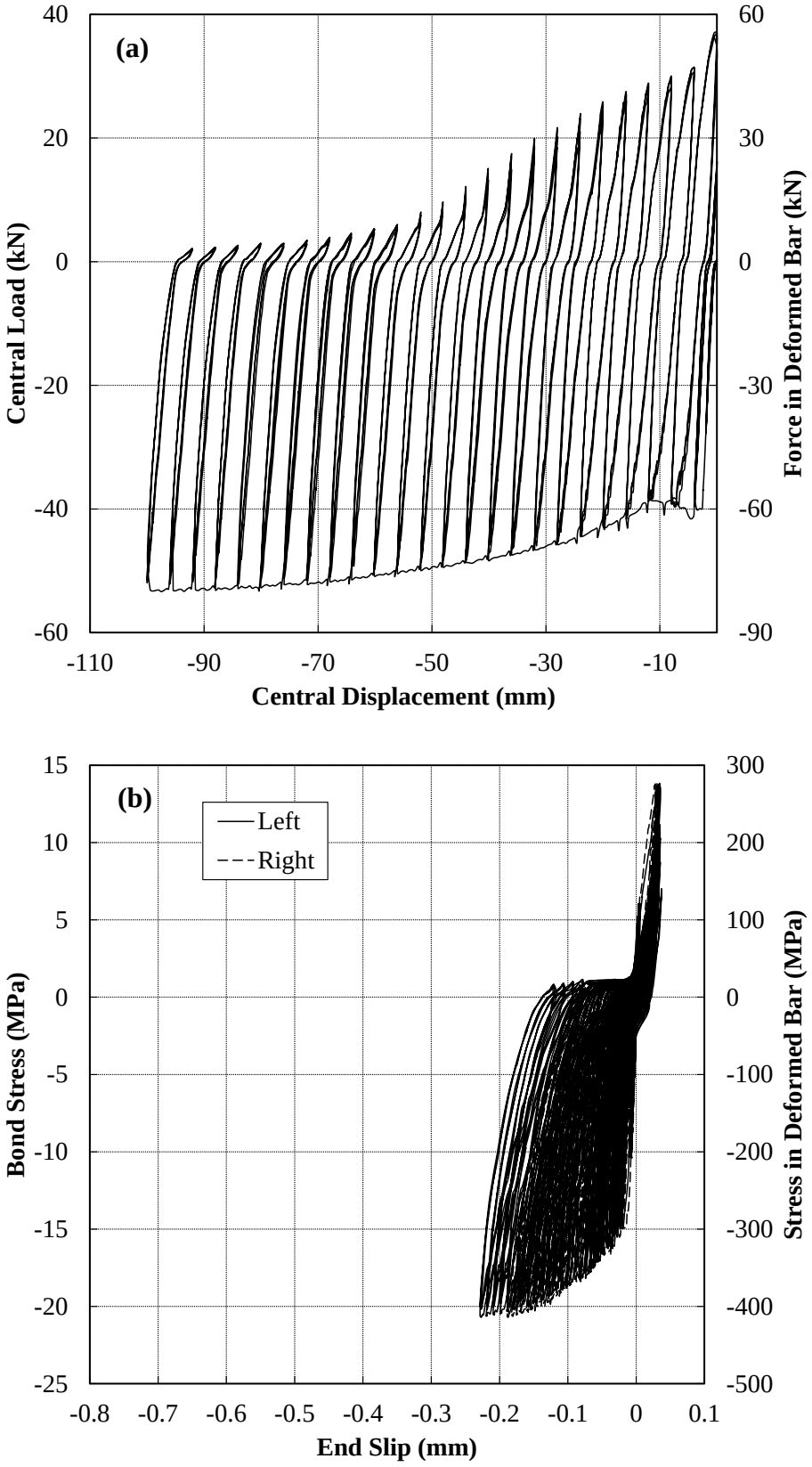

Figure 4.19: (a) Load vs. displacement and (b) averaged bond-stress vs. slip for CVHSC-D16-300G-5D-S2

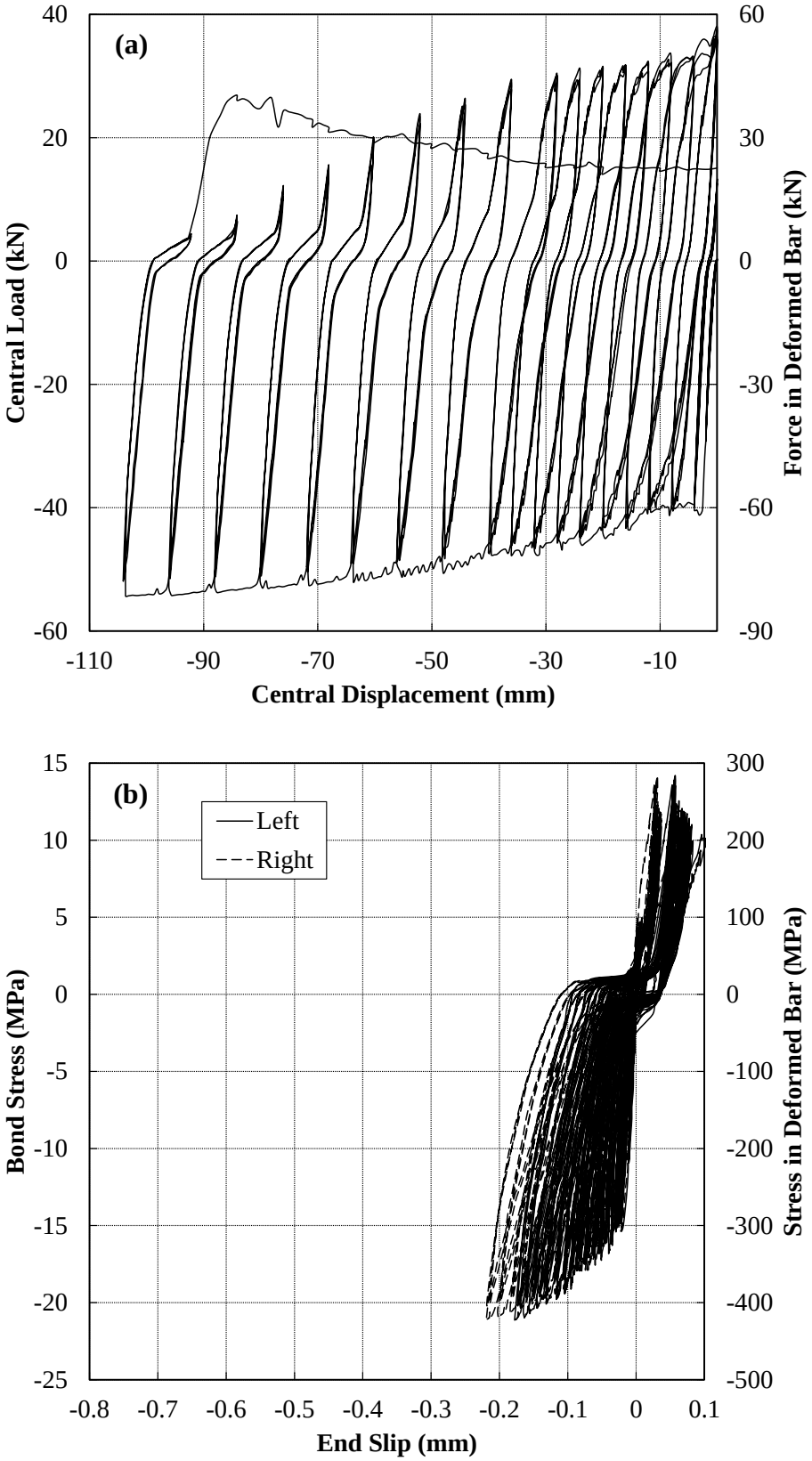

Figure 4.20: (a) Load vs. displacement and (b) averaged bond-stress vs. slip for CVHSC-D16-300G-5D-S3

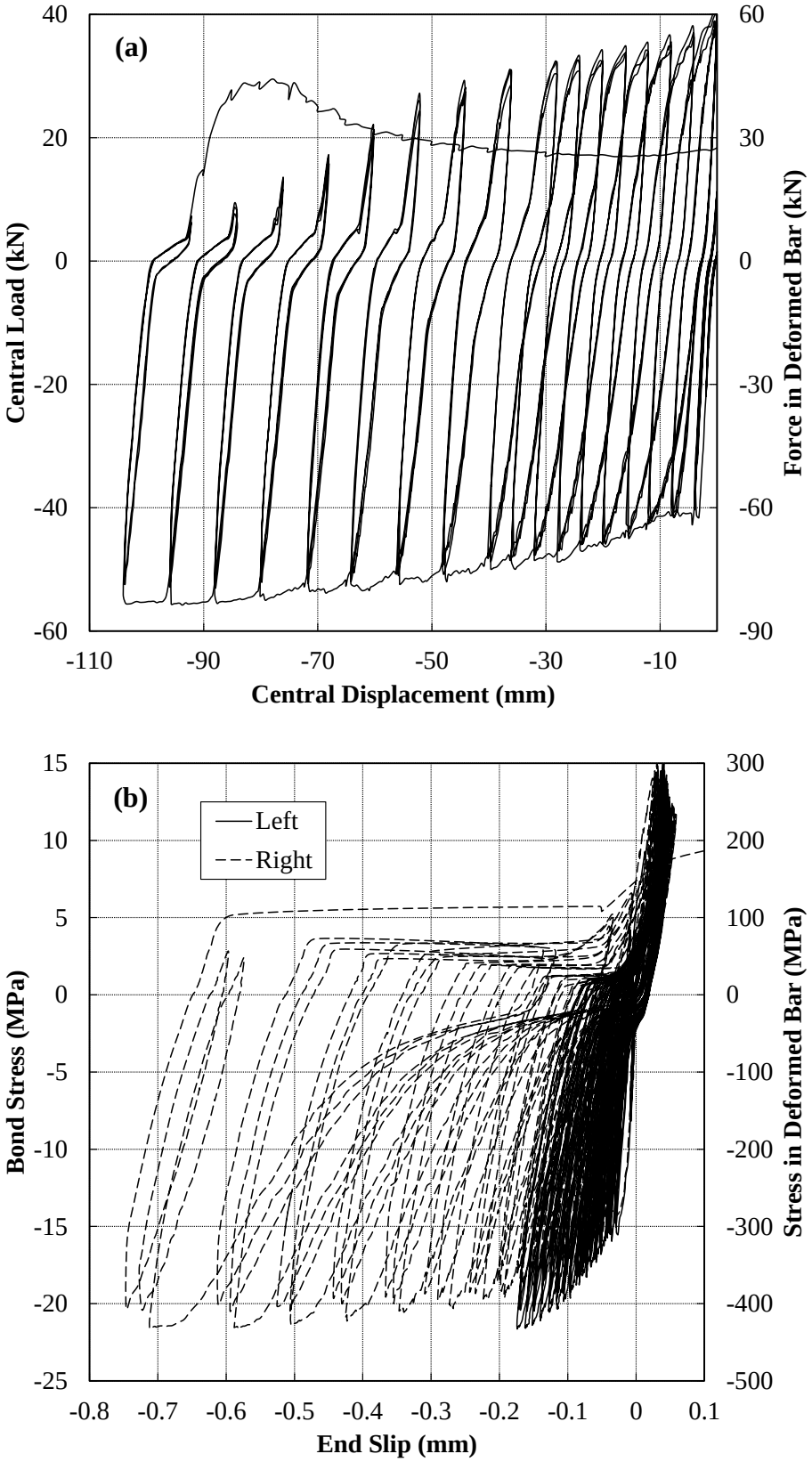

Figure 4.21: (a) Load vs. displacement and (b) averaged bond-stress vs. slip for HSSCC-D16-300G-5D-S2

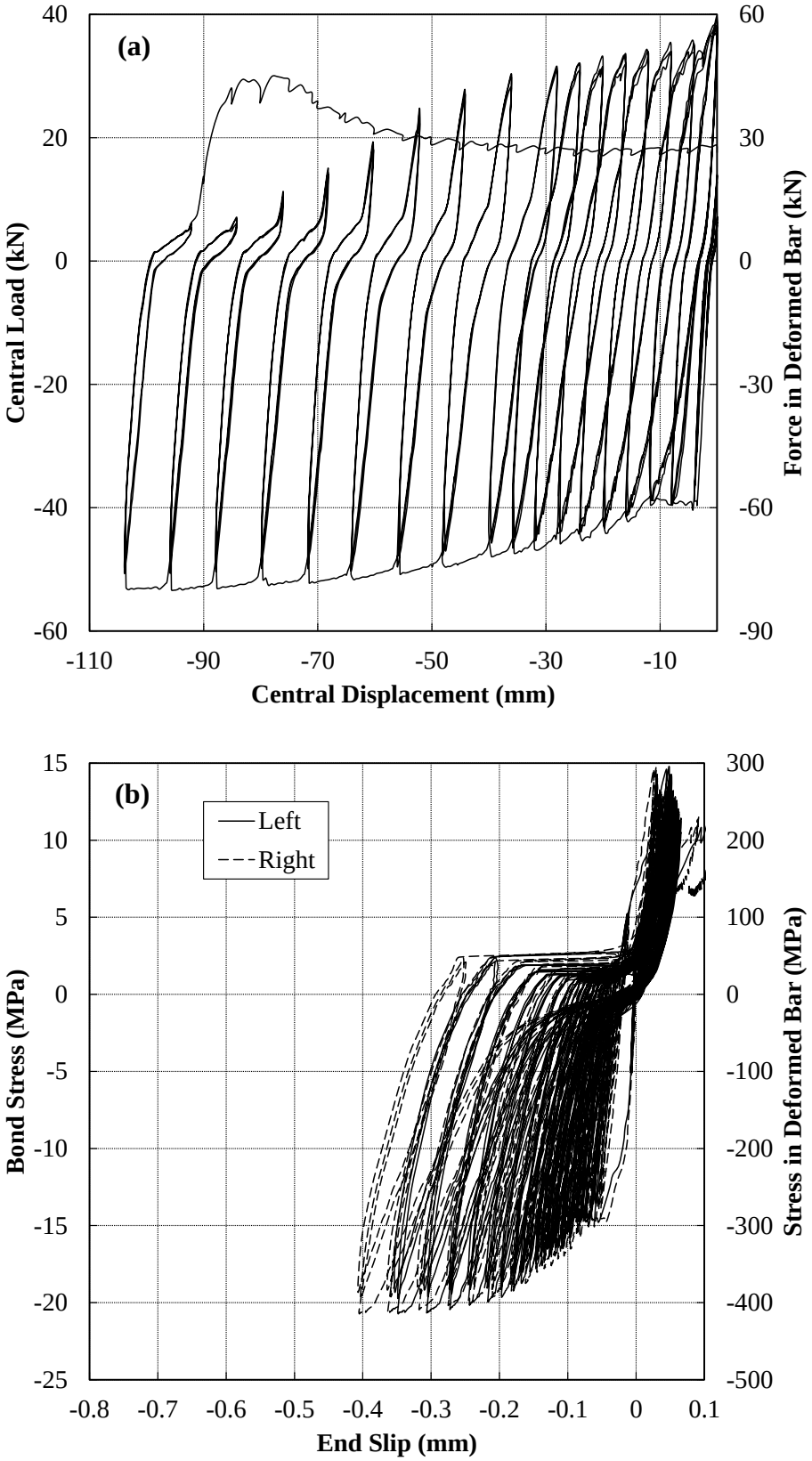

Figure 4.22: (a) Load vs. displacement and (b) averaged bond-stress vs. slip for HSSCC-D16-300G-5D-S3

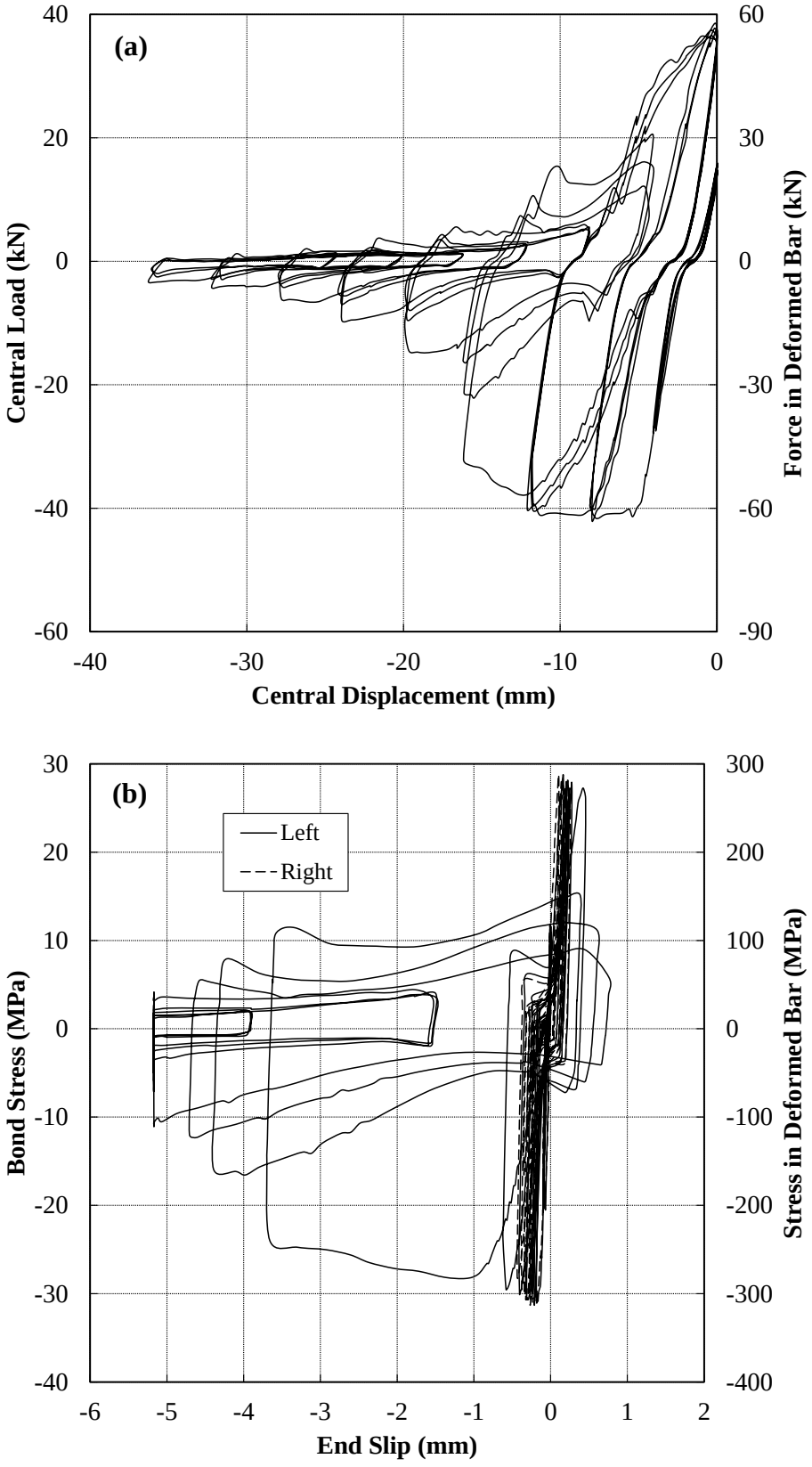

Figure 4.23: (a) Load vs. displacement and (b) averaged bond-stress vs. slip for HSSCC-D16-300G-2.5D-S1

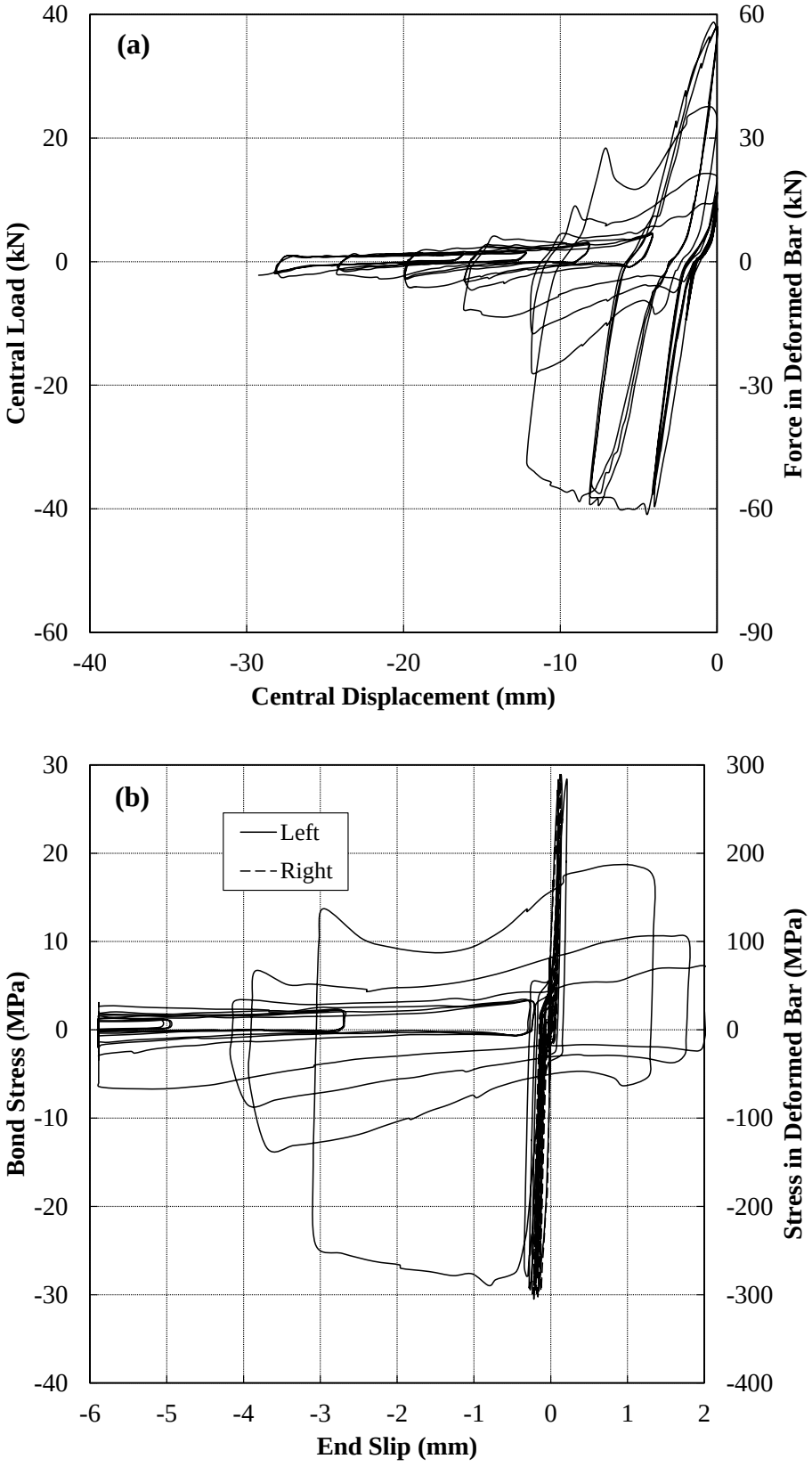

Figure 4.24: (a) Load vs. displacement and (b) averaged bond-stress vs. slip for HSSCC-D16-300G-2.5D-S2

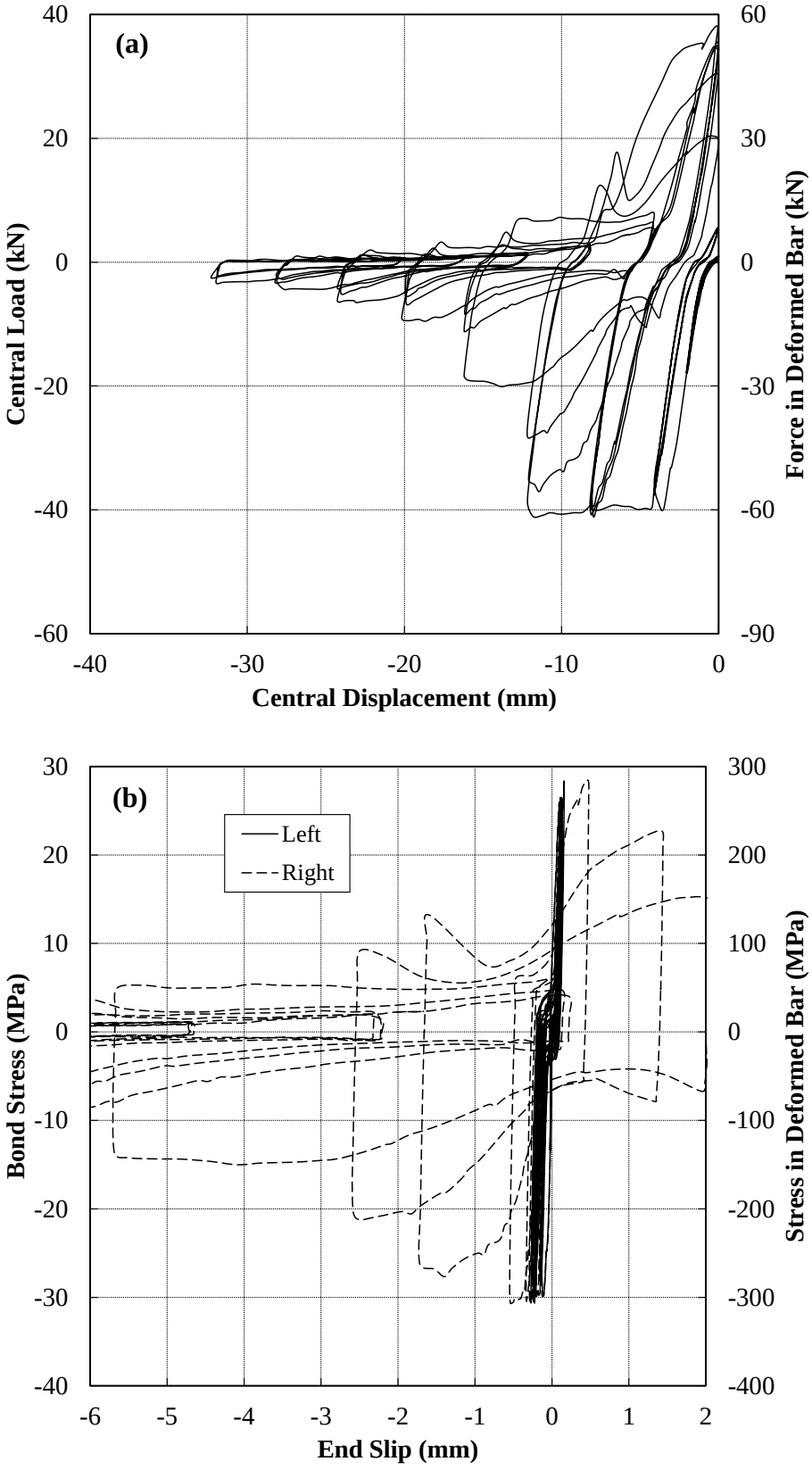

Figure 4.25: (a) Load vs. displacement and (b) averaged bond-stress vs. slip for HSSCC-D16-300G-2.5D-S3

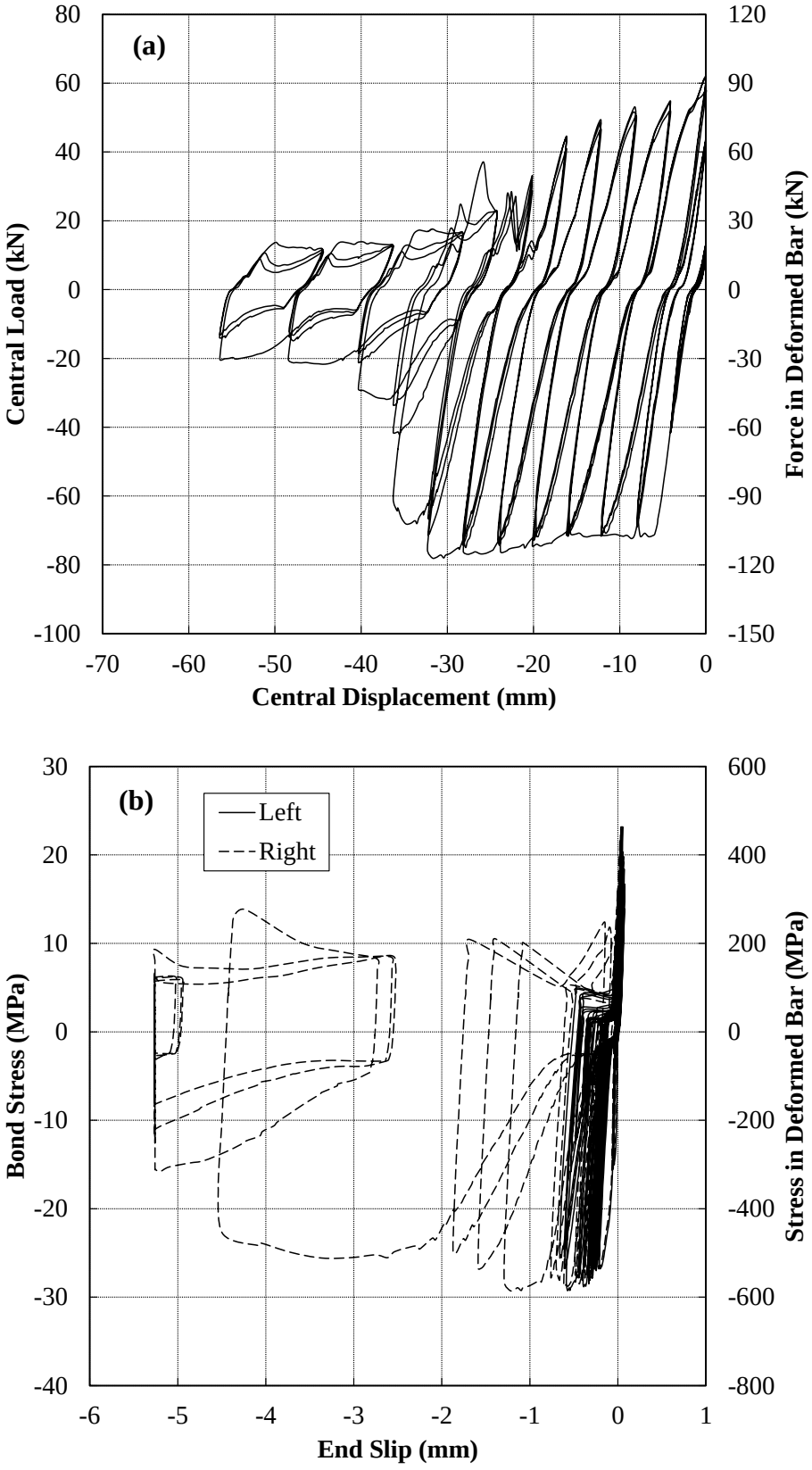

Figure 4.26: (a) Load vs. displacement and (b) averaged bond-stress vs. slip for HSSCC-D16-500G-5D-S1

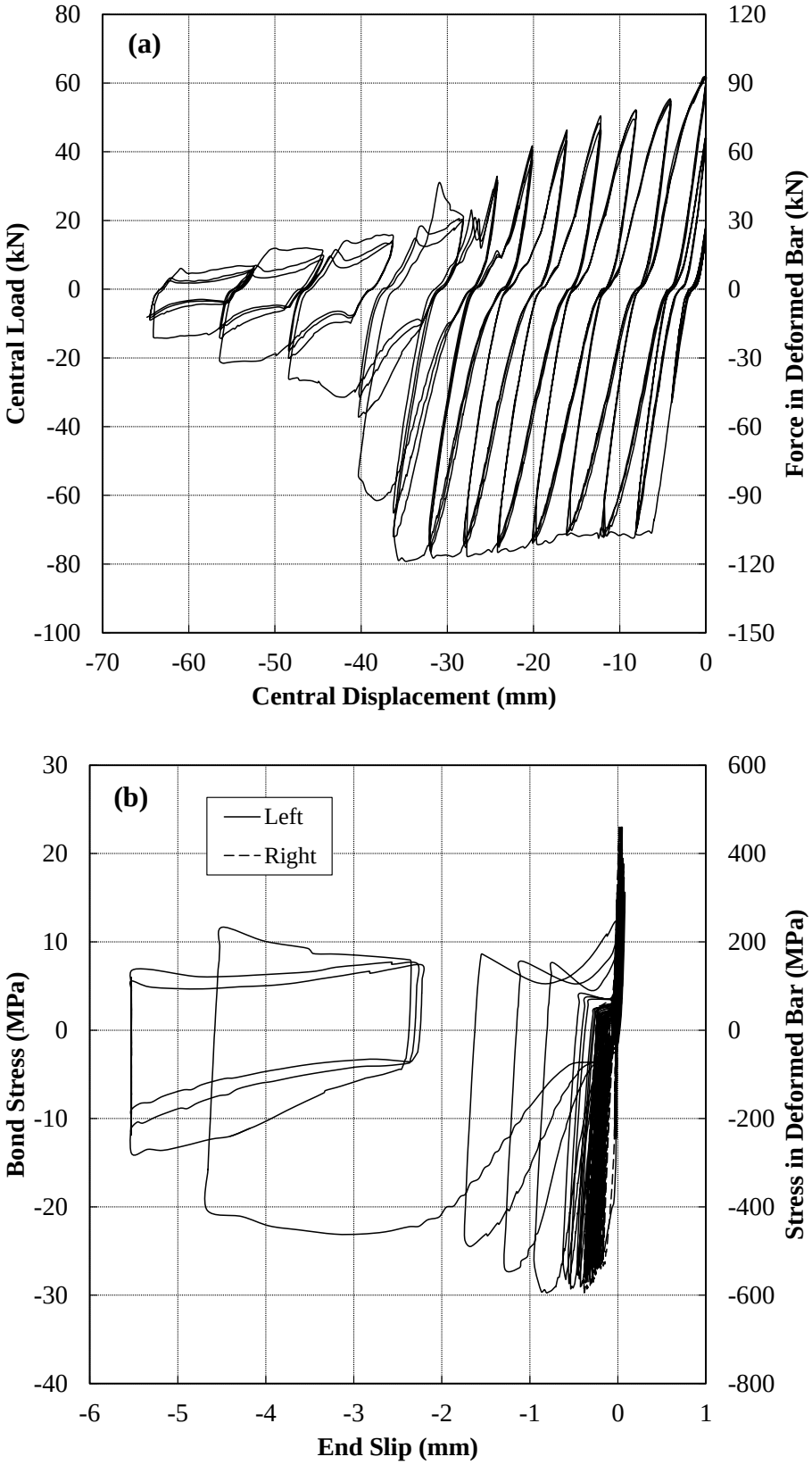

Figure 4.27: (a) Load vs. displacement and (b) averaged bond-stress vs. slip for HSSCC-D16-500G-5D-S2

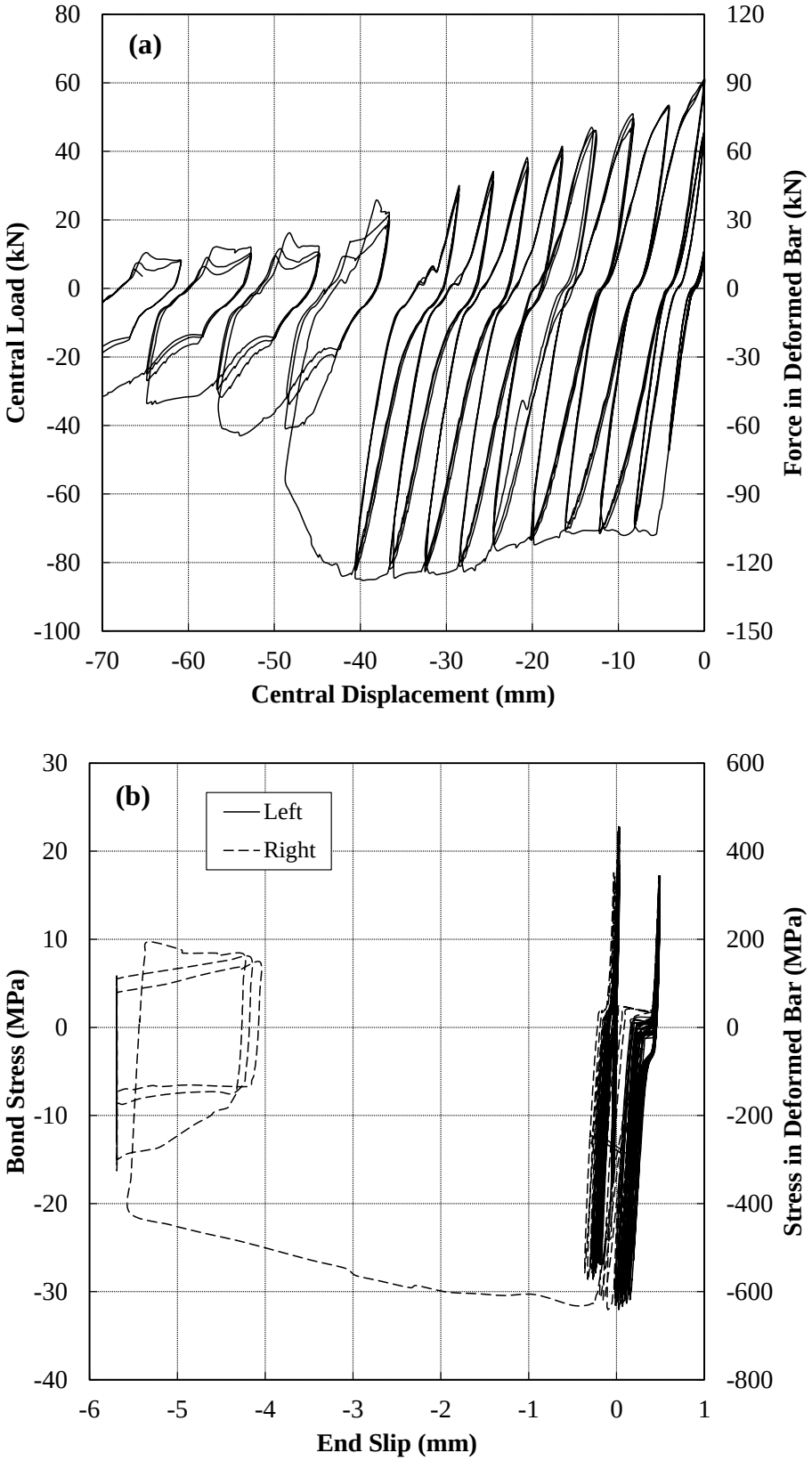

Figure 4.28: (a) Load vs. displacement and (b) averaged bond-stress vs. slip for HSSCC-D16-500G-5D-S3

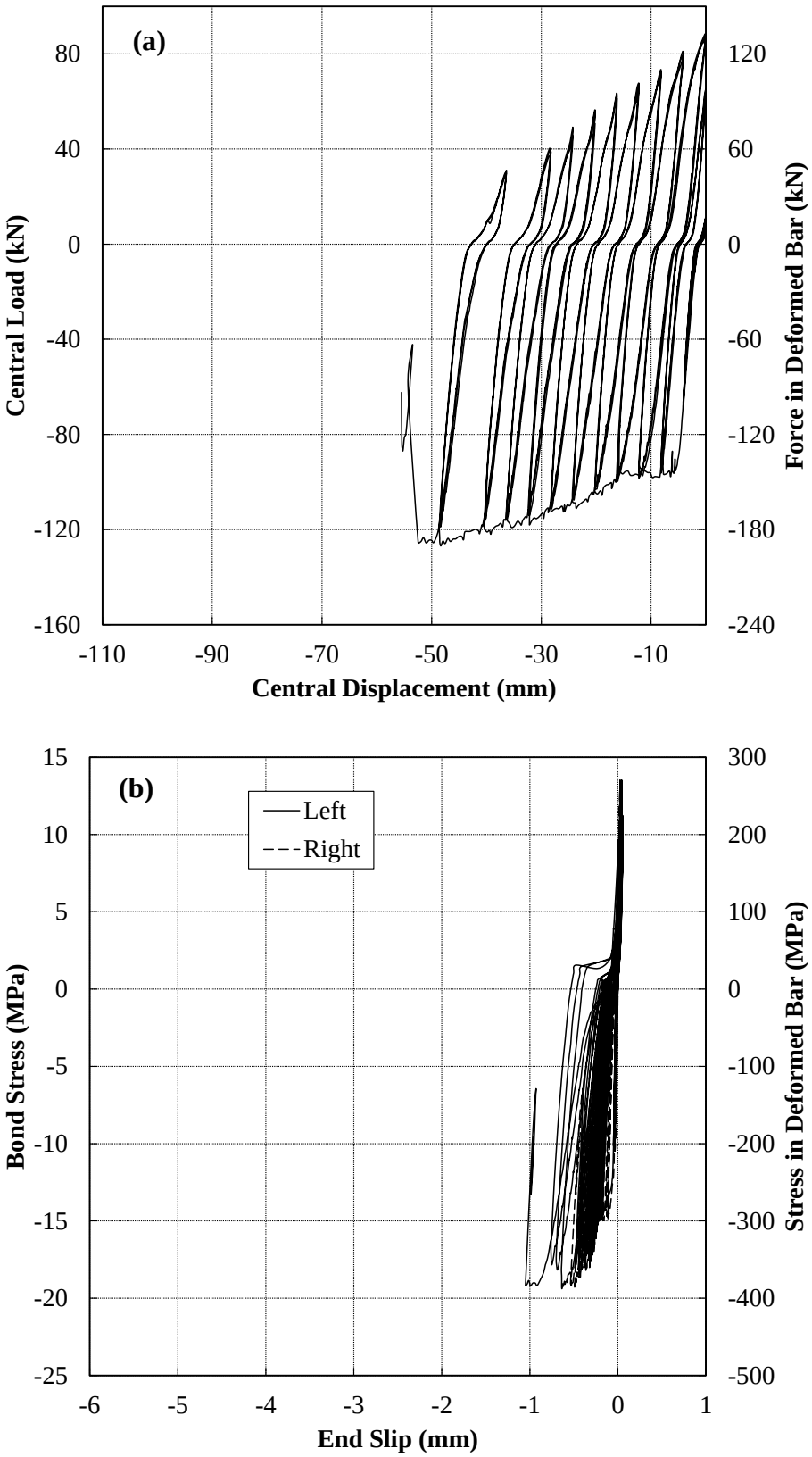

Figure 4.29: (a) Load vs. displacement and (b) averaged bond-stress vs. slip for HSSCC-D25-300G-5D-S1

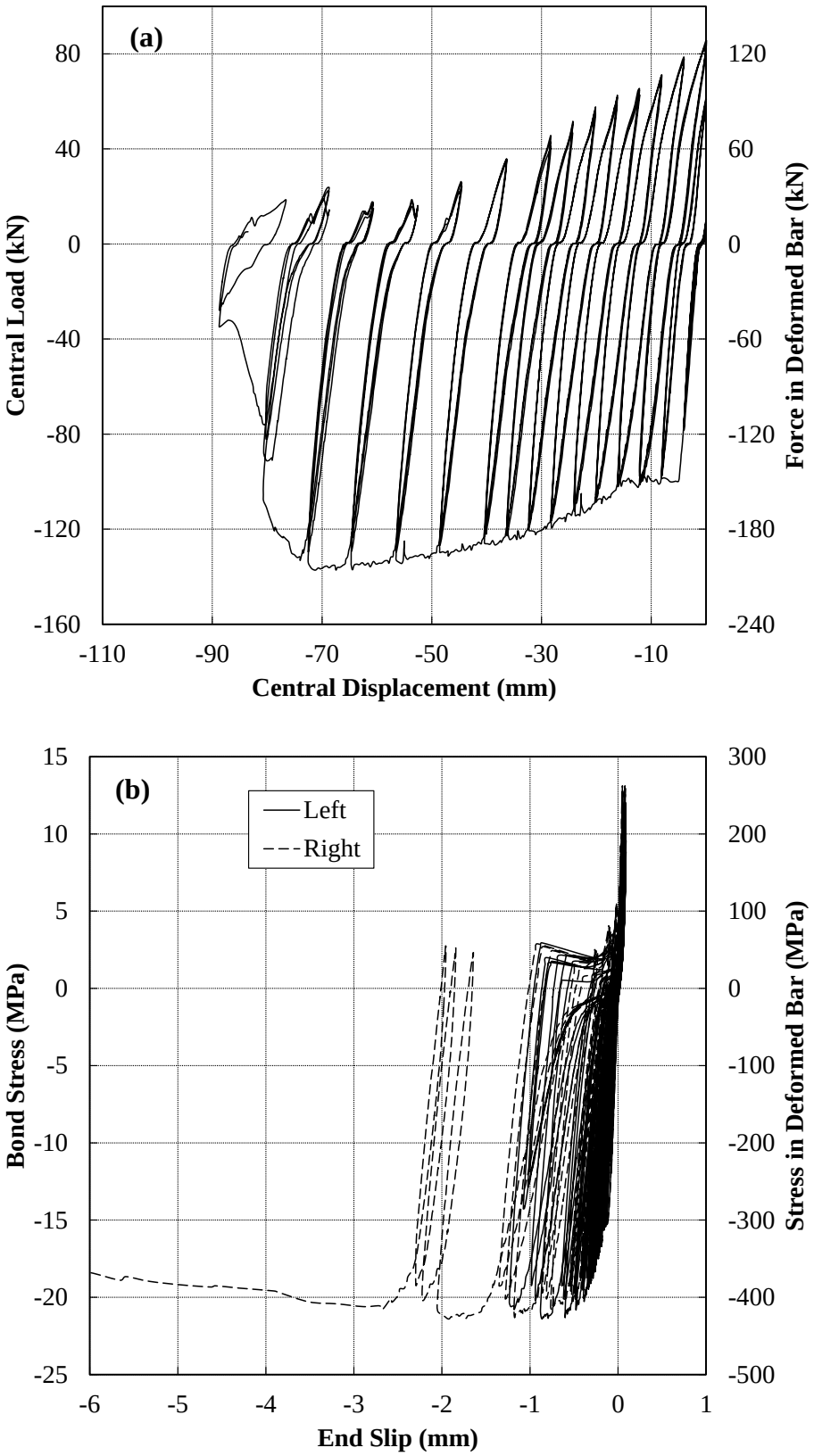

Figure 4.30: (a) Load vs. displacement and (b) averaged bond-stress vs. slip for HSSCC-D25-300G-5D-S2

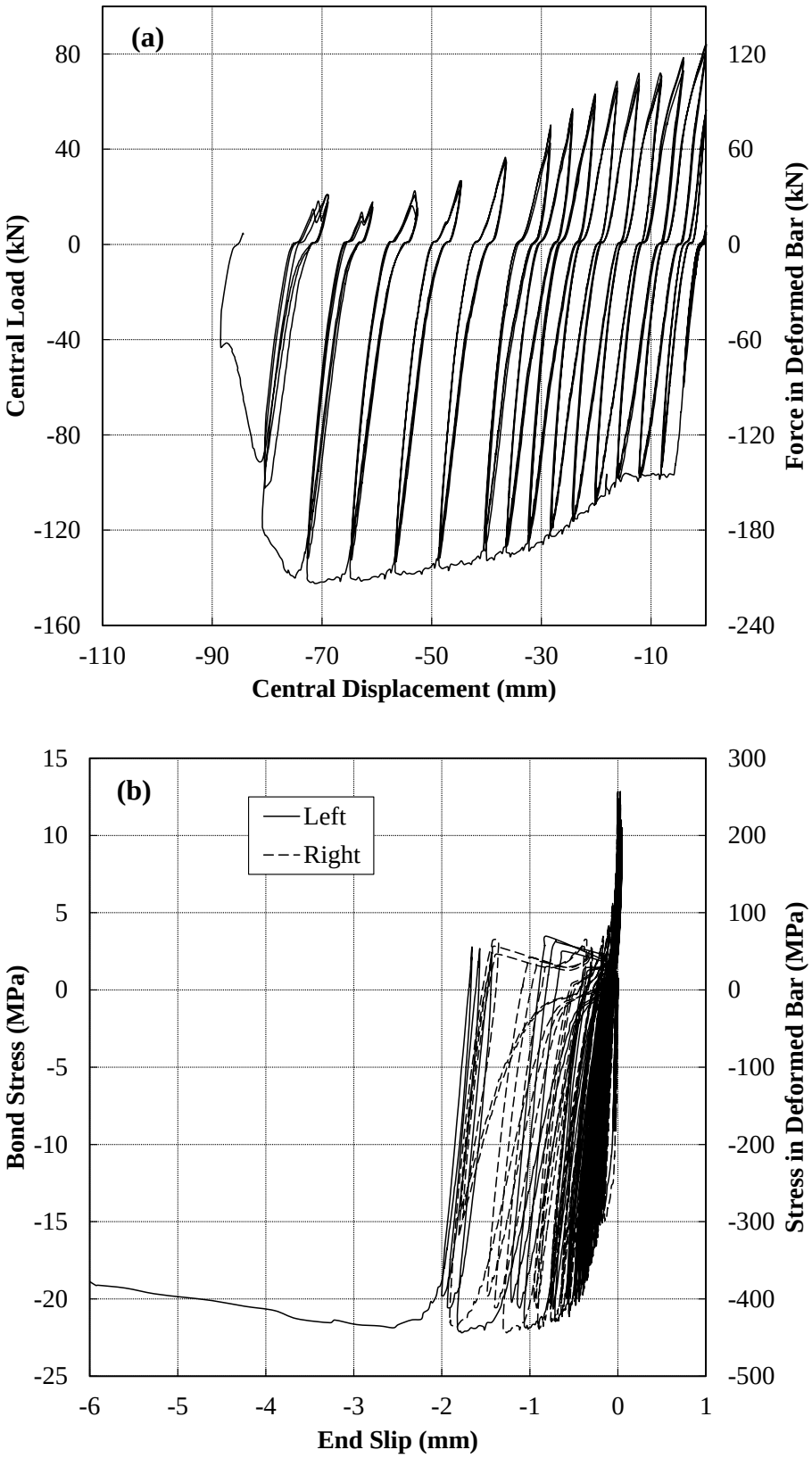

Figure 4.31: (a) Load vs. displacement and (b) averaged bond-stress vs. slip for HSSCC-D25-300G-5D-S3

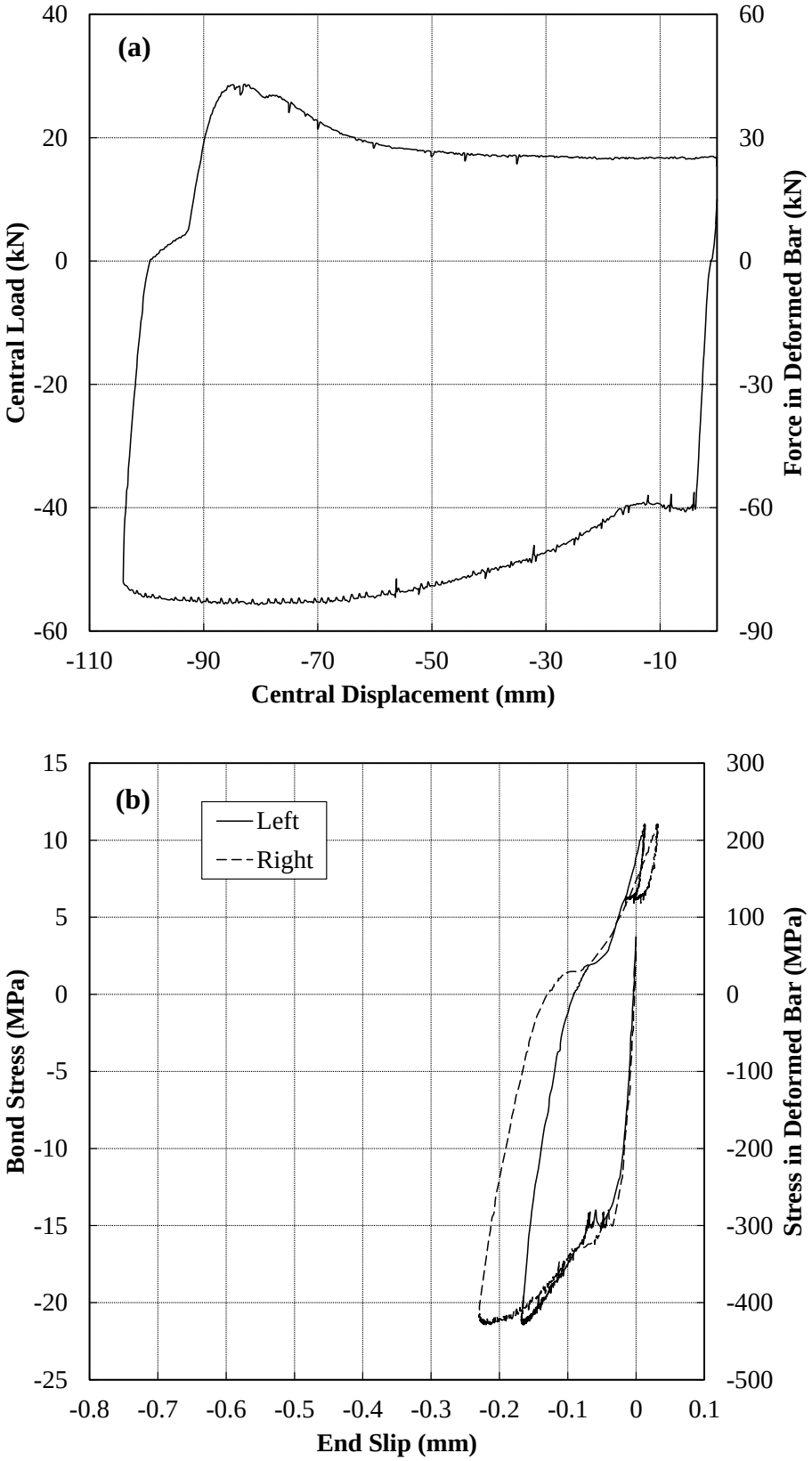

Figure 4.32: (a) Load vs. displacement and (b) averaged bond-stress vs. slip for HSSCC-D16-300G-5D-Mono-S1

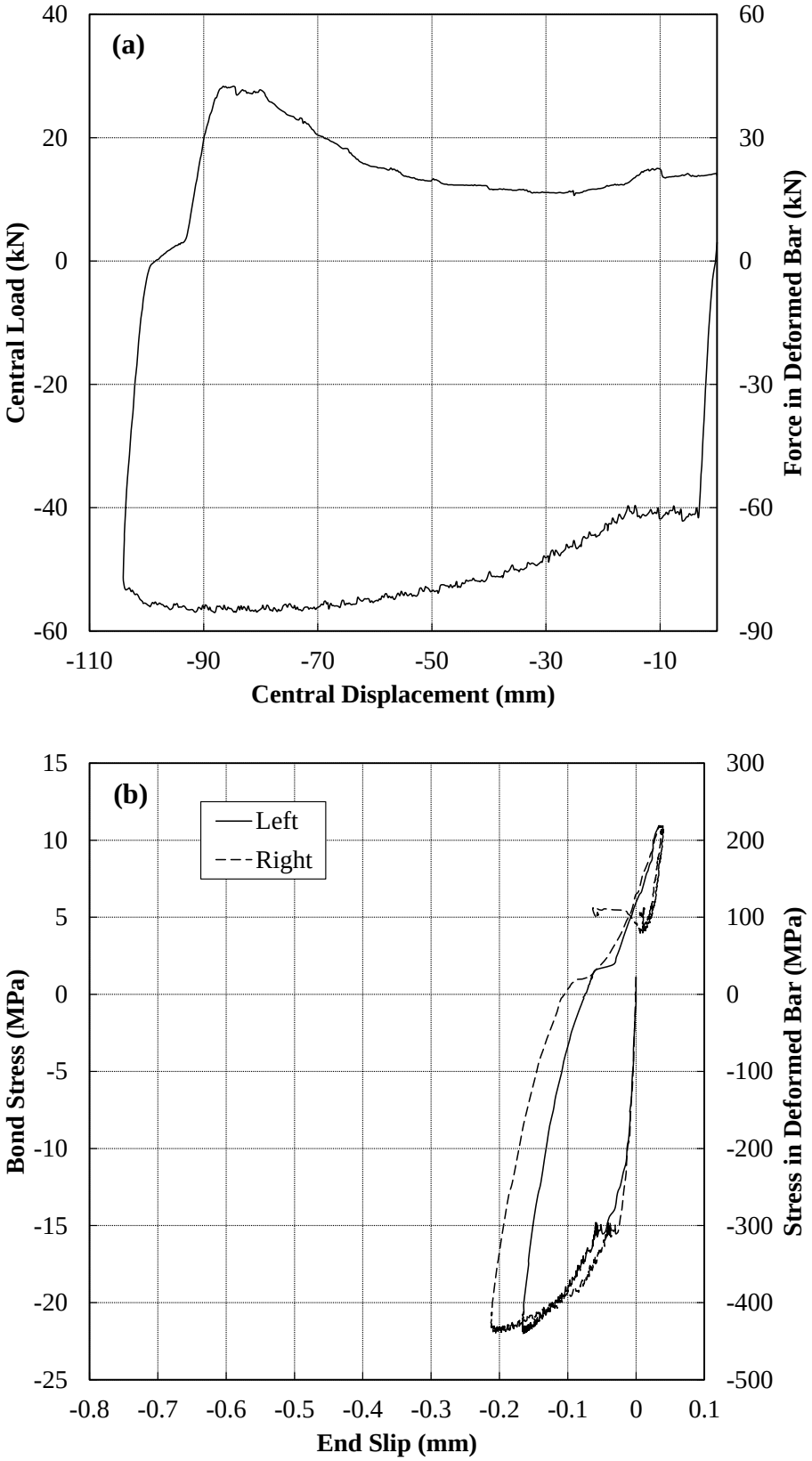

Figure 4.33: (a) Load vs. displacement and (b) averaged bond-stress vs. slip for HSSCC-D16-300G-5D-Mono-S2

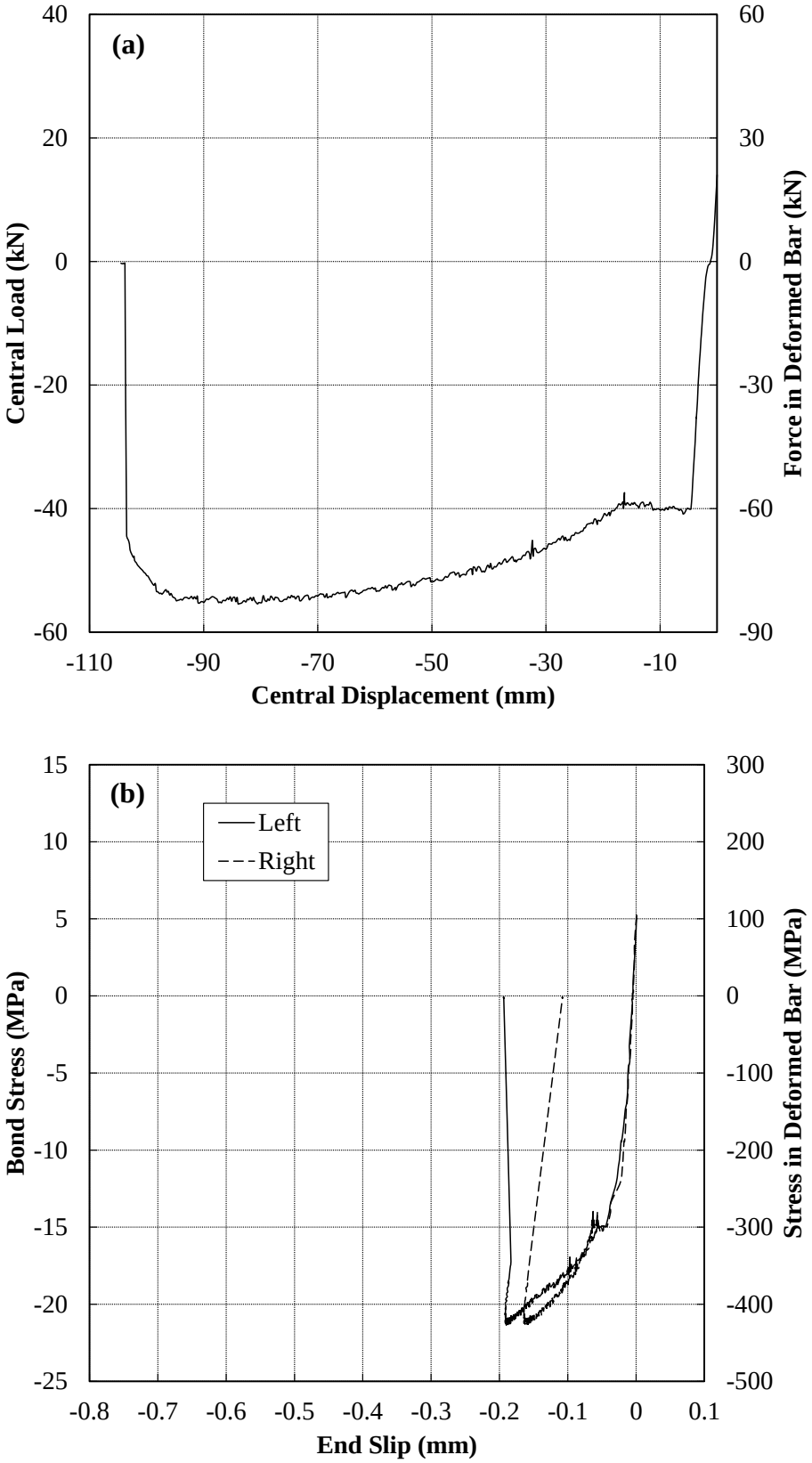

Figure 4.34: (a) Load vs. displacement and (b) averaged bond-stress vs. slip for HSSCC-D16-300G-5D-Mono-S3

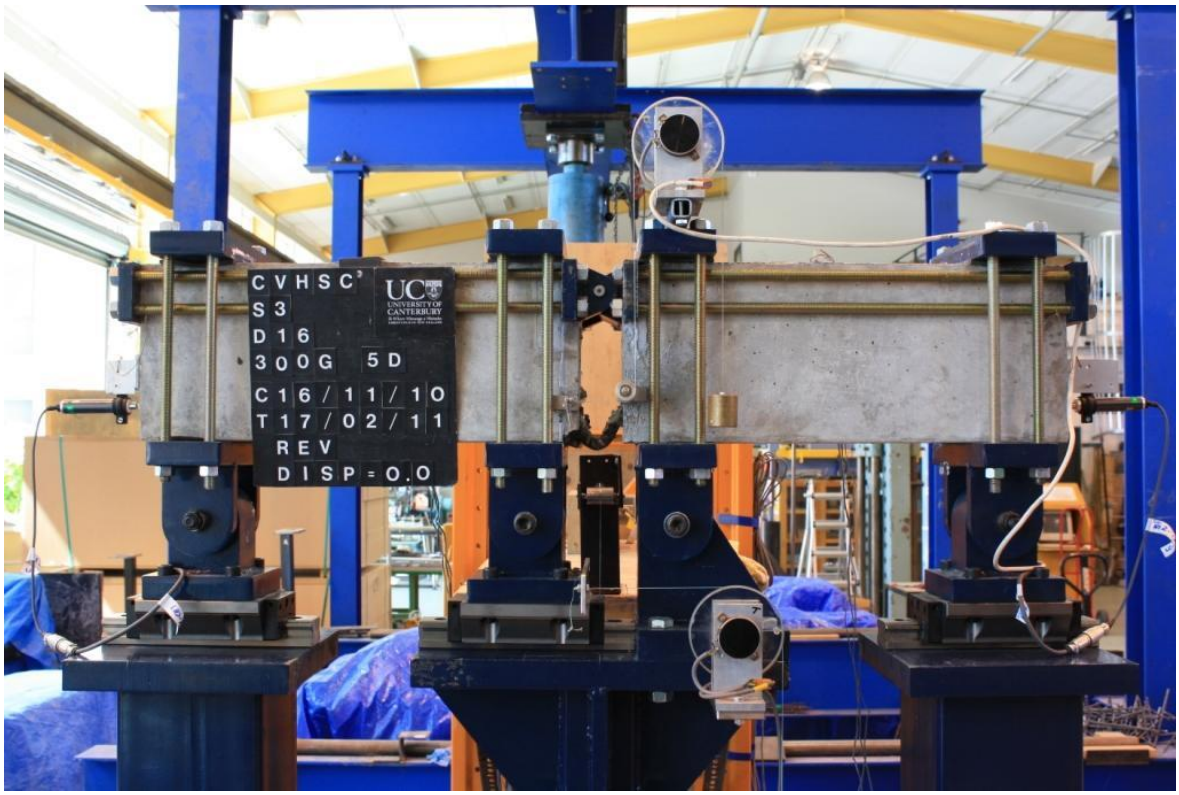

Figure 4.35: Buckling of the bar at the end of the test after returning the beam to the zero displacement point

Specimens HSSCC-D16-300G-5D-S2 and S3 were tested under the finalized cyclic load protocol, which resulted in very similar load-displacement and bond-slip behaviour (Figure 4.21 & Figure 4.22) to that of the CVHSC one (Figure 4.20). Although the peak force and maximum achieved bond stress were almost identical in the HSSCC and CVHSC specimens, the end-slip was two to four times larger in the former. Note that the slip values were very small (below 0.8 mm); without any debonding between reinforcement and concrete (no pullout failure occurred). This can be attributed to the more amount fine aggregates and less coarse aggregates in HSSCC compared to those in CVHSC. Given the steel ultimate capacity of about 440 MPa and the maximum steel stress of 420 MPa achieved in these tests (Figure 4.21-b & Figure 4.22-b), it was not expected that the difference between slips in HSSCC and CVHSC would change the final mode of failure.

The HSSCC-D16-300G-2.5D-S1 to S3 beam specimens which had a smaller bond length (2.5 times the bar diameter) were also tested under the same cyclic loading protocol (Figure 4.17-c). As the bond length was 50% smaller compared to the previous specimens, it was expected that the mode of failure would change to pullout and it did (Figure 4.23 to

Figure 4.25). Bond strength of about 30 MPa was achieved in both directions (tensile and compressive) which started to deteriorate only after about 12 mm central displacement. The bond was almost fully lost after the center of the beam was displaced about 30 mm from its neutral location. Note that due to the limitation of LVDT, the slip could only be measured up to about 5 mm. Specimens with higher grade of steel (i.e. HSSCC-D16-500G-5D-S1 to S3) were tested cyclically. Although the bond length was 5 times the bar diameter, because the steel could undergo higher forces before yielding, pullout was the final mode of failure (Figure 4.26 to Figure 4.28). The maximum bond stress peaked at 30 MPa and the bond deterioration started after about 1 mm slip occurred during the previous cycles.

The same test setup and loading protocol were used to test the HSSCC-D25-300G-5D-S1 to S3 specimens. However as the applied load increased substantially (because a larger bar diameter was used), the pin at the centre of the steel hinge broke while the first specimen was being tested; this can clearly be seen in Figure 4.29. Initially the bond behaviour of these specimens was following the same pattern as that of D16 ones of similar parameters. However, pullout failure started to happen after the first 10 cycles were finished and became the governing mode of failure. This is attributed to the fact that, the same amount of transverse reinforcement was used to confine the radial cracks which were now being generated as a result of greater forces. In other words, the effect confinement was not the same for the 16 mm and 25 mm diameter bars. Therefore, more cracks developed in each half beam (see Appendix C for more photos) which finally led to the loss and failure of bond in these specimens.

Monotonic loading of HSSCC specimens (Figure 4.32 to Figure 4.34) resulted in substantial reduction (about 60%) in the slip compared to the cyclic test results which characterizes the effect of load reversals on the bond-slip behaviour.

4.7 FINITE ELEMENT SIMULATION OF CYCLIC BOND-SLIP BEAM TEST

4.7.1 INTRODUCTION

Capability of the finite element analysis (FEA) software DIANA (2012) in modelling reinforced concrete (RC) members (beam-column joints specifically), is investigated in Chapter 6. Nevertheless, as those specimens were designed based on the current standards, debonding of the beam bars through the joint was not expected to be a possible mode of failure. Therefore, full bond between the reinforcement and concrete was considered when modelling the specimens in DIANA. However, DIANA is also capable of capturing the response of RC members when the bond between the two materials is not perfect. In DIANA, reinforcement can be connected to the surrounding concrete using various methods, including that of the perfect bond, no bond (as in case of the unbounded tendons), automatic bond-slip reinforcements, and manual interface elements.

In the last two methods, a stress-slip law is defined either in the steel properties (automatic bond-slip reinforcement) or in the interface properties (manual interface elements). Depending on the application and modelling requirements, the reinforcements can be defined either as beam or truss elements. In order to scrutinize the accuracy and capability of DIANA in dealing with bond-slip type problems, an attempt has been made to model the cyclic sample beam specimen (proposed in section 4.4) using DIANA in order to capture its bond-slip response under monotonic and cyclic loading. The specimen is modelled using curved shell elements (for concrete), one dimensional beam elements (for steel) and interface elements to connect the concrete and steel. The backbone of the cyclic bond-slip response resulted in the experiments is fed into the interface property as an input and the overall response of the specimen is investigated under different loading types.

4.7.2 MATERIAL MODELS

The total strain rotating crack model was used to model the concrete constitutive behaviour; details of which can be found in section 6.3.1 of Chapter 6. The steel was modelled using both elastic and Menegotto et al. (1973) models for the auxiliary and main

reinforcements, respectively (see section 6.3.4 of Chapter 6 for details of the Menegotto-Pinto model). However, the bond between the deformed bar and concrete was modelled using the line-to-shell interface elements for which the hysteresis rules governing the loading-unloading-reloading are summarized below.

- ✓ A single shear stress vs. slip relationship must be specified to represent the back-bone of the bond-slip response.
- ✓ The defined shear stress vs. slip relation is the same for both positive and negative values of slip.
- ✓ Unloading follows the secant modulus back to the origin which means there is no consideration for the residual slips.
- ✓ Irrespective of the cycle number, when slip reversal happens, the reloading always follows the full backbone curve which means there is no consideration for bond deterioration under cyclic loading.

The line-to-shell elements consist of a line at one side and a curved shell at the other side of the interface. These elements can be used to connect a beam or a truss to a curved shell element in which the beam or truss is located. More details of the line-shell interface elements can be found in DIANA (2012) manual.

4.7.3 DEVELOPMENT OF THE FINITE ELEMENT MODEL

To facilitate the explanations pertaining to the development of the FE modelling of the beam specimen, a completed model of the beam is presented and labelled in Figure 4.36. The concrete was modelled using the two-dimensional curved-shell elements which were explained in Chapter 6. In order to avoid the stability and convergence issues in the FEA, linear material properties were defined for the areas near the supports and loading points (shown in dark grey in Figure 4.36). However, the rest of the concrete was modelled incorporating the relevant nonlinear material properties derived from the experiment and available formulations in the literature (also see Chapter 6).

The steel hinge was modelled using a rigid truss element pinned at both ends. Although this looks different to the actual steel hinge (with one pin at the centre), the forces would

remain unchanged due to the shape of the bending moment diagram (constant moment between the loading points). As the loading points in the FE modelling did not impose any constraints in directions other than specified, it sufficed to define a roller (right side) and a pin (left side) support in order to generate a stable and determinate structural system. Note that the loading protocol used in the experiment (Figure 4.9a) was applied at the loading points in the form of a displacement control regime. In order to add to the stability of the FE model, all of the nodes at the top and bottom edges of the beam were restricted from moving in the 'z' direction (perpendicular to the beam plane). The auxiliary reinforcements in each half-beam were modelled using the full bond embedded reinforcement option in DIANA (explained in Chapter 6) in their exact locations in the beam cross-section (Figure 4.37).

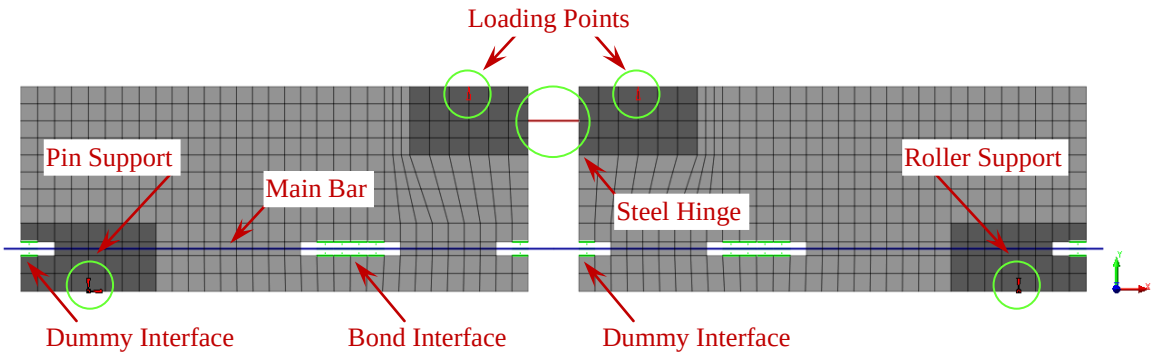

Figure 4.36: Finite element model of the beam specimen

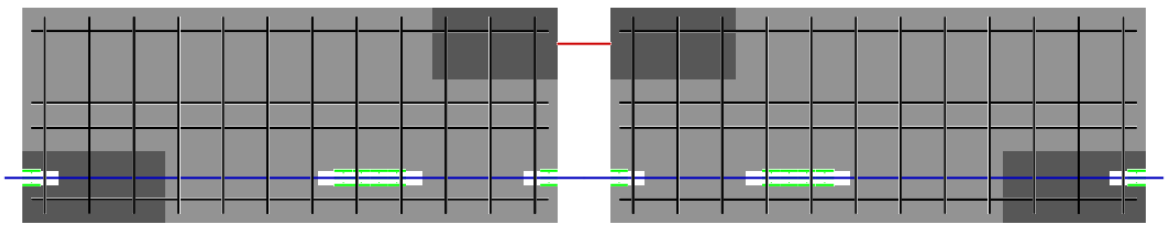

Figure 4.37: Location of the auxiliary reinforcements in the FE model of the beam

The deformed bar was modelled using beam elements and cross sectional properties of a deformed bar of 16 mm diameter to represent the main bar under investigation. Although the deformed bar looks to be connected to the concrete in the areas in which it should be unbonded, debonding was guaranteed by choosing different/separate nodal points for the line element representing the reinforcing bar and the shell element representing the concrete. Line-to-shell interface elements were defined in the two bonded regions where the deformed bar was supposed to be connected to the concrete. The backbone bond-slip

relation derived from the experiment was fed to the properties of these interface elements (Figure 4.38). Dummy interface elements with zero shear-slip properties were also defined at the inner and outer edges of each half-beam such that the deformed bar remains inside the concrete. While this allows for the bar and surrounding concrete elements to move together, the physical interaction between the two is actually zero.

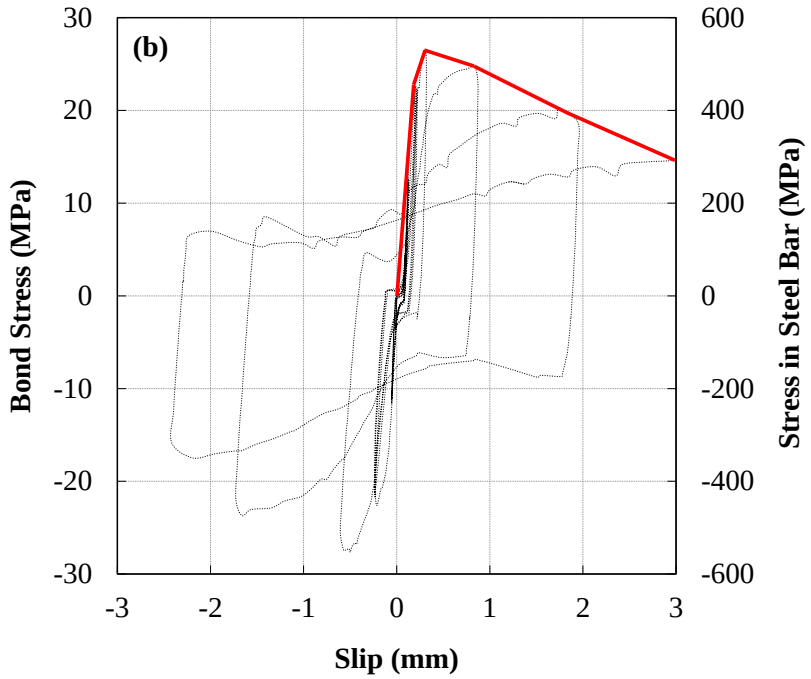

Figure 4.38: Backbone curve of the bond-slip response for the interface element

4.7.4 FINITE ELEMENT ANALYSIS

After the finite element model of the beam specimen was completed and all of the relevant material models, mesh discretization, loading, and boundary conditions were implemented in the data file, a nonlinear analysis was performed on the FE model. Note that because the deterioration of bond (see section 4.7.2) has not been yet implemented in DIANA, in the finite element analysis each loading cycle was repeated only once (as opposed to three times in the actual test). Here again, a pushover analysis was first performed in order to check the stability of the analysis and accuracy of the results. Figure 4.39 shows the comparison between the experimental cyclic and analytical pushover bond stress versus slip plots. Note that although the backbone curve was fed to the properties of the interface elements, after the FEA was performed the average bond-slip response was derived indirectly from the forces, moments and displacements to make sure that the expected

behaviour could be captured. In other words, the generated forces at the loading points were derived from the FEA, the vertical support reactions were found, the maximum bending moment at the centre of the beam was calculated, the force in the bar was determined using the bending moment, and finally the bond stress was worked out by dividing this force by the bond surface. The slip was worked out by calculating the relevant displacement between the concrete and deformed bar at two adjacent mesh nodes. As a result, the bond-slip response shown in Figure 4.39 is obtained.

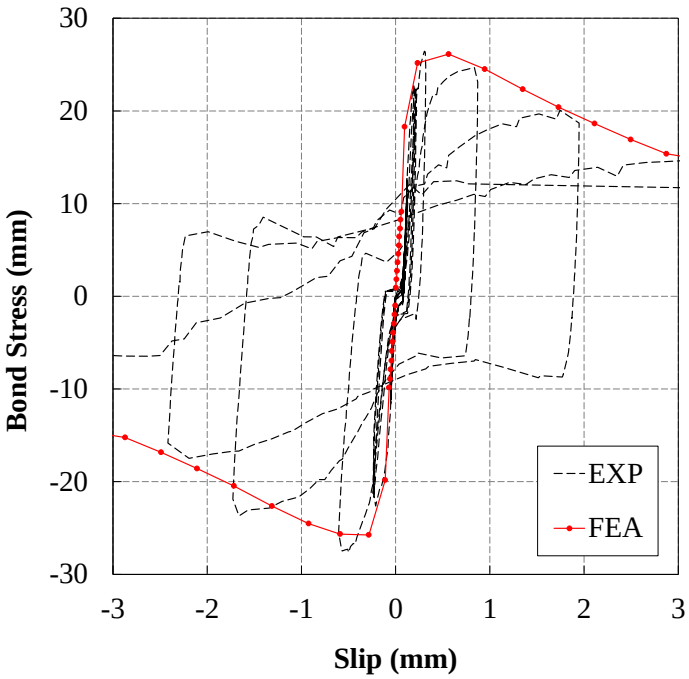

Figure 4.39: Comparison of the bond stress vs. slip between FEA and experiment

The FE predictions of the load versus central displacement of the beam specimen were also compared to the experimental results (Figure 4.40). It is clear from the figure that the initial stiffness predicted in FEA was slightly higher than the experimental results. Because of the nature of this test (two half-beams and a gap at the centre) and that the interaction between concrete and the deformed bar is only through the bonded zones, cracking was expected to occur only around the bonded area. This was proved to be the case in the experimental testing of the beams (Figure 4.41). The FEA predictions of the crack patterns and location (Figure 4.42) were also checked in order to make sure that the FEA could also predict other pertinent properties associated with steel-concrete bond. As it is clear, the crack patterns predicted by FEA were exactly located around the bonded regions and

directed towards the centre of the beam. This shows that the mechanism of the load transfer from steel to the concrete happens in an appropriate way.

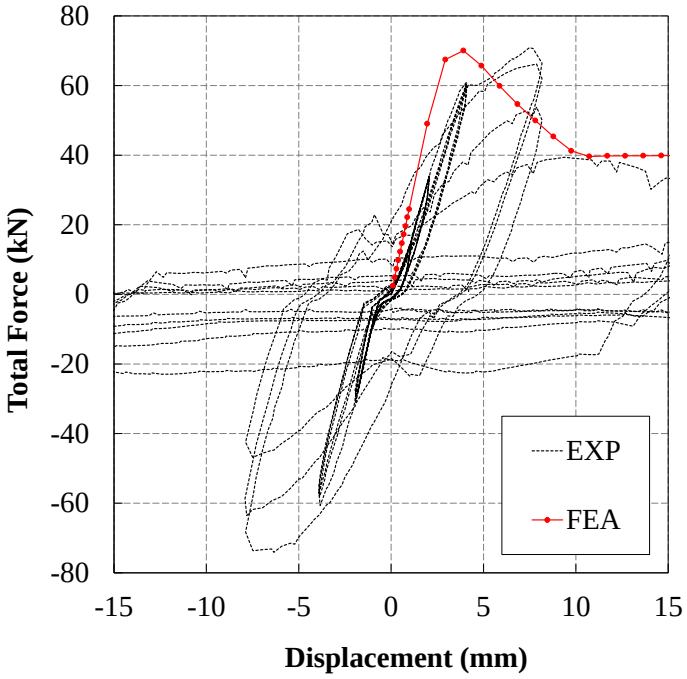

Figure 4.40: Comparison of the load vs. central displacement between FEA and experiment

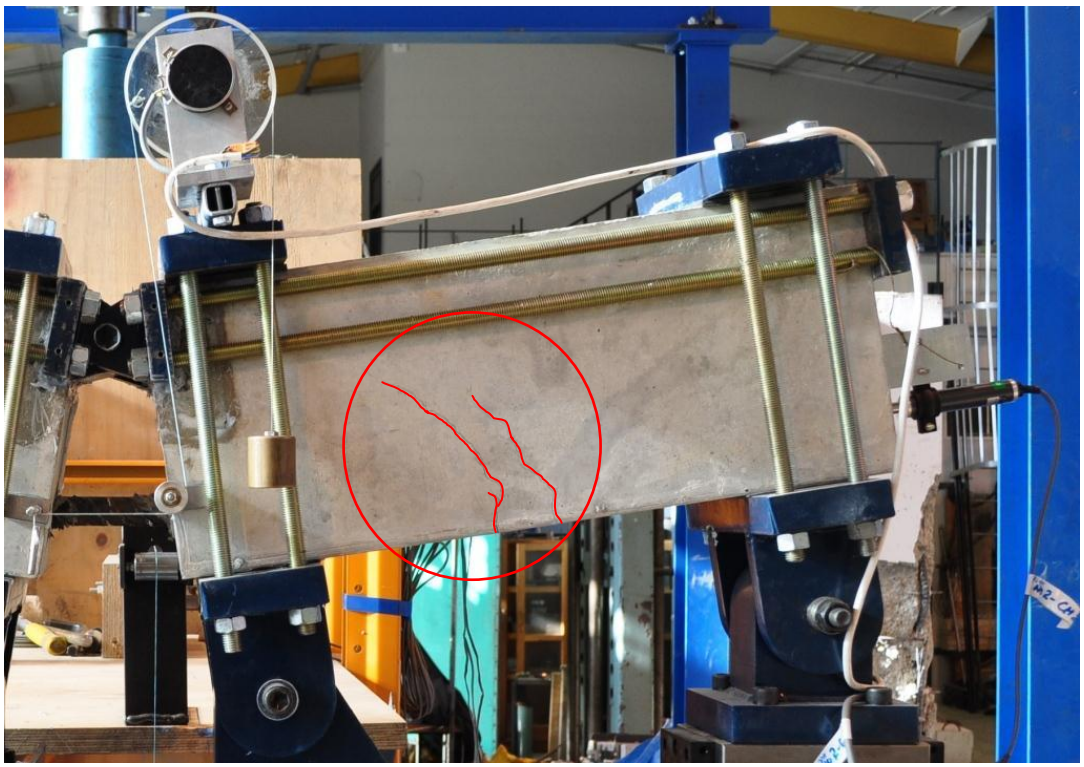

Figure 4.41: Cracking pattern in the experiment

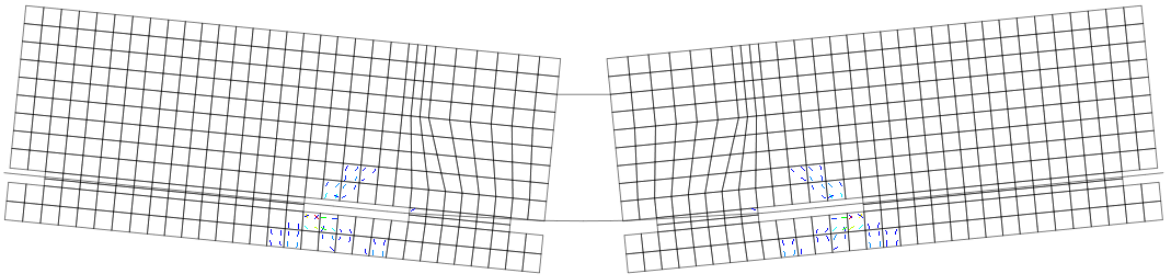

Figure 4.42: Crack patterns predicted by FEA

The stress distribution across the face of the beam also indicates load transfer passage and the possible locations of cracking (Figure 4.43). As expected, the areas around the steel hinge and the bonded zones had the highest stress concentrations and the stress field diminished further from these areas.

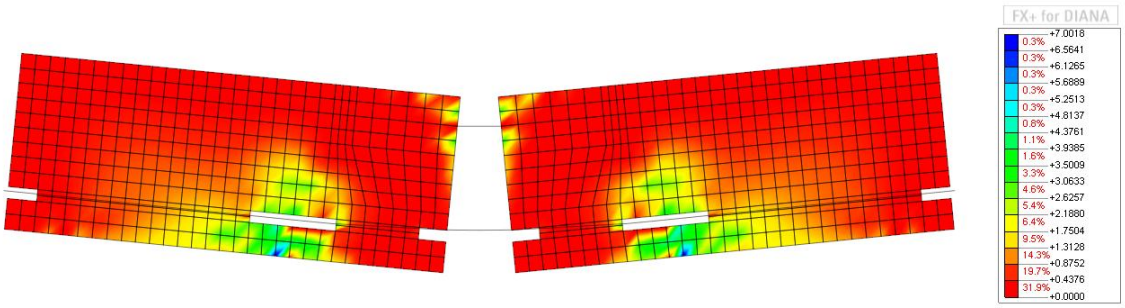

Figure 4.43: Stress distribution

One of the other interesting outcomes of the FEA was the strain distribution along the length of the deformed bar. Figure 4.44 shows the strain profile in the bar at different displacements. In the central region where the bar is unbounded from the concrete, the strain remained constant between the interior faces of the bonded zones. However, it started decreasing substantially as soon as the bar enters the bonded zone in the concrete and transfers the forces from the bar to the concrete. The strain value reached very close to zero at the exterior portions of the bar outside concrete and remained almost constant. This was expected from the geometry of the specimen and was therefore a logical prediction by the FEA. In addition, before the slip started (upto and including the 4 mm displacement cycle) the bar strain increased as the displacement grew larger. However, when the slip started and a longer bar length contributed in taking the tensile force, the strain in the bar started to reduce.

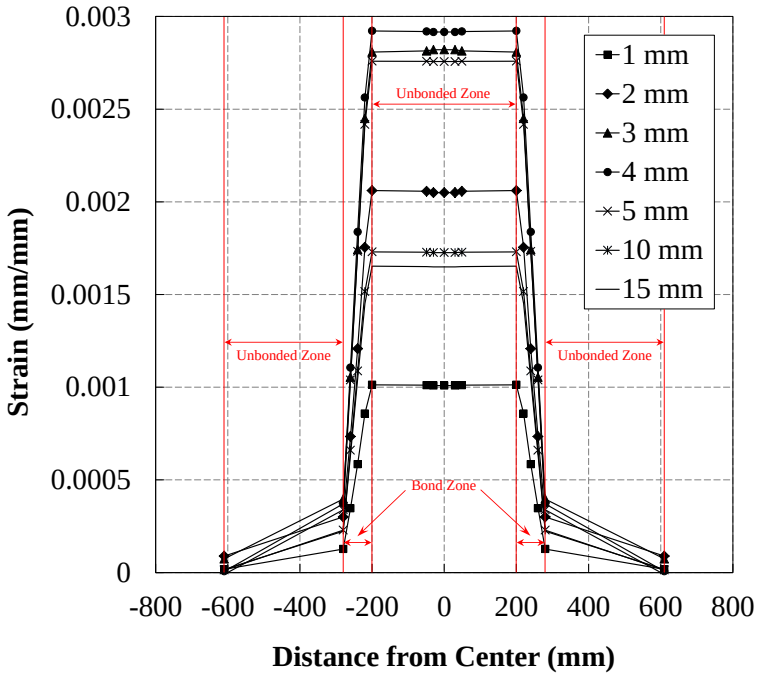

Figure 4.44: Strain profile along the bar length at different displacements

Once the stability and convergence of the nonlinear analysis and performance of the interface elements in representing the bond between steel and concrete was scrutinized through the pushover analysis, the cyclic loading protocol (Figure 4.9a) used in the experiment was applied to the FEA. Figure 4.45a shows the comparison of central displacement of the beam versus slip between the FEA and experiment. It is clear that in the initial cycles, an identical slip value predicted by the FEA happened from a lower displacement of the beam compared to the experimental results. However, this was compensated in the bigger cycles where the FEA provided a better agreement to the experimental values. Figure 4.45b illustrates the FE predictions for bond stress versus slip derived in the same fashion as the ones in pushover analysis. Due to the crude cyclic loops implemented in the bond model in DIANA as explained before (see section 4.7.2), the unloading always headed back towards the origin and reloading followed the full push-over curve. This means that the residual slip and bond capacity in the reversed cycles could not be captured by the FEA.

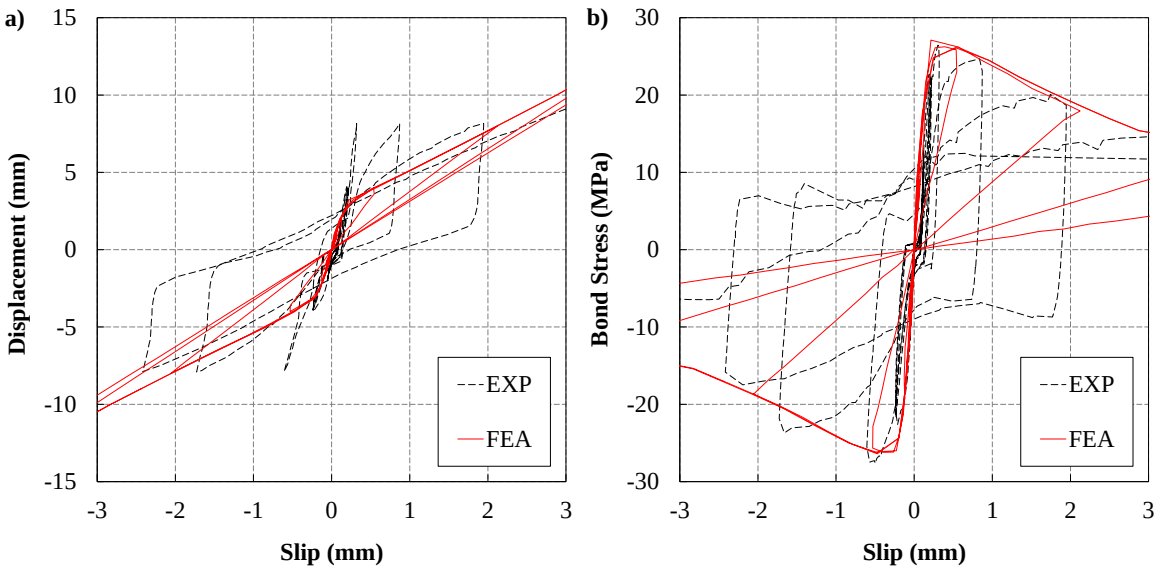

Figure 4.45: Comparison of the cyclic displacement (a) and bond stress (b) vs. slip between FEA and experiment

Figure 4.46 shows the FE prediction of load vs. central displacement response under cyclic loading. As it was expected from the pushover response (Figure 4.40), a higher initial stiffness was predicted by the FE cyclic analysis. In addition, the origin oriented behaviour of the bond interface response under cyclic loading also affected the load-displacement relationship. This means that a much lesser energy dissipation was predicted by the FE results. This can be further improved by implementation of a modified interface properties under cyclic loading to account for residual slip and paths dependent strength deterioration.

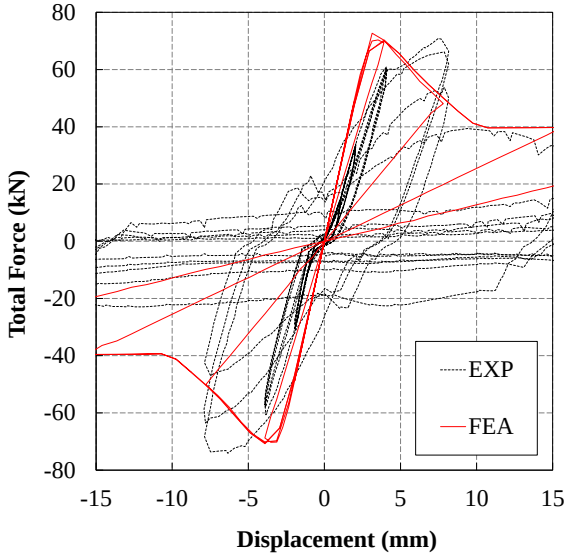

Figure 4.46: Comparison of the cyclic load vs. central displacement between FEA and experiment

4.8 CONCLUSIONS

The available methods to assess bond under reversed cyclic loading are limited to the pullout type tests where the state of stresses in the steel and concrete are different from the actual stress states in RC structural members. In the present study, the beam specimen specified by RILEM for testing monotonic bond behaviour has been modified in such a way that it can sustain cyclic loading. Moreover, a suitable test setup has also been designed to test the modified beam specimen under two-point cyclic loading. The devised test setup was stable and capable of subjecting the modified beam specimen to reverse cyclic displacements; it enabled the cyclic bond-slip relationship to be obtained experimentally.

The validity and applicability of the proposed cyclic test method was assessed by comparing the obtained bond-slip relationship with experimental results of pullout-based monotonic and cyclic tests. It was observed that the bond strength was similar in the monotonic pullout and the proposed cyclic tests when similar material properties and equal bond lengths were used. However, unlike in the monotonic test which maintained the maximum bond stress as the slip increased, the bond stress was found to reduce considerably in the beam specimen under reversed cyclic loading once the maximum bond strength was achieved. Therefore, as opposed to the ductile bond-slip envelope observed under monotonic loading, a substantial deterioration of bond stress occurred under cyclic loading which can potentially have a marked influence on seismic performance of RC structures.

In order to investigate possible effects of bar buckling and loading protocols on the results, eighteen additional high-strength concrete beam specimens with different bar diameter, bond length and steel grade were cast and tested under monotonic and cyclic loading protocols. Initially, fully and symmetrically reversed displacement cycles (with equal peaks in the positive and negative directions) were applied which led to premature buckling and subsequent fracture of the bar at the center which turned out to be the governing mode of failure. However, after applying some adjustments (including the omission of positive cycles) to the loading protocol, an optimized cyclic load protocol was

achieved. Stability, repeatability and reliability of the proposed test setup and experimental results were checked. It was found that when loading is of cyclic nature, more slip occurs for the same overall displacement. Moreover, concrete composition (the proportion of coarse and fine aggregates) was found to affect the slip values. Overall, the test method developed in this study enables researchers to investigate cyclic bond performance in RC members with any type of concrete and reinforcing bars under representative loading condition and more realistic states of stresses.

The nonlinear finite element analysis (FEA) software DIANA was used to predict the monotonic and cyclic bond behaviour of high-strength self-compacting concrete. The analysis was capable of predicting the monotonic bond-slip response envelope, cracking pattern and stress development. However, the currently implemented bond-slip unloading/reloading loops in DIANA were unable to capture the cyclic bond performance accurately. An improved cyclic bond-slip constitutive response will have to be implemented in DIANA so that the residual slips (during unloading/reloading) are better represented. This will potentially improve the FEA results of other bond-critical structural members.

4.9 REFERENCES

Alavi-Fard, M & Marzouk, H 2002, 'Bond behavior of high strength concrete under reversed pull-out cyclic loading', Canadian Journal of Civil Engineering, vol. 29, no. 2, pp. 191-200.

Campione, G, Cucchiara, C, La Mendola, L & Papia, A 2005, 'Steel-concrete bond in lightweight fiber reinforced concrete under monotonic and cyclic actions', Engineering Structures, vol. 27, no. 6, pp. 881-890.

Cattaneo, S & Rosati, G 2009, 'Bond between Steel and Self-Consolidating Concrete: Experiments and Modeling', ACI Structural Journal, vol. 106, no. 4, pp. 540-550.

Chan, Y-W, Chen, Y-S & Liu, Y-S 2003, 'Development of bond strength of reinforcement steel in self-consolidating concrete', ACI Structural Journal, vol. 100, no. 4, pp. 490-498.

Dancygier, AN, Katz, A & Wexler, U 2010, 'Bond between deformed reinforcement and normal and high-strength concrete with and without fibers', Materials and Structures/Materiaux et Constructions, vol. 43, pp. 839-856.

De Almeida Filho, FM, El Debs, MK & El Debs, ALHC 2008, 'Bond-slip behavior of self-compacting concrete and vibrated concrete using pull-out and beam tests', Materials and Structures/Materiaux et Constructions, vol. 41, no. 6, pp. 1073-1089.

Desnerck, P, De Schutter, G & Taerwe, L 2010, 'Bond behaviour of reinforcing bars in self-compacting concrete: Experimental determination by using beam tests', Materials and Structures/Materiaux et Constructions, vol. 43, pp. 53-62.

Dhakal, RP & Maekawa, K 2002, 'Reinforcement stability and fracture of cover concrete in reinforced concrete members', Journal of Structural Engineering, vol. 128, no. 10, pp. 1253-1262.

DIANA 2012, DIANA Manual Release 9.4.4, TNO DIANA BV, Delft, The Netherlands.

EFNARC 2002, Specification and Guidelines for Self-Compacting Concrete, European Federation of Procedures and Applicators of Specialist Products for Structures

EFNARC 2005, The European Guidelines for Self-Compacting Concrete Specification, Production and Use, European Federation of Procedures and Applicators of Specialist Products for Structures

El-Hacha, R, El-Agroudy, H & Rizkalla, SH 2006, 'Bond characteristics of high-strength steel reinforcement', ACI Structural Journal, vol. 103, no. 6, pp. 771-782.

Fang, CQ, Gylltoft, K, Lundgren, K & Plos, M 2006, 'Effect of corrosion on bond in reinforced concrete under cyclic loading', Cement and Concrete Research, vol. 36, no. 3, pp. 548-555.

Menegotto, M & Pinto, E 1973, 'Method of Analysis for Cyclically Loaded Reinforced Concrete Plane Frames Including Changes in Geometry and Non-Elastic Behaviour of Elements Under Combined Normal Force and Bending ', in IABSE Symposium on the Resistance and Ultimate Deformability of Structures Acted on by Well-Defined Repeated Loads, Lisbon, Portugal.

Popov, EP 1984, 'Bond and Anchorage of Reinforcing Bars Under Cyclic Loading', Journal of the American Concrete Institute, vol. 81, no. 4, pp. 340-349.

RILEM-FIP-CEB 1973, 'Tentative recommendations, recommendations for reinforcing steel, bond test for reinforcing steel: 1- Beam test (7-II-28 D) 2- Pull-out test (7-II-128)', Materials and Structures, vol. 6, no. 2, pp. 79-118.

Soleymani Ashtiani, M, Dhakal, RP & Scott, AN 2011a, 'Bond properties of reinforcement in high-strength self-compacting concrete', in Proceedings of the 9th Symposium on High Performance Concrete Design, Verification and Utilization, Rotorua, New Zealand.

Soleymani Ashtiani, M, Scott, AN & Dhakal, RP 2011b, 'Mechanical properties of high-strength self-compacting concrete', in 21st Australasian Conference on the Mechanics of Structures and Materials, ACMSM21, December 7, 2010 - December 10, 2010. CRC Press, Melbourne, VIC, Australia, pp. 827-832.

Soleymani Ashtiani, M, Scott, AN & Dhakal, RP 2013, 'Mechanical and Fresh Properties of High-Strength Self-Compacting Concrete Containing Class C Fly Ash', Construction and Building Materials, vol. 47, pp. 1217-1224.

Su, N, Hsu, K-C & Chai, H-W 2001, 'A simple mix design method for self-compacting concrete', Cement and Concrete Research, vol. 31, no. 12, pp. 1799-1807.

5 EXPERIMENTAL INVESTIGATIONS ON CYCLIC PERFORMANCE OF HSSCC INTERIOR BEAM-COLUMN JOINTS

Soleymani Ashtiani, M, Dhakal, RP & Scott, AN 2013, 'Seismic Performance of High-Strength Self-Compacting Concrete in Reinforced Concrete Beam-Column Joints', *journal of structural Engineering*, DOI: 10.1061/(ASCE)ST.1943-541X.0000973 (Published)

Soleymani Ashtiani, M, Dhakal, RP & Scott, AN 2012, 'Seismic Performance of High-Strength Self-Compacting Concrete in Reinforced Concrete Beam-Column Joints', in *15th World Conference on Earthquake Engineering*, Lisbon, Portugal.

Soleymani Ashtiani, M, Dhakal, RP & Scott, AN 2012, 'Combining high-strength self-compacting and normal-strength concretes in reinforced concrete frame structures', in *22nd Australasian Conference on the Mechanics of Structures and Materials, ACMSM22, December, 2012*, Sydney, Australia.

Soleymani Ashtiani, M, Dhakal, RP & Scott, AN 2013, 'Using High-Strength Self-Compacting Concrete in Reinforced Concrete Beam-Column Joints', in *New Zealand Society for Earthquake Engineering*, Wellington, New Zealand.

Soleymani Ashtiani, M, Dhakal, RP & Scott, AN 2013, 'Shear behavior of high-strength self-compacting concrete beam-column joint panels', in *Fifth North American Conference on the Design and Use of Self-Consolidating Concrete*, Chicago, Illinois, USA.

5.1 ABSTRACT

Due to its potentially beneficial properties, there has been an increased interest in recent years on performance of self-compacting concrete (SCC) in structural members. The capability of SCC in flowing through and filling in even the most congested areas makes it ideal for being used in congested reinforced concrete (RC) structural members such as beam-column joints (BCJ). However, members of tall multi-storey structures impose high capacity requirements where implementing normal-strength self-compacting concrete (NSSCC) is not preferable.

In the present study seven beam-column joints (BCJ) were designed following the guidelines of the New Zealand concrete standards NZS3101; namely four high-strength self-compacting concrete (HSSCC), one conventionally vibrated high-strength concrete (CVHSC), one conventionally vibrated concrete (CVC), and one CVC with HSSCC in its joint region. Factors such as the concrete type, grade of reinforcement, amount of joint shear stirrups, axial load, and direction of casting were considered variables in designing these specimens. All BCJs were tested under a displacement-controlled quasi-static reversed cyclic regime. It was found that not only none of the seismically important features were compromised by using HSSCC, but also the quality of material and ease of construction boosted the performance of beam-column subassemblies.

5.2 INTRODUCTION

Due to its special fresh and mechanical properties, self-compacting concrete (SCC) has been regarded as one of the most important advances in concrete technology after its advent more than two decades ago. It has a unique ability to flow into a uniform level under the influence of gravity with the ability to compact by means of its self-weight without any internal or external vibration. Based on its exceptional flowing properties, SCC is able to be implemented in complex formworks even in highly congested reinforced concrete (RC) members. Therefore, the interest in utilizing SCC in members of concrete framed structures has increased manifold over the recent years.

The intersection of beams and columns represents one of the most congested parts of RC framed structures. Placing and consolidating concrete in such areas has often imposed difficulties which results in imperfect compaction and/or segregation of concrete. This entails other side effects such as deteriorated bond properties which leads to a greater column depth requirement than otherwise required to meet the bond demand. The flowing and filling capability of SCC makes it ideal for being used in RC members such as beam-column joints (BCJ) of high-rise buildings. However, members of tall multi-storey structures impose high capacity requirements where implementing normal-strength self-compacting concrete (NSSCC) is not preferable. At the same time, BCJs are subjected to large horizontal shear forces in the joint panel which requires large amount of shear reinforcement between the top and bottom beam bars. Therefore considering the

advantages (noise reduction, reduced labour force, higher material quality and better surface finish) of high-strength self-compacting concrete (HSSCC) over conventionally vibrated concrete (CVC), if the seismic performance is not compromised, the implementation of HSSCC in BCJs could be an answer to all of the mentioned problems (i.e. compaction, bond and shear requirements).

Fresh and mechanical properties (compressive, splitting tensile, and flexural strengths as well as modulus of elasticity, shrinkage and bond strength) of SCC including their comparison with that of CVC have been extensively investigated (De Almeida Filho et al., 2008; Desnerck et al., 2010; Domone, 2006; Persson, 2001; Soleymani Ashtiani et al., 2011; Soleymani Ashtiani et al., 2010; Soleymani Ashtiani et al., 2013b; Valcuende et al., 2009). Bond properties between deformed bars and HSSCC (including post-yield performance) has also been investigated (Soleymani Ashtiani et al., 2013a) which found that bond performance of HSSCC is superior. More recently, researchers have also looked at the structural performance of RC members cast with SCC under monotonic loads (Hassan et al., 2008; Lachemi et al., 2005; Sonebi et al., 2003). Nevertheless to the best of the authors' knowledge, investigation of seismic behaviour of reinforced concrete beam-column joints cast with SCC is very scarce in literature (Said et al., 2007), and no studies have addressed seismic performance of HSSCC. Following the Canadian and American Standards, Said et al. (2007) fabricated a SCC exterior beam-column joint with 28-day compressive strength of 50 MPa and investigated its performance under reversed cyclic loading. They also compared the behaviour of the SCC joint with that of a CVC benchmark specimen of the same concrete compressive strength range. They reported that the SCC specimen showed comparable cracking behaviour, load and displacement capacities and mode of failure to that of CVC up to 4.5% drift after which a faster reduction in load carrying capacity for SCC was observed. They attributed this to the lower coarse aggregate content in SCC which results in lesser friction due to aggregate interlocking; thus smaller contribution in the total shear resistance mechanism especially at higher drifts. This was also reported to have resulted in a lower concrete contribution towards shear resistance in the beam for SCC specimen compared to that of CVC.

In the present study, a commercially reproducible HSSCC mix (100 MPa compressive strength) was designed using locally available materials in Christchurch, New Zealand. For comparison a conventionally vibrated high-strength concrete (CVHSC) mix of equivalent

compressive strength and a normal-strength conventionally vibrated concrete (CVC) were also developed. Seven beam-column joints (four HSSCC, one CVHSC, one CVC, and one CVC with HSSCC in its joint area) were designed following the guidelines of the New Zealand concrete standard (NZS3101, 2006). Parameters such as concrete and steel type, joint shear reinforcement, axial load, and casting direction were considered variables in designing the specimens. Except for one HSSCC specimen in which 500 grade steel was used, in the rest of the specimens 300 grade reinforcement (having identical features with minor variations) was utilized. Out of the four HSSCC subassemblies one was designed with only about half (56% to be precise) of the required joint shear reinforcement in order to investigate the relative contribution of concrete and joint shear reinforcement on the shear resistance of HSSCC beam-column subassemblies. One specimen was cast vertically and tested under lower axial force in order to investigate the effects of these parameters. All specimens were instrumented with linear variable displacement transducers (LVDT) on the joint and beam regions, strain gauges on both longitudinal and transverse reinforcements at different locations, load-cells at the lateral loading point and beam tips and pressure transducer at the hydraulic jack pipeline to measure the column axial load. All BCJs were tested under a displacement-controlled quasi-static reversed cyclic regime. Recorded data was used to calculate the load vs. displacement, ductility, plastic hinge zone (beam) elongation, stiffness degradation, energy dissipation, deformation components, and contribution of steel and concrete in the joint shear stress. The experimental results of this study were used in identifying the pros and cons of using HSSCC in beam-column joints of the RC structures.

5.3 SPECIMEN PROPERTIES AND TEST SETUP

In the present investigation, locally available materials in Christchurch, New Zealand were used in order to design different concrete mixes (Table 5.1). Details of physical properties of the cement, fly ash, and aggregates as well as the mixing method and procedure are described elsewhere (Soleymani Ashtiani et al., 2010; Soleymani Ashtiani et al., 2013b). All concrete mixes were supplied by a ready mix concrete plant and the concrete quality control and results were acceptable; except for CVHSC mix in which the variation of the designed and actual w/b ratio resulted in lower compressive strength (82.5 MPa) than

required. Note that for CVHSC and CVC mixes the slump and for HSSCC mixes the slump flow diameter were measured.

Table 5.1: Different concrete mix proportions and properties

	HSSCC BCJ1	HSSCC BCJ2	HSSCC BCJ3	HSSCC BCJ4	CVHSC BCJ5	CVC BCJ 6	CVC/HSSC C BCJ7
Coarse (kg/m^3)	880	880	880	880	1145	1045	1045 / 880
Fine (kg/m^3)	870	870	870	870	695	930	930 / 870
Cement (kg/m^3)	385	385	385	385	385	265	265 / 385
Fly ash (kg/m^3)	165	165	165	165	165	-	- / 165
Water (kg/m^3)	165	165	165	165	148.5	158	158 / 165
SP* (kg/m^3)	3.58	3.58	3.58	3.58	1.93	0.79	0.79 / 3.58
w/b (designed)	0.30	0.3	0.30	0.3	0.27	0.6	0.6 / 0.3
w/b (actual)	0.28	0.29	0.32	0.28	0.29	0.61	0.6 / 0.3
Slump (mm)	600	715	700	740	150	80	180 / 740
Comp. st (MPa)**	124.3	112.9	101.1	121.6	82.5	48.4	45.7 / 109.9
Splitting tensile strength (MPa)**	7.0	7.3	7.4	7.0	7.0	4.7	4.8 / 7.4

* SP: Super plasticizer ** These were measured at the day of test (about 90 days after pouring)

Seven standard beam-column joints (Table 5.2), namely BCJ1, BCJ2, BCJ3 and BCJ4 (using HSSCC), BCJ5 (using CVHSC), BCJ6 (using CVC), and BCJ7 (using CVC with HSSCC in the joint area) were designed following the current New Zealand Standard (NZS3101, 2006) requirements to achieve a strong-column-weak-beam hierarchy where the final expected mode of failure was hinging of the beam at the column face. Based on capacity design principals, column was designed to remain elastic throughout the test; this was ensured by keeping the ratio of the factored yield moment of the column (φM_y) to the over-strength moment of the beam ($M_{o,b}$) well above 1.0 for all specimens. The specimen BCJ2 was originally designed to have only the direction of casting as variable. However when the other specimens were being tested, it was decided to reduce the axial load to obtain more information from this specimen. The detailing of the reinforcement was identical in all seven specimens except for slight variations in BCJ3 (amount and type of joint shear reinforcement) and BCJ4 (500 grade steel instead of 300 grade). BCJ2 was cast vertically and tested under lower axial force. Figure 5.1 and Figure 5.2 shows detailing of the shear and longitudinal reinforcement in the beam-column joints. Ratios of the longitudinal reinforcement in the beam (tension side) and column were 0.011 and 0.025,

respectively which were within the limits specified by the New Zealand Standard (NZS3101, 2006).

Table 5.2: Details of all beam-column joint specimens

Specimen ID	Concrete Type	Steel Grade (MPa)	Axial Load (kN)	Beam (T/B)	Column	Joint
BCJ1	HSSCC	300	1500	2(D25+D20)	14 D20	2(HR12+HR10)
BCJ2	HSSCC	300	200	2(D25+D20)	14 D20	2(HR12+HR10)
BCJ3	HSSCC	300	1500	2(D25+D20)	14 D20	4 R10
BCJ4	HSSCC	500	1500	4 HD20	12 HD16	2HR12+HR10
BCJ5	CVHSC	300	1500	2(D25+D20)	14 D20	2(HR12+HR10)
BCJ6	CVC	300	650	2(D25+D20)	14 D20	2(HR12+HR10)
BCJ7	CVC	300	650	2(D25+D20)	14 D20	2(HR12+HR10)

In order to measure the local strains, strain gauges with 3 mm gauge length were installed on the top and bottom longitudinal beam bars as well as the shear reinforcement in the joint, beam and column (only the two stirrups adjacent to the joint). In addition, the beam plastic-hinge zone, beam-column interface and the joint panel were instrumented with LVDTs (installed on the surface) in order to measure the average strains, beam flexural and shear deformations, plastic-hinge zone elongation and joint shear deformations. It should be noted that as the column was designed to remain elastic, monitoring its deformations was not necessary; thus it was not instrumented with LVDTs or strain gauges (Figure 5.2). The lateral load was applied to the top of the column through a 400 kN capacity hydraulic actuator (ram) and measured using a load-cell. The ram was supported on the west by a strong reaction frame designed to take twice the actuator maximum capacity. The displacement was fed to the hydraulic actuator through a portable computer and associated controller. This was measured with a rotary potentiometer (located at the level of the actuator) which was connected to an independent frame to make sure that any slack in the setup did not affect the loading history. The designed axial load was applied through a 2500 kN capacity hydraulic jack and transferred to the column through the top and bottom plates and Macalloy bars. The bottom of the column and beam-ends were fixed to the strong floor using a pin and two roller supports, respectively. The generated loads at the end of the beams were measured using two load-cells. Figure 5.4 shows a schematic view of the setup used to test the beam-column subassemblies. A quasi-static displacement-controlled loading regime (Figure 5.4b) was adopted following the ACI guidelines for moment resisting frames (ACI374.1-05, 2005).

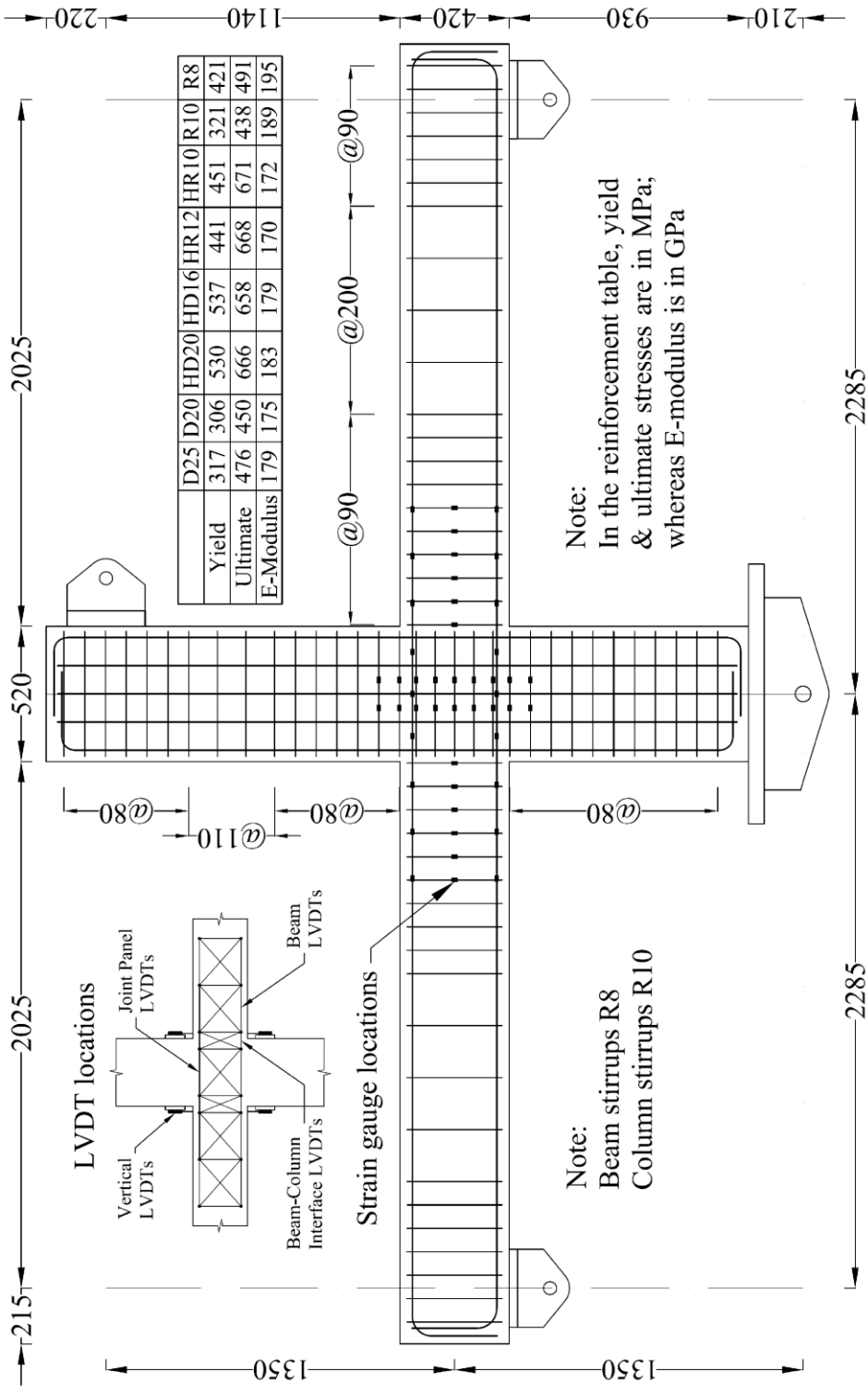

Figure 5.1: Typical details of reinforcement and instrumentation on a beam-column subassembly (dimensions are in ‘mm’)

Figure 5.2: Typical details of reinforcement in the beam, column and joint sections (dimensions are in 'mm')

The positive (+) and negative (-) drift directions were chosen based on the sign convention given in Figure 5.3. Up to the 0.5% drift cycles, displacement increments of 0.5 mm were used in each loading step; however 1 mm increments were used for the rest of the cycles. Each displacement cycle was repeated 3 times and starting after the 0.5% drift cycle, a small cycle (1/3 magnitude of the preceding one) followed each cycle set. The axial load was monitored and maintained throughout the test (using a pressure transducer) such that the axial load to capacity ratio remained almost the same (except for BCJ2) for all specimens (0.07, 0.01, 0.08, 0.07, 0.1, 0.08, and 0.08 for BCJ1 to BCJ7, respectively). The test was paused at both '+' and '-' peaks of the 3rd cycle of each drift set. At each pause, cracks were marked and labelled with the drift, crack-widths were measured (using a hand microscope of 0.01 mm accuracy) and pictures were taken of the overall specimen and different damaged parts. In order to follow the crack patterns more efficiently, two grids of size 65 mm and 100 mm were drawn on the joint and beam surfaces, respectively. A test report was completed at every pause in order to associate the observations to the manually collected data.

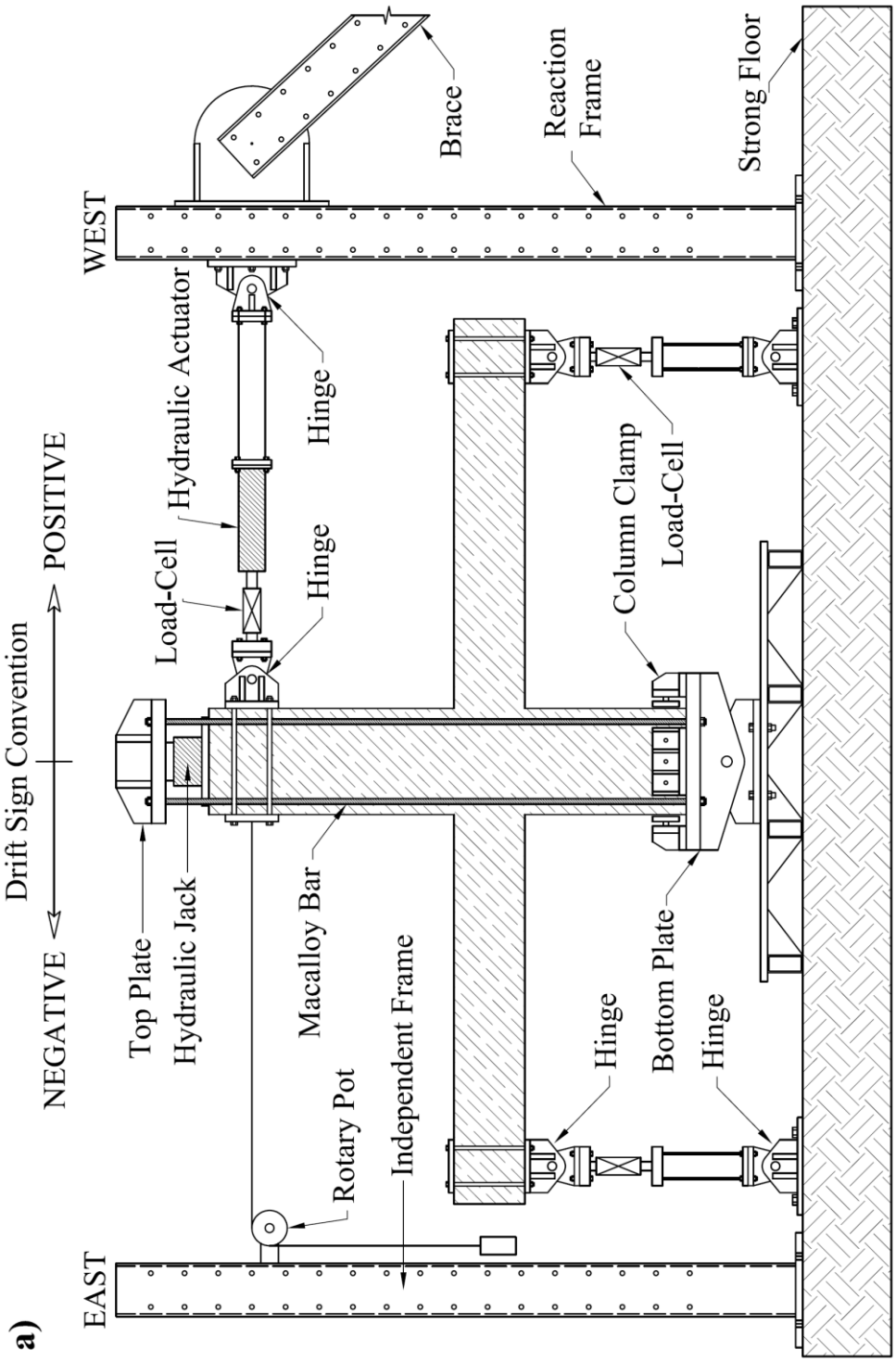

Figure 5.3: Schematic view of the test setup

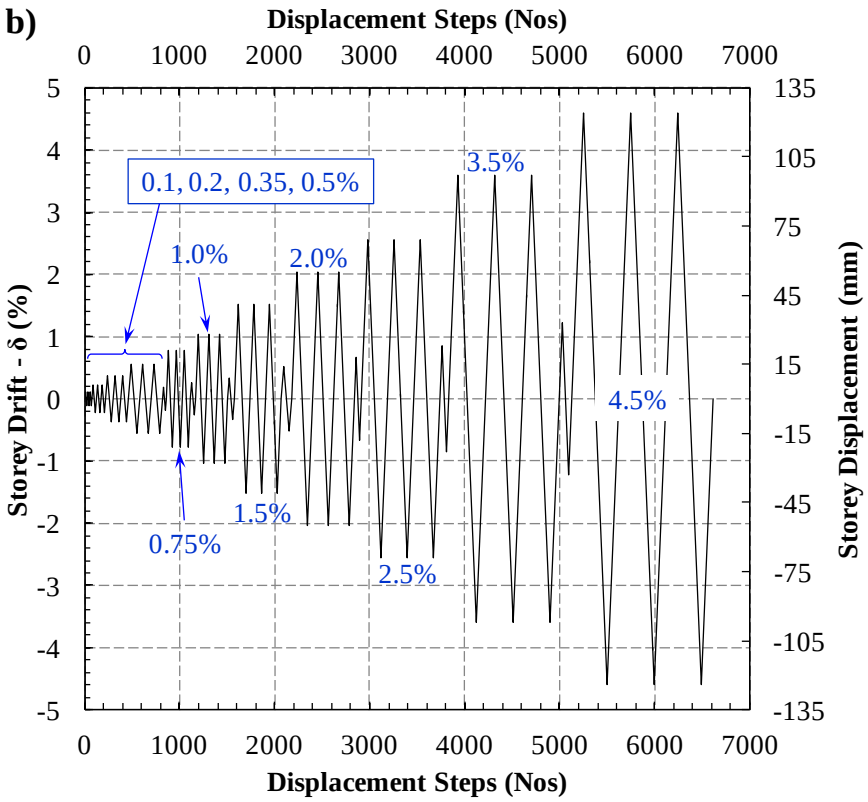

Figure 5.4: Applied displacement history

5.4 RESULTS AND DISCUSSIONS

5.4.1 HYSTERESIS RESPONSE AND CRACKING

Figure 5.5a to Figure 5.5g show the storey-shear versus drift responses for the seven specimens. The yield and test-end points (including displacement 'Δ', drift 'δ', and the storey shear) are annotated based on the test observations and the change in stiffness. The horizontal solid lines in Figure 5.5 (just above the yield points) show the predicted shear strength of the specimens calculated based on the factored nominal moment capacity of the beam (φM_n). Based on the ACI recommendations (ACI374.1-05, 2005) the limiting drift value for the RC moment resisting frames is 3.5%. However, the adopted test setup in this study limited the maximum applicable drift to 4.5%, and none of the specimens had failed when the test was terminated after applying the 4.5% drift cycles. The measured drift (δ) values were converted to equivalent ductility (μ) defined as the ratio of drift (δ) at any stage to the drift at yield (δ_y); this is illustrated on a secondary axis parallel to the drift axis in Figure 5.5. According to the hysteresis loops for an identical ultimate drift of 4.5%, all

BCJs proved to be almost equally ductile with the ductility value of around 5 for all specimens (except for BCJ4). This contradicts the general notion that high-strength concrete (HSC) behaves in a brittle manner; in fact the better bond between concrete and reinforcement resulted in higher strain compatibility between the two materials; resulting in a relatively high ductility. In case of BCJ4 and considering a high-strength steel (of grade 500 MPa with lower ductility) was used for longitudinal reinforcement, the lower ductility of 3.18 was not beyond expectation.

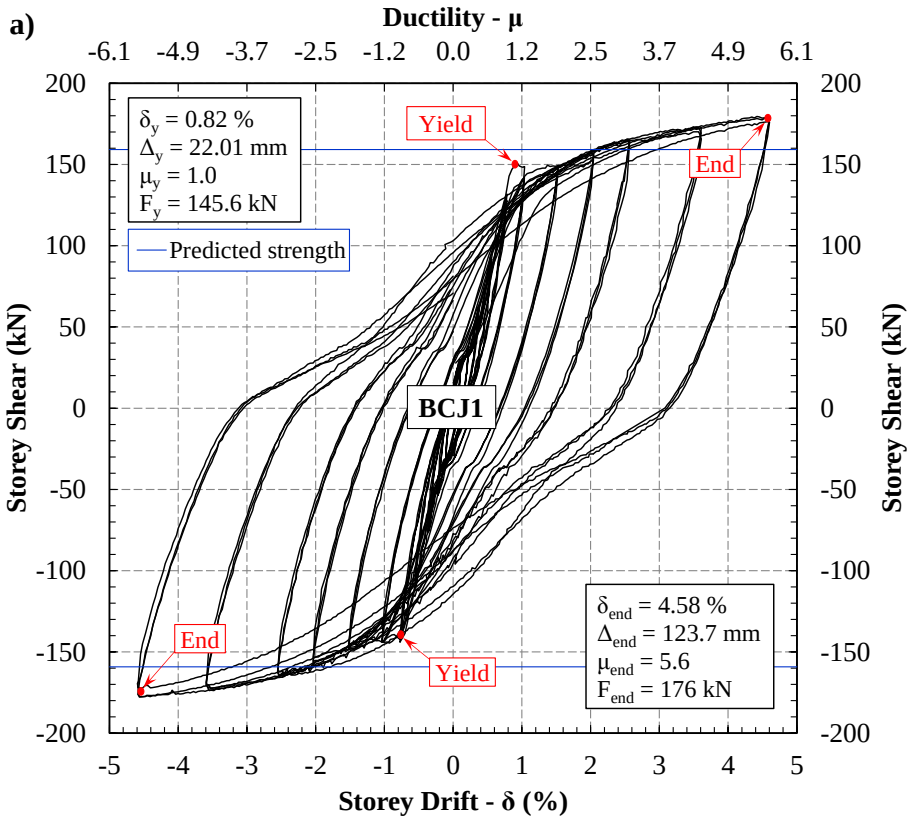

b)

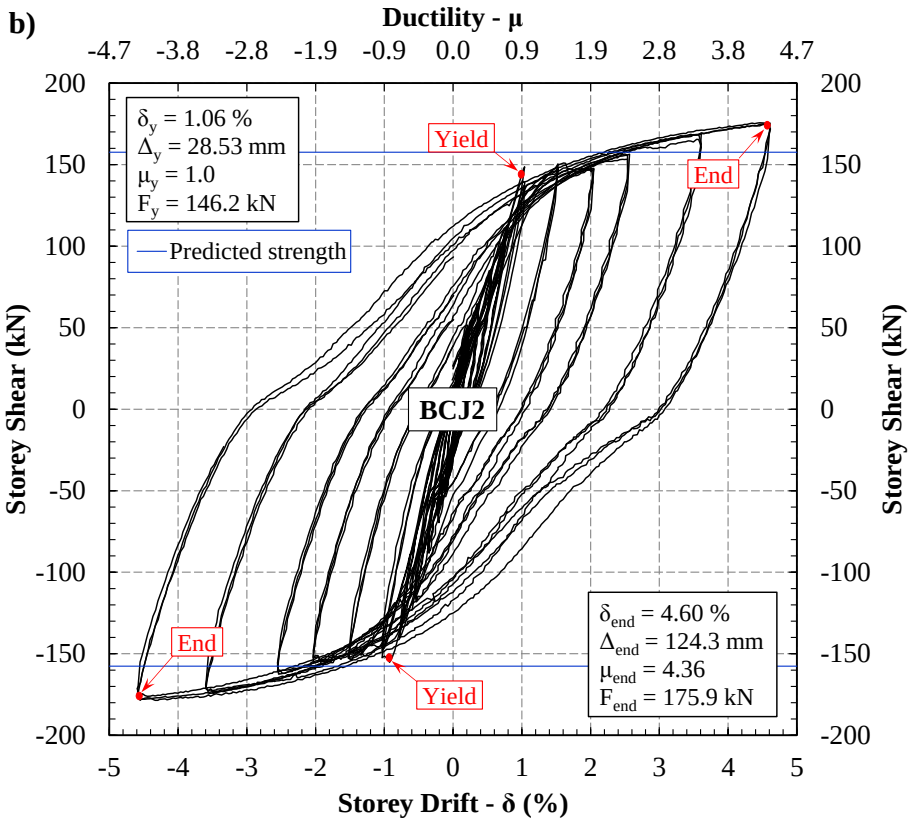
Ductility - μ
-4.7 -3.8 -2.8 -1.9 -0.9 0.0 0.9 1.9 2.8 3.8 4.7
δy = 1.06 %
Δy = 28.53 mm
μy = 1.0
Fy = 146.2 kN
Predicted strength
Yield
End
BCJ2
End
Yield
δend = 4.60 %
Δend = 124.3 mm
μend = 4.36
Fend = 175.9 kN
Storey Shear (kN)
200 150 100 50 0 -50 -100 -150 -200
-5 -4 -3 -2 -1 0 1 2 3 4 5
Storey Drift - δ (%)

c)

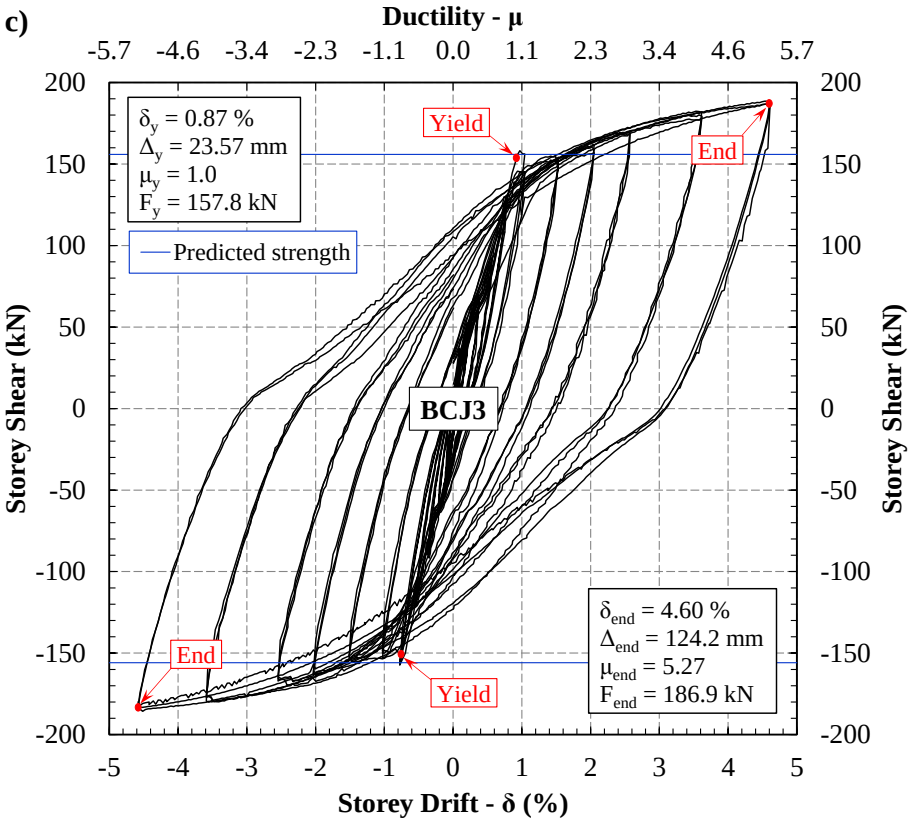
Ductility - μ
-5.7 -4.6 -3.4 -2.3 -1.1 0.0 1.1 2.3 3.4 4.6 5.7
δy = 0.87 %
Δy = 23.57 mm
μy = 1.0
Fy = 157.8 kN
Predicted strength
Yield
End
BCJ3
End
Yield
δend = 4.60 %
Δend = 124.2 mm
μend = 5.27
Fend = 186.9 kN
Storey Shear (kN)
200 150 100 50 0 -50 -100 -150 -200
-5 -4 -3 -2 -1 0 1 2 3 4 5
Storey Drift - δ (%)

d)

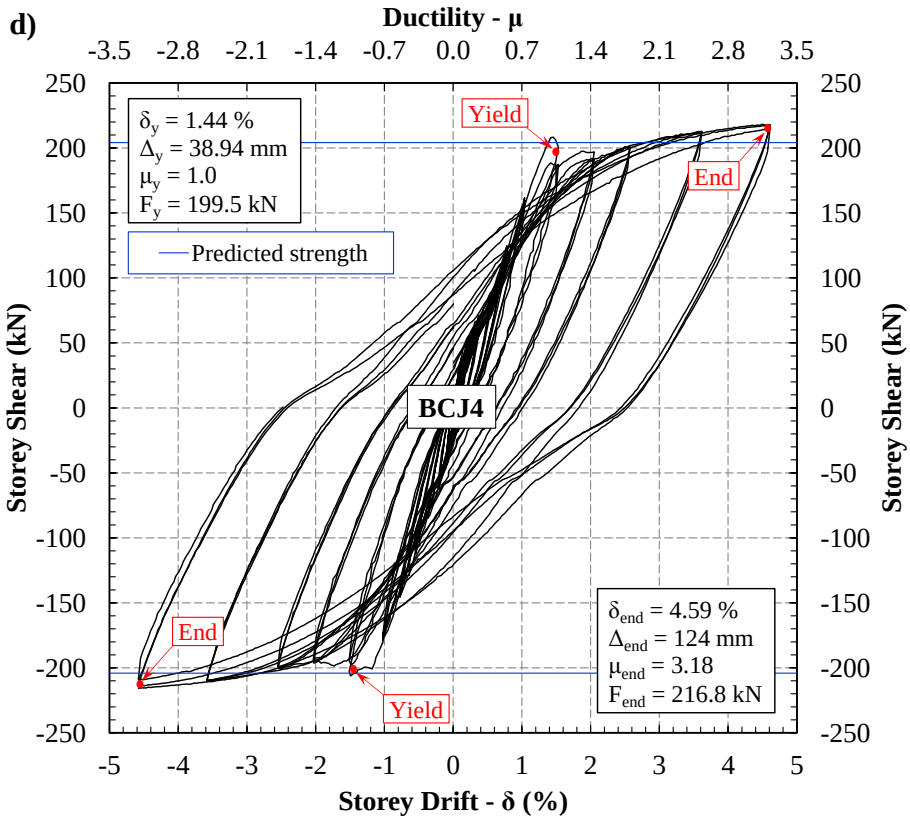
Ductility - μ
-3.5 -2.8 -2.1 -1.4 -0.7 0.0 0.7 1.4 2.1 2.8 3.5
δy = 1.44 %
Δy = 38.94 mm
μy = 1.0
Fy = 199.5 kN
Predicted strength
Yield
End
BCJ4
End
Yield
δend = 4.59 %
Δend = 124 mm
μend = 3.18
Fend = 216.8 kN
Storey Shear (kN)
Storey Drift - δ (%)

e)

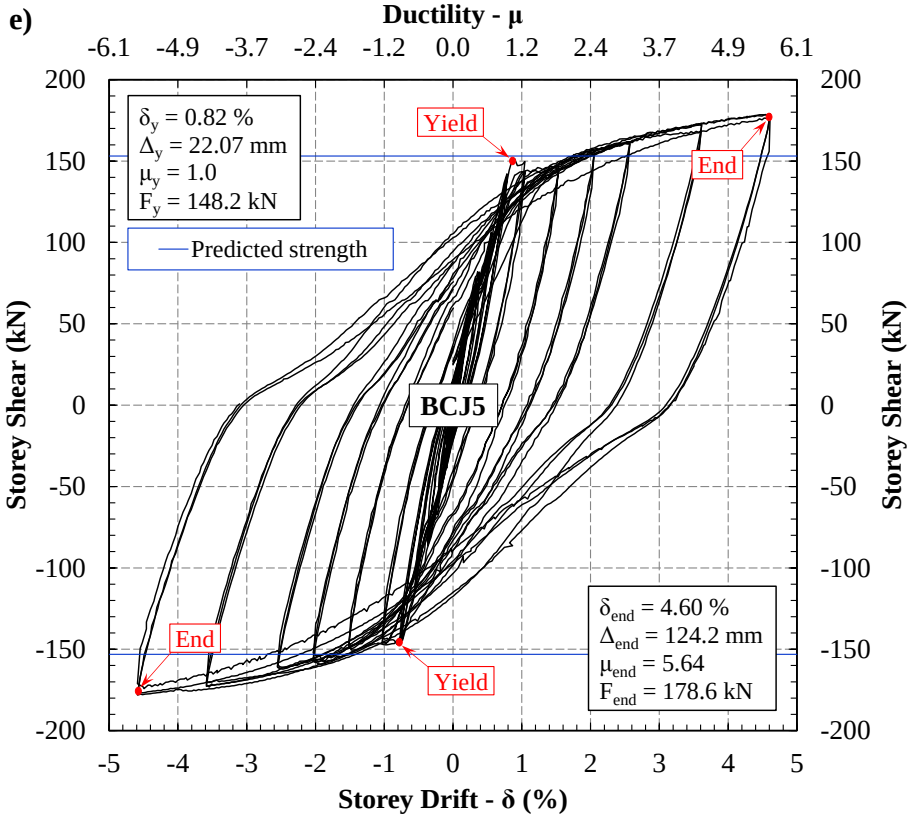
Ductility - μ
-6.1 -4.9 -3.7 -2.4 -1.2 0.0 1.2 2.4 3.7 4.9 6.1
δy = 0.82 %
Δy = 22.07 mm
μy = 1.0
Fy = 148.2 kN
Predicted strength
Yield
End
BCJ5
End
Yield
δend = 4.60 %
Δend = 124.2 mm
μend = 5.64
Fend = 178.6 kN
Storey Shear (kN)
Storey Drift - δ (%)

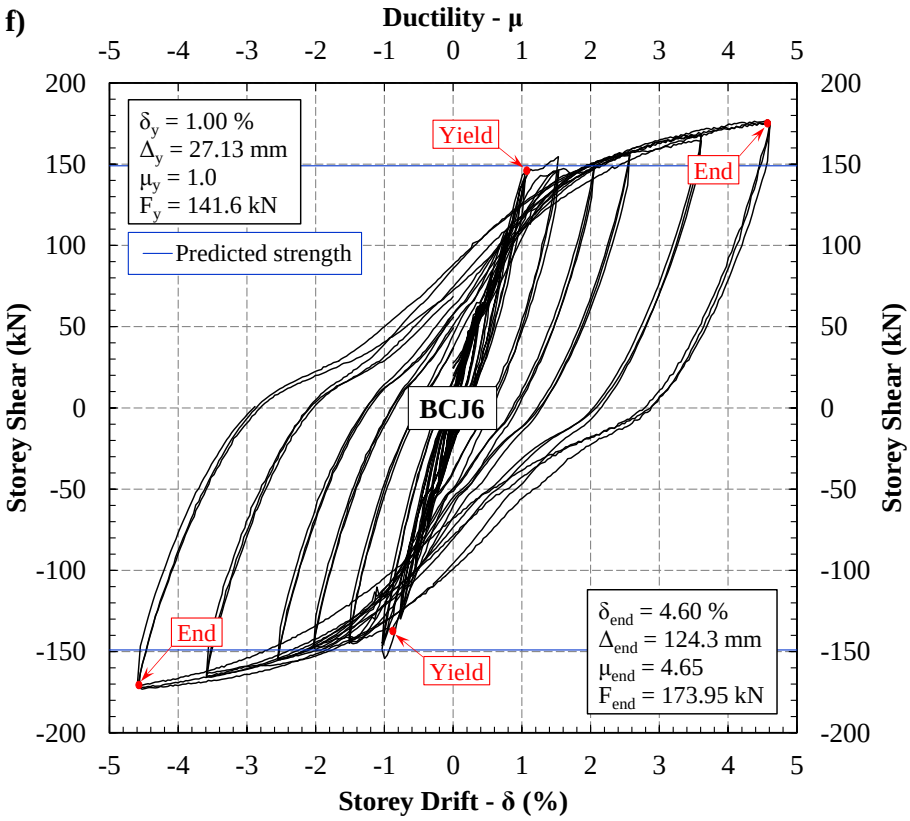

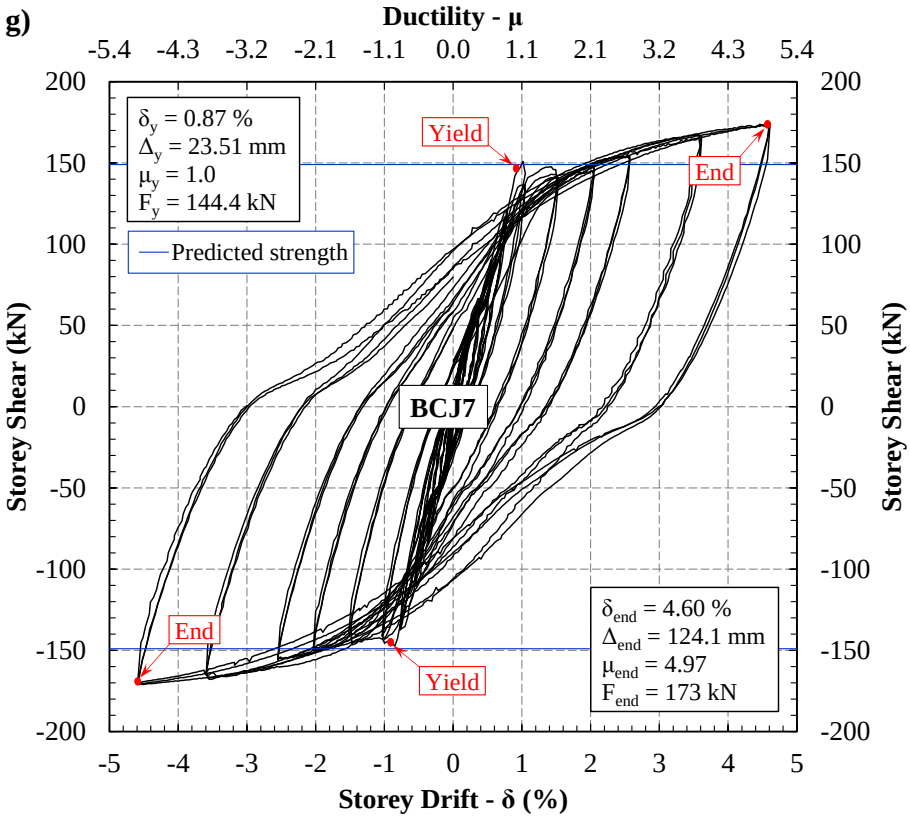

Figure 5.5: Storey shear vs. drift response of all specimens

Although some of the parameters (axial load, concrete type, joint shear reinforcement, and casting direction) were different between BCJ1, BCJ2, BCJ3, and BCJ5, their overall storey-shear vs. drift response (Figure 5.5a, b, c, and e) was very similar with respect to the maximum achieved capacity (about 180 kN), overall ductility (around 5) and pinching behaviour (insubstantial). The slightly higher pinching in BCJ1 during the last two cycle series occurred due to the fact that the broken concrete pieces were forcibly removed from the specimen (see BCJ1 at drift ratio 4.5% in Figure 5.7 and compare to other specimens). This intervention also reduced the maximum achieved capacity of BCJ1 by about 6% compared to that of BCJ3 irrespective of the fact the latter had only about half of the recommended joint shear reinforcement. As removing the broken concrete pieces was found to be deleterious for the cyclic response of the specimen; it was not repeated in testing of the rest of the specimens.

The lower axial load ratio of 0.01 (as opposed to that of about 0.1 for other specimens) applied on BCJ2, did not significantly affect the overall performance of this specimen with respect to the maximum achieved capacity, pinching and ductility. The hysteresis loops of BCJ6 (cast with CVC) showed a considerably thinner response curve (Figure 5.5f) with a more amplified pinching towards the end of the test compared to the other specimens. This was attributed to a combination of the following two reasons: lower concrete compressive strength (48.4 MPa) which is easier to be crushed in the compression zone and possible slippage of the reinforcement through the joint panel resulting from lower bond capacity of CVC. Although no physical measurements were taken to prove the occurrence of the latter, comparison between Figure 5.5f and Figure 5.5g reveals that the hysteresis behaviour of BCJ7 (with HSSCC in its joint zone) showed fatter and less pinched loops compared to that of BCJ6. Note that both specimens reached the same flexural capacity at the end of the test. Nevertheless, the maximum achieved capacity of BCJ6 was not overly affected by the lower concrete compressive strength as it is mostly governed by the longitudinal bars which had the same strength and arrangement as the other specimens. The behaviour of BCJ4 (Figure 5.5d) was slightly different to other specimens in that it dissipated lesser energy in its hysteresis loops and very minimal pinching was observed. Unfortunately due to a misunderstanding between the design and fabrication of this specimen, HD20 bars were used for the longitudinal beam bars instead of HD16. This resulted in considerably

higher flexural capacity (20% more compared to the other specimens) at the end of 4.5% drift cycle.

Figure 5.6 shows the maximum values of crack width measurements in the plastic hinge zone and the joint panel at each drift ratio. Note that due to excessive crack width opening (more than 5 mm) at the end of 4.5% drift, they were not measured in the plastic hinge zone; therefore, crack widths at the plastic hinge zone are reported up to the end of 3.5% drift. Comparison of the crack width measurements in the joint panel (Figure 5.6b) of BCJ6 and BCJ7 shows that although the joint panel of BCJ7 was poured using HSSCC, it experienced larger crack widths, which is contrary to the higher concrete compressive strength. However, this can be explained assuming that slippage of the beam bars had occurred through the joint panel in BCJ6 resulting in lesser transfer of shear forces into the joint area of this specimen. Whereas in BCJ7, no slippage occurred and all of the shear force was transferred from the beam bars to the joint; resulting in slightly larger crack widths. This explanation also supports the previous observation of more pinching in BCJ6 compared to that of BCJ7.

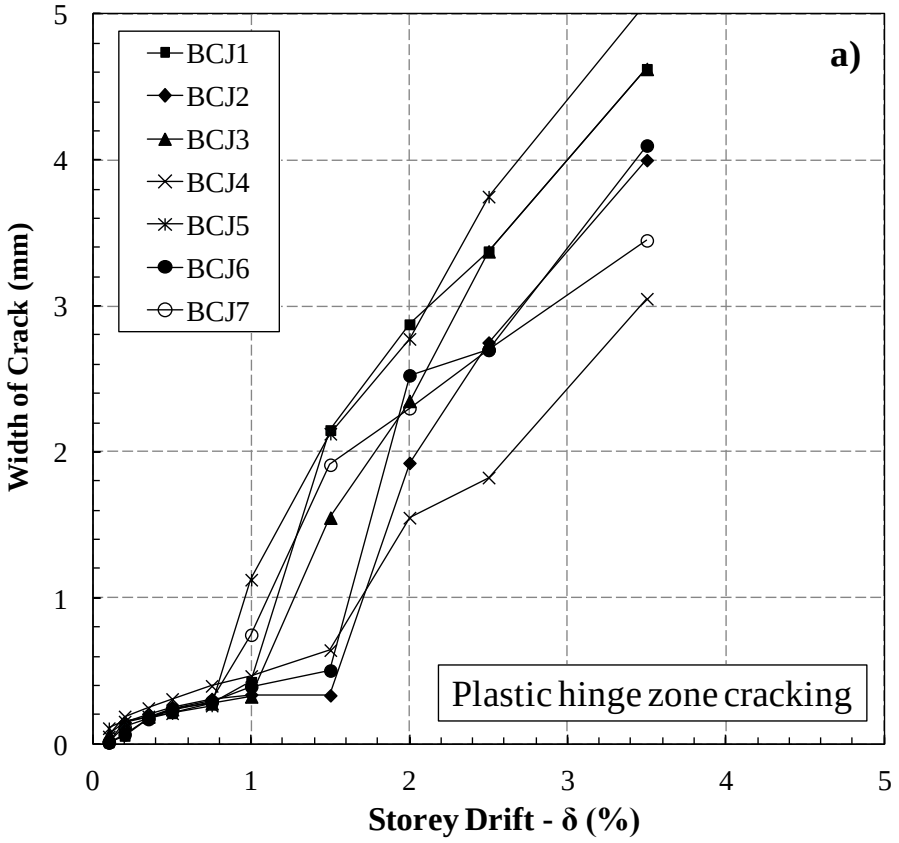

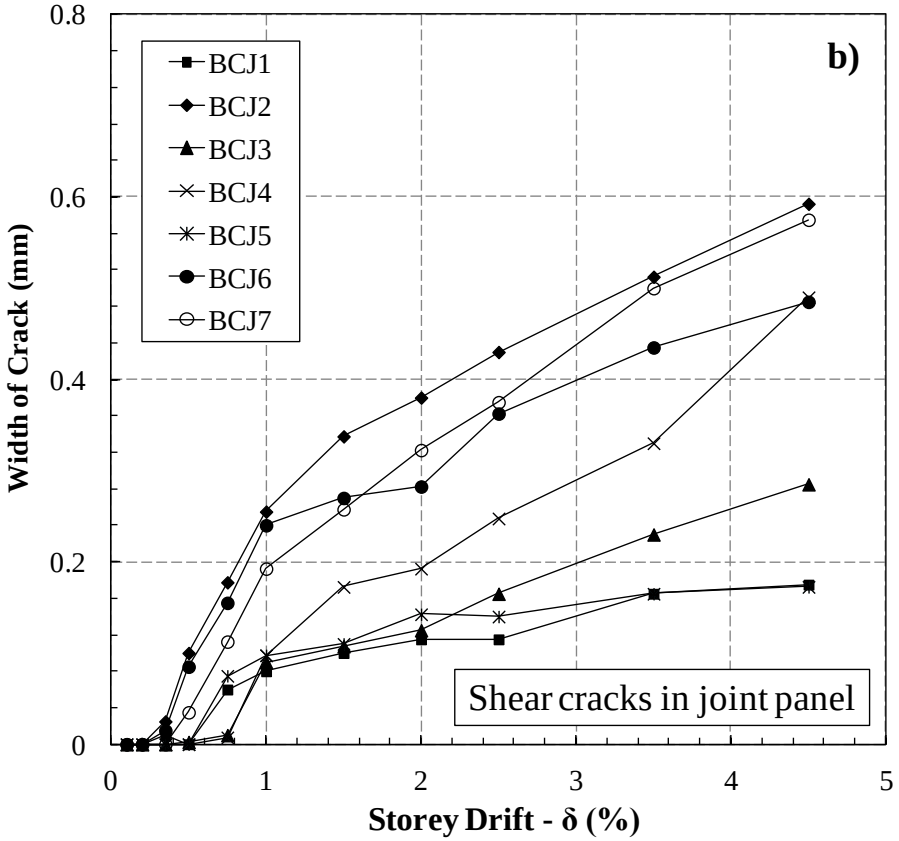

Figure 5.6: Width of cracks in the a) plastic hinge zone and b) joint panel

Figure 5.7 to Figure 5.10 shows the physical condition of cracking in the plastic hinge zone and joint panel in different specimens at positive drift ratios of 1.5%, 2.5% and 4.5%. Although none of the specimens had failed at the end of the 4.5% drift ratio, it is evident that major cracking occurred in the beam plastic hinge zone and if the loading was continued, the specimens were expected to fail at the beam hinges at the column faces This visual observation is also justified by the large contribution of the beam flexure in overall drift of the specimen (to be discussed later). The cracks were dispersed along the length of the plastic hinge zone which shows reasonable distribution of plastic curvature rather than strain concentration and its associated drawbacks.

Although the concrete compressive strength was different in BCJ1 and BCJ5, the joint cracking pattern and width of cracks (Figure 5.6b) were comparable. As mentioned before, only about half of the otherwise prescribed joint shear reinforcement was used in BCJ3, nevertheless the amount, pattern and width of cracks in the joint panel of BCJ3 were comparable to that of BCJ1 and BCJ5. This shows that the amount of shear reinforcement

suggested by NZ3101 standard is highly conservative for high-strength concrete. This will be more evident when the contribution of steel and concrete in taking the shear forces transferred to the joint is investigated later. Due to lower axial load ratio in BCJ2, it expectedly had more cracks in its joint region which had wider cracks (up to 0.6 mm) than the other high-strength specimen. In fact the crack opening of BCJ2 was similar to that of BCJ6 and BCJ7 with lower strength concrete. BCJ4 had more cracks developed in its joint panel with a maximum crack width of about 0.5 mm; this is attributed to higher amount of forces exerted on the joint panel (as stated earlier). Finally, BCJ6 had the most cracks in its joint region due a considerably lower concrete compressive strength. As mentioned before and based on the observations from hysteresis loops (Figure 5.5f, g) and crack width measurements (Figure 5.6b), it is believed that slippage of beam bars through the joint occurred in this specimen which in turn limited both the number and width of the cracks.

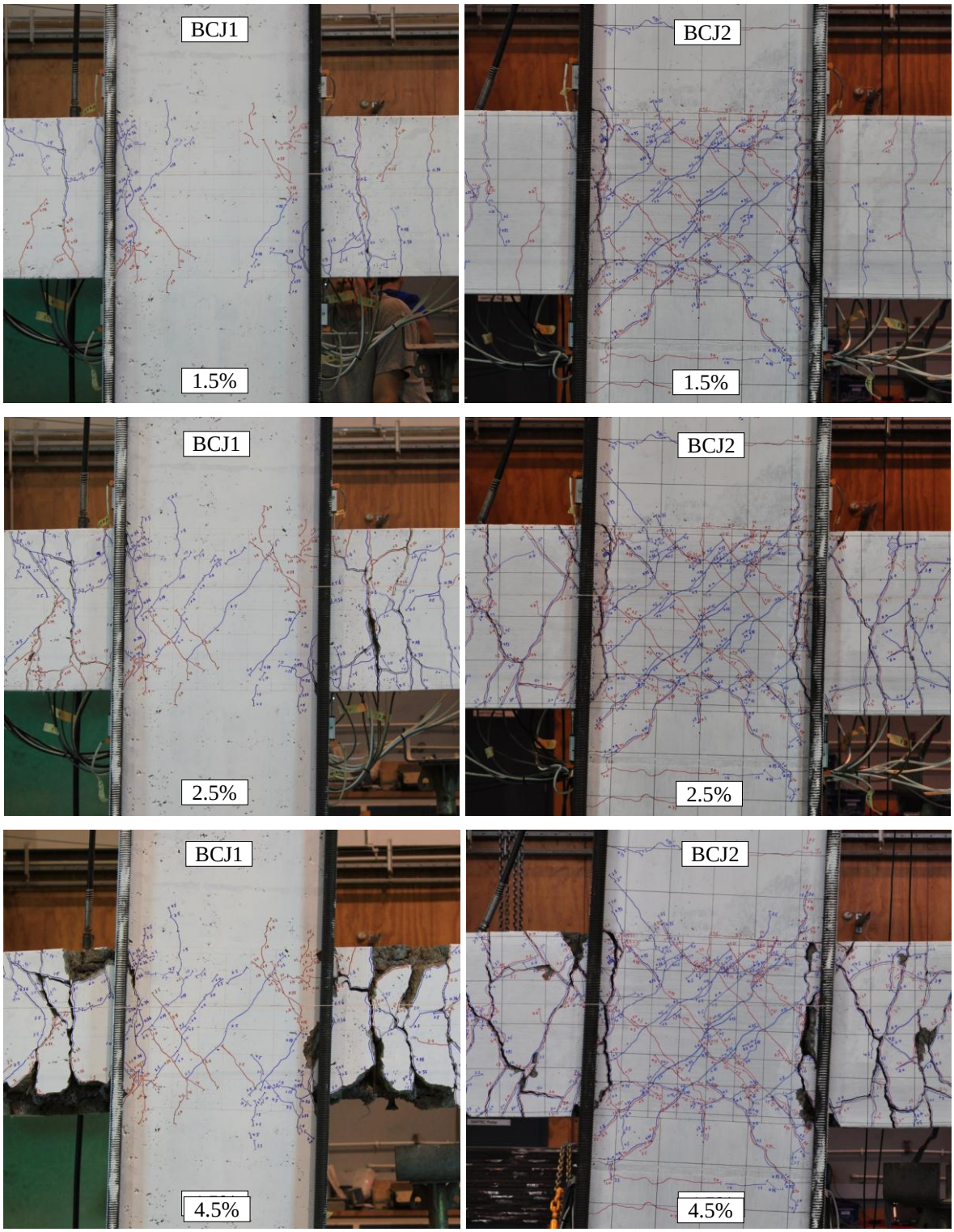

Figure 5.7: Cracking condition in BCJ1 and BCJ2 at drift ratios 1.5%, 2.5% and 4.5%

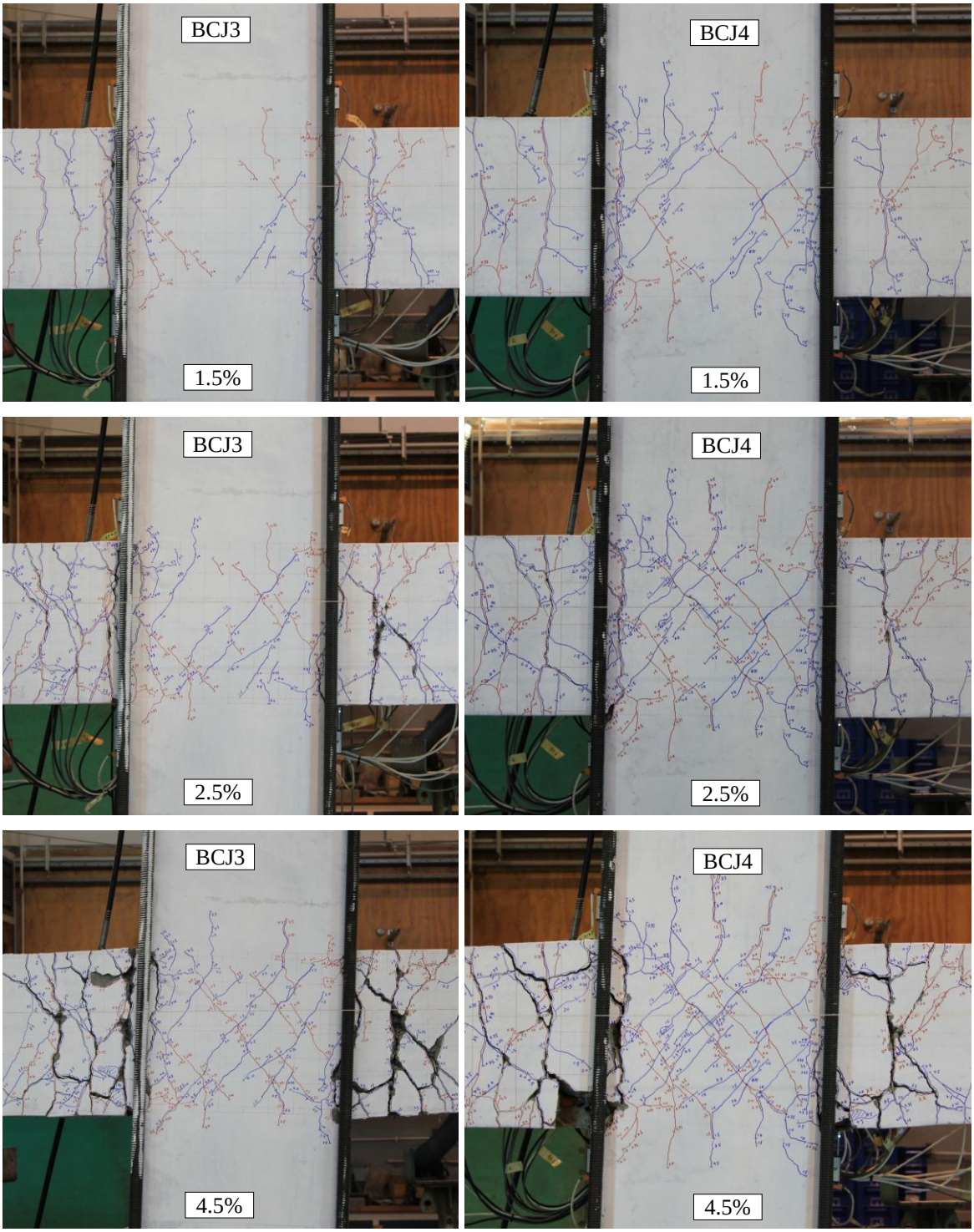

Figure 5.8: Cracking condition in BCJ3 and BCJ4 at drift ratios 1.5%, 2.5% and 4.5%

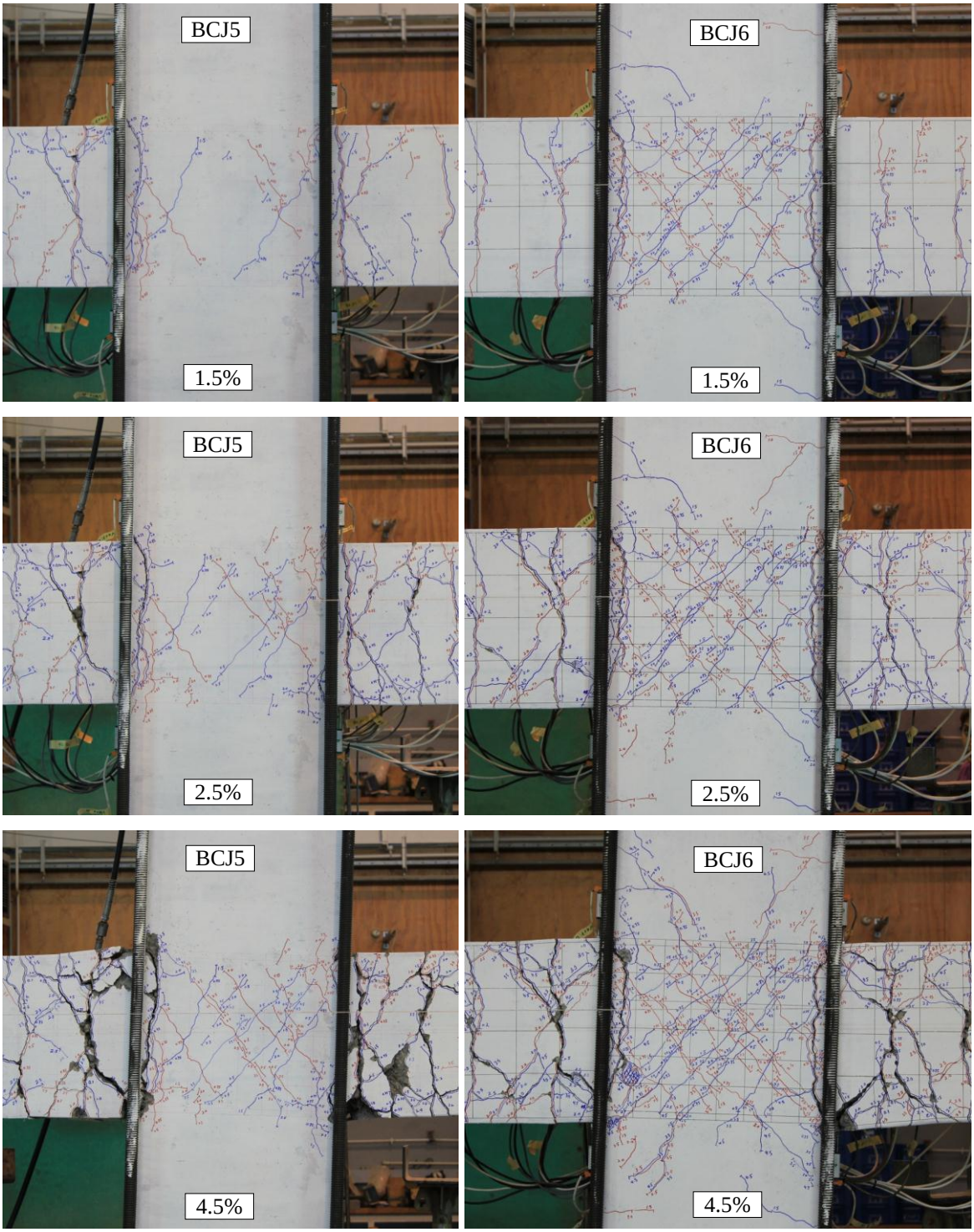

Figure 5.9: Cracking condition in BCJ5 and BCJ6 at drift ratios 1.5%, 2.5% and 4.5%

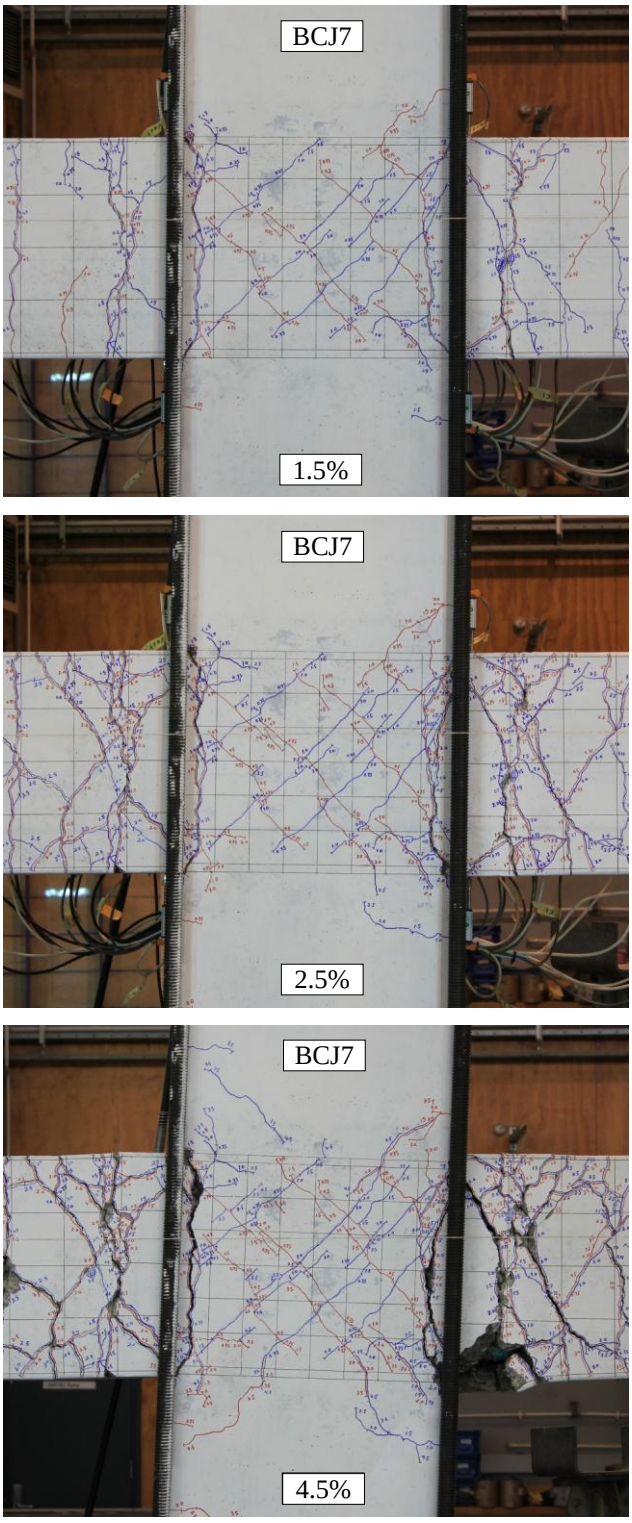

Figure 5.10: Cracking condition in BCJ7 at drift ratios 1.5%, 2.5% and 4.5%

5.4.2 DAMPING AND STIFFNESS PROPERTIES

The dissipated energy was measured from the hysteresis loops to calculate the equivalent viscous damping for all specimens (Equations 5.1 to 5.3). This calculation was performed in order to provide a better understanding of the hysteresis and pinching behaviours. In addition, the peak-to-peak secant stiffness degradation was also calculated (Equation 5.4) for all specimens. Results of damping and stiffness degradation are shown in Figure 5.11.

$$\xi_{eq} = \frac{E_D}{4\pi . E_{sto}} \tag{5.1}$$

$$E_D = \sum \frac{(\Delta_{i+1} - \Delta_i)(F_{i+1} + F_i)}{2} \tag{5.2}$$

$$E_{sto} = \frac{F_0 \Delta_0}{2} \tag{5.3}$$

$$k_p = \frac{(F_{+ve} - F_{-ve})}{(\Delta_{+ve} - \Delta_{-ve})} \tag{5.4}$$

In the above equations, 'ξ_{eq}' is the equivaleant viscous damping, 'E_D' is the dissipated energy per cycle (N.mm), 'E_{sto}' is the equivalent elastic stored energy per cycle (N.mm), 'F_i' is the load at each step (N), 'Δ_i' is the displacement at each step (mm), 'F_0' is the peak load of each cycle (N), 'Δ_0' is the peak displacement of each cycle (mm), 'k_p' is the peak-to-peak stiffness (N/mm), 'F_{+ve}' and 'F_{-ve}' are the maximum and minimum forces of the intended cycle (N) and 'Δ_{+ve}' and 'Δ_{-ve}' are the maximum and minimum displacements of the intended cycle (mm).

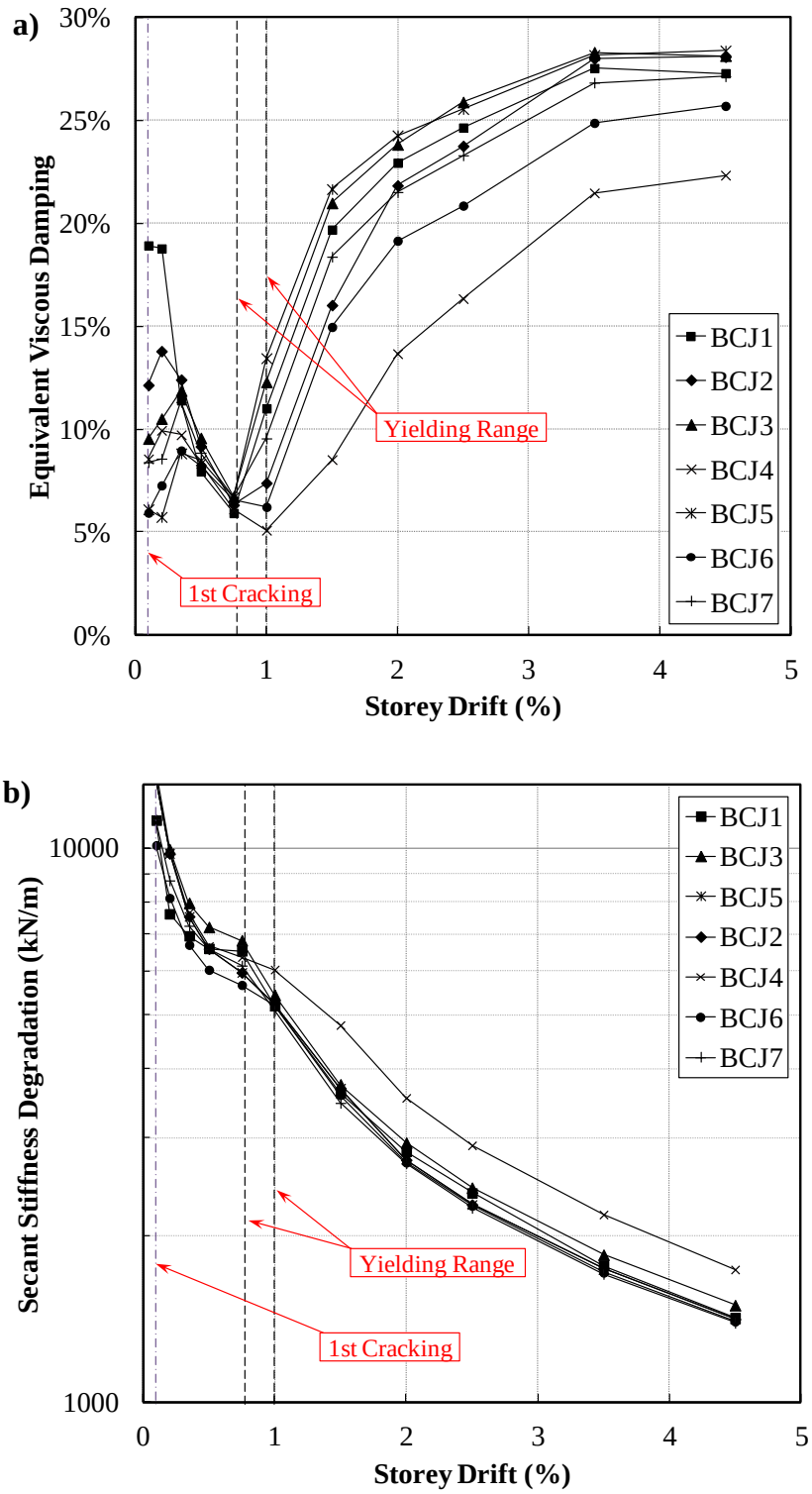

Figure 5.11: a) Equivalent viscous damping and b) Peak-to-peak secant stiffness degradation

According to Figure 5.11a and based on the previous observations (Figure 5.5) at a given drift ratio after yielding, all specimens (except for BCJ4) show similar damping properties with only slight variations. Before yielding, BCJ1 shows considerably higher damping

compared to the others; however these initially high values decrease quite fast so that the damping values become almost the same for all specimens around the yielding point. Note that the calculation of equivalent viscous damping requires division by the elastic stored energy 'E_{sto}', which is very small in the elastic response range; hence the calculated pre-yield damping values cannot be relied upon as they are very sensitive even to small discrepancies in estimating E_{sto}. Similarly in Figure 5.11b, all specimens show comparable stiffness degradation in the pre-yield range; with almost equal values after the yielding point. BCJ4 showed lower stiffness degradation which is most possibly attributed to its higher steel grade and flexural capacity. Note that the vertical axis in Figure 5.11b is drawn in logarithmic scale.

5.4.3 JOINT SHEAR RESPONSE

The total joint shear force 'V_{jh}' and the horizontal joint shear stress 'v_{jh}' at each drift peak were calculated using the geometry of the test setup and specimens. The contribution of the joint shear reinforcement to the total joint shear stress was calculated using the results of the strain gauges installed on the joint stirrups (Figure 5.12). Note that the half-yield dashed-line shown in Figure 5.12 is not straight (except for Figure 5.12c where the same shear reinforcement is used) due to the different shear reinforcement grade (300 and 500 MPa) used in the joint and the column; (see also Figure 5.2 and Table 5.2).

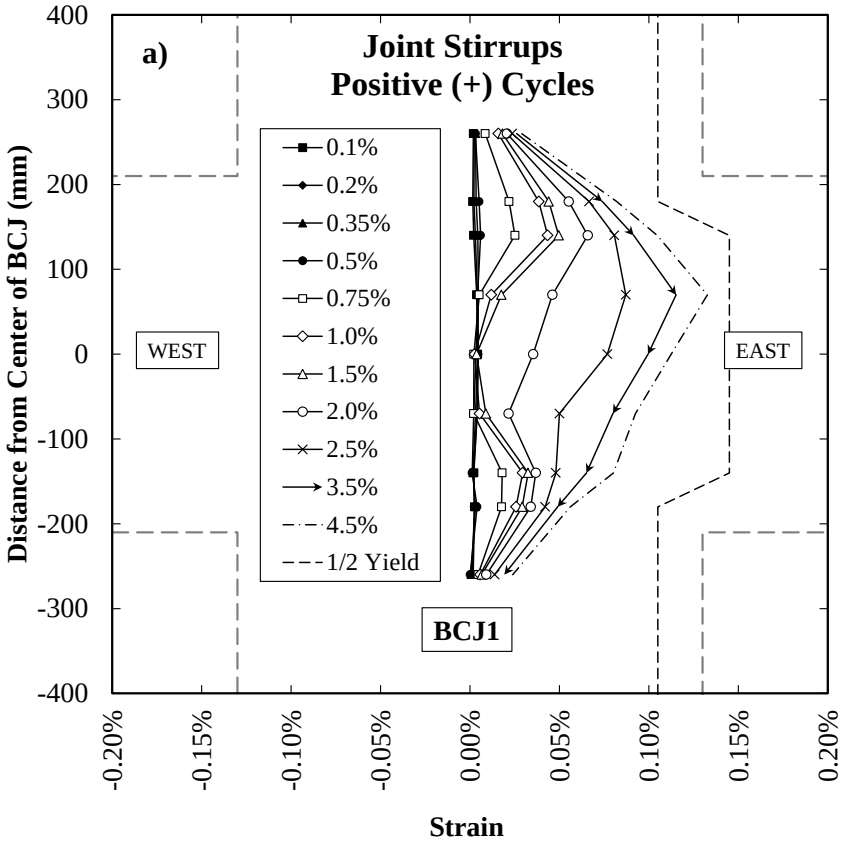
a)
Joint Stirrups
Positive (+) Cycles
0.1%
0.2%
0.35%
0.5%
0.75%
1.0%
1.5%
2.0%
2.5%
3.5%
4.5%
1/2 Yield
WEST
EAST
BCJ1
Distance from Center of BCJ (mm)
400
300
200
100
0
-100
-200
-300
-400
-0.20%
-0.15%
-0.10%
-0.05%
0.00%
0.05%
0.10%
0.15%
0.20%
Strain

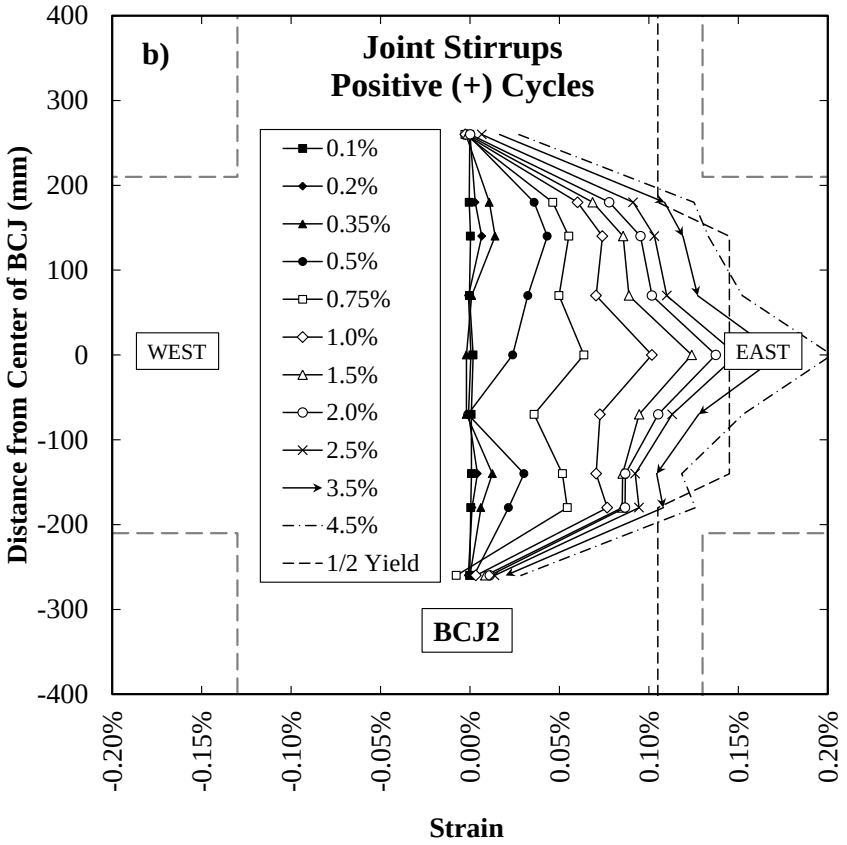
b)
Joint Stirrups
Positive (+) Cycles
0.1%
0.2%
0.35%
0.5%
0.75%
1.0%
1.5%
2.0%
2.5%
3.5%
4.5%
1/2 Yield
WEST
EAST
BCJ2
Distance from Center of BCJ (mm)
400
300
200
100
0
-100
-200
-300
-400
-0.20%
-0.15%
-0.10%
-0.05%
0.00%
0.05%
0.10%
0.15%
0.20%
Strain

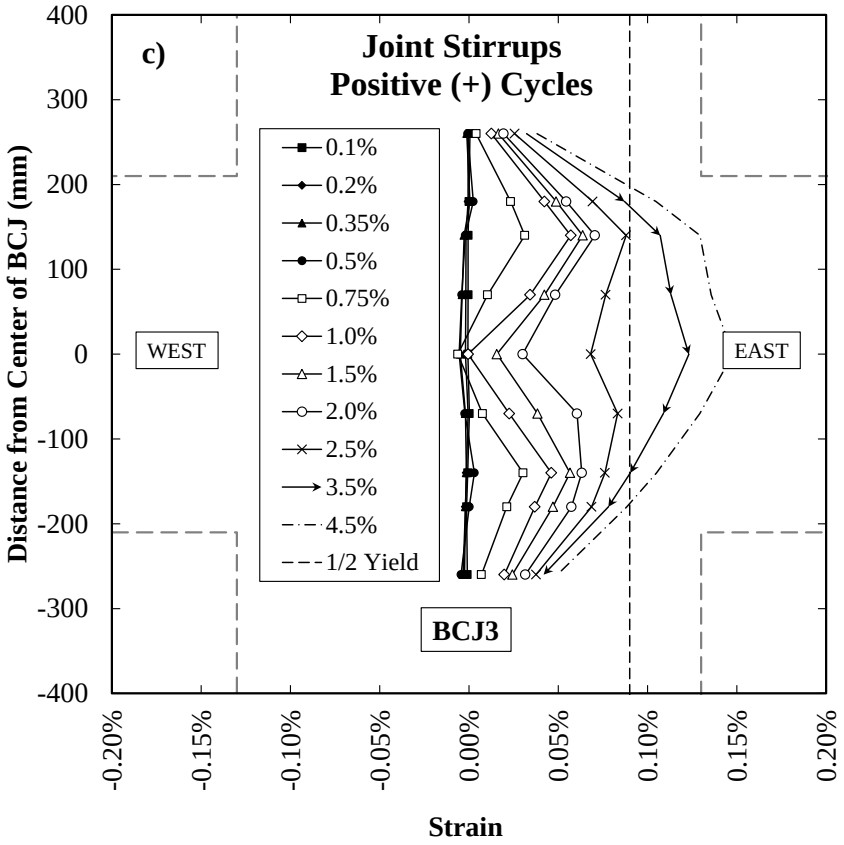
c)
Joint Stirrups
Positive (+) Cycles
0.1%
0.2%
0.35%
0.5%
0.75%
1.0%
1.5%
2.0%
2.5%
3.5%
4.5%
1/2 Yield
WEST
EAST
BCJ3
Distance from Center of BCJ (mm)
400
300
200
100
0
-100
-200
-300
-400
-0.20%
-0.15%
-0.10%
-0.05%
0.00%
0.05%
0.10%
0.15%
0.20%
Strain

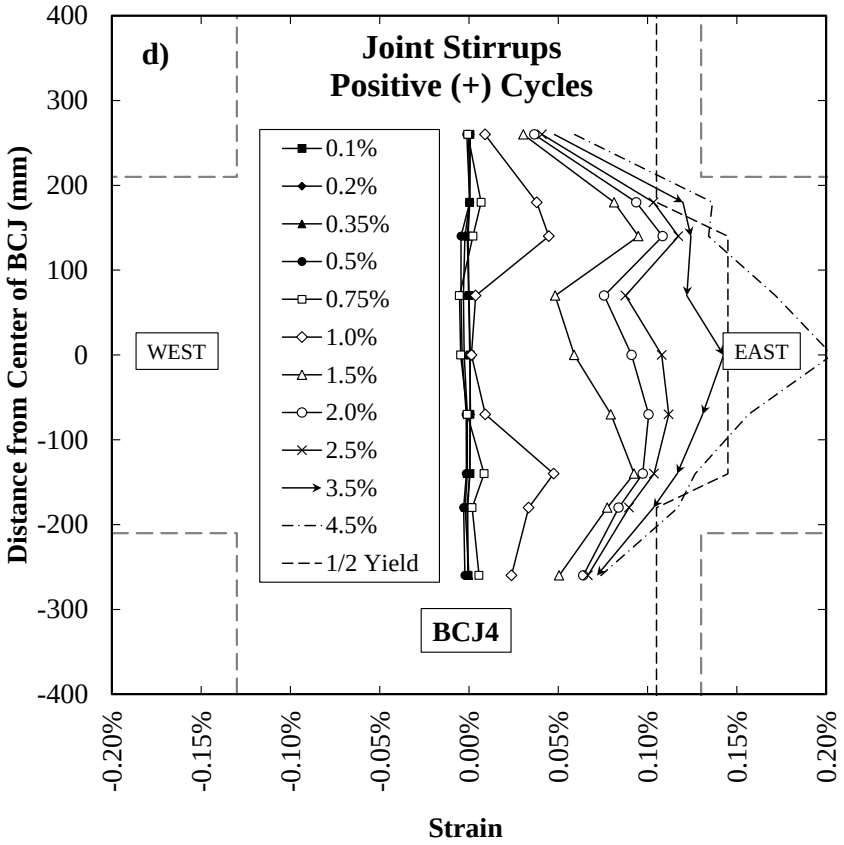
d)
Joint Stirrups
Positive (+) Cycles
0.1%
0.2%
0.35%
0.5%
0.75%
1.0%
1.5%
2.0%
2.5%
3.5%
4.5%
1/2 Yield
WEST
EAST
BCJ4
Distance from Center of BCJ (mm)
400
300
200
100
0
-100
-200
-300
-400
-0.20%
-0.15%
-0.10%
-0.05%
0.00%
0.05%
0.10%
0.15%
0.20%
Strain

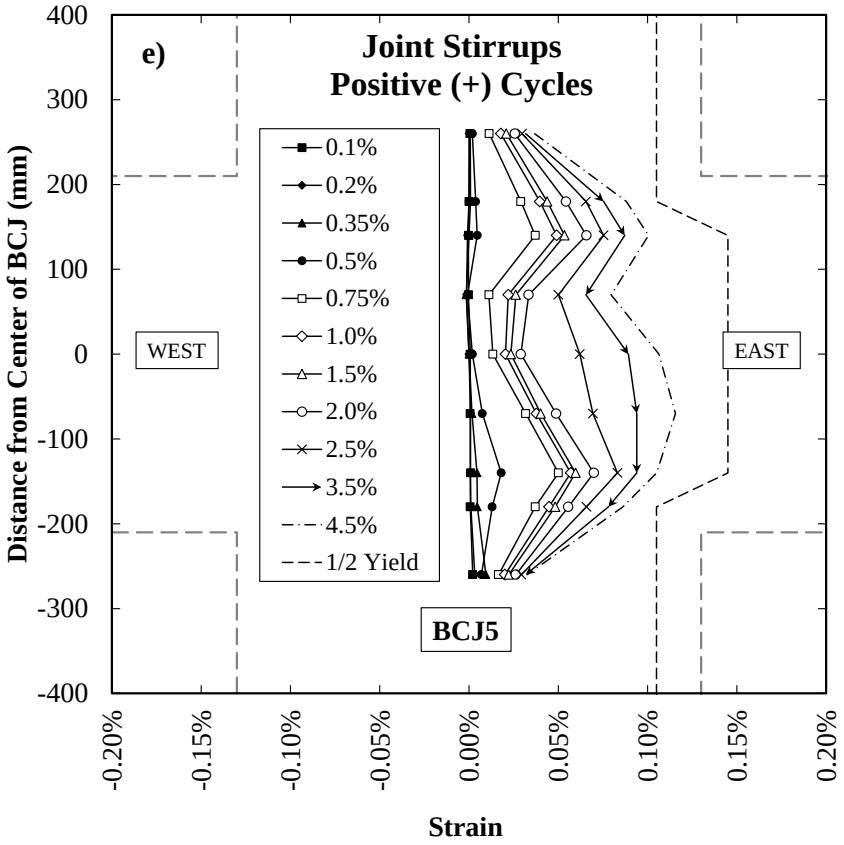
e)
Joint Stirrups
Positive (+) Cycles
0.1%
0.2%
0.35%
0.5%
0.75%
1.0%
1.5%
2.0%
2.5%
3.5%
4.5%
1/2 Yield
WEST
EAST
BCJ5
Distance from Center of BCJ (mm)
400
300
200
100
0
-100
-200
-300
-400
-0.20%
-0.15%
-0.10%
-0.05%
0.00%
0.05%
0.10%
0.15%
0.20%
Strain

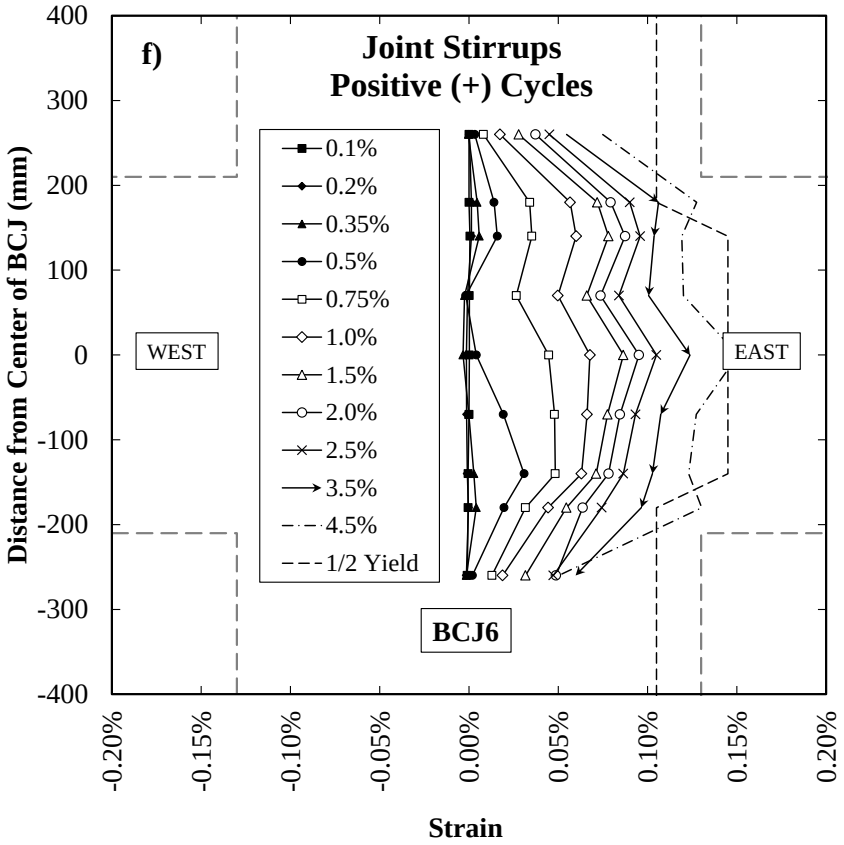
f)
Joint Stirrups
Positive (+) Cycles
0.1%
0.2%
0.35%
0.5%
0.75%
1.0%
1.5%
2.0%
2.5%
3.5%
4.5%
1/2 Yield
WEST
EAST
BCJ6
Distance from Center of BCJ (mm)
400
300
200
100
0
-100
-200
-300
-400
-0.20%
-0.15%
-0.10%
-0.05%
0.00%
0.05%
0.10%
0.15%
0.20%
Strain

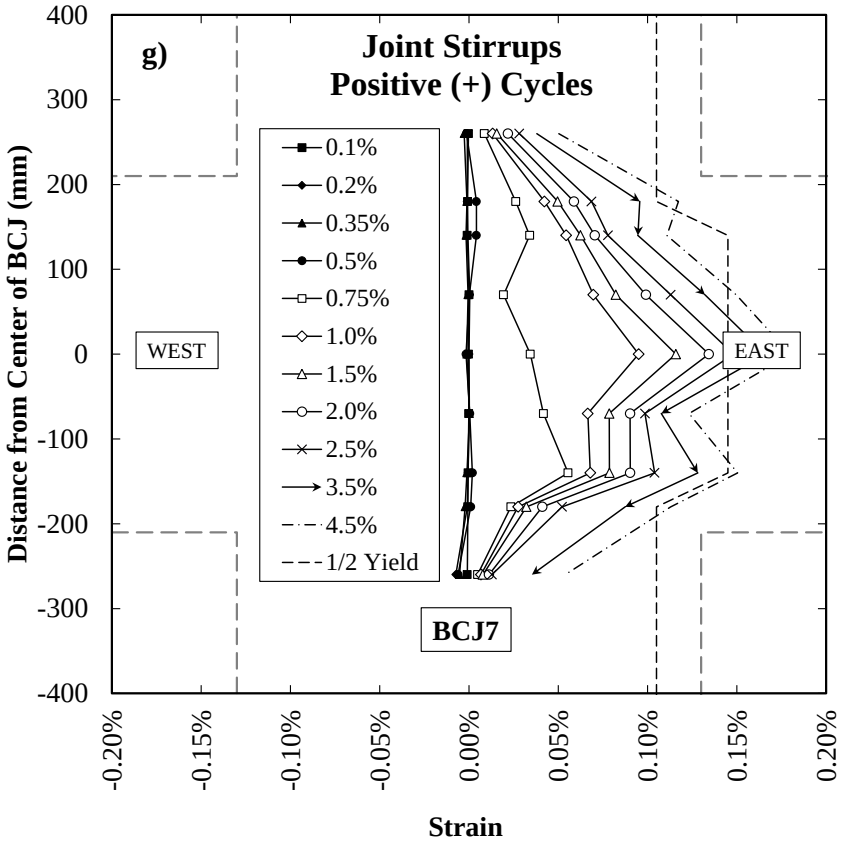

Figure 5.12: Reading of strain gauges installed on the joint shear reinforcement

According to the strain gauge readings, even at the highest storey drift of 4.5% none of the joint stirrups yielded. In fact they all remained elastic around half-yield levels except for the joint shear reinforcement of BCJ3 (with about half of the prescribed joint shear reinforcement) which passed the half-yield point but remained elastic. Therefore stresses were calculated using Hooke's law and the corresponding forces were determined by multiplying the stresses and the area of stirrups. Shear stress of the joint was also normalized with respect to the square root of concrete compressive strength '$\sqrt{f'_c}$' to provide an unbiased assessment of the steel and concrete contributions to the total joint shear stress (Figure 5.13). Despite the joint shear stress being similar in all specimens, the steel contribution to joint shear was more in BCJ2 and BCJ3 compared to the others. This is attributed to the lower amount of axial force ratio in BCJ2 (0.01 as opposed to about 0.1 in the others) and less shear reinforcement in BCJ3 (only 56% of the required amount based on code recommendations). The maximum limit of joint shear stress for all specimens, calculated as per the American and New Zealand standards (ACI318M-08, 2008; NZS3101, 2006) are also shown in Figure 5.13 for comparison. As mentioned earlier, all specimens were designed to the New Zealand Standard (NZS3101, 2006),

therefore it was expected that the maximum joint shear stress would not exceed the codal limits.

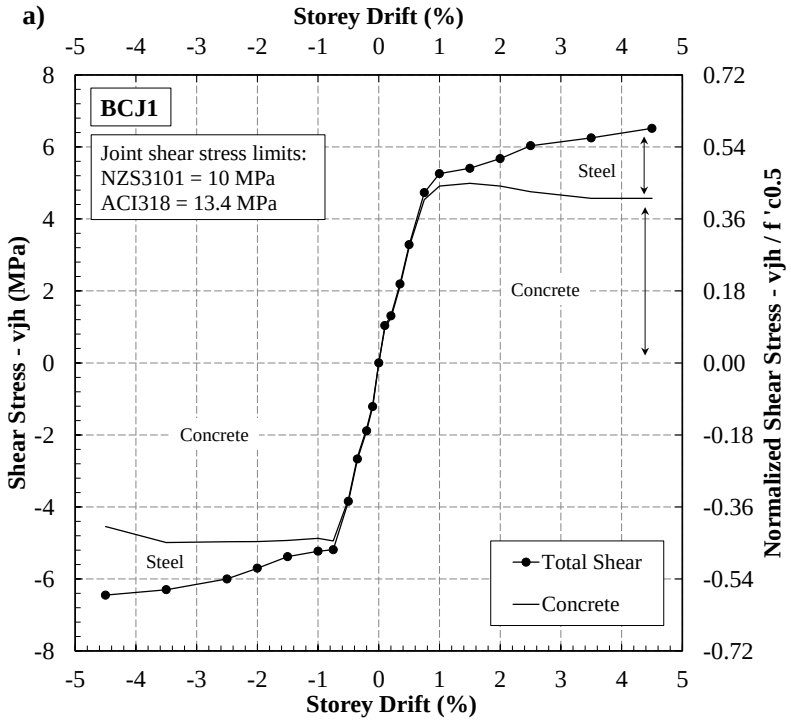

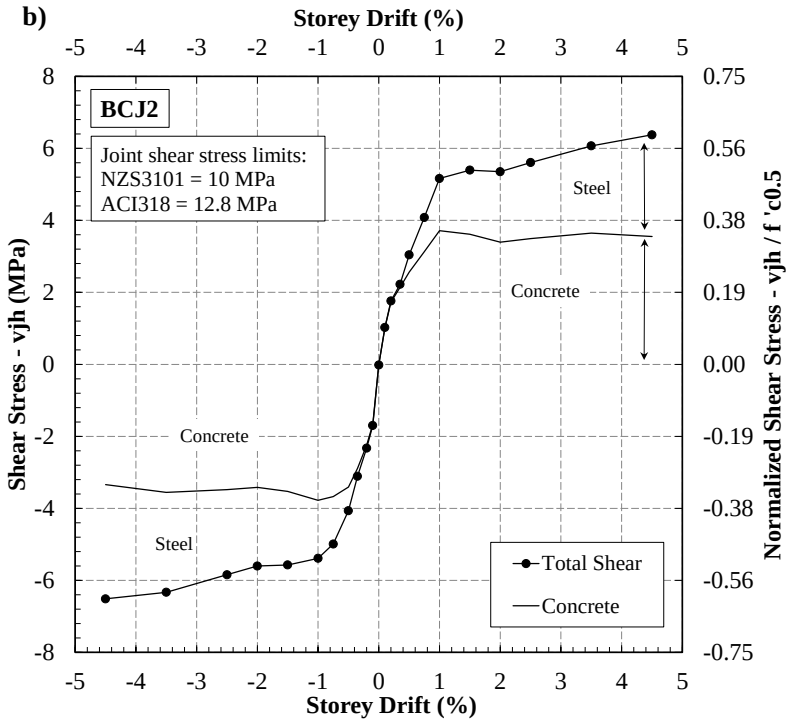

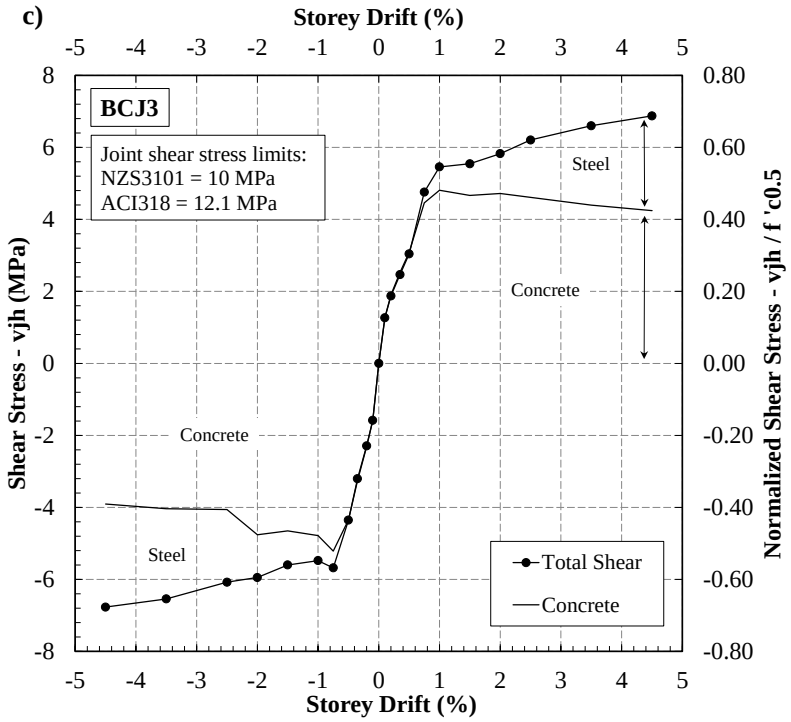
c)
Storey Drift (%)
BCJ3
Joint shear stress limits:
NZS3101 = 10 MPa
ACI318 = 12.1 MPa
Steel
Concrete
Concrete
Steel
Total Shear
Concrete
Shear Stress - vjh (MPa)
Normalized Shear Stress - vjh / f 'c0.5
Storey Drift (%)

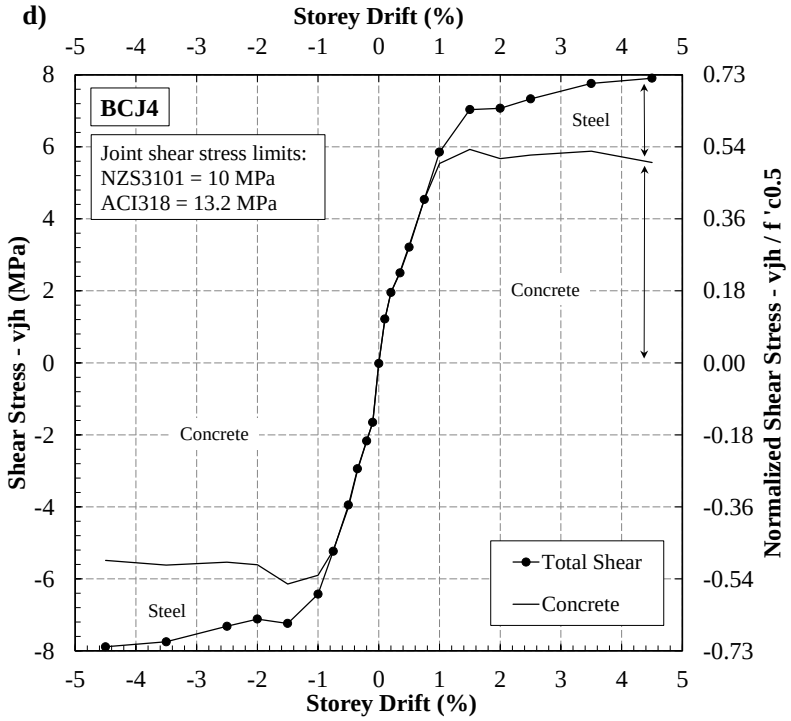
d)
Storey Drift (%)
BCJ4
Joint shear stress limits:
NZS3101 = 10 MPa
ACI318 = 13.2 MPa
Steel
Concrete
Concrete
Steel
Total Shear
Concrete
Shear Stress - vjh (MPa)
Normalized Shear Stress - vjh / f 'c0.5
Storey Drift (%)

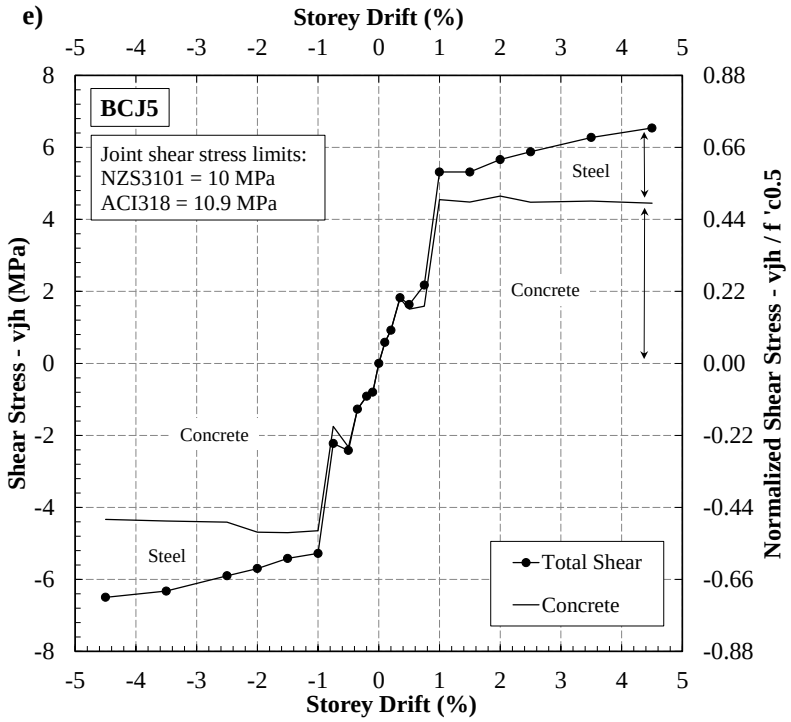
e)
Storey Drift (%)
BCJ5
Joint shear stress limits:
NZS3101 = 10 MPa
ACI318 = 10.9 MPa
Steel
Concrete
Concrete
Steel
Total Shear
Concrete
Shear Stress - vjh (MPa)
Normalized Shear Stress - vjh / f 'c0.5
Storey Drift (%)

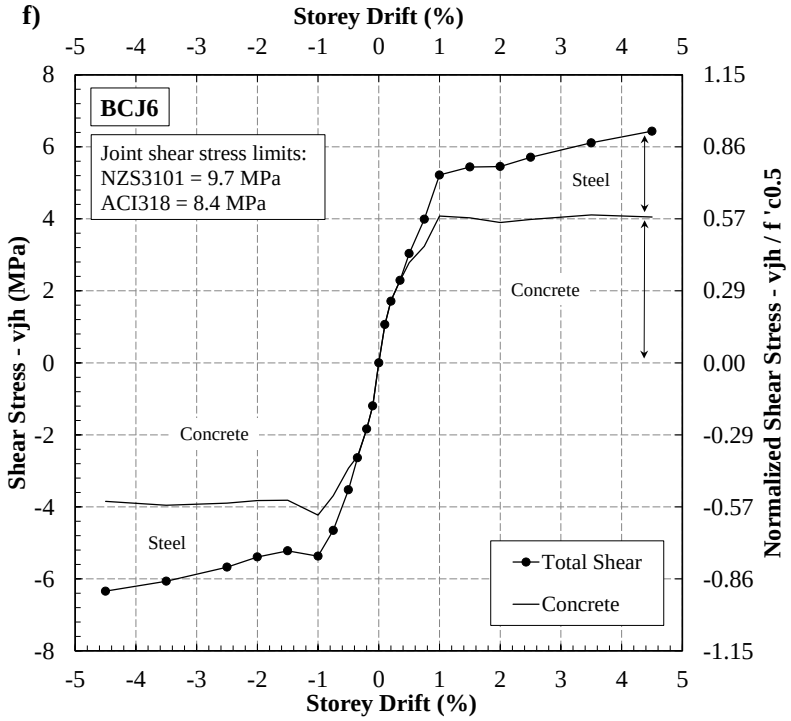
f)
Storey Drift (%)
BCJ6
Joint shear stress limits:
NZS3101 = 9.7 MPa
ACI318 = 8.4 MPa
Steel
Concrete
Concrete
Steel
Total Shear
Concrete
Shear Stress - vjh (MPa)
Normalized Shear Stress - vjh / f 'c0.5
Storey Drift (%)

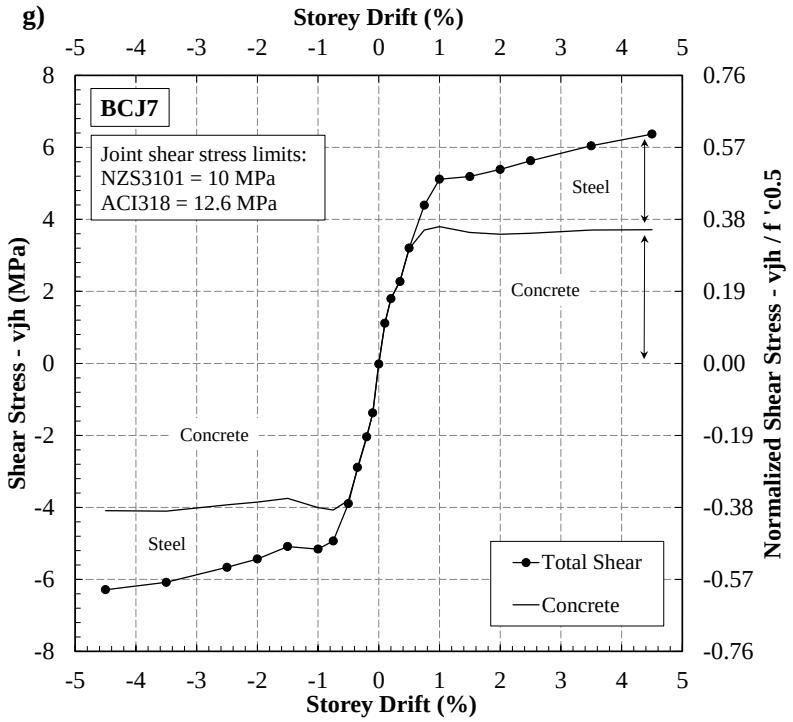

Figure 5.13: Contribution of concrete and steel in joint shear capacity

5.4.4 CONTRIBUTION OF DIFFERENT COMPONENTS TO OVERALL DRIFT

The overall deformation of a beam-column subassembly comprises of beam, column and joint deformations. As the specimens were designed to fail by the formation of plastic hinge in the beam region, the beam deformation would be contributed by four different components: elastic flexure, fixed-end rotation (i.e. rocking), plastic hinge rotation and shear deformations. On the contrary, as the column was designed to remain elastic throughout the test, the column deformation comprises only of the elastic flexure and shear deformations. It should be mentioned that the beam and column shear deformations were considerably small compared to the other components; hence they are neglected in the discussion to follow. Finally, the joint contribution to the overall deformation comes solely from the shear deformation of the joint panel. Figure 5.14 shows the contributions of the different elements (beam, column and joint) to the overall displacement of each specimen at the peak drifts. As could be expected based on the designed failure mode (beam hinging), the beam contributed considerably more towards the overall specimen drift than the column and the joint did. The components of deformation were almost the same amongst BCJ1, BCJ3, BCJ5 and BCJ7; however the contribution of joint deformation to

the overall drift was considerably higher in BCJ2 and BCJ6 due to lower axial load ratio and lower concrete compressive strength, respectively.

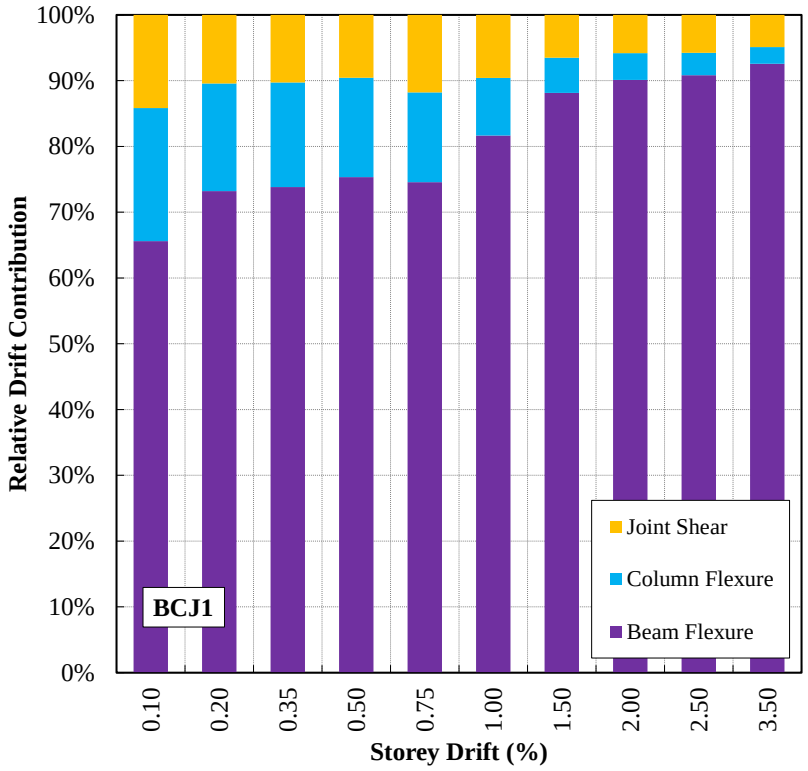

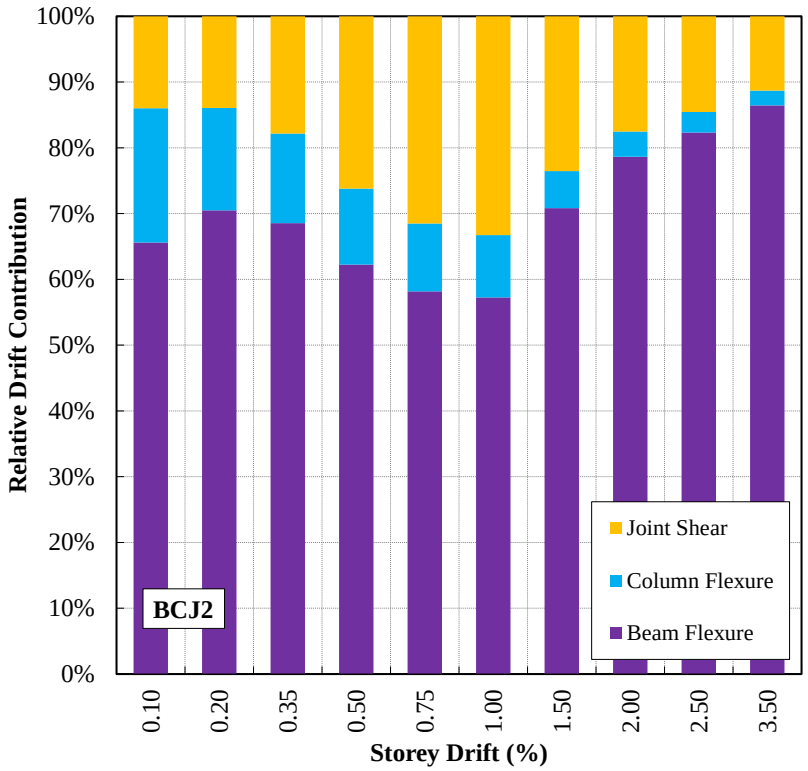

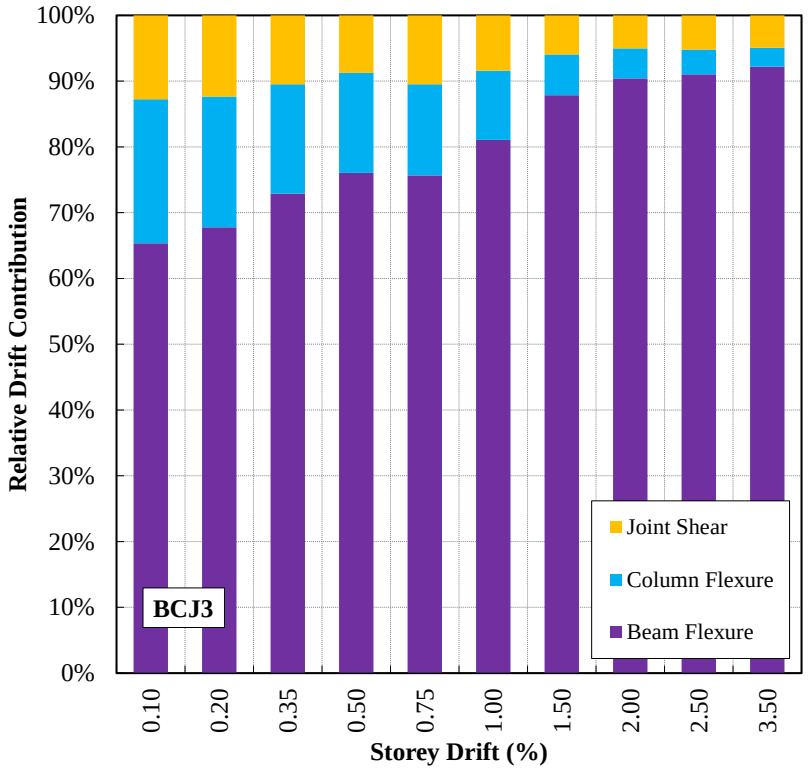
100%
90%
80%
70%
60%
50%
40%
30%
20%
10%
0%
Relative Drift Contribution
BCJ3
Joint Shear
Column Flexure
Beam Flexure
0.10
0.20
0.35
0.50
0.75
1.00
1.50
2.00
2.50
3.50
Storey Drift (%)

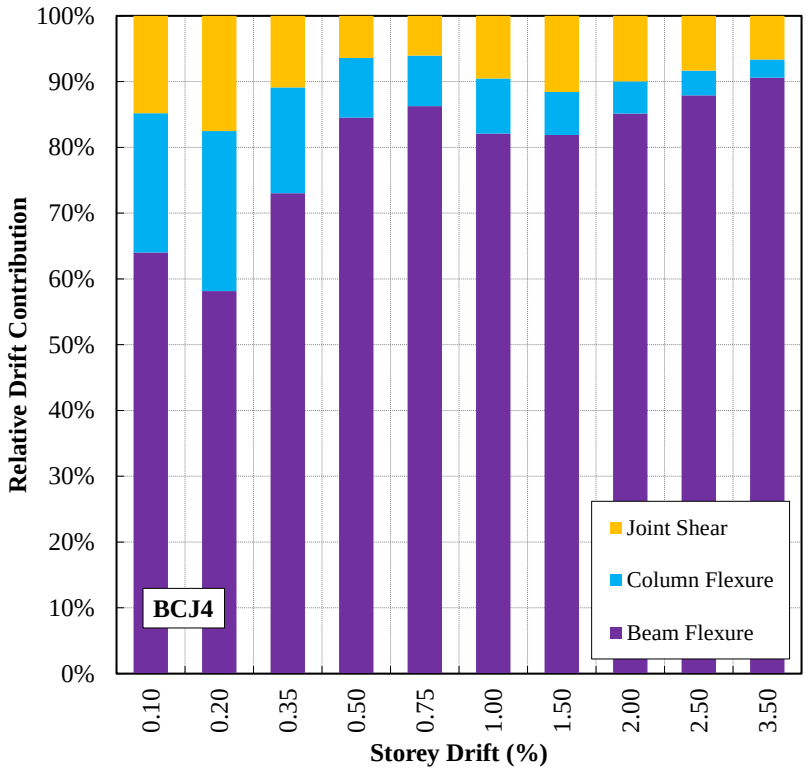
100%
90%
80%
70%
60%
50%
40%
30%
20%
10%
0%
Relative Drift Contribution
BCJ4
Joint Shear
Column Flexure
Beam Flexure
0.10
0.20
0.35
0.50
0.75
1.00
1.50
2.00
2.50
3.50
Storey Drift (%)

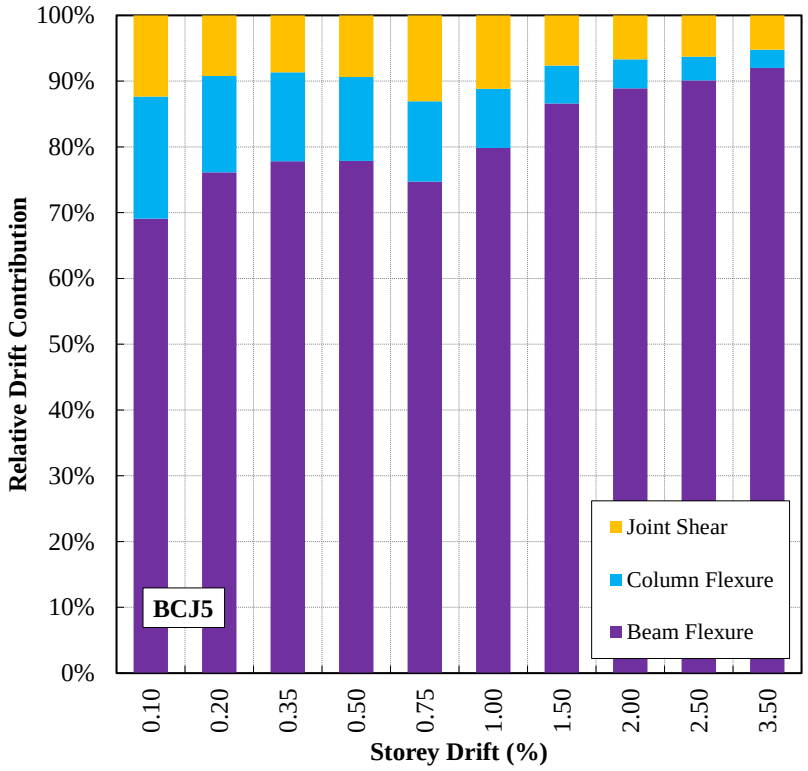
100%
90%
80%
70%
60%
50%
40%
30%
20%
10%
0%
Relative Drift Contribution
BCJ5
Joint Shear
Column Flexure
Beam Flexure
0.10
0.20
0.35
0.50
0.75
1.00
1.50
2.00
2.50
3.50
Storey Drift (%)

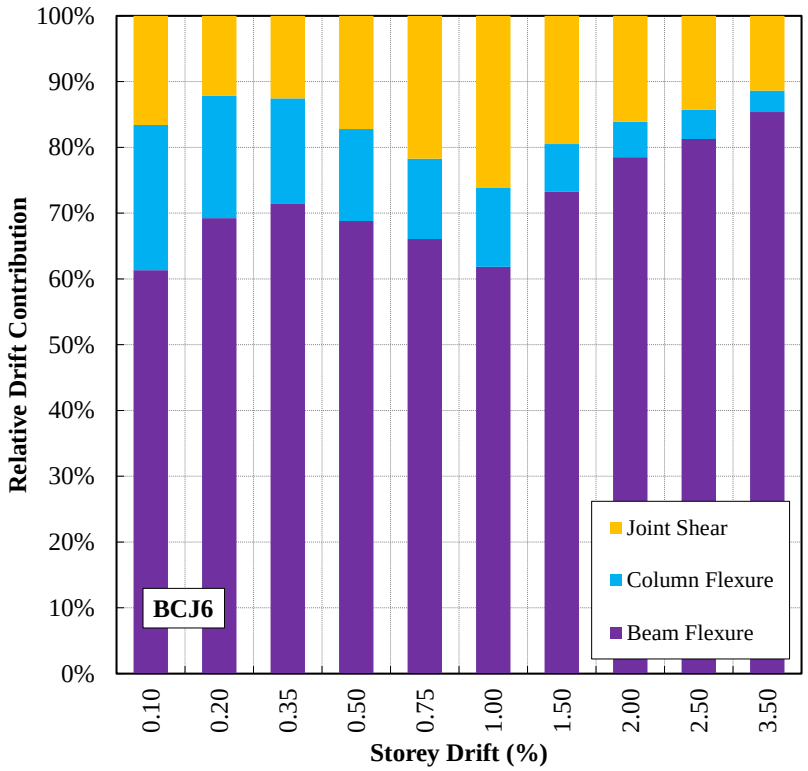
100%
90%
80%
70%
60%
50%
40%
30%
20%
10%
0%
Relative Drift Contribution
BCJ6
Joint Shear
Column Flexure
Beam Flexure
0.10
0.20
0.35
0.50
0.75
1.00
1.50
2.00
2.50
3.50
Storey Drift (%)

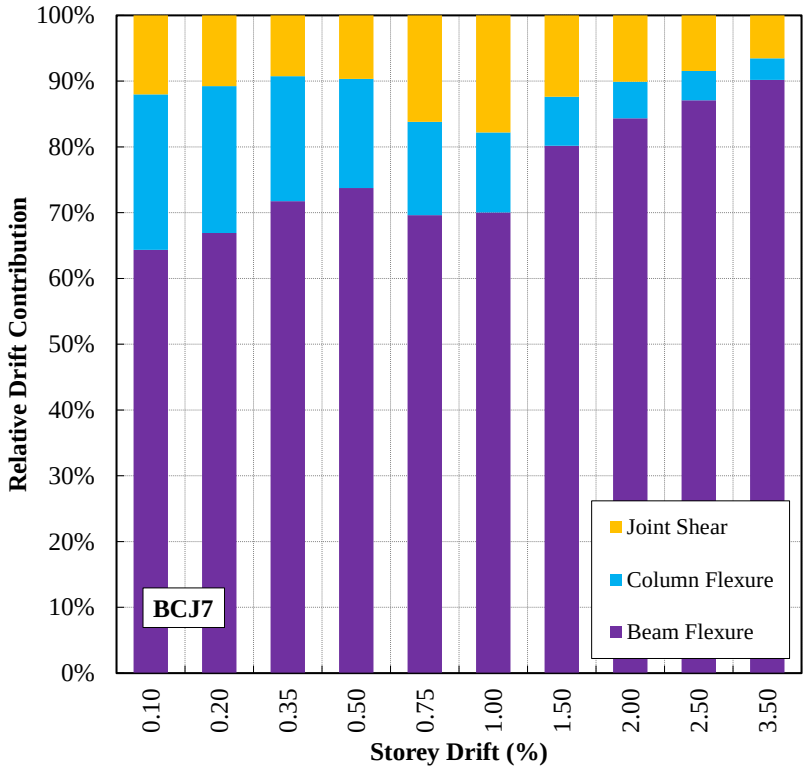

Figure 5.14: Relative contributions of different components to the overall specimen drift

5.4.5 BEAM ELONGATION

Using the LVDTs installed on the surface of specimens, the elongation of the plastic hinge zone was also calculated for the west and east beams. Total elongation (sum of the west and east) of each specimen is shown in Figure 5.15. A closer look at the elongation graphs reveals that before yielding the elongation was very small and reversible to zero for all specimens. However, it started to increase and became irreversible at higher drifts (after yielding). This can be explained by the fact that when the specimens were in their elastic response region, the cracks were small and closed completely during unloading; consequently the elongations were small and reversible. However when the cracks started to widen in the larger post-yield drift cycles, small pieces of concrete dropped into the void created by the cracks. In the reverse loading, these concrete parts started transferring the forces from one side of the crack to the other before these cracks closed completely. As a result, the reinforcement in the tension side started elongating before the cracks on the compression side fully closed down. This caused the cracks to open up in the next cycle even more and the process continued throughout the loading regime; thereby gradually increasing the permanent elongation of the plastic hinge zone. In addition to the explained

phenomenon, plastic strain of the top and bottom beam bars after yielding may also have added to the overall elongation of the plastic hinge zone. This observation is in agreement with elongation of plastic hinges reported in normal RC frames (Peng et al., 2013). As can be seen in the figures, all specimens elongated to similar extent; the total elongation (after 3.5% drift) in some specimens was about 30 mm; which is more than 7% of the beam depth. However, for BCJ4 (500 grade steel) and BCJ6 (CVC) elongation was slightly less; i.e. about 6%. In case of the former, lesser elongation can be explained by the lower ductility of the higher grade steel. However as BCJ6 was cast using lower strength concrete (48.4 MPa), the crushed concrete in the compression zone lost its strength and could not transfer the force from one side to the other side of the crack compared to a higher strength concrete.

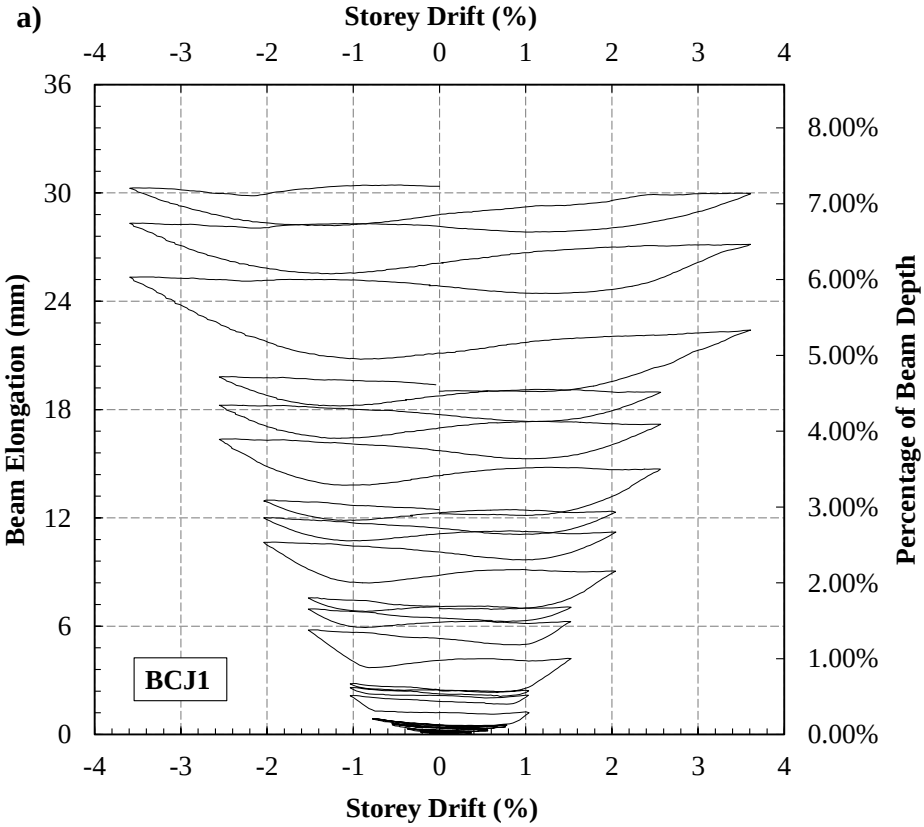

b)

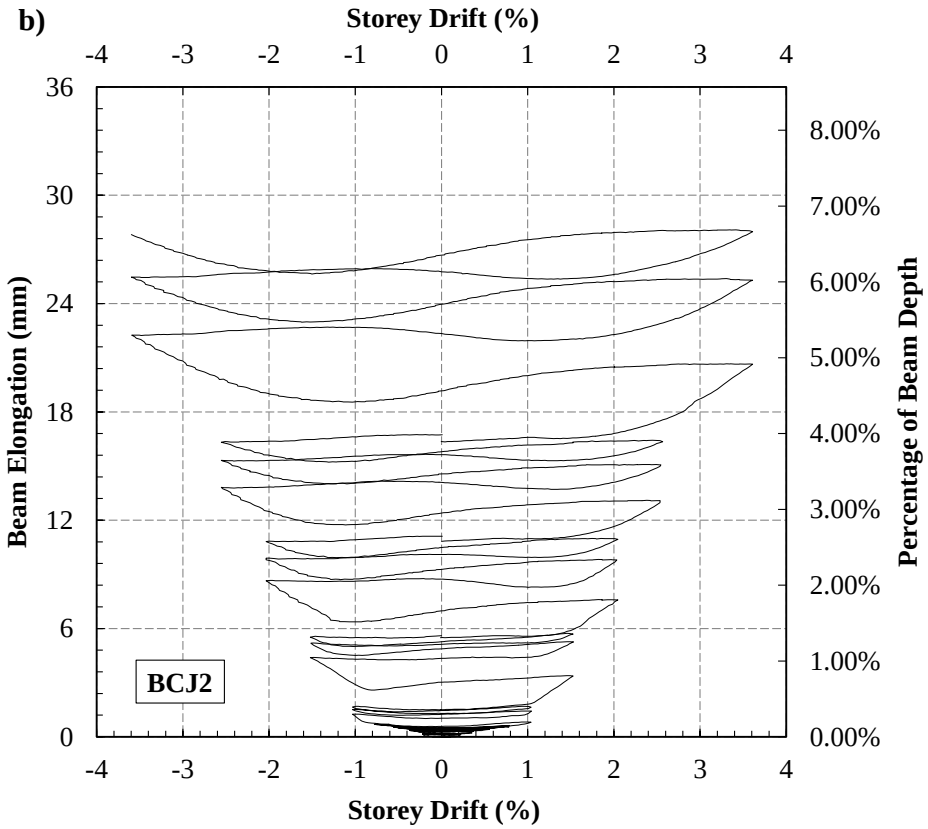
Storey Drift (%)
-4 -3 -2 -1 0 1 2 3 4
Beam Elongation (mm)
0 6 12 18 24 30 36
Percentage of Beam Depth
0.00% 1.00% 2.00% 3.00% 4.00% 5.00% 6.00% 7.00% 8.00%
BCJ2
Storey Drift (%)

c)

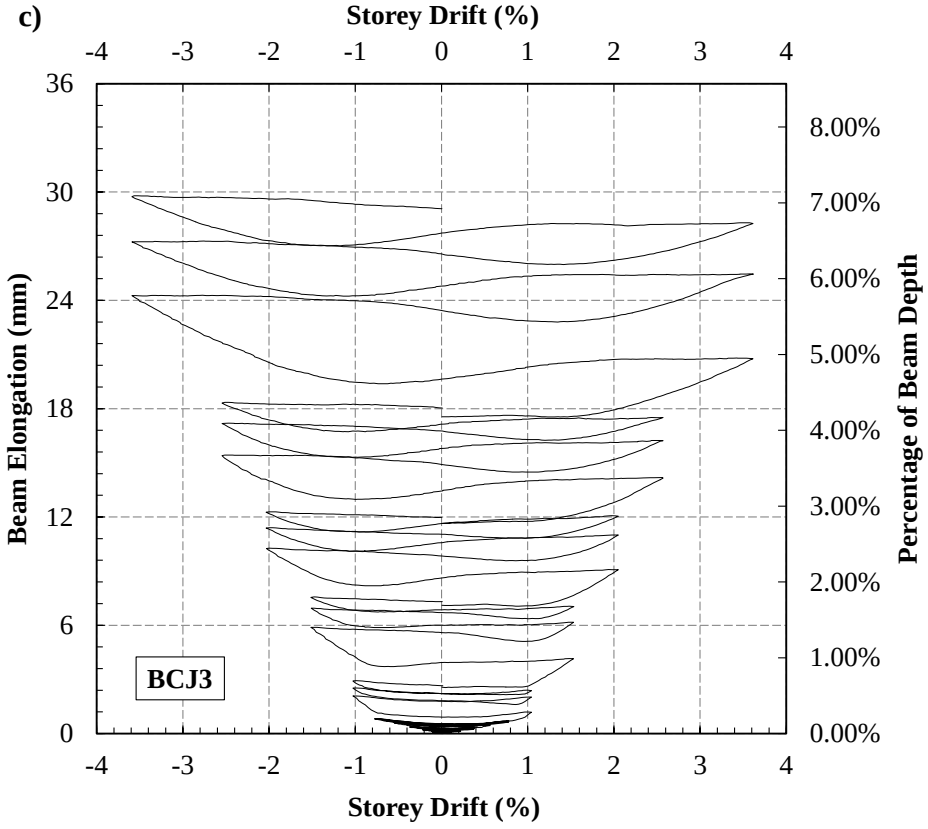
Storey Drift (%)
-4 -3 -2 -1 0 1 2 3 4
Beam Elongation (mm)
0 6 12 18 24 30 36
Percentage of Beam Depth
0.00% 1.00% 2.00% 3.00% 4.00% 5.00% 6.00% 7.00% 8.00%
BCJ3
Storey Drift (%)

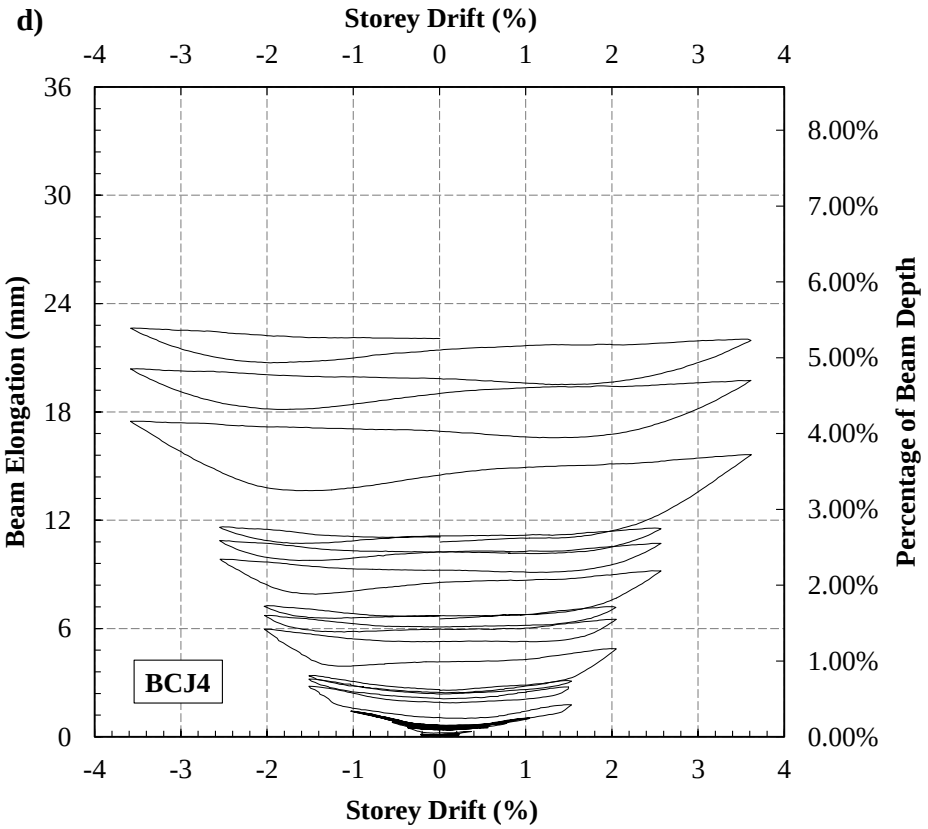
d)
Storey Drift (%)
-4 -3 -2 -1 0 1 2 3 4
36 30 24 18 12 6 0
Beam Elongation (mm)
8.00% 7.00% 6.00% 5.00% 4.00% 3.00% 2.00% 1.00% 0.00%
Percentage of Beam Depth
BCJ4
Storey Drift (%)

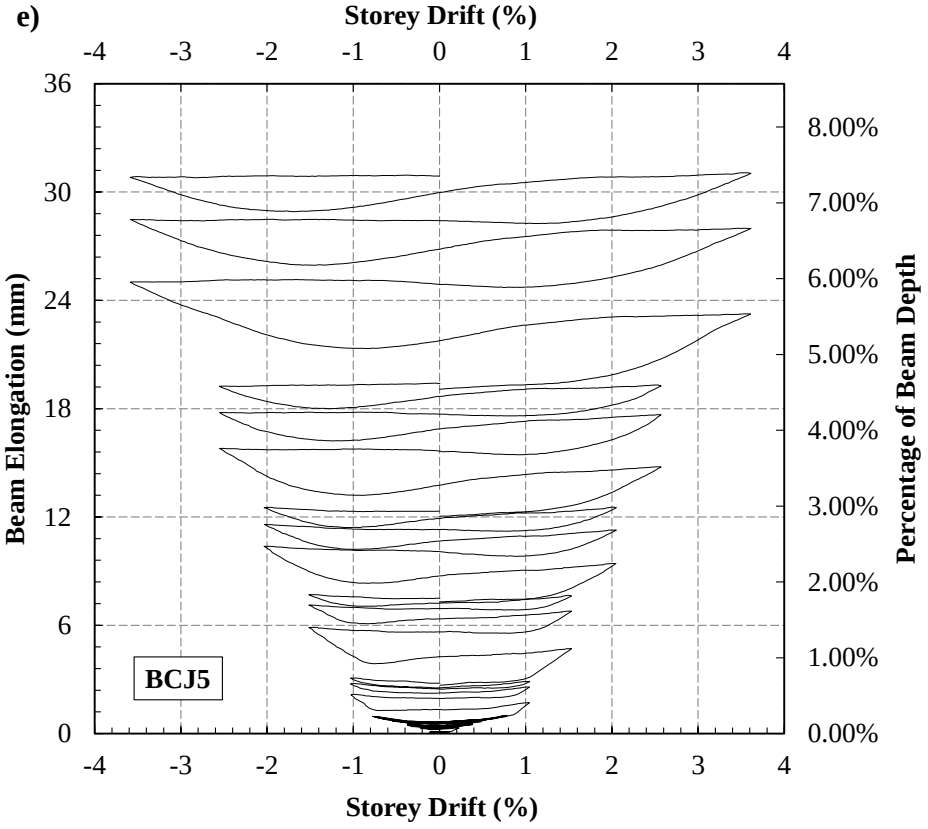
e)
Storey Drift (%)
-4 -3 -2 -1 0 1 2 3 4
36 30 24 18 12 6 0
Beam Elongation (mm)
8.00% 7.00% 6.00% 5.00% 4.00% 3.00% 2.00% 1.00% 0.00%
Percentage of Beam Depth
BCJ5
Storey Drift (%)

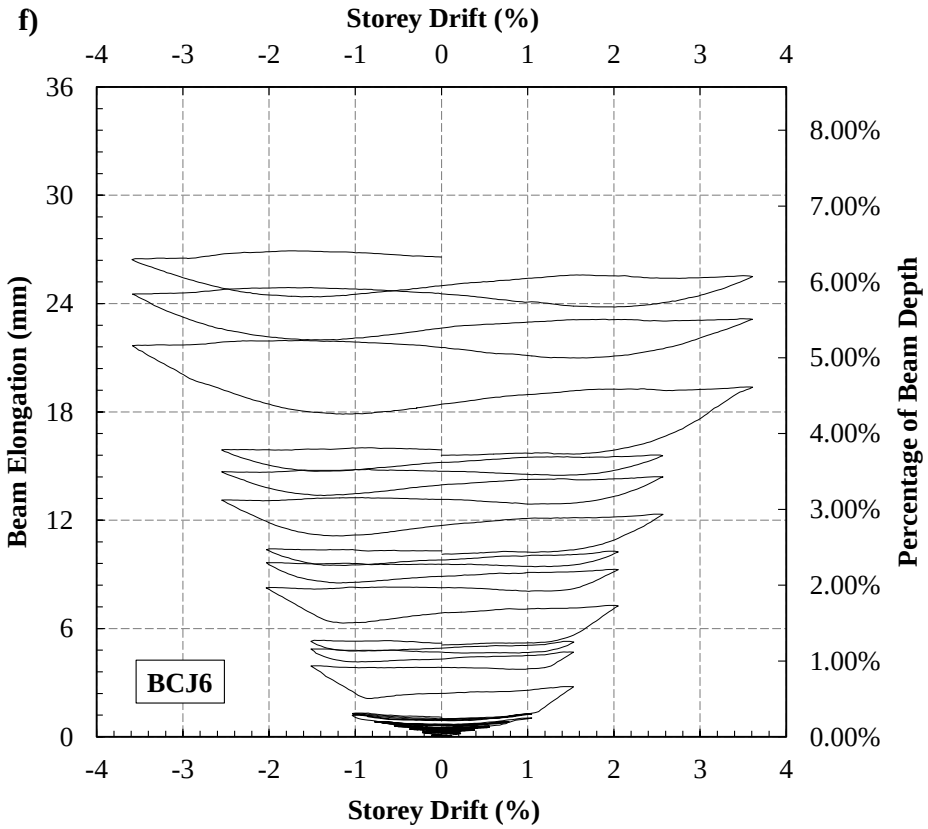

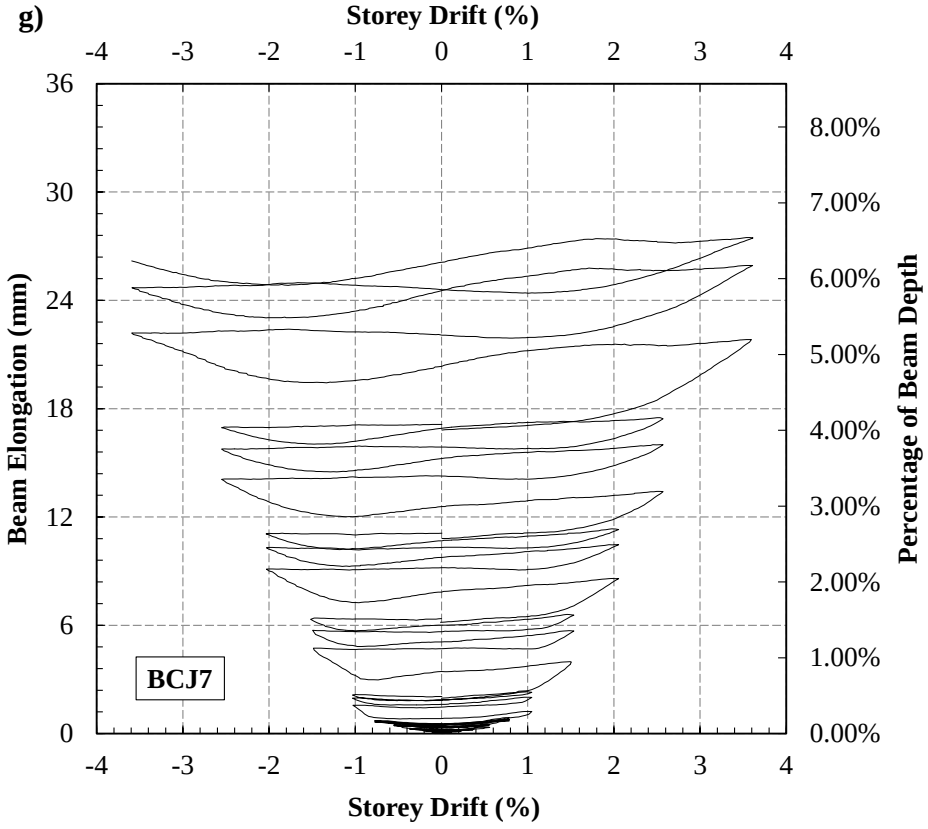

Figure 5.15: Total elongation of the plastic hinge zone (west and east beam)

5.5 CONCLUSIONS

In this paper seven beam-column joint specimens made of high-strength self-compacting concrete (HSSCC), conventionally vibrated high-strength concrete (CVHSC) and normal strength conventionally vibrated concrete (CVC) were designed, fabricated and tested under reversed cyclic loading. The effect of variables such as concrete type and strength, joint shear reinforcement, casting direction, axial load and steel grade on the seismic performance of BCJs were investigated. The three different concrete mixes (HSSCC, CVHSC and CVC) were developed using locally available materials in New Zealand to ensure that they can be commercially reproduced in a ready mix concrete plant.

Although none of the specimens failed within the tested regime (4.5% drift), it was apparent that the likely mode of failure (had the loading been continued) was the formation of plastic hinges in the beam close to the column faces. All specimens showed a relatively ductile behaviour as opposed to the general notion of brittle failure in high-strength concrete. This can be attributed to the better strain compatibility between high-strength concrete and reinforcing steel. At a given drift ratio, HSSCC incurred less cracks in the joint area compared to CVHSC and CVC specimens because of higher compressive strength and stronger bond of HSSCC. The hysteretic damping and stiffness reduction characteristics were similar in all specimens except for the CVC specimen which showed lower damping.

Except for slight variations, the relative contribution of joint shear reinforcement and concrete in the joint shear stress was similar amongst all specimens. As expected, the joint stirrups in the HSSCC specimen with a lower quantity of shear reinforcement experienced higher strain compared to the other two specimens. However, the joint stirrups remained well below the yielding level in all specimens, indicating that the codal requirements for the amount of shear reinforcement may be too conservative. As expected, the maximum shear stress in the joint remained within the allowable standard limits.

The beam flexural deformation was observed to contribute the most towards the specimen overall drift in all specimens; the contribution of column and joint were very small

compared to that of the beam. Lower axial load ratio and reduced amount of shear reinforcement were found to increase the joint contribution.

The beam elongation trends of all specimens (except for the higher grade steel specimen) were similar; the maximum total elongation (at 3.5% drift) was about 6% to 7% of the beam depth (i.e. about 24 to 30 mm). The lower beam elongation in the specimen with higher grade steel resulted from the lower ductility of the steel used.

Overall, seismic behaviour of the HSSCC specimens were quite similar to the CVHSC ones and none of the key parameters pertinent to the seismic performance were compromised by using HSSCC. In fact, the better bond properties and very high compressive strength resulted in better overall performance of HSSCC specimens. In addition, using HSSCC in the joint area of CVC specimen improved its seismic performance. Hence, HSSCC may offer an easier option (compared to CVHSC and CVC) for heavily congested areas like beam-column connections in RC frame structures without deleteriously affecting the seismic performance of the structure.

As mentioned previously, the amount of research on the seismic performance of SCC is very limited in the accessible literature and there is no information available on the cyclic behaviour of HSSCC under earthquake type excitations. It should be noted that the findings and recommendations of this study were based on a limited number of laboratory experiments conducted on HSSCC and CHVSC beam-column joint subassemblies. As the concept of HSSCC is relatively new in the field of structural engineering, more investigations are required to supplement the results obtained in this study; so that design guidelines could be developed for generic uses of HSSCC in RC structures in seismic regions.

5.6 ACKNOWLEDGMENTS

The authors would like to acknowledge the funding provided for the project by the Earthquake Commission (EQC) New Zealand, the University of Canterbury and the Department of Civil and Natural Resources Engineering. Authors would like to extend their sincere thanks to Tim Perigo, technician of the structures laboratory at the University

of Canterbury, for his continuous support throughout the experimental stage of this study. Without his diligent efforts and high-quality inputs, fabrication and testing of the beam-column subassemblies would have become a much more tedious task.

5.7 REFERENCES

ACI318M-08 2008, 'ACI318M-08 Building Code Requirements for Structural Concrete and Commentary'. ACI Committee 318, p. 479.

ACI374.1-05 2005, 'ACI374.1-05 Acceptance criteria for moment frames based on structural testing and commentary'. ACI Committee 374, p. 9.

De Almeida Filho, FM, El Debs, MK & El Debs, ALHC 2008, 'Bond-slip behavior of self-compacting concrete and vibrated concrete using pull-out and beam tests', Materials and Structures/Materiaux et Constructions, vol. 41, no. 6, pp. 1073-1089.

Desnerck, P, De Schutter, G & Taerwe, L 2010, 'Bond behaviour of reinforcing bars in self-compacting concrete: Experimental determination by using beam tests', Materials and Structures/Materiaux et Constructions, vol. 43, pp. 53-62.

Domone, PL 2006, 'Self-compacting concrete: An analysis of 11 years of case studies', Cement and Concrete Composites, vol. 28, no. 2, pp. 197-208.

Hassan, AAA, Hossain, KMA & Lachemi, M 2008, 'Behavior of full-scale self-consolidating concrete beams in shear', Cement and Concrete Composites, vol. 30, no. 7, pp. 588-596.

Lachemi, M, Hossain, KMA & Lambros, V 2005, 'Shear resistance of self-consolidating concrete beams - Experimental investigations', Canadian Journal of Civil Engineering, vol. 32, no. 6, pp. 1103-1113.

NZS3101 2006, 'NZS3101 Concrete structures standard Parts 1 & 2: The Desing of Concrete Structures and Commentary'. Standards New Zealand, Wellington, New Zealand, p. 698.

Peng, B, Dhakal, R, Fenwick, R, Carr, A & Bull, D 2013, 'Multispring Hinge Element for Reinforced Concrete Frame Analysis', Journal of Structural Engineering, vol. 139, no. 4, pp. 595-606.

Persson, B 2001, 'A comparison between mechanical properties of self-compacting concrete and the corresponding properties of normal concrete', Cement and Concrete Research, vol. 31, pp. 193-198.

Said, A & Nehdi, M 2007, 'Behaviour of reinforced self-consolidating concrete frames', Proceedings of the Institution of Civil Engineers: Structures and Buildings, vol. 160, no. 2, pp. 95-104.

Soleymani Ashtiani, M, Dhakal, RP & Scott, AN 2011, 'Bond properties of reinforcement in high-strength self-compacting concrete', in Proceedings of the 9th Symposium on High Performance Concrete Design, Verification and Utilization, Rotorua, New Zealand.

Soleymani Ashtiani, M, Dhakal, RP & Scott, AN 2013a, 'Post-yield bond behaviour of deformed bars in high-strength self-compacting concrete', Construction and Building Materials, vol. 44, no. 0, pp. 236-248.

Soleymani Ashtiani, M, Scott, AN & Dhakal, RP 2010, 'Mechanical properties of high-strength self-compacting concrete', in Proceedings of the 21st Australasian Conference on the Mechanics of Structures and Materials, Melbourne, Australia, pp. 827-832.

Soleymani Ashtiani, M, Scott, AN & Dhakal, RP 2013b, 'Mechanical and Fresh Properties of High-Strength Self-Compacting Concrete Containing Class C Fly Ash', Construction and Building Materials (Submitted)

Sonebi, M, Tamimi, AK & Bartos, PJM 2003, 'Performance and Cracking Behavior of Reinforced Beams Cast with Self-Consolidating Concrete', ACI Materials Journal, vol. 100, no. 6, pp. 492-500.

Valcuende, M & Parra, C 2009, 'Bond behaviour of reinforcement in self-compacting concretes', Construction and Building Materials, vol. 23, no. 1, pp. 162-170.

6 FINITE ELEMENT MODELLING AND ANALYSES OF HSSCC BEAM-COLUMN JOINTS

Soleymani Ashtiani, M, Dhakal, RP & Scott, AN 2014, 'Analytical Investigation on Seismic Performance of a High-Strength Self-Compacting Concrete Beam-Column Joint', in *Tenth U.S. National Conference on Earthquake Engineering*, Anchorage, Alaska.

6.1 ABSTRACT

The finite element analysis (FEA) software "DIANA" was implemented to simulate the results of experimental investigations on seismic performance of full-scale beam-column joints (BCJ). All specimens were designed following the New Zealand concrete standards (NZS3101:2006). Material models for concrete and steel were calibrated based on the physical characteristics of the materials derived from either the laboratory tests or available expressions in the literature. Specimens were modelled using two-dimensional curved-shell elements capable of capturing in and out of plane forces and deformations. In order to achieve a higher accuracy, both the longitudinal and transverse reinforcement were modelled in their actual locations as per the detail drawings. As the specimens were designed following the code requirements for seismic actions, the bond between reinforcement and concrete was defined as fully bonded.

Axial load was transferred to the column through four pre-stressed tendons connected to rigid plates located at the top and bottom of the column. Pushover analysis was first conducted to calibrate the results and check the mesh sensitivity; after which the exact cyclic loading applied in the laboratory was applied to the modelled specimens. Effectiveness of the FEA model in predicting the seismic behaviour of the specimens was judged based on the comparison between the peak loads and the shape of the load vs. displacement loops. When a good agreement was found between the FEA and experimental results, further seismically important features (namely damping, stiffness, concrete and steel contributions in the joint shear force, joint shear deformations, strain development in the joint stirrups, elongation of the plastic hinge zone, development of

compressive stress, and cracking pattern) were investigated. It was found that the FEA performed using DIANA were capable of providing reasonable predictions for the BCJ specimens tested in the laboratory.

6.2 INTRODUCTION

Reinforced concrete (RC) beam-column joints (BCJ) behave in a very complex manner; therefore an analytical joint model should be capable of capturing numerous characteristics for it to accurately predict the joint behaviour. In general, an RC BCJ may exhibit a combination of different failure mechanisms such as diagonal joint shear cracking, flexural cracking, hinging of beams, yielding of reinforcement, and excessive bond slip resulting in loss of anchorage of beam longitudinal bars. However, considering that the BCJs tested in this study were designed based on the current NZ concrete standard NZS3101 (2006) to withstand seismic forces, it is expected that beam hinging will be the predominant mode of failure (as experimentally shown in Chapter 5).

Finite element analysis (FEA) of BCJs accounting for such behaviours has been the focus of many previous research studies. Early efforts in modelling nonlinear behaviour of beam-column joints tackled the problem by manually updating the material properties at the onset of cracks or through the specification of discrete cracks. However, limitations such as the requirement of crack locations motivated the researchers to adopt continuum-based elasto-plastic fracture models. Amongst the most commonly used models are the Drucker-Prager plasticity model paired with a multidirectional non-orthogonal fixed crack model, the micro-plane models, the Willam-Warnke plasticity model in conjunction with a smeared rotating crack model, and the smeared rotating crack model along with the Modified Compression Field Theory. Explanation of the details of these analytical models is out of the scope of this study.

As the aim of the intended analysis is to capture the cyclic performance of RC beam-column joints, selection of an appropriate FEA program was mainly based on its capabilities in dealing with the associated issues. DIANA (2012) is a general purpose finite element program (three dimensional and nonlinear) which works based on displacement method. DIANA has been under development since 1972 and the name is an abbreviated

form of “DIsplacement method ANAlyser”. The software has been developed by civil engineers originating from Delft University of Technology. Dealing with the complexities involved in modelling reinforcement and bond in RC structures and availability of material models to incorporate cyclic loading are some of many appealing features of the software. DIANA has a range of extensive material, element and procedure libraries which make it ideal for research investigations. As a result DIANA (2012) was chosen for this study not only because of its reported success in simulating highly nonlinear problems in the literature (Deaton, 2013; Kulkarni et al., 2009; Kulkarni et al., 2008; Li et al., 2009a; Li et al., 2010; Li et al., 2009b), but also because it had multiple constitutive models for concrete and steel.

6.3 MATERIAL MODELS

6.3.1 TOTAL STRAIN ROTATING CRACK MODEL FOR CONCRETE

The total strain constitutive crack model for concrete is developed based on the Modified Compression Field Theory (MCFT), originally developed by Vecchio et al. (1986) and it follows a smeared crack approach for the fracture energy (Litton, 1974). The smeared crack concept assumes that the cracks are uniformly distributed over the entire volume of a finite element (De Borst, 1987). The implemented formulation in DIANA includes three-dimensional extension of the MCFT theory proposed by Selby et al. (1997; 1996) which accounts for lateral expansion and changes of concrete strength due to confinement and/or transverse cracking. A summary of this constitutive model is presented in the following section and the full theoretical formulation can be found in the DIANA material library reference manual (2012).

The total strain crack model describes stress as a function of strain in which the loading and unloading follow the same stress-strain path. As currently implemented in DIANA, the loading is modelled differently under tension and compression; however the unloading follows a secant path back to the origin (Figure 6.1).

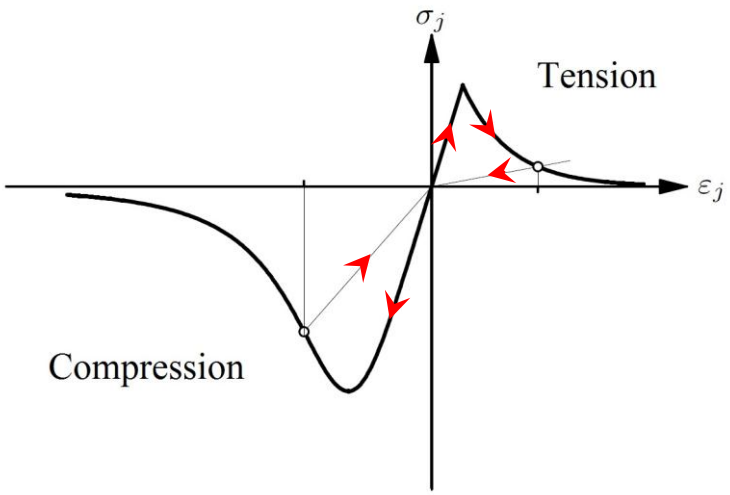

Figure 6.1: Total strain crack model: loading and unloading paths

In the ‘rotating crack model’ the crack direction is allowed to continuously adjust itself to the direction of principal strain. Although this approach bears less physical meaning than the ‘fixed crack model’ (where crack direction remains the same after its occurrence), it has been successfully applied to simulate the behaviour of reinforced concrete structures for a long time. A rotating crack model is advantageous over a fixed crack model in shear-failure type problems because the specification and validation of a shear retention factor is not required. However the assumption that the principal stresses and strains remain coincident is considered a limitation of this approach.

As mentioned before, the constitutive response consists of uniaxial stress-strain envelopes for tension and compression which are detailed in the next sections. During loading, the material is subjected to both tensile and compressive stresses which can result in cracking and crushing. Deterioration of concrete material due to cracking and crushing is monitored with internal damage variables which track the maximum (tensile) and minimum (compressive) strains reached at each integration point. In the total strain rotating crack model, it is assumed that once the material (concrete in this case) is damaged it will not recover. Therefore the absolute values of the internal damage variables and thus the stiffness degradation can only increase.

The lateral deformations of a specimen subjected to uniaxial tensile or compressive loadings are determined by the Poisson effect. However a passive lateral confinement

emerges when these displacements are constrained; which is an important characteristic in a three dimensional modelling of RC structures. When the material is cracked, the Poisson effect is no longer valid. This means that expansion in the cracked direction will not result in contraction of the transverse direction. As concrete is a pressure-dependent material, confinement plays an important role in changing its strength and ductility; this is also implemented in DIANA (2012). Compressive behaviour is also affected by the lateral cracking, or in other words by the tensile strength deterioration of the material in the transverse direction.

The concrete constitutive model detailed above depends on the selection of uniaxial concrete tensile and compressive behaviour. This means that the total strain rotating crack model may be coupled with various choices of tension and compression curves to simulate the concrete behaviour. A summary of the selected uniaxial concrete tensile and compressive responses is given in the following sections.

6.3.2 CONCRETE UNIAXIAL COMPRESSION RESPONSE

Under uniaxial compressive loading, the concrete response remains elastic only up to about 30% of its ultimate compressive strength. At the onset of inelastic deformations, the concrete shows a very high nonlinearity. As soon as the peak stress is passed, the compressive stress starts decreasing until the crushing (failure) strain is reached. Various models are reported in literature to model the behaviour of unconfined and confined concrete under compression such as Popovics (1973), Thorenfeldt et al. (1987), Mander et al. (1988a), Mander et al. (1988b) and Hoshikuma et al. (1997). As the influence of confinement and lateral cracking is incorporated in the total strain rotating crack model, it is not necessary to include the confinement in the uniaxial compression response separately.

DIANA (2012) provides different options for definition of the concrete compressive response such as linear, constant, Thorenfeldt, linear hardening, and multi-linear curves. Out of the above mentioned curves, Thorenfeldt et al. (1987) was chosen to model the concrete constitutive response in compression. One can always opt to use the ‘multi-linear’

curve, in order to input any of the other concrete compression models available in literature. The formulation of the Thorenfeldt et al. (1987) model is given below.

$$\sigma = f_c' \left(\frac{\varepsilon}{\varepsilon_0} \right) \frac{n}{n-1+\left(\frac{\varepsilon}{\varepsilon_0} \right)^{nk}} \tag{6.1}$$

$$\varepsilon_0 = \frac{f_c'}{E_c} \cdot \frac{n}{n-1} \tag{6.2}$$

$$n = 0.8 + \frac{f_c'}{17} \tag{6.3}$$

$$k = \begin{cases} 1.0 & \varepsilon_0 > \varepsilon \\ 0.67 + \frac{f_c'}{62} \geq 1.0 & \varepsilon > \varepsilon_0 \end{cases} \tag{6.4}$$

In the above equations, ‘σ’ is the concrete stress (MPa), ‘ε’ is the concrete strain (mm/mm), ‘f'_c’ is the concrete compressive strength (MPa), ‘E_c’ is the concrete modulus of elasticity (MPa), and ‘n’ and ‘k’ are the parameters of the Thorenfeldt model as defined above.

The modulus of elasticity of concrete is estimated using the Dinakar et al. (2008) formulae expressed in Chapter 2.

$$E_c = 4180\sqrt{f_c'} \tag{6.5}$$

When experimental results of a typical uniaxial concrete compressive stress-strain curve are available (unconfined or confined), one can always calibrate the Thorenfeldt et al. (1987) model to match those results and then use the corrected ‘n’ and ‘k’ parameters in the input file of DIANA. Unfortunately in this research due to the time and laboratory limitations, the high-strength concrete responses under tension and compression were not tested. Therefore, the models available in the literature (Mander et al., 1988b; Thorenfeldt et al., 1987) were used to generate appropriate responses using the compressive and split

tensile strength of concrete tested in the laboratory. In order to validate the FEA results against the Thorenfeldt et al. (1987) formulation, a three-dimensional single solid element was modelled and analysed nonlinearly in DIANA (Figure 6.2).

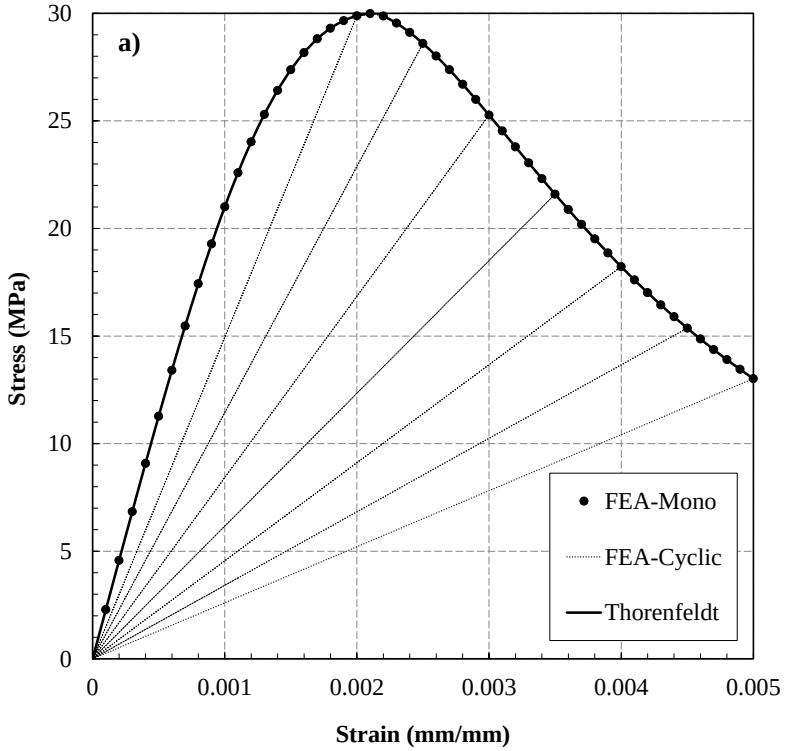

Figure 6.2: Validation of the Thorenfeldt model implemented in DIANA

As it can be seen in Figure 6.2, there is a perfect match between the validation of FEA result performed by DIANA and the actual Thorenfeldt formulation under monotonic loading. However, the cyclic response of the model currently implemented in DIANA does not account for the residual plastic strain; thus the unloading path follows a secant line which passes through the origin. This means that the analysis shows a substantially higher pinching compared to the actual concrete behaviour under cyclic loading (Deaton, 2013). Nevertheless as the behaviour of RC BCJs is highly dependent on the steel response, the overall pinching in the RC member response will be influenced by the analytical model proposed for steel in DIANA (this is discussed in section 6.3.4). Deaton (2013) validated the Thorenfeldt et al. (1987) formulation implemented in DIANA against previous experimental tests and reported an acceptable match under monotonic and cyclic loads.

6.3.3 CONCRETE UNIAXIAL TENSION RESPONSE

Tensile cracking is one of the other nonlinearities in dealing with concrete. When it comes to design, concrete contribution in taking tensile forces is neglected after cracking. However, experimental investigations (Belarbi et al., 1994) suggest that the concrete contribution under tension is continued even after reaching its maximum tensile capacity. This behaviour is known as "tension softening" in RC concrete members.

One of the other inputs required for the total strain rotating crack model is the concrete response under uniaxial tensile loads. If the reinforcement is modelled discretely with bond-slip interface elements a tension softening curve is required for the concrete response under tension. On the other hand, a tension stiffening response more suites the uniformly distributed reinforcement with perfect bond. In this study, the uniaxial concrete response under tension is defined following the model proposed by Hordijk (1991) with the following formulation.

$$\sigma_{cr} = f_t \left[\left(1 + \left(c_1 \frac{\varepsilon_{cr}}{\varepsilon_{cr,ult}} \right)^3 \right) e^{\left(-c_2 \frac{\varepsilon_{cr}}{\varepsilon_{cr,ult}} \right)} - \frac{\varepsilon_{cr}}{\varepsilon_{cr,ult}} \left(1 + c_1{}^3 \right) e^{-c_2} \right] \qquad 6.6$$

$$\varepsilon_{cr,ult} = 5.136 \frac{G_f}{h.f_t} \qquad 6.7$$

Where 'c_1' and 'c_2' are 3 and 6.93 respectively, '$\varepsilon_{cr,ult}$' is the maximum plastic strain, 'G_f' is the mode-I fracture energy (N/mm), 'f_t' is the concrete tensile strength (MPa), and 'h' is the crack bandwidth (characteristic length providing mesh objectivity with respect to the fracture energy). When the concrete is modelled using linear two-dimensional, higher order two-dimensional and solid elements, the crack bandwidth is defined as $(2A)^{0.5}$, $(A)^{0.5}$ and $(V)^{1/3}$, respectively. Note that 'A' and 'V' are the total area and volume of the element, respectively. The tensile strength 'f_t' is estimated using the expression given by Felekoglu et al. (2007) as detailed in Chapter 2 (Equation 2.4) and the fracture energy 'G_f' is determined using Equation 6.9.

$$f_t = 0.43 f_c'^{0.6} \quad 6.8$$

$$G_f = 0.065 \times \ln\left(1 + \frac{f_c'}{10}\right) \quad 6.9$$

Figure 6.3 provides a comparison between the tension model proposed by Hordijk (1991) and the implementation of the same in DIANA.

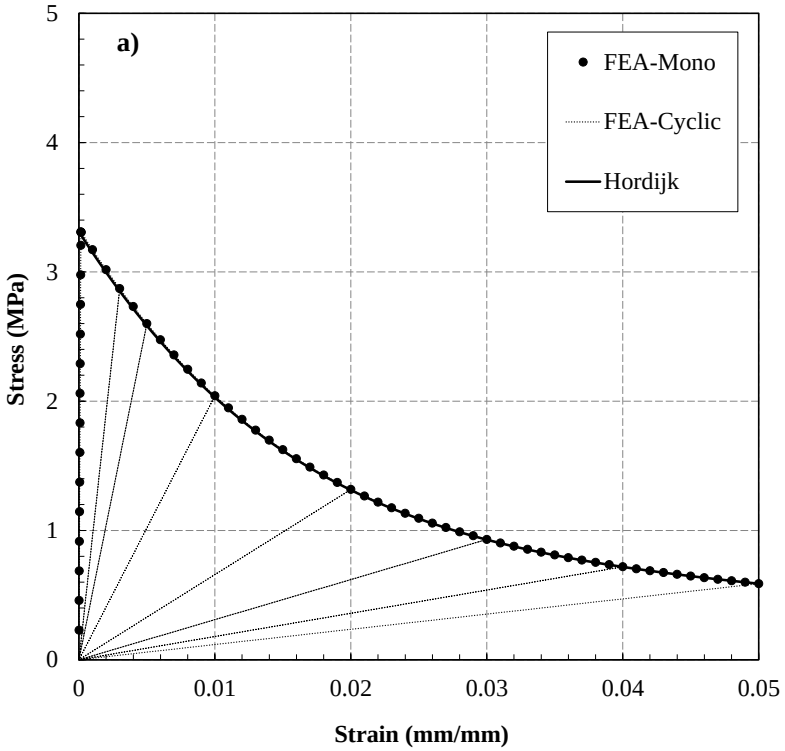

Figure 6.3: Validation of the Hordijk model implemented in DIANA

Here again the monotonic FEA provides a perfect match for the Hordijk (1991) formulation; whereas the cyclic response neglects the effect of inelastic tensile strains and the contact stress effect. Therefore an unrealistic pinching, resulting from secant unloading and reloading, remains the deficiency of DIANA's uniaxial tensile response. The Hordijk (1991) model has also been validated against experimental tests by Deaton (2013). It is reported that the FEA results show a reasonable match against the experimental result once the model limitations were accepted.

6.3.4 MENEGOTTO-PINTO MODEL FOR STEEL REINFORCEMENT

Cyclic performance of reinforced concrete beam-column joints is highly dependent on the nonlinear response of reinforcing bars under cyclic loading. One of the important features of the nonlinear behaviour of reinforcing bars under cyclic excitations is the yielding during loading reversal; more commonly known as the Bauschinger effect. Previous research scrutinized the effect of Bauschinger phenomenon on the simulation of cyclically loaded joints (Fleury et al., 1999; Sasmal et al., 2010) as it enables the cracks to close easily during the load reversals and also affects the performance of the compression zone. Many researchers have successfully investigated the Bauschinger effect in the behaviour of reinforcing steel (Balan et al., 1998; Cofie et al., 1985; Dodd et al., 1995; Heo et al., 2009; Hoehler et al., 2006; Menegotto et al., 1973). Some have also accounted for buckling effect in their models (Dhakal et al., 2002a,b; Gomes et al., 1997; Monti et al., 1992; Rodriguez et al., 1999). Although incorporation of the Bauschinger and buckling effects increase the accuracy of the BCJ analytical model, some studies have successfully used a simple elastic-perfectly-plastic steel response to model the hysteresis response of BCJs (Li et al., 2009a; Li et al., 2009b).

Out of the above mentioned steel hysteresis response models, currently the Menegotto et al. (1973) model coupled with a bilinear backbone curve is implemented in DIANA which can be incorporated in modelling reinforcement of the BCJs investigated in this research. The detailed formulation of the model can be found in many of the previous studies (Deaton, 2013; Dhakal et al., 2002b; Gomes et al., 1997; Menegotto et al., 1973); however a summary of the model concept along with the calibration of some of the parameters is presented here. The model accounts for Bauschinger effect as well as the isotropic strain hardening and is expressed in terms of non-dimensional stress ‘σ*’ and strain ‘ε*’ correlation as follows. Figure 6.4 and Figure 6.5 illustrate the parameters used in the Menegotto-Pinto model.

$$\sigma^* = b\varepsilon^* + \frac{(1-b)\varepsilon^*}{\left(1+\varepsilon^{*R}\right)^{\frac{1}{R}}} \qquad 6.10$$

$$R = R_0 - \frac{A_1 \varepsilon_{p,\max}}{A_2 + \varepsilon_{p,\max}} \qquad 6.11$$

Where ‘b’ is the ratio of strain hardening to elastic modulus, ‘R’ is the curvature parameter controlling the shape of the hysteresis response, ‘R_0’ is the initial curvature parameter, and ‘$\varepsilon_{p,max}$’ is the maximum plastic excursion during the previous half-cycle.

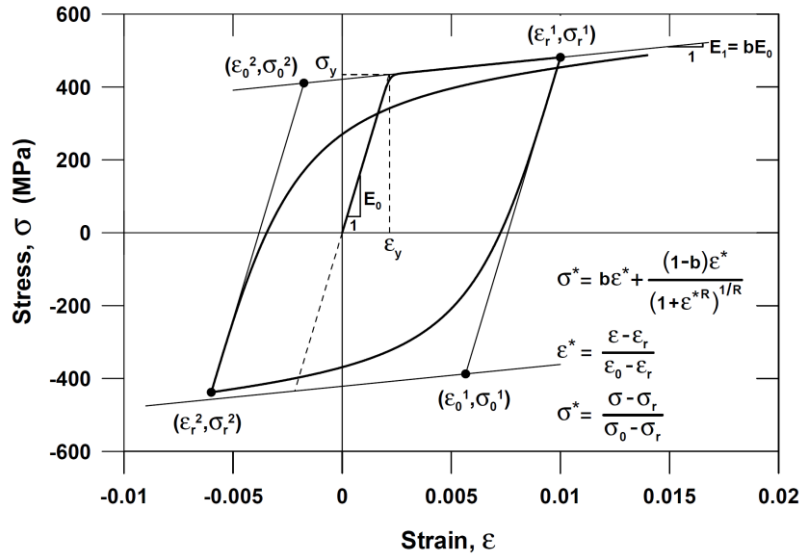

Figure 6.4: Schematic view of the parameters of Menegotto-Pinto model

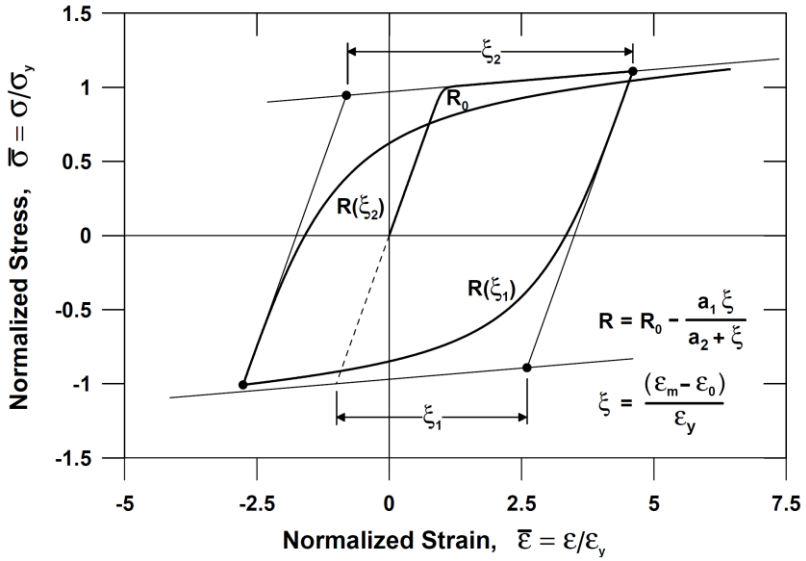

Figure 6.5: Degradation of cyclic curvature

A stress shift 'σ_{sh}' in the linear yield asymptote is proposed to account for the isotropic hardening (Figure 6.6); which depends on the maximum plastic strain and determined from Equation 6.12.

$$\frac{\sigma_{sh}}{\sigma_{y0}} = A_3\left(\frac{\varepsilon^t_{\max}}{\varepsilon_{y0}} - A_4\right) \qquad 6.12$$

Where 'σ_{y0}' and 'ε_{y0}' are the initial yield stress and corresponding strain and 'ε^t_{max}' is the maximum absolute total strain at the instant of strain reversal. 'A_1' to 'A_4' in Equations 6.11 and 6.12 are the material constants which should be determined experimentally.

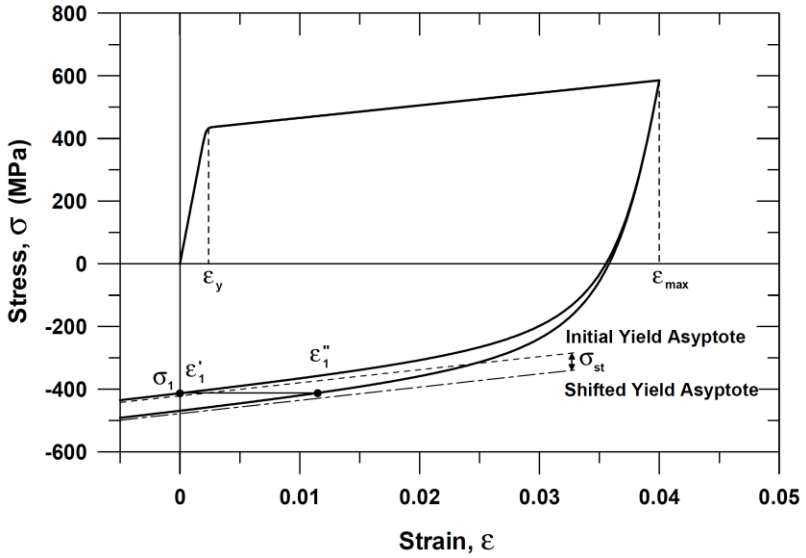

Figure 6.6: Stress shift due to isotropic strain hardening

In addition to the material constants ('A_1' to 'A_4'), the initial curvature 'R_0' and the ratio of strain hardening 'b' should also be calibrated to the specific cases of reinforcement. In order to determine an appropriate value for the strain hardening ratio 'b', experimental stress-strain curves for the reinforcement were used. Figure 6.7 shows the experimental response of a typical D25 bar under axial tension. The Menegotto et al. (1973) model follows a bilinear curve in which the first branch connects the origin and the yielding point so that the elastic behaviour of the reinforcement can be predicted accurately. The ratio of strain hardening 'b' should be calculated in such a way that the second branch fits the post-yield phase of the steel response. The first choice is to determine 'b' so that the second branch of the model connects the yielding point to the maximum strain before failure (b =

0.004 line in Figure 6.7). However the problem with this way of determining 'b' is that, after yielding, the model constantly underestimates the response of reinforcement by upto about 20%; which is a substantial compromise in one of the main material models.

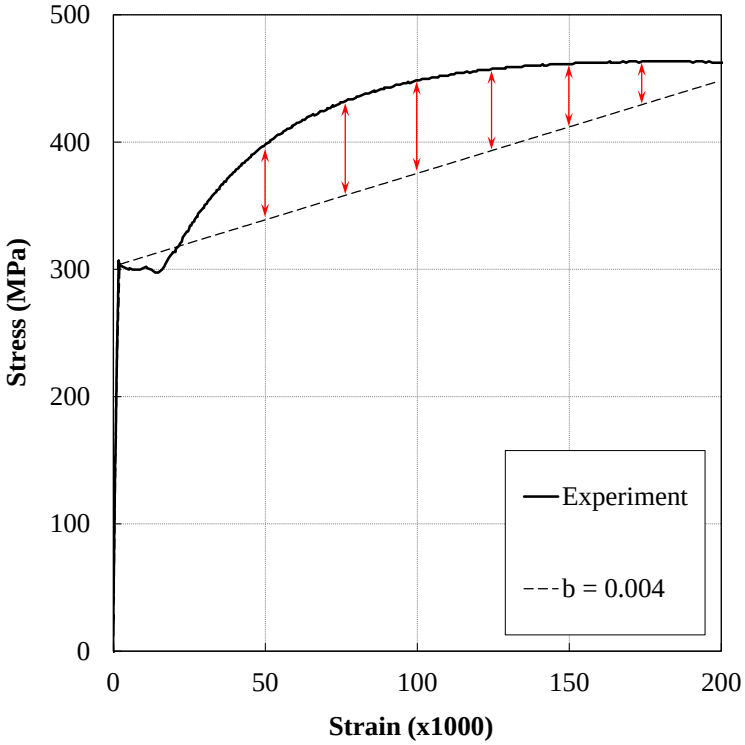

Figure 6.7: Selection of the ratio of strain hardening 'b'

Therefore, a more realistic approach was chosen to determine the ratio of strain hardening which is detailed herein. As explained before (Chapter 5 and Appendix F), potentiometers were installed on the surface of the specimens in order to measure the average strains at the level of reinforcement. At the same time, it is known that the maximum elongation of the reinforcement happens in the plastic hinge zone. Therefore, the readings of the potentiometers were used to determine the maximum strain that the reinforcement had undergone at the end of the test (average maximum of about 0.1 mm/mm). The corresponding stress was then found from the experimental stress-strain curves for reinforcement. The achieved point was connected to the yield point and the slope of this line provided a more realistic value for the strain hardening ratio (b = 0.008) which was used in the Menegotto et al. (1973) model. Figure 6.8 shows the comparison of the two (b = 0.004 and 0.008) values chosen for the strain hardening ratio. After the steel strain reaches a value of 0.1 mm/mm, the model (incorporating b = 0.008) starts overestimating the stress-strain response. However, as mentioned before the maximum measured strain in

the steel was well below 0.1 mm/mm. Thus, it is expected that a 'b' value of 0.008 well serves the purpose of FEA modelling of the specimens used in this study. Nevertheless, DIANA (2012) developers should consider the implementation of a multi-linear backbone for the Menegotto et al. (1973) model in order to improve its capabilities.

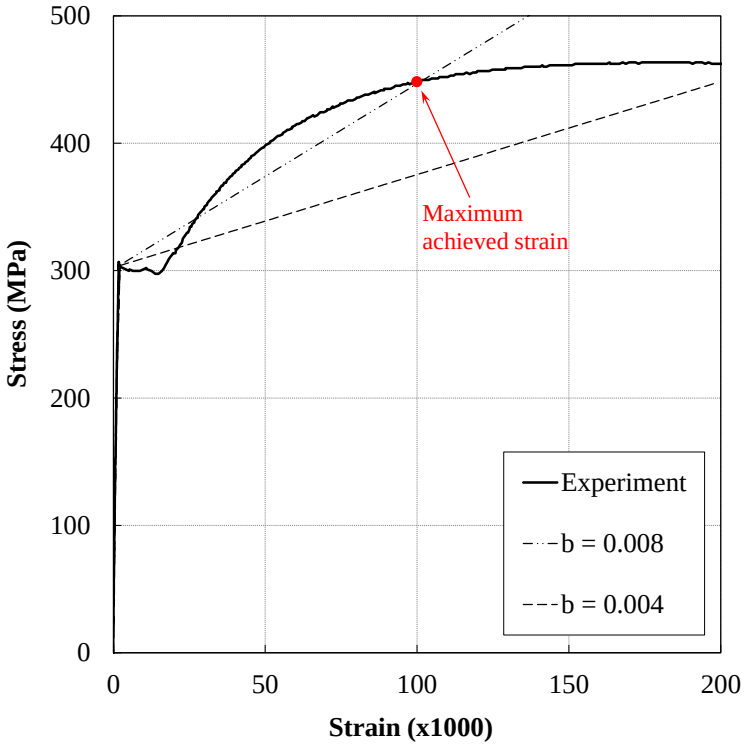

Figure 6.8: Comparison of different strain hardening ratios

Other parameters were set based on a parametric analysis and recommendations from literature (Deaton, 2013; Menegotto et al., 1973; Monti et al., 1992; Orakcal et al., 2006) as R_0 = 19.5, A_1 = 18.5, A_2 = 0.1, A_3 = 0.0, and A_4 = 0.0. The reason to choose A_3= 0.0 was to overrule the isotropic hardening as it gave unrealistic results compared to the experimental curve (see Figure 6.9). Figure 6.10 shows the finalized cyclic response of a typical steel bar (D25) predicted using the Menegotto et al. (1973) model and the calibrated parameters explained before. Using another set of parameters, Deaton (2013) validated the implemented Menegotto et al. (1973) model in DIANA against some of the experimental tests performed by other researchers and reported acceptable predictions. Note that the maximum strain excursion in those experimental results were well below 0.05 mm/mm which is less than half of the strain the reinforcement had undergone in the tested specimens.

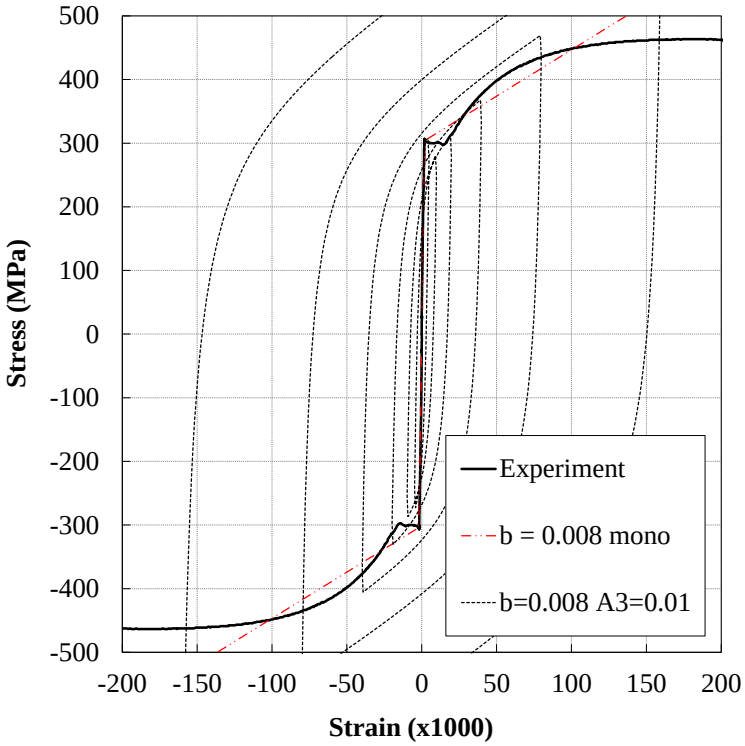

Figure 6.9: Cyclic response of reinforcement using b=0.008 and A_3=0.01

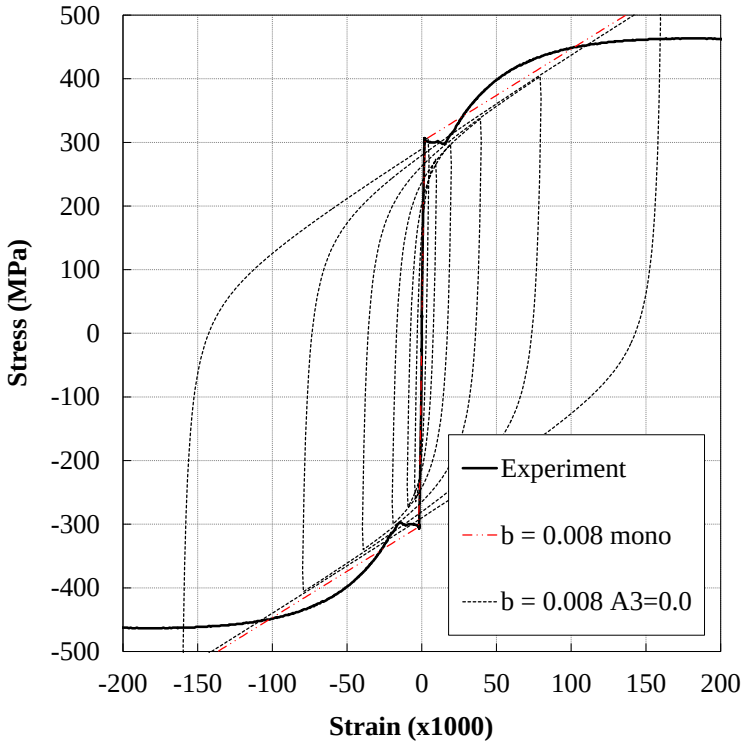

Figure 6.10: Menegotto-Pinto model for capturing cyclic response of reinforcement

6.3.5 BOND-SLIP RESPONSE

Reinforcing steel can be modelled using three different options in DIANA; namely embedded reinforcement, discrete reinforcement and bond-slip reinforcement. Employing discrete reinforcement elements and connecting them to concrete using interface elements (such as bond-slip) is advantageous only when a detailed bond-slip analysis is required. However in most of the other cases (such as BCJs), embedded reinforcement is normally used which can be coupled with the bond-slip option if necessary (such as for non-seismically detailed BCJs where slipping of the beam bars through the joint might happen). Depending on the distribution of reinforcement over the RC section, either 'bar' or 'grid' reinforcement options can be utilized. Note that for the 'bar' reinforcement option, the exact location of bars can be determined; even when the embedded reinforcement is used.

In the current research the bond-slip reinforcement has not been used for the following two reasons. First, as the BCJs were designed based on the current NZS3101 (2006) standard to resist seismic actions, the slippage of bars through the joint is not considered a probable failure mechanism. Second, in the current version of DIANA (2012) the bond-slip for embedded reinforcement has not been coupled with the Menegotto et al. (1973) model. Therefore, if the bond-slip has to be used, the Menegotto-Pinto model should be replaced with the Von Mises Plasticity model for reinforcement. However, the latter was found to be less effective in predicting the cyclic response of steel bars and overestimates the energy dissipation in each cycle. As the importance of the steel model is much higher than the effect of bond-slip behaviour for the seismically detailed BCJs, it was decided to rule out the bond-slip implementation in the finite element modelling.

6.4 DEVELOPMENT OF THE FINITE ELEMENT MODEL

6.4.1 SELECTION OF THE MESH ELEMENTS

DIANA (2012) provides a wide selection of different elements (detailed in the "element library" manual) including but not limited to the truss, beam, plane stress, plane strain, axisymmetric, plate bending, flat shell, curved shell, solid, and interface elements. Due to the geometry of BCJ specimens and test setup as well as the loading direction, it is not

necessary to choose three-dimensional (solid) elements. Selection of solid elements for such analysis will only increase the computation effort and time required for the analysis without adding any significant value to the final outcome. Therefore, the finite element analysis was decided to consist of two-dimensional elements.

The applicable 2D elements which could be employed in the FE model were channelled down to the plane stress, plate bending, flat shell, and curved shell elements (Figure 6.11). In the plate bending elements (Figure 6.11b), the direction of load should be perpendicular to the plane of the element; which is not the case in the analysis of BCJs. Therefore, the 2D plate bending elements are ruled out. In DIANA, the embedded reinforcement option cannot be used in the flat shell elements (Figure 6.11c); which makes the usage of these elements out of question. However, when using the curved shell elements (Figure 6.11d), there is an option for flat surfaces which is equivalent to the flat shell elements in which the embedded reinforcements may be used.

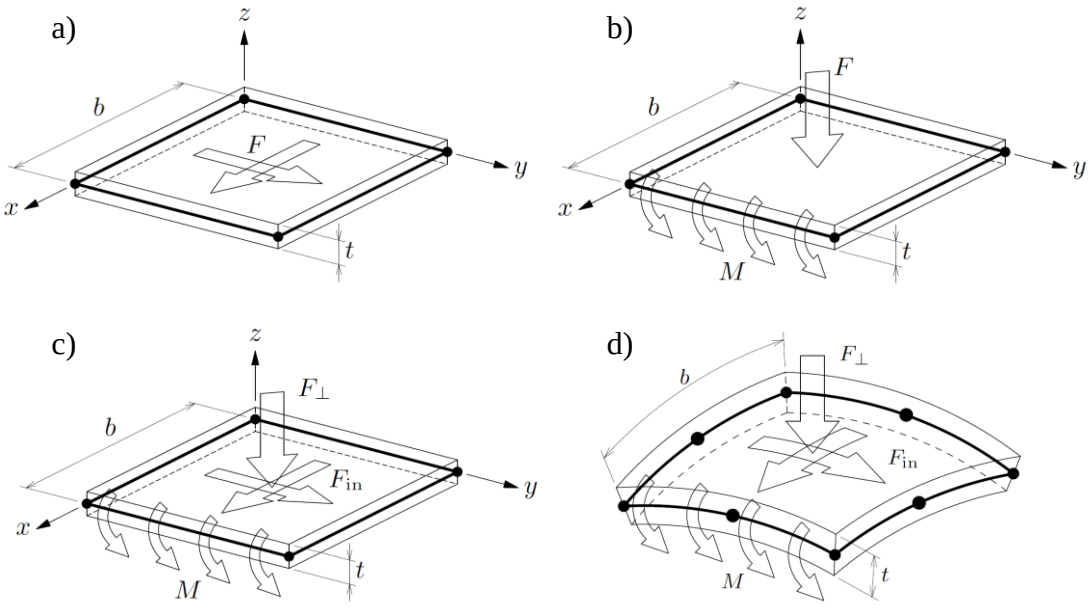

Figure 6.11: a) Plane stress, b) plate bending, c) flat shell, and d) curved shell elements

If the plane stress elements (Figure 6.11a) are chosen for the FE modelling, all of the reinforcement which is otherwise distributed along the thickness (340 mm) of the BCJs should be lumped into one plane. Although the computation effort and analysis time would decrease, this assumption unnecessarily reduces the accuracy of the generated FE model. This is important when bars of different diameter and yield strength are utilized along the

thickness of the specimen; which was the case for the tested BCJs in this study. By employing curved shell elements, the location of reinforcements (longitudinal and transverse) along the thickness of BCJs can be maintained and different diameter bars can easily be modelled. In addition, different material properties can be defined by incorporating different layers along the thickness and the out of plane deformations may be accounted for should any asymmetric or out of plane loadings are presented in the model.

6.4.2 FINITE ELEMENT DISCRETIZATION OF THE MODEL

In generating the FE model, attention was paid to replicate different parts of the actual experiment in such a way that a balance of accuracy and simplicity in modelling was achieved. As explained in the previous section, curved shell elements (Figure 6.11d) were chosen to model the two-dimensional parts (joint region, beam, column, linear concrete, and steel plates) of the BCJ as shown in Figure 6.12. Note that the nonlinear concrete used in the joint, beam and column have different material numbers assigned; which enables defining different material properties when dissimilar concrete mixes are used in various locations of the same specimen (BCJ7).

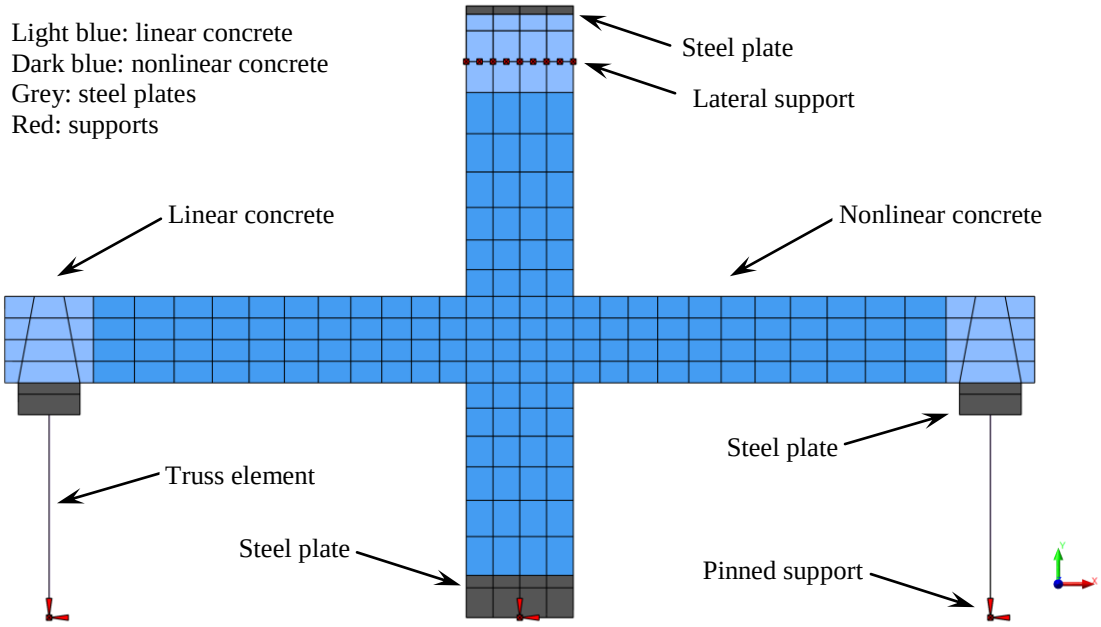

Figure 6.12: Different parts of the finite element model

Steel plates of linear material properties and very high stiffness were used at the top and bottom of the column as well as the tip of the beams. Truss element of 300 mm diameter

circular cross section, linear steel and high stiffness were employed to connect the beam ends to their supports as in the experiments. Note that the truss elements can only take axial loads and are pinned at their nodes; therefore they were discretized into a single mesh which would accurately replicate the actual test setup conditions. The column and beam supports were all pinned and the column was also supported laterally in the 'z' direction (perpendicular to the BCJ plane). The additional lateral support of the column was provided to increase the stability of the FE model against the out of plane deformations of the curved shell elements.

The axial load was applied through four pre-stressed steel tendons (35 mm diameter) connected to the top and bottom steel plates of the column (Figure 6.13). The 2D presentation in Figure 6.12 shows the mid-plane of the curved shell elements and the thickness offsets into two equal halves on each side of the mid-plane to form the full thickness. Note that the thickness of the 2D curved shell elements in 'z' direction was 340 mm; equal to the actual thickness of the specimens.

In the experiment the pre-stressed tendons were located outside of the BCJ. However due to the modelling considerations in DIANA for embedded reinforcement and also simplicity of the model, they were modelled inside the BCJ in the FE model. In order to defuse the influence of embedded tendons on the concrete, they were defined as 'NOBOND' reinforcement connected only to the outer points of the steel plates. As a result, the axial load was first transferred to the steel plates and then to the column through the plates; which was the same as what happened in the experiment. The three-dimensional nature of the 2D curved shell elements can be shown by activating the cross sectional properties in DIANA (Figure 6.13).

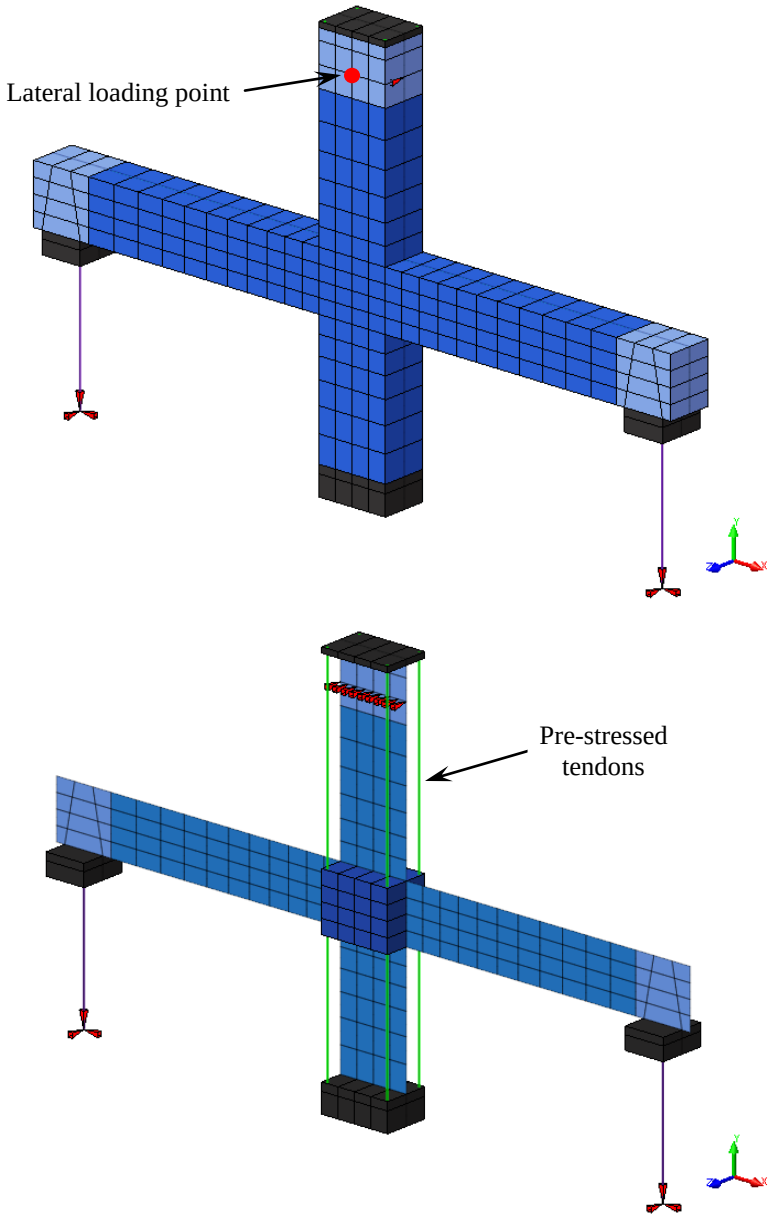

Figure 6.13: Three-dimensional presentation of the curved shell elements

Both the longitudinal and transverse reinforcement were modelled in their actual locations (Figure 6.14) without compromising their distribution in 'z' direction (over the thickness) using the full bond embedded reinforcement option in DIANA (2012). In this method, the physical properties (diameter and yield stress) of each bar were defined in an identical material property for which the Menegotto et al. (1973) model was activated incorporating the relevant material constants (explained in section 6.3.4).

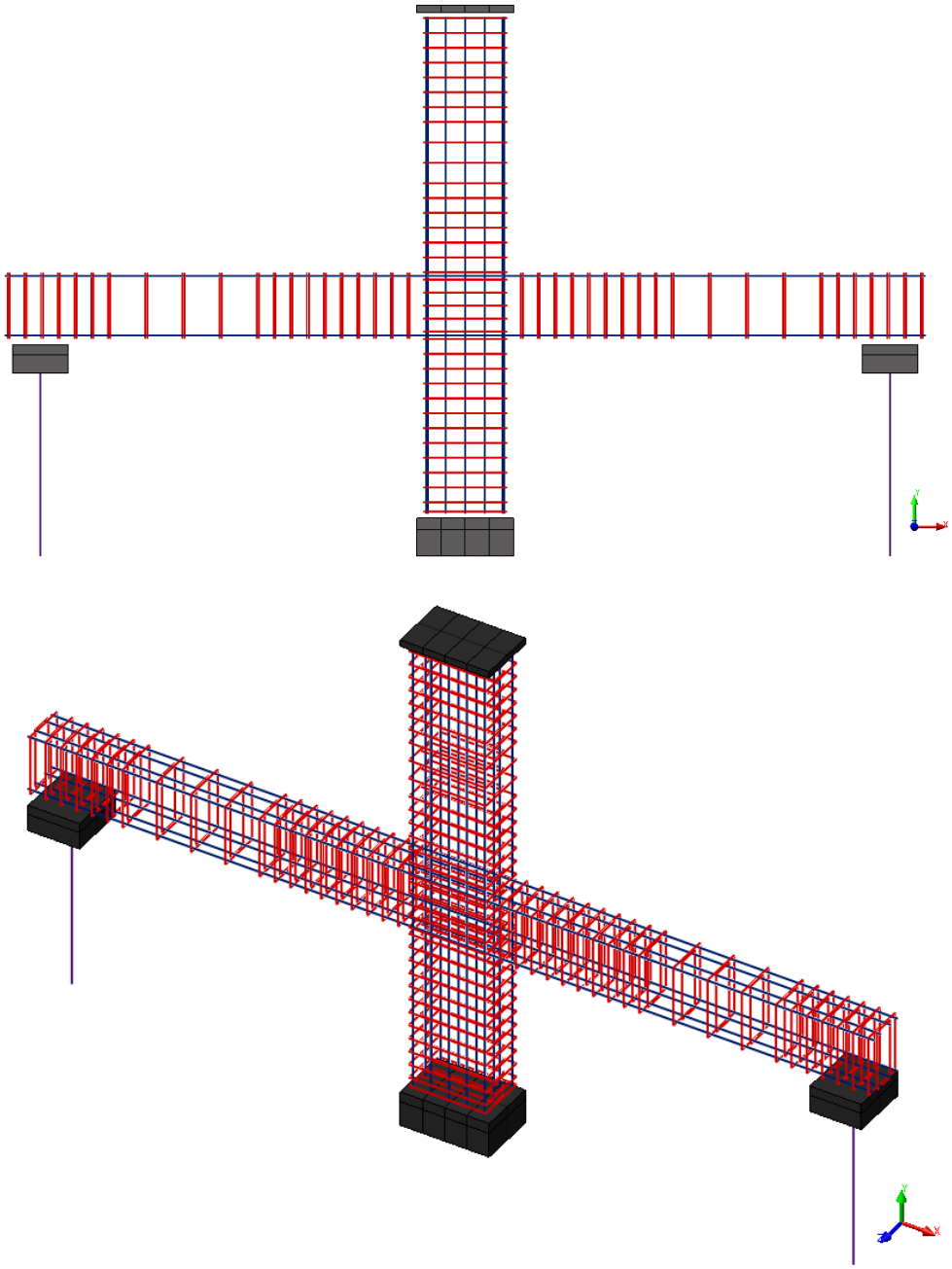

Figure 6.14: Details of the embedded reinforcement modelled in DIANA

As mentioned before, the axial load was exerted to the column through the four pre-stressing tendons. However it was applied in 10 equal loading steps to ensure that the stability of the analysis was maintained. The lateral loading protocol which was used in the laboratory, was adopted, adjusted and applied to the top of the column in the form of a displacement control regime as in the experiments. Note that as opposed to the experiments where each loading cycle was repeated three times, in the FEA only one cycle was applied for each drift. Although this was done to reduce the required time for analysis, for one case

the results were compared between the two analyses and no significant difference was observed. Therefore, the remaining cases were analysed using the non-repetitive loading regime. The displacement increment at each loading step was limited to 1 mm so that equilibrium could be achieved quickly and divergence was avoided. In order to avoid the associated problems of applying load to the FE model where nonlinear material properties exist, concrete properties were defined to be linear in the regions near the loading point and also near the beam supports (Figure 6.13).

The size of the mesh elements was adapted such a way that it reflects the nonlinearity and cracking of each part of the BCJ based on the visual observations from the experiments. This meant that the joint region and the plastic hinge zone of the beam had a finer mesh and a coarser mesh was used for the remaining parts. Mesh sensitivity analysis was also performed in order to determine the most suitable mesh size so that a balance between computational effort and accuracy is achieved.

6.5 FINITE ELEMENT ANALYSIS

After the finite element model was prepared, an analysis file (*.dcf) was written following DIANA (2012) manual recommendation. To account for the effect of material nonlinearities on the analysis, a nonlinear analysis procedure had to be adopted. The solution to a nonlinear analysis involves selecting an appropriate iterative procedure. DIANA offers four different iterative procedures; namely Newton-Raphson, Quasi-Newton, Linear Stiffness, and Constant Stiffness. The Quasi-Newton (otherwise known as the Secant) method was chosen based on its capability in maintaining a stable analysis. The method proposed by Broyden was selected to solve the Secant iterative procedure. Details of the selected procedure and method can be found in the "Analysis Procedures" manual of DIANA. When strong nonlinearities (like cracking in RC structures) are present in a model, the ordinary iteration process may have problem in converging. This is when applying a "Line Search" algorithm would be beneficial in keeping the iterative procedure stable to avoid divergence. The line search method was employed in the analysis whenever divergence occurred.

The analysis involved two main stages: the application of axial load and lateral displacement cycles consecutively. As the axial and lateral loads were applied in the form of force and displacement controlled procedures, respectively; an "Energy Norm" of 0.0025 was used to control the convergence at each loading step for both loading types. The maximum number of iterations was set to 1000; however if convergence was not achieved after the end of the 1000^{th} iteration, the analysis was set to continue in the next step. At the end of the analysis, the results of those steps which did not converge after 1000 iterations were checked to make sure they were reasonable or otherwise omitted from the analysis. It is worth mentioning that most of the loading steps converged after about a maximum of 30 iterations and only a few steps needed higher number of iterations to converge. Note that all analyses were performed on a "Windows 7 Enterprise" based 64-bit operating system on a desktop computer with "Intel(R) Core(TM) i7 – 2600 CPU @ 3.40 GHz" and 16 GB of RAM.

6.5.1 PUSHOVER ANALYSIS

The finite element model of BCJ1 was prepared following the details explained in section 4.7.3 and incorporating the material properties for concrete and reinforcement mentioned in Chapter 5. However before applying the cyclic loading to the model, a pushover analysis was first performed in order to check that the overall features of the response (such as the initial stiffness, yield point and peak load of each cycle) were comparable to that of the experiment. Figure 6.15 shows the load vs. displacement results of the FE pushover analysis of BCJ1 against the experimental result.

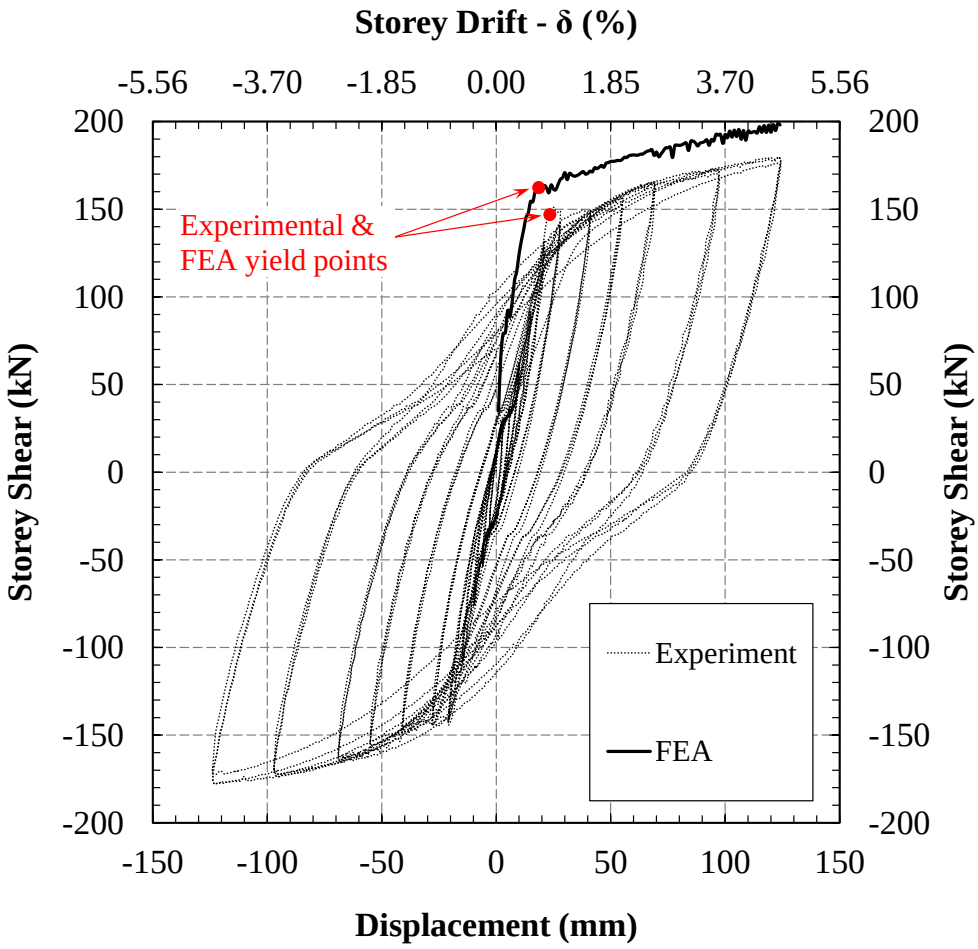

Figure 6.15: FE Pushover analysis of BCJ against the experimental results

As it can be seen in Figure 6.15, the overall trend of the pushover curve follows the backbone of the experimental cyclic response. The yielding and post-yielding loads given by the FEA were higher compared to the experiment. However, such difference can occur between a pushover and cyclic experimental test, and one needs to conduct a cyclic FEA (presented in the following sections) to confirm if there is indeed a significant mismatch. In addition, the initial stiffness of the FE model seems to be slightly higher than the actual specimen. Due to the location of the bolts on the strong floor, the pin support at the base of the column had to be connected to the strong floor through a stiffened steel base (Figure 6.16). As the steel based was about 200 mm high off the ground, suitable length bolts were used to fix it to the strong floor. As a result, a slight movement was observed at the steel base when the column top was at its peak displacement. This displacement was not measured actively during the test; but it was attempted to be minimized using a bracing at the base. This may have been the reason for the higher stiffness in the FE model compared to that of the experiment. Due to the nature of the movement, it could be modelled using a

linear spring quite accurately Therefore, two other pushover analyses were performed on models by adding linear springs (of 35,000 N/mm and 17,500 N/mm stiffness) along the 'x' direction at the column support (Figure 6.17). The results of the three cases are compared in Figure 6.18.

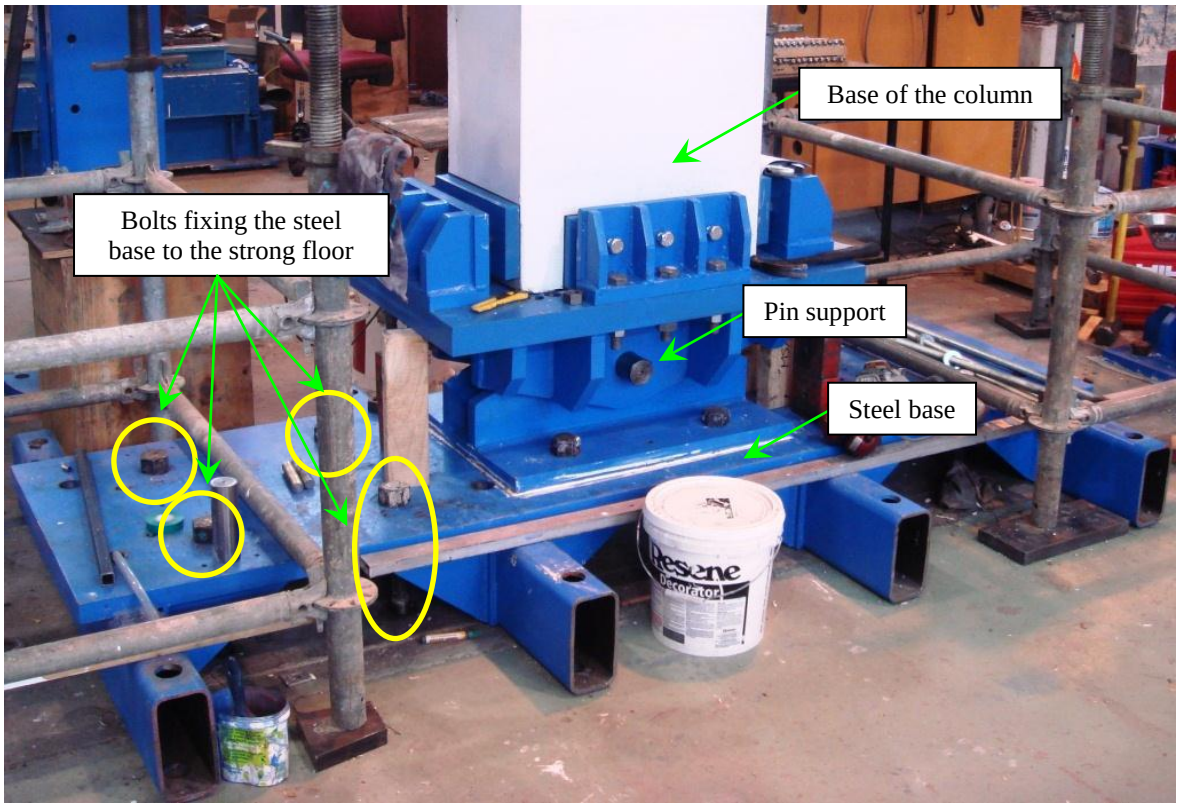

Figure 6.16: Arrangement of the test setup at the base of the column

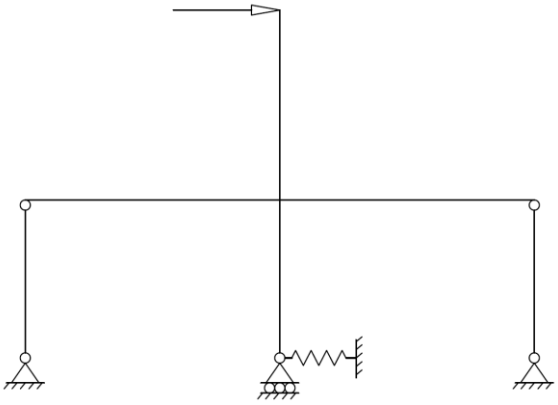

Figure 6.17: Schematic view of the spring support at the column base

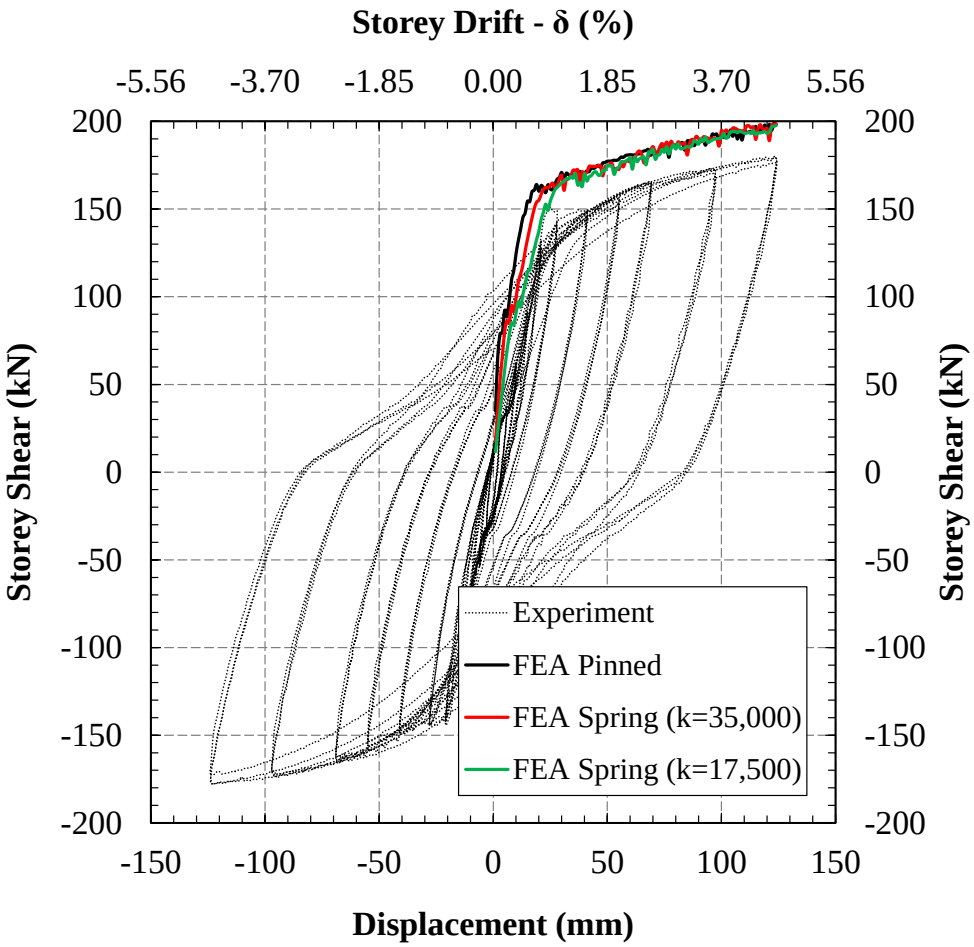

Figure 6.18: Effect of spring support in 'x' direction at the column base on FEA

As it can be seen, the initial stiffness reduces without changing any other properties of the curve when a linear spring is added in the 'x' direction at the column base. It is clear from Figure 6.18 that the spring with stiffness k = 17,500 N/mm provides a closer prediction of the experimental backbone curve. Although the addition of the linear spring adds to the accuracy of the model, the nonlinearity of the FE model also increases substantially which makes it difficult to achieve convergence in the cyclic analysis. At the same time, addition of the spring only affects the linear portion of the response and the post yield response does not show substantial difference with or without the spring. As a result, when convergence could not be achieved, the spring was removed. It is worth mentioning that the analysis time of the pinned support and spring support took 4 and 5 minutes, respectively. Table 6.1 shows the peak forces obtained from the FEA of the pinned and spring (k = 17,500 N/mm) models against the experimental ones. It is obvious from the ratio of the FEA to EXP peak forces that, the FE predictions were substantially improved in the elastic range once the spring was added.

Table 6.1: Comparison of the FE (pinned and spring) pushover and experimental results

Drift (%)	Storey shear				
	EXP (kN)	FEA (kN)		FEA/EXP	
		Pinned	Spring	Pinned	Spring
0.1	27.88	78.98	34.93	2.833	1.253
0.2	35.01	88.54	68.72	2.529	1.963
0.35	59.50	124.53	90.79	2.093	1.526
0.5	89.07	154.46	113.97	1.734	1.280
0.75	128.80	163.46	144.04	1.269	1.118
1.0	143.27	166.99	162.34	1.166	1.133
1.5	147.33	171.75	166.00	1.166	1.127
2.0	155.12	178.33	173.80	1.150	1.120
2.5	164.72	180.68	182.02	1.097	1.105
3.5	170.43	192.26	189.89	1.128	1.114
4.5	177.85	198.11	197.63	1.114	1.111

Before applying the cyclic loading to the FE model, the sensitivity of the pushover analysis to the mesh discretization was checked. For this purpose, four different mesh sizing were considered and pushover analysis was performed for each of these cases. In order to choose a referencing method, the number of elements in the joint area was chosen to name different mesh discretization. The joint area was divided into 4x4, 5x5, 7x6, and 9x7 elements which resulted in a total of 204, 393, 603, and 742 elements, respectively (Figure 6.19).

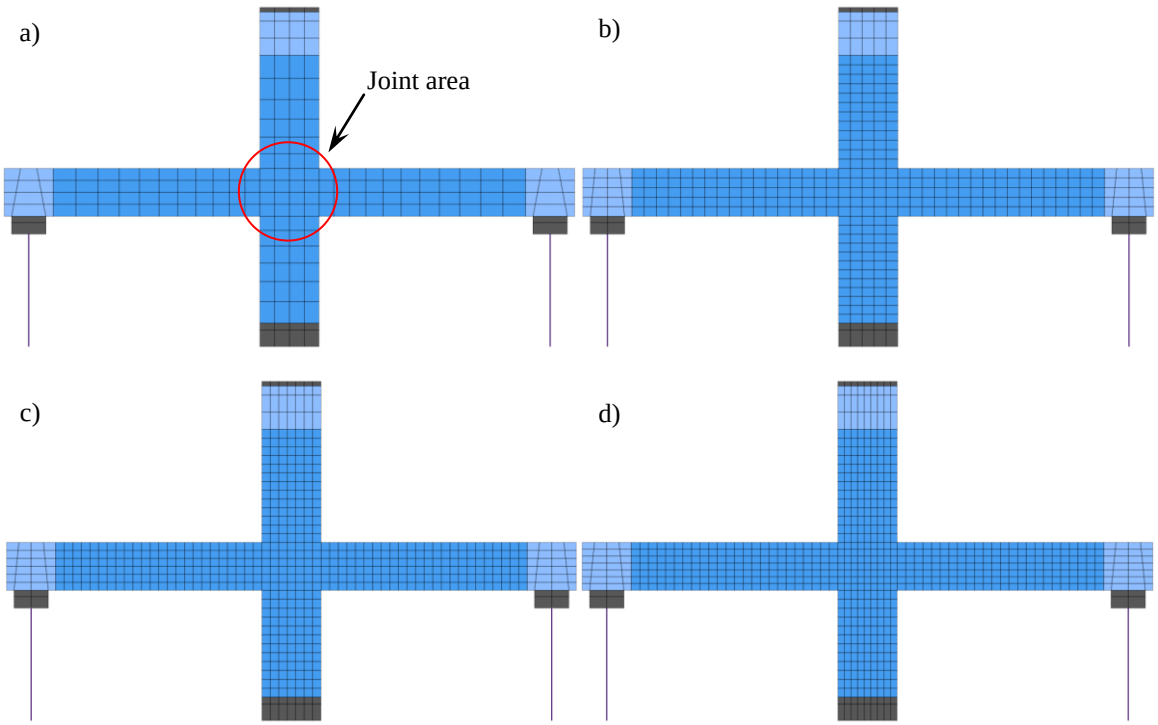

Figure 6.19: Different mesh discretization for FE model; a) 4x4, b) 5x5, c) 7x6, and d) 9x7 number of elements on the joint area

The spring based column support with the spring constant 17,500 N/mm was chosen for the purpose of mesh sensitivity analysis. Figure 6.20 shows the results of pushover FEA for the different mesh discretizations. As it can be seen, increasing the number of elements did not affect the results substantially. Interestingly, the 4x4 and 5x5 graphs showed identical results to those of 7x6 and 9x7. The same mesh sensitivity analysis was also performed on the cyclic FEA (section 6.5.2) before the appropriate mesh discretization was selected.

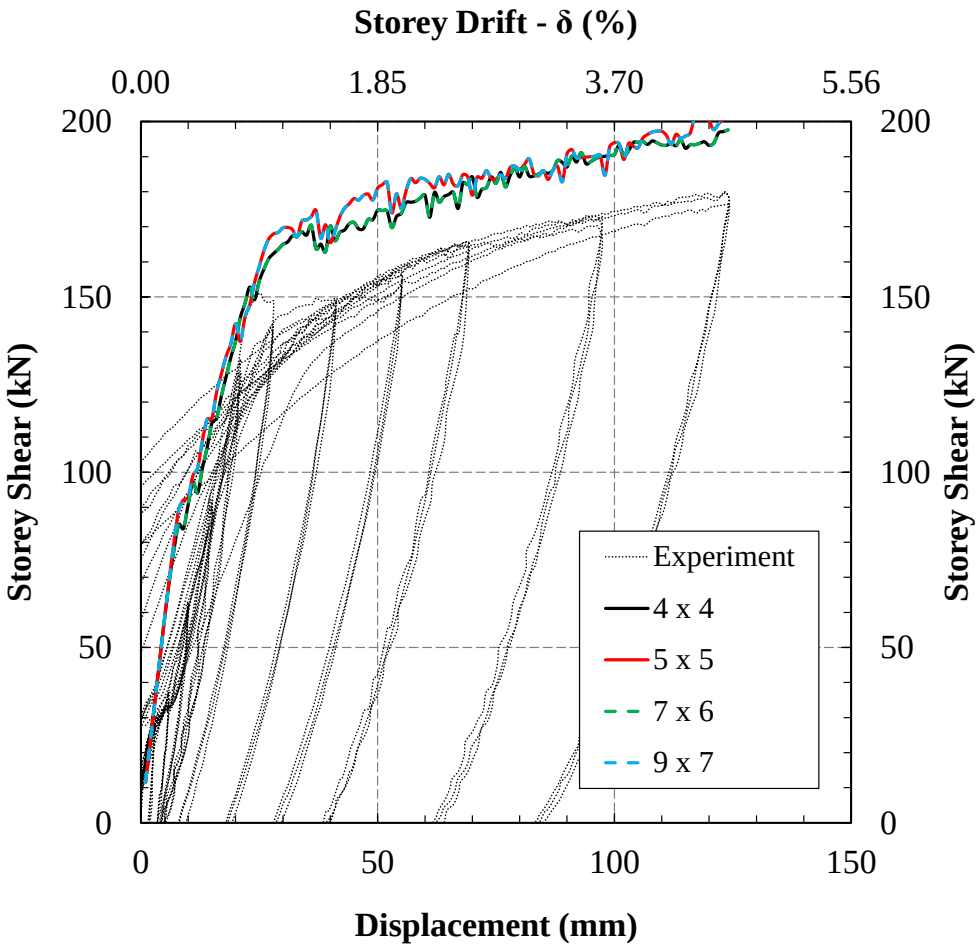

Figure 6.20: Load vs. displacement pushover curves for mesh sensitivity

6.5.2 CYCLIC ANALYSIS

Separate cyclic analyses were performed on FE models with pinned and spring (k = 17,500 N/mm) supports. The analysis took about 2 hours in each case and the load vs. displacement curves are reported in Figure 6.21 and Figure 6.22.

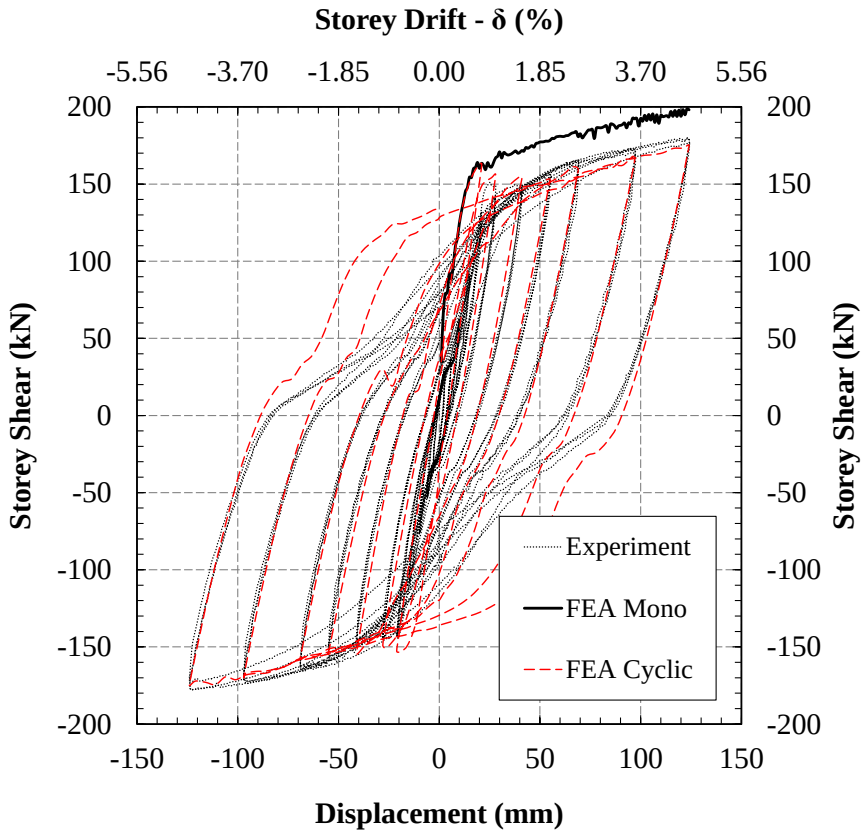

Figure 6.21: FEA vs. experimental results of BCJ1 with pinned column base

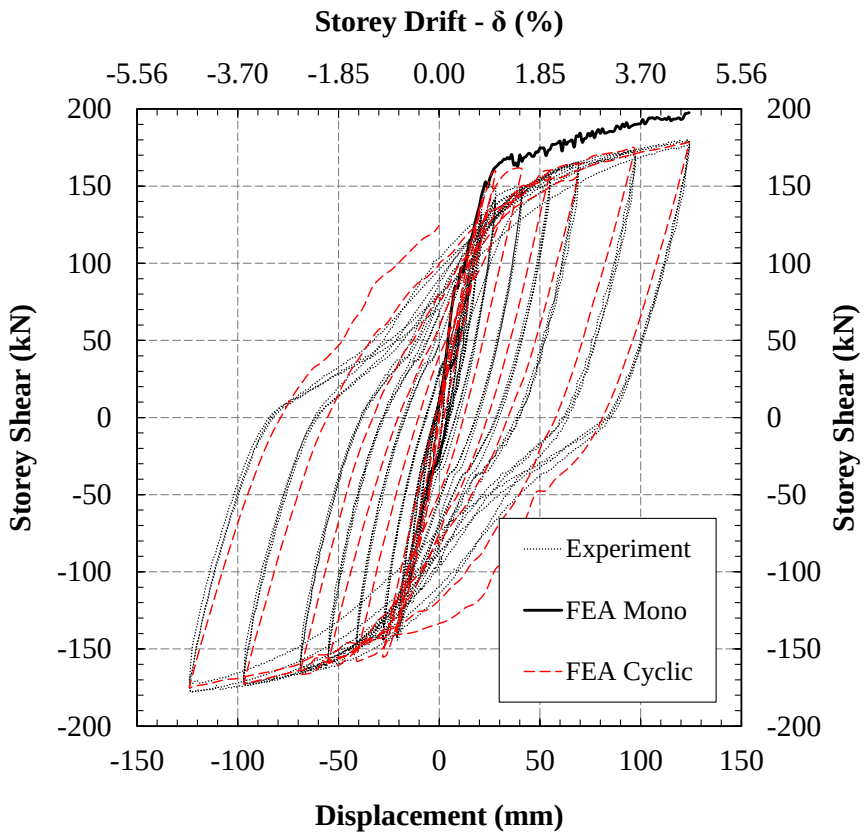

Figure 6.22: FEA vs. experimental results of BCJ1 with spring column base

As it can be seen in Figure 6.21, after yielding the strength degradation in the cyclic analysis is substantially higher compared to that in the pushover analysis; which is due to the deleterious effects of cyclic loading on the material properties. In fact, the peak lateral forces achieved in the experiment were comparable to the peak forces obtained from the cyclic FEA (Table 6.2). Except for the initial elastic stiffness, the loading and unloading stiffnesses were predicted with a very good accuracy. The FE response showed lesser pinching compared to the experiment; especially in the larger displacement cycles (2.5%, 3.5% and 4.5% drift ratios). Considering that the concrete constitutive response (see sections 6.3.2 and 6.3.3) had a very high pinching, the lower pinching of the FE model comes from the steel constitutive response. It is believed that once the effect of buckling is incorporated in the steel constitutive model in DIANA, the FE results should predict the pinching a bit better. Nevertheless considering that in the FE analysis the material properties from a micro level are applied to predict the macro level response of the structure, the predictions are considered acceptable. Once the linear spring was added in the 'x' direction of the column support, the FE predictions became even more accurate during the initial cycles (Figure 6.22). The prediction of the peak forces and loading-unloading stiffness remained accurate (Table 6.2); in addition a higher pinching was predicted for the higher displacement cycles which was much closer to the experimental results compared to the predictions with pinned column base.

Table 6.2: Comparison of the FE (pinned and spring) cyclic and experimental results

Drift (%)	Direction	Storey shear				
		EXP (kN)	FEA (kN)		FEA/EXP	
			Pinned	Spring	Pinned	Spring
0.75	+	128.80	163.46	140.89	1.269	1.094
	−	-142.45	-153.14	-138.98	1.075	0.976
1.0	+	143.27	156.28	159.94	1.091	1.116
	−	-143.35	-148.96	-155.17	1.039	1.082
1.5	+	147.33	154.99	161.16	1.052	1.094
	−	-146.93	-154.73	-157.76	1.053	1.074
2.0	+	155.12	153.17	159.50	0.987	1.028
	−	-155.35	-154.98	-159.13	0.998	1.024
2.5	+	164.72	159.68	156.64	0.969	0.951
	−	-163.10	-157.97	-165.82	0.969	1.017
3.5	+	170.43	165.34	173.85	0.970	1.020
	−	-170.93	-170.00	-172.66	0.995	1.010
4.5	+	177.85	175.23	178.24	0.985	1.002
	−	-174.15	-174.94	-174.82	1.005	1.004

In order to show the difference between the cyclic and pushover analyses results, the FEA/EXP ratios of the peak forces at drift ratios 0.75% to 4.5% are compared between the two loading types and support conditions (Figure 6.23). It is obvious that irrespective of the support condition (pinned or spring), when FEA was performed with cyclic loading the ratios of FEA/EXP peak storey shear were closer to one compared to the pushover analysis.

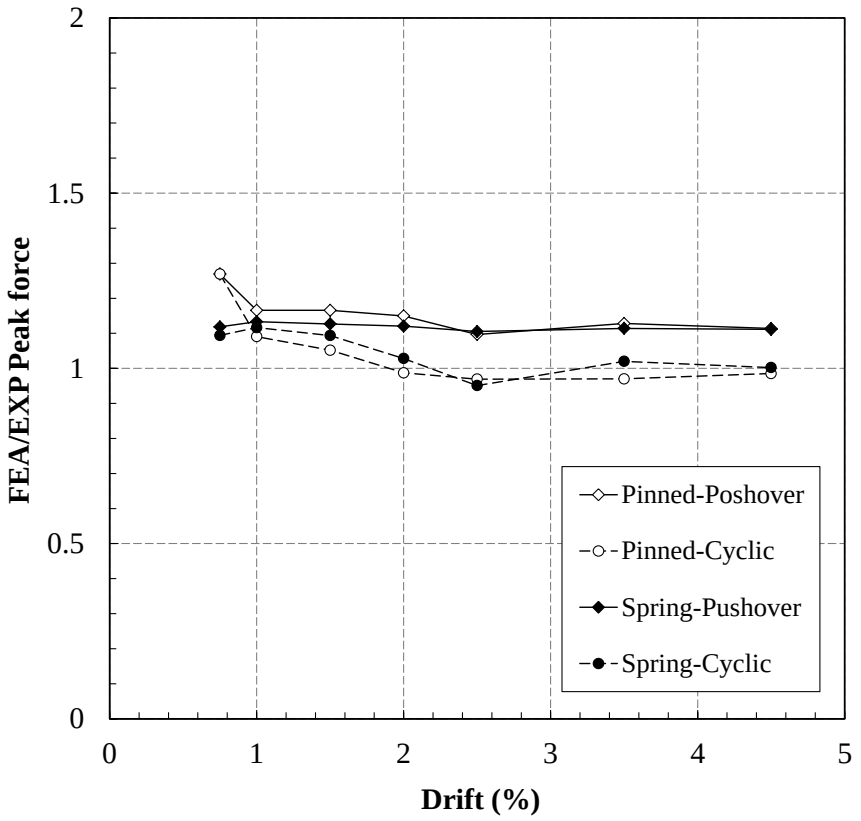

Figure 6.23: Comparison of FEA/EXP storey shear ratios for cyclic and pushover analysis

As in the pushover analysis, a mesh sensitivity analysis was performed on the cyclic FEA in order to check any possible effect of mesh size on the cyclic response of BCJ. Here again 4x4, 5x5, 7x6, and 9x7 discretization of the joint were the four different cases applied on the spring (with stiffness 17,500 N/mm) column support FE model. Note that the number of integration points was different between the analyses in order to control the stability of the analysis and avoid divergence of the results. A 2x2x3 integration scheme was used for the 4x4 and 9x7 models and the analysis took 1:40 and 2:20 hours, respectively. Whereas, a 3x3x3 integration scheme was employed to the 5x5 and 7x6

models which took 2:30 and 2:50 hours to complete. The lateral force vs. displacement responses (Figure 6.24) of these models were compared to evaluate the appropriateness of each mesh discretization. Although the mesh was very coarse in the first model (Figure 6.24a) and reasonably fine in the last one (Figure 6.24d), the influence on the overall response was insubstantial. However after scrutinizing the FE and experimental curves closely, it was observed that the 4x4 and 9x7 mesh models provided a slightly better prediction of the cyclic response. Considering that the 9x7 model required 40% higher computational effort compared to the 4x4 one, it was decided that the latter was used for further investigation. Nevertheless, a finer mesh discretization was utilized for comparison if any of the other properties were considerably different from the experimental results.

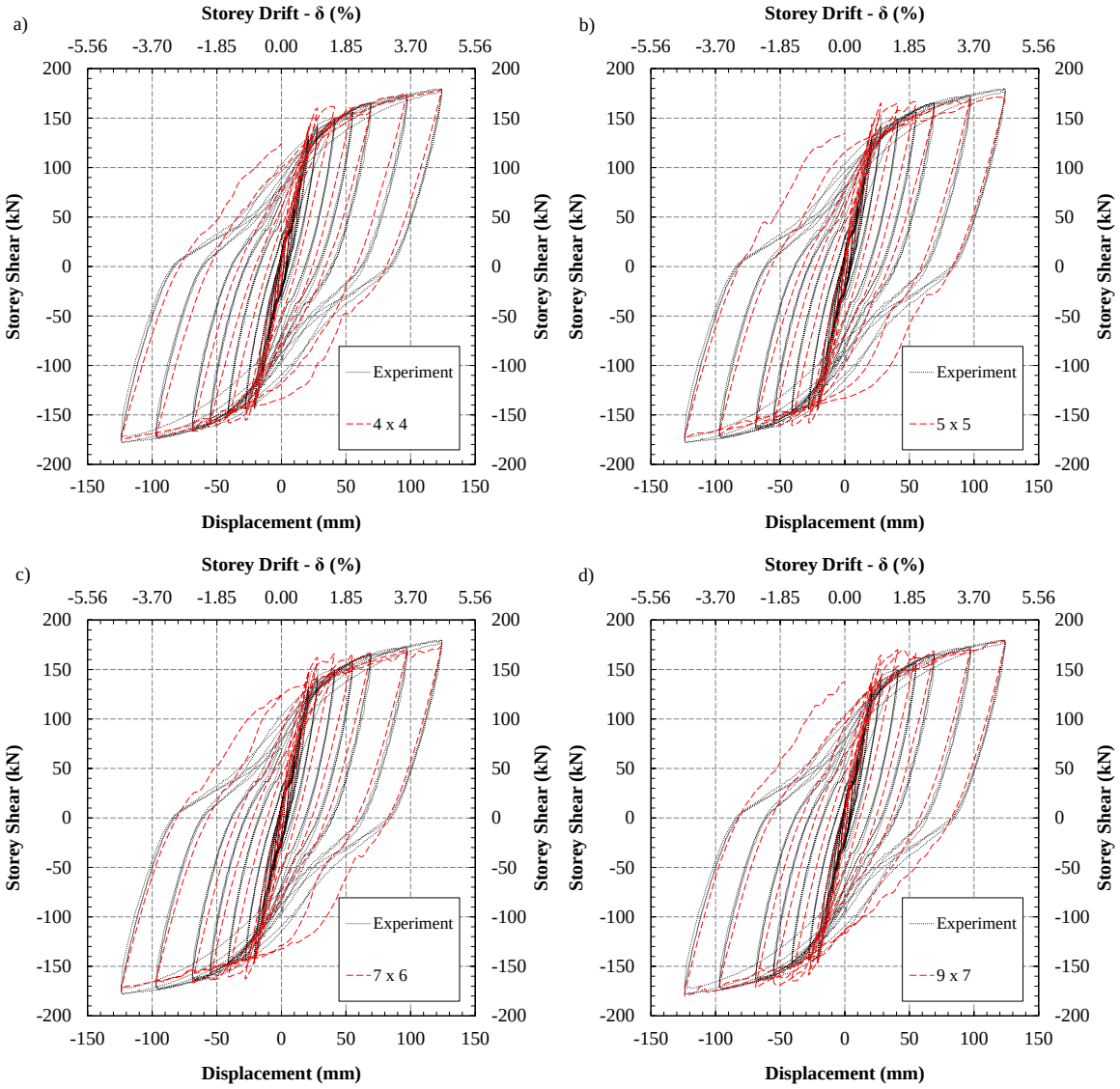

Figure 6.24: Mesh sensitivity analysis for the cyclic FEA

After the mesh sensitivity analysis was performed and the suitable mesh was decided to be the 4x4 discretization of the joint, a full cyclic analysis including all of the smaller drift ratios (namely 0.1%, 0.2%, 0.35%, and 0.5%) was performed for which the column shear vs. drift ratio is given in Figure 6.25. Note that like before, each loading cycle was applied once only to reduce the computational time; yet the analysis took about 2 hours for completion (A sample FE analysis was also performed where each cycle was repeated three times in which the FEA took about 18 hours to complete and no significant difference was observed between the two).

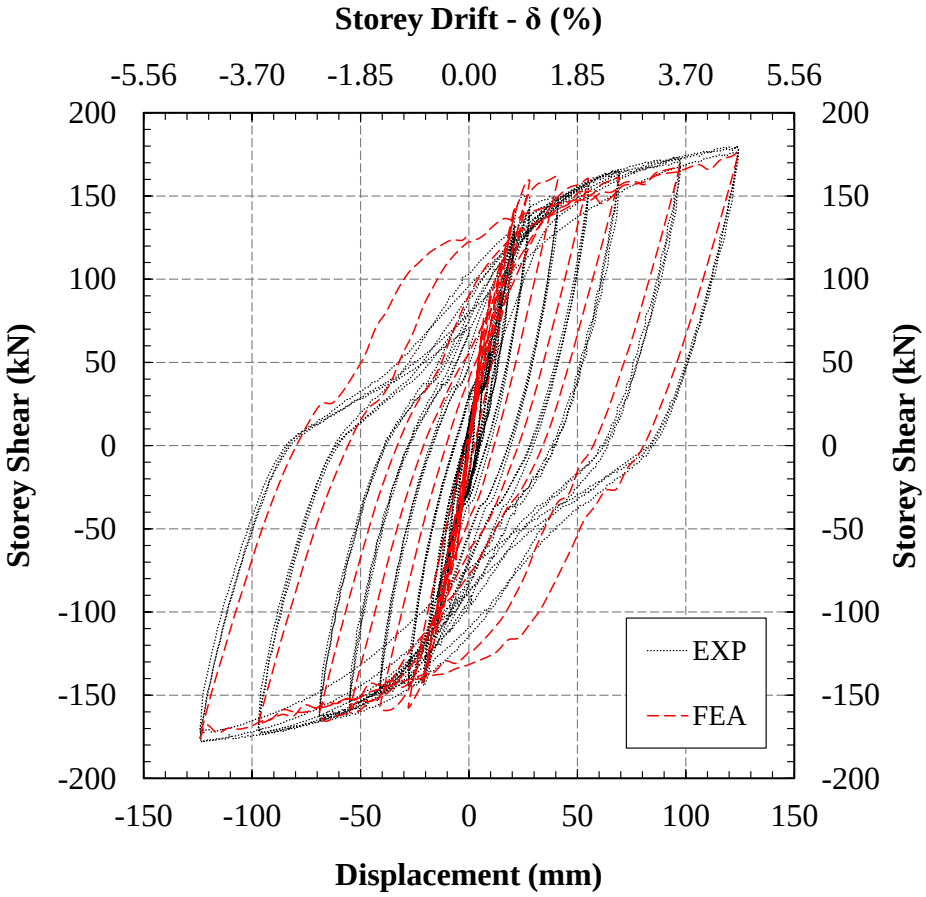

Figure 6.25: Storey shear vs. drift ratio of the 4x4 mesh under full cyclic

Damping and peak-to-peak secant stiffness of the FE model were calculated based on the formulation given in Chapter 5 and comparison between the experimental and FEA results is given in Figure 6.26.

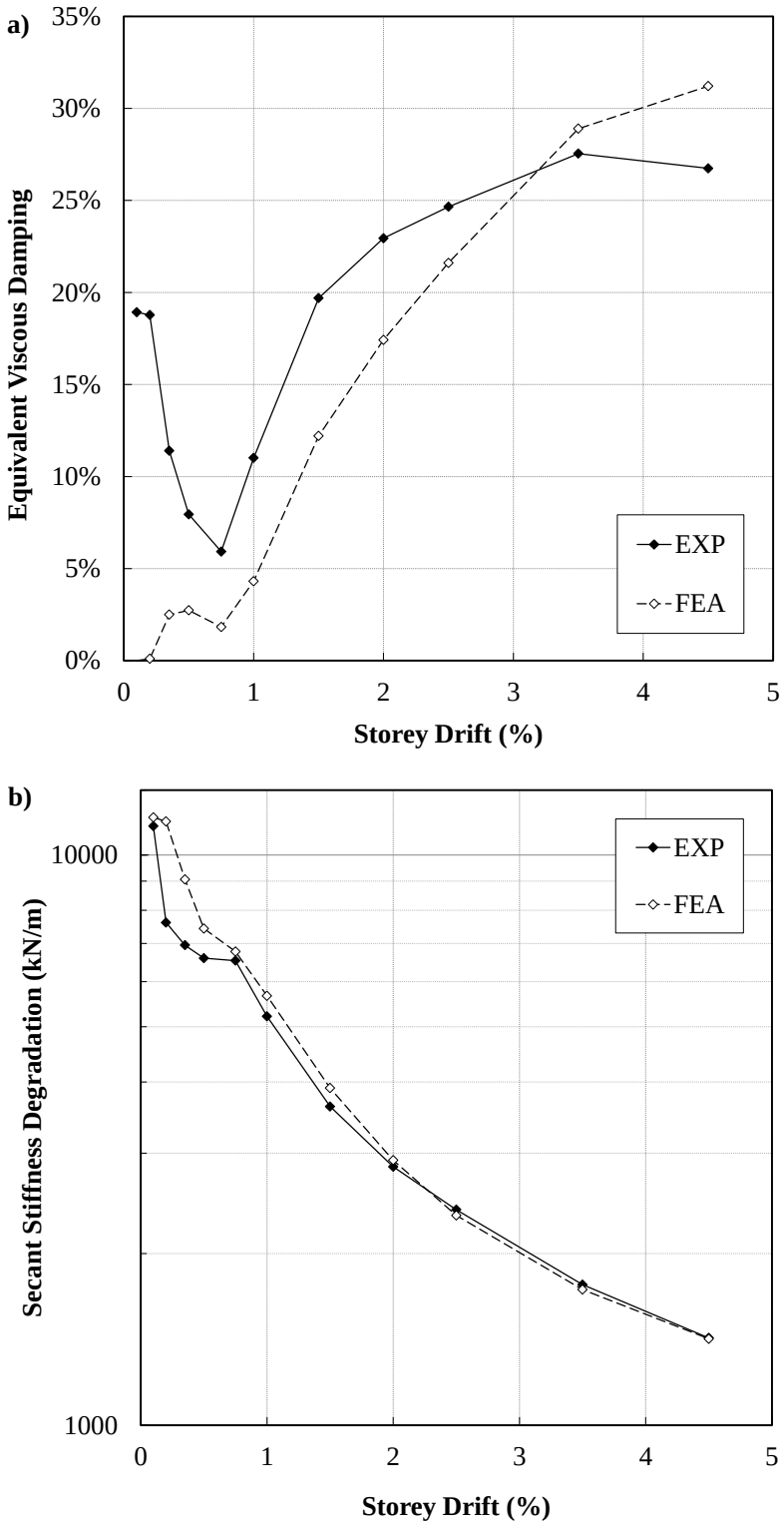

Figure 6.26: Comparison of a) damping and b) stiffness between the experiment and FEA

As it was mentioned in the discussion of damping formulation (see Chapter 5) the hysteresis loops were very sensitive before yielding and do not provide reliable values of damping calculated according to the adopted formulation. This is also apparent in the predicted FE results. The FEA underestimates the damping properties from 8% to 60%

between the 0.75% and 2.5% drift ratios (after yield); but it overestimates the damping by 1% and 15% for the last two cycles, respectively. The difference between the FE predictions and experimental results came from the mobility of the analysis in accurately predicting the pinching. However, the overall predicted FEA trend shows acceptable correlation to that of the experimental results. The FE predictions for the peak-to-peak secant stiffness shows close match with that of the experiment; this is because the peak loads were predicted very accurately by the FE analyses (see Figure 6.25).

The beam support reactions which were registered in the FEA were used to calculate the total shear force applied at the joint face from west and east sides (see Chapter 5 for directions and sign conventions). Then the stress developed in the joint shear reinforcement was transformed to the equivalent forces. The summation of forces in all joint shear stirrups, formed the contribution of steel and the remaining was considered the concrete contribution in taking the joint shear force. Comparison between the experimental and analytical results for the shear contribution of steel and concrete in the joint is shown in Figure 6.27. Here again a close agreement is observed between the FEA and experimental results which further illustrates the capability and accuracy of the FE model in predicting the results.

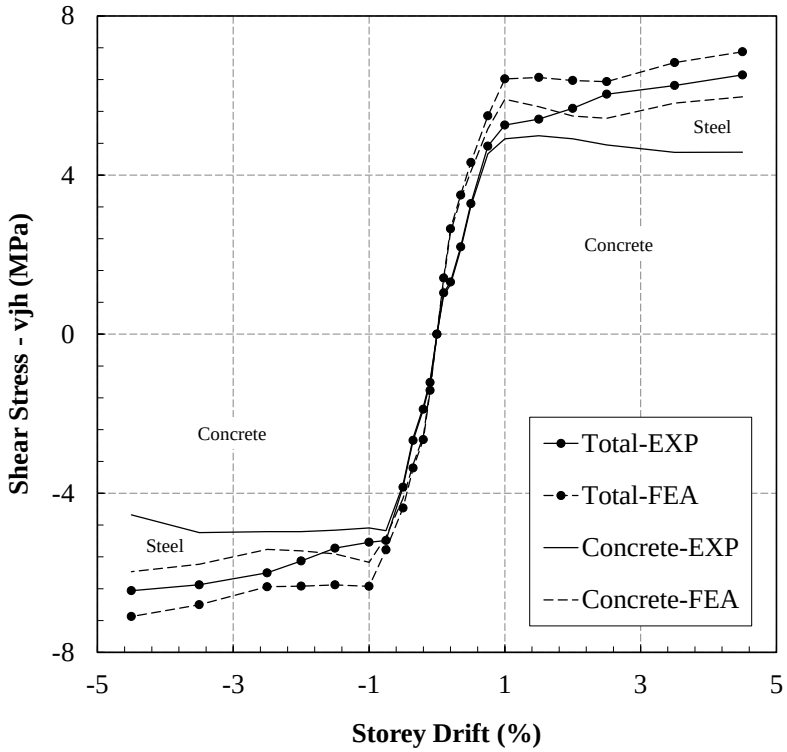

Figure 6.27: Steel and concrete contributions in taking joint shear force (FEA vs. EXP)

Shear deformation of the joint panel was calculated following the procedure given in Appendix F. However, due to the restrictions exerted by the finite element discretization, element sizes and node locations (Figure 6.28), it was not feasible to keep the panel size (shown in red) exactly the same as the one on which potentiometers were placed (shown in yellow) on the actual specimen. Nevertheless, the width-to-length ratios of the panels under investigation were kept as close as possible (0.89 and 0.81 for the experiment and FE model, respectively). The joint shear deformations were compared in the form of the deformation angle 'γ_j' detailed in Appendix F and results are presented in Figure 6.29.

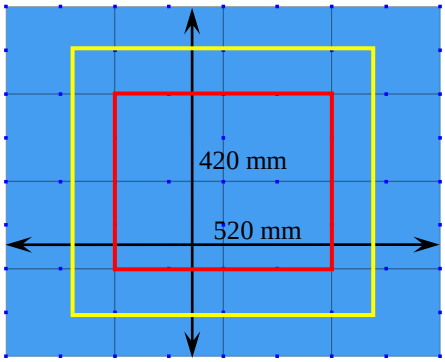

Figure 6.28: Finite element discretization of the joint panel and location of element nodes

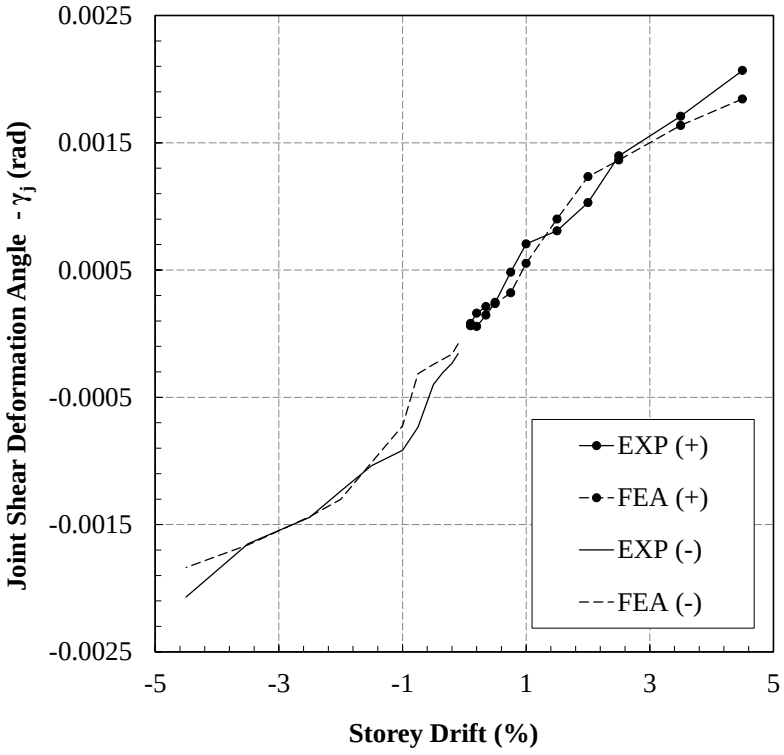

Figure 6.29: Comparison of the predicted joint shear deformation angle vs. experiment

It is important noticing that the joint shear force does not result from direct shear force application; rather it comes indirectly from the transformation of beam bending at the face of the column to a force couple in beam bars and then transferred into the joint. Therefore, such accuracy in predicting the joint shear deformations can only result from a very capable material model in conjunction with proper structural performance in the FE model and analysis. In order to go even deeper into the details, strain development in the joint shear stirrups were scrutinized and compared with the readings of strain gauges installed on the surface of the joint shear reinforcement (Figure 6.30).

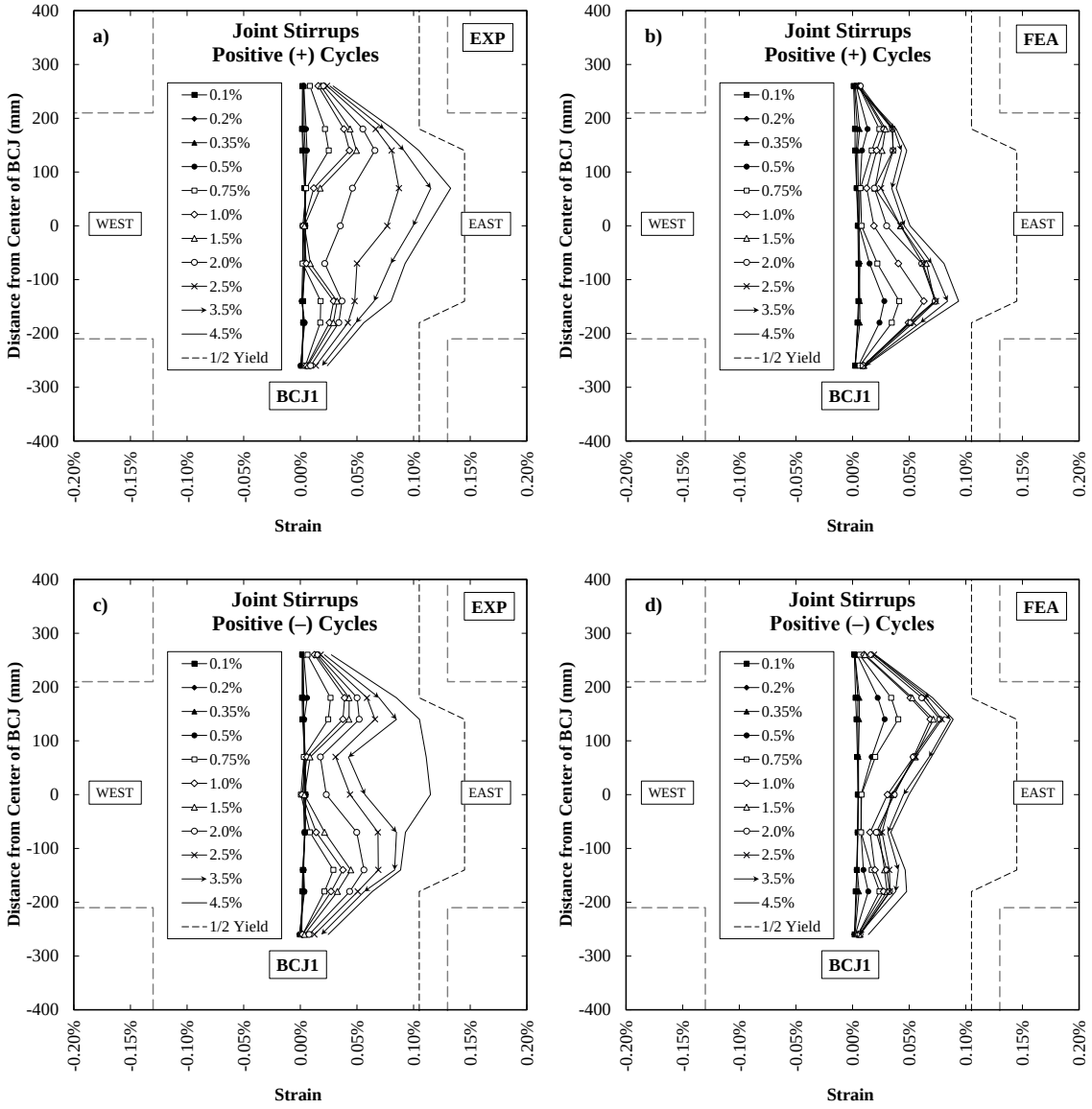

Figure 6.30: Strain development in joint shear stirrups in a) +ive cycles EXP b) +ive cycles FEA c) –ive cycles EXP d) –ive cycles FEA

The FE results for the strain in joint shear reinforcement at different drift ratios confirm that like in the experimental readings, the strains remain well below the half-yield line indicated by the dashed line in Figure 6.30. Note that the two top and bottom stirrup sets were those of the column shear reinforcement. As different shear reinforcement were used in the joint and column (HR10 & HR12 in joint and R10 in column), the half-yield line is not straight. The strain profile observed in the negative cycles of the test (Figure 6.30c) was predicted more accurately (Figure 6.30d) compared to the ones in the positive cycles. Nevertheless, considering that the readings of strain gauges are always subjected to statistical dispersion and also the fact that it is a very detailed result extracted from the FEA, the overall prediction of strain level in joint stirrups were acceptable.

Elongation of the beam at the plastic hinge zone was also compared with the FEA (Figure 6.31). Alike in the joint shear deformations, the length of consideration for calculating the elongation was limited by the element sizes and location of nodes (Figure 6.32). The length over which the elongation of plastic hinge zone was measured in the experiment was 490 mm, however the restrictions in the FE model dictated an approximately 475 mm length for calculation of elongation.

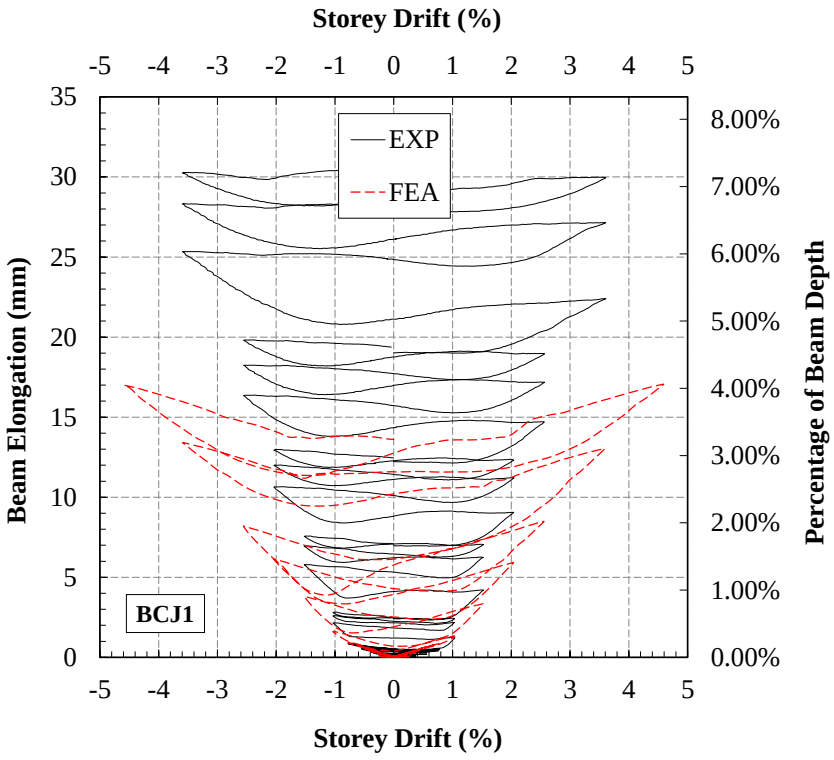

Figure 6.31: Elongation of beam at the plastic hinge zone

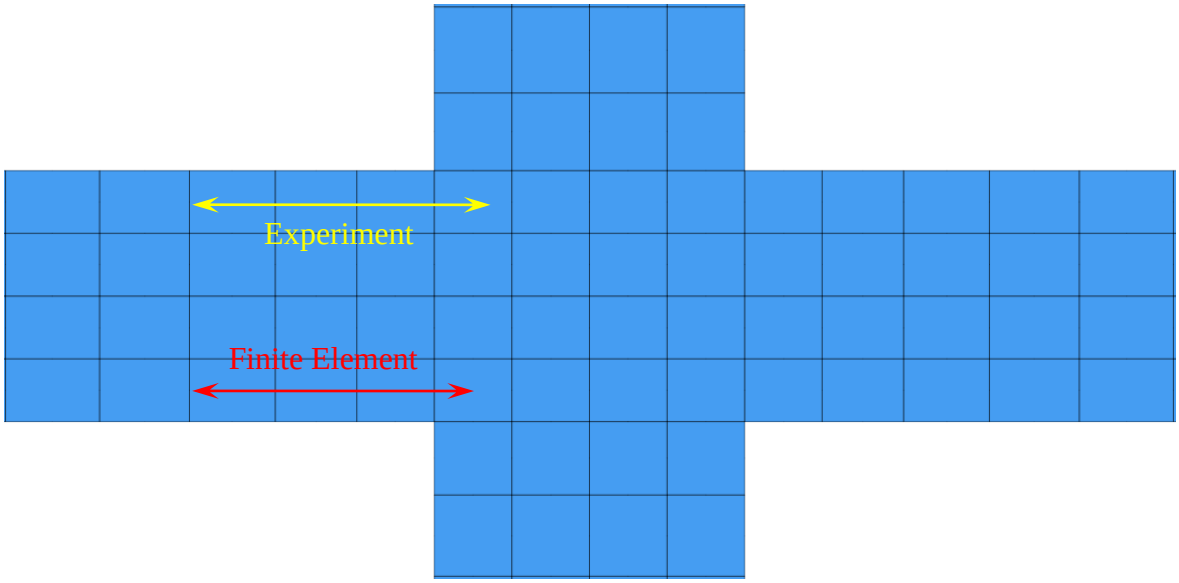

Figure 6.32: Length considerations for the purpose of elongation

It is obvious from Figure 6.31 that the FE model could predict that the elongation occurs in the plastic hinge zone, however only about half of the actual elongation was predicted in the FEA. Note that in the experiment, elongation measurements were performed only up to the end of the 3.5% drift ratio after which the potentiometers had to be removed in order to avoid being damaged; this was obviously not the case in FEA. At the end of the 3.5% drift, the FEA predicted only about 13 mm elongation as opposed to that of 30 mm in the experiment. Also at the end of each loading cycle when displacement was reversed, the predicted elongation retrieved considerably when the column was returned to zero displacement position; which did not happen in the experiment. In addition in the FEA due to the definition of the material models, deterioration of the material is not considered to the same extent as in the experiment. Therefore, even after repeating each drift cycle three times (same as in the test), the resulted elongation did not change considerably in the FEA. In order to take this into consideration, the experimental elongation results were modified in such a way that the effect of the two repeated cycles on beam elongation was omitted and the modified results were compared to the elongation captured in FEA (Figure 6.33). It is clear from Figure 6.33 that once the two additional drift cycles were removed from the recorder elongation data, the FEA and experimental result showed a considerably closer agreement. At drift ratio of 3.5%, the experiment and FEA showed an elongation of about 4% and 3% of the beam depth, respectively.

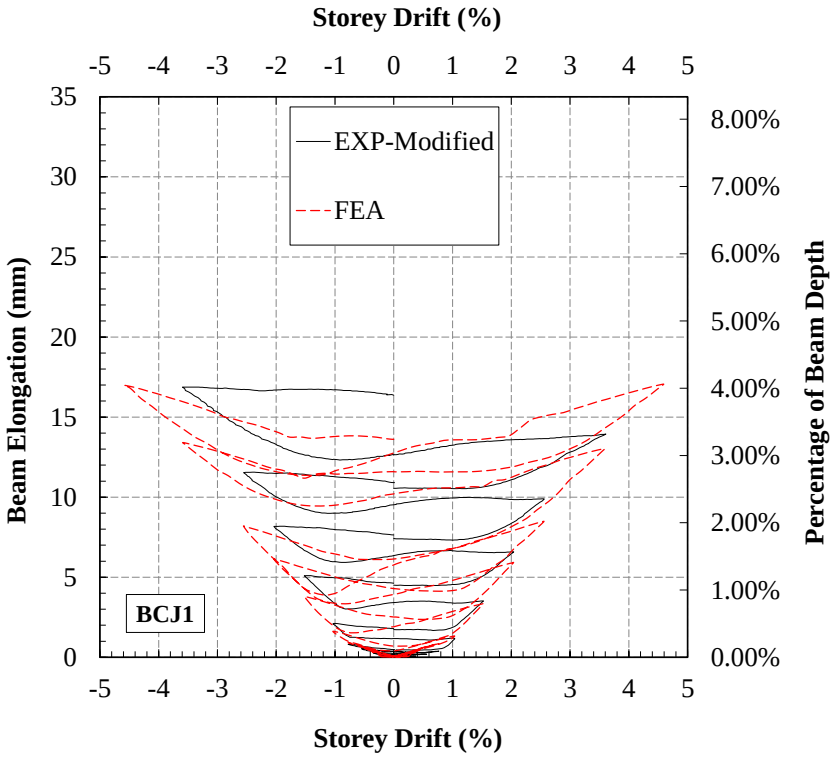

Figure 6.33: Modified experimental elongation against FEA

Although after adjusting the experimental beam elongation (by removing the two additional cycles) the FEA and experimental results were reasonably close, a difference of about 1% of the beam depth still existed between the two results. It is believed that this may be attributed to the material models (section 4.7.2). Although the residual strain is captured in the constitutive model for reinforcing bars, the total strain concrete model did not account for the residual strain in concrete. As a result, the contribution of concrete in plastic hinge zone elongation is not accounted for in the FE predictions (see Chapter 5 for more details). Therefore, it is not surprising that the elongation captured by the FEA was lower than that in the experiment.

The evolution of the principal compressive stress in the joint, beam and column at different analysis stages (namely 1.5%, 3.5% and 4.5% drift ratios) is shown in Figure 6.34.

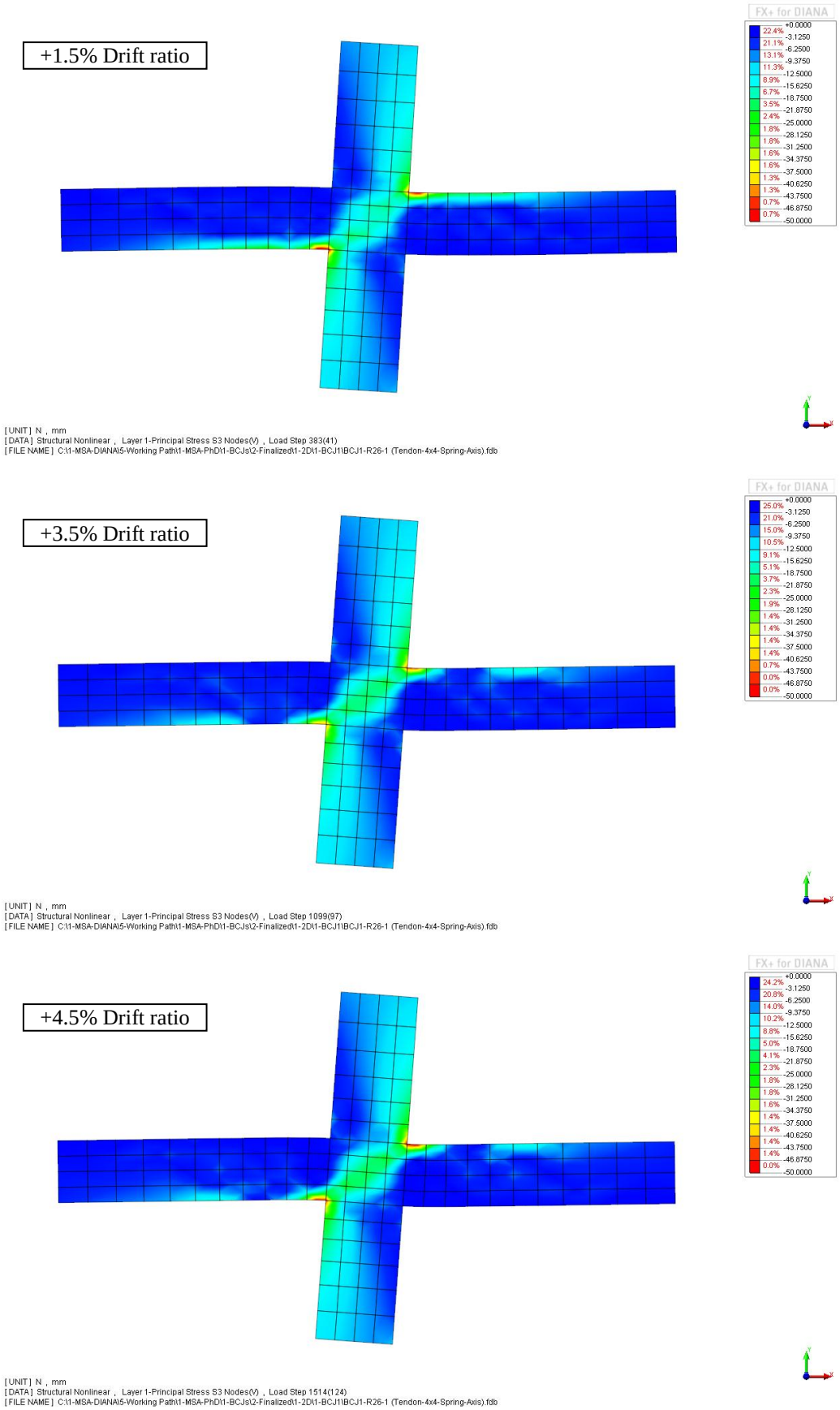

Figure 6.34: Evolution of the principal compressive stress in joint, beam and column

The compressive stress development illustrated in Figure 6.34 ranges from zero (dark blue) to 50 MPa (red) and depicts the stress evolution in the positive cycles. As expected, stress concentration occurred at the top-west and bottom-east corners of the beam and column intersection where the compressive stress reached its maximum value of about 50 MPa. Distribution of the compressive stress at the maximum positive displacement cycle (+4.5 % drift) in the joint compressive strut is shown in Figure 6.35. As soon as the compressive strut goes further away from the corner points, the stress level drops from about 50 MPa to around 25 MPa. This explains the cover concrete cover spalling at these regions.

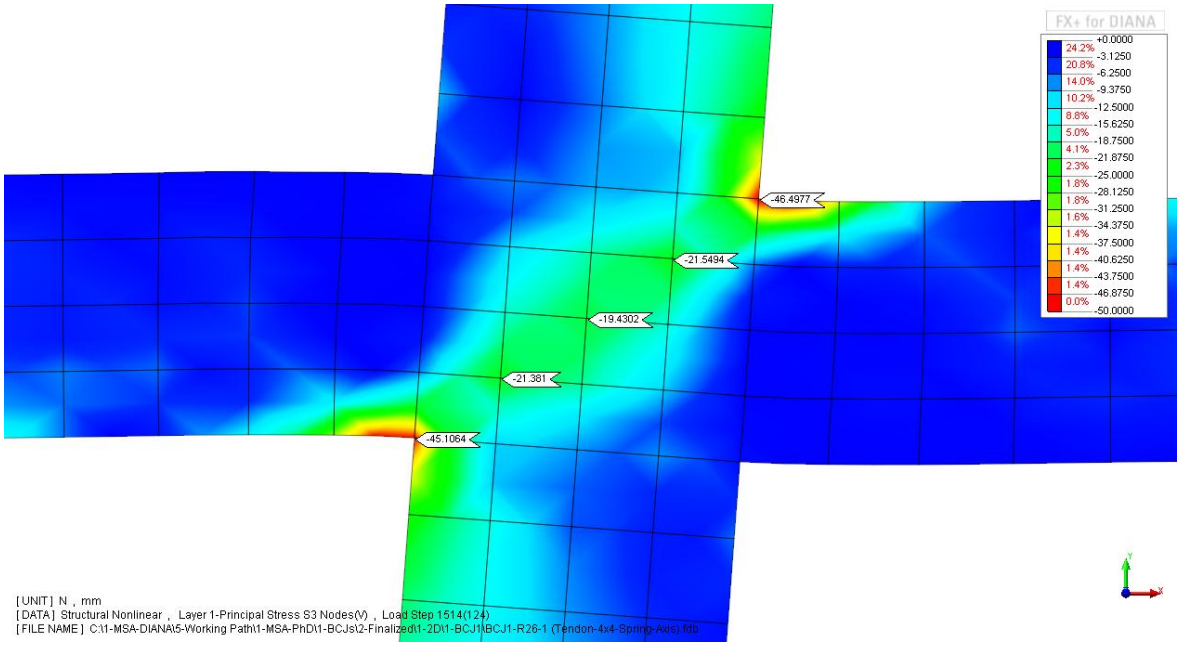

Figure 6.35: Stress distribution in the joint compressive strut

The FEA also captured the cracking based on the total strain rotating crack model explained in section 6.3.1 for concrete (Figure 6.36). The crack patterns predicted by the FEA were also compared to that of the experimental results (Figure 6.37). Note that the cracks marked in ‘blue’ and ‘red’ had opened during the positive and negative cycles, respectively. Comparison between Figure 6.36 and Figure 6.37 shows the accuracy of the FE model in predicting the location and direction of the cracks. Severity of the cracks had increased (in the joint and beam) as the drift cycles got bigger (Figure 6.38 and Figure 6.39). Note that because of the rotating nature of the model in capturing the cracks, cracks which appeared in the previous cycle would disappear on load reversal which is equivalent to crack closure in the experiment (Figure 6.38).

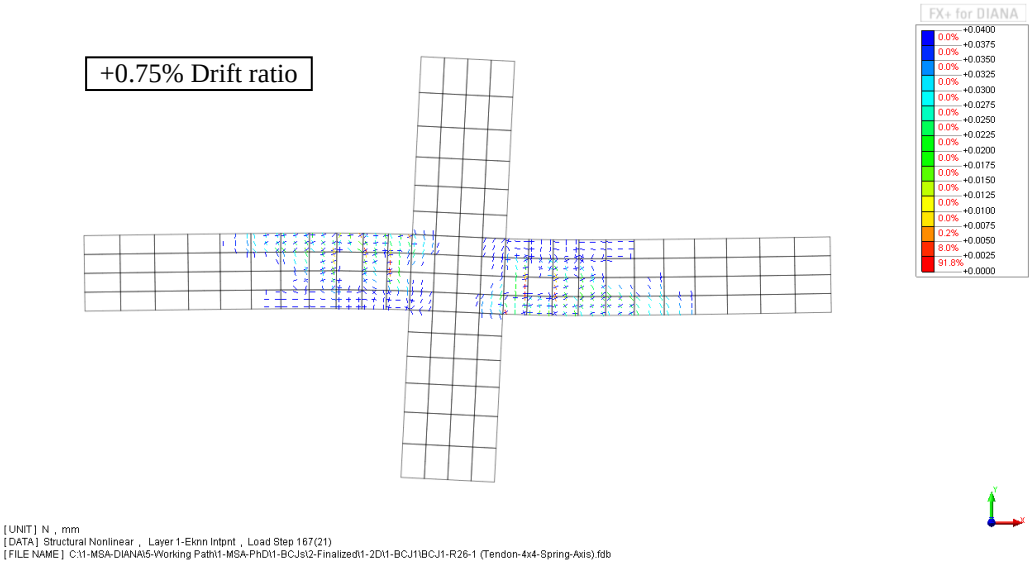

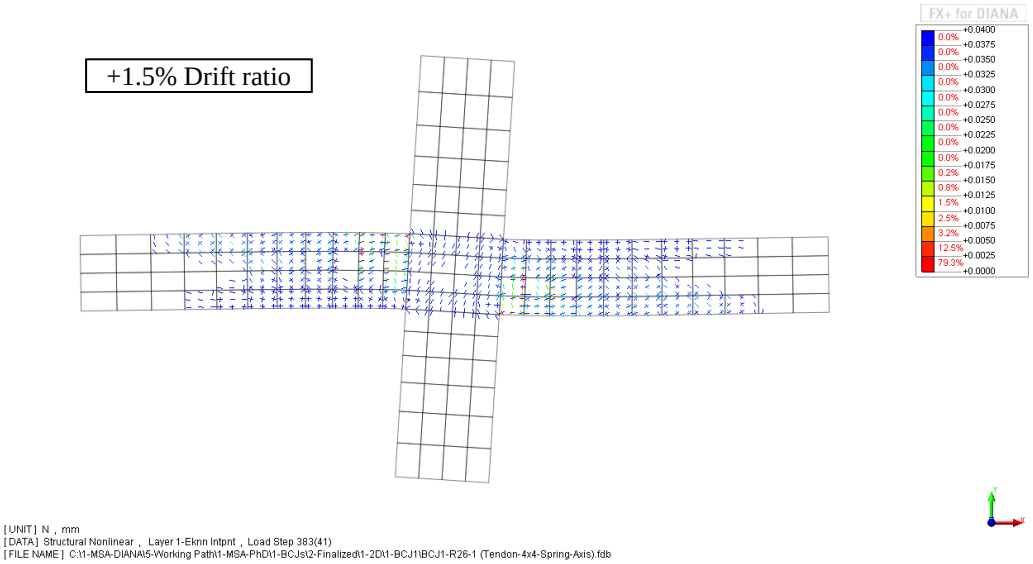

Figure 6.36: Crack formation at different drift ratios predicted by the FEA

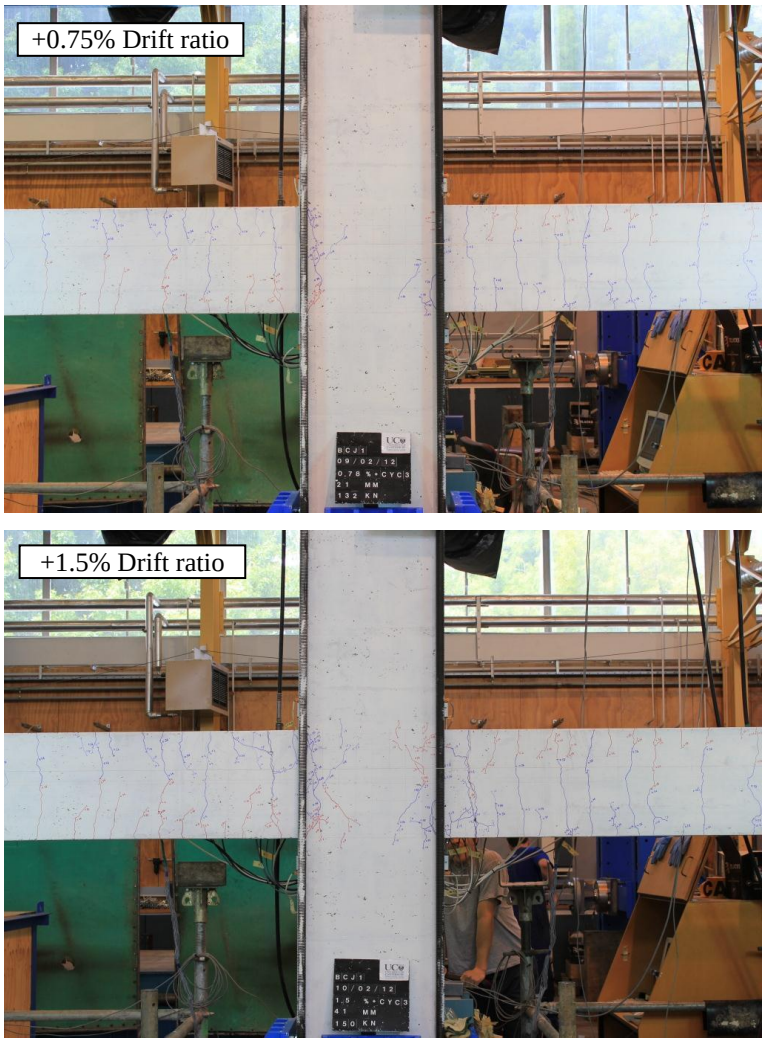

Figure 6.37: Crack patterns at the end of +0.75% and +1.5% drift ratios

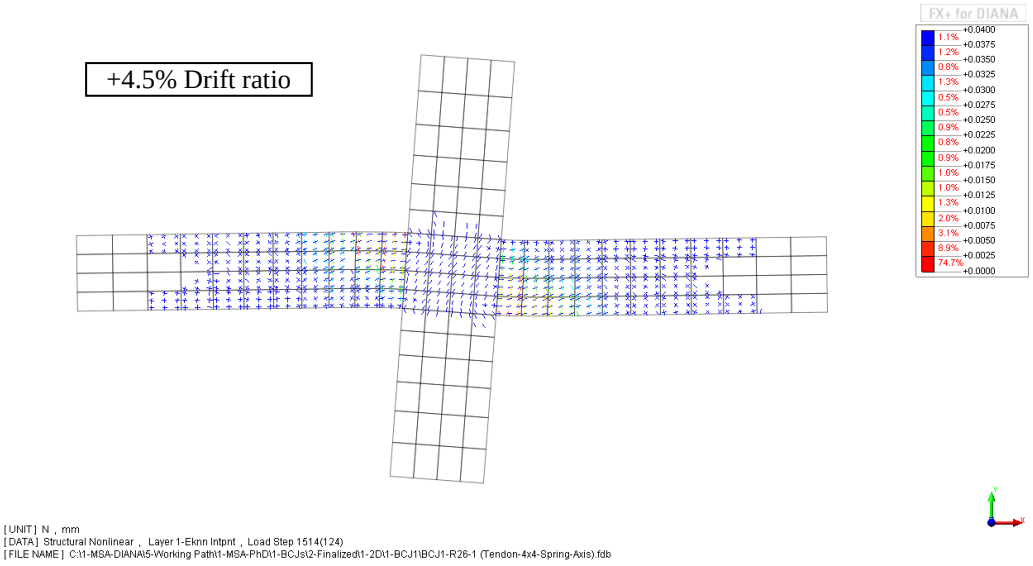

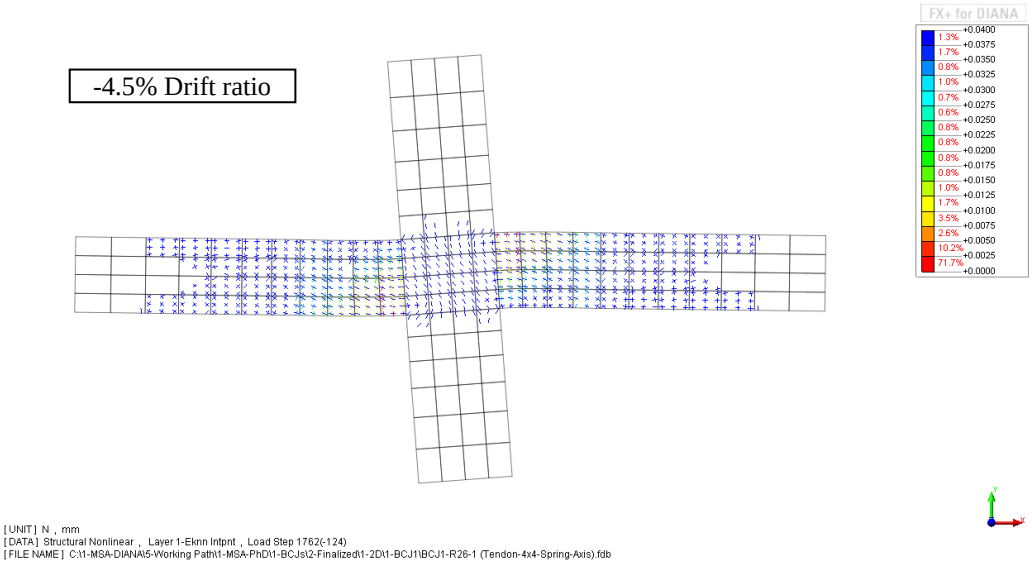

Figure 6.38: Closure and disappearance of the cracks in (+)ive and (–)ive cycles

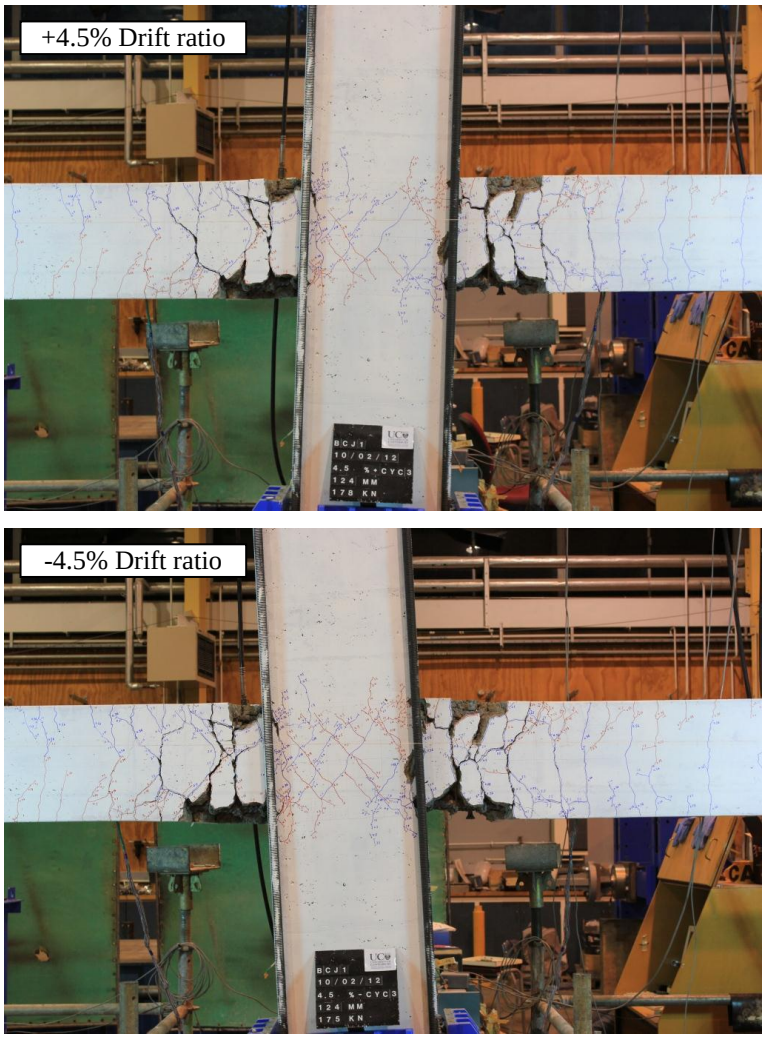

Figure 6.39: Crack patterns at the end of +4.5% and -4.5% drift ratios

6.5.3 FEA SIMULATION AND RESULTS OF OTHER TESTED BCJS

The remaining six specimens were also modelled following the procedure explained in section 4.7.3. Note that except for BCJ1 for which a detailed comparison of FEA and experimental results was provided in the previous section, for other specimens only the main features were compared and results are reported in the following sections. Note that like in the BCJ1 specimen, the experimental results of the beam plastic hinge zone elongation were modified for the exclusion of the effect of additional loading cycles.

6.5.3.1 FEA OF BCJ2

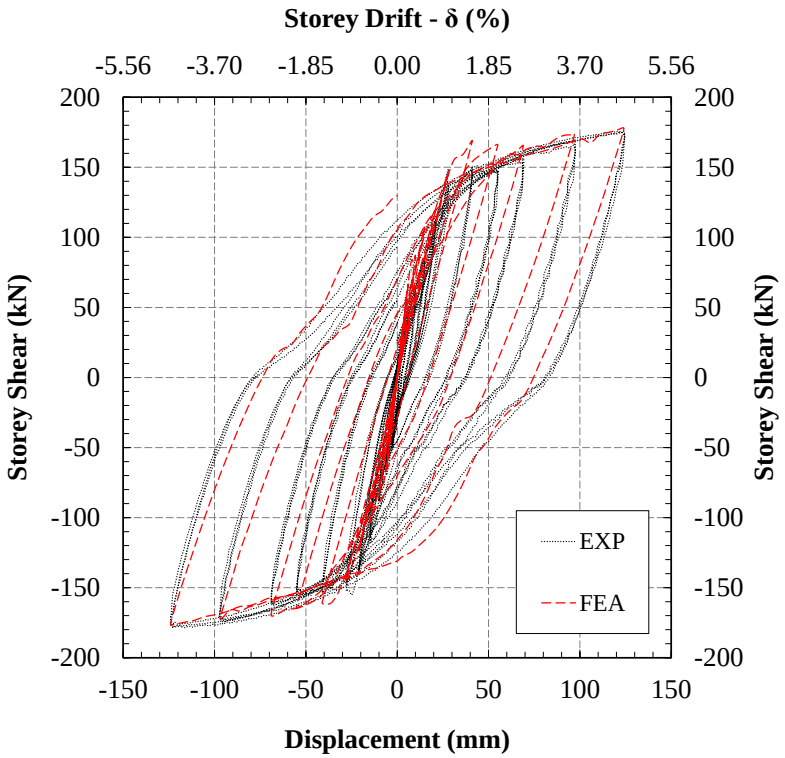

Figure 6.40: Storey shear vs. drift ratio of the 4x4 mesh under full cyclic

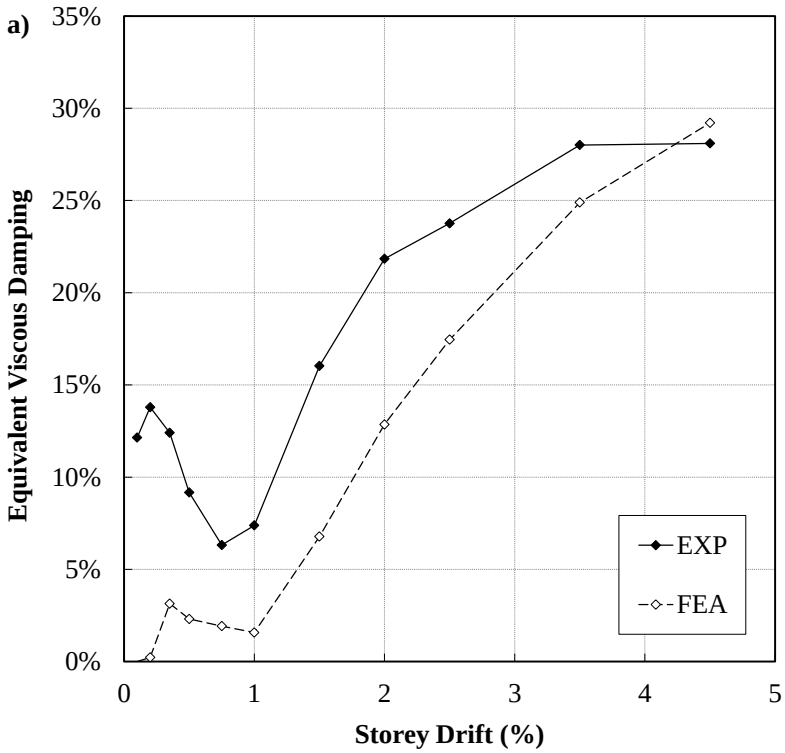

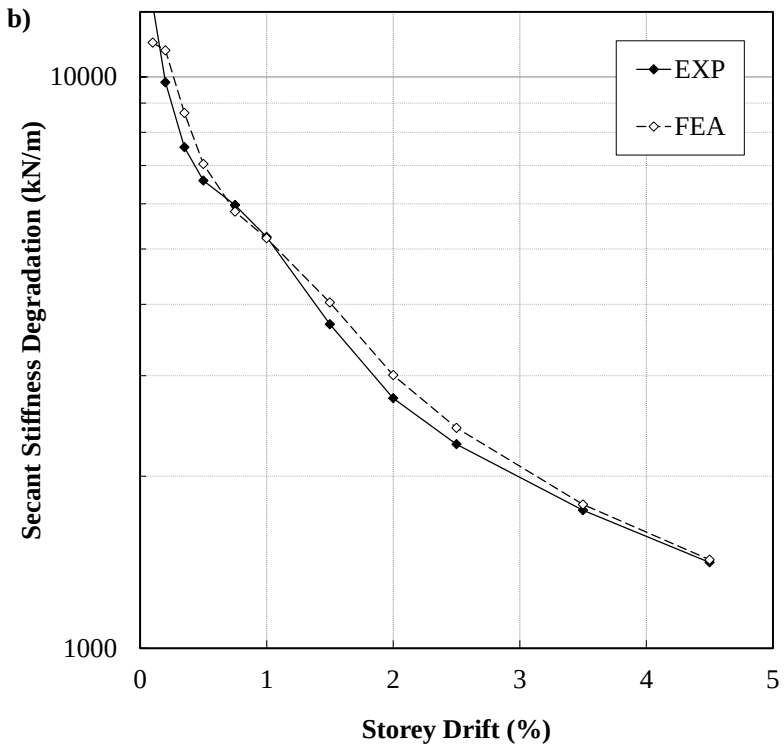

Figure 6.41: Comparison of a) damping and b) stiffness between the experiment and FEA

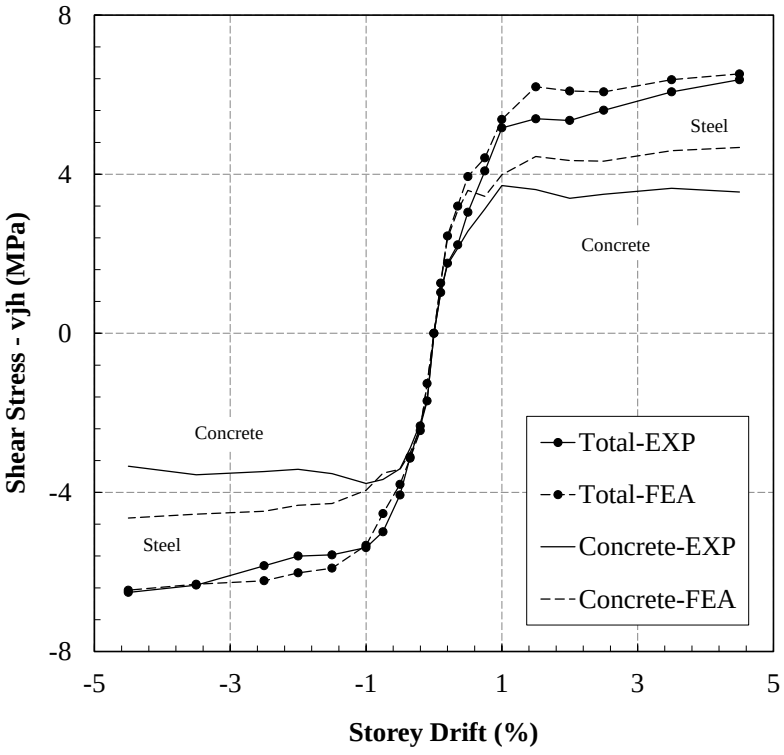

Figure 6.42: Steel and concrete contributions in taking joint shear force (FEA vs. EXP)

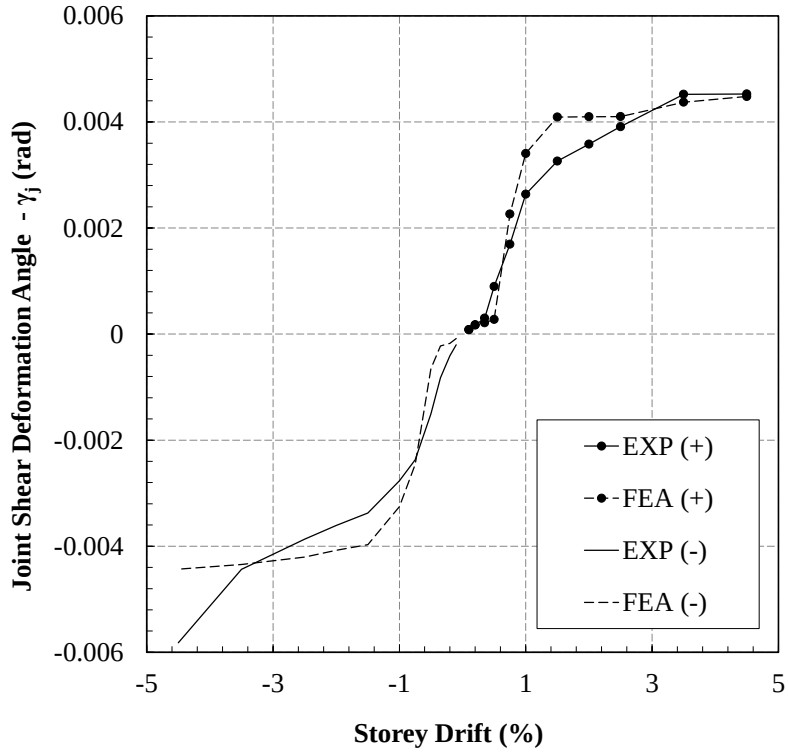

Figure 6.43: Comparison of the predicted joint shear deformation angle vs. experiment

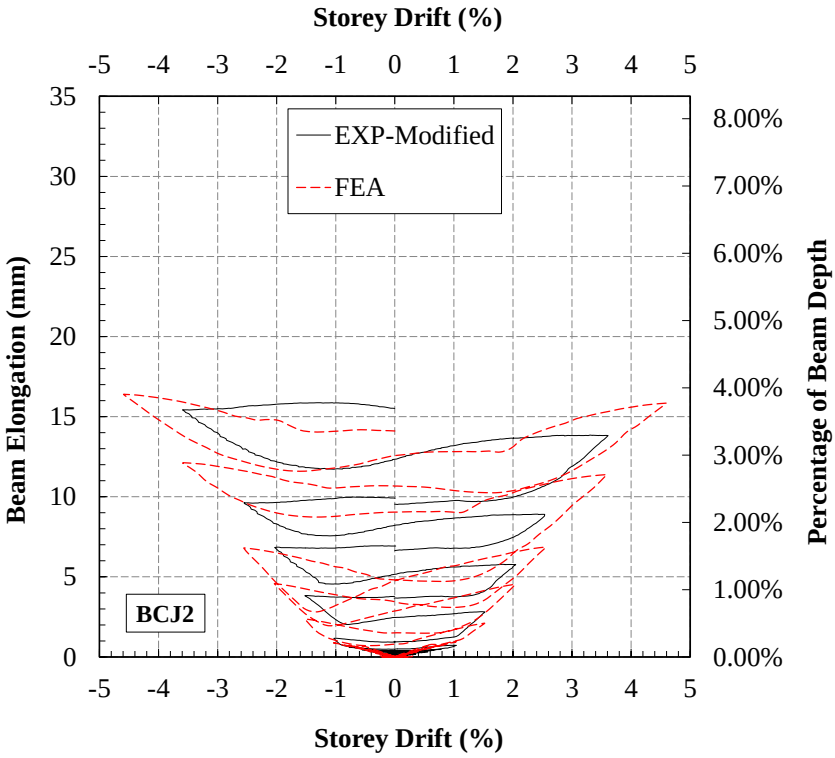

Figure 6.44: Elongation of beam at the plastic hinge zone

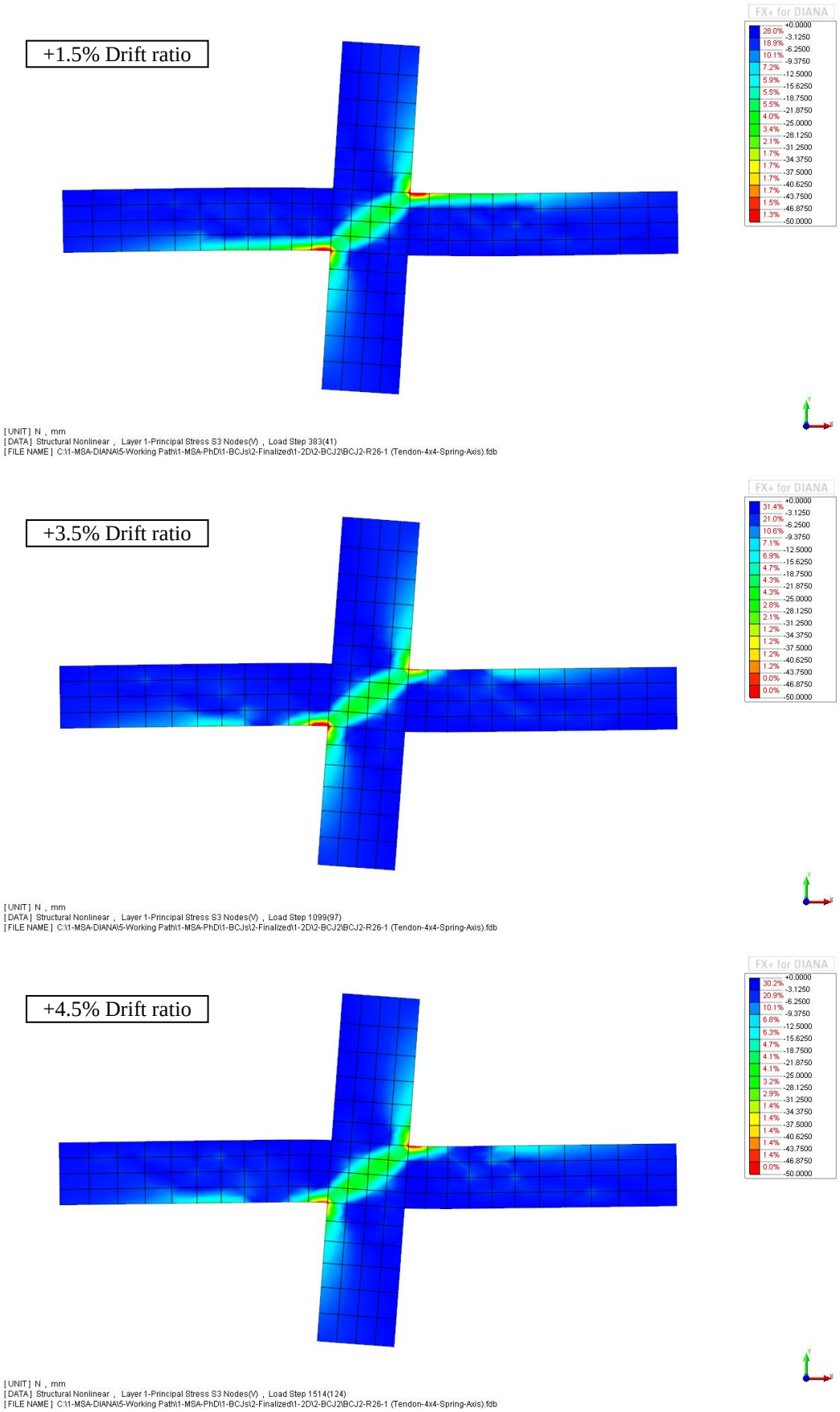

Figure 6.45: Evolution of the principal compressive stress in joint, beam and column

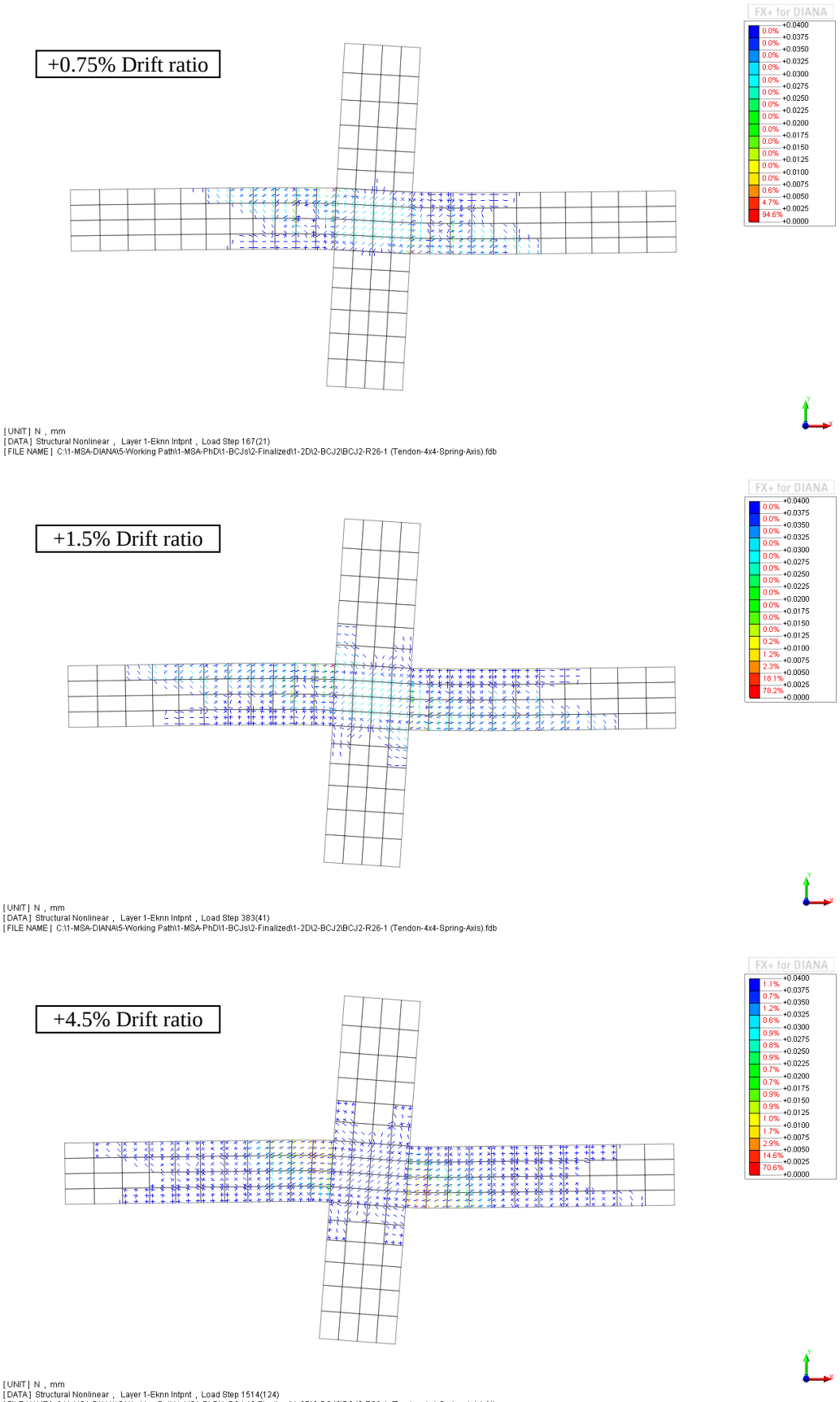

Figure 6.46: Crack formation in different drift ratios predicted by the FEA

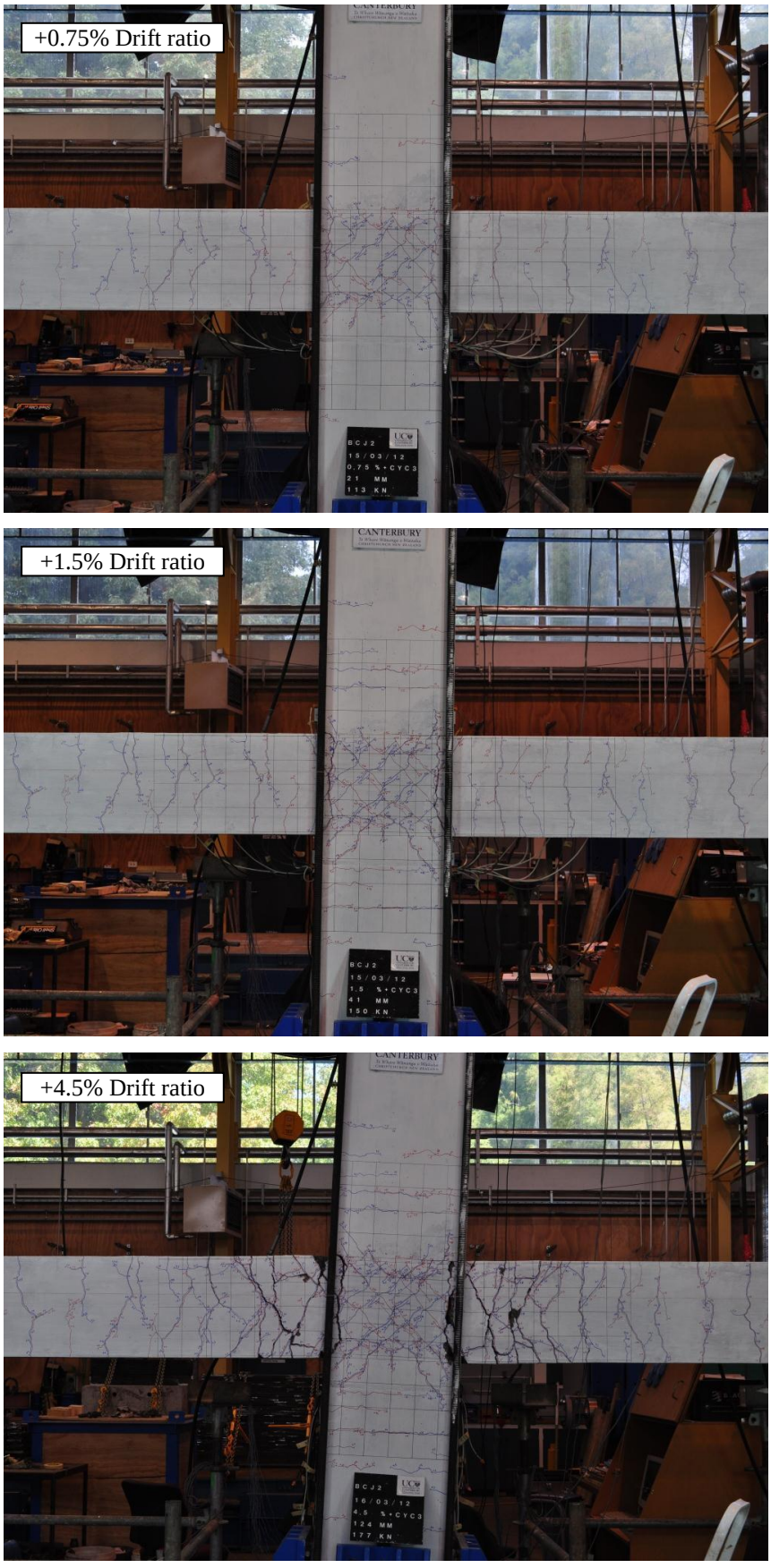

Figure 6.47: Experimental crack formation in different drift ratios

6.5.3.2 FEA OF BCJ3

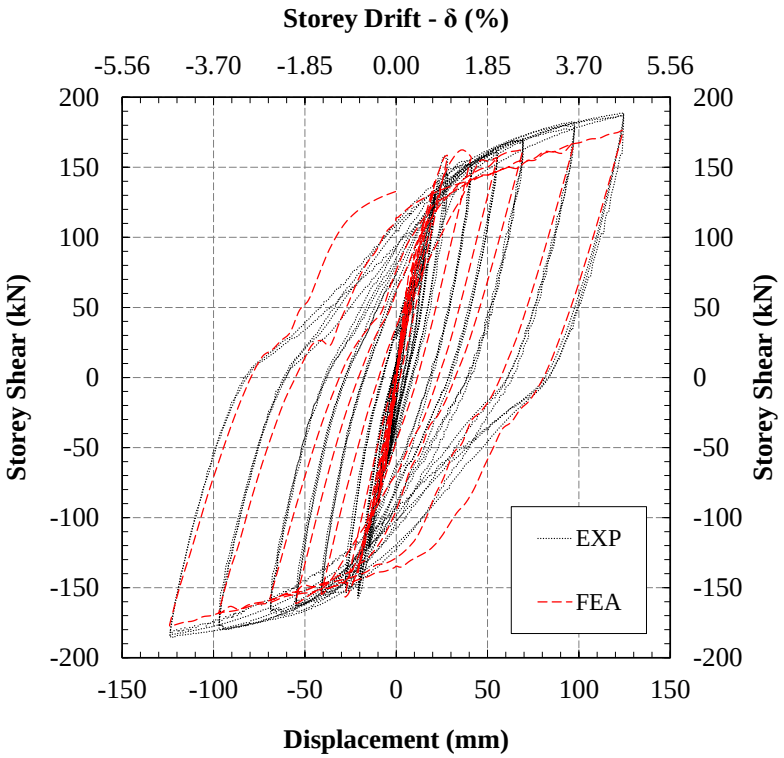

Figure 6.48: Storey shear vs. drift ratio of the 4x4 mesh under full cyclic

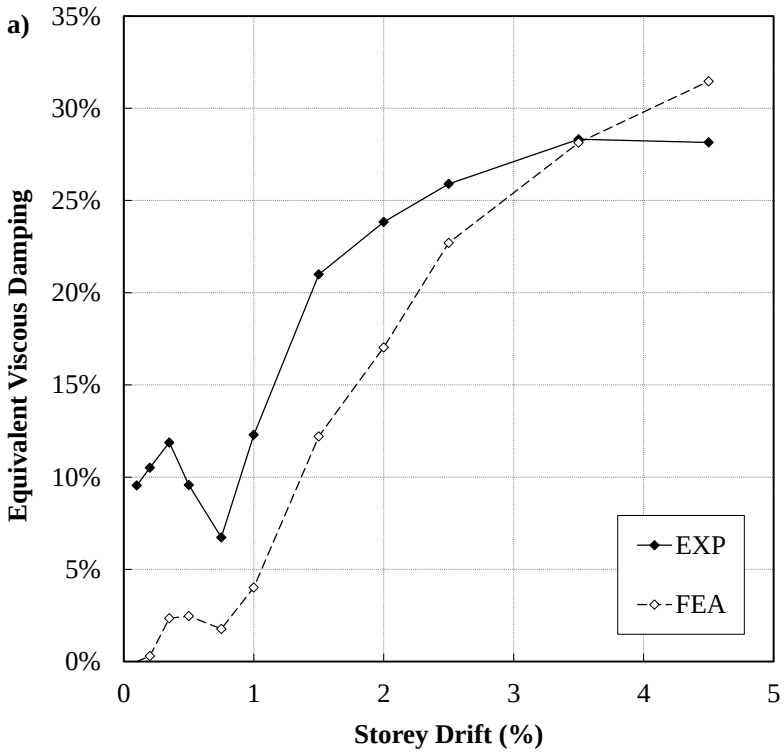

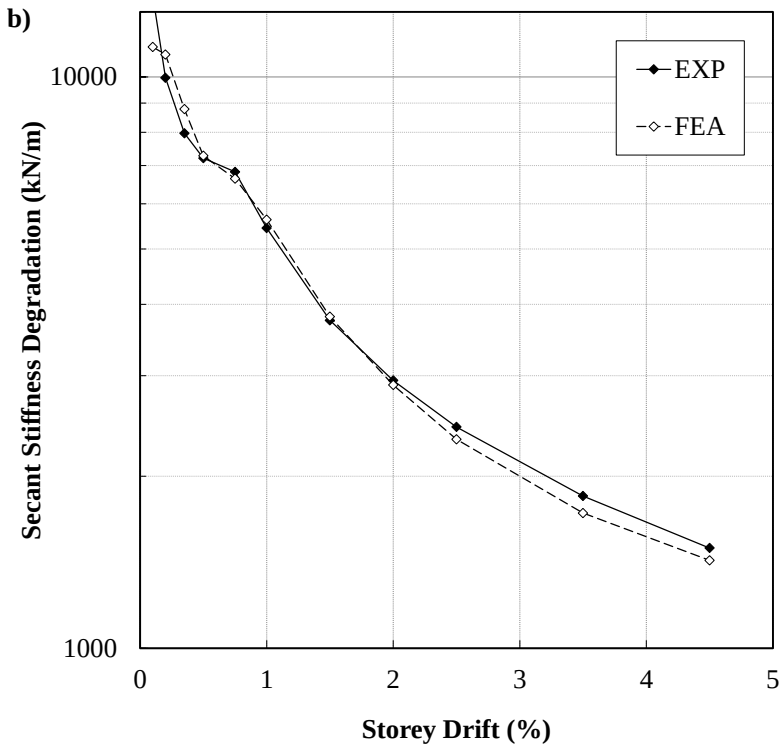

Figure 6.49: Comparison of a) damping and b) stiffness between the experiment and FEA

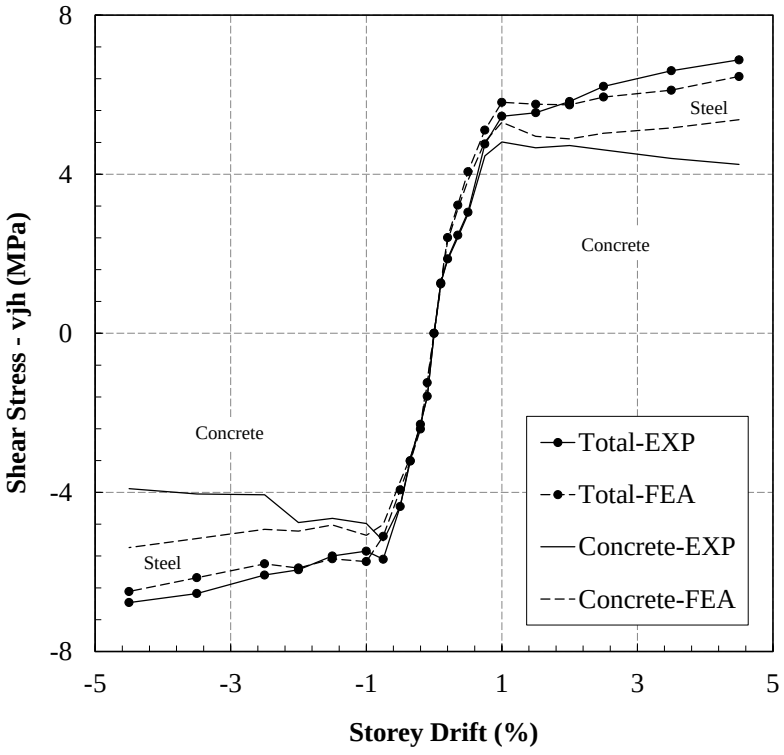

Figure 6.50: Steel and concrete contributions in taking joint shear force (FEA vs. EXP)

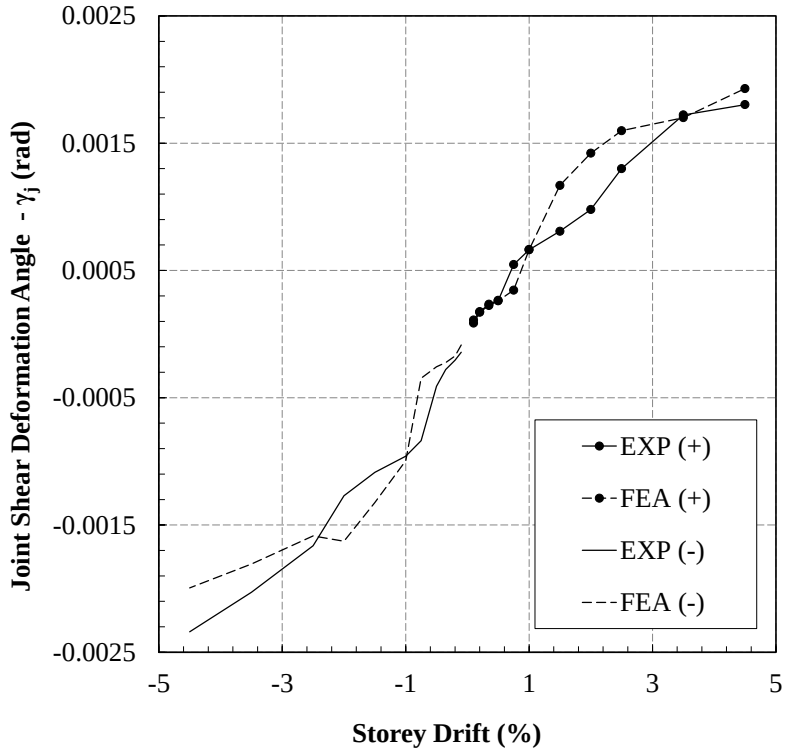

Figure 6.51: Comparison of the predicted joint shear deformation angle vs. experiment

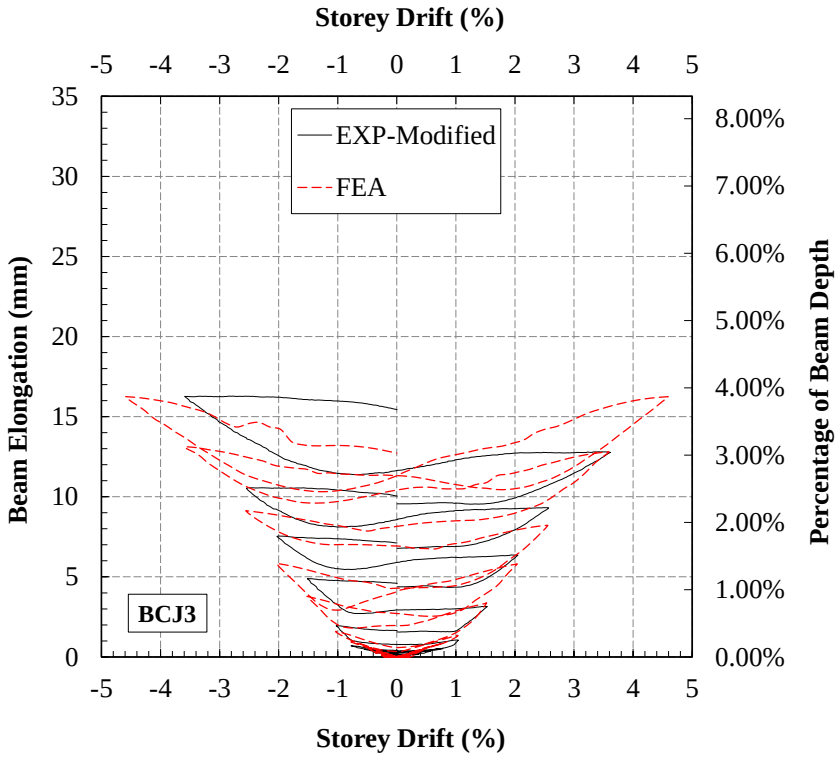

Figure 6.52: Elongation of beam at the plastic hinge zone

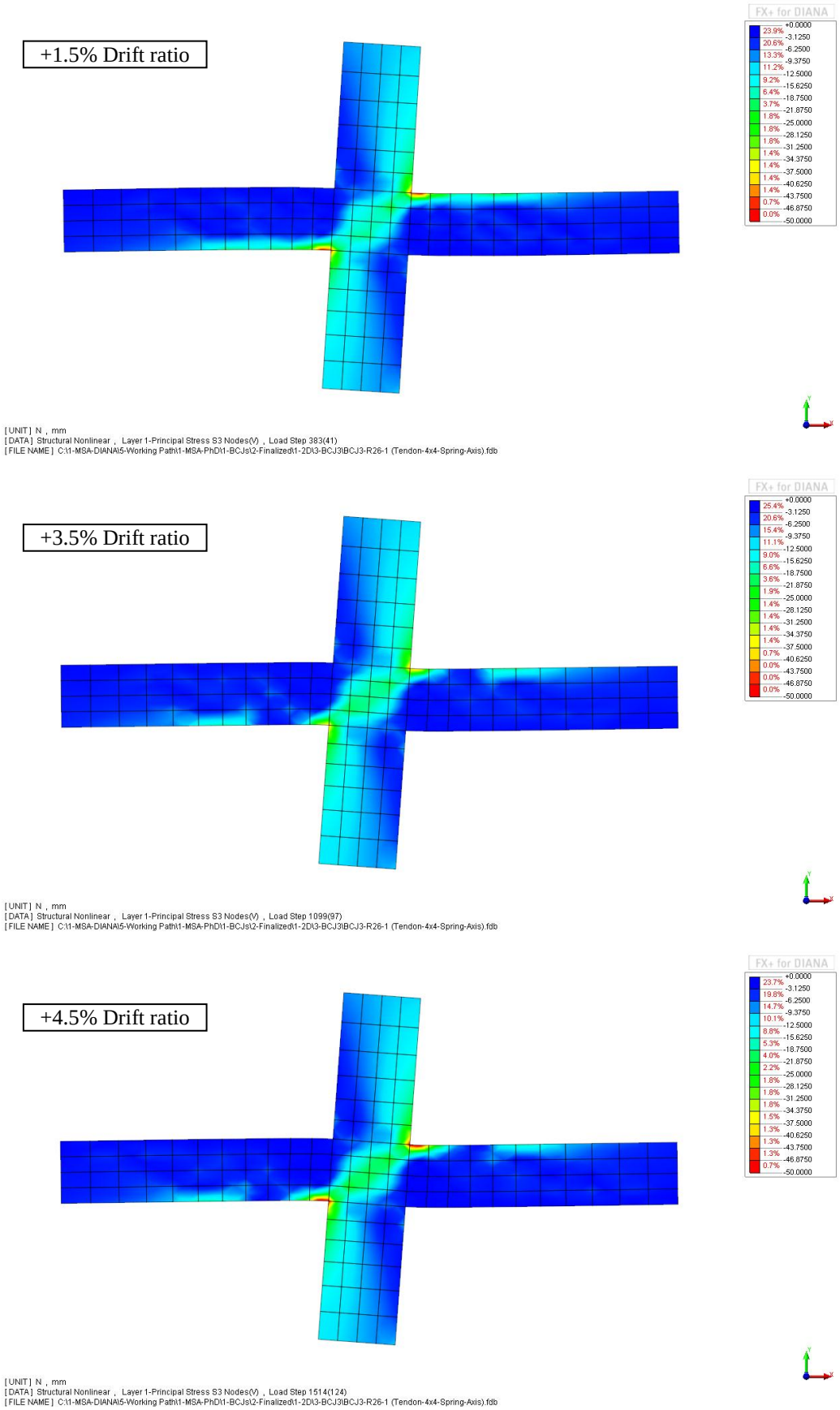

Figure 6.53: Evolution of the principal compressive stress in joint, beam and column

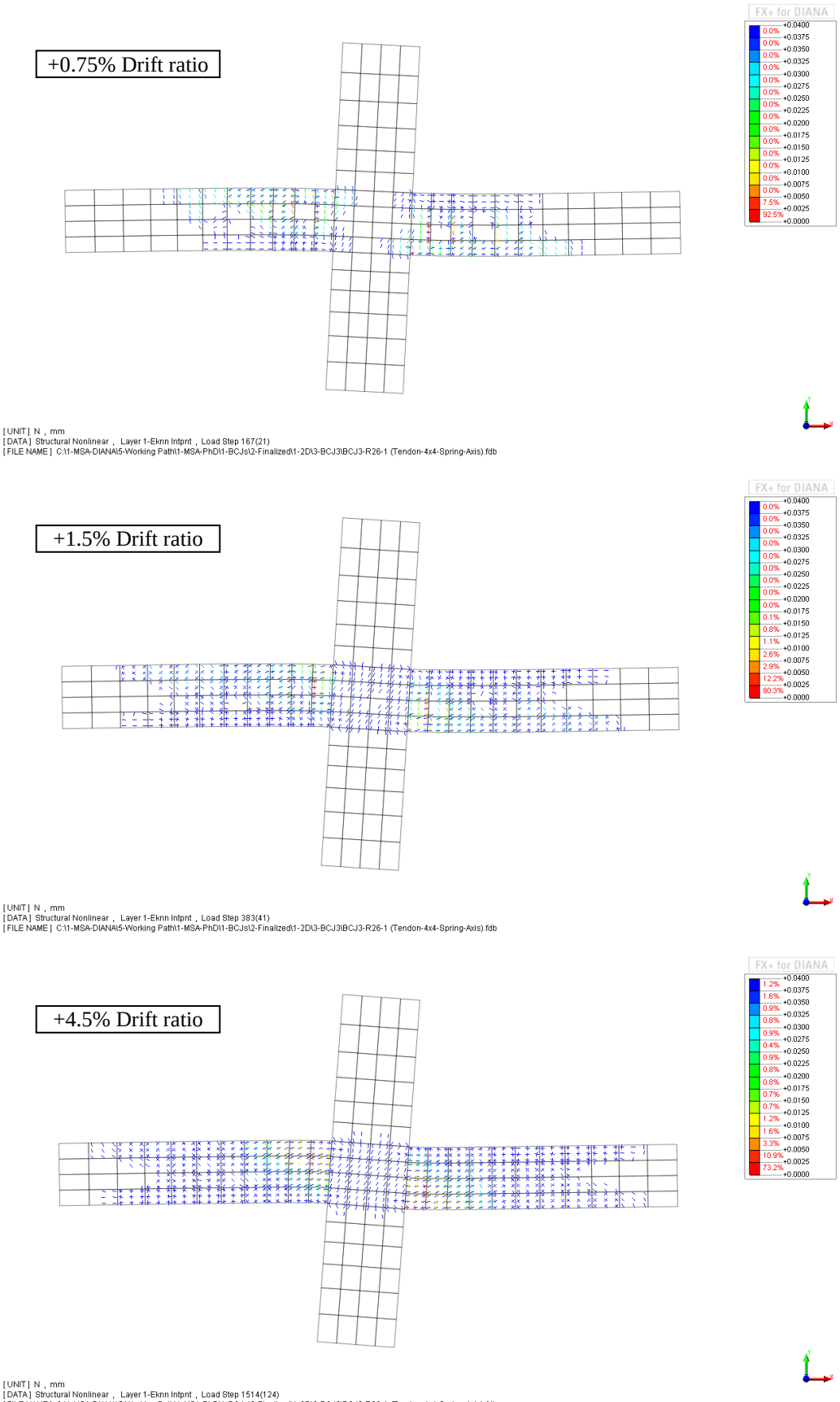

Figure 6.54: Crack formation in different drift ratios predicted by the FEA

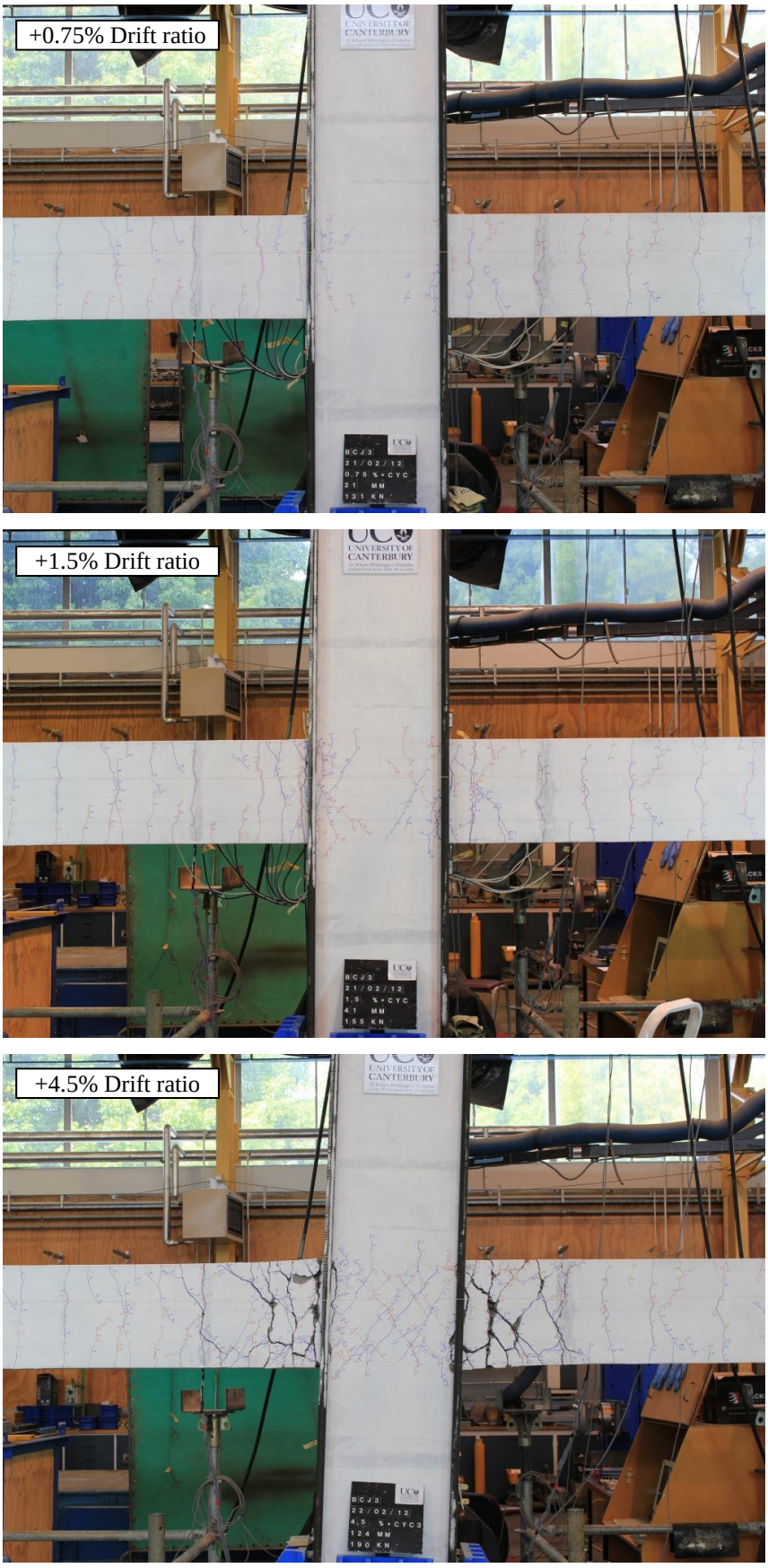

Figure 6.55: Experimental crack formation in different drift ratios

6.5.3.3 FEA OF BCJ4

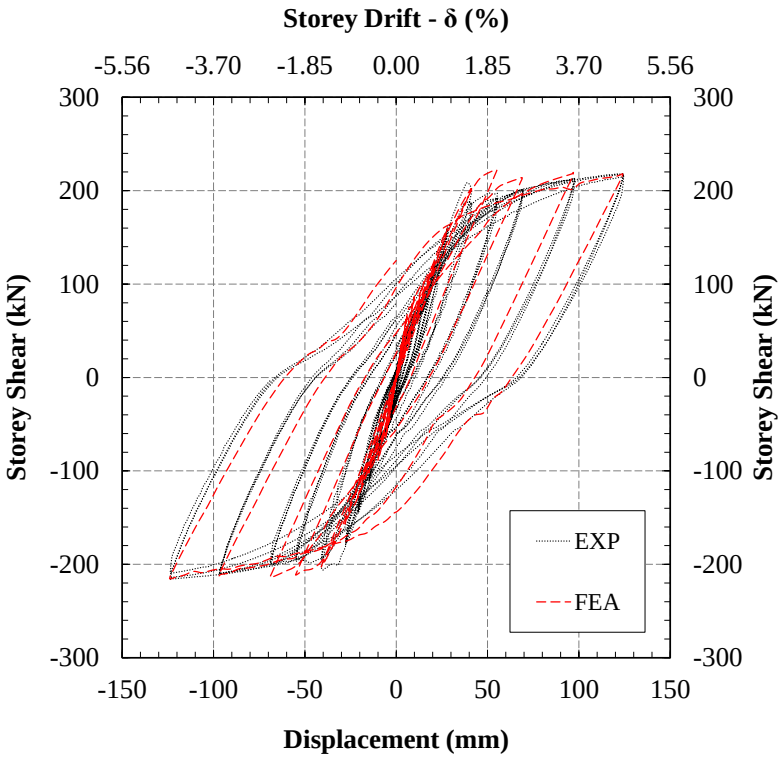

Figure 6.56: Storey shear vs. drift ratio of the 4x4 mesh under full cyclic

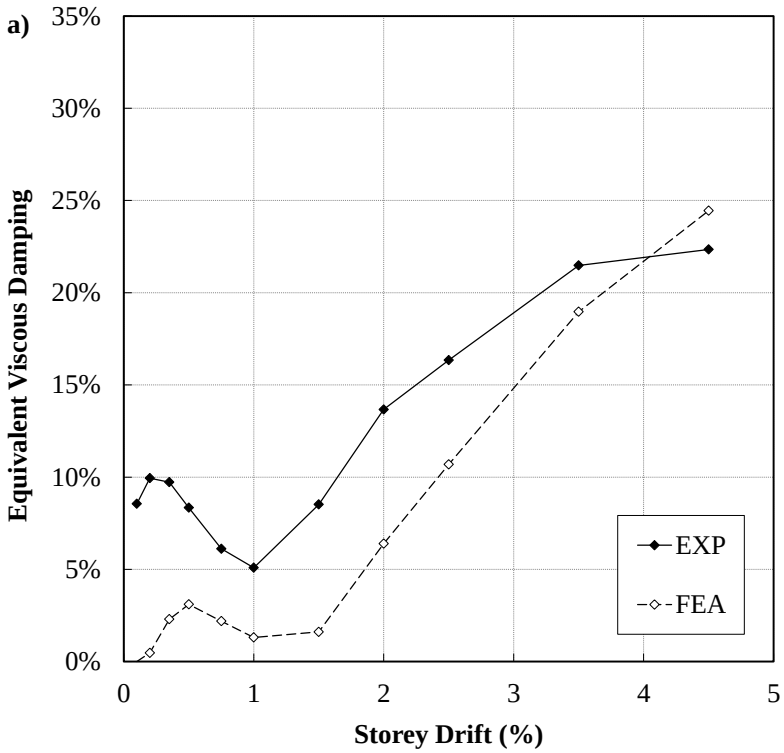

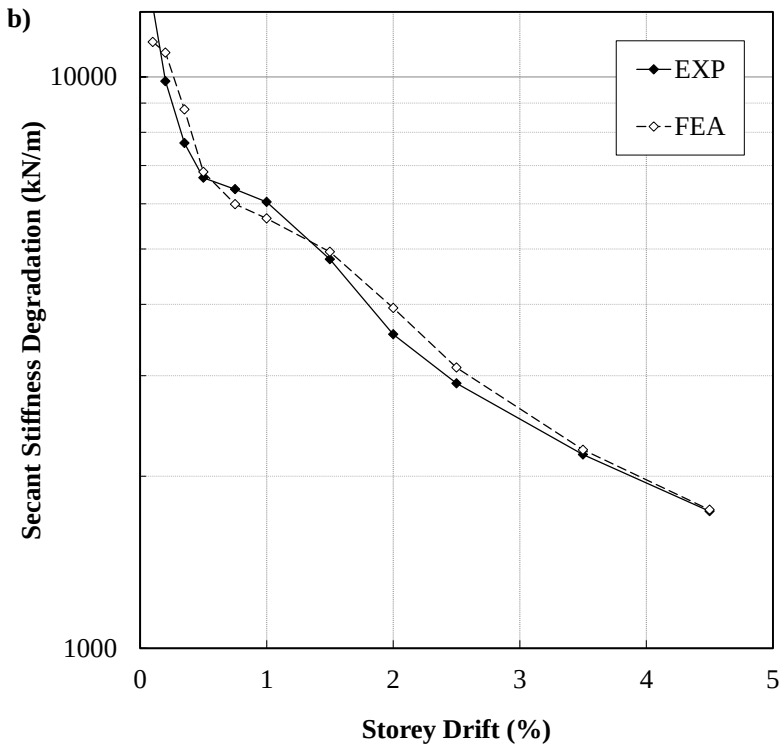

Figure 6.57: Comparison of a) damping and b) stiffness between the experiment and FEA

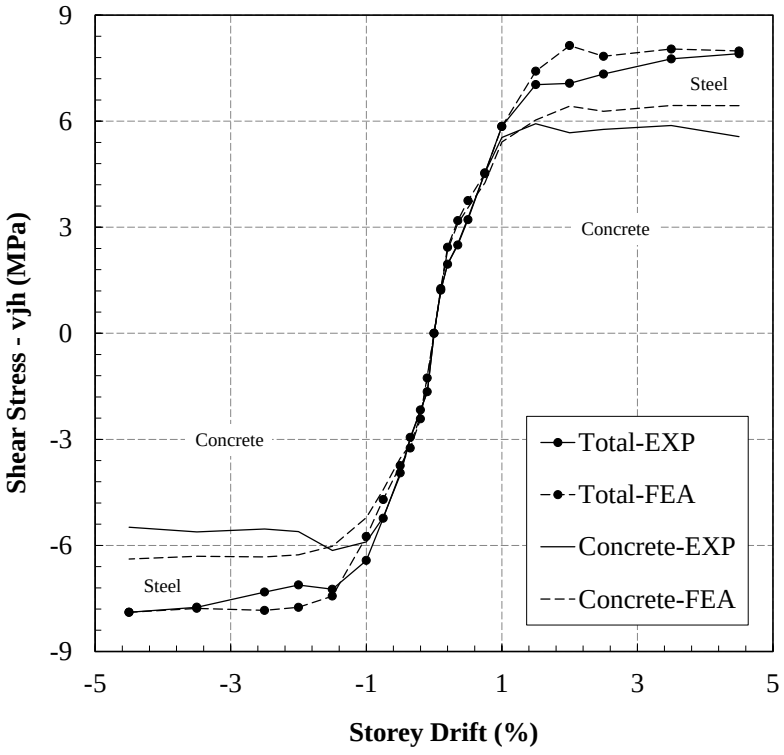

Figure 6.58: Steel and concrete contributions in taking joint shear force (FEA vs. EXP)

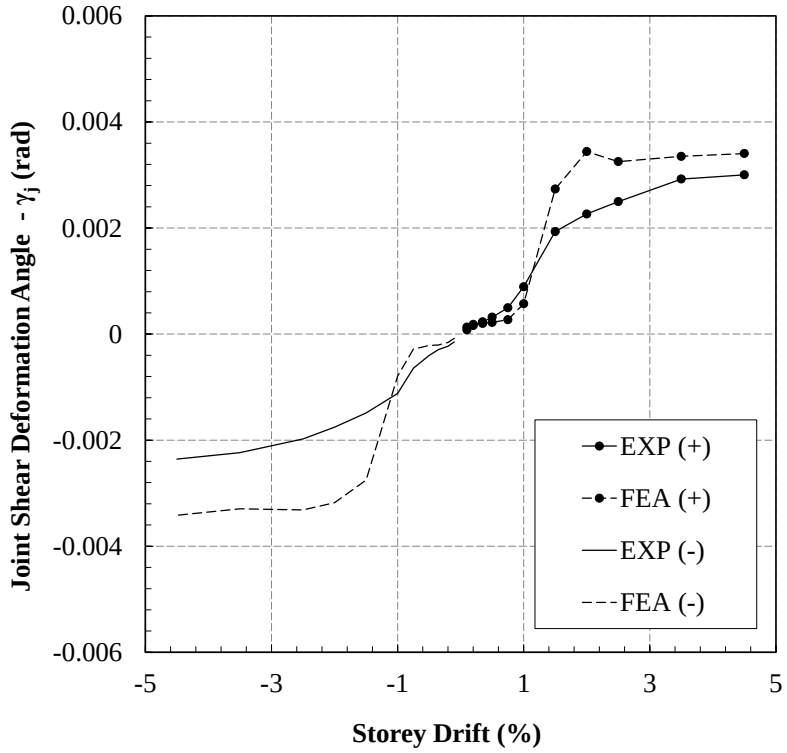

Figure 6.59: Comparison of the predicted joint shear deformation angle vs. experiment

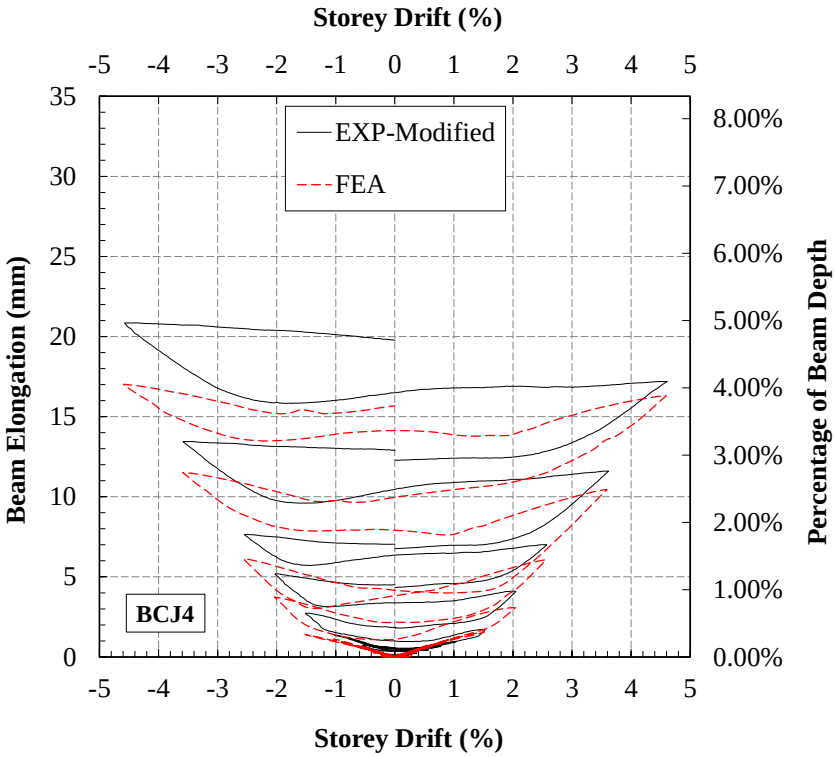

Figure 6.60: Elongation of beam at the plastic hinge zone

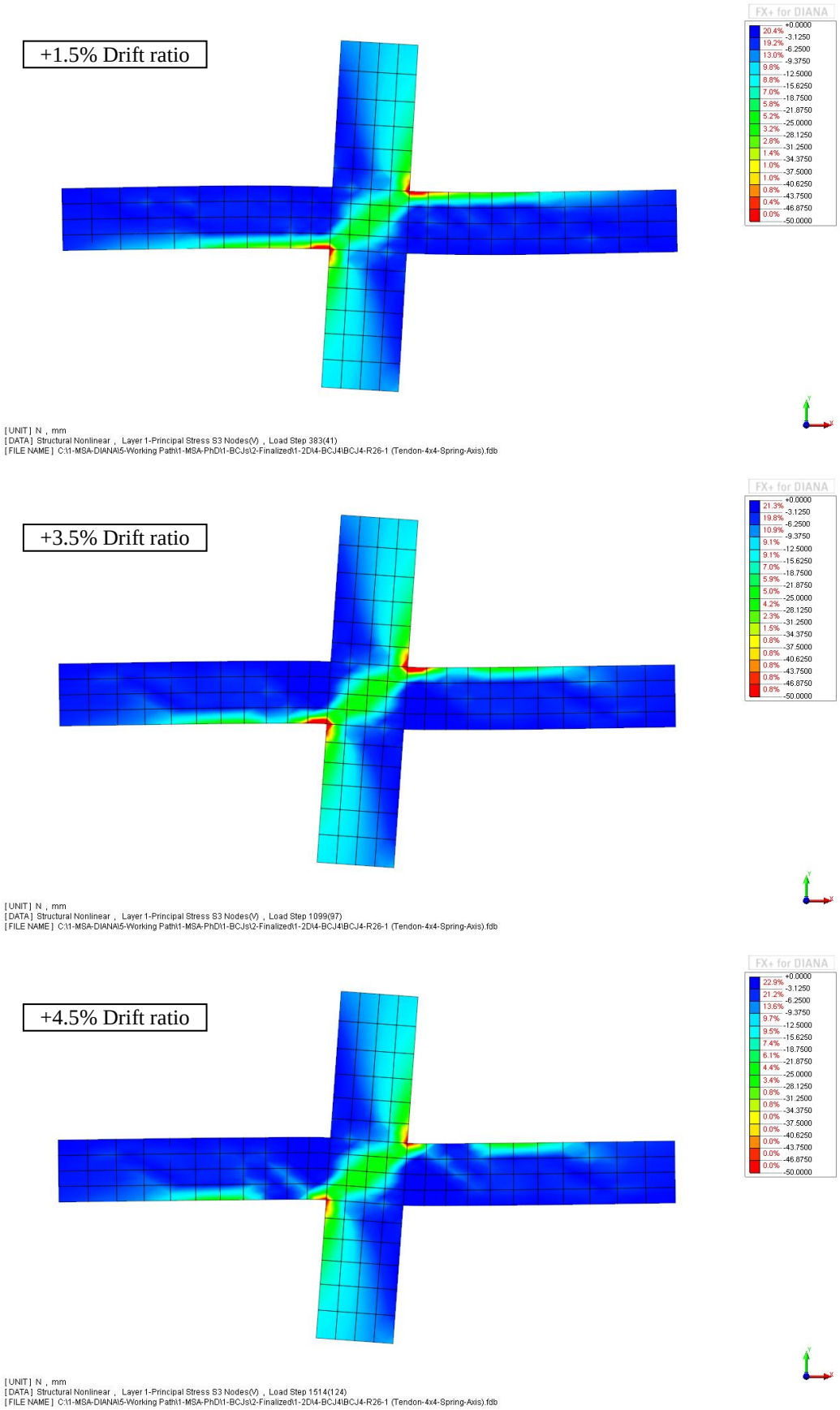

Figure 6.61: Evolution of the principal compressive stress in joint, beam and column

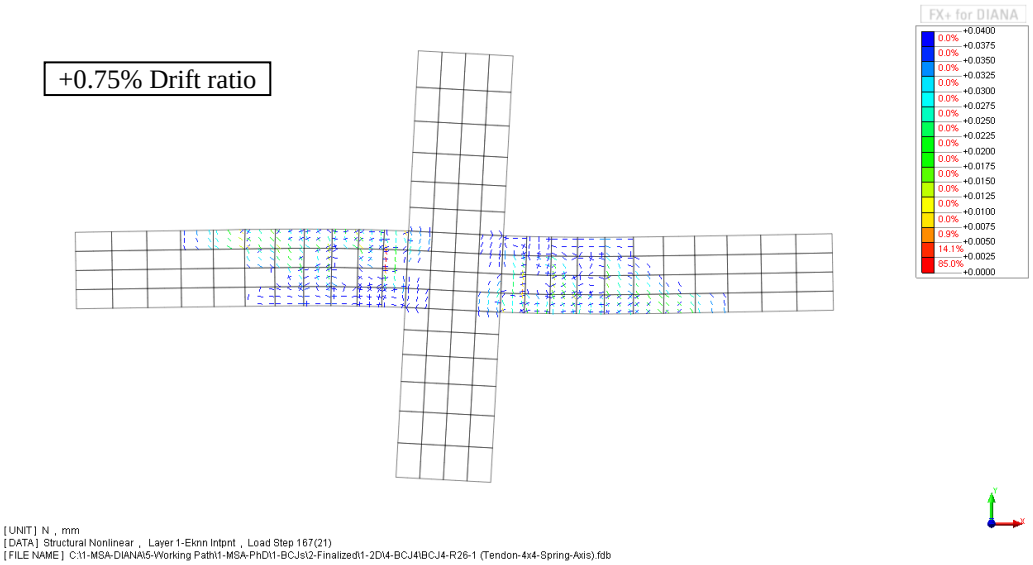

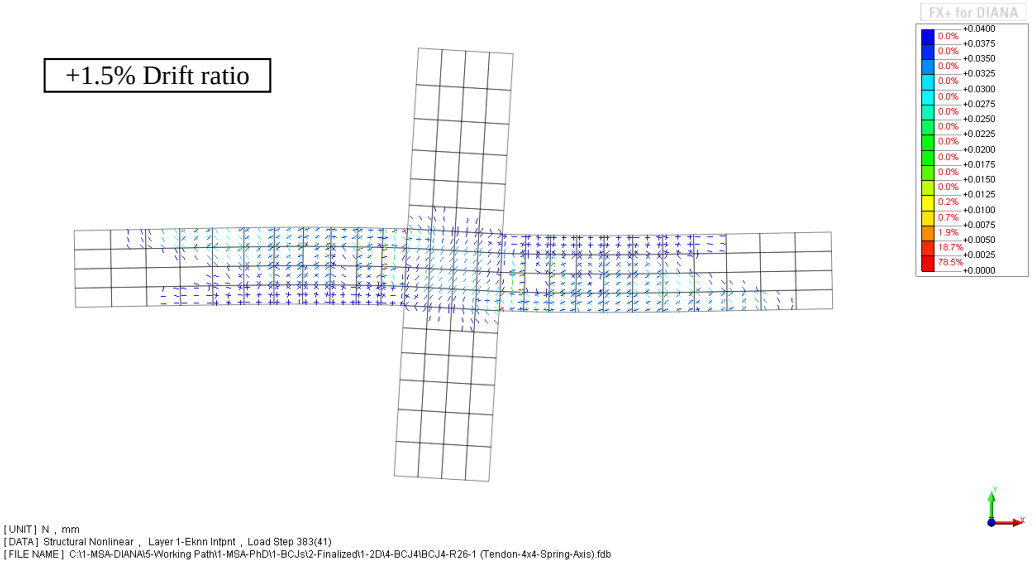

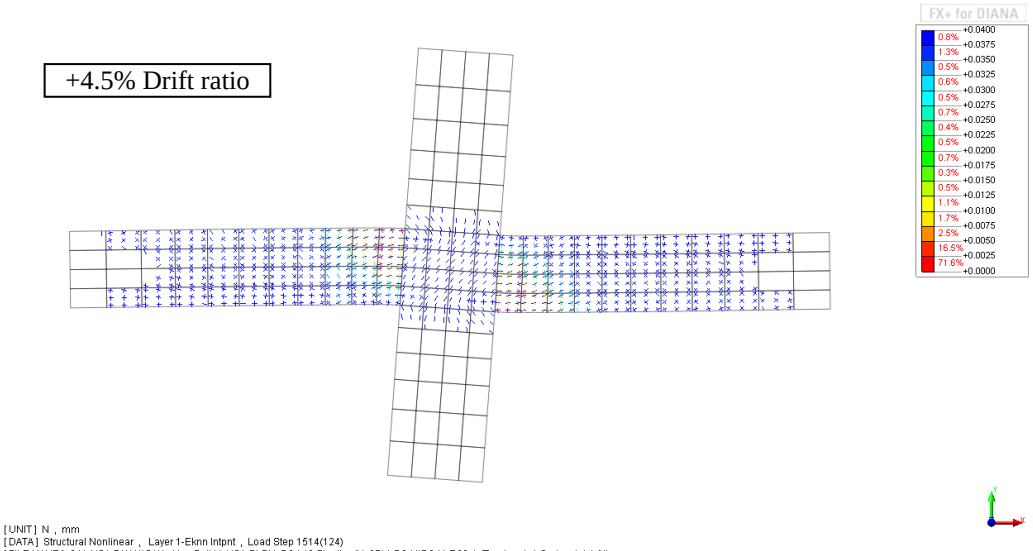

Figure 6.62: Crack formation in different drift ratios predicted by the FEA

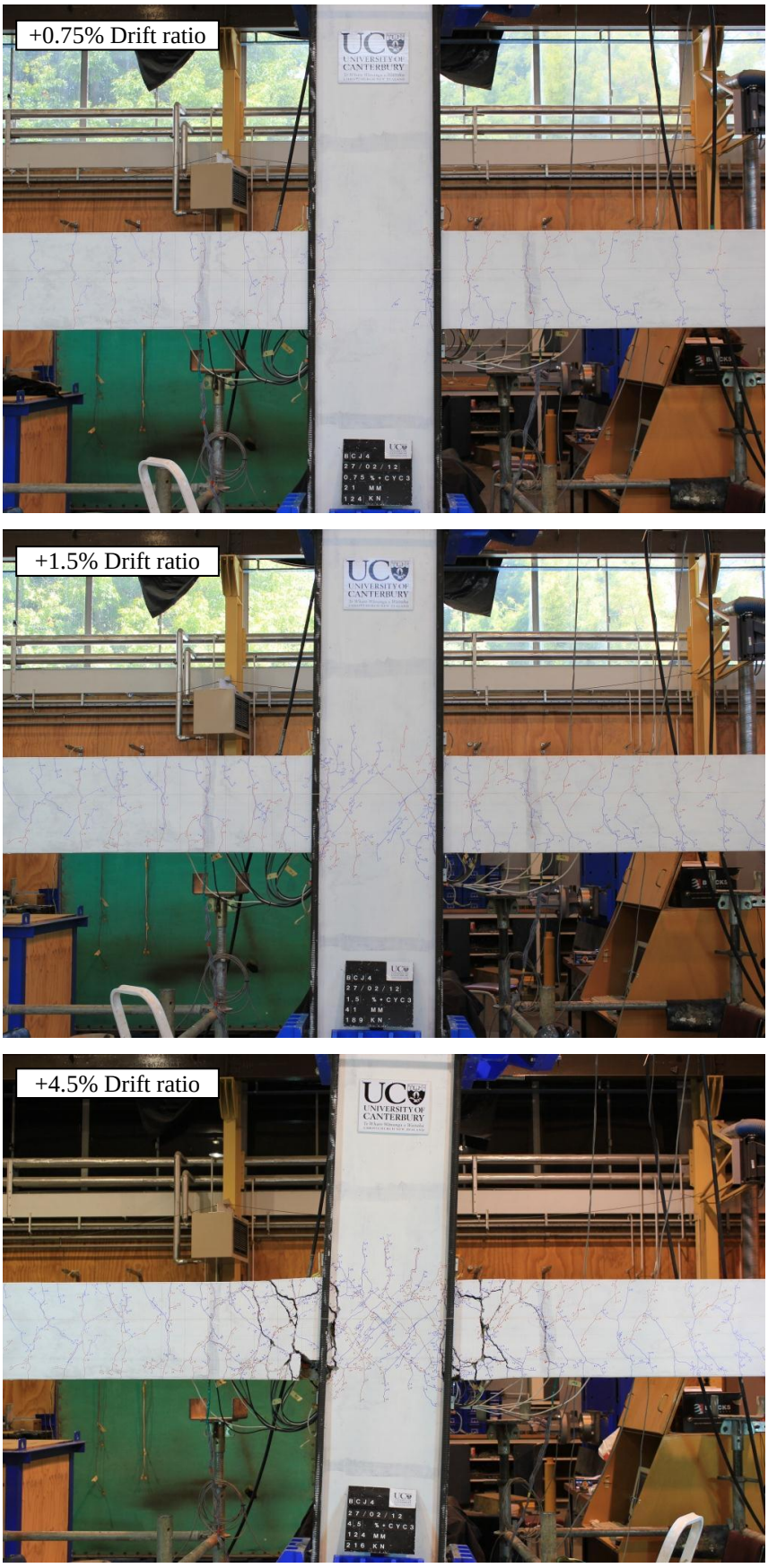

Figure 6.63: Experimental crack formation in different drift ratios

6.5.3.4 FEA OF BCJ5

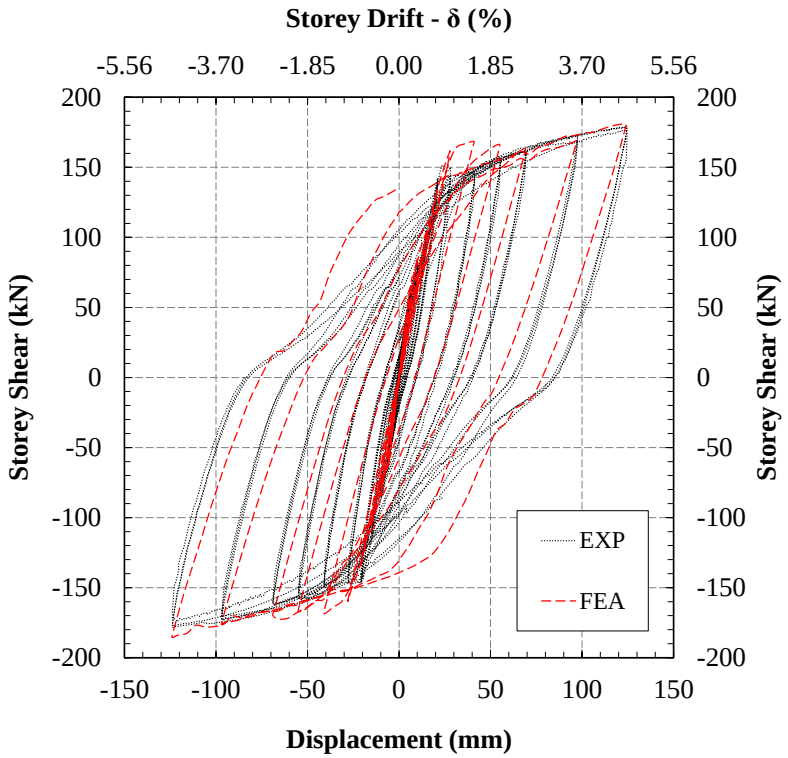

Figure 6.64: Storey shear vs. drift ratio of the 4x4 mesh under full cyclic

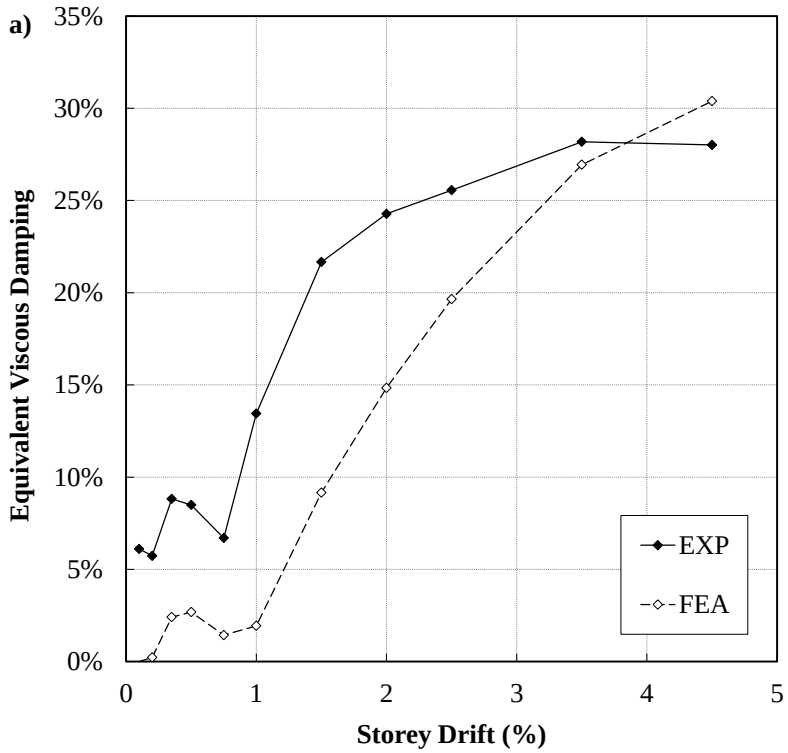

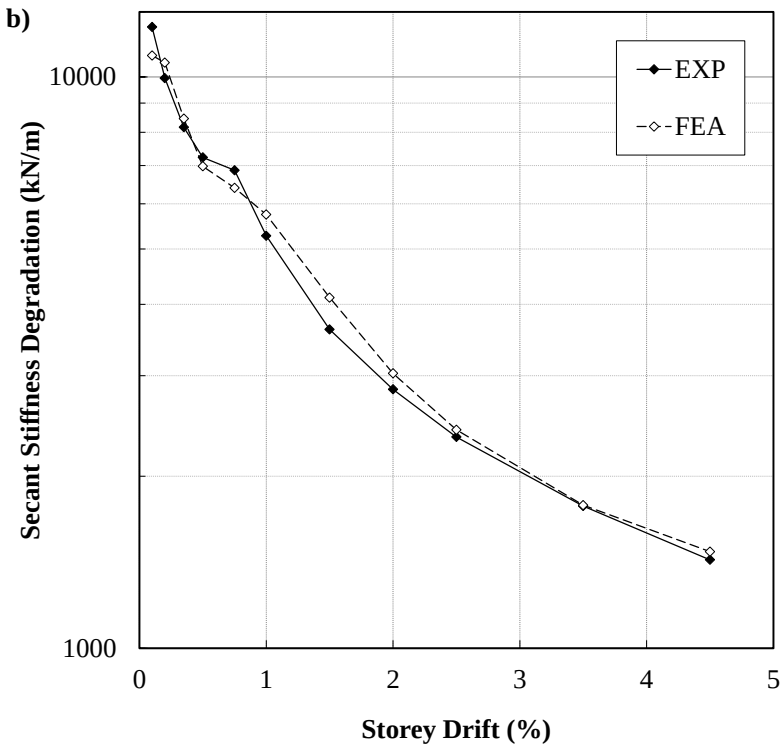

Figure 6.65: Comparison of a) damping and b) stiffness between the experiment and FEA

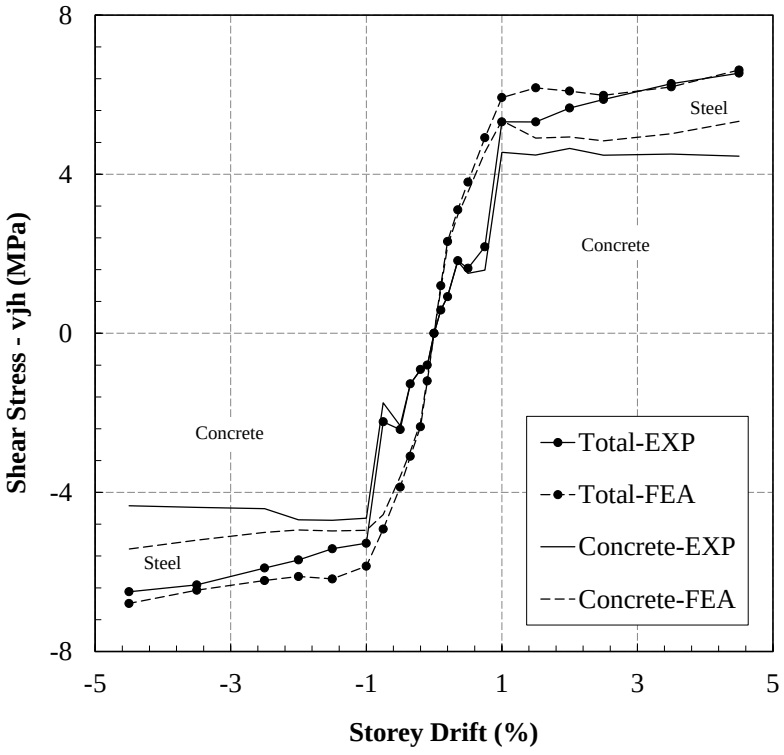

Figure 6.66: Steel and concrete contributions in taking joint shear force (FEA vs. EXP)

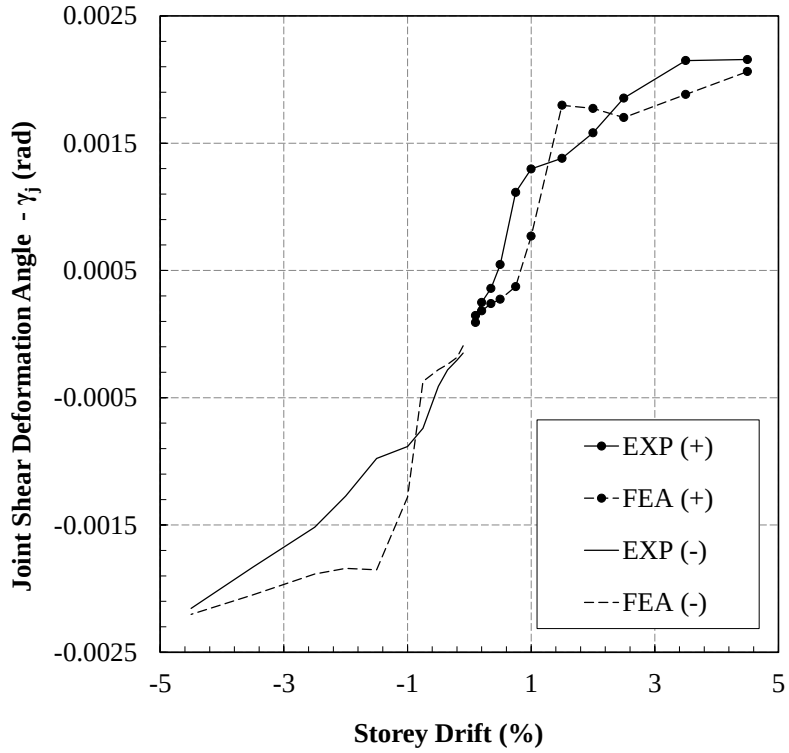

Figure 6.67: Comparison of the predicted joint shear deformation angle vs. experiment

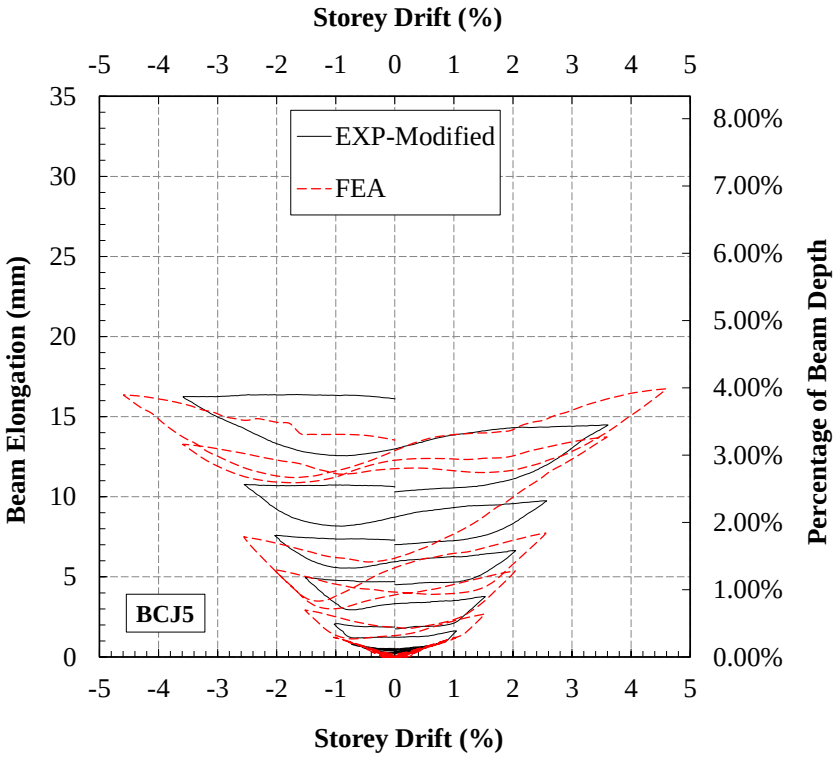

Figure 6.68: Elongation of beam at the plastic hinge zone

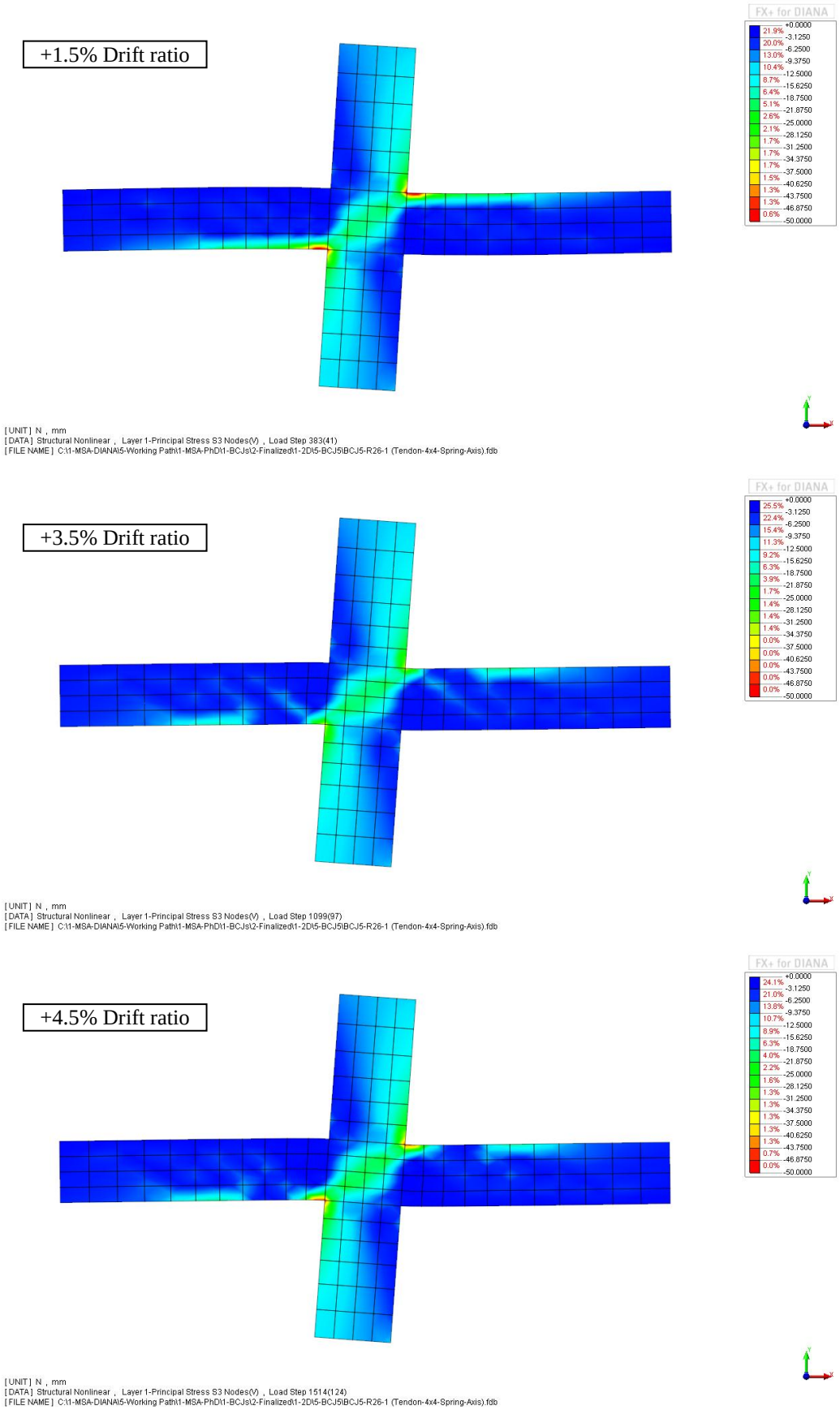

Figure 6.69: Evolution of the principal compressive stress in joint, beam and column

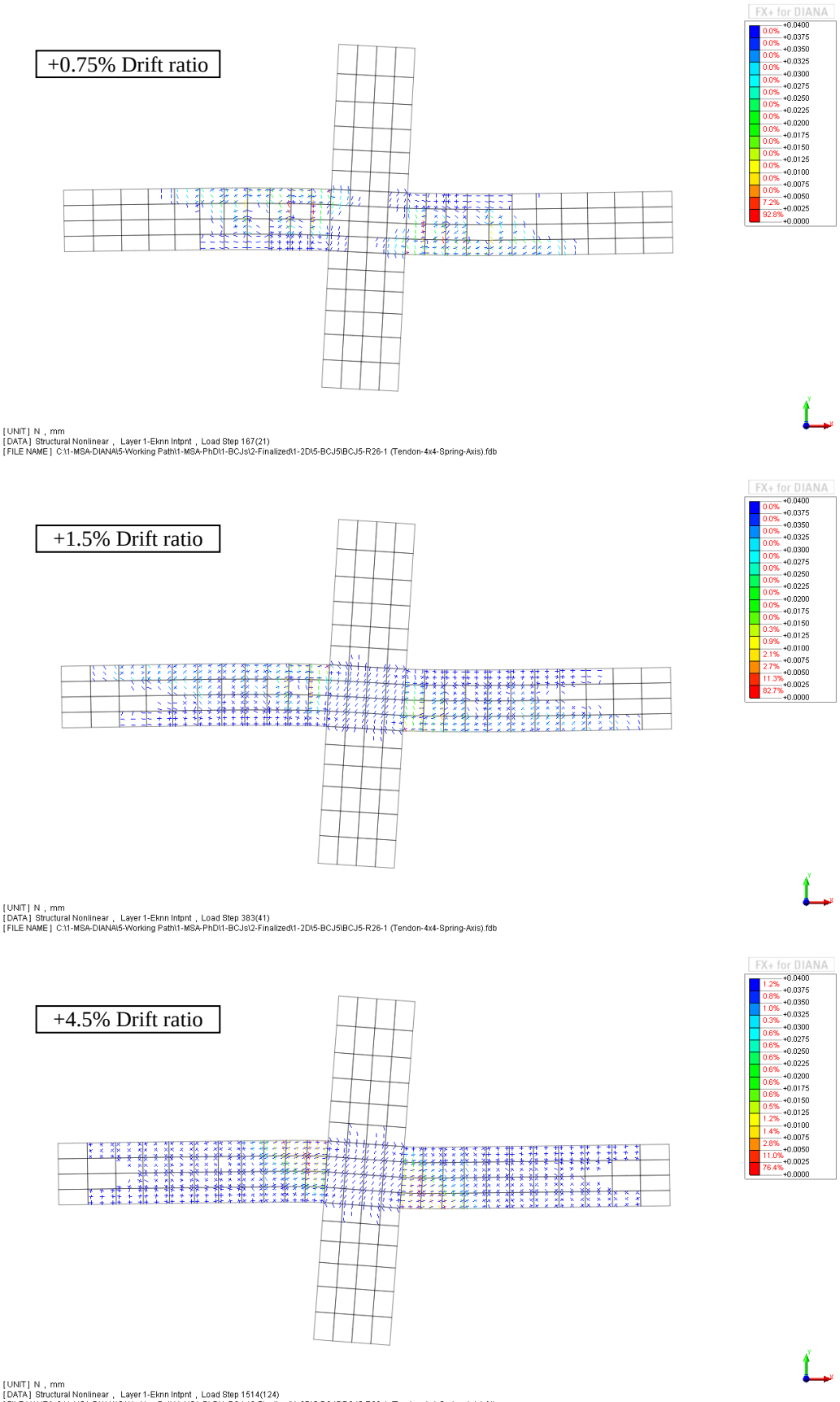

Figure 6.70: Crack formation in different drift ratios predicted by the FEA

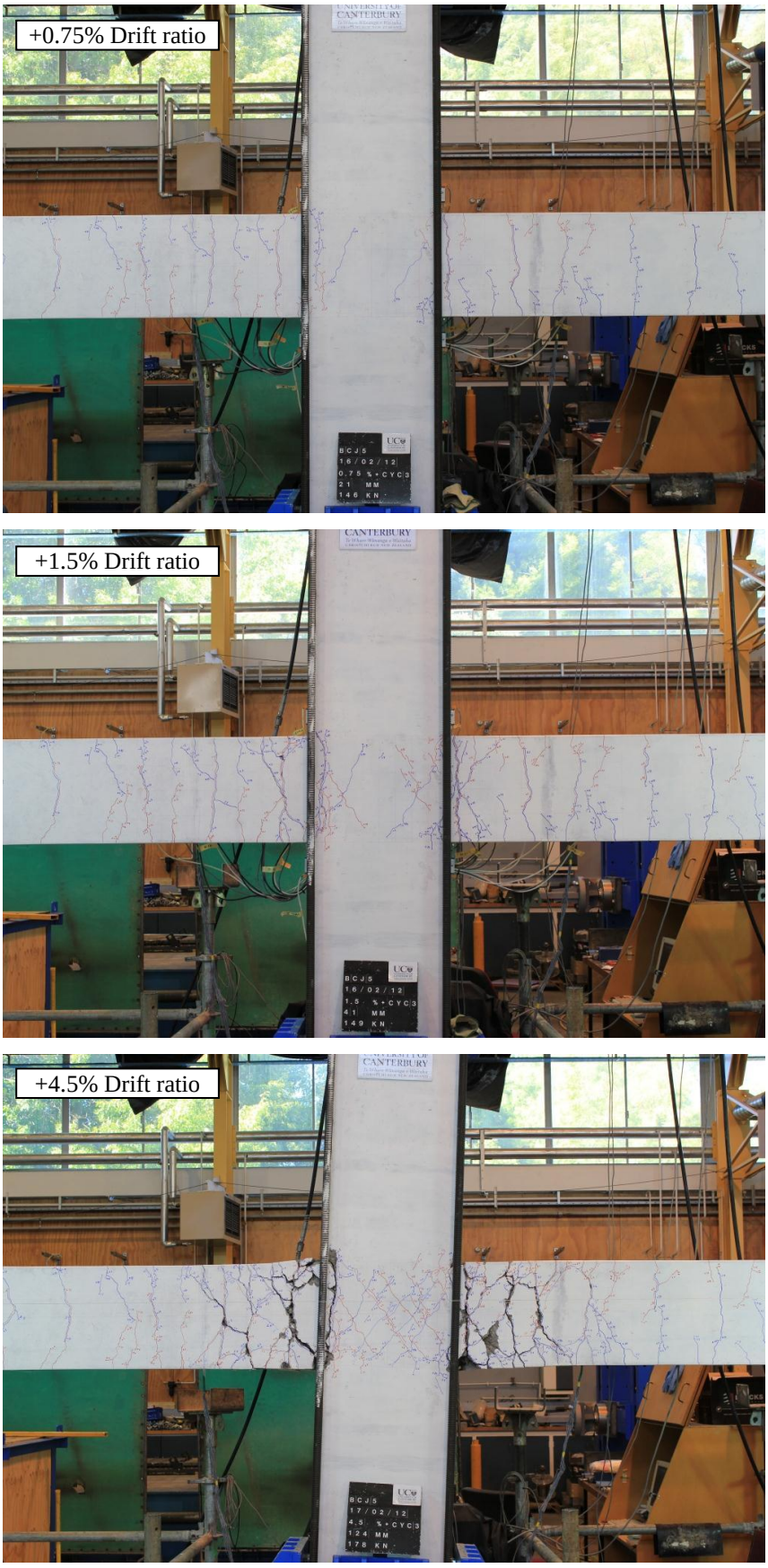

Figure 6.71: Experimental crack formation in different drift ratios

6.5.3.5 FEA OF BCJ6

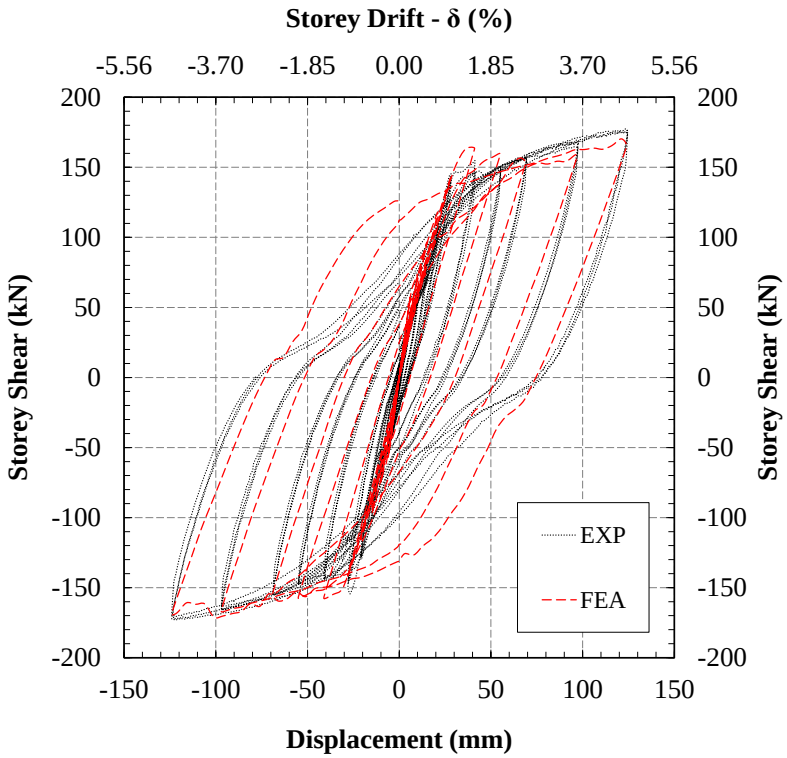

Figure 6.72: Storey shear vs. drift ratio of the 4x4 mesh under full cyclic

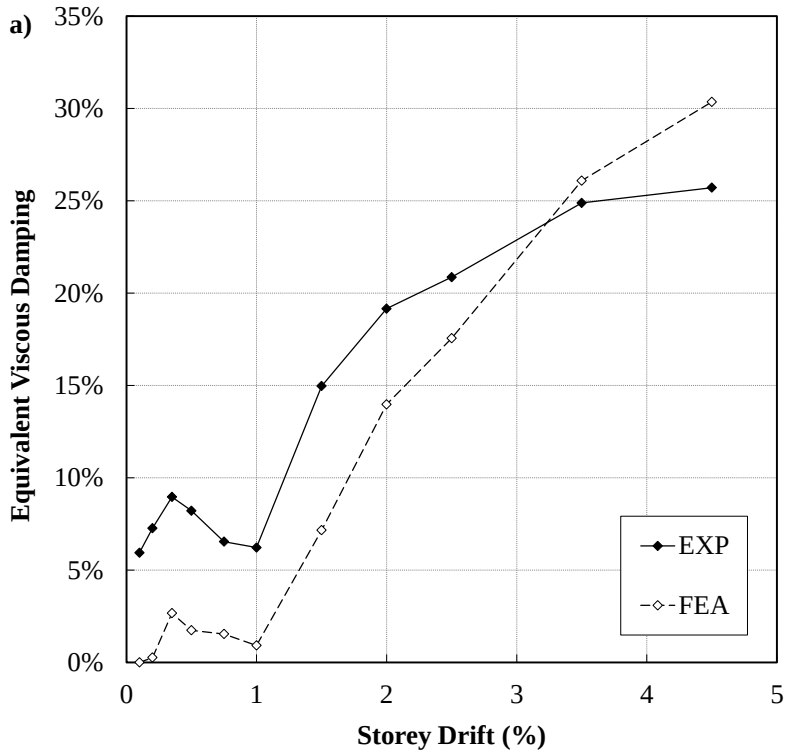

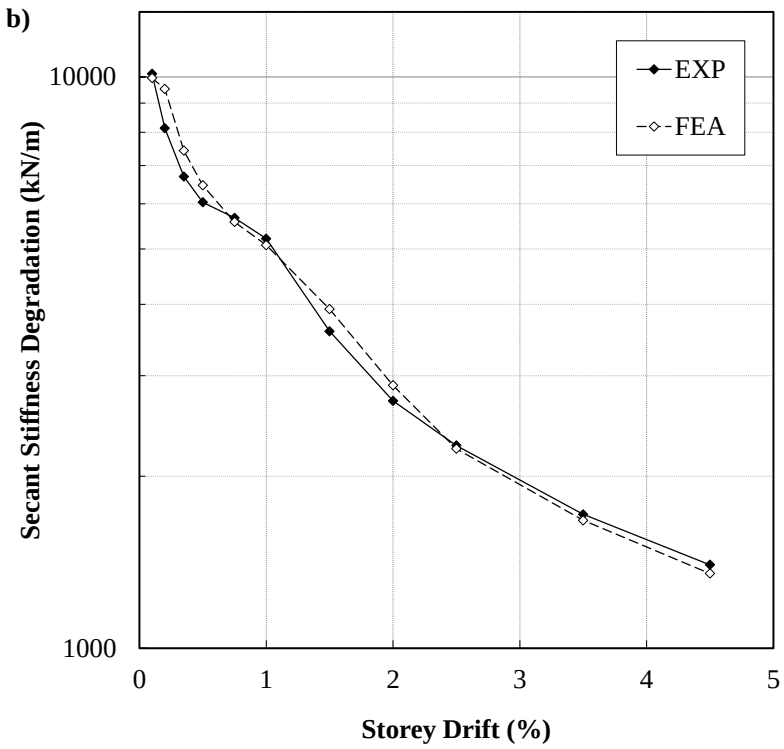

Figure 6.73: Comparison of a) damping and b) stiffness between the experiment and FEA

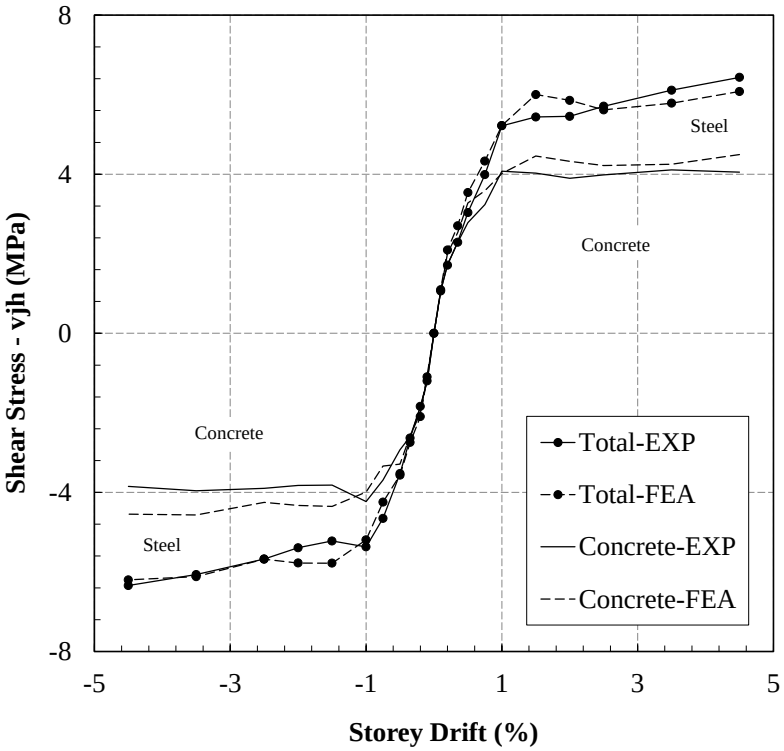

Figure 6.74: Steel and concrete contributions in taking joint shear force (FEA vs. EXP)

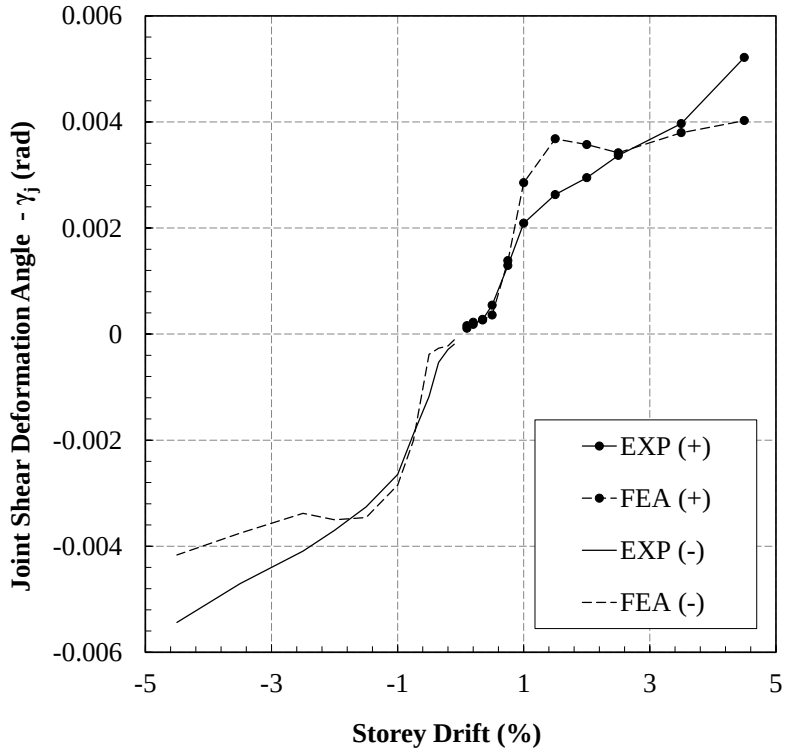

Figure 6.75: Comparison of the predicted joint shear deformation angle vs. experiment

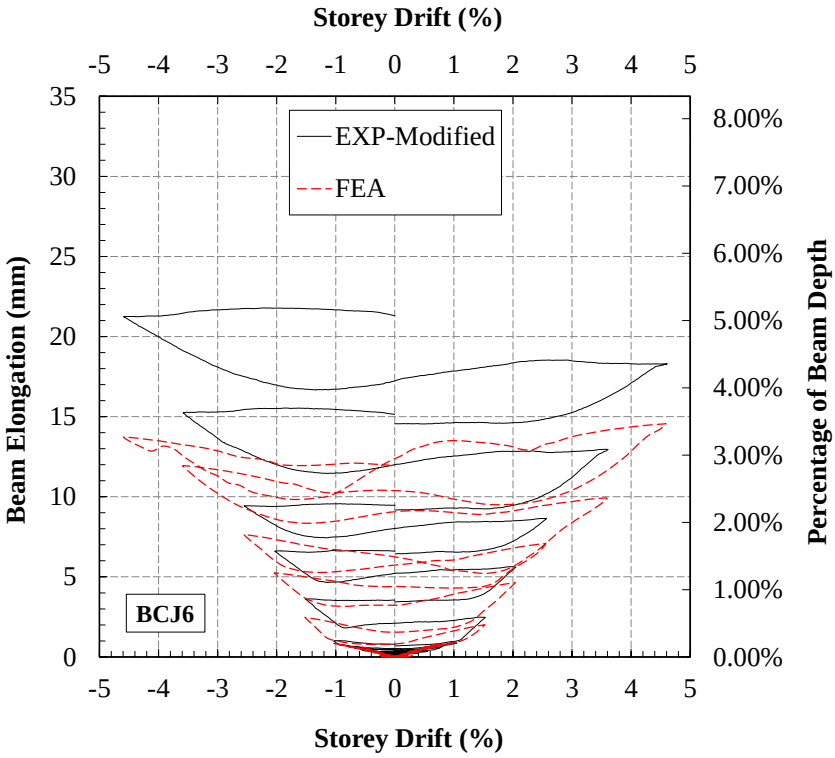

Figure 6.76: Elongation of beam at the plastic hinge zone

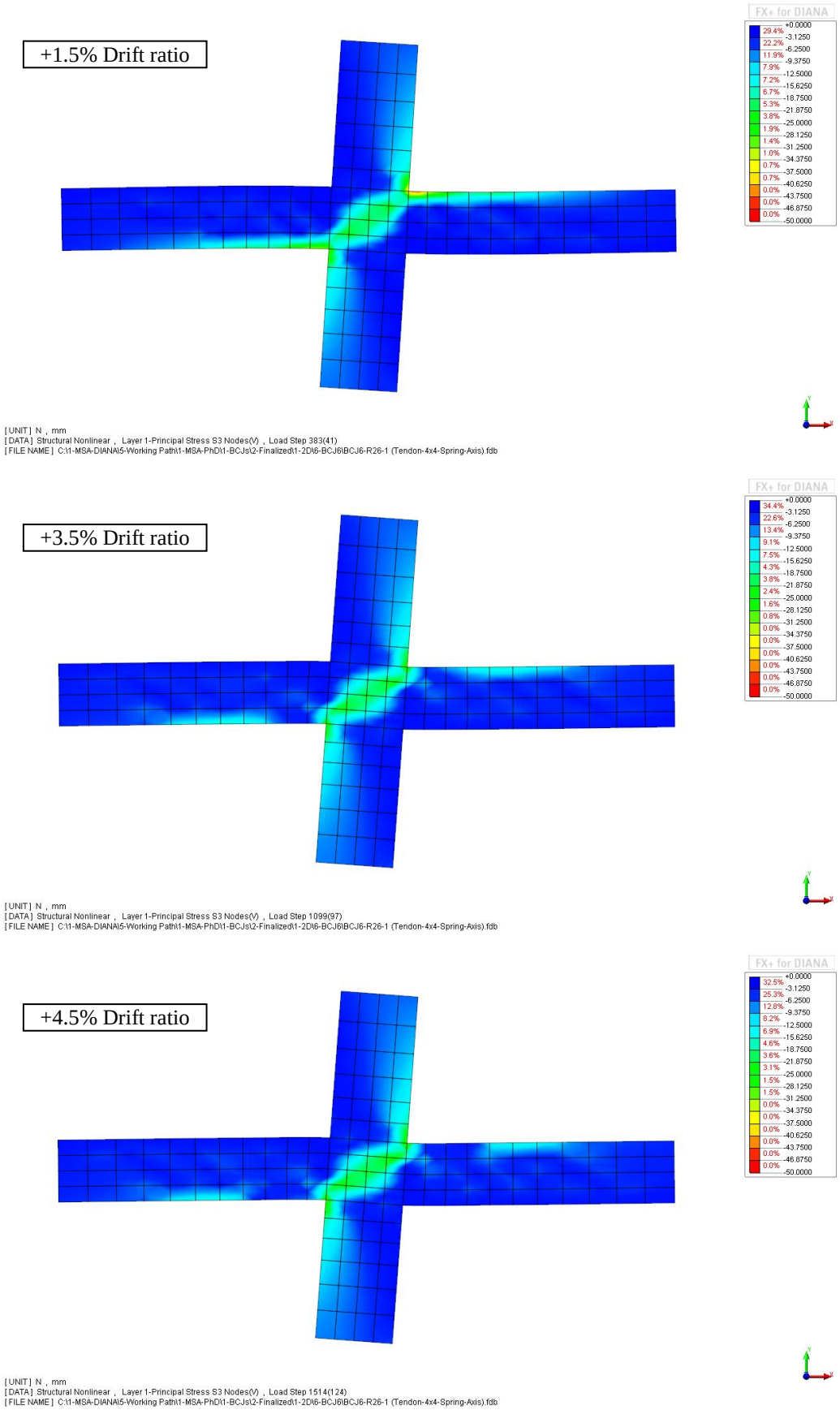

Figure 6.77: Evolution of the principal compressive stress in joint, beam and column

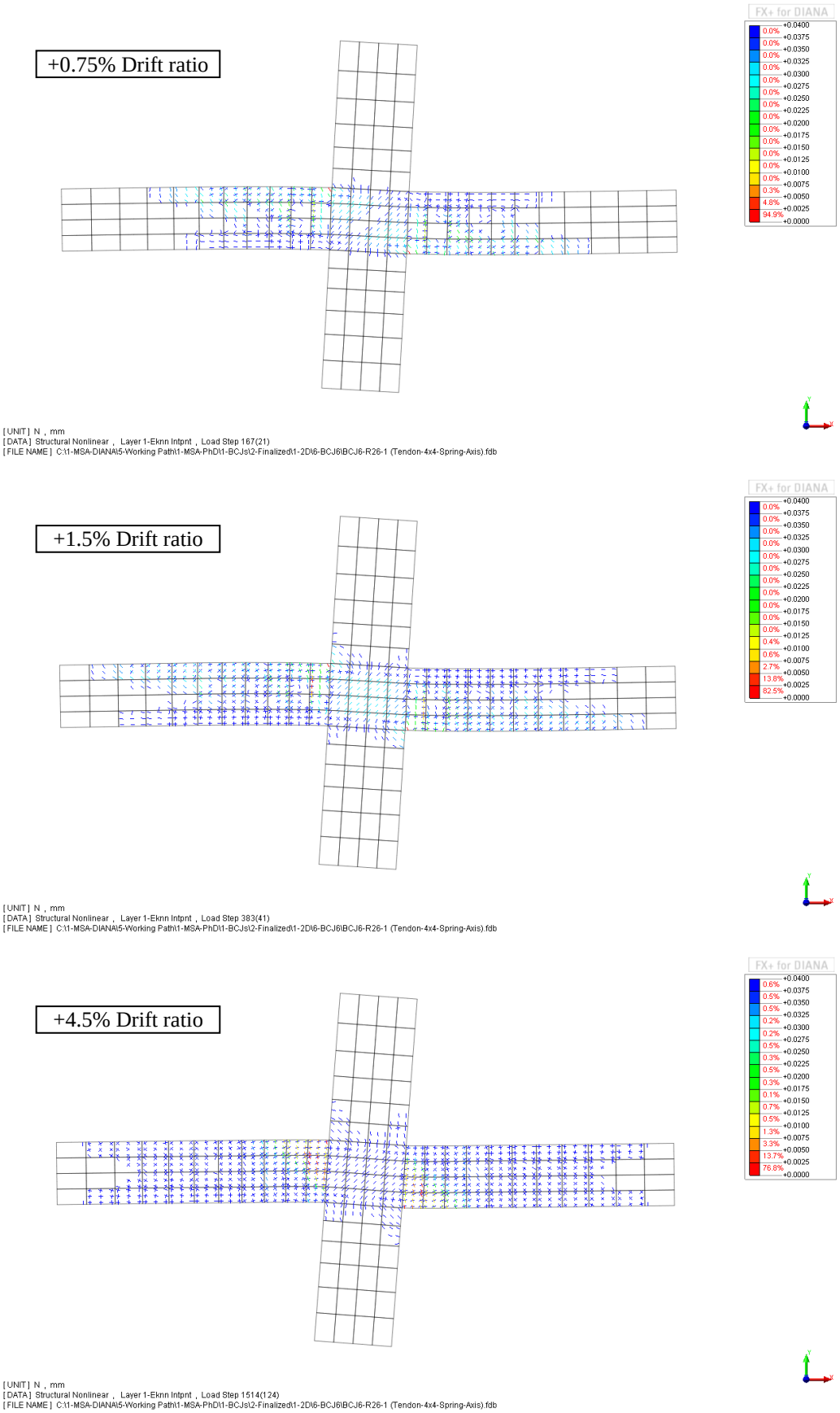

Figure 6.78: Crack formation in different drift ratios predicted by the FEA

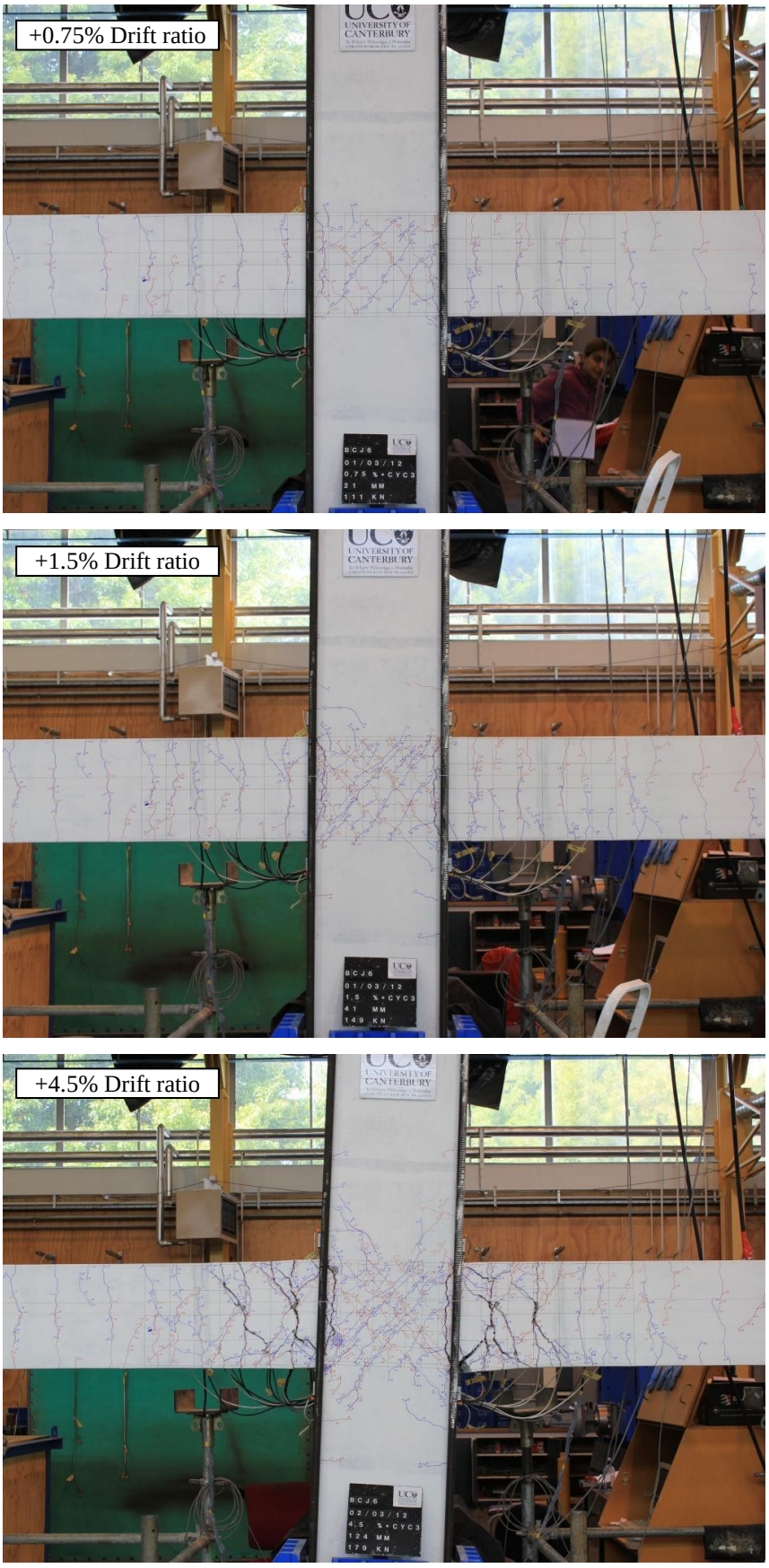

Figure 6.79: Experimental crack formation in different drift ratios

6.5.3.6 FEA OF BCJ7

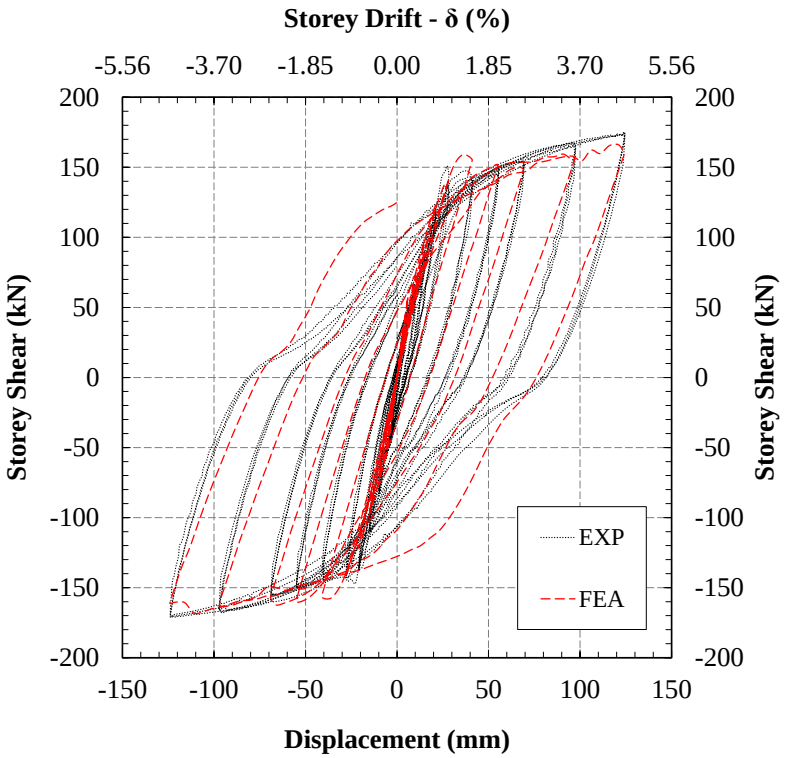

Figure 6.80: Storey shear vs. drift ratio of the 4x4 mesh under full cyclic

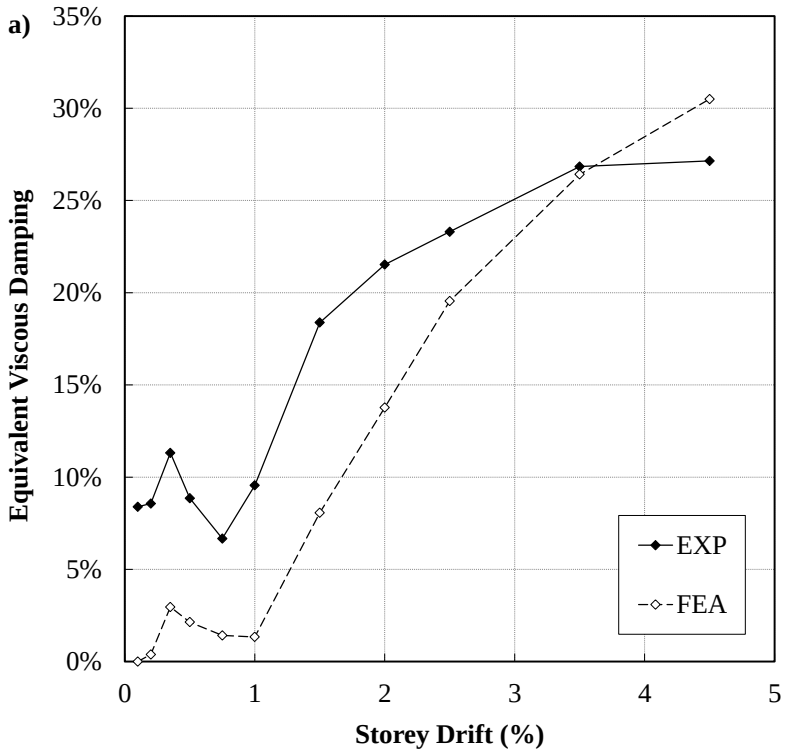

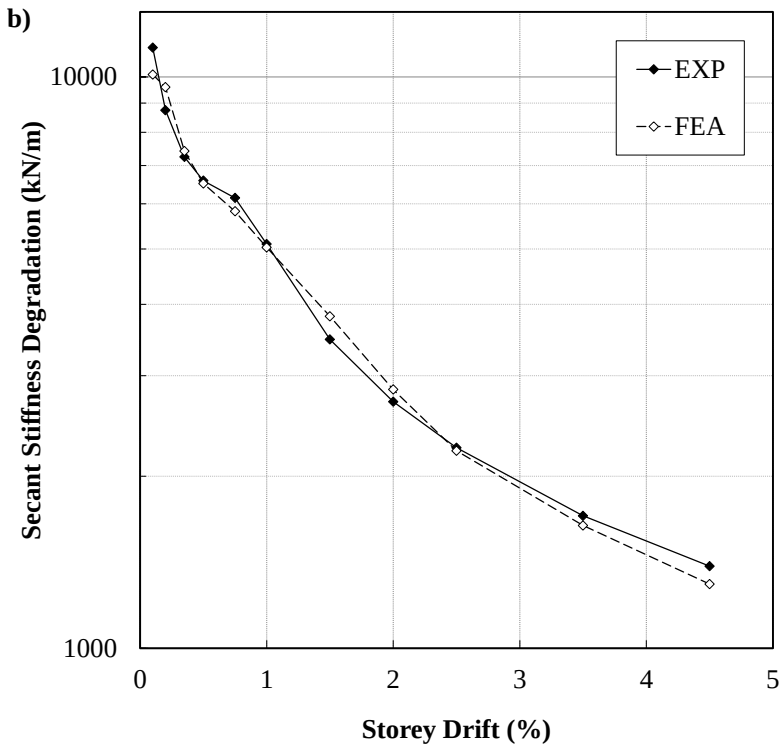

Figure 6.81: Comparison of a) damping and b) stiffness between the experiment and FEA

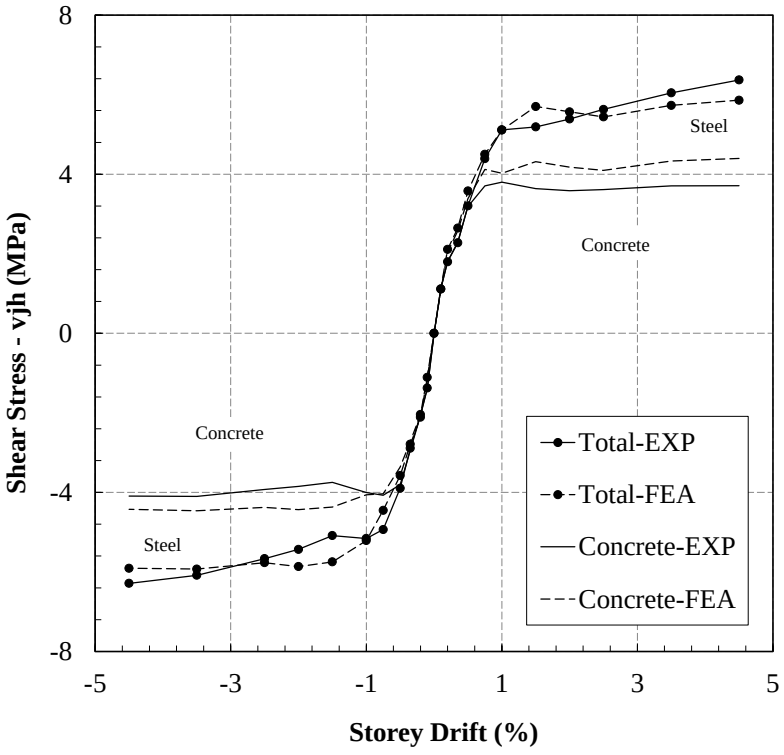

Figure 6.82: Steel and concrete contributions in taking joint shear force (FEA vs. EXP)

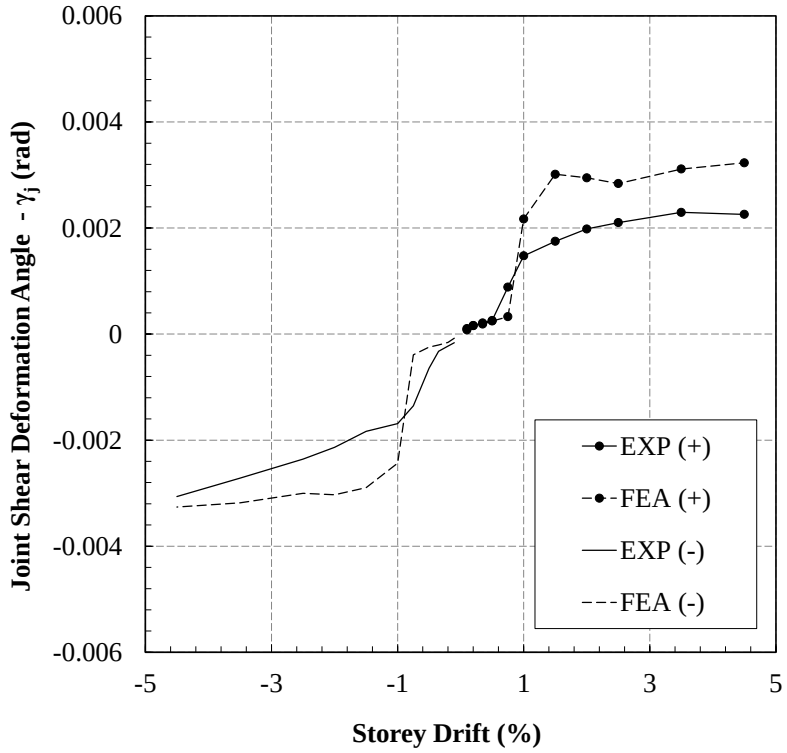

Figure 6.83: Comparison of the predicted joint shear deformation angle vs. experiment

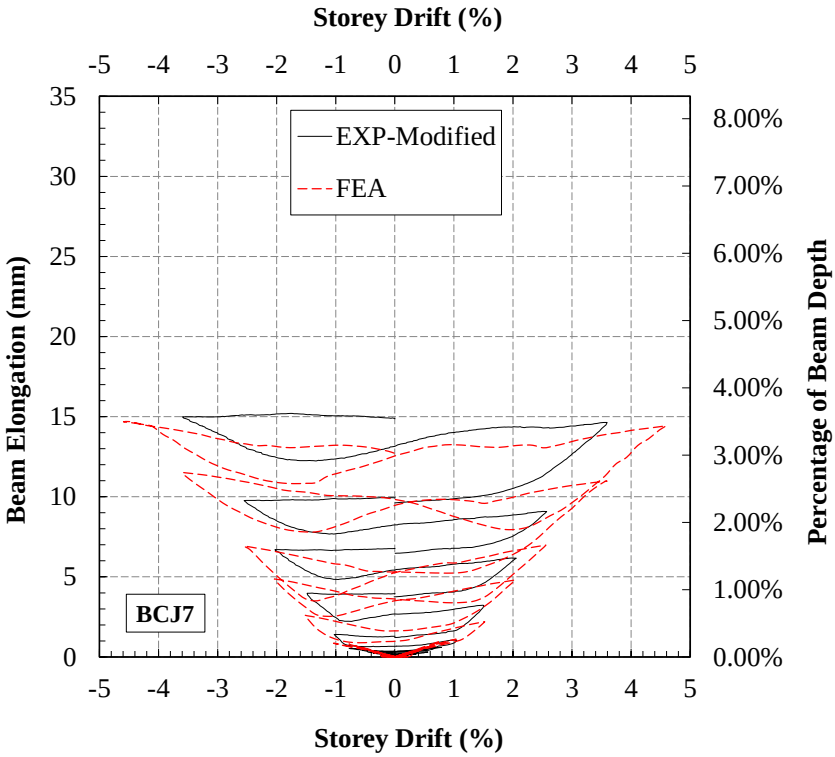

Figure 6.84: Elongation of beam at the plastic hinge zone

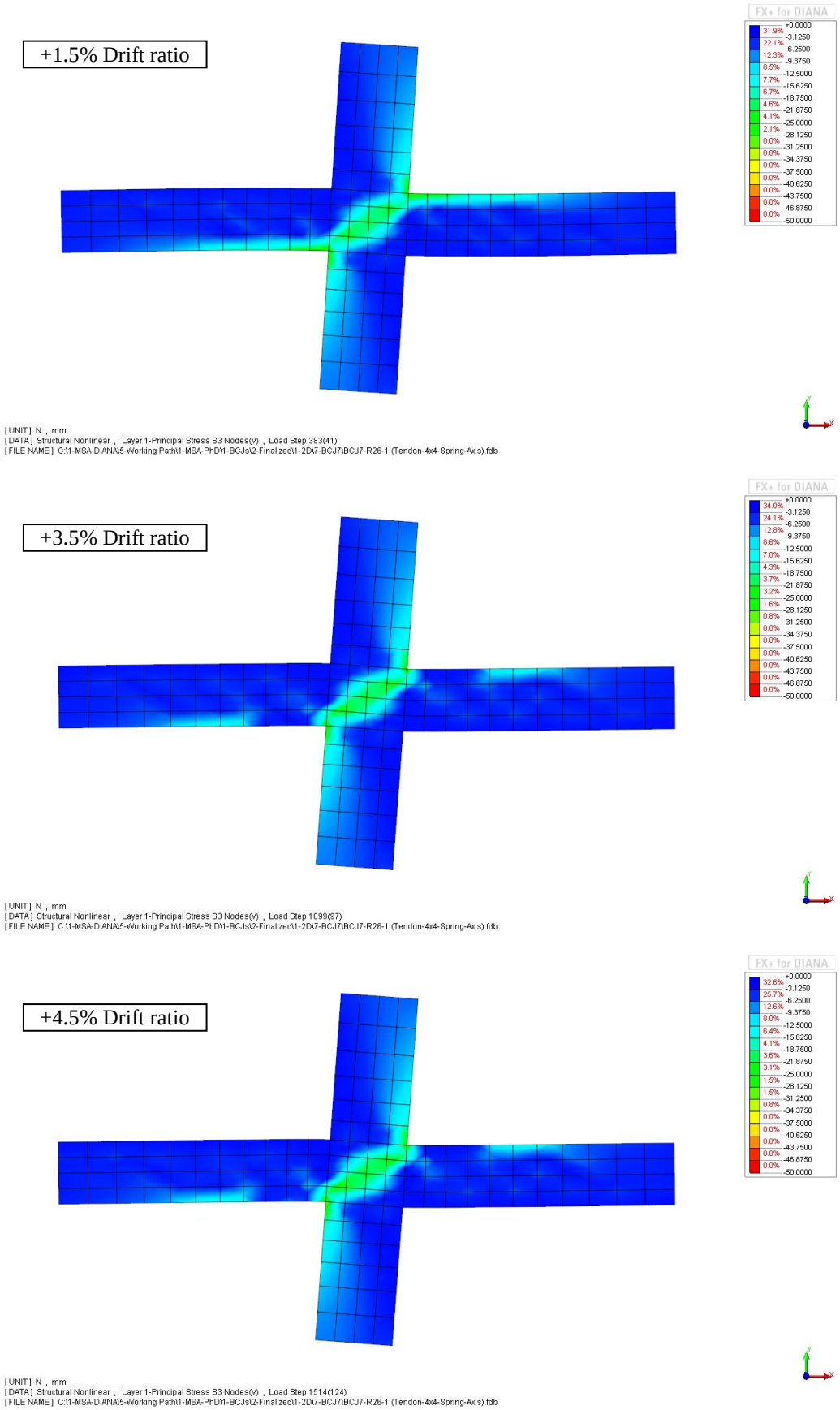

Figure 6.85: Evolution of the principal compressive stress in joint, beam and column

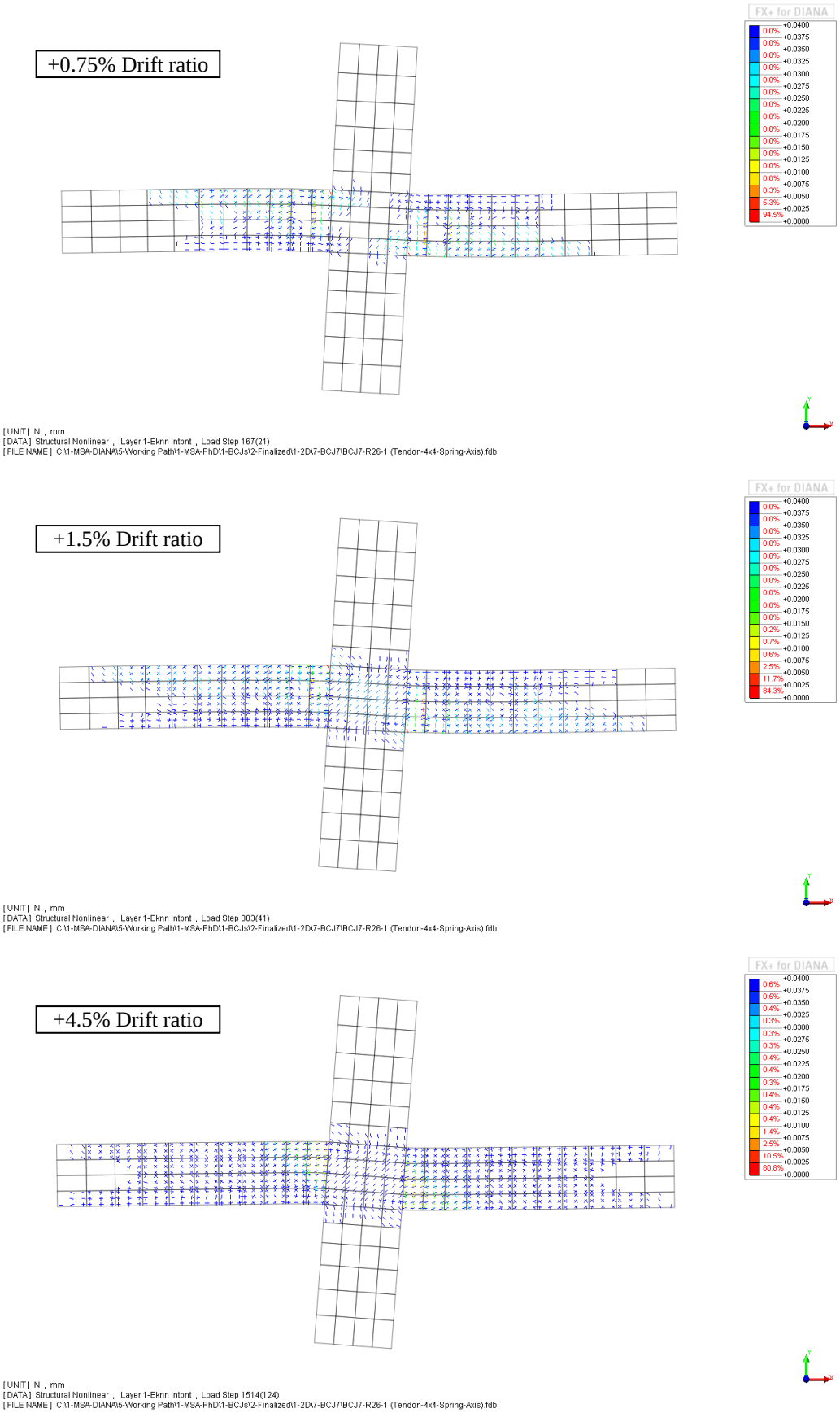

Figure 6.86: Crack formation in different drift ratios predicted by the FEA

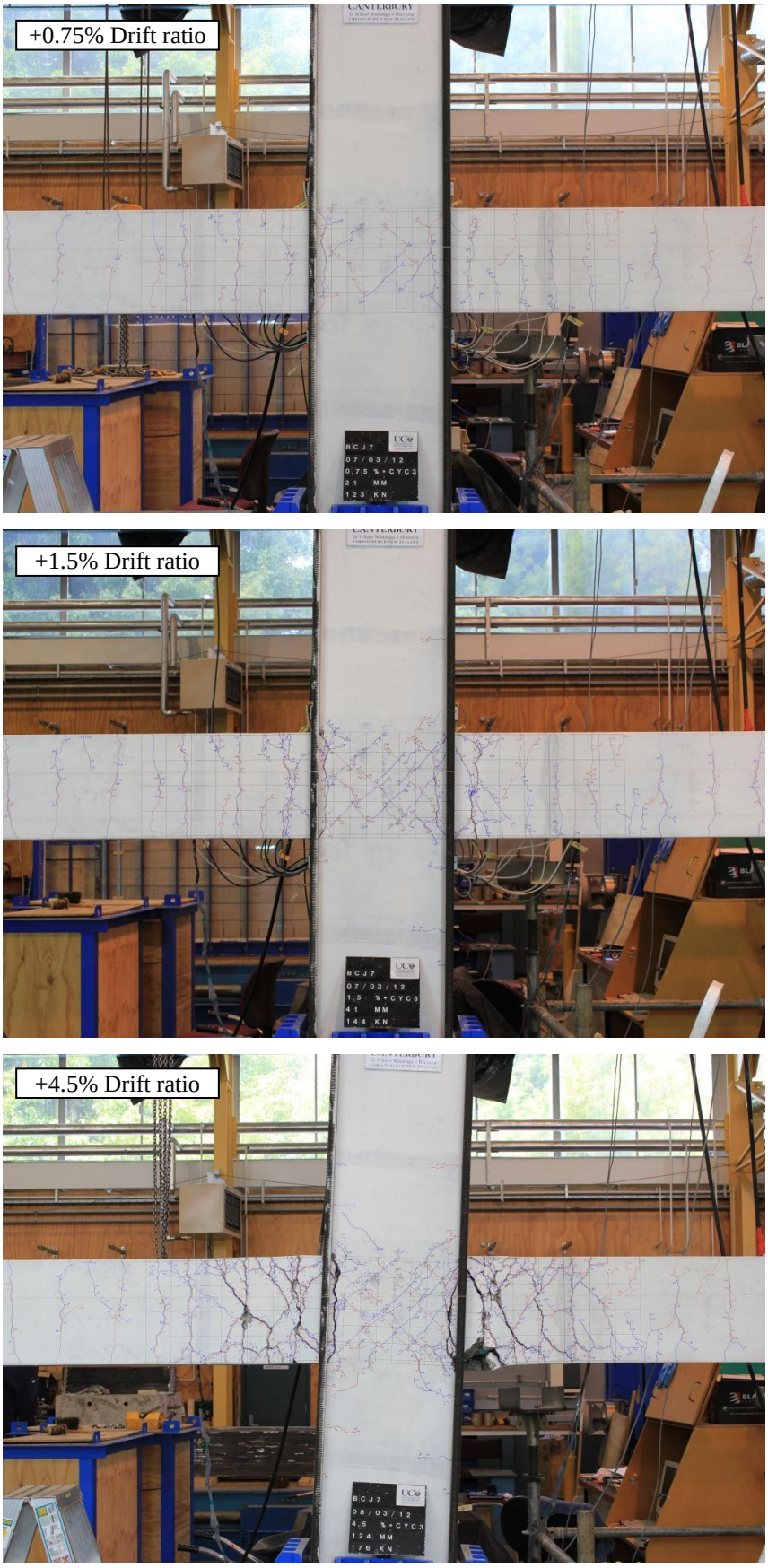

Figure 6.87: Experimental crack formation in different drift ratios

6.6 CONCLUSIONS

In this study, the finite element based computer software "DIANA" was used to model the seismic performance of HSSCC beam-column joints (BCJ) under cyclic loading. The concrete and steel were modelled used the total-strain rotating crack and Menegotto-Pinto constitutive material models, respectively. Full bond between reinforcement and concrete was defined because the BCJs were designed following the current New Zealand standards for seismic forces and debonding of main bars was not an expected mode of failure. Two-dimensional curved-shell elements (capable of capturing both in and out of plane displacements and forces) were utilized for modelling concrete. Both longitudinal and transverse reinforcement were defined using the perfect-bond embedded reinforcement option available in DIANA. Nonlinear analysis was performed on the simulated specimens and the following conclusions were deduced.

Pushover analyses were conducted first to get basic idea of the pros and cons of the model developed; pushover analysis was chosen for its simplicity, stability of analysis, better convergence of the results and lesser time requirement. The appropriateness of the finite element model and mesh sensitivity were checked and it was found that the model was not very sensitive to the mesh discretization. Fine tuning of the model and suitability of the material models were decided at this stage. As expected, the peak loads showed higher values in the pushover analysis compared to the back bone of the experimental cyclic load-displacement curves.

Simulated BCJs were also subjected to the same cyclic loading protocol as in the experiments. A much closer match was observed between the peak loads of the FEA and experimental results at each drift cycle; which proved that the material models could reasonably capture cyclic deterioration. The hysteresis response captured by FEA also showed a very close agreement to that of the actual tests. However, a lower pinching was predicted in the FEA; which was attributed to the limitations of the material models. Mesh sensitivity was also performed for the cyclic loading and again little dependency to mesh discretization was observed.

The equivalent viscous damping and peak to peak secant stiffness were calculated using the FE results and compared with those of the experimental ones. In both cases, a reasonable agreement was observed between the analysis and experimental results. The contributions of concrete and shear reinforcement to the applied joint shear force were calculated and a close agreement between the FEA and experimental values was noticed. In addition, the predicted joint shear deformations closely agreed with those derived from the potentiometers installed on the joint panel.

The analytical strain profiles in the joint shear stirrups were compared with the results of strain gauges in the experiment and the overall pattern and extent of strain development in FEA conformed to those in experiments. Elongation of the beam in the plastic hinge zones was also extracted from the FEA results. Due to the fact that the FE analysis was unable to capture the additional material deterioration once a loading cycle was repeated more than once, the initial elongations were not close enough between the analysis and experiment. However once the experimental results were modified and the effect of additional loading cycles on elongation were excluded, results were comparable.

Development of compression strut within the joint and its evolution in the subsequent cycles were illustrated in the form of contour graphs. The cracking pattern at different drift ratios were further compared to the one recorded in the experiment and a close agreement was observed. Overall, the FE predictions performed using nonlinear analysis with DIANA, showed a reasonable agreement with the actual experimental test results. This also shows that the selected finite element based software with its implemented material models and element library was capable of dealing with the complexities involved in modelling and analysing HSSCC reinforced concrete beam-column joints.(Soleymani Ashtiani et al., 2014)

6.7 REFERENCES

Balan, TA, Filippou, FC & Popov, EP 1998, 'Hysteretic Model of Ordinary and High-Strength Reinforcing Steel', Journal of structural engineering New York, N.Y., vol. 124, no. 3, pp. 288-297.

Belarbi, A & Hsu, TTC 1994, 'Constitutive laws of concrete in tension and reinforcing bars stiffened by concrete', ACI Structural Journal, vol. 91, no. 4, pp. 465-474.

Cofie, N & Krawinkler, H 1985, 'Uniaxial Cyclic Stress-Strain Behavior of Structural Steel', Journal of Engineering Mechanics, vol. 111, no. 9, pp. 1105-1120.

De Borst, R 1987, 'Smeared cracking, plasticity, creep, and thermal loading—A unified approach', Computer Methods in Applied Mechanics and Engineering, vol. 62, no. 1, pp. 89-110.

Deaton, JB 2013, Nonlinear Finite Element Analysis of Reinforced Concrete Exterior Beam-Column Joints with Nonseismic Detailing Georgia Institute of Technology, Atlanta, Georgia, The United States of America.

Dhakal, RP & Maekawa, K 2002a, 'Modeling for postyield buckling of reinforcement', Journal of Structural Engineering, vol. 128, no. 9, pp. 1139-1147.

Dhakal, RP & Maekawa, K 2002b, 'Path-dependent cyclic stress-strain relationship of reinforcing bar including buckling', Engineering Structures, vol. 24, no. 11, pp. 1383-1396.

DIANA 2012, DIANA Manual Release 9.4.4, TNO DIANA BV, Delft, The Netherlands.

Dinakar, P, Babu, KG & Santhanam, M 2008, 'Mechanical properties of high-volume fly ash self-compacting concrete mixtures', Structural Concrete, vol. 9, no. 2, pp. 109-116.

Dodd, LL & Restrepo-Posada, JI 1995, 'Model for predicting cyclic behavior of reinforcing steel', Journal of structural engineering New York, N.Y., vol. 121, no. 3, pp. 433-444.

Felekoglu, B, Turkel, S & Baradan, B 2007, 'Effect of water/cement ratio on the fresh and hardened properties of self-compacting concrete', Building and Environment, vol. 42, no. 4, pp. 1795-1802.

Fleury, F, Reynouard, JM & Merabet, O 1999, 'Finite element implementation of a steel-concrete bond law for nonlinear analysis of beam-column joints subjected to earthquake type loading', Structural Engineering and Mechanics, vol. 7, no. 1, pp. 35-52.

Gomes, A & Appleton, J 1997, 'Nonlinear cyclic stress-strain relationship of reinforcing bars including buckling', Engineering Structures, vol. 19, no. 10, pp. 822-826.

Heo, Y, Zhang, G, Kunnath, S & Xiao, Y 2009, 'Modeling cyclic behavior of reinforcing steel: Relevance in seismic response analysis of reinforced concrete structures', Key Engineering Materials, vol. 400-402, pp. 301-309.

Hoehler, MS & Stanton, JF 2006, 'Simple phenomenological model for reinforcing steel under arbitrary load', Journal of Structural Engineering, vol. 132, no. 7, pp. 1061-1069.

Hordijk, D 1991, Local Approach to Fatigue of Concrete Delft University of Technology, Delft, The Netherlands.

Hoshikuma, J, Kawashima, K, Nagaya, K & Taylor, AW 1997, 'Stress-strain model for confined reinforced concrete in bridge piers', Journal of structural engineering New York, N.Y., vol. 123, no. 5, pp. 624-633.

Kulkarni, SA & Li, B 2009, 'Seismic behavior of reinforced concrete interior wide-beam column joints', Journal of Earthquake Engineering, vol. 13, no. 1, pp. 80-99.

Kulkarni, SA, Li, B & Yip, WK 2008, 'Finite element analysis of precast hybrid-steel concrete connections under cyclic loading', Journal of Constructional Steel Research, vol. 64, no. 2, pp. 190-201.

Li, B & Cao Thanh Ngoc, T 2009a, 'Seismic behavior of reinforced concrete beam-column joints with vertically distributed reinforcement', ACI Structural Journal, vol. 106, no. 6, pp. 790-799.

Li, B & Kulkarni, SA 2010, 'Seismic behavior of reinforced concrete exterior wide beam-column joints', Journal of Structural Engineering, vol. 136, no. 1, pp. 26-36.

Li, B, Tran, CTN & Pan, T-C 2009b, 'Experimental and numerical investigations on the seismic behavior of lightly reinforced concrete beam-column joints', Journal of Structural Engineering, vol. 135, no. 9, pp. 1007-1018.

Litton, RW 1974, A Contribution to the Analysis of Concrete Structures Under Cyclic Loading University of California, Berkeley,

Mander, JB, Priestley, MJN & Park, R 1988a, 'Observed Stress-Strain Behavior of Confined Concrete', Journal of structural engineering New York, N.Y., vol. 114, no. 8, pp. 1827-1849.

Mander, JB, Priestley, MJN & Park, R 1988b, 'Theoretical Stress-Strain Model for Confined Concrete', Journal of structural engineering New York, N.Y., vol. 114, no. 8, pp. 1804-1826.

Menegotto, M & Pinto, E 1973, 'Method of Analysis for Cyclically Loaded Reinforced Concrete Plane Frames Including Changes in Geometry and Non-Elastic Behaviour of Elements Under Combined Normal Force and Bending ', in IABSE Symposium on the Resistance and Ultimate Deformability of Structures Acted on by Well-Defined Repeated Loads, Lisbon, Portugal.

Monti, G & Nuti, C 1992, 'Nonlinear cyclic behavior of reinforcing bars including buckling', Journal of structural engineering New York, N.Y., vol. 118, no. 12, pp. 3268-3284.

NZS3101 2006, 'NZS3101 Concrete structures standard Parts 1 & 2: The Desing of Concrete Structures and Commentary'. Standards New Zealand, Wellington, New Zealand, p. 698.

Orakcal, K, Massone, LM & Wallace, JW 2006, Analytical Modeling of Reinforced Concrete Walls for Predicting Flexural and Coupled-Shear-Flexural Responses, Pacific Earthquake Engineering Research Center, University of Californina, Los Angeles

Popovics, S 1973, 'A Numerical Approach to the Complete Stress-Strain Curve of Concrete', Cement and Concrete Research, vol. 3, no. 5, pp. 583-599.

Rodriguez, ME, Botero, JC & Villa, J 1999, 'Cyclic stress-strain behavior of reinforcing steel including effect of buckling', Journal of structural engineering New York, N.Y., vol. 125, no. 6, pp. 605-612.

Sasmal, S, Novak, B & Ramanjaneyulu, K 2010, 'Numerical analysis of under-designed reinforced concrete beam-column joints under cyclic loading', Computers and Concrete, vol. 7, no. 3, pp. 203-220.

Selby, RG & Vecchio, FJ 1997, 'A constitutive model for analysis of reinforced concrete solids', Canadian Journal of Civil Engineering, vol. 24, no. 3, pp. 460-470.

Selby, RG, Vecchio, FJ & Collins, MP 1996, 'Analysis of reinforced concrete members subject to shear and axial compression', ACI Structural Journal, vol. 93, no. 3, pp. 306-315.

Soleymani Ashtiani, M, Dhakal, RP & Scott, AN 2014, 'Analytical Investigation on Seismic Performance of a High-Strength Self-Compacting Concrete Beam-Column Joint', in Tenth U.S. National Conference on Earthquake Engineering, Anchorage, Alaska.

Thorenfeldt, E, Tomaszewicz, A & Jensen, JJ 1987, 'Mechanical Properties of High-Strength Concrete and Applications in Design', in Proc. Symp. Utilization of High-Strnegth Concrete, Stavanger, Norway.

Vecchio, FJ & Collins, MP 1986, 'Modified Compression-Field Theory for Reinforced Concrete Elements Subjected to Shear', Journal of the American Concrete Institute, vol. 83, no. 2, pp. 219-231.

7 CONCLUSIONS AND RECOMMENDATIONS

In this research, seismic performance of reinforced concrete (RC) structures with high-strength self-compacting concrete (HSSCC) was investigated. The study focused on the following five main objectives as set out earlier in Chapter 1: (i) development and material characterisation of a HSSCC mix; (ii) laboratory investigations on monotonic bond performance of deformed bars in HSSCC; (iii) design and fabrication of a modified beam specimen and an innovative test setup to investigate cyclic bond performance of deformed bars in HSSCC; (iv) experimental investigations on seismic performance of RC beam-column joint (BCJ) subassemblies cast with HSSCC; and (v) nonlinear finite element analysis (FEA) of the tested BCJ specimens using DIANA. These objectives were thoroughly investigated and described in different chapters of this dissertation. The main findings and limitations of this research are presented in this chapter and possible areas for future research are also identified.

7.1 MAIN FINDINGS

7.1.1 MIX DESIGN AND MATERIAL CHARACTERISATION OF HSSCC

Self-compacting concrete (SCC) has undergone more than twenty years of advancement since it was first introduced to the field of civil engineering. Researchers have investigated its fresh and mechanical properties; some have also scrutinized the performance of SCC in structural members. Nevertheless, some large-scale and complex structures (such as high-rise buildings, towers and offshore structure) require special concrete types with high-strength and high-performance characteristics. As a result, development and characterisation of material properties of such concrete mixes are of great interest to researchers. However, there exist only a few studies focusing on the material characterisation of HSSCC with no investigations on other properties (including seismic performance) of this concrete type. Chapter 2 of the thesis focused on investigating and responding to the first objective as set out earlier.

Following the Su et al. (2001) guidelines for normal strength SCC, HSSCC mix of compressive strength above 100 MPa was developed through several lab trials using locally available materials in New Zealand. This mix was later proved to be commercially reproducible and used in the fabricating RC BCJs. Two comparable benchmark concrete mixes of conventionally vibrated high-strength concrete (CVHSC), were also developed for comparison purpose; namely CVHSC-1 (comparable mix proportions and w/b ratio) and CVHSC-2 (comparable compressive strength). Rheological properties of HSSCC were thoroughly investigated using the available fresh property test methods and checked against the admissible limits suggested in different standards (EFNARC, 2002,2005) and literature (Hwang et al., 2006). Specimens were cast using both HSSCC and CVHSC mixes and tested following the ASTM, New Zealand and Australian testing protocols. The microstructural (resistivity and scanning electron microscope) and physical properties (compressive, splitting tensile and flexural strengths as well as modulus of elasticity and shrinkage) of the two concrete mixes were determined.

It was found that when the mix proportions were the same (HSSCC and CVHSC-1) HSSCC developed a considerably higher (by 15 MPa) compressive strength compared to that of CVHSC. It was believed that the higher strength of HSSCC was due to the improved homogeneity, lower possibility of segregation, better packing factor, and larger quantity of super plasticizer (SP) in HSSCC compared to those in CVHSC. Therefore, CVHSC with a lower w/b ratio was required in order to achieve compressive strength comparable to HSSCC. As a result, CVHSC-2 mix was designed using a w/b ratio of 0.27 as opposed to that of 0.3 of the HSSCC; both mixes developed virtually equal compressive strengths.

Compressive strength development of HSSCC versus time was checked against the model proposed in EN1992-2 (2005) and the model was found to be inefficient in predicting the results. Thus a new model was proposed based on the 3-day strength of HSSCC (as opposed to the 28-day strength based EN1992 model) which was more effective in predicting the strength development versus time at an early age. In the proposed model, the effect of incorporating fly ash in the concrete mix was taken care of through the correction factors which can be calibrated to predict the strength development of other concrete types. The splitting tensile strength of CVHSC was slightly higher than that of HSSCC before the age of 28 days; this was compensated by a higher homogeneity and lower amount of voids

in HSSCC after 28 days. Similar pattern was observed in the flexural strengths (inherently resulting from tensile strength) of the different concrete types. The available expressions underestimated the flexural strength of HSSCC; thus a model was proposed to agree better with the experimental results. As expected, HSSCC showed a smaller modulus of elasticity resulting from its lower coarse aggregate content. HSSCC also exhibited a slightly higher shrinkage resulting from its higher amount of paste. The EN1992-2 (2005) model was modified using relevant correcting factors such that it could predict the drying shrinkage results accurately.

7.1.2 MONOTONIC BOND PERFORMANCE OF DEFORMED BARS IN HSSCC

Bond between reinforcement and concrete is the governing factor in assuring that the composite reaction between the two materials takes place in an RC member. Most of the RC analysis theories have formed around the fact that a perfect bond exists between the concrete and steel. However, the highly nonlinear behaviour of RC members after cracking contradicts this assumption. Given an identical geometry of reinforcement, when the mix proportion, compressive strength and splitting tensile strength of concrete changes, bond could still vary considerably. SCC has shown different bond behaviour compared to that of conventionally vibrated concrete (CVC). Many researchers have investigated the bond performance of different reinforcement in SCC. However, even the amount of research on bond behaviour of CVHSC is very limited let alone that of HSSCC. Also little research has been performed on bond performance of deformed bars and concrete in the post-yield stage. Therefore, Chapter 3 focused on investigating the bond between HSSCC and deformed bars under monotonic loading as an effort to respond to the second objective stated in the Chapter 1.

The HSSCC and CVHSC-2 mix proportions designed earlier (see Chapter 2) were used to fabricate specimens for two different series of commonly used pullout tests (see Chapter 3); a total of twenty-one and thirty specimens in the first and second series, respectively. The concrete type, compressive strength, bond length, bar diameter, steel grade, and loading type were considered as variables. The first series was mainly designed to characterize the different bond characteristics of HSSCC and CVHSC. It was observed that the difference of bond behaviour between HSSCC and CVHSC diminished along with an

increase in the strength of concrete. However, a unique phenomenon was noticed in the bond behaviour of different steel grades in the post-yield region; i.e. higher grade steel bars showed greater bond strength compared to the lower grade steel ones. This coincidence was first correlated with possible differences in the geometry of the ribs between the two grade bars; this was later ruled out as measurements showed that the rib geometries were identical between the two bars. A second hypothesis formed around the lower lateral stiffness of ribs in the lower grade steel bars; this was also refuted by cutting open the specimens and measuring the rib geometry of different steel grades. Finally, the observed behavioural difference was hypothetically associated with the different nature of bar diameter reduction between the lower and higher grade steel reinforcement. However, delving the available literature on bond did not reveal any supporting evidence.

This necessitated the design and fabrication of the second series pullout specimens instrumented such that the observed phenomenon could be captured. The new bond pullout specimens were equipped with strain gauges and they were tested in a slightly different test setup with more control and accuracy. In addition, changes of bar diameter before and after the test were measured. The reasons as to why the other investigations were unable to identify the mentioned phenomenon were classified; namely choosing short bond lengths, employing normal strength concretes, considering the elastic response range of steel bars, focusing on other parameters affecting bond, and not incorporating different grade bars within an investigation with no comparison between their behaviour. The diameter of the higher grade bars showed about half of the reduction occurred to the diameter of lower grade ones. This meant that the physical bearing of the ribs was considerably higher in higher grade bars resulting in higher bond strength. Whereas the bar diameter of the lower grade steel was reduced such that the ribs were pulled out of their locations, the bearing was deteriorated and bond failure triggered.

Also noticed was a yield plateau in the bond vs. slip curves; this was similar to the one in the axial stress-strain curves. Here again not only the previous literature did not explicitly discern the occurrence of such plateau; but also described how the yield plateau of the steel stress-strain behaviour disappears in the member response (Fib-Bulletin-10, 2000). The only indirect suggestion of such behaviour was found in the studies performed by Maekawa et al. (2003); suggesting that a unique relationship existed between the bond stress, slip and strain. The model proposed by Maekawa et al. (2003) for predicting the

interrelationship between the three components was modified and expanded such that it could reasonably match the experimental study of this research. The CEB-FIP-MC (1993) model code prosed for bond-slip behaviour of bars in concrete was modified such that it could predict the occurrence of the yield plateau in the bond-slip response. Relevant factors capable of being calibrated for different test situations were also implemented in the proposed model.

7.1.3 CYCLIC BOND PERFORMANCE OF DEFORMED BARS IN HSSCC

Bond between reinforcing steel and concrete in RC members is of great importance. As bond varies considerably under different loading types, it is therefore imperative that laboratory investigations are conducted to obtain a proper picture of bond performance under the most realistic conditions representing real structures. In service conditions, RC structures are always subjected to some form of reversed (cyclic) type loading; be it earthquake, wind or live loads. Therefore, while developing simple experimental tests (such as pullout) is crucial for basic understanding of bond mechanisms, they may not necessarily form an appropriate representation of real conditions. Therefore, there is a need to scrutinizing bond using a cyclic specimen and test setup (the third objective of this research); this has been addressed in Chapter 4.

Pullout specimens and test setups are considered the most commonly used method for testing bond between reinforcing steel and concrete even under cyclic loads. Nevertheless, the concrete and steel are always under opposing state of stresses; i.e. when the concrete is under compression, the steel is under tension and vice versa. However, in RC members both materials work under the same state of stress. As a solution to this problem, RILEM-FIP-CEB (1973) provided a beam specimen (see Chapter 4 for details) in which bond can be investigated under realistic stress conditions. But the specimen proposed by RILEM can only take monotonic loads. In this research, the RILEM beam specimen was modified such that it could take reversed cyclic loads. In addition, an innovative test setup was proposed to complement the modified specimen for being tested under a fully reversed cyclic loading regime.

The main modifications applied to the specimen included the reduction of bond length to suit the higher strength of the HSSCC, relocation of the bond position towards the centre of the beam to decrease the vulnerability of the bar to premature buckling and design of a steel hinge capable of taking both tensile and compressive forces. The specimen was clamped to the test setup using an arrangement of nuts and bolts, and supports and loading points consisted of special rollers and pins (see Chapter 4). The functionality of both the specimen and test setup was checked in a sample test, and eighteen beam specimens were tested using different variables to ensure the repeatability of the test results. It was shown that the designed test setup was suitably capable of applying reversed cyclic loads to the modified beam specimen. The test results were compared with those of benchmark specimens (pullout tests) and the validity of the results were confirmed. It was observed that the maximum bond strength was similar between the pullout and beam specimens under monotonic and cyclic loading, respectively. However, substantial deterioration of the bond stress occurred in the cyclic test once the maximum bond strength was achieved. Concrete composition (proportion of coarse and fine aggregates) was found to affect the slip values.

In an effort to scrutinize the performance of the modified test specimen and cyclic setup, possible drawbacks of the proposed testing method were investigated. The unsupported portion of the bar between the two bonded regions could possibly trigger premature buckling; specially in the gap between the two half-beams. If pull out does not happen (due to longer bond length and higher concrete strength) before the steel bar enters its post-yield phase or larger fully reversed displacement cycles are applied to the specimen, the unsupported portion of the bar starts to buckle. This was proved in one of the beam specimens where a combination of these critical factors was present in the test; therefore, the specimen failed due to breakage of the bar resulting from buckling. The premature buckling of the bar can be avoided by supporting the free length of the bar, reducing the bond length, or limiting the compressive displacement cycles. Another limiting factor of the proposed test was the physical constraint in upward and downward movement of the centre of the specimen. This limitation was imposed by the roller supports and the length of their rails. However, this was not found to affect the cyclic nature of the test as pullout would have initiated and full bond deterioration could be captured before reaching the displacement limits.

The sample beam specimen was modelled using DIANA (nonlinear finite element analysis software) in order to examine the capability of the software in predicting bond. The steel, concrete and the bond between the two materials were modelled using one-dimensional (1D) beam, two-dimensional (2D) curved shell and 2D interface elements, respectively. The interface elements were characterized by the monotonic bond-slip envelope derived from the experiments. Under monotonic loading, the implemented bond model in DIANA was capable of accurately predicting the bond-slip behaviour, cracking pattern and stress development. However, the FE hysteresis cyclic loops were deficient in correctly representing the experimental results due to the secant unloading/reloading stiffness defined in the concrete cyclic model. Therefore, an improved cyclic bond constitutive model should be implemented in DIANA to enhance the agreement between the FEA and experimental results. This will potentially increase the accuracy of the software in predicting bond critical problems such as non-seismically detailed BCJs.

7.1.4 EXPERIMENTAL INVESTIGATIONS ON SEISMIC PERFORMANCE OF BCJS CAST WITH HSSCC

The BCJs of RC structures are known for their behavioural complexity and their performance substantially affects the overall response of the structure. Therefore, numerous investigations have focused on explaining the behaviour, identifying the failure mechanisms and proposing improvements on the performance of BCJs. As mentioned before, HSSCC has gained interest only in the past few years and the amount of research on its structural performance is very limited. Considering the advantages of HSSCC, its applications in structural members can potentially enhance the performance of RC structures. This might be of more interest in seismically active regions like New Zealand where dealing with RC BCJs becomes highly intricate. Nevertheless, before this special concrete can widely be used in earthquake prone areas, its seismic performance needs to be fully scrutinized. As a result, the fourth objective of this study was set to investigate the seismic performance of internal BCJs cast with HSSCC; this was achieved in Chapter 5.

Seven full-scale RC interior BCJs were designed following the current concrete structure standard in New Zealand (NZS3101, 2006); namely four of HSSCC, one of CVHSC, one of CVC, and one of CVC with HSSCC in the joint area. Variables such as concrete type

and strength, steel grade, joint shear stirrups, axial load, and direction of casting were considered in the design of BCJs. All specimens were tested under a displacement controlled reversed cyclic loading regime to simulate the impact of seismic excitations. BCJ subassemblies were instrumented with load cells, potentiometers and strain gauges to facilitate capturing the required data for analysis of seismically important features. Experimental data collected from the tests was used to calculate the hysteresis response, damping, stiffness, strain development in the joint stirrups, contribution of steel and concrete in joint shear stress, contribution of different components in overall drift, and elongation of plastic hinge zone.

All specimens were tested up to 4.5% drift (which was the limiting displacement imposed by the geometry of the test setup) and plastic hinges were formed in beams near the column faces. None of the specimens had failed at the end of the 4.5% drift cycle; but the detected mode of failure (plastic hinge formation in the beams) remained the expected final mode of failure with excessive loss of capacity if higher drifts were applied. Higher and lower strength subassemblies developed similar levels of ductility. Due to higher compressive strength and better bond properties, HSSCC specimens developed less cracks in their joint area. Hysteresis damping and stiffness reduction were similar between the BCJs of comparable strength. The contribution of steel and concrete in joint shear force were comparable between different BCJs. Even the subassembly with about half of the joint shear stirrups did not show any signs of joint failure and the stirrups in the joint did not yield. As expected, beam deformation contributed the most towards the overall drift of the specimens. Elongation of plastic hinge followed a similar pattern among the specimens; only the BCJ with higher grade steel showed a slightly lower elongation.

Overall, the laboratory tests performed in this research proved that HSSCC can safely be incorporated in structural members with high congestion of reinforcement. In addition, the seismic performance of HSSCC was verified in comparison with the benchmark CVC and CVHSC specimens with no noticeable compromise in any of the seismically important features. As a result, designing engineers and builder can now confidently use HSSCC in construction of RC members and structures subjected to earthquake excitations.

7.1.5 NONLINEAR FINITE ELEMENT ANALYSIS OF HSSCC BCJS

Investigating the performance of RC structures and structural members through experimental tests has always been popular among researchers. Nevertheless, due to limited time and availability of resources it is not always feasible to consider the effect of all parameters involved in experimental investigations. Thus, analytical modelling and numerical simulations have frequently been used to complement the laboratory tests. Finite element (FE) method has been utilized in many investigations to model the behaviour of RC structures. It has become famous for its ability to deal with the complex nonlinearity involved in concrete cracking. Therefore, the last objective of this study was set to incorporate DIANA (a nonlinear FE based software) in modelling and prediction of the laboratory experiments performed on cyclic response of BCJs. This objective was achieved in Chapter 6.

Total strain rotating crack model and Menegotto et al. (1973) model were used to simulated concrete and steel, respectively. As the BCJ subassemblies were modelled based on the current New Zealand concrete standard, bond between reinforcement and concrete was not expected to be an issue; therefore, bond was assumed to be perfect in modelling considerations. The material models were calibrated using the laboratory test results and available expressions in the literature. Thorenfeldt et al. (1987) and Hordijk (1991) models were used for compression and tension responses of the total strain rotating crack model, respectively. Suitable element sizes were chosen after performing a mesh sensitivity analysis. Two-dimensional curved shell elements were utilized to model the concrete and steel supports; whereas, the reinforcing bars were modelled using perfect-bond embedded uniaxial elements. Nonlinear pushover and cyclic analyses were performed on the model and the results were compared between the experiments and the FEA.

Pushover analysis was initially performed in order to check the functionality of the model, mesh sensitivity, stability of the analysis, convergence of the results, and time requirements. The model and constitutive material responses were fine-tuned at this stage. As expected, the FE pushover backbone curve showed slightly higher values compared to those of the experimental cyclic ones. However, the overall trend showed good agreement between the FEA and experimental results. The cyclic loading protocol used in the tests

was also applied to the FE model. The FE cyclic backbone curve showed a very close agreement with that obtained from the experiment; this resulted from the implementation of the material degradation under cyclic loading. In addition, the hysteresis response of the BCJ subassemblies was accurately predicted by the FEA. A lower pinching was predicted by the FEA which was attributed to the material model limitations. Except for the elongation of the plastic hinge zone, all of the other seismically important features (detailed in Chapter 5 and 6) were reasonably predicted by the FEA.

Stress development, force transfer and cracking patterns derived from the FE model, showed that the mechanics of BCJ behaviour were well captured by DIANA. Modelling facilities, material library, nonlinear analysis procedures, and post processing of the results implemented in DIANA proved to be versatile and comprehensive. Overall, the FE software DIANA was capable of dealing with the complex nature of the BCJ response to reversed cyclic loading.

7.2 RECOMMENDATIONS FOR FUTURE RESEARCH

After achieving the objectives set forth in this research, here an effort has been made towards identifying possible areas for future research in order to complement the results accomplished in this study.

7.2.1 MIX DESIGN AND MATERIAL CHARACTERISATION OF HSSCC

Considering the current status of the available literature on HSSCC, this research provided a good database for microstructural and mechanical properties of this concrete type. However, there are a couple of areas demanding improvement and/or focused investigation in order to fully understand the behaviour of HSSCC.

- ✓ Developing a solid mix design procedure for designing HSSCC which is not yet explicitly available.
- ✓ Investigations on various mix proportions and influence of different constituent materials on the fresh and hardened properties of this special concrete type.

- ✓ Due to different proportions of coarse and fine aggregates in HSSCC and also the nature of higher strength material, an appropriate of concrete compressive stress block to be used in the design of HSSCC needs to be explored.
- ✓ The indirect tension test (splitting tensile strength) was used as an indication of the HSSCC tensile strength. Further research incorporating the direct tension test on HSSCC would facilitate a better understanding of its cracking behaviour.

7.2.2 MONOTONIC BOND PERFORMANCE OF DEFORMED BARS IN HSSCC

A thorough investigation was performed on bond performance of reinforcing steel in HSSCC and CVHSC with a focus on post-yield bond properties. It was found that the two concrete types performed equally well with similar bond performance under monotonic loading. Reduction of bar diameter after yielding was found to markedly affect the bond performance; however, more investigation is required on the following issues to provide a complete picture.

- ✓ Post-yield bond performance of reinforcement in concrete has not been the focus of many previous studies. As a result, this needs to be further investigated in order to isolate the impact of bond parameters on the post-yield bond performance.
- ✓ In this research, the reduction of bar diameter was only measured before and after the tests. Further research is necessary with progressive measurement of the bar diameter and observing the level and extent of the impact of this phenomenon on bond performance.
- ✓ The impact of bar diameter reduction on bond performance needs to be correlated with the available bond theories. Modifications should be proposed to the available predicting equations where necessary.
- ✓ The observed phenomenon should be implemented in analytical software (such as DIANA). This way the reduction of bar diameter and its impact on overall bond performance of deformed bars in concrete can be captured.

7.2.3 CYCLIC BOND PERFORMANCE OF DEFORMED BARS IN HSSCC

The RILEM monotonic beam specimen was modified and an innovative test setup was designed to cyclically test the specimen. Limitations and possible issues of the new test method were investigated; however, further improvement and additional research are required to expand the scope of the proposed method.

- ✓ In order to avoid premature buckling trigger, the loading protocol had to be adjusted and/or the bond length reduced to ensure bond failure before yield point. Further research is required on different methods of buckling control (such as using steel sheath) for the unsupported length of the bar between bond regions.
- ✓ The beam specimen consists of two half-beams and slip is measured for both parts. However, at the time of failure only one half-beam undergoes the full pullout. Considering the complexity of the test, obtaining failure in both half-beams can be of great interest. Therefore, research is required to develop a clamping mechanism capable of withstanding reversed loads. This way, once the bond strength is reached in one of the half-beams, the reinforcing bar can be clamped and test be continued until the failure occurs in the second half.
- ✓ It was observed that the current bond model implemented in DIANA was deficient in capturing the cyclic bond hysteresis loops. Improvement is necessary to increase its accuracy which would result in more accurate prediction of bond critical problems by DIANA.

7.2.4 EXPERIMENTAL INVESTIGATIONS ON SEISMIC PERFORMANCE OF BCJS CAST WITH HSSCC

Although investigating seismic performance of RC beam-column joints has been the focus of many previous studies, the amount of research is very limited on the behaviour of HSSCC under seismic excitations. This research provided an insight to the suitability and performance of HSSCC BCJs considering different variables. Yet it is necessary to delve more into the impact of critical factors affecting the performance of BCJs under cyclic loading.

- ✓ The amount of joint shear reinforcement suggested by the New Zealand concrete standard (NZS3101, 2006) was shown to be excessive to the shear demand requirement for HSSCC. More in-depth research is needed to find out the critical limits for the joint shear stirrups considering important parameters.
- ✓ An attempt was made towards designing a 500 grade steel BCJ specimen having comparable design capacity with that of 300 grade ones. Unfortunately, due to a mistake between drawings and fabrication, wrong diameter bars were used and the results were not comparable. It is advised that the seismic performance of HSSCC with high-strength steel is investigated.
- ✓ The casting direction was among the variables considered in design of BCJs in this research. No apparent differences were found between the seismic response of horizontally and vertically cast specimens. This proved that a properly designed HSSCC was not sensitive to the direction of casting. This needs to be further scrutinized in more laboratory tests.

7.2.5 NONLINEAR FINITE ELEMENT ANALYSIS OF HSSCC BCJS

Nonlinear finite element analysis software DIANA was used to model the experimentally tested specimens and the experimental results were successfully predicted by the analysis. Simplifying assumptions were used in modelling and analysis which can further be improved by incorporating the following recommendations.

- ✓ The hysteresis response of the implemented total strain rotating crack model in DIANA does not account for residual strains. This means that the cyclic response of concrete becomes overly pinched. In the current research, this was not an issue due to the BCJ response depending more on the steel hysteresis loops than the concrete model. However, the mentioned issue would become problematic in many other situations (like non-seismically detailed BCJ). Therefore, the implemented concrete cyclic model should further be improved.
- ✓ The currently implemented material models in DIANA do not account for progressive deterioration under repetitive loading. This means that even if an identical cycle is repeated more than once, there will not be any further degradation

of the material properties. Therefore, an improvement to the cyclic deterioration of the materials in DIANA could be an attractive research topic.

- ✓ The steel constitutive models currently implemented in DIANA do not account for deleterious effects of buckling. Incorporating one of the available buckling models into the steel hysteresis loops of DIANA would substantially increase the capability of the software in predicting buckling critical problems. In addition, the selection of backbone curve of the Menegotto-Pinto model is limited to a simple bilinear curve which reduces the accuracy of the model. Implementation of a multi-linear backbone curve would significantly increase the applicability of the model.
- ✓ As the BCJs were designed following the current New Zealand concrete standard, bond failure was avoided. Therefore, reinforcing bars were modelled assuming perfect bond with concrete. However, should the application of bond-slip be necessary, the cyclic response would not be accurately captured due to imperfect implementation of bond in DIANA. As a result, the bond model should further be improved for better prediction of cyclic behaviour.

7.3 REFERENCES

CEB-FIP-MC 1993, 'Model Code 1990: Design Code'. T. Telford, London.

EFNARC 2002, Specification and Guidelines for Self-Compacting Concrete, European Federation of Procedures and Applicators of Specialist Products for Structures

EFNARC 2005, The European Guidelines for Self-Compacting Concrete Specification, Production and Use, European Federation of Procedures and Applicators of Specialist Products for Structures

EN1992-2 2005, 'EN1992-2 Design of concrete structures'. Comite Europeen de Normalisation (CEN), Brussels, Belgium.

Fib-Bulletin-10 2000, 'Fib (CEB-FIP) Bulletin 10, Bond of reinforcement in concrete: state-of-art report', vol. 10., no. Book, Whole

Hordijk, D 1991, Local Approach to Fatigue of Concrete Delft University of Technology, Delft, The Netherlands.

Hwang, S-D, Khayat, KH & Bonneau, O 2006, 'Performance-based specifications of self-consolidating concrete used in structural applications', ACI Materials Journal, vol. 103, no. 2, pp. 121-129.

Maekawa, K, Pimanmas, A & Okamura, H 2003, Nonlinear mechanics of reinforced concrete, Spon Press, New York.

Menegotto, M & Pinto, E 1973, 'Method of Analysis for Cyclically Loaded Reinforced Concrete Plane Frames Including Changes in Geometry and Non-Elastic Behaviour of Elements Under Combined Normal Force and Bending ', in IABSE Symposium on the Resistance and Ultimate Deformability of Structures Acted on by Well-Defined Repeated Loads, Lisbon, Portugal.

NZS3101 2006, 'NZS3101 Concrete structures standard Parts 1 & 2: The Desing of Concrete Structures and Commentary'. Standards New Zealand, Wellington, New Zealand, p. 698.

RILEM-FIP-CEB 1973, 'Tentative recommendations, recommendations for reinforcing steel, bond test for reinforcing steel: 1- Beam test (7-II-28 D) 2- Pull-out test (7-II-128)', Materials and Structures, vol. 6, no. 2, pp. 79-118.

Su, N, Hsu, K-C & Chai, H-W 2001, 'A simple mix design method for self-compacting concrete', Cement and Concrete Research, vol. 31, no. 12, pp. 1799-1807.

Thorenfeldt, E, Tomaszewicz, A & Jensen, JJ 1987, 'Mechanical Properties of High-Strength Concrete and Applications in Design', in Proc. Symp. Utilization of High-Strength Concrete, Stavanger, Norway.

APPENDIX A – DEVELOPMENT AND PROPERTIES OF HIGH-STRENGTH SELF-COMPACTING CONCRETE (HSSCC)

A-1: TESTING FRESH PROPERTIES OF HSSCC

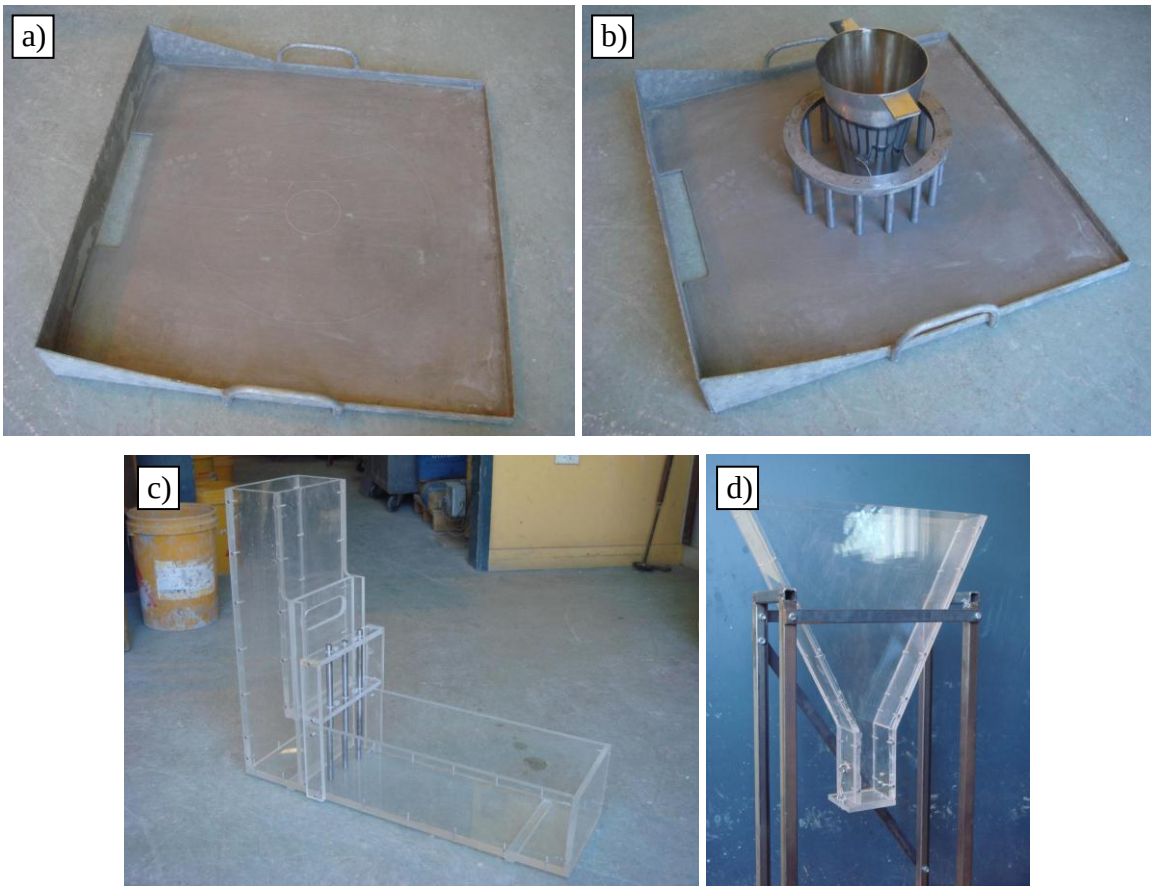

Figure A-1: Instruments for testing fresh properties of SCC; Slump flow base with marked circles locating the centre and 500 mm circles (a), Inverted slump flow cone and J-ring (b), L-box (c), and V-funnel (d)

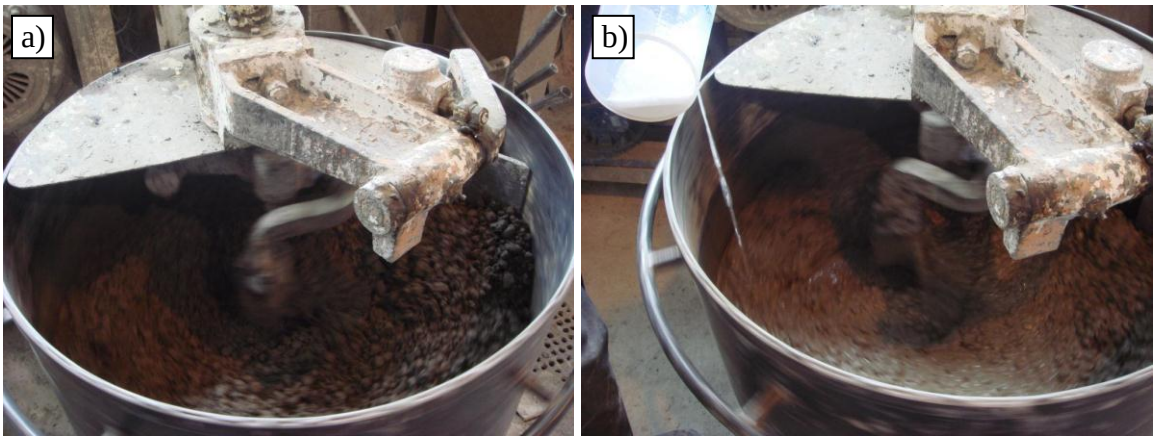

Figure A-2: A typical concrete mix in the pan mixer; before adding SP (a) and after adding SP (b)

Figure A-3: Slump flow test (a) and measurement of flow diameter (b)

Figure A-4: J-ring test (a) and measurement (b)

Figure A-5: L-box test (a, b) and measurement (c, d)

Figure A-6: V-funnel test and time measurement

A-2: MECHANICAL PROPERTIES OF HSSCC

Figure A-7: Mould and formwork for cylinders (a), shrinkage (b) and flexural beam (c) specimens

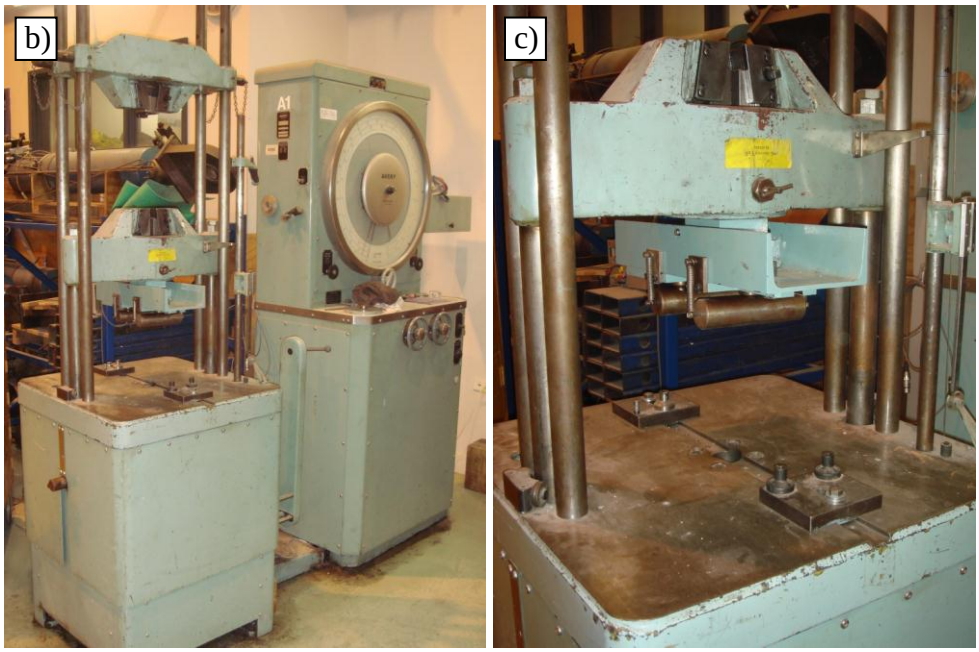

Figure A-8: Test devices for compression, split tensile and modulus of elasticity (a) and flexural strength (b, c) of concrete

Figure A-9: Pouring of concrete specimens

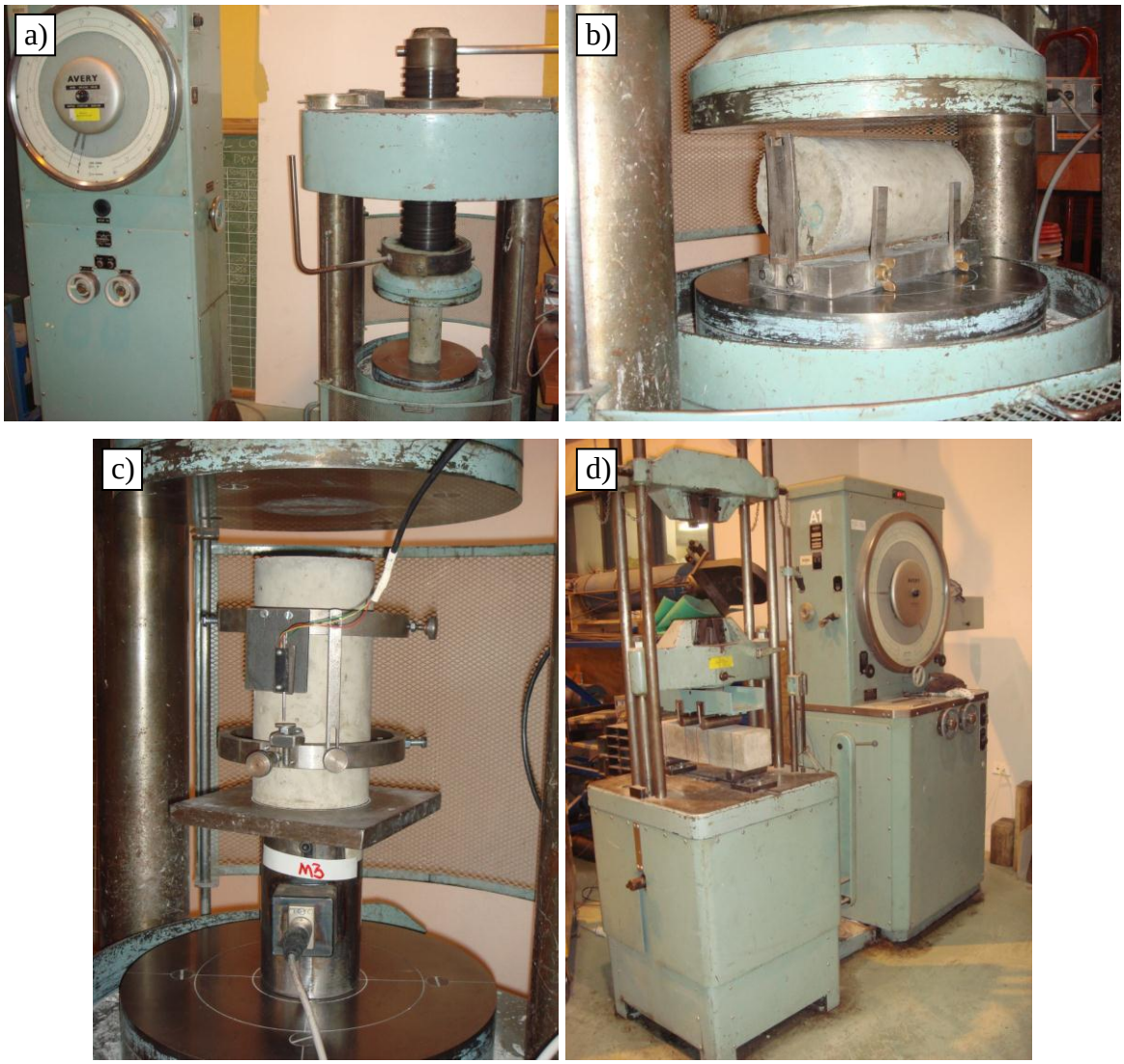

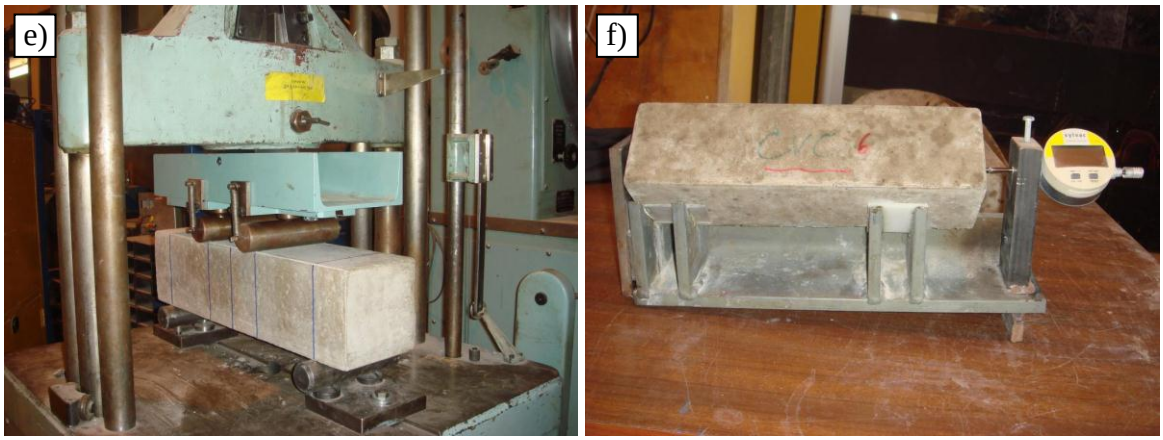

Figure A-10: Testing compressive strength (a) split tensile strength (b) modulus of elasticity (c) flexural strength (d, e), and shrinkage (f) of concrete specimens

APPENDIX B – EXPERIMENTAL EVALUATION OF MONOTONIC BOND BETWEEN DEFORMED BARS AND HSSCC

B-1: PULLOUT TESTING OF HSSCC

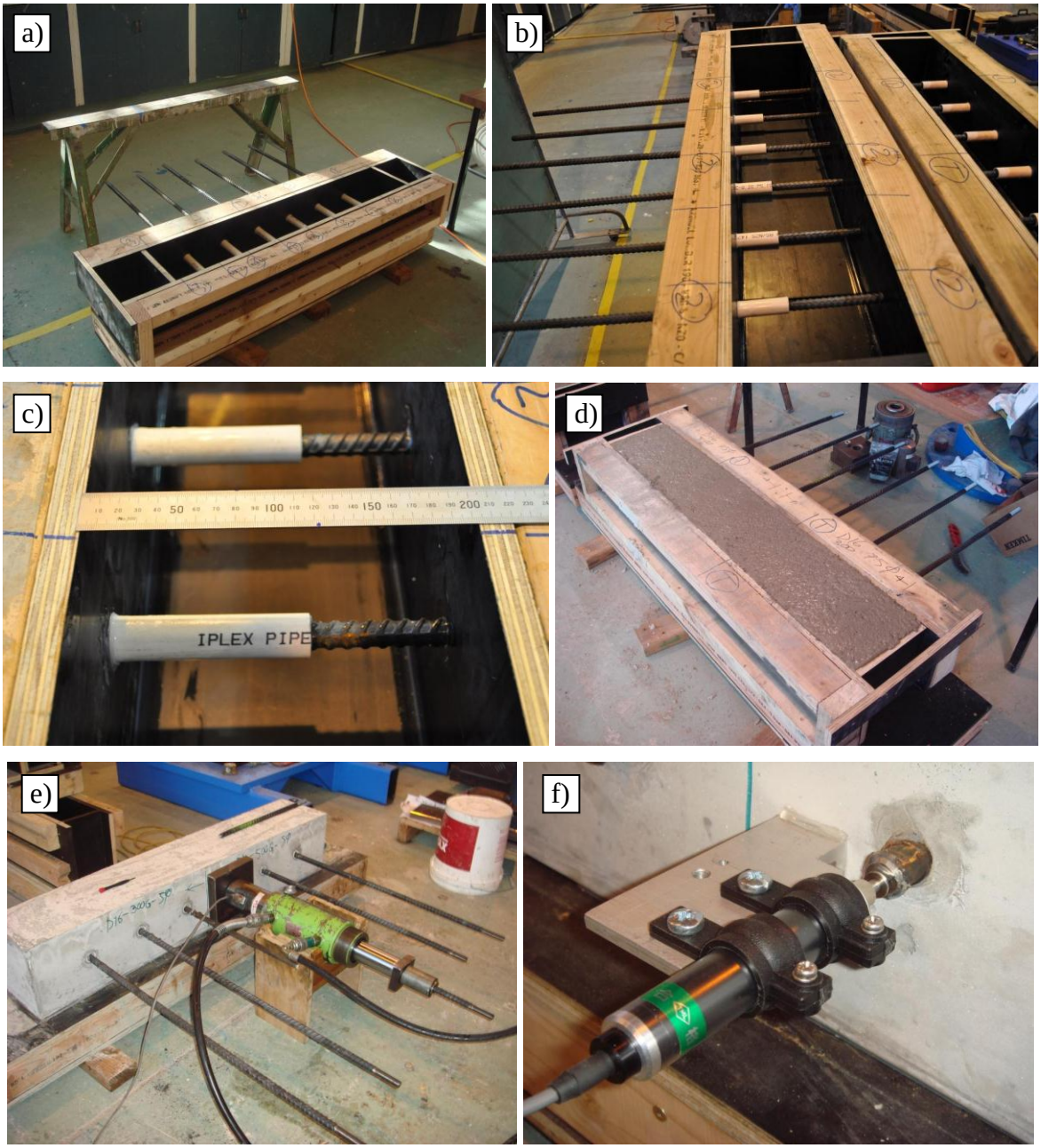

Figure B-1: HSSCC pullout specimens Preparation (a, b, c), pouring (d) and testing (e, f)

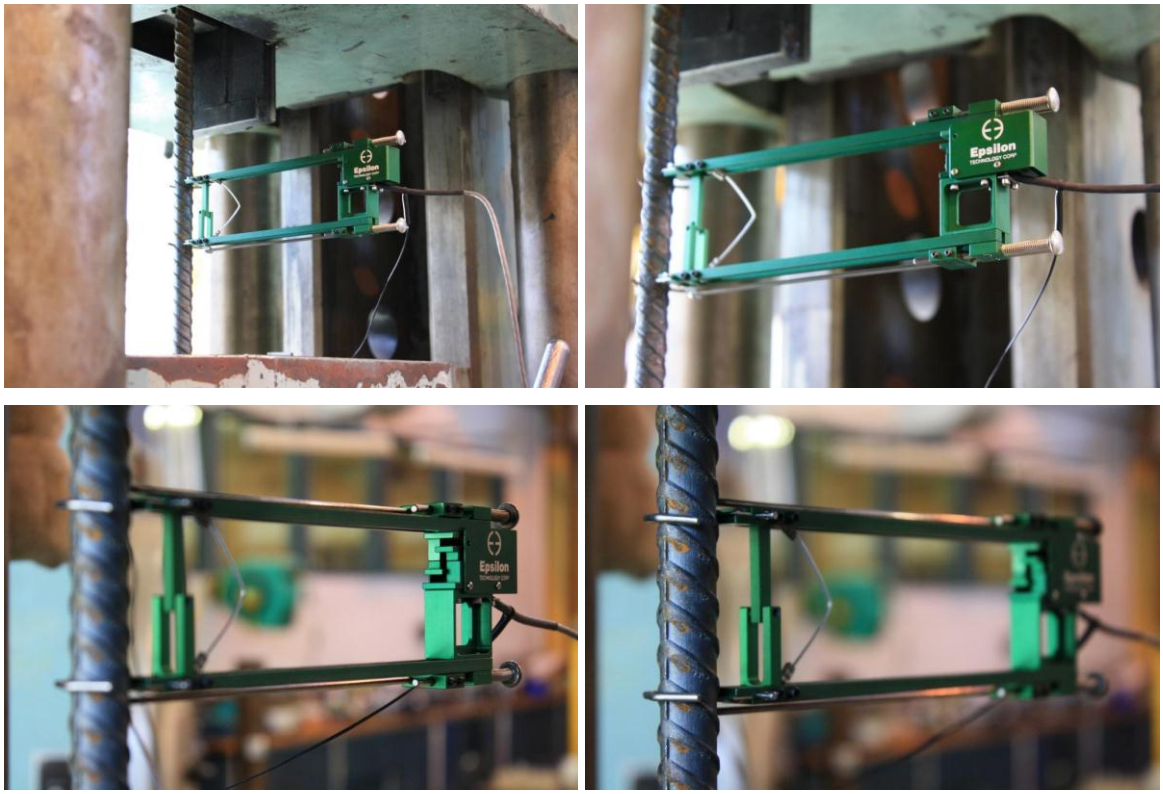

Figure B-2: Typical testing deformed bars for capturing stress-strain relationship

B-2: POST-YIELD PULLOUT TESTS OF HSSCC

Figure B-3: Preparation and casting of HSSCC pullout specimens

Figure B-4: Pullout specimen and test setup

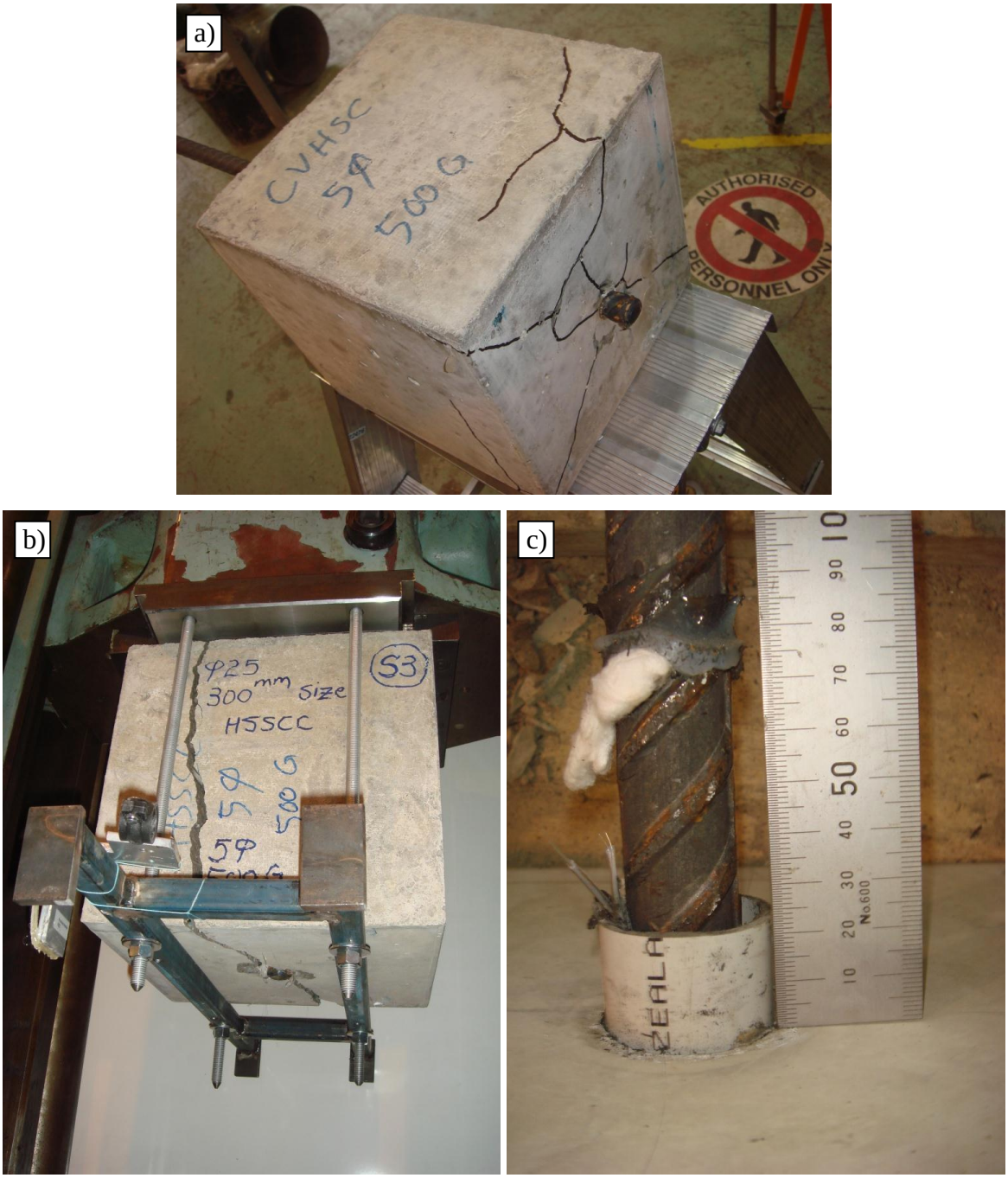

Figure B-5: Typical tested specimens (a, b) and bar elongation (c)

APPENDIX C – CYCLIC BOND BEHAVIOUR OF DEFORMED BARS IN HSSCC

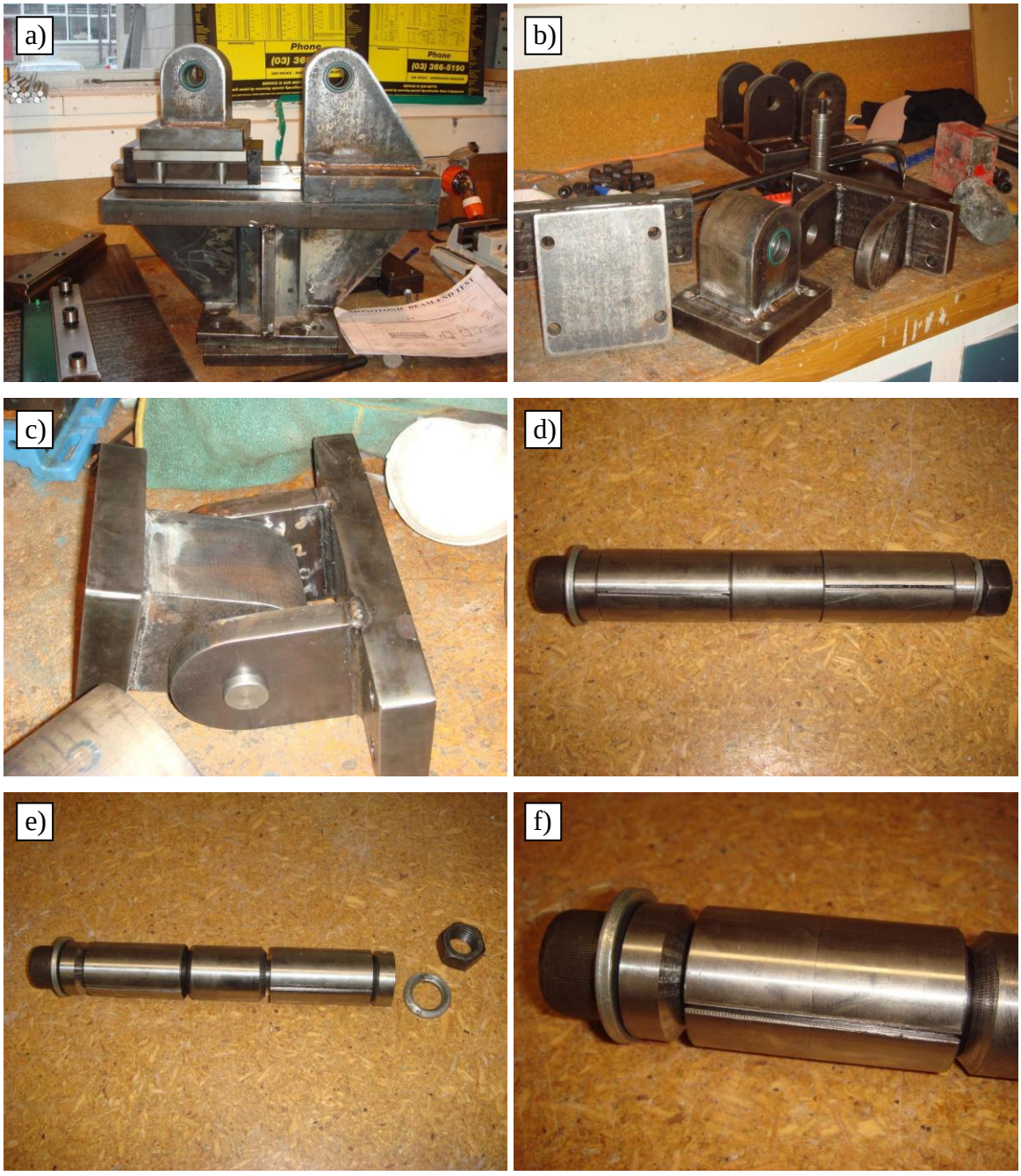

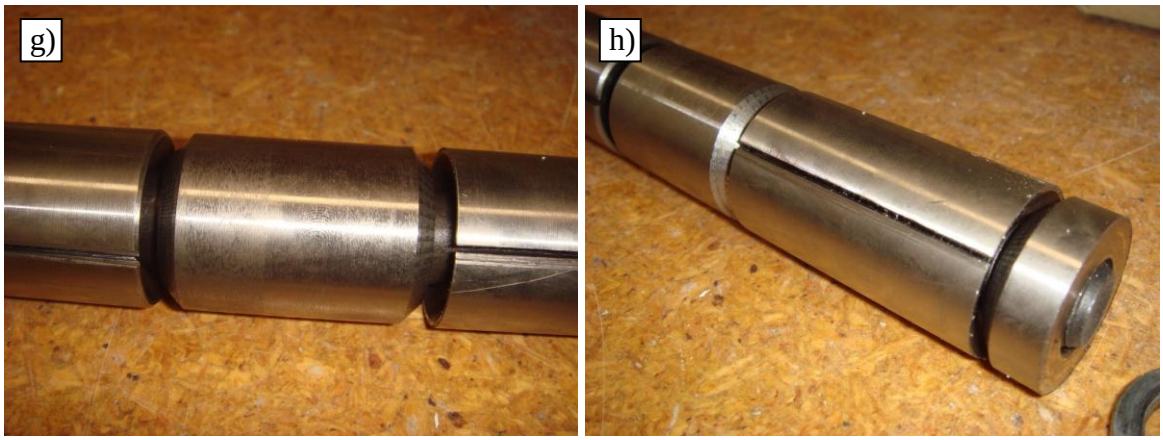

Figure C-1: Bits and pieces of the cyclic test setup; loading head (a), unassembled steel hinge (b), assembled steel hinge (c), expandable pin (d-h)

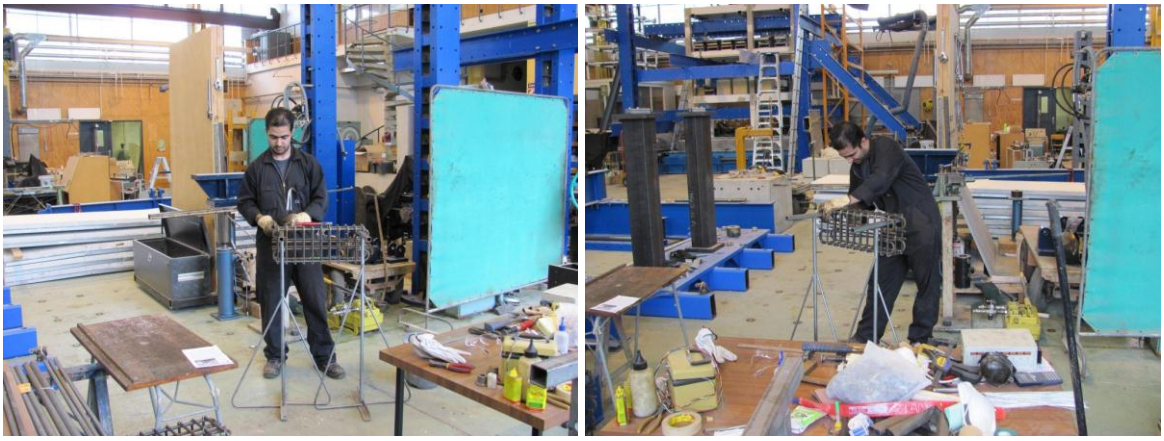

Figure C-2: Bar bending of the auxiliary reinforcement of each half beam

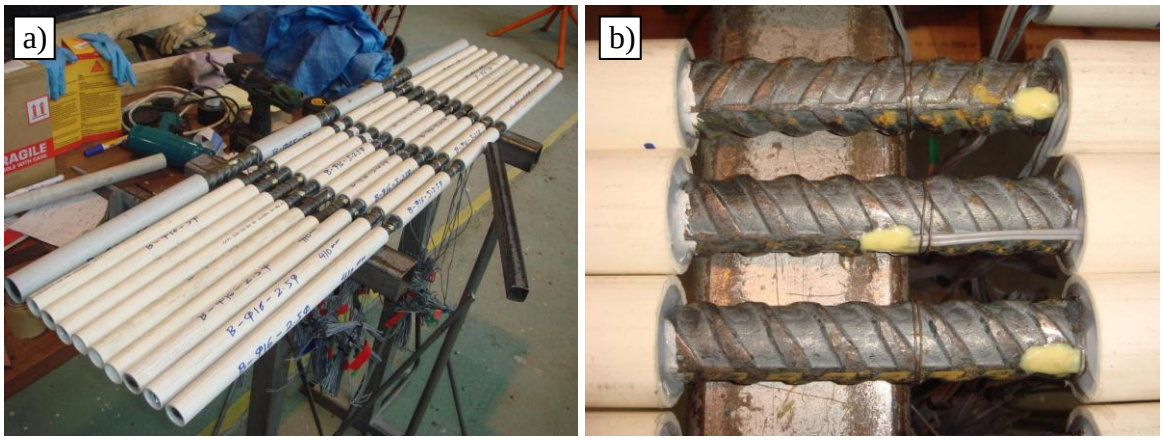

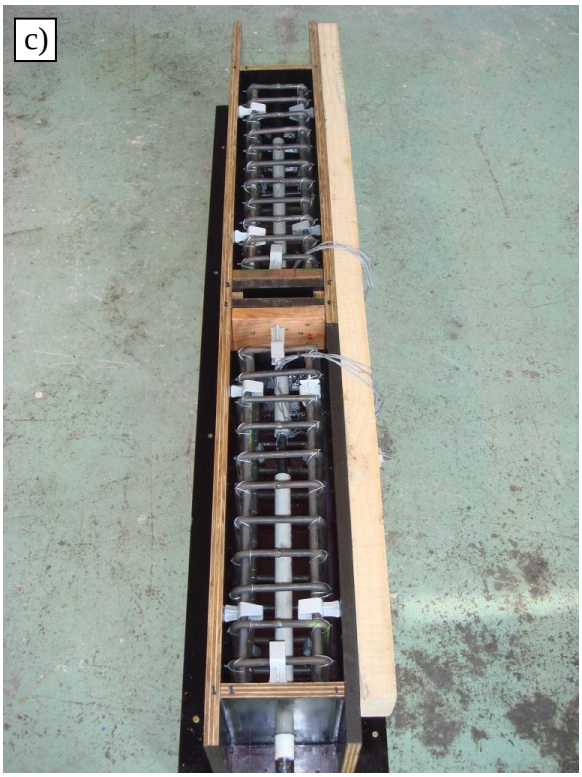

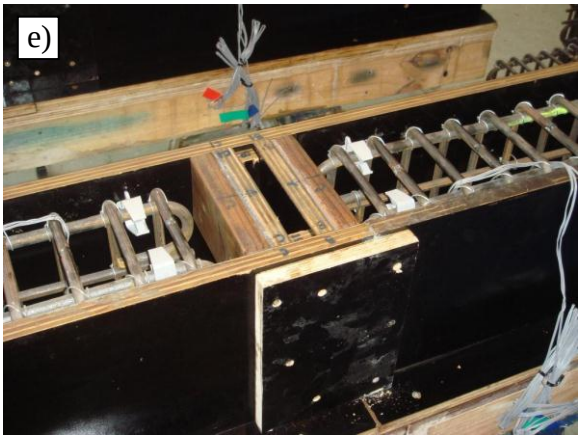

Figure C-3: Preparation and strain gauging of the main bar (a, b) and placing reinforcement cages in the formwork (c, d, e)

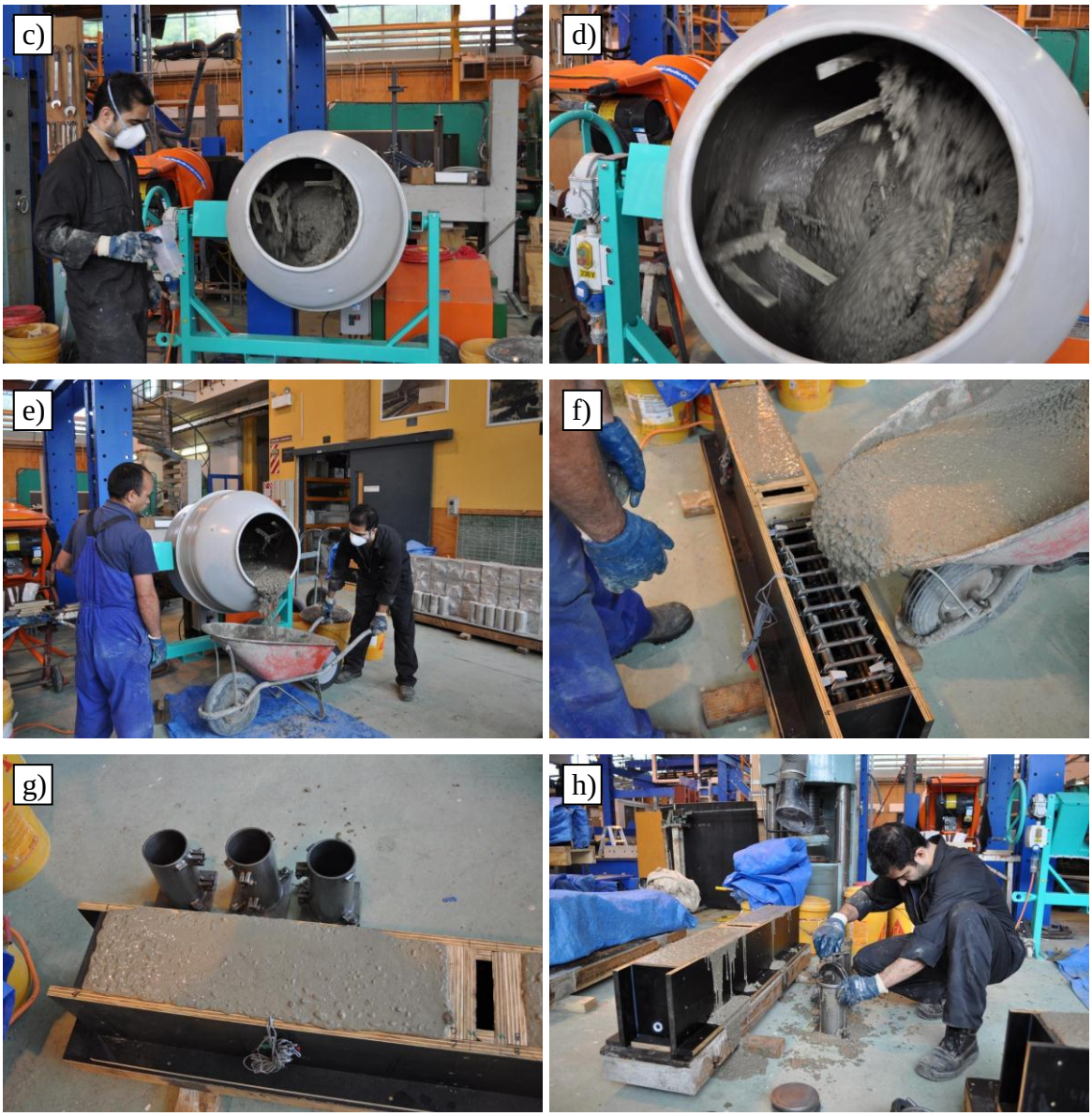

Figure C-4: Mixing HSSCC for beam specimens (a-d) and pouring HSSCC into the formwork (e-h)

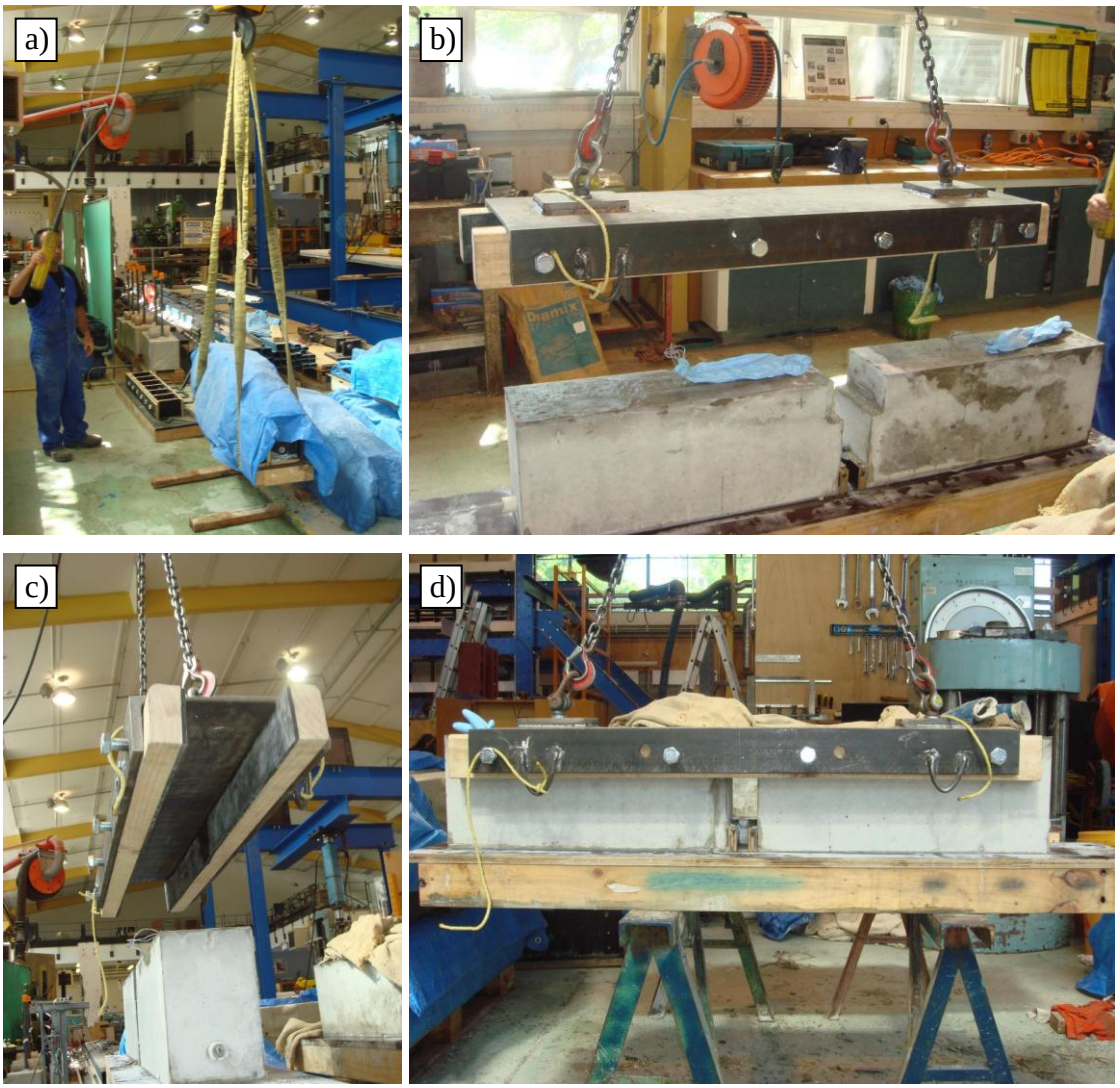
a)
b)
c)
d)

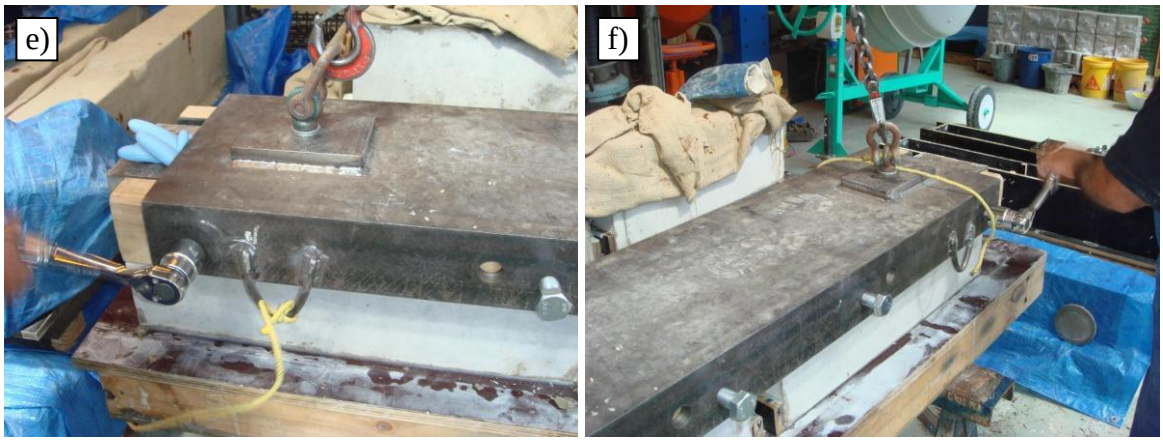
e)
f)

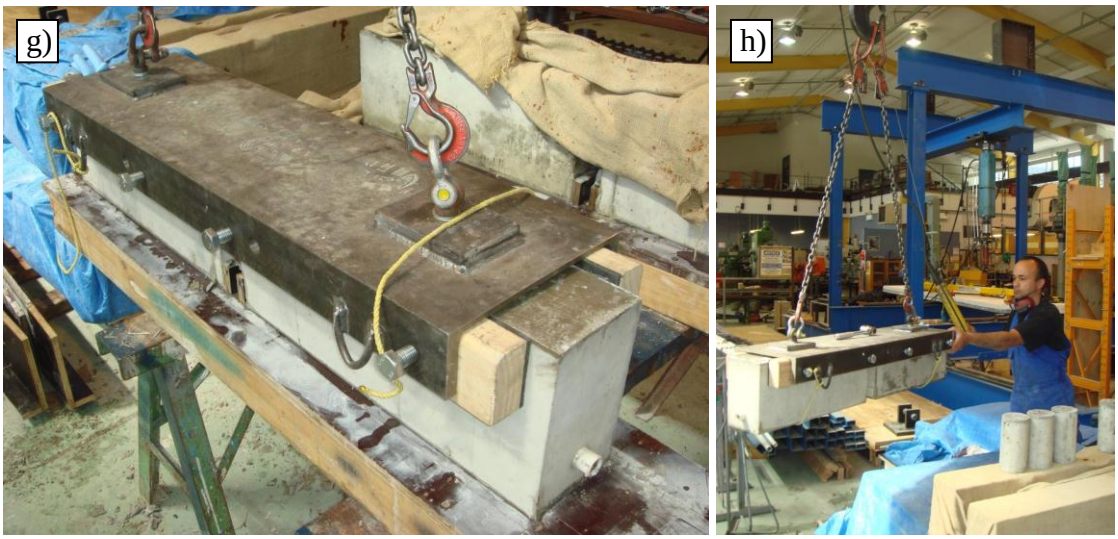

Figure C-5: Moving beam specimen when still in the formwork (a), special frame to move the beam specimen (before steel hinge installation) after stripping the formwork (b-h)

Figure C-6: Preparation of the steel hinge for pouring high-strength epoxy

Figure C-7: Filling the gaps between the beam specimen and steel hinge with high-strength epoxy

Figure C-8: Handling the beam specimen with the steel hinge installed

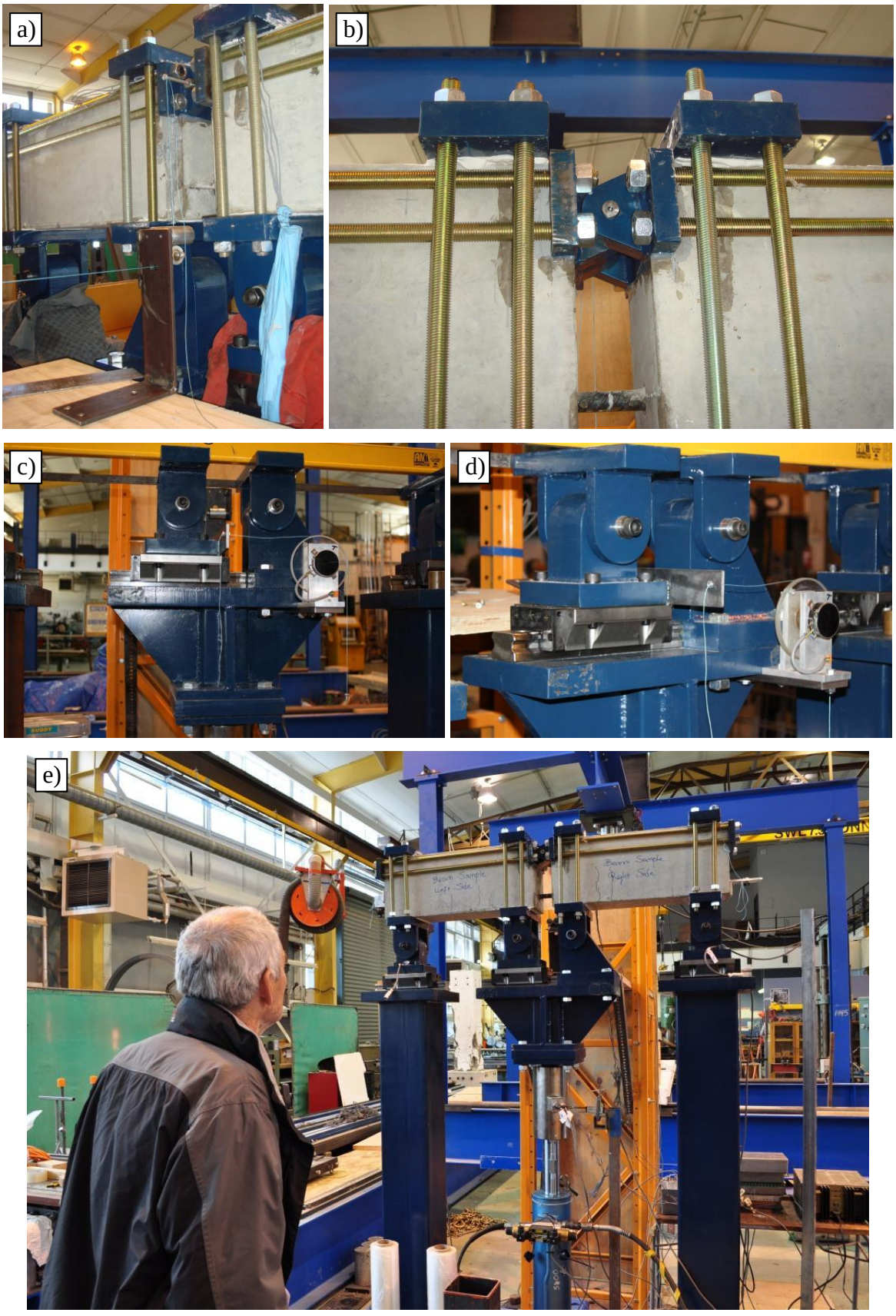

Figure C-9: Beam bending test setup; central deflection measurement (a), steel hinge and beam clamping mechanisms (b), loading head and lateral movement measurement (c, d), and complete test setup (e)

Figure C-10: Typical cyclic testing of beam specimens; start point (a), 40 mm central displacement (b), 56 mm central displacement (c), 104 mm central displacement (d), reversed loading at 45 mm central displacement (e), and end of the test (f)

APPENDIX D – SAMPLE DESIGN OF A BCJ BASED ON THE NEW ZEALAND STANDARD NZS3101 (2006)

In this section, a sample design of a typical reinforced concrete beam-column joint is presented following the requirements of the New Zealand Standards NZS3101 (2006). Note that the cross sectional dimensions of the specimens were worked out in a trial and error procedure and the limits were decided based on the maximum capacity of the hydraulic actuator, reaction frame and strong floor in which the beam-column subassemblies were tested.

The section analysis for both the beam and column was performed using a simple Microsoft Excel spread sheet and also compared with the results of Response 2000 (Bentz, 2001); this is not presented in this thesis. The amount of applied forces and moments as well as the amount of longitudinal reinforcement in both beam and column cross sections were taken from the spread sheet. However, the design for shear reinforcement and other required checks for beam, column and joint based on the NZS3101 (2006) are explained in this example. The relevant section or equation number of the NZS3101 (2006) is quoted in parenthesis wherever necessary. Note that in the following calculations, in many cases the concrete compressive strength is limited by the NZS3101 (2006) due to the limited research and available database on the behaviour of high-strength concrete.

GENERAL INFORMATION

f'_c = 124.3 MPa (concrete compressive strength)

ε_{cu} = 0.003 (assumed concrete strain at crushing)

L_b = 2285 mm (beam length from the centre of column to support)

Lc = 2700 mm (column length from support to loading point)

h_b = 420 mm (beam height)

b_w = 340 mm (beam breadth)

h_c = 520 mm (column height)

b_c = 340 mm (column breadth)

BEAM DESIGN

The following information is extracted from the Excel spread sheet and used for further checking and design of the beam section.

$f_y = f'_y$ = 312.6 MPa (yield strength of steel in tension and compression, respectively)

f_{yt} = 300 MPa (lower characteristic yield strength of transverse reinforcement)

E_s = 177.7 GPa (modulus of elasticity of steel)

d' = 48 mm (dist. from the concrete comp. fibre to the centre of steel in comp.)

d = 372 mm (dist. from the concrete comp. fibre to the centre of steel in tension)

$A_s = A'_s$= 1610.1 mm^2 (2 D25 + 2 D20 top and bottom)

MAXIMUM LONGITUDINAL REINFORCEMENT IN BEAMS CONTAINING DUCTILE PLASTIC HINGES (9.4.3.3)

$$\rho_{max} = \frac{f'_c + 10}{6 f_y} \leq 0.025 \qquad 1$$

ρ_{max} = maximum permitted value of the ratio of tensile reinforcement computed using width of web

f'_c = specified compressive strength of concrete (MPa)

f_y = lower characteristic yield strength of longitudinal reinforcement (MPa)

$$\rho_{max} = \frac{124.3 + 10}{6 \times 312.6} = 0.0716 \leq 0.025 \rightarrow \rho_{max} = 0.025$$

$$\rho_{max} = \frac{A_{s,max}}{d \times b_w} \rightarrow A_{s,max} = 0.025 \times 372 \times 340 = 3162\, mm^2 \geq 1610.1\, mm^2$$

MINIMUM LONGITUDINAL REINFORCEMENT IN BEAMS CONTAINING DUCTILE PLASTIC HINGES (9.4.3.4)

$$\rho_{\min} = \frac{\sqrt{f_c'}}{4 f_y} \qquad 2$$

ρ_{min} = minimum permitted value of the ratio of tensile reinforcement computed using width of web

$$\rho_{\min} = \frac{\sqrt{124.3}}{4 \times 312.6} = 0.0089$$

$$\rho_{\min} = \frac{A_{s,\min}}{d \times b_w} \rightarrow A_{s,\min} = 0.0089 \times 372 \times 340 = 1125\, mm^2 < 1610.1\, mm^2$$

MAXIMUM LONGITUDINAL BEAM BAR DIAMETER TO COLUMN DEPTH (9.4.3.5.2)

$$\frac{d_b}{h_c} \le 3.3 \alpha_f \alpha_d \frac{\sqrt{f_c'}}{1.25 f_y}; \qquad \text{where } (f_c' \le 70\, MPa) \qquad 3$$

d_b = nominal diameter of longitudinal reinforcing bar (mm)

h_c = overall depth of column (mm)

α_f = 1.0 for one-way frames

α_d = 1.0 for ductile plastic regions

f'_c = specified compressive strength of concrete (MPa)

f_y = lower characteristic yield strength of longitudinal reinforcement (MPa)

$$\frac{d_b}{h_c} \le 3.3 \times 1 \times 1 \times \frac{\sqrt{70}}{1.25 \times 300} = 0.0736 \rightarrow \frac{d_b}{520} \le 0.0736 \rightarrow d_b \le 38.3\, mm$$

$$\rho_w = \frac{A_{s,provided}}{d \times b_w} = \frac{1610.1}{372 \times 340} = 0.01273$$

DESIGN FOR SHEAR

Based on NZS3101 (2006), the parameters of the concrete compression block are derived as follows (7.4.2.7). These were used in the Excel spread sheet for performing section analysis and evaluating depth of neutral axis.

$$\alpha_1 = 0.85 - 0.004 \times (f_c' - 55) \geq 0.75 \rightarrow \alpha_1 = 0.75 \quad (4)$$

$$\beta_1 = 0.85 - 0.008 \times (f_c' - 30) \geq 0.65 \rightarrow \beta_1 = 0.65 \quad (5)$$

The following data is extracted from the Excel spread sheet:

c = 36.9 mm (depth of neutral axis)

M_{ob} = 238.1 kN.m (overstrength moment of the beam)

$$V_0^* = \frac{M_{ob}}{L_b - h_c/2} = \frac{238.1 \times 10^6}{2285 - 520/2} = 117580\ N \rightarrow V_0^* = 117.6\ kN \quad (6)$$

V_0^* = Factored design shear force for calculation of shear design

$$V_c = v_c \times A_{cv} \quad (9.3.9.3.4) \quad (7)$$

$$A_{cv} = b_w d \quad (8)$$

$$v_c = k_d k_a v_b \quad (9)$$

$$v_b = \min\left((0.07 + 10\rho_w) \times \sqrt{f_c'} \text{ and } 0.2 \times \sqrt{f_c'}\right) \geq 0.08\sqrt{f_c'} \quad (\text{where } f_c' \leq 50\ MPa) \quad (10)$$

V_c = nominal shear strength provided by the concrete (N)

v_c = shear stress resisted by concrete (MPa)

A_{cv} = effective shear area used to calculate shear stress (mm^2)

k_d = factor allowing for the influence of aggregate size on shear strength (0.895 for 13 mm coarse aggregate used in this research)

k_a = factor allowing for the influence of member depth on shear strength (1.0)

$\rho_w = A_s/b_w.d$; (A_s is the area of flexural tension reinforcement in mm^2)

$$v_b = \min\left((0.07 + 10 \times 0.01273) \times \sqrt{50} \text{ and } 0.2 \times \sqrt{50} \right) \geq 0.08 \times \sqrt{50}$$

$$v_b = \min\left(1.395 \text{ and } 1.414 \right) \geq 0.566 \rightarrow v_b = 1.414$$

$$v_c = 1.414\ MPa$$

$$V_c = 1.414 \times 340 \times 372 = 178842\ N = 178.8\ kN$$

$$V_{s,required} = \frac{V_0^*}{\phi} - V_c \quad (9.3.9.3.6) \qquad 11$$

V_s = nominal shear strength provided by the shear reinforcement (N)

ϕ = load amplification factor (1.0 when shear is derived from overstrength actions)

$$V_{s,required} = \frac{117.6}{1} - 178.8 = -61.2\ kN$$

The negative value for the required shear force (which should be taken by transverse reinforcement) means that the concrete is strong enough in taking the applied shear. Nevertheless, the minimum shear reinforcement should be provided based on code requirements.

$$A_{v,\min} = \frac{1}{16} \times \sqrt{f_c'} \times \frac{b_w s_{\max}}{f_{yt}} \quad (9.3.9.4.15) \qquad 12$$

$A_{v,min}$ = min area of shear reinforcement (mm^2)

s_{max} = maximum spacing of the transverse reinforcement (mm)

Providing 4 legs of R8 (8 mm diameter round) stirrups we have:

$$s_{\max} = \frac{4 \times \pi \times 8^2 / 4 \times 16 \times 300}{\sqrt{100} \times 340} = 283\ mm \geq s_{provided} \rightarrow s_{provided} = 250\ mm$$

The provided shear reinforcement is therefore: 4 R8 @ 250 mm c/c in the non-plastic hinge zone.

$$V_{s,provided} = A_v f_{yt} \frac{d}{s} \quad (9.3.9.4.2) \qquad 13$$

A_v = area of shear reinforcement perpendicular to the span within a distance 's' (mm^2)
s = spacing of transverse reinforcement in direction parallel to the longitudinal reinforcement (mm)

$$V_{s,provided} = 4 \times \frac{\pi \times 8^2}{4} \times 300 \times \frac{372}{250} = 89754\ N = 89.7\ kN$$

ADDITIONAL REQUIREMENTS FOR EARTHQUAKE

$$A_{v,\min} = \frac{1}{12} \times \sqrt{f_c'} \times \frac{b_w s_{\max}}{f_{yt}} \quad (9.4.4.1.6) \qquad 14$$

$$V_{s,required} = \frac{V_0^*}{\phi} - V_c \quad (V_c = 0.0 \text{ for earthquake design})$$

$$V_{s,required} = \frac{117.6}{1} - 0.0 = 117.6\ kN$$

Considering 4 R8 we have:

$$s_{\max} = \frac{4 \times \pi \times 8^2 / 4 \times 12 \times 300}{\sqrt{100} \times 340} = 212\ mm \geq s_{provided}$$

$$s_{\max} = \min\left(12 d_b \text{ and } d/2\right) \quad (9.4.4.1.6) \qquad 15$$

d_b = diameter of the smallest longitudinal bar in the corners of the stirrups near the top and bottom faces of the beam

$$s_{\max} = \min\left(12 \times 20 \text{ and } 372/2\right) = \min\left(240, 186\right) = 186\, mm \geq s_{provided}$$

Therefore provide 4 R8 @ 150 mm c/c

$$V_{s,provided} = 4 \times \frac{\pi \times 8^2}{4} \times 300 \times \frac{372}{150} = 149590\ N = 149.6\, kN \geq 117.6\, kN$$

CHECK FOR LATERAL RESTRAINT (9.4.5)

$$s_{\max} = \min\left(6d_b \text{ and } d/4\right) \qquad 16$$

$$s_{\max} = \min\left(6 \times 20 \text{ and } 372/4\right) = \min\left(120, 93\right) = 93\, mm \geq s_{provided}$$

$$s_{provided} = 90\, mm$$

$$A_{te} = \frac{\sum A_b \times f_y}{96 f_{yt}} \times \frac{s}{d_b} \qquad 17$$

A_{te} = area of one leg of stirrup-tie (mm^2)

ΣA_b = sum of the areas of the longitudinal bars reliant on one corner of the tie (mm^2)

$$A_{te} = \frac{\pi \times 25^2/4 \times 312.6}{96 \times 300} \times \frac{90}{25} = 19.2\, mm^2$$

$$A_{te,provided} = \frac{\pi \times 8^2}{4} = 50.3\, mm^2 \geq 19.2\, mm^2$$

Therefore provide 4 R8 @ 90 mm c/c. The finalized cross section of the beam is shown below.

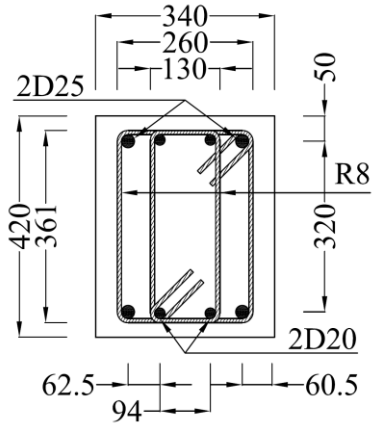

Figure D-1: Schematic view of the beam cross section

COLUMN DESIGN

The applied moment to the column should be calculated using the overstrength moment of the beam (238.1 kN.m) and the column should be designed to withstand this moment along with the applied axial load. The overstrength moment of the beam at the face of column is first calculated at the centre of the column based on the geometry of the specimen and test setup as follows.

$$M^*_{col} = M_{ob,cc} = M_{ob} \times \frac{L_b}{L_b - h_c/2} \qquad 18$$

M^*_{col} = factored design moment of the column

$M_{ob,cc}$ = overstrength moment of the beam at the centre of the column

$$M^*_{col} = M_{ob,cc} = 238.1 \times \frac{2285}{2285 - 520/2} = 268.6\, kN.m$$

In order to satisfy the strong-column-weak-beam design concept, the column needs to remain elastic during the course of the test. This means that the factored yield moment of the column ($\phi M_{col,yield}$) should be well above the factored design moment of the column (M^*_{col}). In a process of trial and error in the Excel spread sheet and considering the above criterion, the size and arrangement of longitudinal bars were achieved.

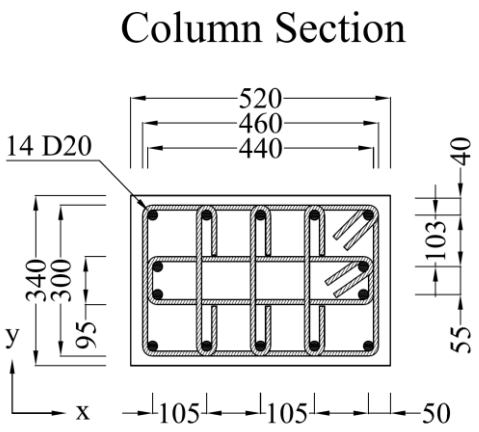

Figure D-2: Schematic view of the column cross section

This arrangement of reinforcements resulted in the following information (taken from the Excel spread sheet):

$$M_{col,yield} = 493.7\,kN$$

$$\phi \times M_{col,yield} = 0.85 \times 493.7 = 419.6\,kN$$

$$\frac{\phi \times M_{col,yield}}{M^{*}_{col}} = \frac{419.6}{268.6} = 1.56 >> 1$$

$$d = 520 - 50 = 470\,mm$$

$$A_s = 14 \times \frac{\pi \times 20^2}{4} = 4398\,mm^2$$

LIMITS FOR AREA OF LONGITUDINAL REINFORCEMENT (10.3.8.1)

The area of longitudinal reinforcement for columns and piers shall be greater than 0.008 and less than 0.08 times the gross area (A_g) of the section.

$$\rho_w = \frac{A_{s,provided}}{d \times b_w} = \frac{4398}{470 \times 340} = 0.0275$$

DESIGN FOR SHEAR

$$V_c^* = \frac{2M_{col}^*}{L_c} = \frac{2 \times 268.6}{2.7} = 199\,kN \qquad 19$$

This is the predicted maximum force in the hydraulic actuator.

$$V_c = k_a k_n v_b A_{cv} \quad (10.3.10.3.1) \qquad 20$$

V_c = nominal shear strength provided by the concrete mechanisms (N)
k_a = 0.895 for 13 mm coarse aggregate
A_{cv} = area of concrete assumed to resist shear (mm^2)

$$k_n = 1 + \frac{3N^*}{A_g f_c'} \qquad 21$$

N^* = design axial load at ultimate limit state; '+' for compression and '-' for tension (N)
A_g = gross area of section (mm^2)

N^* was chosen to be a compressive force of 1500 kN based on available hydraulic jack capacity which provides an axial load ratio of almost 0.1 or 10% of the column section capacity.

$$k_n = 1 + \frac{3 \times 1500000}{520 \times 340 \times 124.3} = 1.2$$

$$v_b = (0.07 + 10\rho_w)\sqrt{f_c'} \quad (0.08\sqrt{f_c'} < v_b < 0.2\sqrt{f_c'}) \quad \text{and} \quad (f_c' \le 50\ MPa) \qquad 22$$

$$\rho_w = \frac{0.3A_{st}}{0.8 \times b \times H} = \frac{0.3 \times 4398}{0.8 \times 340 \times 520} = 0.0093 \quad \text{(Paulay et al., 1992)} \qquad 23$$

$$\rho_w = \frac{6 \times \pi \times 20^2 / 4}{340 \times 470} = 0.0118 \quad \text{(NZS3101, 2006)}$$

$$v_{b,Paulay} = (0.07 + 10 \times 0.0093) \times \sqrt{50} = 1.15 \quad (0.57 < v_b < 1.41)$$

$$v_{b,NZS3101} = (0.07 + 10 \times 0.0118) \times \sqrt{50} = 1.33 \quad (0.57 < v_b < 1.41)$$

$$v_b = 1.15$$

$$V_c = 0.895 \times 1.2 \times 1.15 \times 340 \times 520 = 218365\, N = 218.3\, kN$$

$$V_{s,required} = \frac{V_0^*}{\phi} - V_c = \frac{199}{0.75} - 218.6 = 46.73\, kN$$

$$V_{s,required} = A_v f_{yt} \frac{d}{s}$$

$$\left(\frac{A_v}{s}\right)_{required} = \frac{46.73 \times 1000}{300 \times 470} = 0.33$$

$$A_{v,\min} = \frac{1}{16} \times \sqrt{f_c'} \times \frac{b_w s_{\max}}{f_{yt}}$$

$$\left(\frac{A_v}{s}\right)_{\min} = \frac{1}{16} \times \sqrt{124.3} \times \frac{340}{300} = 0.79$$

Therefore the minimum amount of 0.79 is used. Using 4 R10 bars as column shear reinforcement we have:

$$s = \frac{4 \times \pi \times 10^2 / 4}{0.79} = 397\, mm$$

DESIGN FOR CONFINEMENT OF CONCRETE AND LATERAL RESTRAINT OF LONGITUDINAL BARS (10.3.10.6.1)

The total effective tie area in each principal directions of the cross section within spacing 's_h' should be greater than equations 24 and 25.

$$A_{sh} = \frac{(1-\rho_t m)s_h h''}{3.3}\frac{A_g}{A_c}\frac{f_c'}{f_{yt}}\frac{N^*}{\phi\, f_c' A_g} - 0.0065 s_h h'' \quad \text{(concrete confinement)} \qquad 24$$

$$A_{te} = \frac{\sum A_b \times f_y}{135 f_{yt}} \times \frac{s_h}{d_b} \quad \text{(lateral restraint of longitudinal bars)} \qquad 25$$

$\rho_t = A_{st}/A_g$

$m = f_y/0.85f'_c$

s_h = centre to centre spacing of hoop sets (mm)

h'' = dimension of concrete core of rectangular section, measured perpendicular to the direction of the hoop bars, measured to the outside of the peripheral hoop (mm)

A_c = are of concrete core of section measured to outside of peripheral hoop (mm^2)

ΣA_b = sum of the areas of the longitudinal bars reliant on one corner of the tie (mm^2)

Note that the values of "$\rho_t.m$" and "A_g/A_c" should not be greater than 0.4and 1.5 respectively.

$$\rho_t = \frac{A_{st}}{A_g} = \frac{4398}{520 \times 340} = 0.025$$

$$m = \frac{f_y}{0.85 f_c'} = \frac{312.6}{0.85 \times 124.3} = 2.96$$

$$\rho_t m = 0.025 \times 2.96 = 0.074 < 0.4$$

$$A_c = (520 - 2 \times 30) \times (340 - 2 \times 20) = 138000\, mm^2$$

$$A_g = 520 \times 340 = 176800\, mm^2$$

$$\frac{A_g}{A_c} = \frac{176800}{138000} = 1.28 < 1.5$$

$h''_{long} = 340 - 2 \times 20 = 300\, mm$ used for the longitudinal direction

$h''_{tran} = 520 - 2 \times 30 = 460\, mm$ used for transverse direction

SPACING OF TIE SETS (10.3.10.6.2)

$$s_{\max} = \min(b/3 \text{ and } 200\,mm) = \min(340/3,\ 200) = 113\,mm \qquad 26$$

Assume spacing of 110 mm between the tie sets we have:

$$A_{sh,long} = \frac{(1 - 0.025 \times 2.96) \times 110 \times 300}{3.3} \times \frac{176800}{138000} \times \frac{124.3}{300} \times \frac{1500000}{1 \times 124.3 \times 176800} - 0.0065 \times 110 \times 300$$

$$A_{sh,long} = 121\,mm^2 < 4 \times \frac{\pi \times 10^2}{4} = 314.2\,mm^2$$

$$A_{sh,tran} = \frac{(1 - 0.025 \times 2.96) \times 110 \times 460}{3.3} \times \frac{176800}{138000} \times \frac{124.3}{300} \times \frac{1500000}{1 \times 124.3 \times 176800} - 0.0065 \times 110 \times 460$$

$$A_{sh,tran} = 185\,mm^2 < 5 \times \frac{\pi \times 10^2}{4} = 392.7\,mm^2$$

$$A_{te} = \frac{\frac{\pi \times 20^2}{4} \times 312.6}{135 \times 300} \times \frac{110}{20} = 13.3\,mm^2$$

Therefore 4 R10 @ 110 mm c/c is used as shear reinforcement for the non-potential plastic hinge region.

ADDITIONAL REQUIREMENTS FOR EARTHQUAKE

LENGTH OF DUCTILE DETAILING ZONE (10.4.5)

The schematic drawing below shows the concept explained in NZS3101 (2006) for finding the length of the potential plastic hinge zone for provision of special requirement for earthquake.

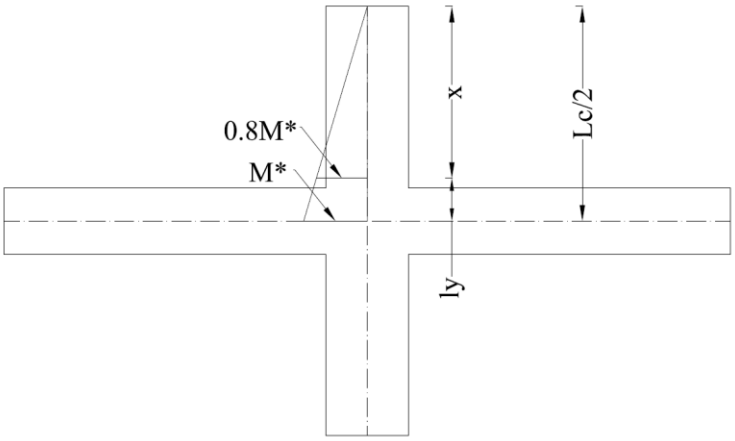

Figure D- 3: Schematic view of the potential plastic hinge zone length calculation

$$\frac{M^*}{L_c/2}=\frac{0.8M^*}{x} \rightarrow x=0.4L_c \rightarrow l_y=\frac{L_c}{2}-x=0.5L_c-0.4L_c \rightarrow l_y=0.1L_c$$

$$l_y=\max\left(h\,,0.1L_c\right) \qquad 27$$

h = dimension in the direction resisting the applied moment (520 mm)

L_c = length of the column (2700 mm)

$$l_y=\max\left(520,270\right)=520\,mm$$

TRANSVERSE REINFORCEMENT IN COLUMNS AND PIERS (10.4.7)

$$v_c=3v_b\sqrt{\left(\frac{N_0^*}{A_g f_c'}\right)-0.1}\geq 0.0 \qquad 28$$

$$v_c=3\times 1.15\times\sqrt{\left(\frac{1500000}{520\times 340\times 124.3}\right)-0.1}=Non-real\,Value$$

$$v_c=0.0$$

$$A_{v,\min}=\frac{1}{12}\times\sqrt{f_c'}\times\frac{b_w s_{\max}}{f_{yt}} \qquad 29$$

$$\left(\frac{A_v}{s}\right)_{\min} = \frac{1}{12} \times \sqrt{124.3} \times \frac{340}{300} = 1.05$$

$$V_{s,required} = \frac{V_c^*}{0.75} = \frac{199}{0.75} = 265.3\,\text{kN}$$

$$V_{s,required} = A_v f_{yt} \frac{d}{s}$$

$$\left(\frac{A_v}{s}\right)_{required} = \frac{265.3 \times 1000}{300 \times 470} = 1.88 > 1.05 \qquad \text{Therefore shear governs}$$

$$A_{sh} = \frac{(1.3 - \rho_t m) s_h h''}{3.3} \frac{A_g}{A_c} \frac{f_c'}{f_{yt}} \frac{N_0^*}{\phi\, f_c' A_g} - 0.006 s_h h'' \qquad 30$$

$$\frac{A_{sh}}{s_h} = \left(\frac{(1.3 - \rho_t m)}{3.3} \frac{N_0^*}{\phi\, A_c f_{yt}} - 0.006 \right) h''$$

$$\left(\frac{A_{sh}}{s_h}\right)_{long} = \left(\frac{(1.3 - 0.025 \times 2.96)}{3.3} \frac{1500000}{1 \times 138000 \times 300} - 0.006 \right) \times 300 = 4.04$$

$$\left(\frac{A_{sh}}{s_h}\right)_{tran} = \left(\frac{(1.3 - 0.025 \times 2.96)}{3.3} \frac{1500000}{1 \times 138000 \times 300} - 0.006 \right) \times 460 = 6.19$$

Assuming spacing of 80 mm for transverse reinforcement we have:

$$\left(\frac{A_{sh}}{s}\right)_{long} = \frac{4 \times \pi \times 10^2 / 4}{80} = 3.93 \qquad \text{(very close to 4.04; therefore O.K.)}$$

$$\left(\frac{A_{sh}}{s}\right)_{tran} = \frac{5 \times \pi \times 10^2 / 4}{80} = 4.91$$

The ratio for the transverse direction looks not O.K.; but because the column is designed to remain elastic, the concrete also takes part in taking the shear force. Besides, no forces are acting in the transverse direction. Therefore, the same amount of reinforcement and spacing is used.

$$A_{te} = \frac{\sum A_b \times f_y}{96 f_{yt}} \times \frac{s_h}{d_b} \qquad 31$$

$$\frac{A_{te}}{s_h} = \frac{\frac{\pi \times 20^2}{4} \times 312.6}{96 \times 300 \times 20} = 0.17 \qquad \text{(O.K.)}$$

Therefore 4 R10 @ 80 mm c/c is used as shear reinforcement for the non-potential plastic hinge region.

BEAM-COLUMN JOINT DESIGN

The shear force transferred to the beam-column joint of a reinforced concrete member is calculated using the equation **Error! Reference source not found.**.

$$V^*_{ojh} = T + C - V_{o,c} \qquad 32$$

V^*_{ojh} = design horizontal shear force across a joint at overstrength (N)
T = tensile force in the beam reinforcement at overstrength (N)
C = compressive force in the beam reinforcement at overstrength (N)
$V_{o,c}$ = column shear force at overstrength (N)

$$T = C = \frac{M_{o,b}}{d - d'} = \frac{238.1 \times 10^6}{372 - 48} = 734876\ N = 734.9\ kN \qquad 33$$

$$V^*_{ojh} = 734.9 + 734.9 - 199 = 1270.8\ kN$$

MAXIMUM HORIZONTAL JOINT SHEAR FORCE (15.3.4)

$$V^*_{jh} = \min\left(0.2 f'_c b_j h_c\ , 10 b_j h_c\right) \qquad 34$$

$$b_j = \min\left(b_c\,,\, b_w + \frac{h_c}{2}\right) \qquad 35$$

V^*_{jh} = design horizontal shear force across a joint (N)

b_j = effective width of joint (mm)

h_c = overall depth of column in the direction of the horizontal shear to be considered (mm)

b_c = overall width of column (mm)

b_w = web width (mm)

$$b_j = \min\left(340\,,\, 340 + \frac{520}{2}\right) = \min\left(340{,}600\right) \rightarrow\ b_j = 340\,mm$$

$$V^*_{jh} = \min\left(0.2\times 124.3\times 340\times 520\,,\, 10\times 340\times 520\right) = \min\left(4395.2\,,\, 1768\right)$$

$$V^*_{jh} = 1768\,kN > 1270.8\,kN$$

ADDITIONAL REQUIREMENTS FOR EARTHQUAKE

HORIZONTAL JOINT SHEAR REINFORCEMENT (15.4.4)

$$A_{jh} = \frac{6V^*_{ojh}}{f'_c\, b_j h_c}\left(\frac{\alpha_i\, f_y A^*_s}{f_{yh}}\right) \geq 0.4\,\frac{V^*_{ojh}}{f_{yh}} \qquad 36$$

$$0.85 \leq \left(\frac{6V^*_{ojh}}{f'_c\, b_j h_c}\right) \leq 1.2 \qquad 37$$

$$0.85 \leq \left(\frac{6\times 1270.8\times 10^3}{124.3\times 340\times 520}\right) \leq 1.2 \ \rightarrow\ 0.85 \leq 0.35 \leq 1.2 \qquad \text{Not O.K.}$$

Therefore: $\dfrac{6V^*_{ojh}}{f'_c\, b_j h_c} = 0.85$

$$\alpha_i = 1.4\,\alpha_n \quad \text{or} \quad \alpha_i = \left(1.4 - 1.6\,\frac{C_j N^*_0}{f'_c A_g}\right)\alpha_n \qquad 38$$

$$C_j = \frac{V_{jh}}{V_{jx} + V_{jz}} \qquad 39$$

V_{jh} = nominal horizontal shear force transferred across a joint in the direction being considered (N)

V_{jx} = nominal horizontal joint shear force transferred in 'x' direction (N)

V_{jz} = nominal horizontal joint shear force transferred in 'z' direction (N)

For a one-way joint we have: $V_{jh} = V_{jx}$ and $V_{jz} = 0 \rightarrow C_j = 1.0$

$$\alpha_i = \left(1.4 - 1.6\frac{1 \times 1500 \times 10^3}{124.3 \times 340 \times 520}\right) \times 1 = 1.29$$

$$A_s^* = \max\left(A_s\ ,\ A_s'\right) \qquad 40$$

A_s = area of the top beam reinforcement (mm^2)

A'_s = area of the bottom beam reinforcement (mm^2)

$$A_s^* = \max\left(1610.1, 1610.1\right) = 1610.1\, mm^2$$

$$A_{jh} = 0.85 \times \left(\frac{1.29 \times 312.6 \times 1610.1}{500}\right) \geq 0.4 \times \frac{1270.8}{500}$$

$A_{jh,required} = 1103.8\, mm^2 \geq 1016.6\, mm^2$ O.K.

DISTRIBUTION OF HORIZONTAL JOINT REINFORCEMENT (15.4.4.4)

Based on the code requirements, the effective horizontal joint shear reinforcement should be placed between (but not immediately adjacent) to the innermost layers of the top and bottom beam bars. These should be distributed in the effective zone as uniformly as practicable. Any tie legs bent around the column bars that do not cross the potential diagonal failure plane (dummy sets) should not be considered in calculations.

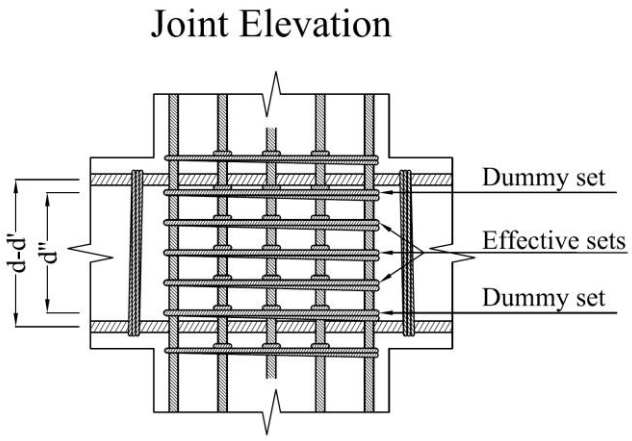

Figure D-4: Schematic view of the effective zone for placing the joint shear reinforcement

$$s_{\max} = \min\left(10\,d_b\,,\,200\,mm\right) \quad (15.4.4.4) \tag{41}$$

$$s_{\max} = \min\left(10\times 20\,,\,200\,mm\right) = 200\,mm$$

$$s = \frac{d''}{n'-1} \tag{42}$$

$$n' = n + 2 \tag{43}$$

d″ = distance over which the effective joint shear reinforcement should be distributed

n´ = total number of joint shear reinforcement sets (including the dummy sets)

n = number of the effective joint shear reinforcement sets

$$d'' = \left(d - d'\right) - 2\times\left(\frac{d_b}{2} + \frac{d_s}{2}\right) \tag{44}$$

$$d'' = \left(372 - 48\right) - 2\times\left(\frac{25}{2} + \frac{12}{2}\right) = 287\,mm$$

Considering (2 HR12 + 2 HR10) bars in each set we have:

$$A_{set} = 2 \times \left(\frac{\pi \times 12^2}{4} + \frac{\pi \times 10^2}{4} \right) = 383.3\, mm^2 \qquad 45$$

$$n = \frac{A_{jh}}{A_{set}} = \frac{1103.8}{383.3} = 2.88 \quad \text{(provide 3 sets in the effective zone)} \qquad 46$$

$$n' = 3 + 2 = 5$$

$$s = \frac{287}{5-1} = 72\, mm$$

Finally provide (2 HR12 + 2 HR10) @ 65 mm c/c

$$A_{jh,provided} = 3 \times \left(2 \times \left(\frac{\pi \times 12^2}{4} + \frac{\pi \times 10^2}{4} \right) \right) = 1149.8\, mm^2 > 1103.8\, mm^2$$

Note that these 3 sets of shear reinforcements are provided in the effective distance of 287 mm. However in order to satisfy the buckling and concrete constraint requirements, two additional dummy sets of shear reinforcement with the same arrangement as the main ones (2 HR12 + 2 HR10) are provided adjacent to the top and bottom beam bars (**Error! Reference source not found.**).

VERTICAL JOINT SHEAR REINFORCEMENT (15.4.5)

$$A_{jv} = \alpha_v A_{jh} \frac{f_{yh}}{f_{yv}} \frac{h_b}{h_c} \qquad 47$$

$$\alpha_v = \frac{0.7}{1 + \frac{N_0^*}{f_c' A_g}} \qquad 48$$

$$\alpha_v = \frac{0.7}{1 + \frac{1500 \times 10^3}{124.3 \times 520 \times 340}} = 0.655$$

$$A_{jv,required} = 0.655 \times 1149.8 \times \frac{500}{312.6} \times \frac{420}{520} = 973\,mm^2$$

Except for the two extreme layers of column bars located at the left and right sides of the column (8 D20), the rest of the column bars (6 D20) can act as vertical shear reinforcement to withstand the vertical shear force.

$$A_{jv,provided} = 6 \times \frac{\pi \times 20^2}{4} = 1885\,mm^2 \geq 918.8\,mm^2$$

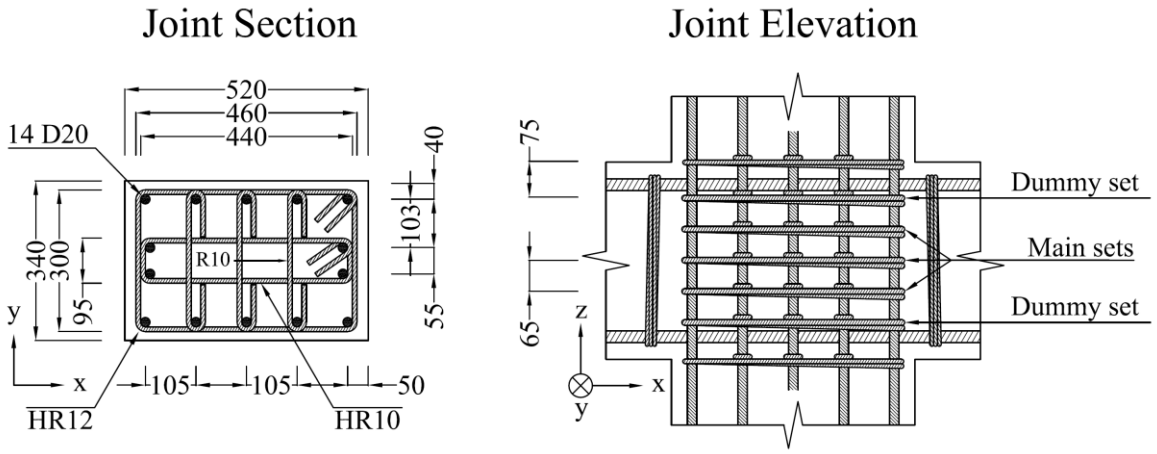

Figure D-5: Schematic view of the joint elevation and cross section

REFERENCE

Bentz, E 2001, Response-2000 User Manual Version 1.1, University of Toronto, Toronto, Ontario, Canada

NZS3101 2006, 'NZS3101 Concrete structures standard Parts 1 & 2: The Desing of Concrete Structures and Commentary'. Standards New Zealand, Wellington, New Zealand, p. 698.

Paulay, T & Priestley, MJN 1992, Seismic design of reinforced concrete and masonry buildings.

APPENDIX E – VISUAL SUPPLEMENT FOR THE BCJ EXPERIMENTAL TESTING

This appendix mostly consisted of a visual supplementation of the photographs taken at different stages of the experimental investigations of beam-column joints. The presentation of the pictures is in the form of three separate sections; namely the casting, preparation and testing of specimens. It is worthwhile mentioning that the reported pictures in this appendix are only a carefully selected pool of more than 10,000 pictures.



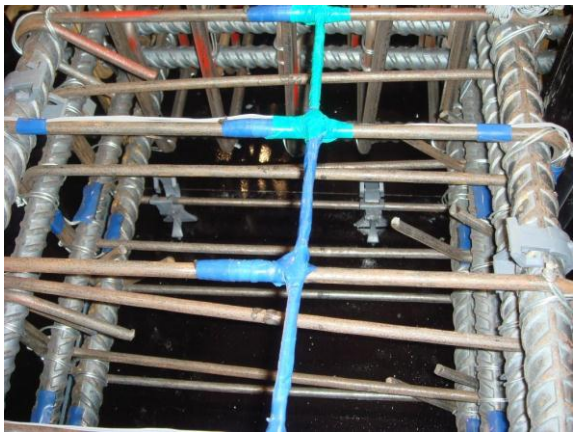


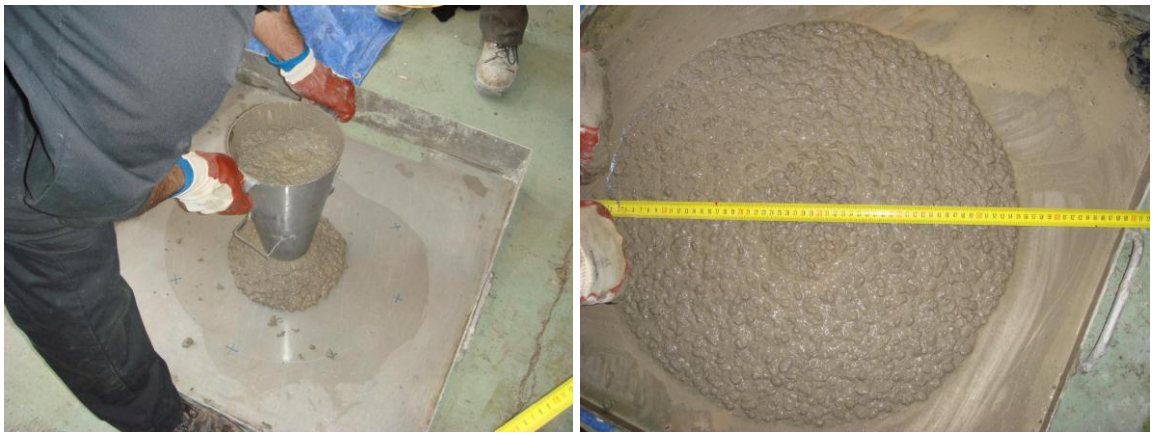

Figure E-1: Casting stages of BCJ1








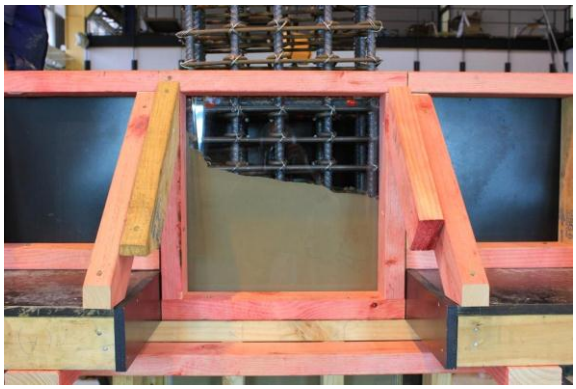


Figure E-2: Casting stages of BCJ2



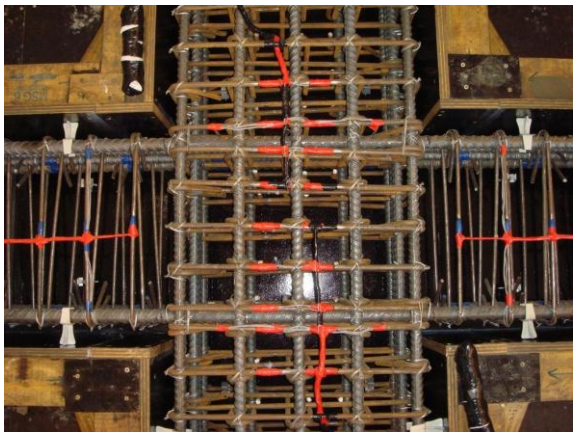

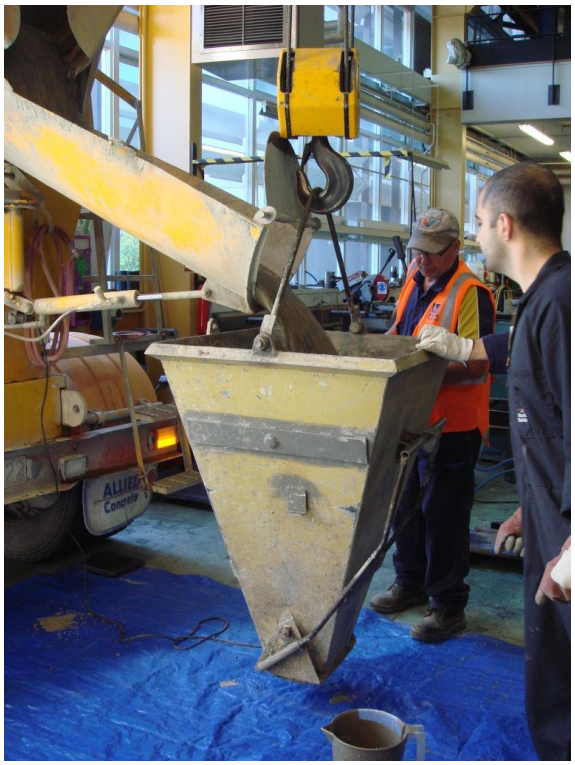






Figure E-3: Casting stages of BCJ3



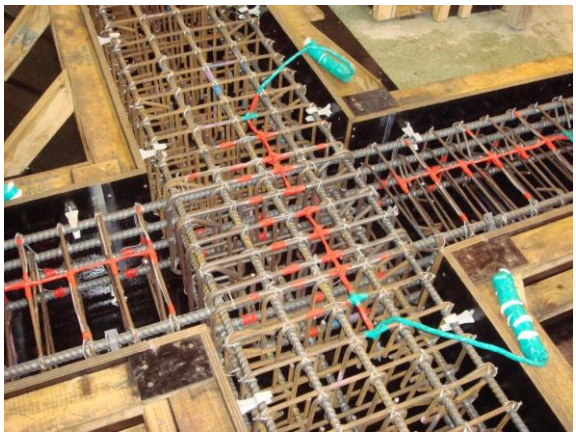
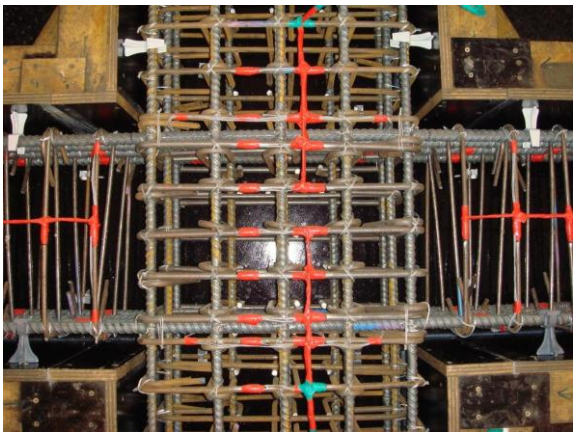


ALLIED
ELE116

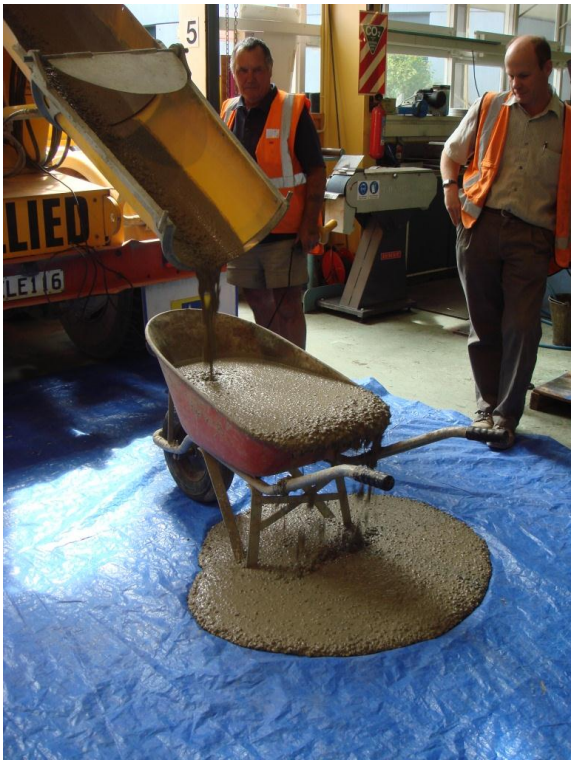
ALLIED
ELE116




Figure E-4: Casting stages of BCJ4



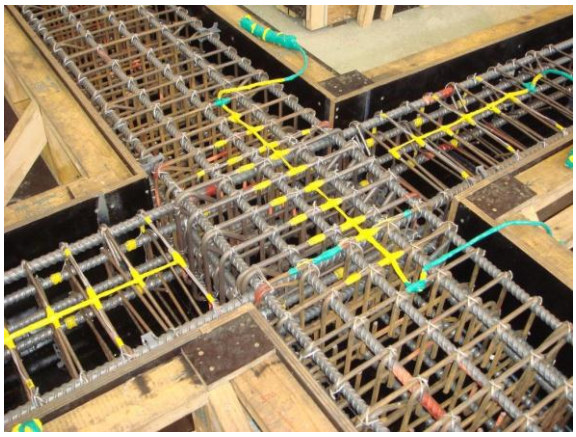
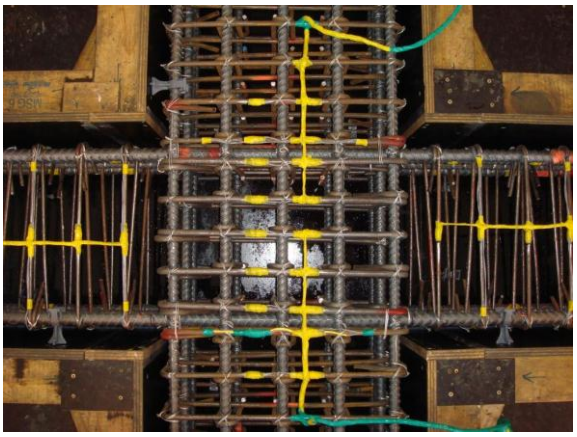




Figure E-5: Casting stages of BCJ5




Figure E-6: Casting stages of BCJ6


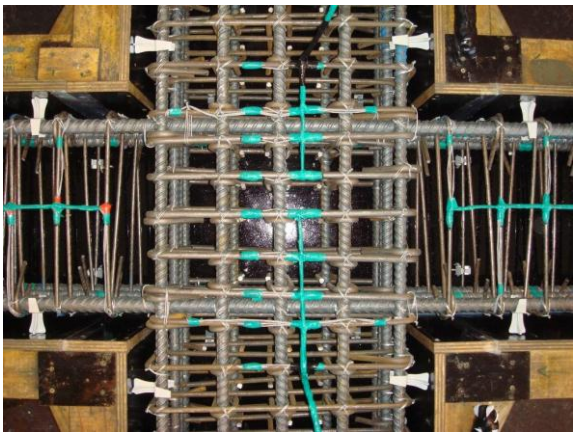

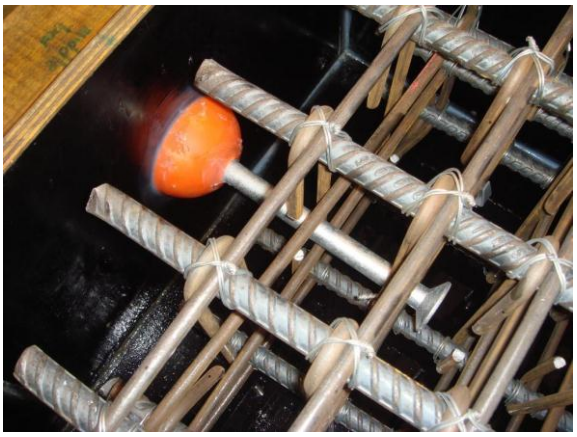



Figure E-7: Casting stages of BCJ7

Figure E-8: Painting a typical BCJ in white for crack identification















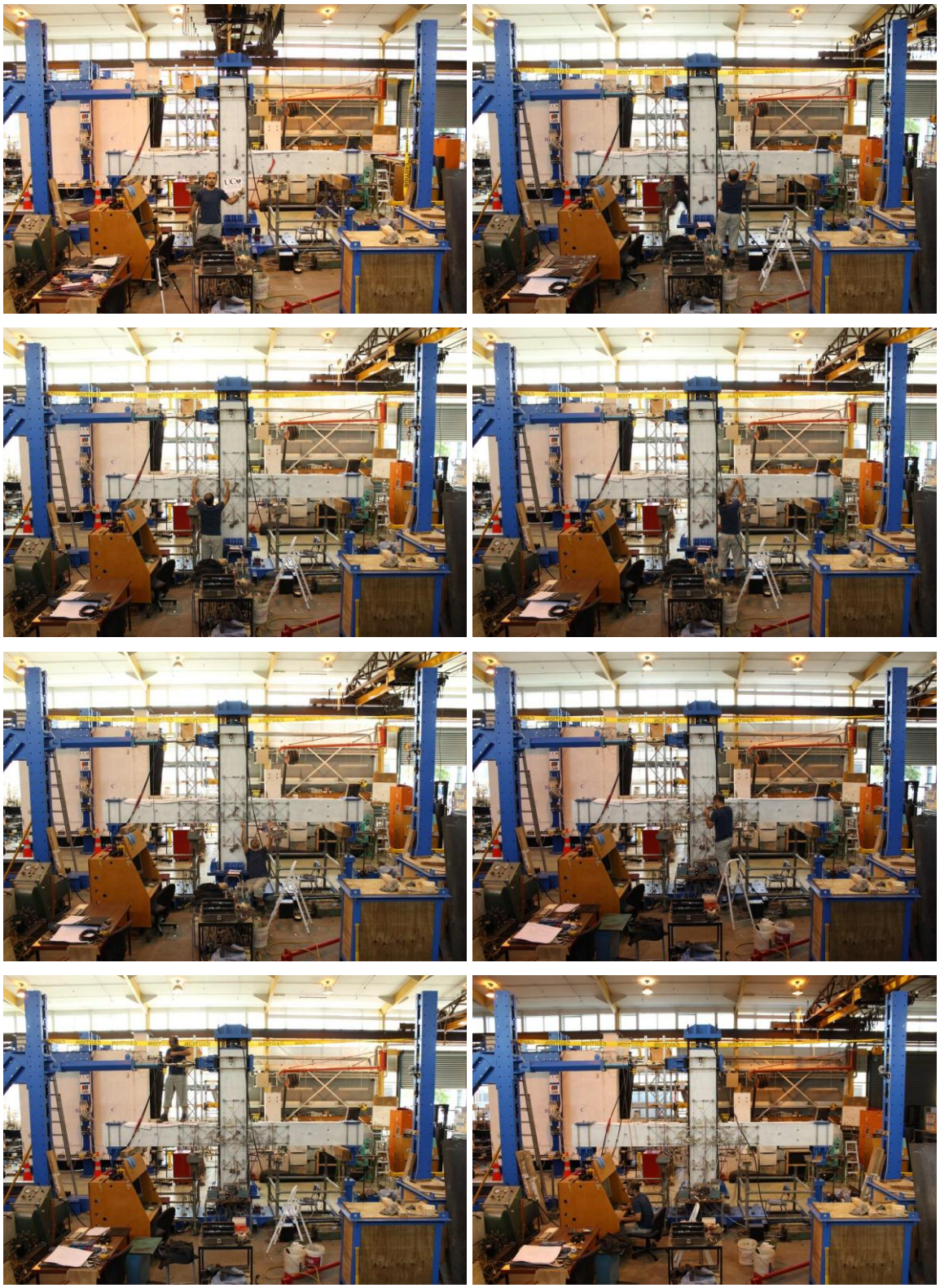

Figure E-9: Erection of a typical BCJ and installation of instrumentation

Figure E-10: Testing of a typical BCJ (3.5% and 4.5%drift ratios)

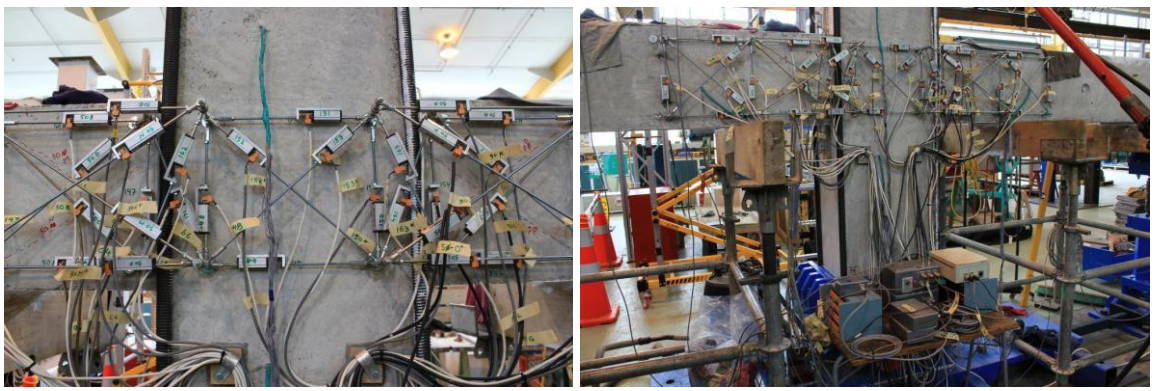



CAUTION CAUTION CAUTION CAUTION

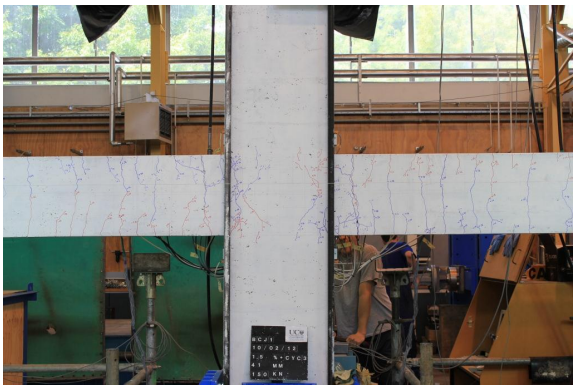

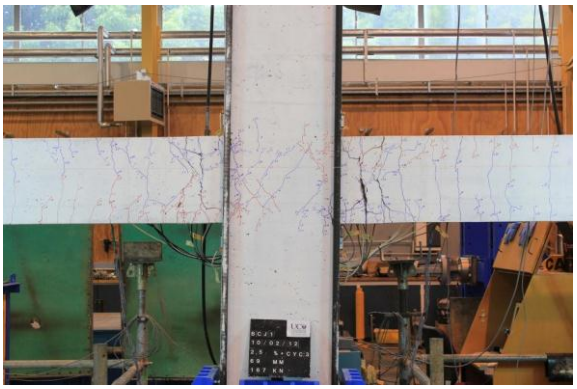
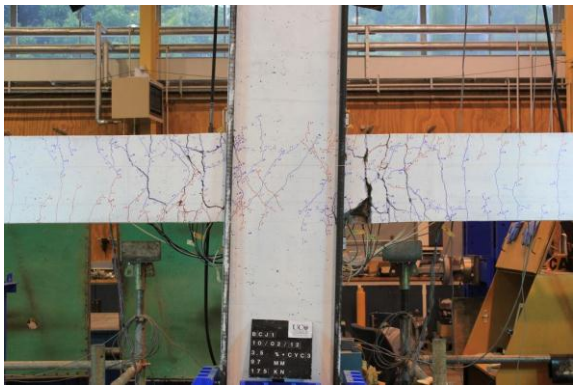
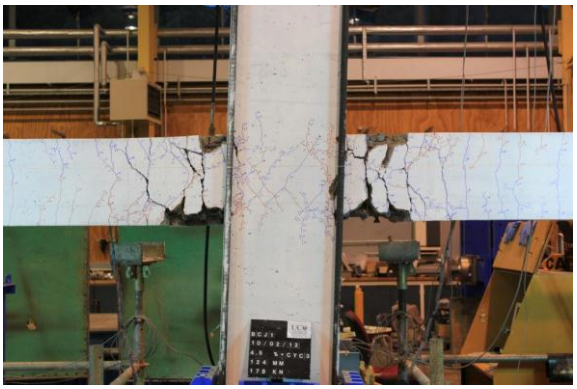

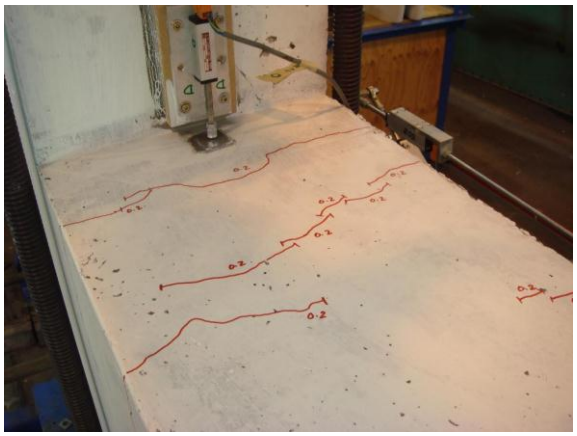

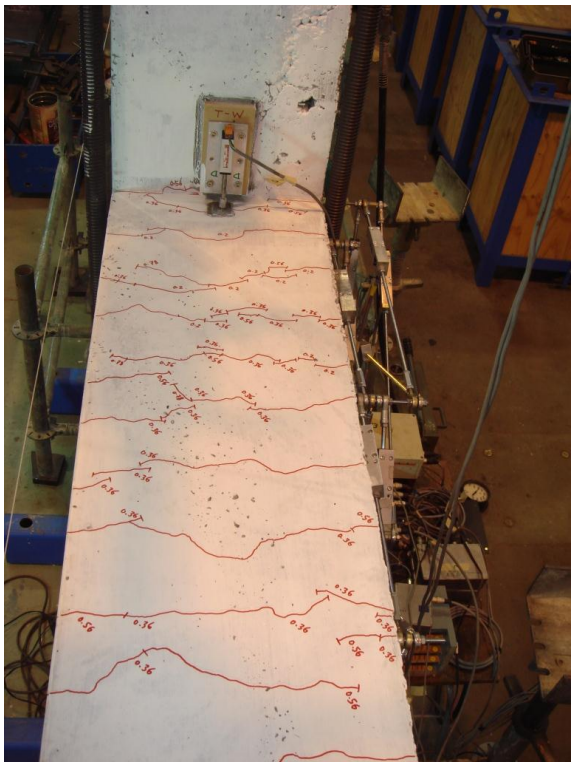
T-W
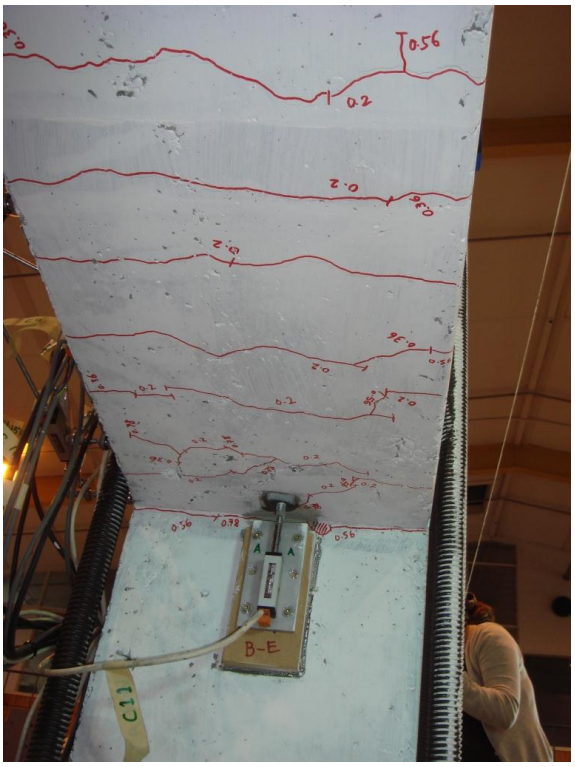
B-E
C11
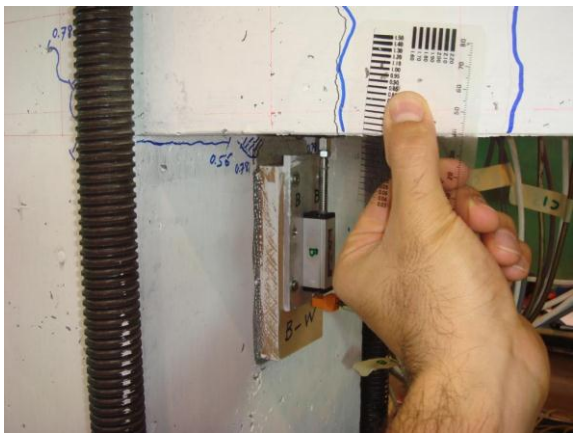
B-W
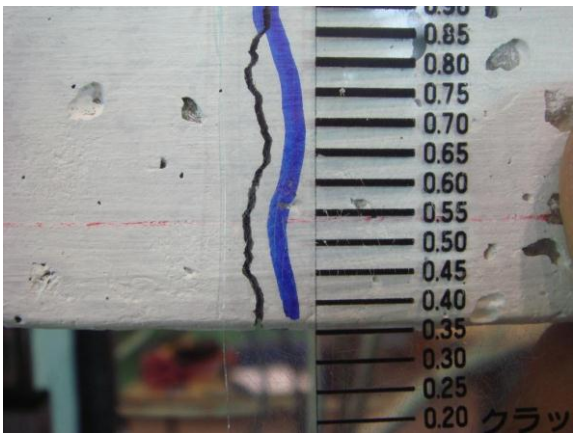
0.85
0.80
0.75
0.70
0.65
0.60
0.55
0.50
0.45
0.40
0.35
0.30
0.25
0.20
クラッ

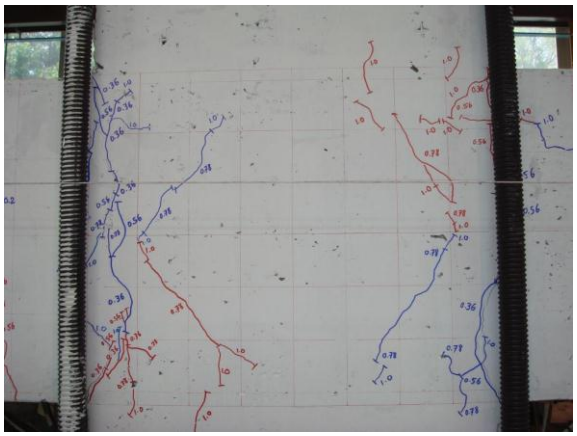


BCJ1
10/02/12
1.5 % + CYC3
41 MM
150 KN

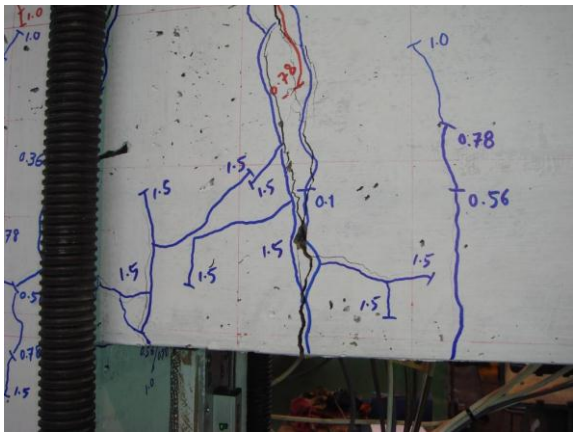
1.0
0.78
0.56
1.5
0.1

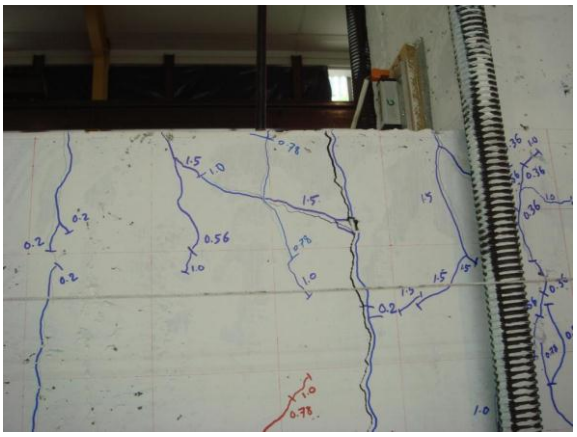


BCJ1
10/02/12
2.0 % + CYC3
55 MM
158 KN

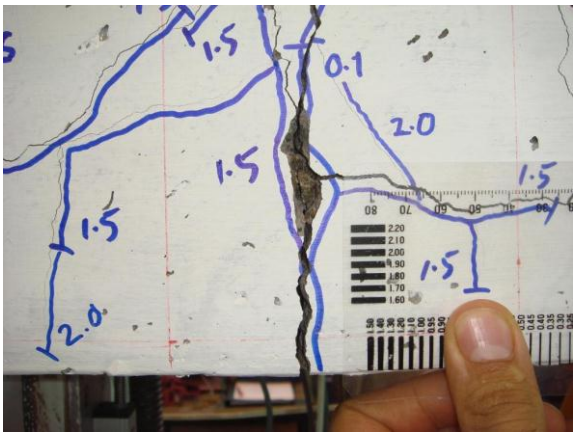
1.5
0.1
2.0
1.5
1.5
1.5
1.5
2.0

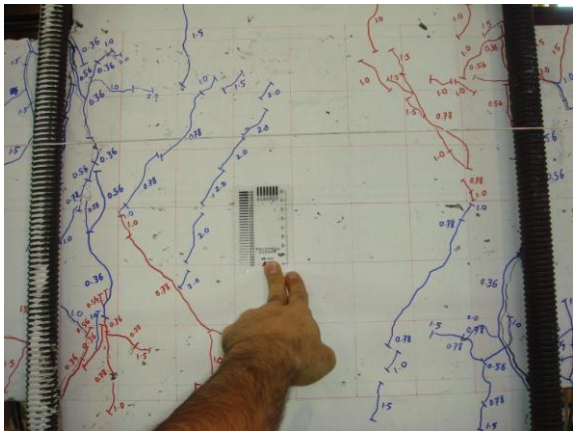


BCJ1
10/02/12
2.5 %+CYC3
69 MM
167 KN

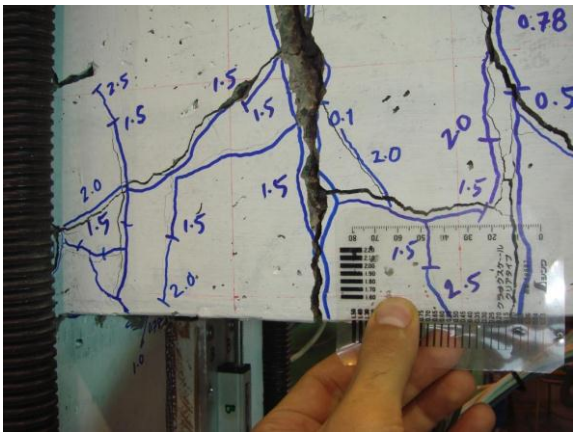

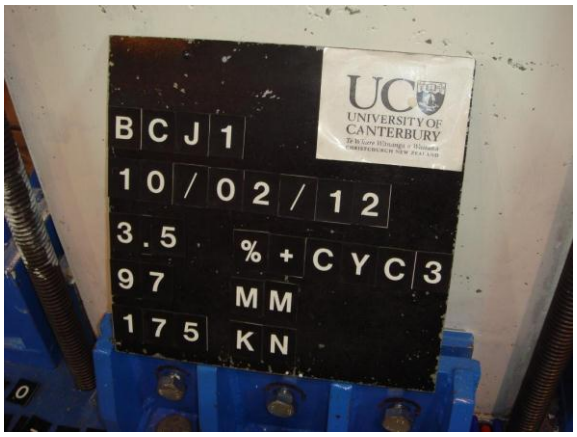
BCJ1
10/02/12
3.5 %+CYC3
97 MM
175 KN

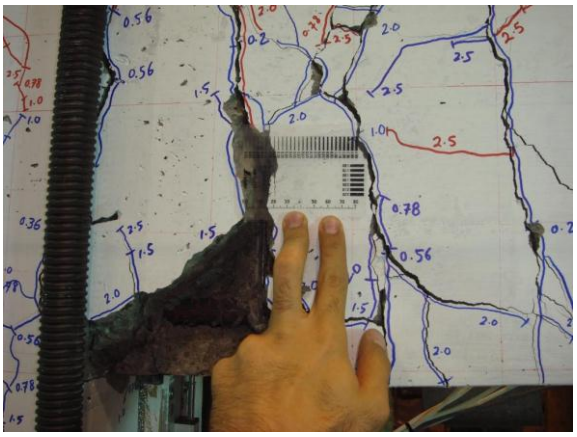

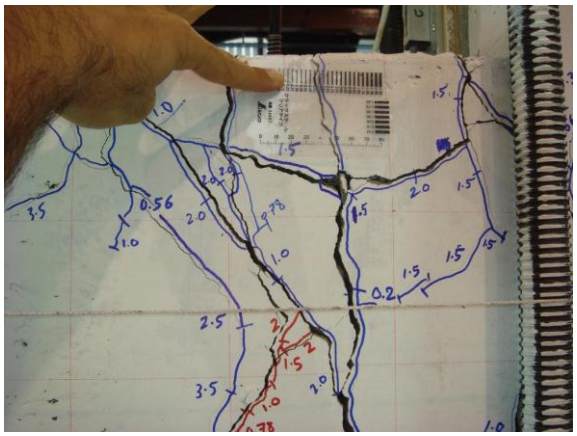


BCJ1
10/02/12
4.5 %+CYC3
124 MM
178 KN

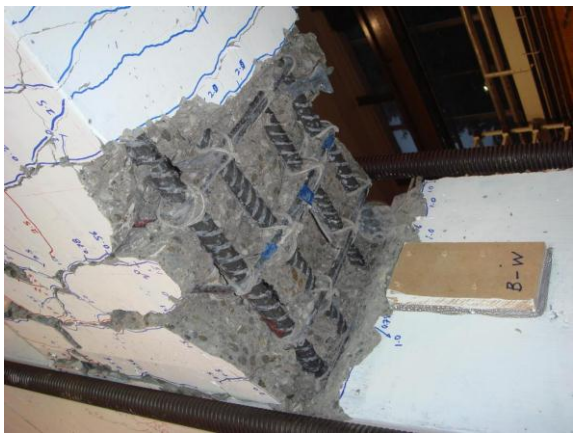
B-W

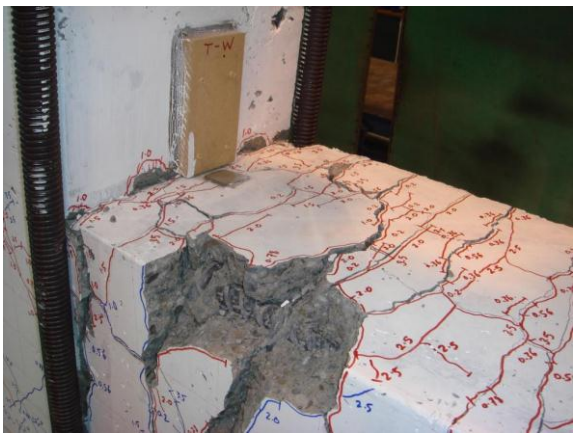
T-W

Figure E-11: Testing of BCJ1

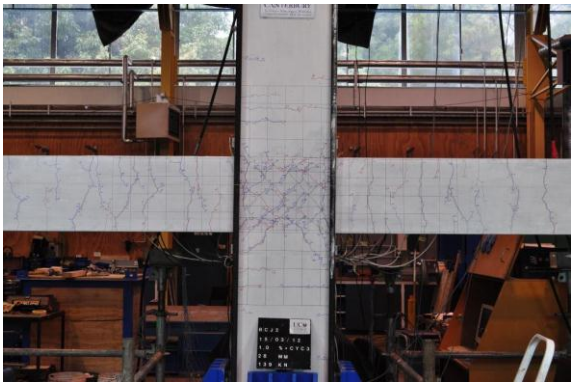
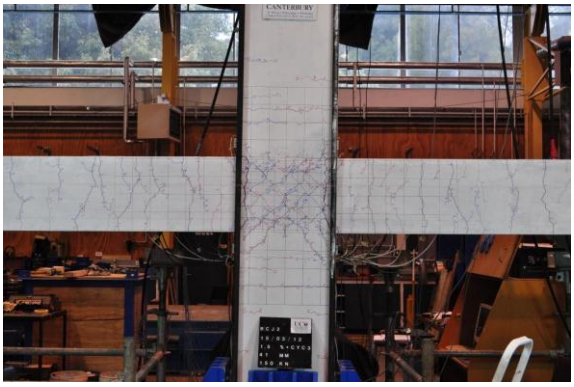
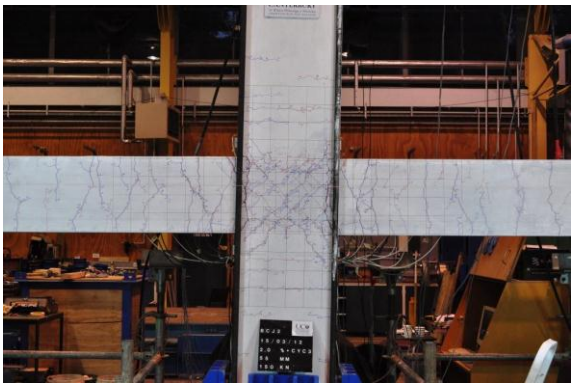
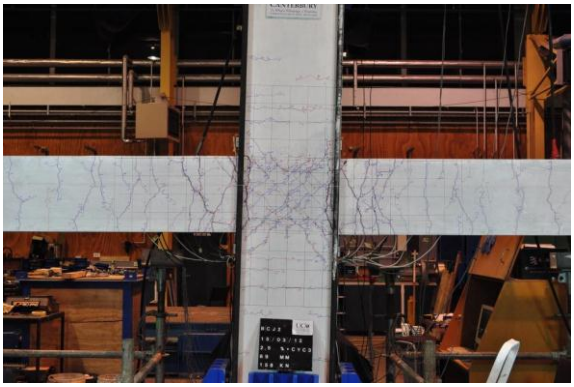
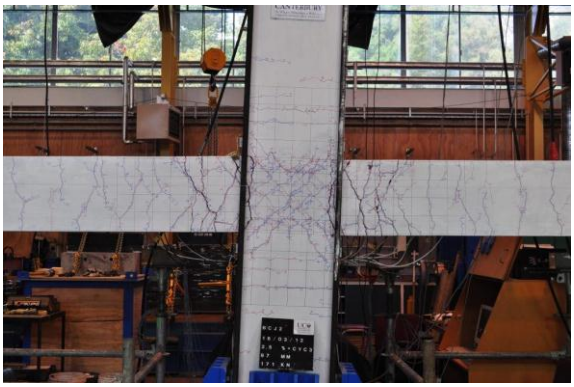
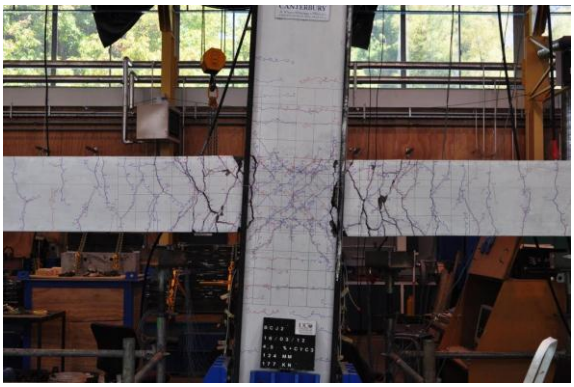
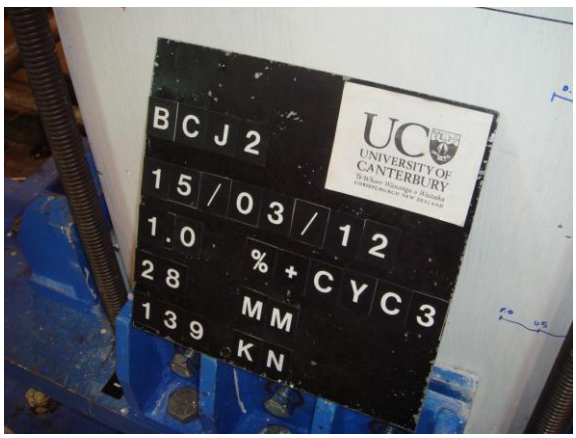
BCJ2
UC
UNIVERSITY OF CANTERBURY
15/03/12
1.0 %+CYC3
28 MM
139 KN
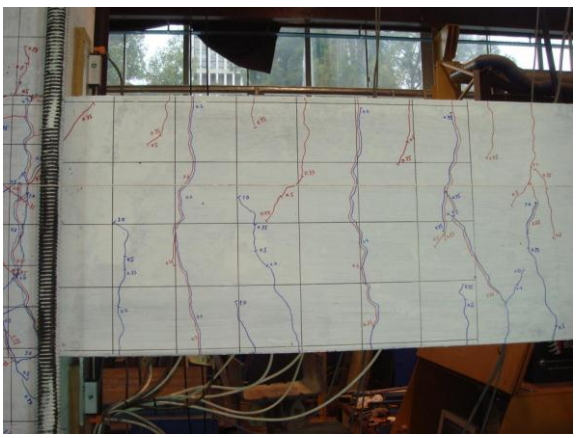

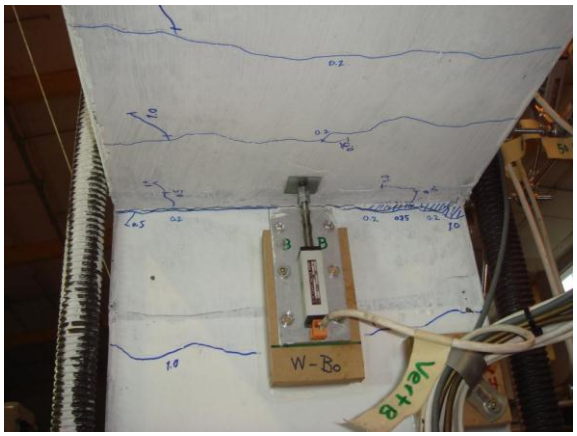
W-Bo
Vert B

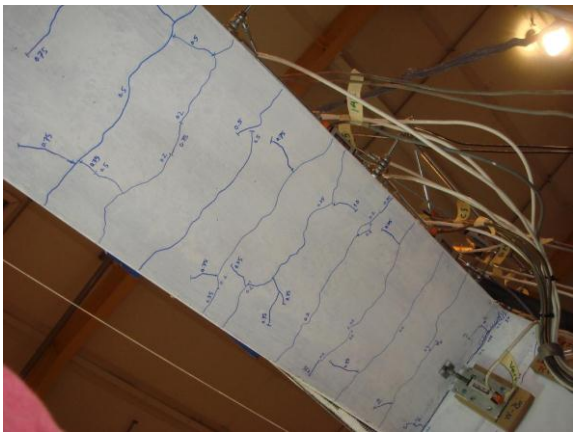

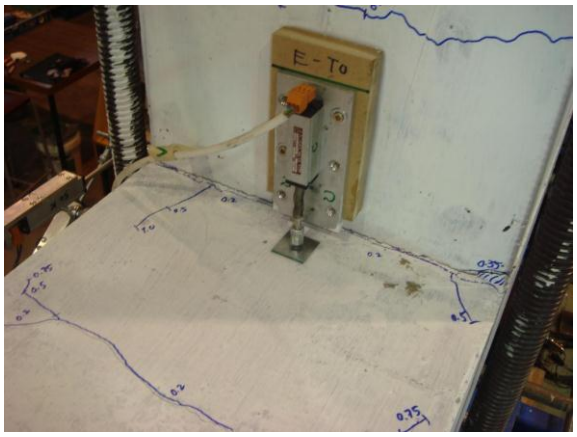
E-To

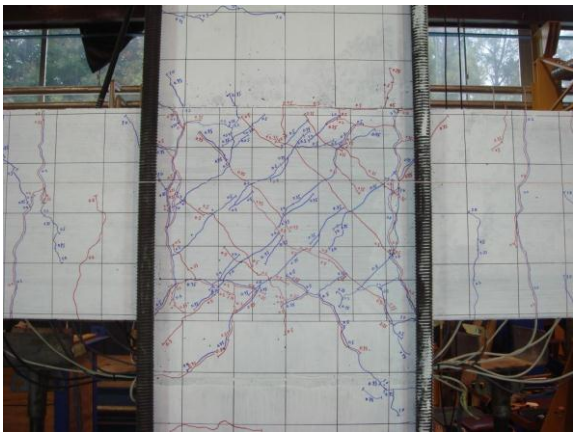

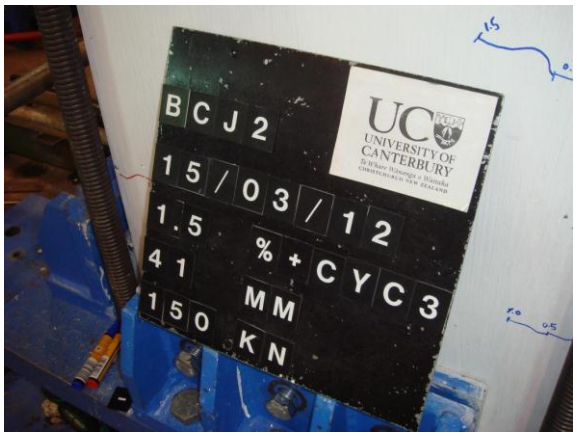
BCJ2
15/03/12
1.5 % + CYC 3
41 MM
150 KN
UC
UNIVERSITY OF CANTERBURY

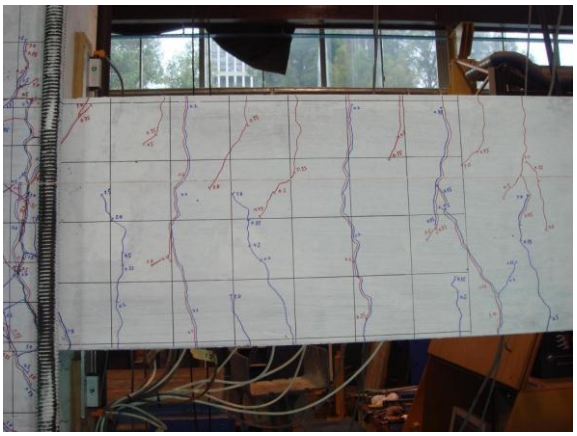

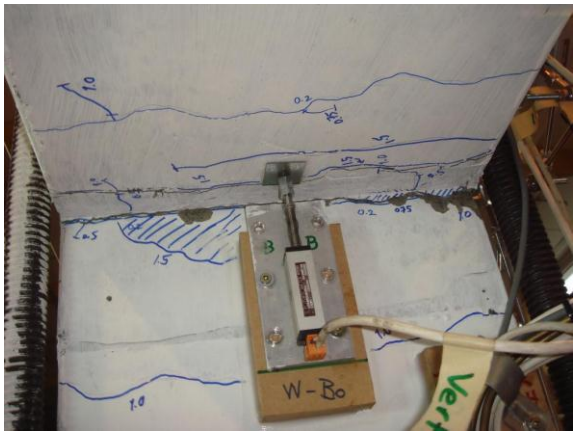
W-Bo

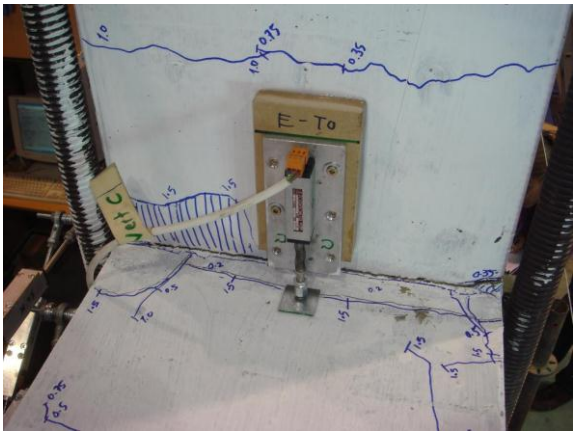
E-To

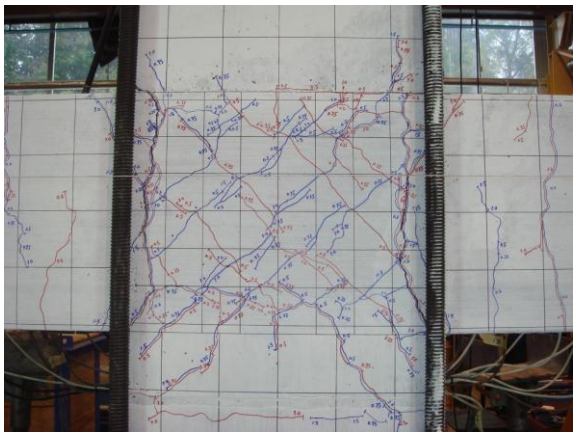

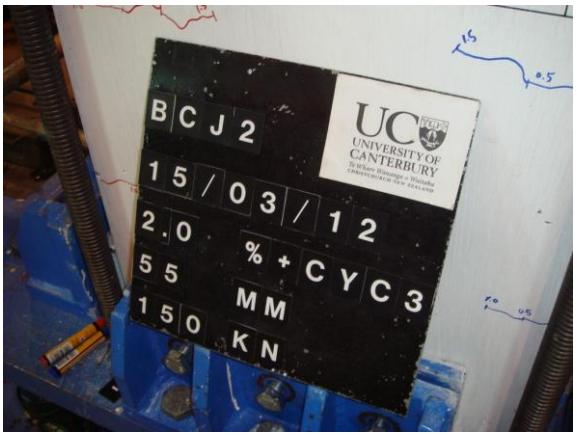
BCJ2
15/03/12
2.0 % + CYC3
55 MM
150 KN
UC
UNIVERSITY OF CANTERBURY

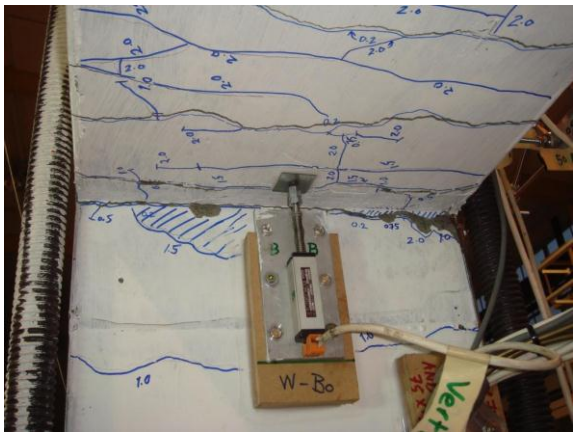
W-Bo

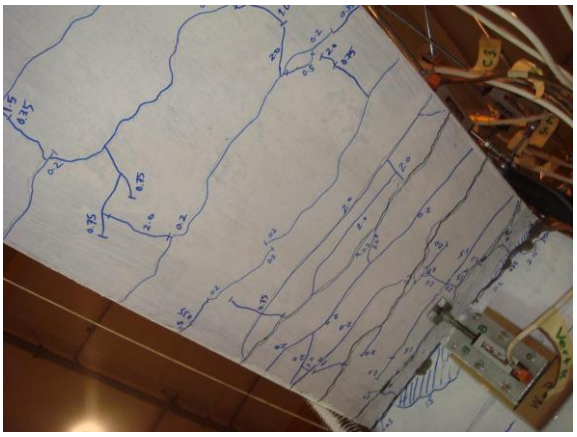

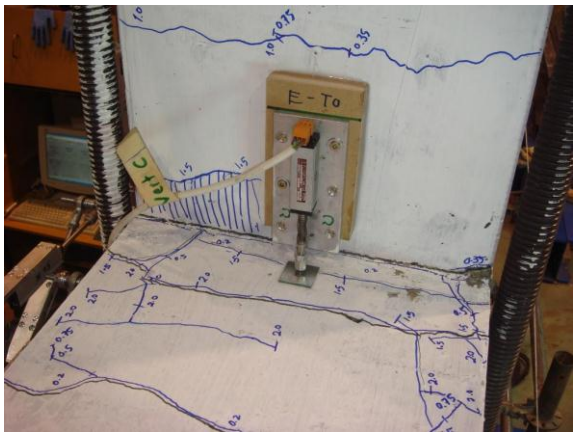
E-To

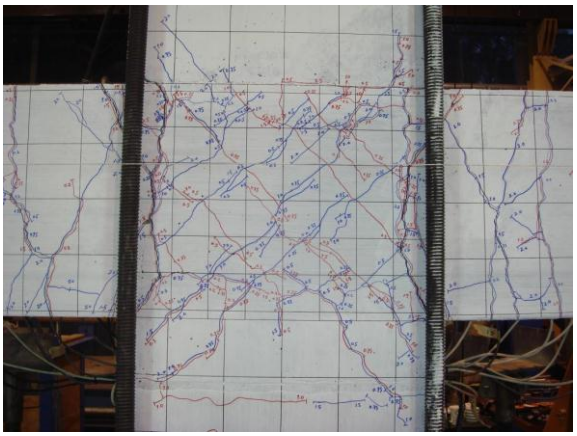

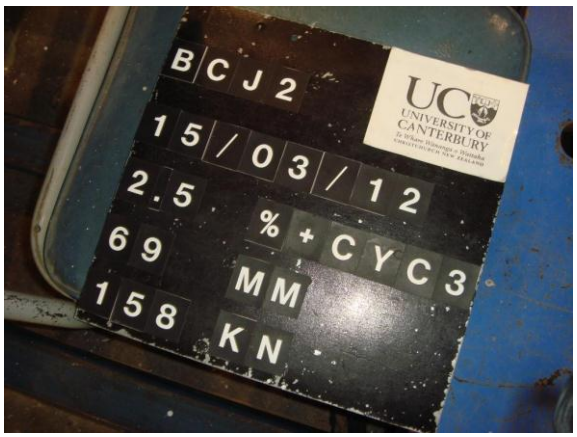
BCJ2
15/03/12
2.5 % + CYC3
69 MM
158 KN
UC
UNIVERSITY OF CANTERBURY

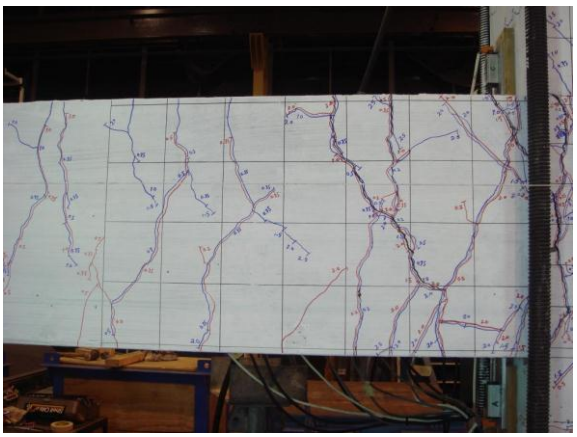

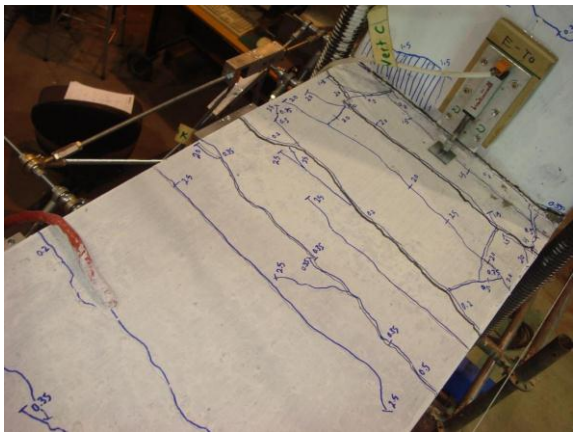
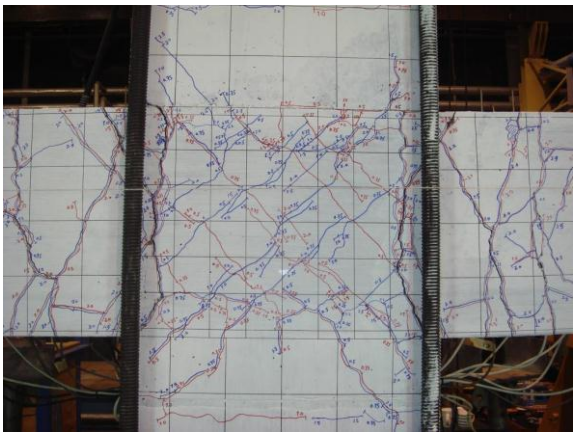
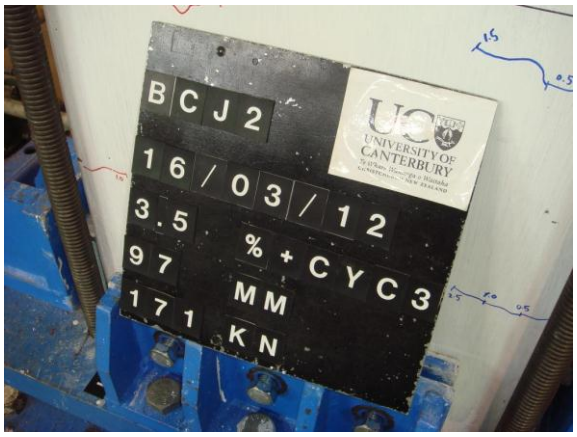
BCJ2
UNIVERSITY OF CANTERBURY
16/03/12
3.5 % + CYC 3
97 MM
171 KN
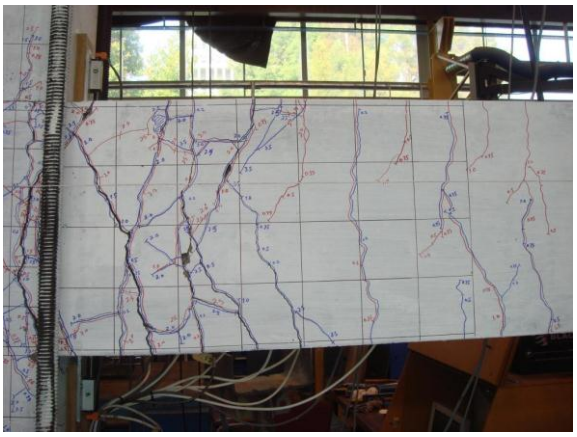
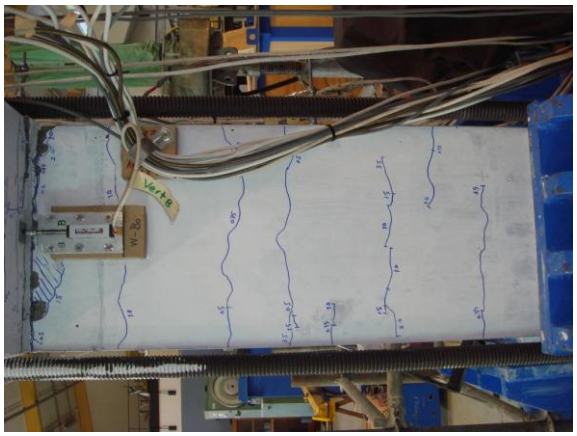
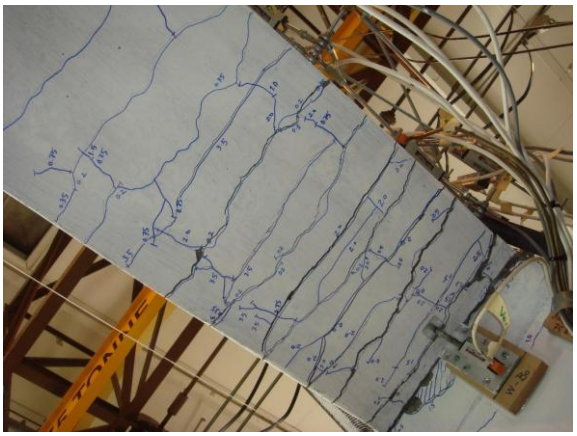
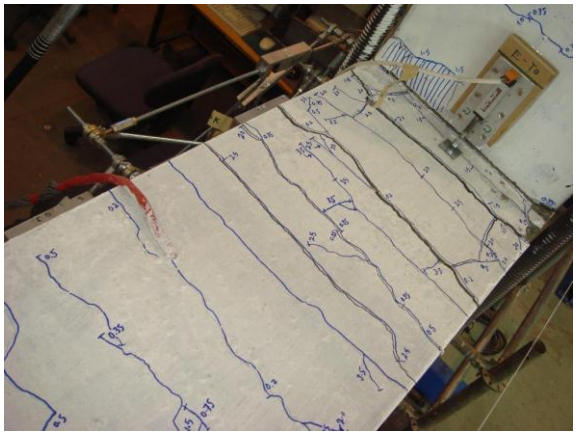
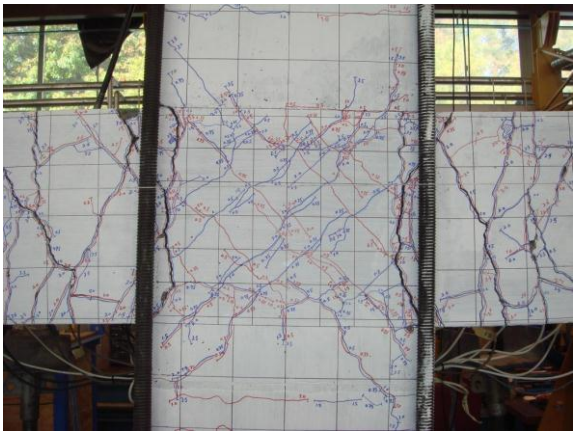

Figure E-12: Testing of BCJ2

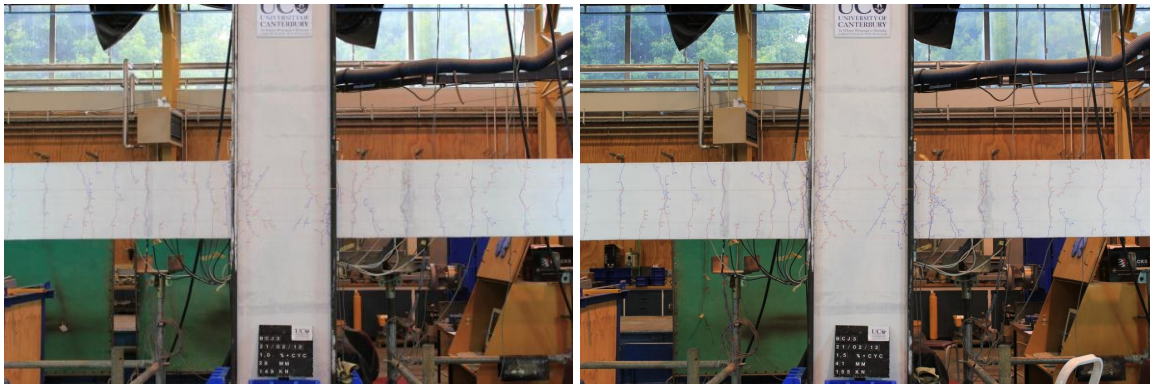

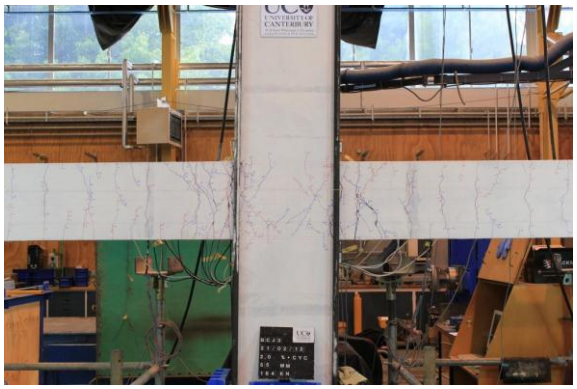
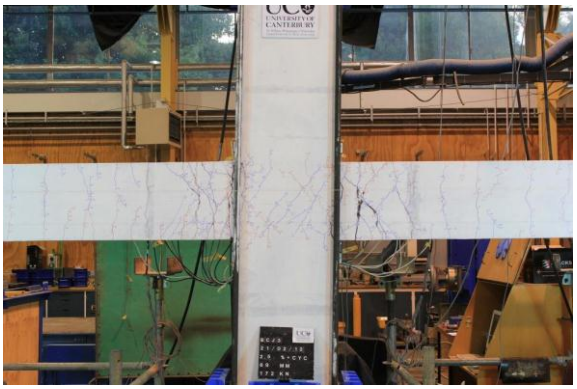



BCJ3
21/02/12
1.0 % + CYC
28 MM
149 KN
UC
UNIVERSITY OF CANTERBURY
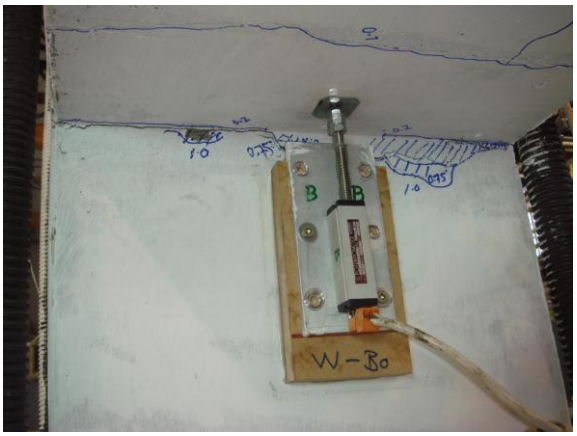
W-Bo
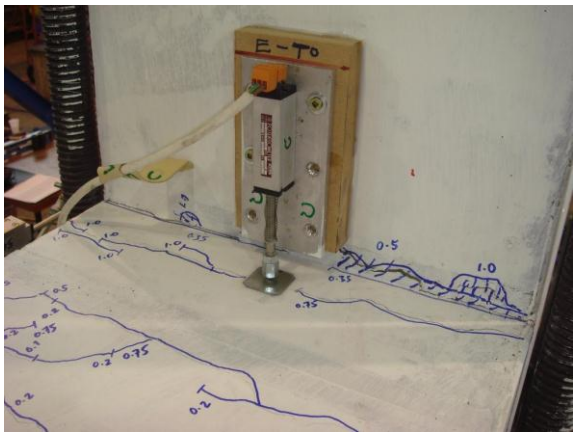
E-To
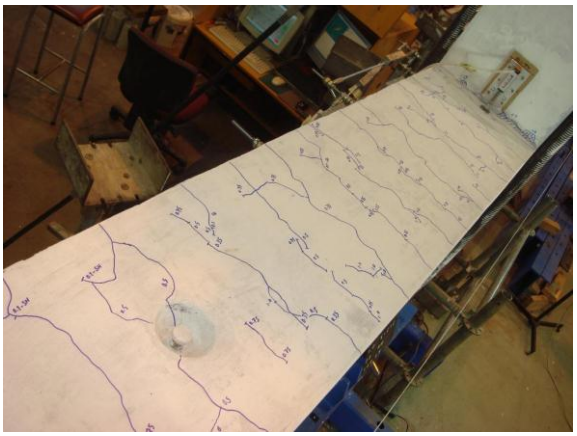

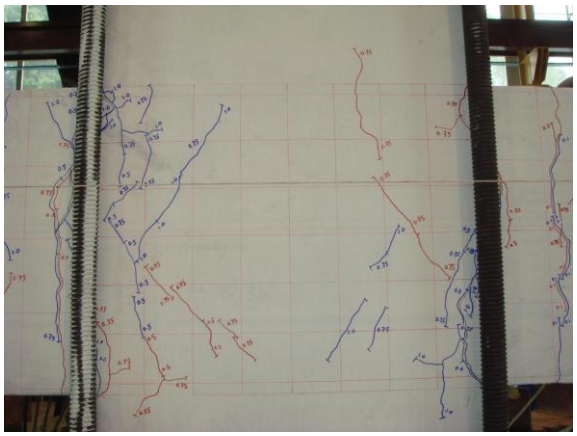


BCJ3
21/02/12
1.5 % + CYC
41 MM
155 KN
UC
UNIVERSITY OF CANTERBURY

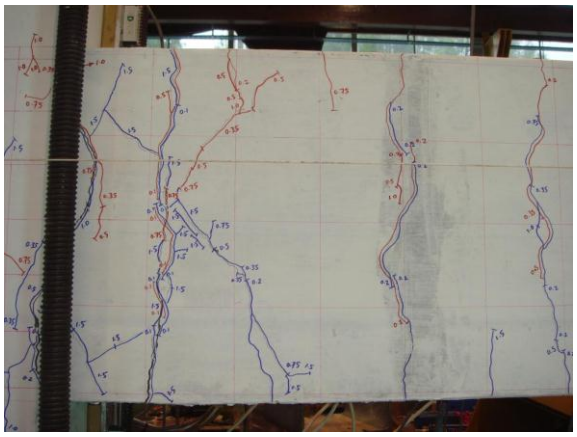

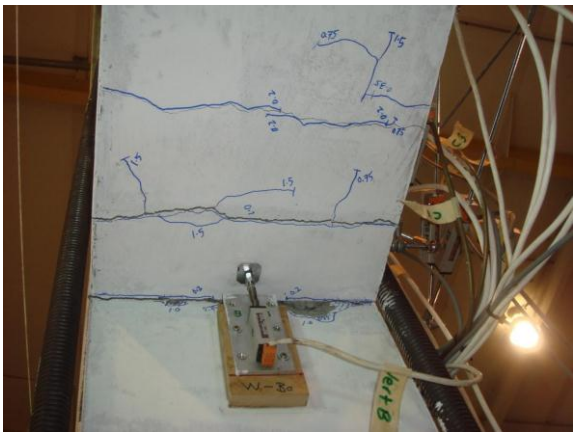

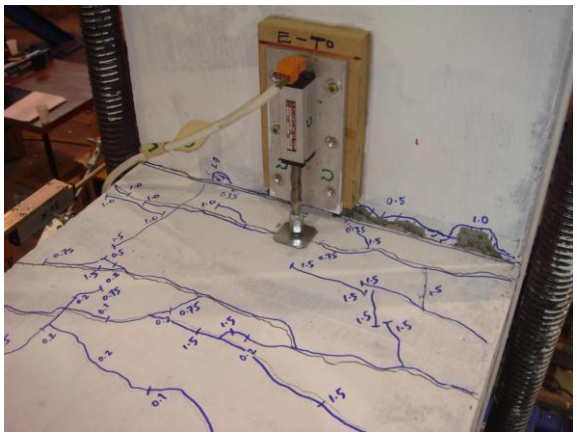

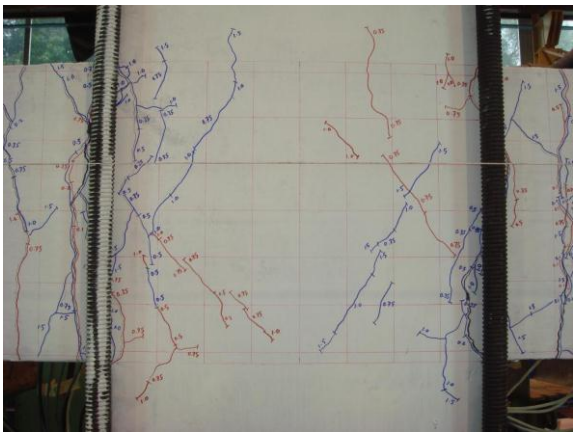


BCJ3
21/02/12
2.0 % + CYC
55 MM
164 KN
UC
UNIVERSITY OF CANTERBURY

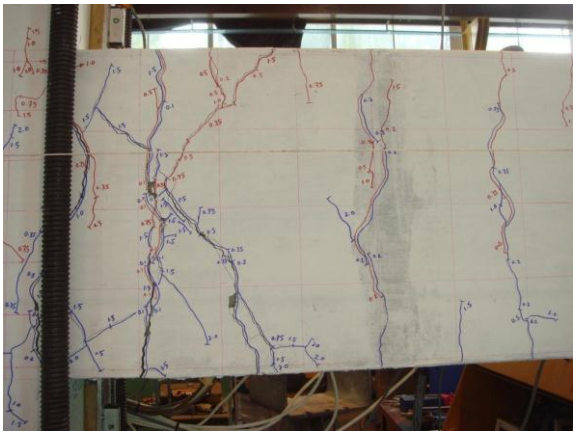

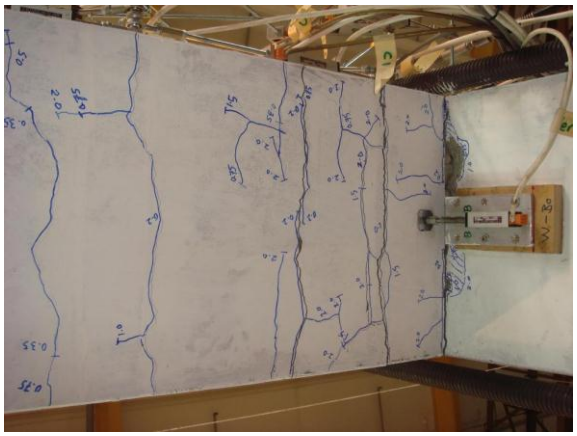
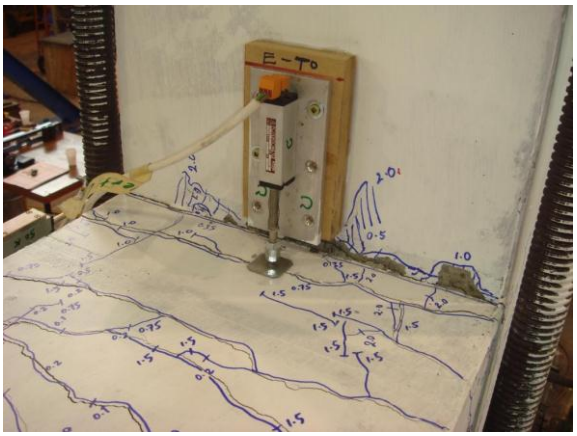
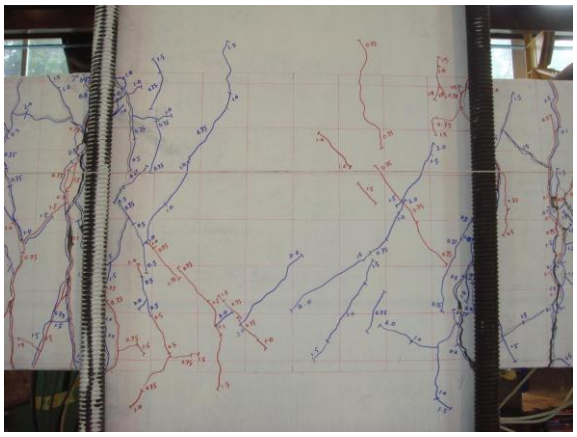
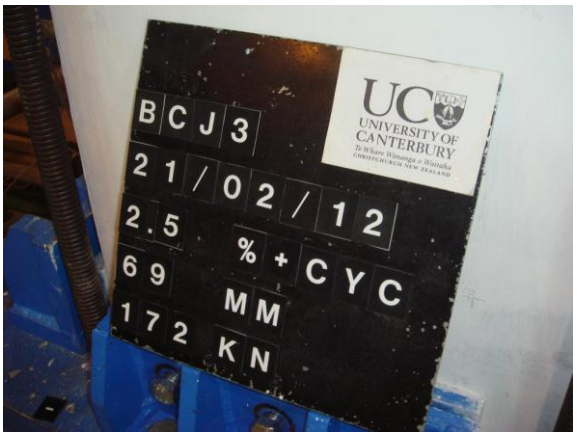
BCJ3
21/02/12
2.5 % + CYC
69 MM
172 KN
UC
UNIVERSITY OF CANTERBURY
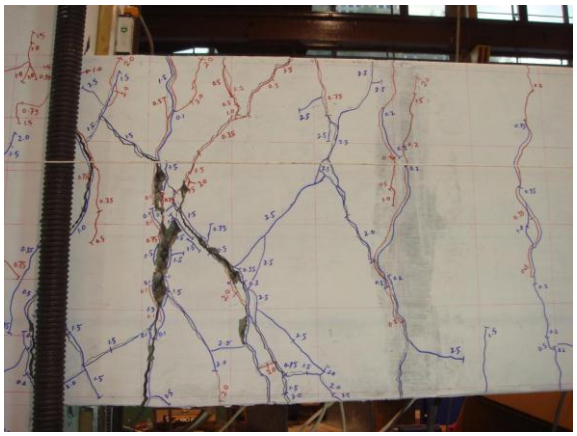
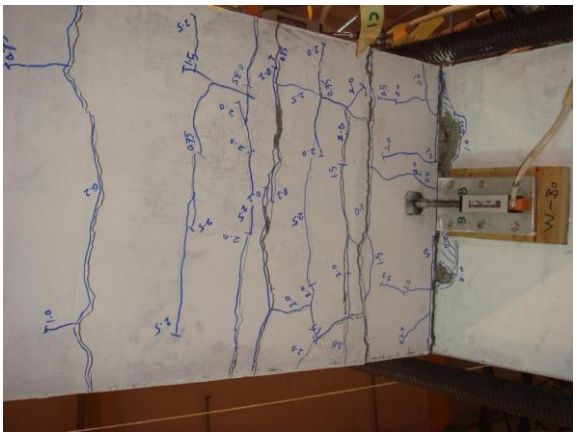
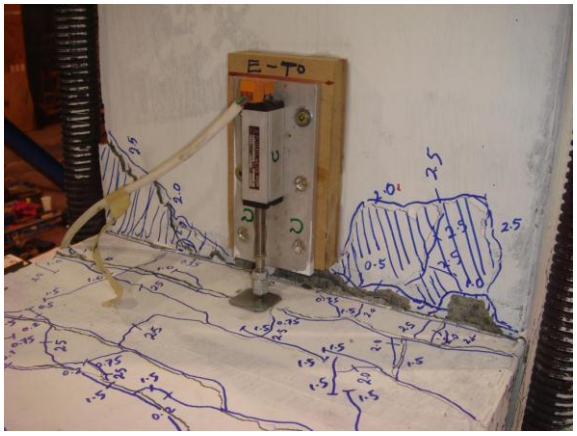
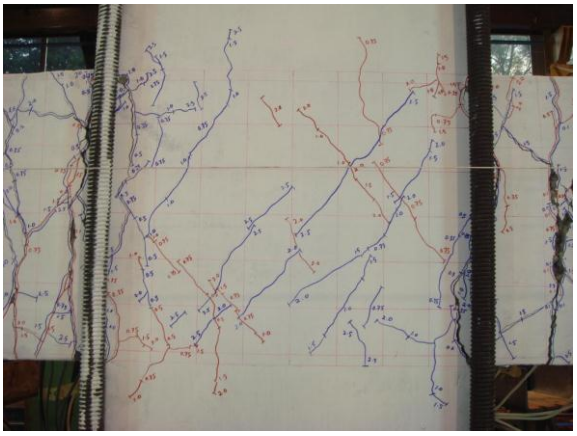

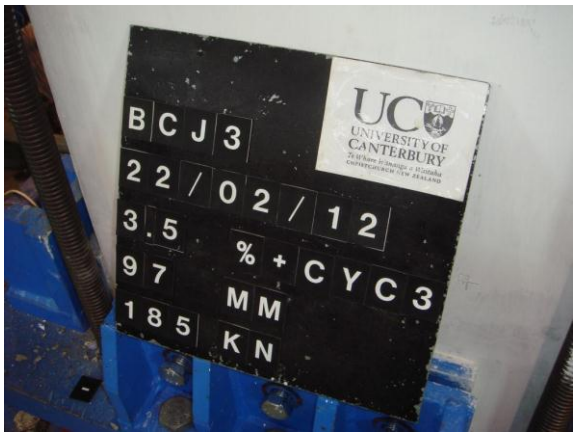
BCJ3
UC
UNIVERSITY OF
CANTERBURY
22/02/12
3.5 % + CYC3
97 MM
185 KN
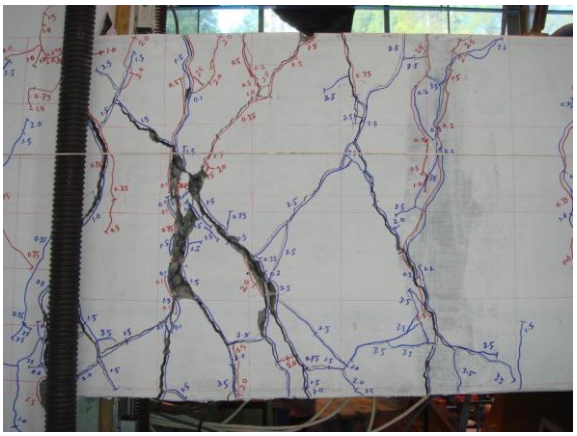

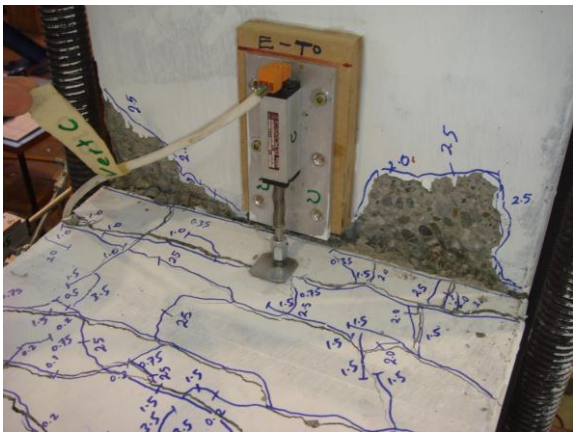
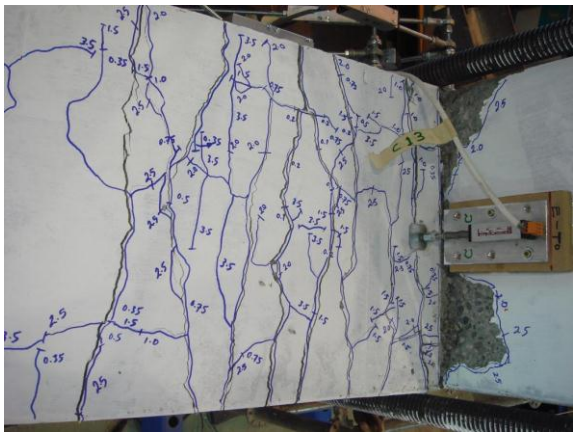
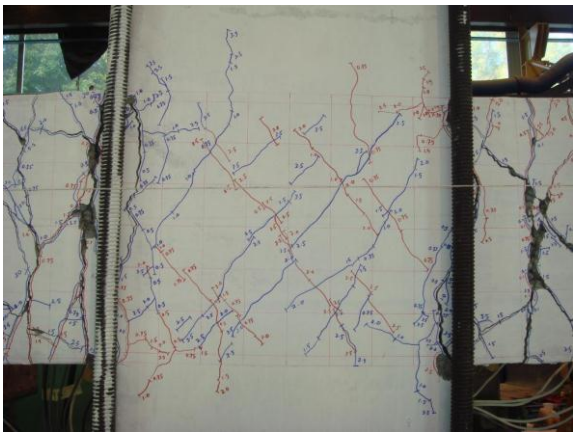

BCJ3
UC
UNIVERSITY OF
CANTERBURY
22/02/12
4.5 % + CYC3
124 MM
190 KN
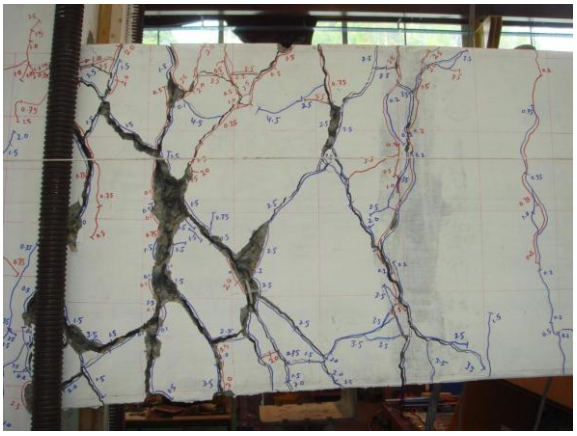

Figure E-13: Testing of BCJ3

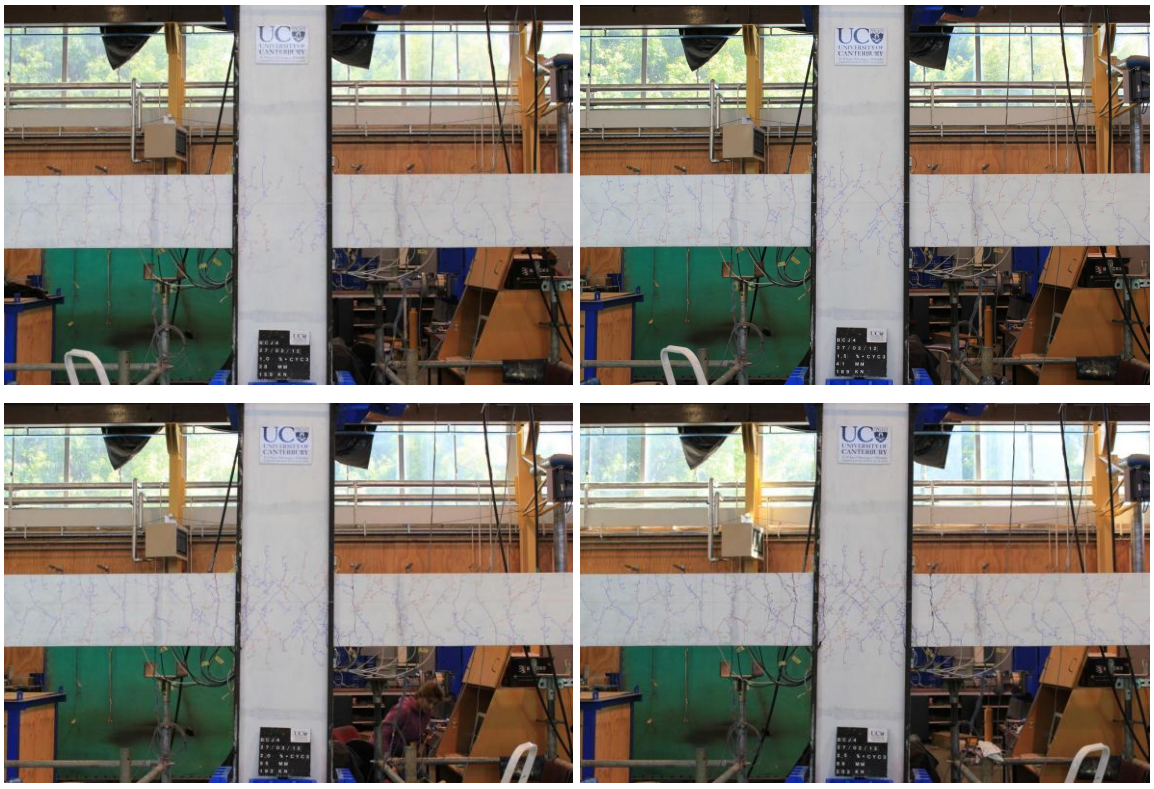

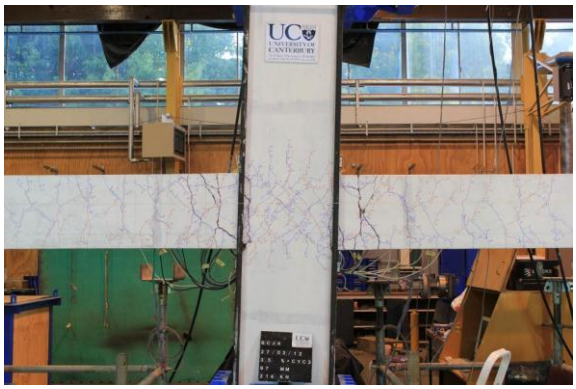

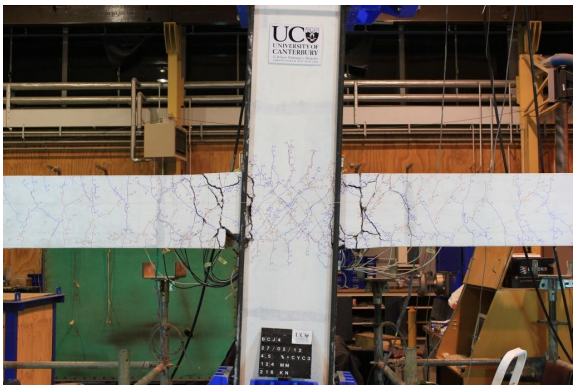


BCJ4
27/02/12
1.0 % + CYC3
28 MM
159 KN

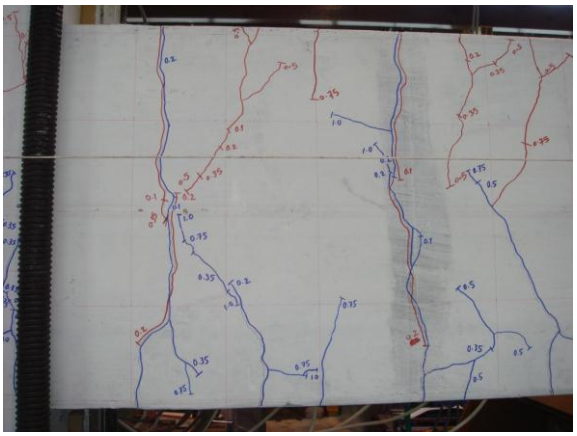

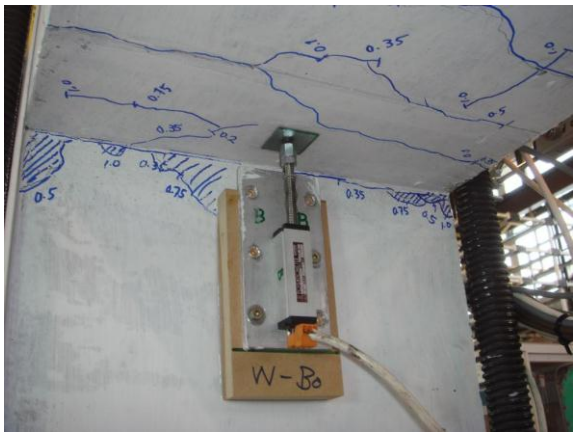
W-Bo

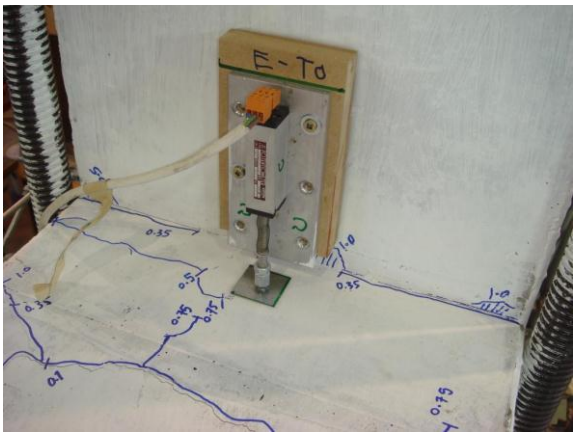
E-To

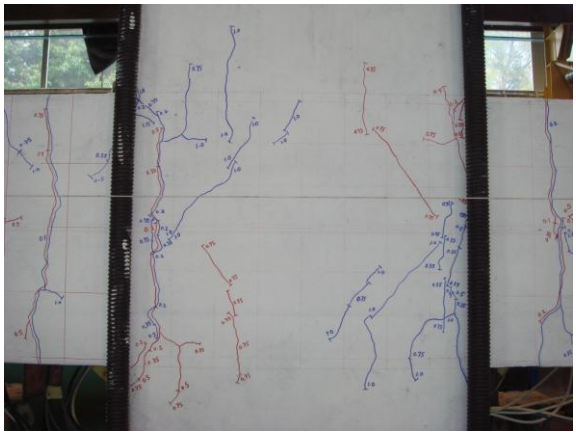

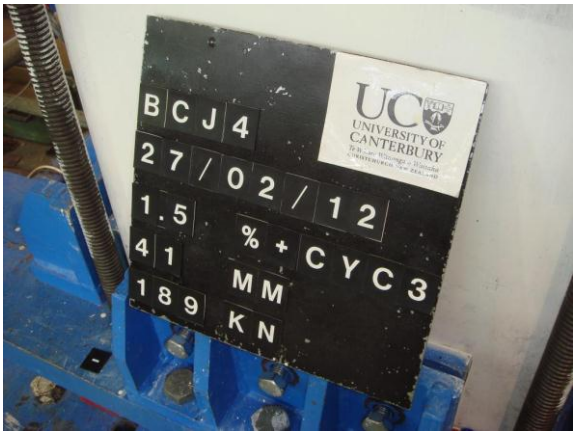
BCJ4
27/02/12
1.5 % + CYC3
41 MM
189 KN

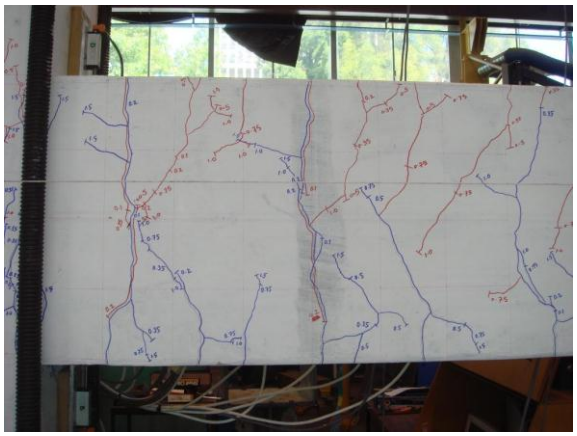
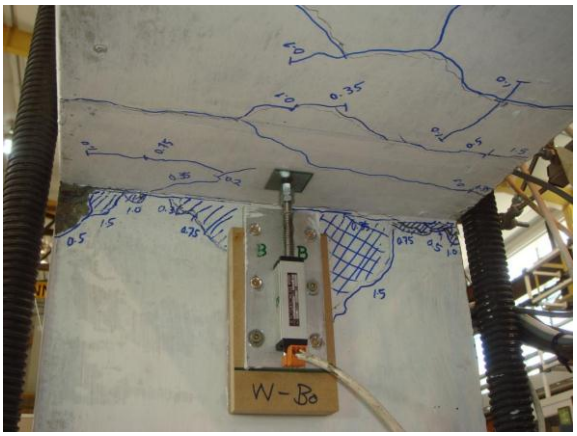
W-Bo
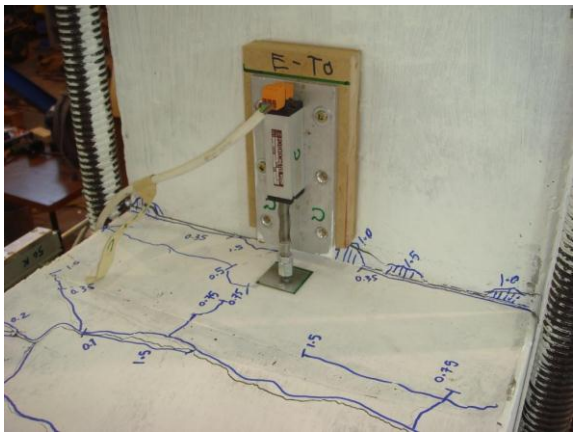
E-To
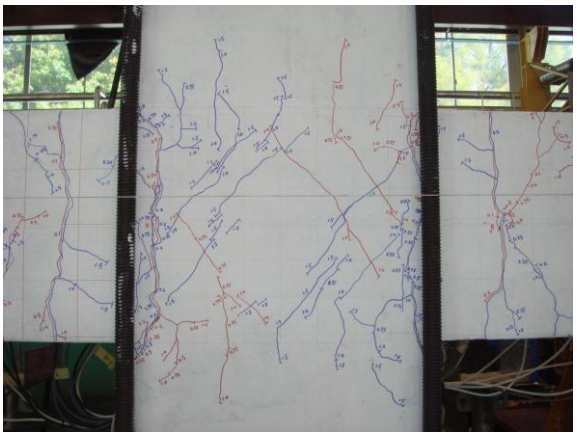
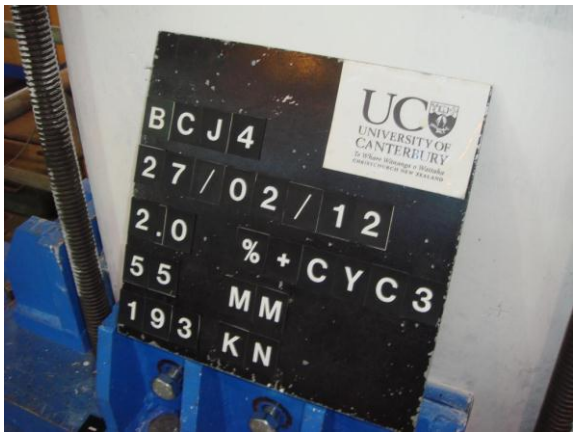
BCJ4
27/02/12
2.0 %+CYC3
55 MM
193 KN
UC
UNIVERSITY OF CANTERBURY
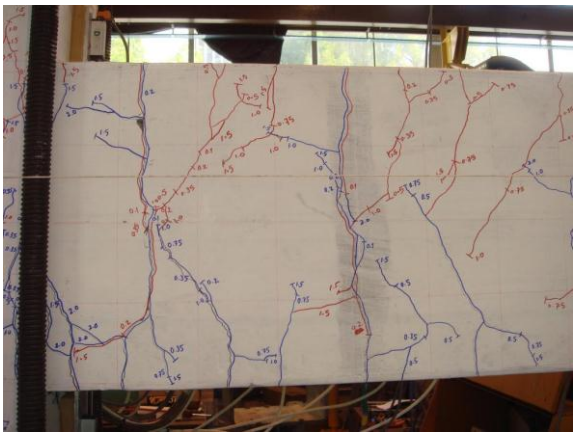

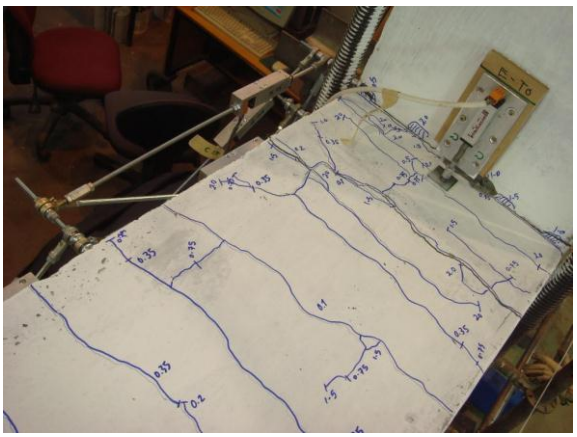

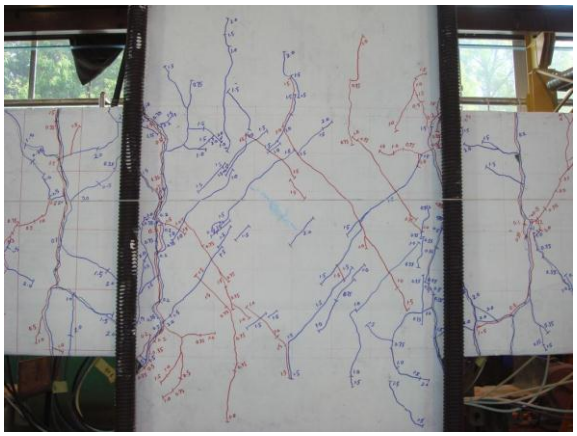
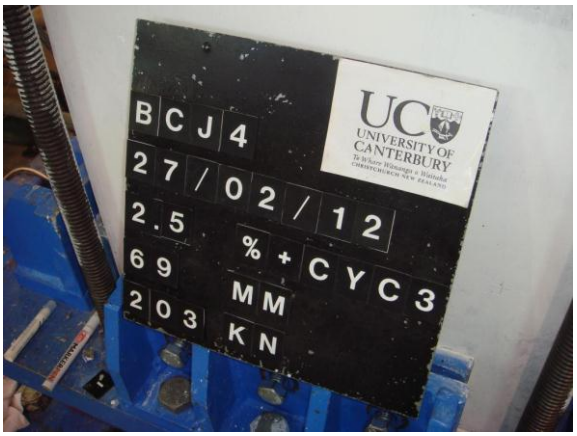
BCJ4
27/02/12
2.5 % + CYC3
69 MM
203 KN
UC
UNIVERSITY OF CANTERBURY
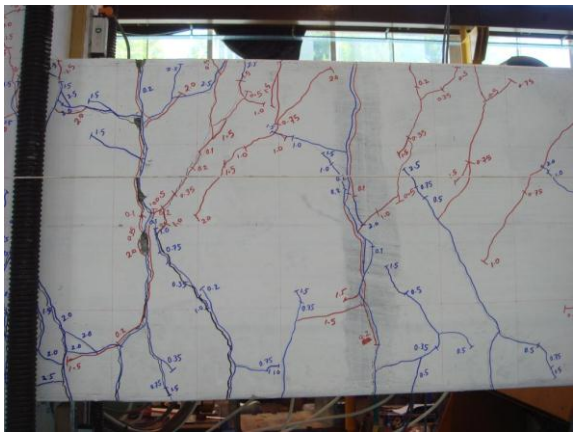
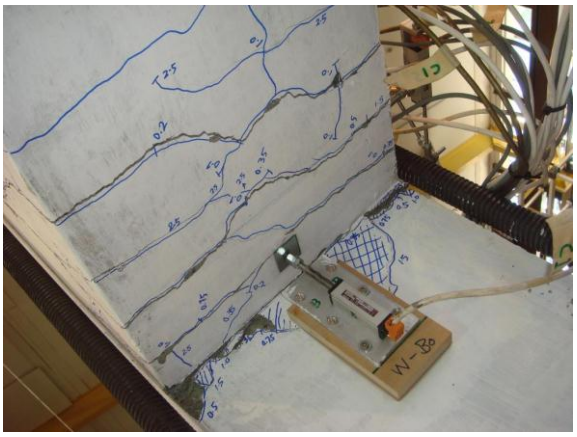
W-B
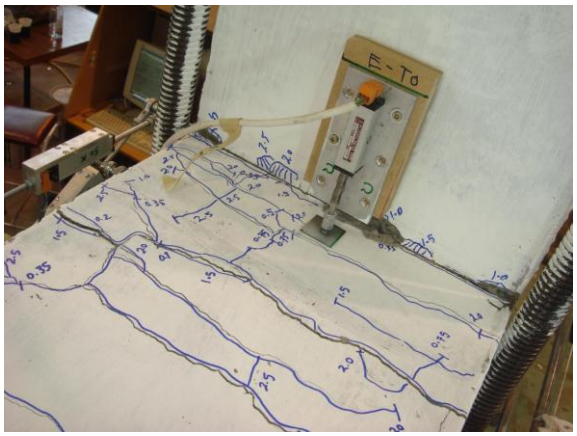
E-To
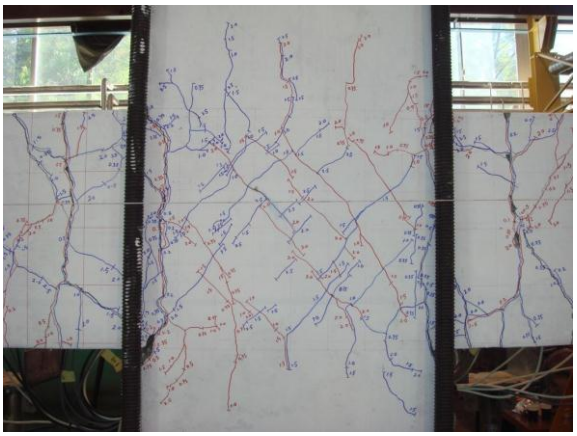
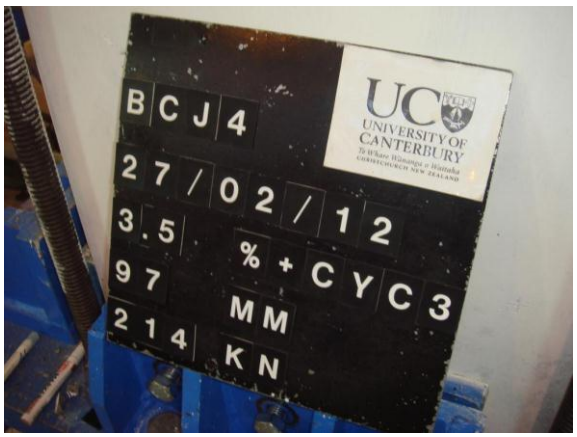
BCJ4
27/02/12
3.5 % + CYC3
97 MM
214 KN
UC
UNIVERSITY OF CANTERBURY
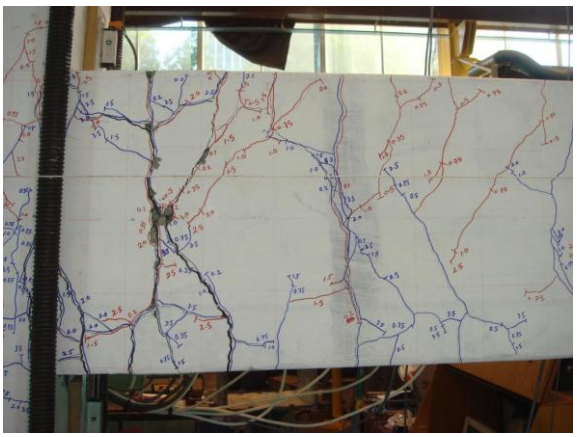

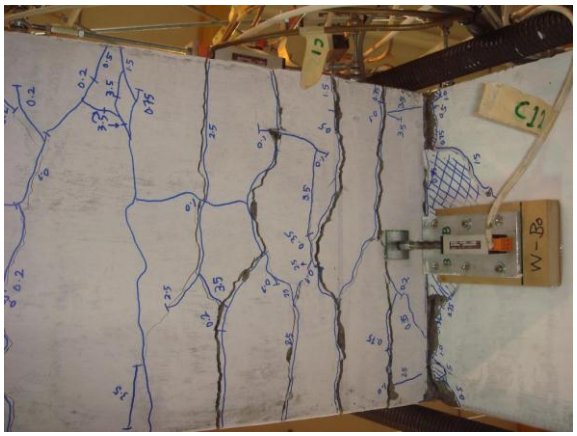
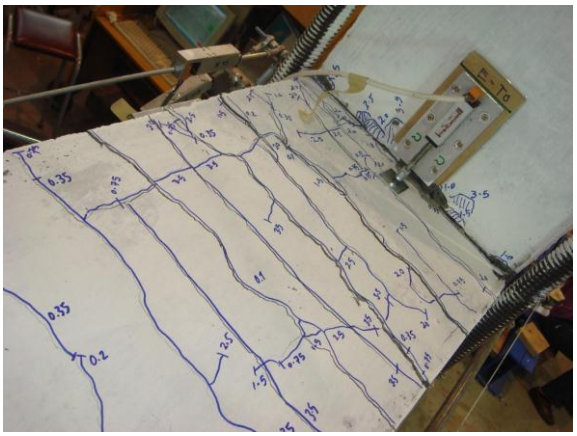
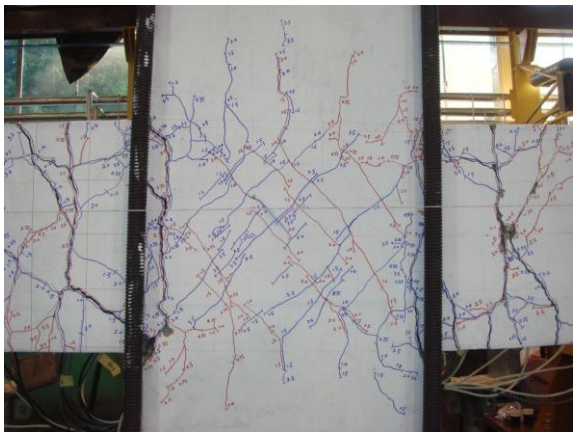
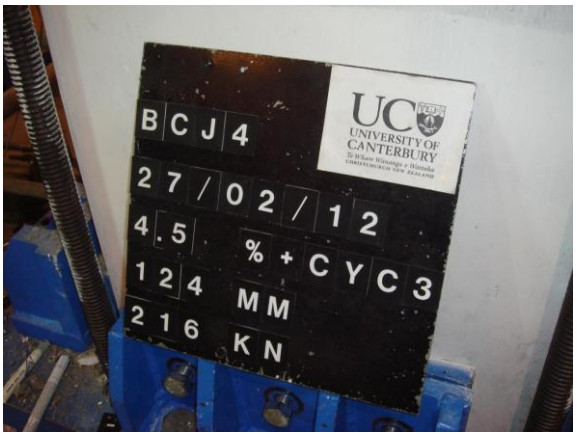
BCJ4
27/02/12
4.5 % + CYC3
124 MM
216 KN
UC
UNIVERSITY OF
CANTERBURY
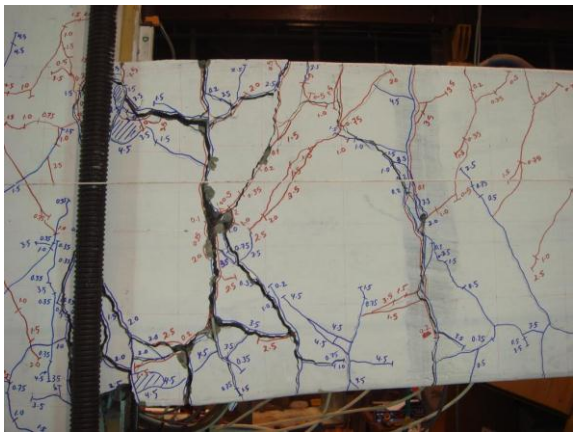
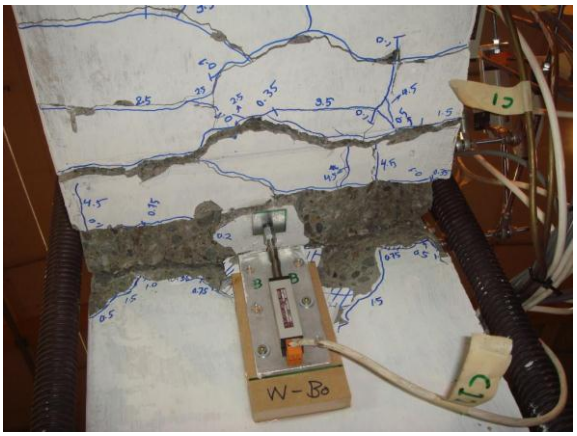

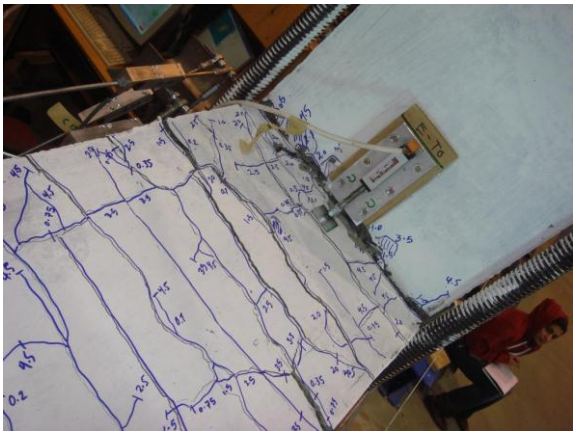

Figure E-14: Testing of BCJ4

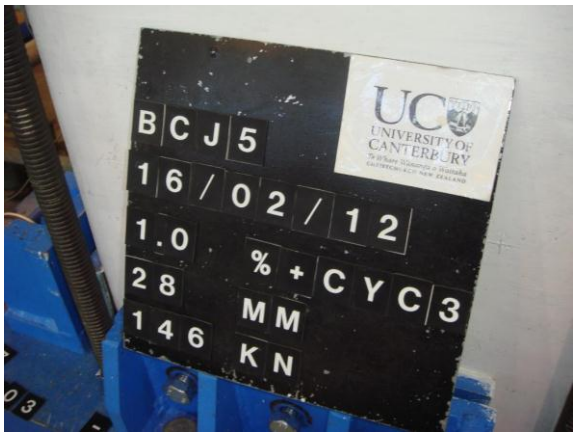
BCJ5
16/02/12
1.0 % + CYC3
28 MM
146 KN

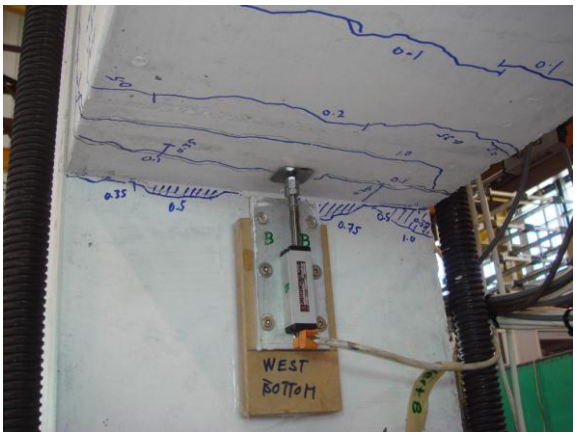
WEST
BOTTOM

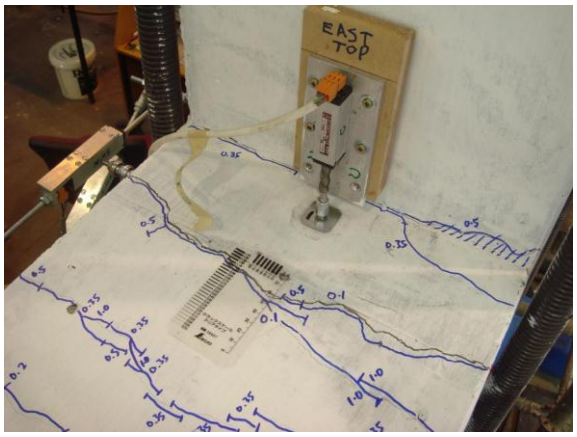
EAST
TOP


BCJ5
16/02/12
1.5 % + CYC3
41 MM
149 KN

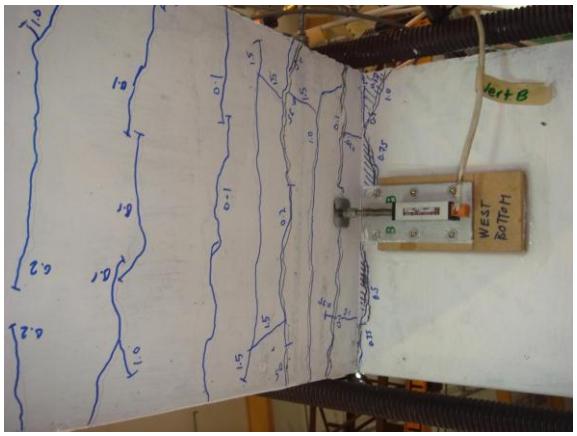
WEST
BOTTOM

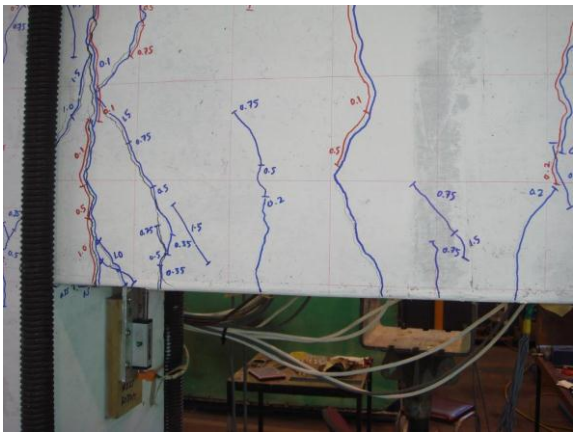

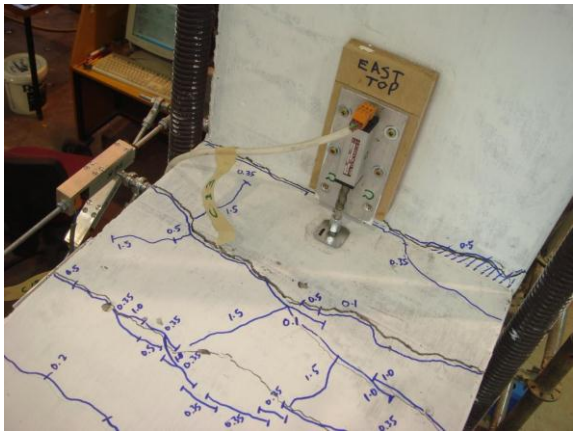
EAST
TOP

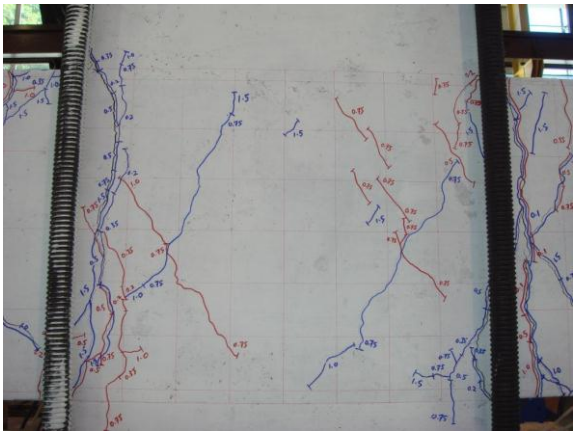


BCJ5
16/02/12
2.0 % + CYC3
55 MM
158 KN

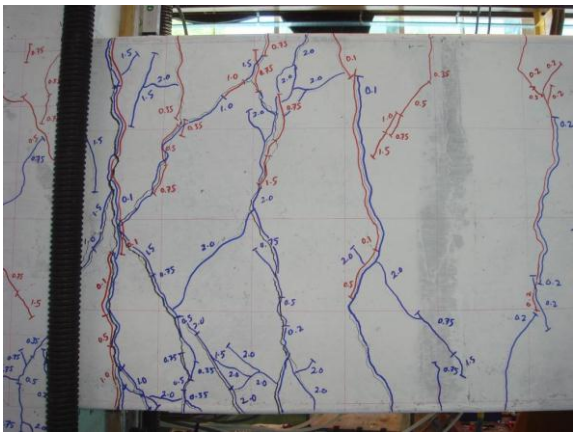

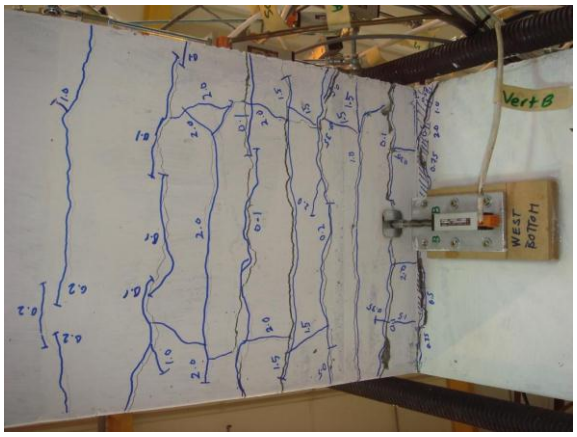
Vert B
WEST BOTTOM

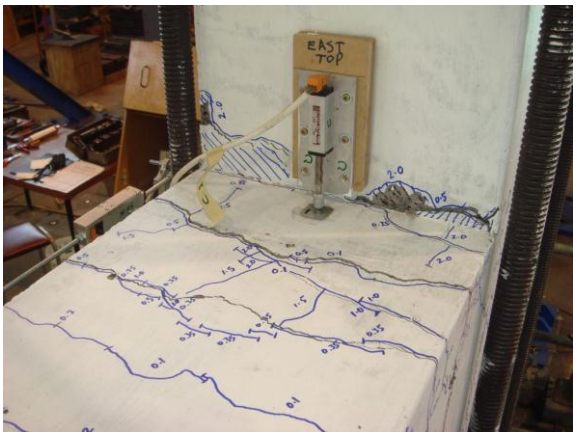
EAST TOP

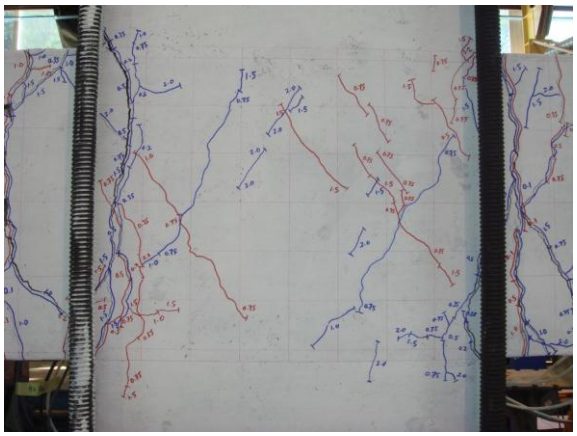

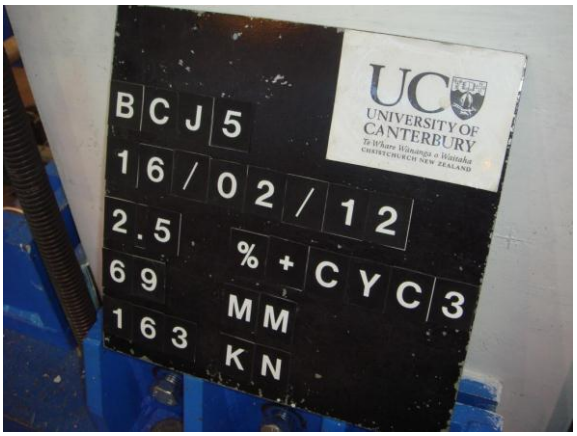
BCJ5
16/02/12
2.5 % + CYC3
69 MM
163 KN

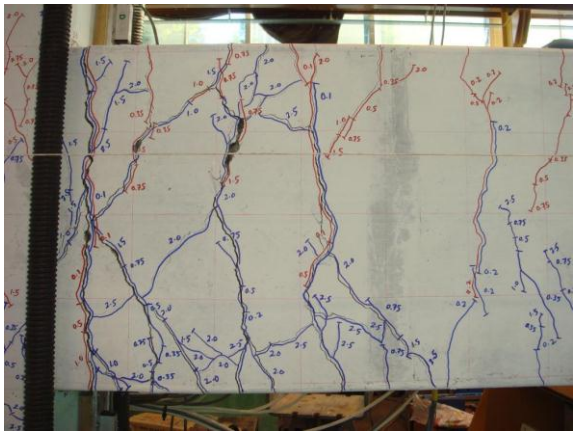


WEST BOTTOM

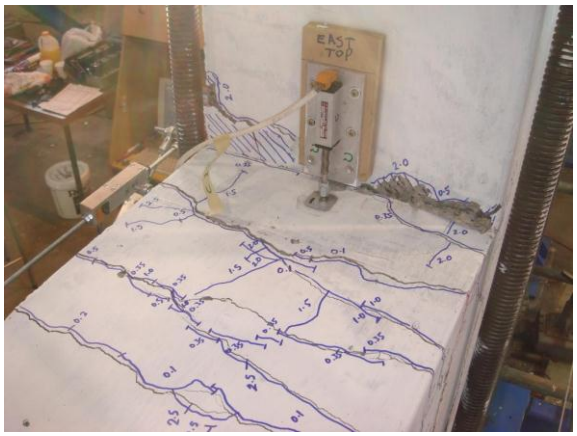
EAST
TOP

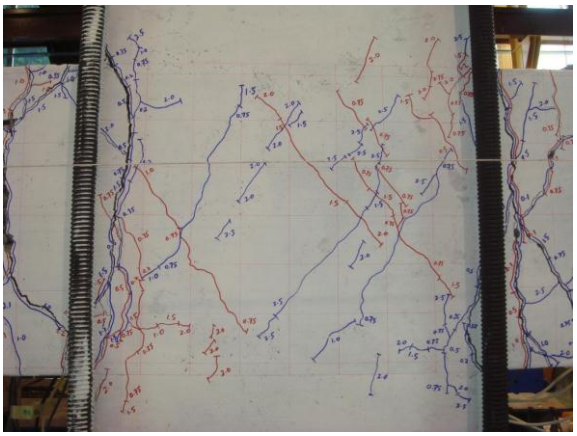

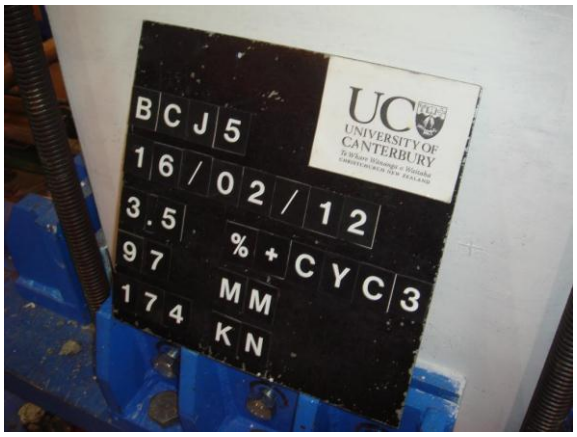
BCJ5
16/02/12
3.5 % + CYC3
97 MM
174 KN
UC
UNIVERSITY OF
CANTERBURY

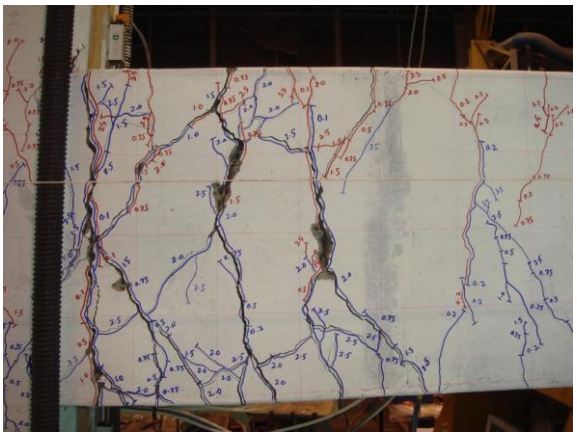

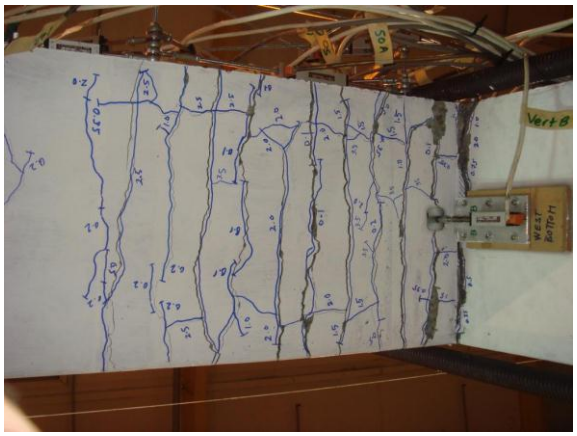
Vert B
WEST
BOTTOM

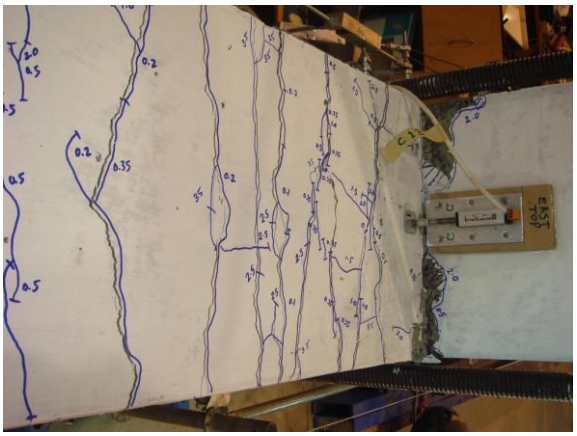

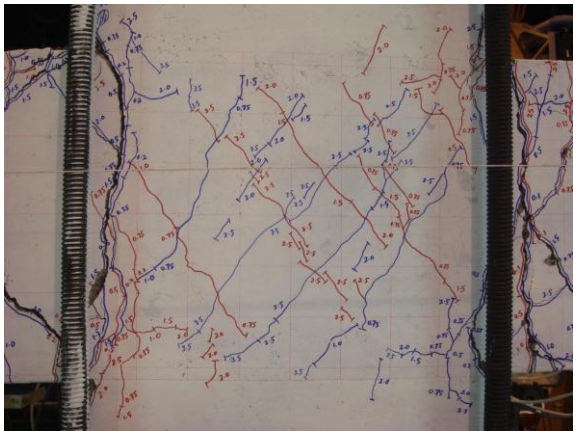

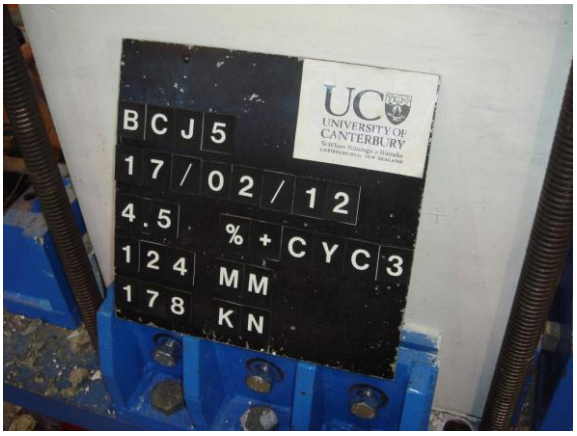
BCJ5
17/02/12
4.5 % + CYC3
124 MM
178 KN
UC
UNIVERSITY OF
CANTERBURY

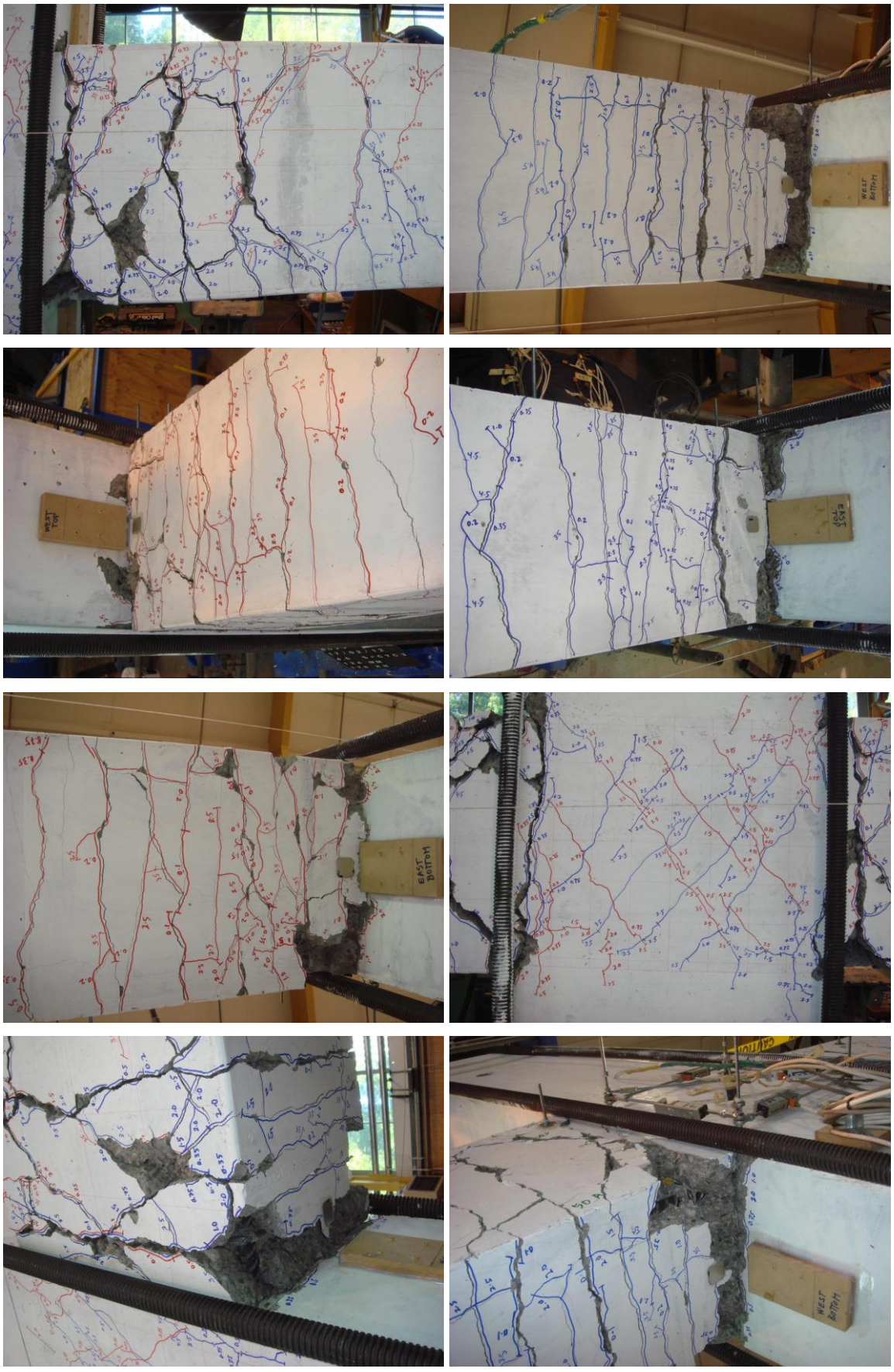

Figure E-15: Testing of BCJ5

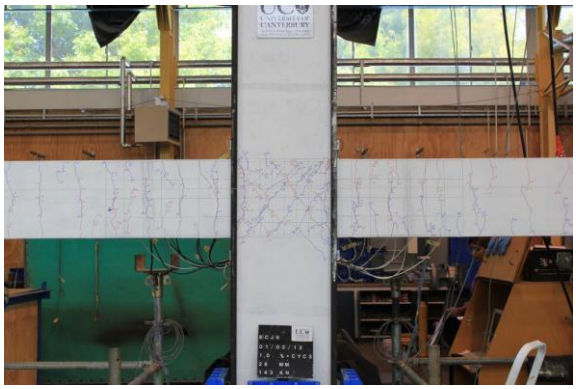
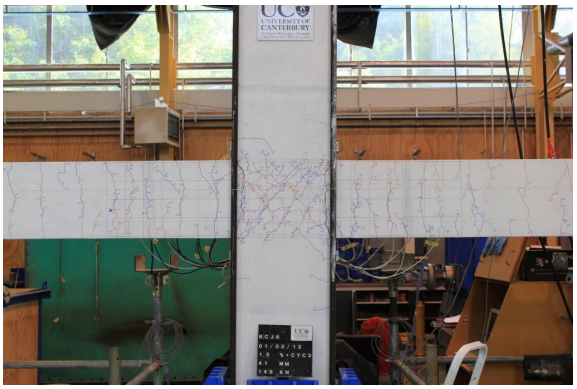
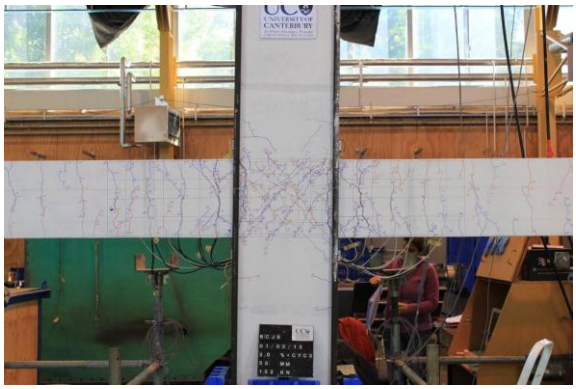
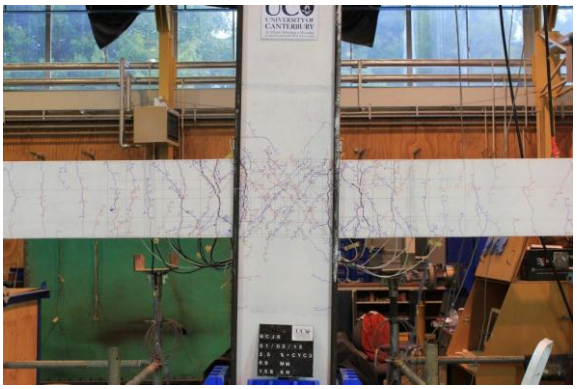
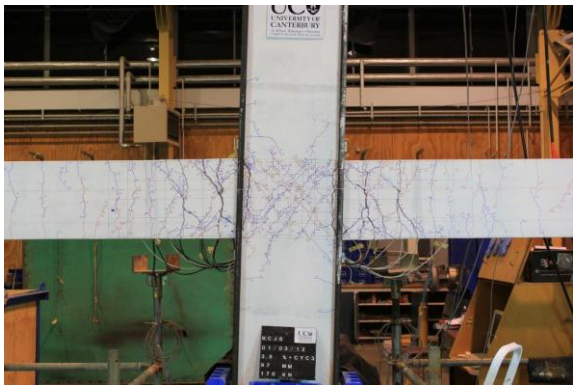
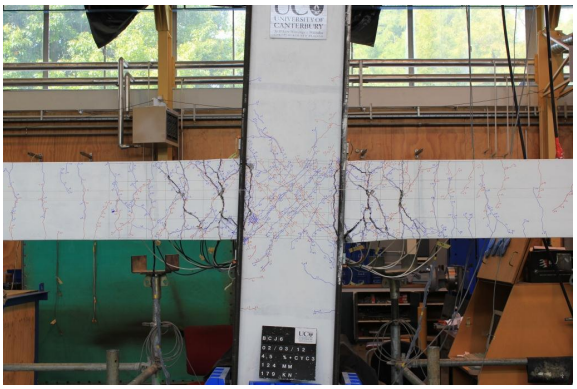
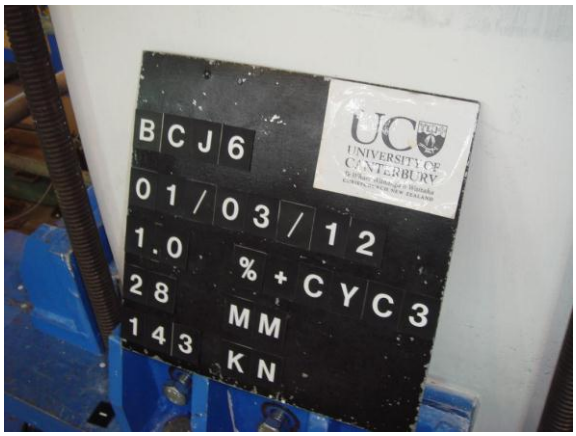
BCJ6
01/03/12
1.0 %+CYC3
28 MM
143 KN
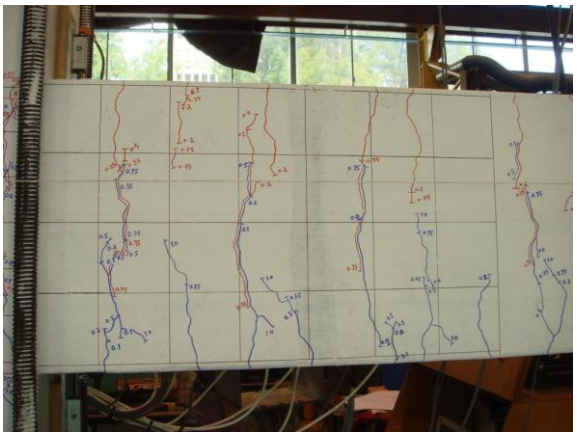

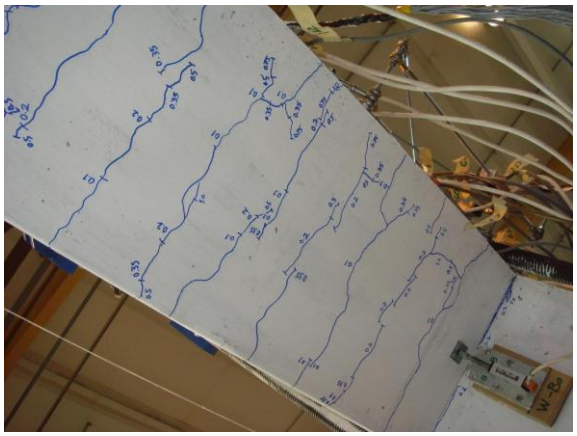

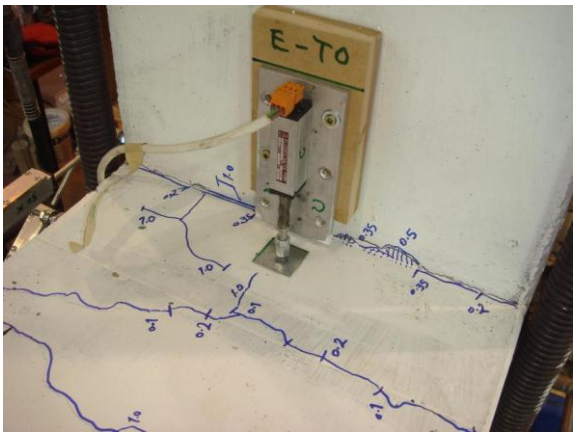
E-T0

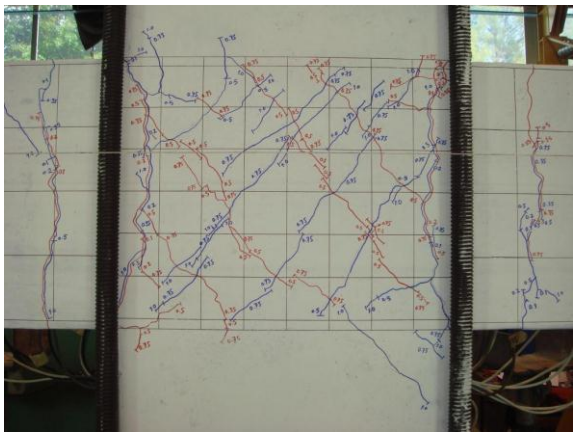

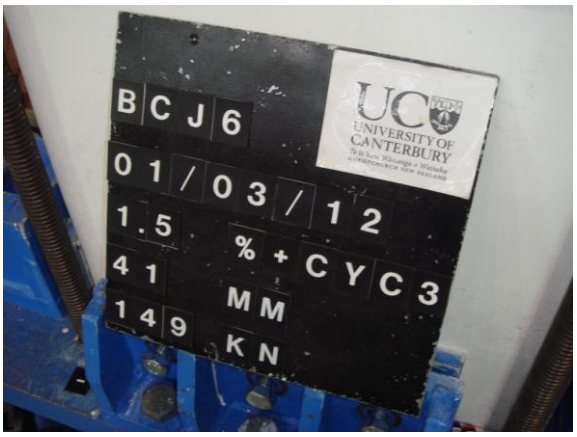
BCJ6
UC
UNIVERSITY OF
CANTERBURY
01/03/12
1.5 % + CYC3
41 MM
149 KN

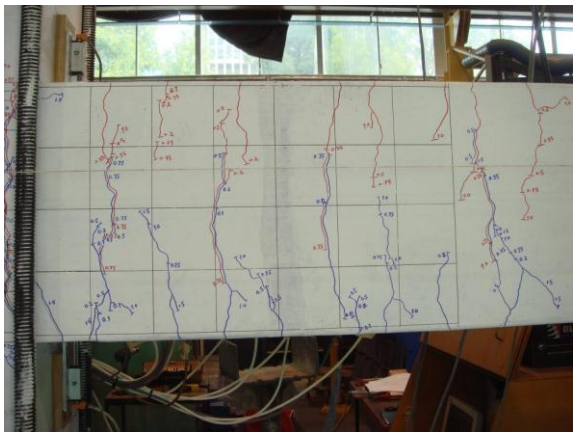

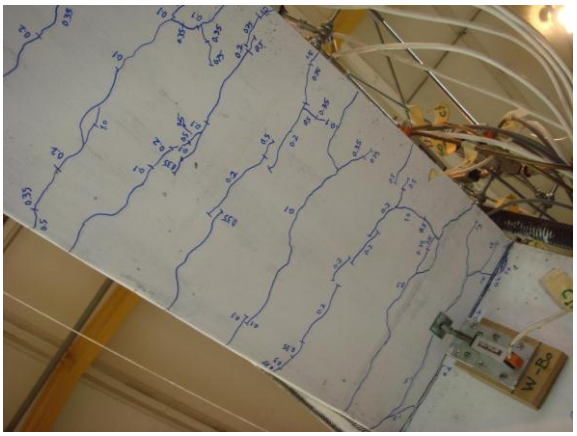

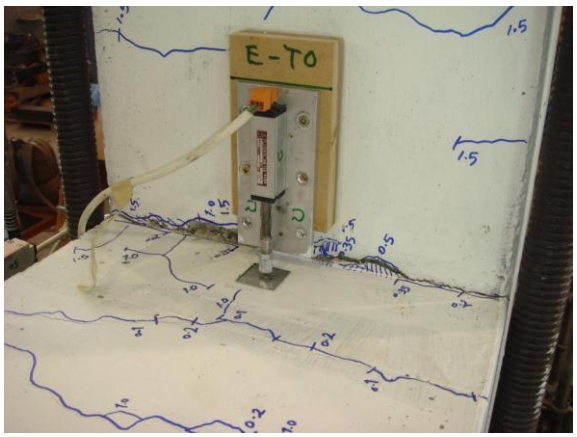
E-T0

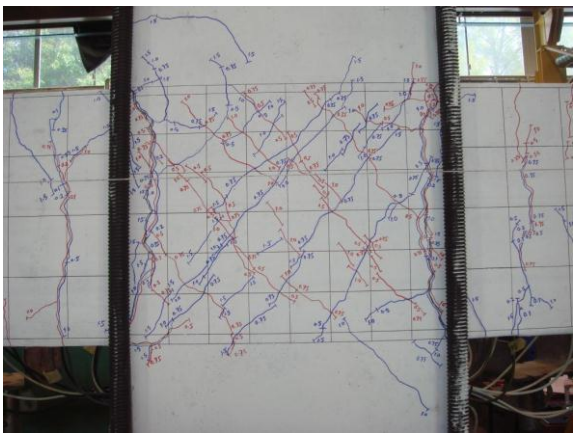

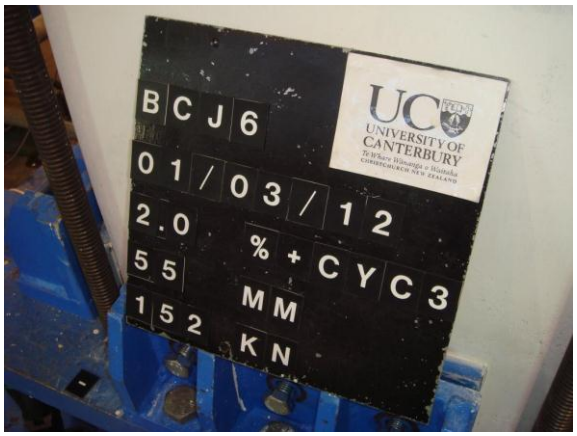
BCJ6
UC
UNIVERSITY OF
CANTERBURY
01/03/12
2.0 % + CYC3
55 MM
152 KN

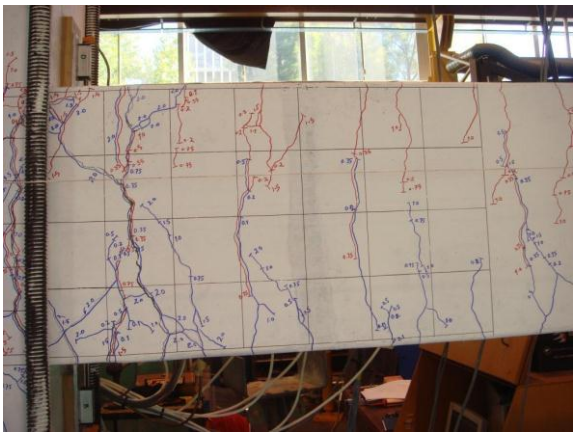

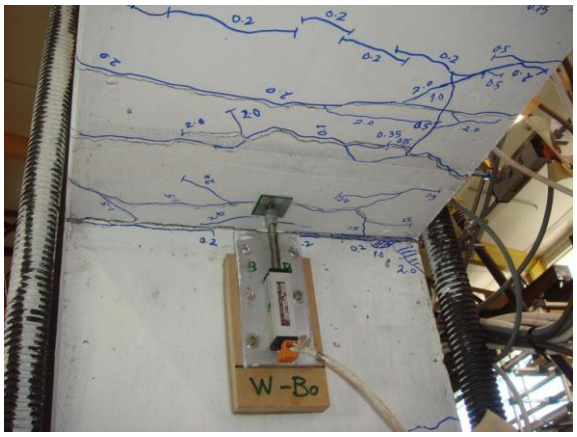
W-Bo

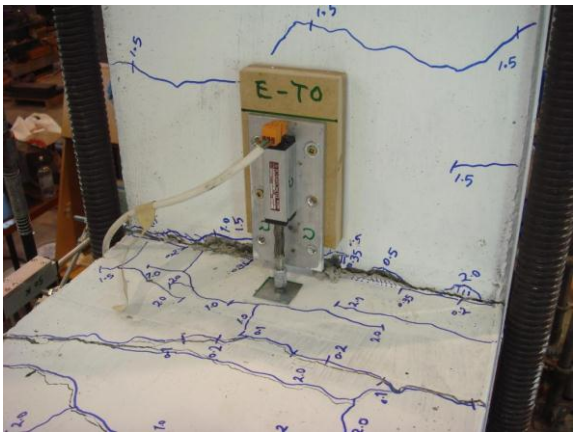
E-TO

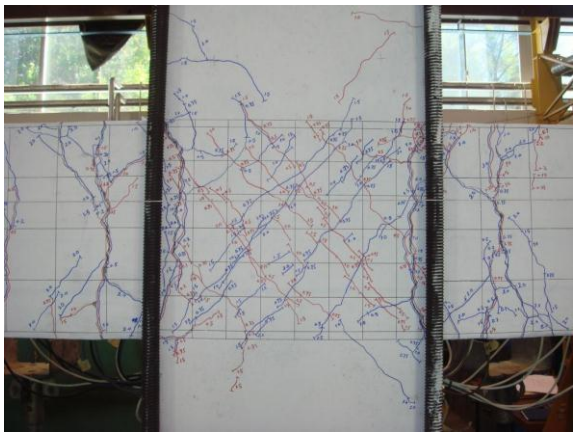

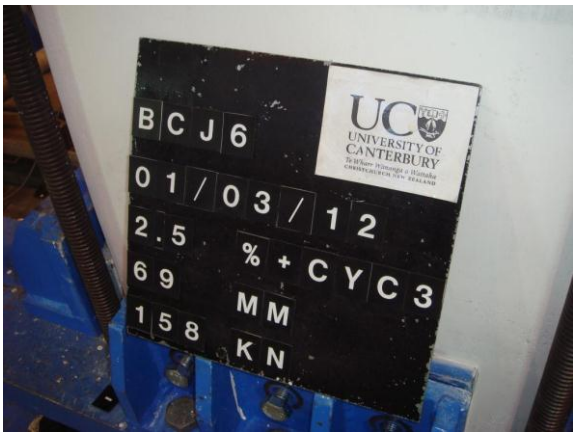
BCJ6
UC
UNIVERSITY OF
CANTERBURY
01/03/12
2.5 % + CYC3
69 MM
158 KN

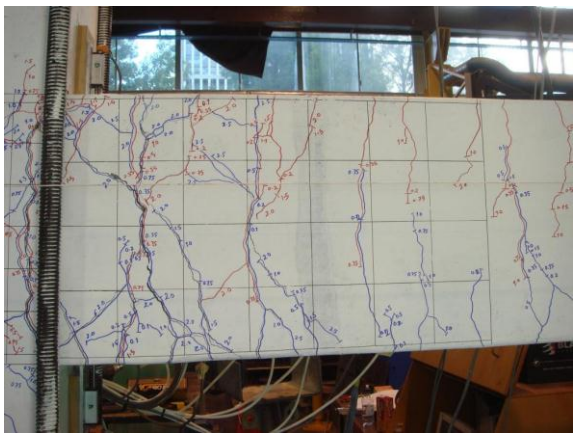

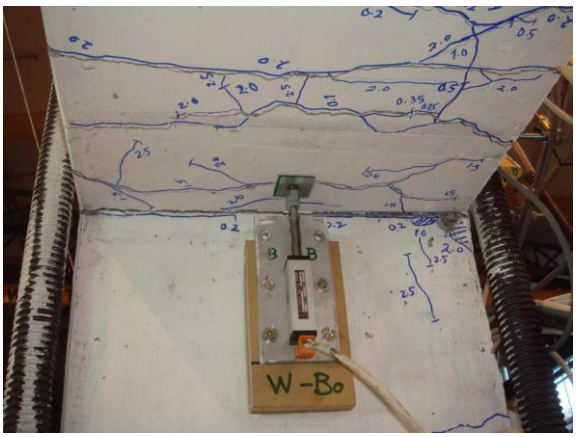
W-Bo

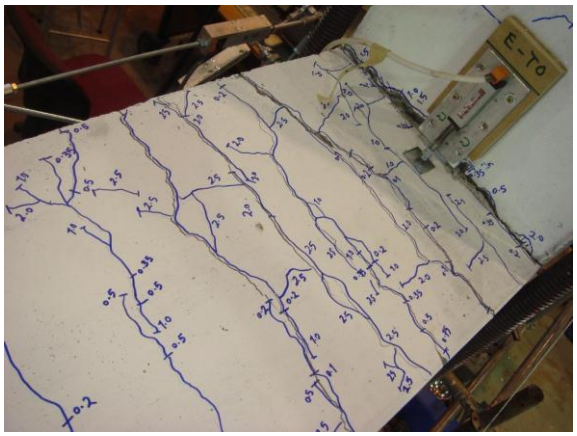
E-T0

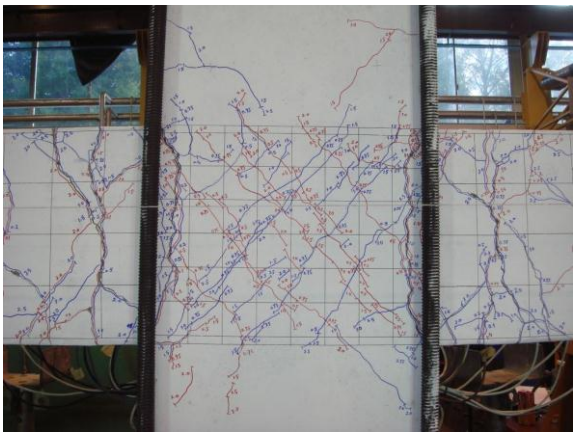

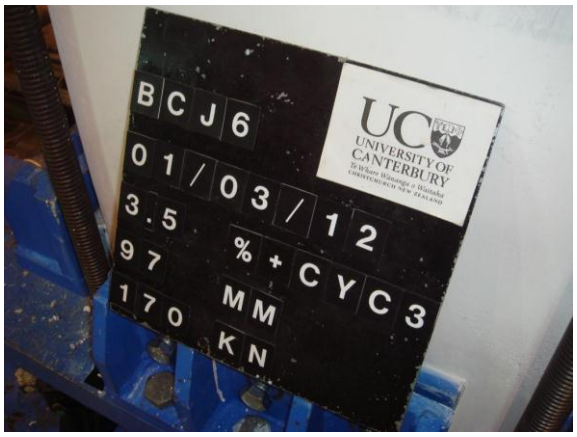
BCJ6
01/03/12
3.5 %+CYC3
97 MM
170 KN
UC
UNIVERSITY OF CANTERBURY

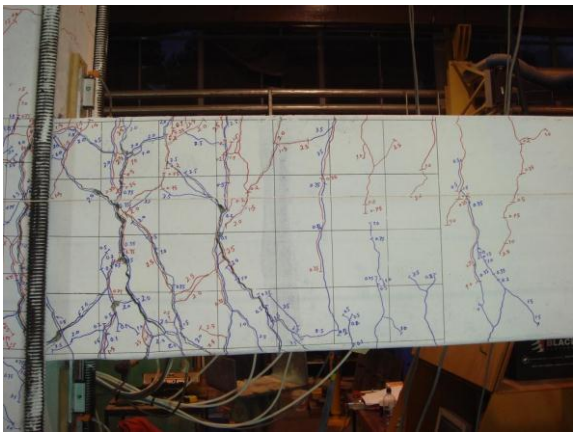


W-R8

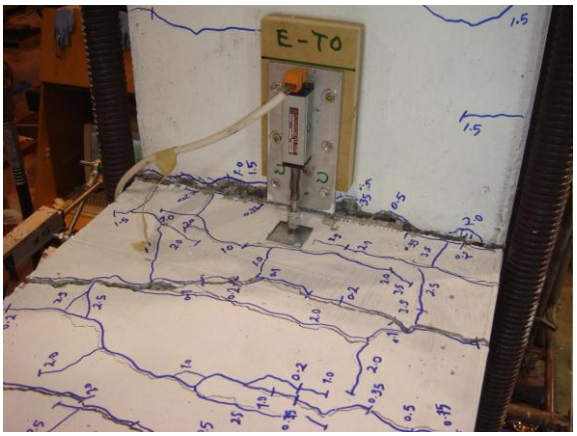
E-T0

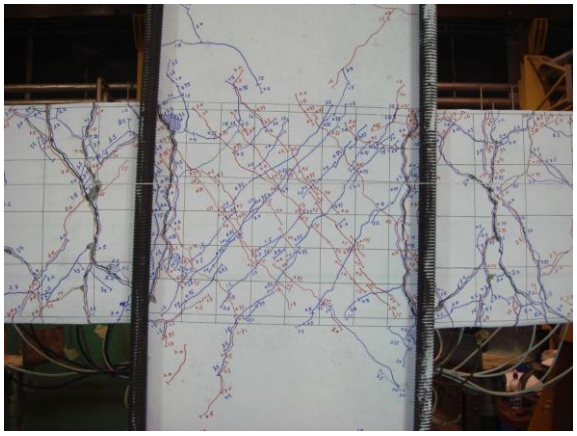

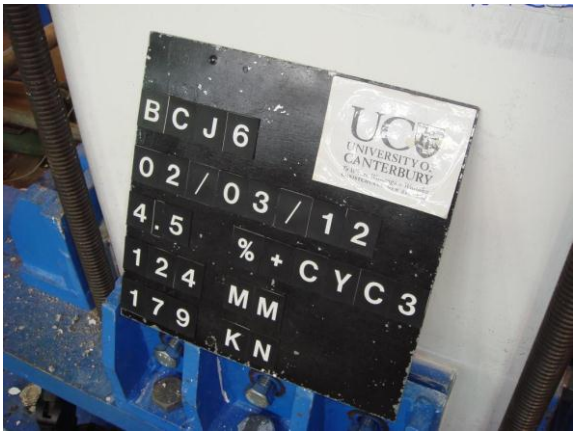
BCJ6
02/03/12
4.5 %+CYC3
124 MM
179 KN
UC
UNIVERSITY OF CANTERBURY

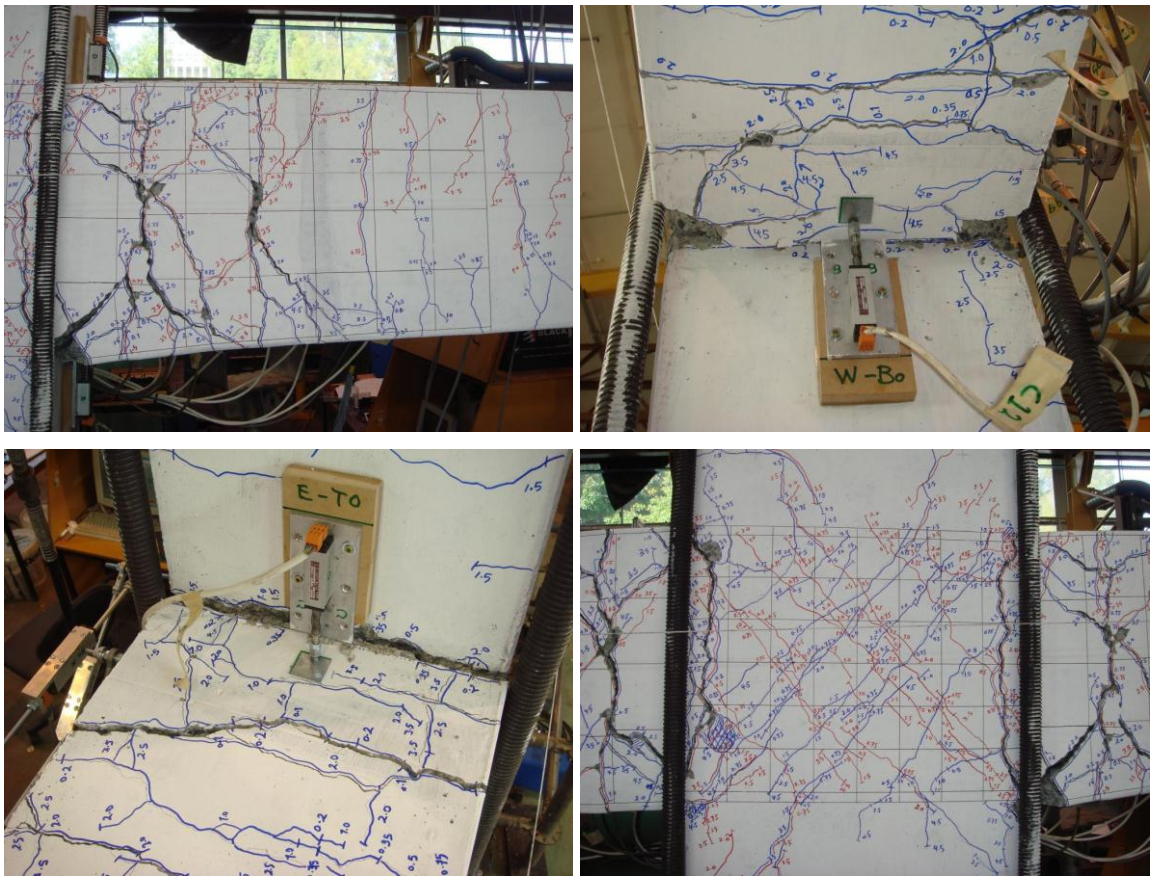

Figure E-16: Testing of BCJ6

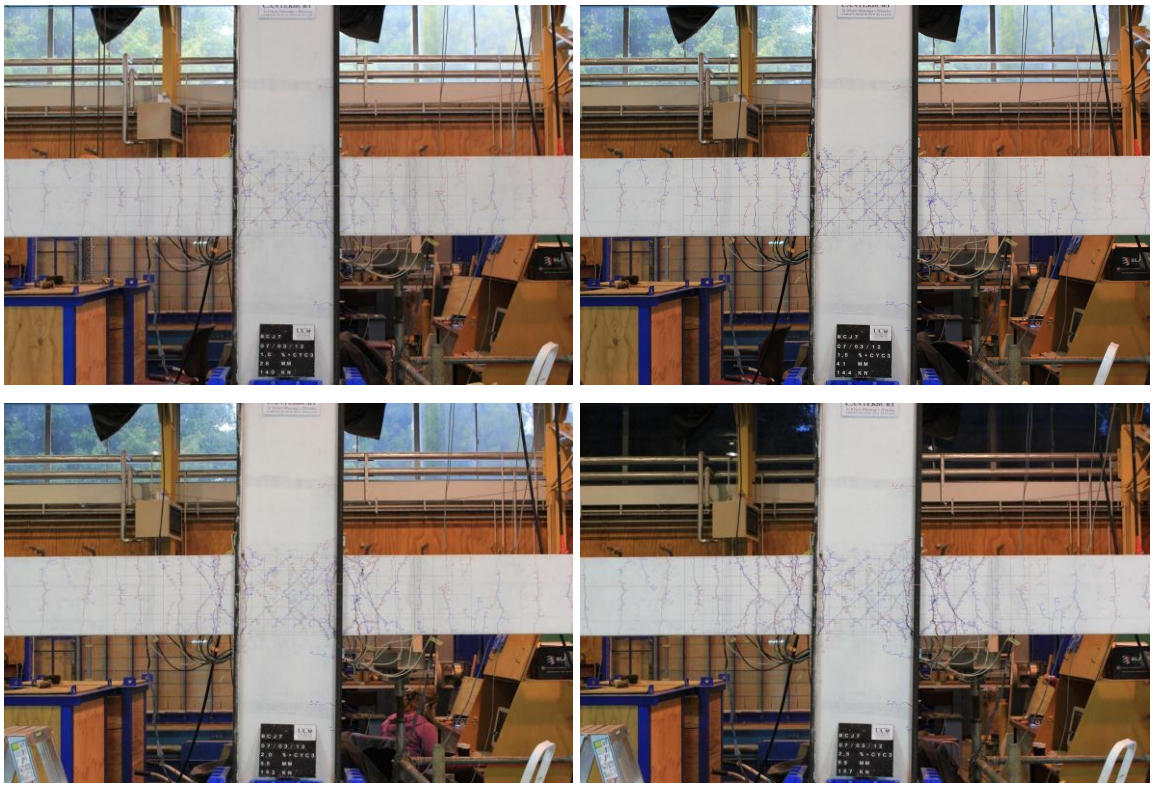

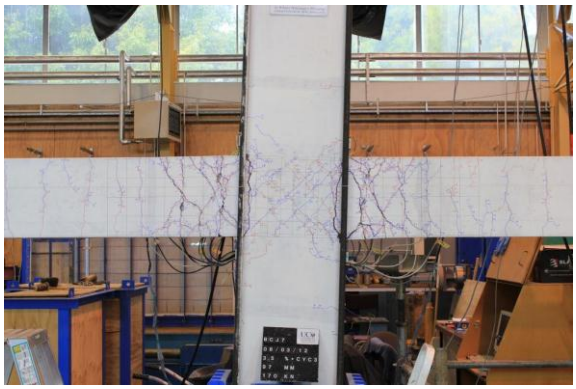
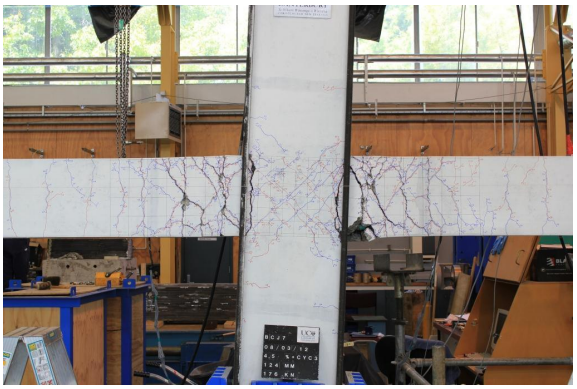

BCJ7
UC
UNIVERSITY OF CANTERBURY
07/03/12
1.0
%+CYC3
28
MM
140
KN
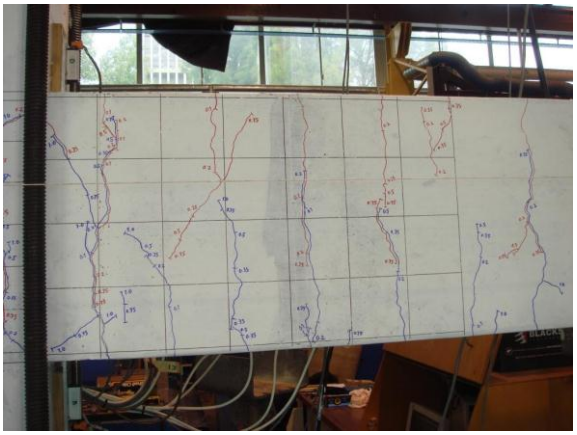
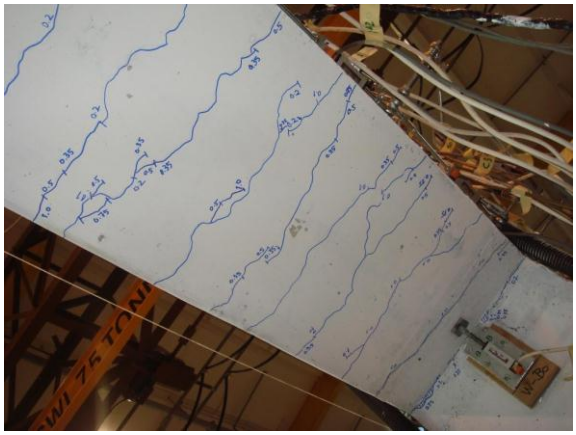
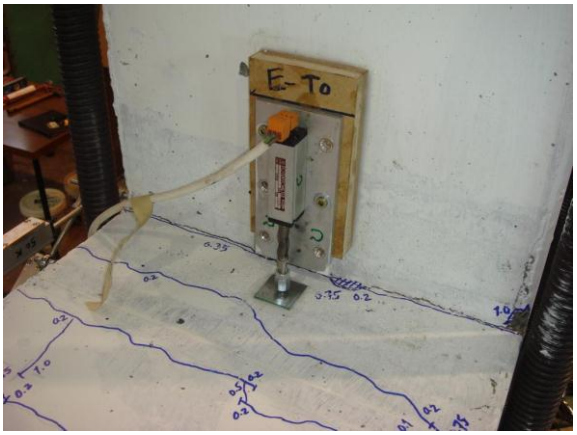
E-To
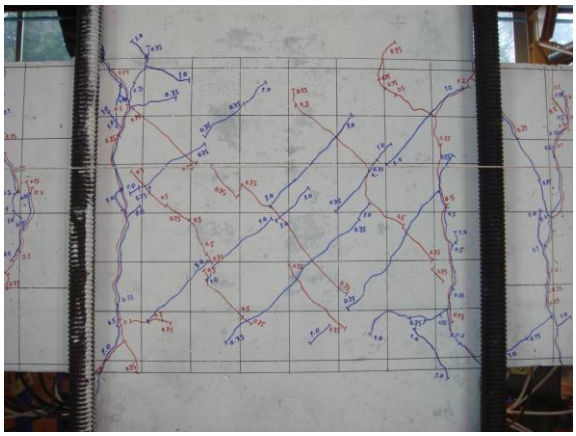
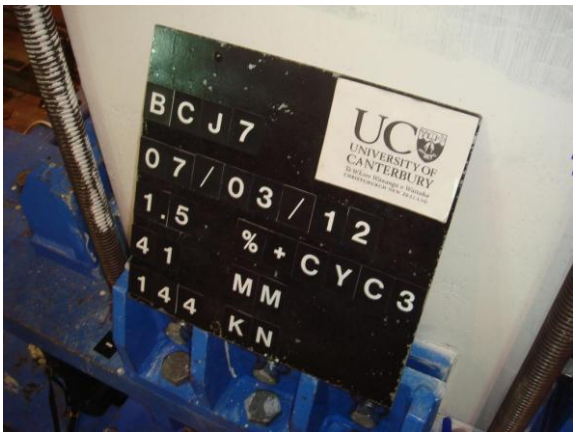
BCJ7
UC
UNIVERSITY OF CANTERBURY
07/03/12
1.5
%+CYC3
41
MM
144
KN

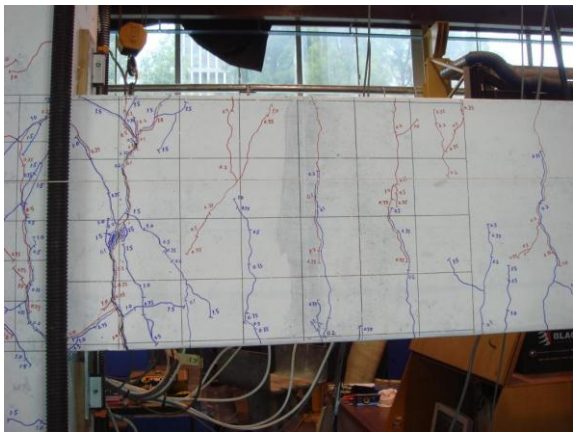

W-Bo
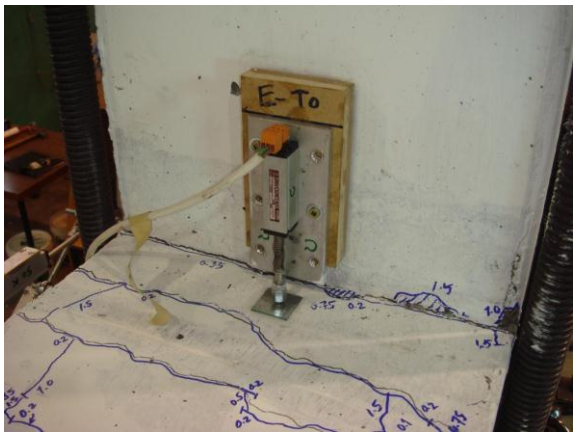
E-To
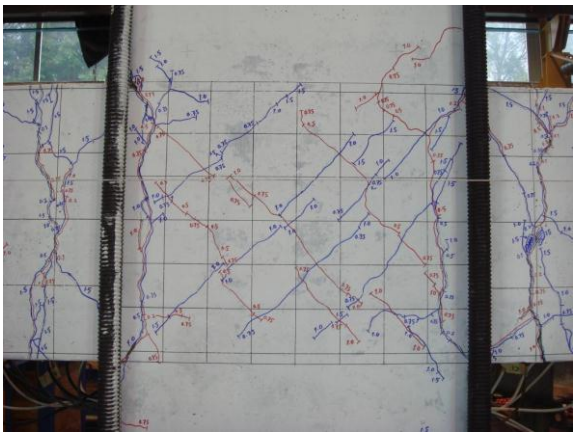
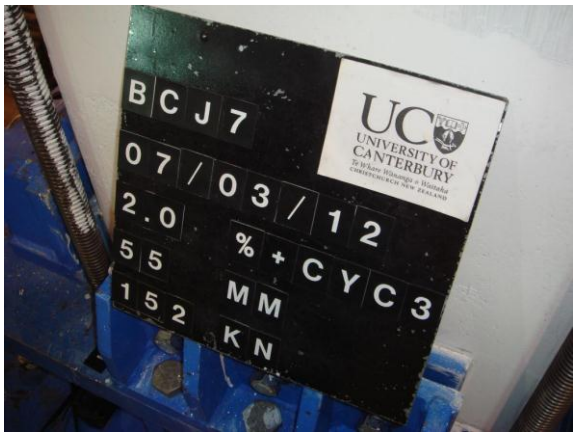
BCJ7
UC
UNIVERSITY OF CANTERBURY
07/03/12
2.0 %+CYC3
55 MM
152 KN
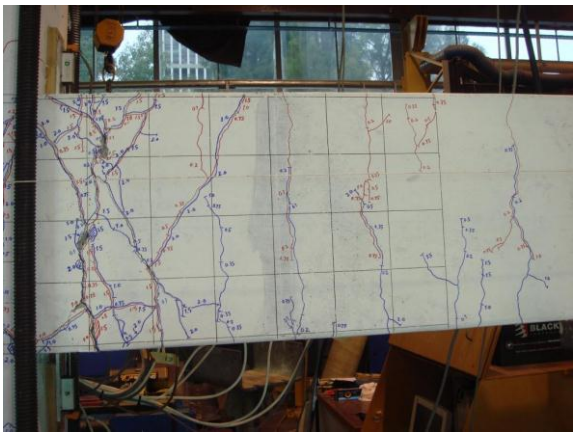
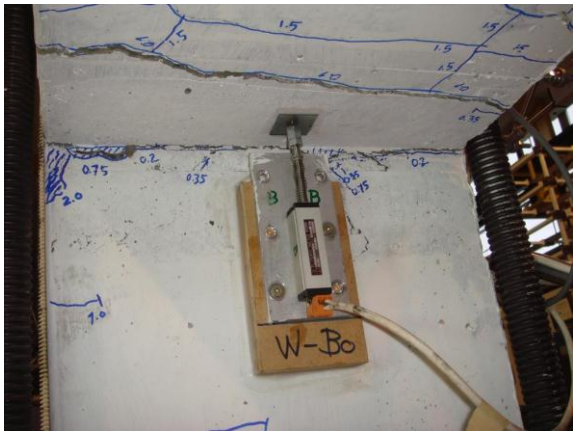
W-Bo
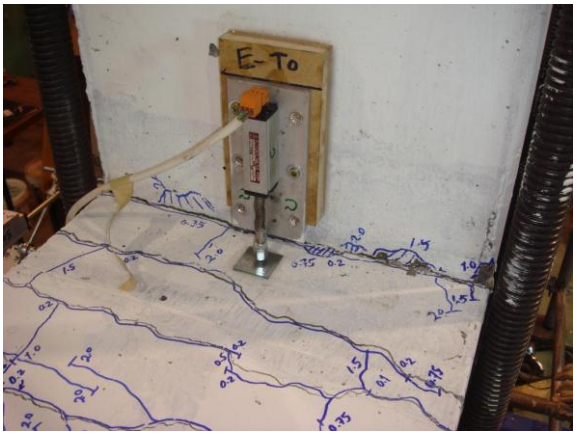
E-To

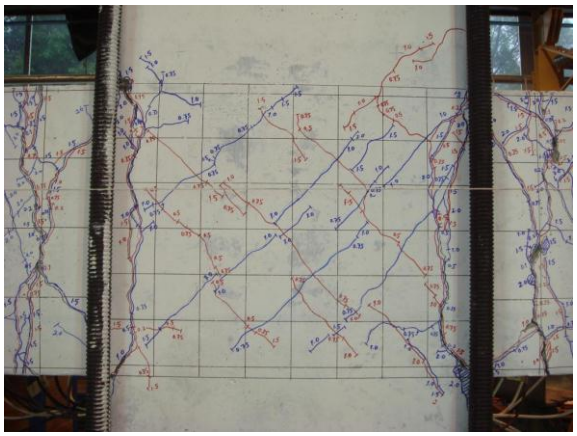
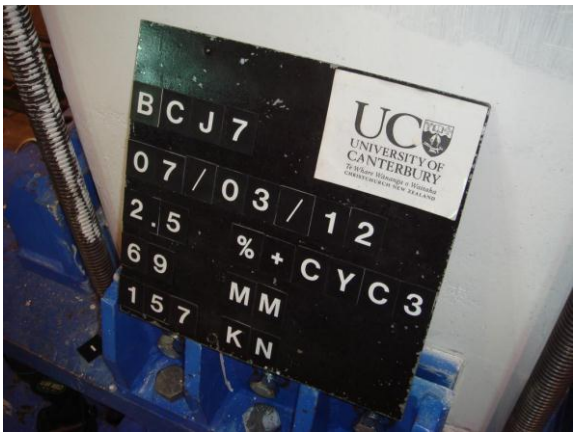
BCJ7
UC
UNIVERSITY OF CANTERBURY
07/03/12
2.5 % + CYC3
69 MM
157 KN
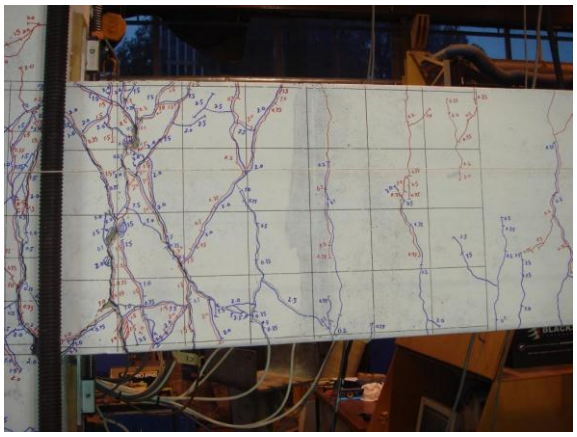
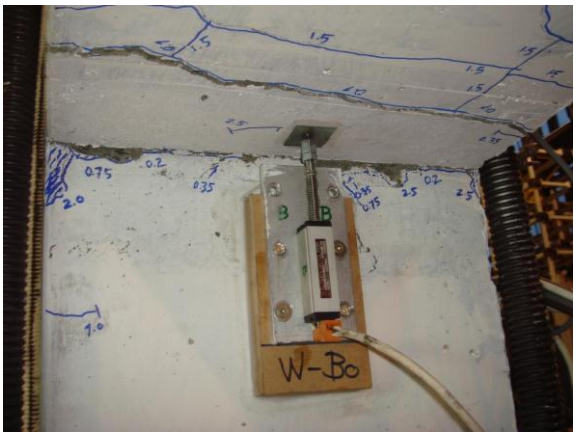
W-Bo
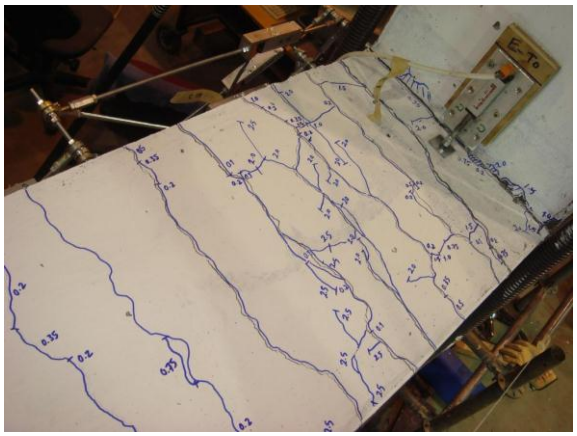
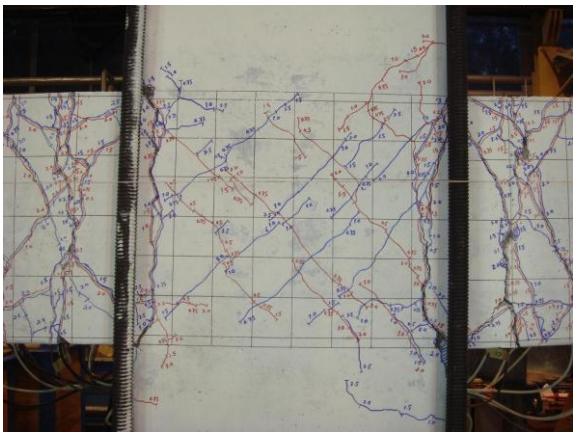

BCJ7
UC
UNIVERSITY OF CANTERBURY
08/03/12
3.5 % + CYC3
97 MM
170 KN
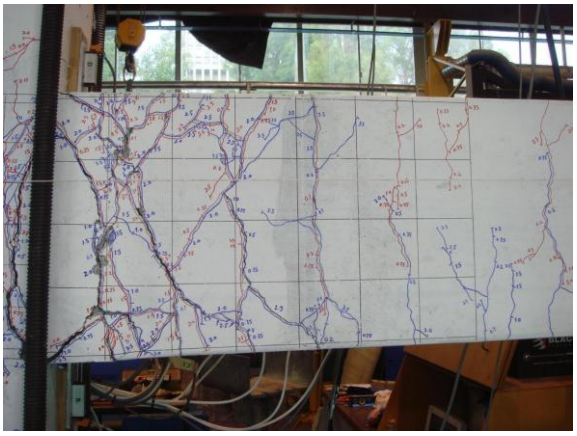

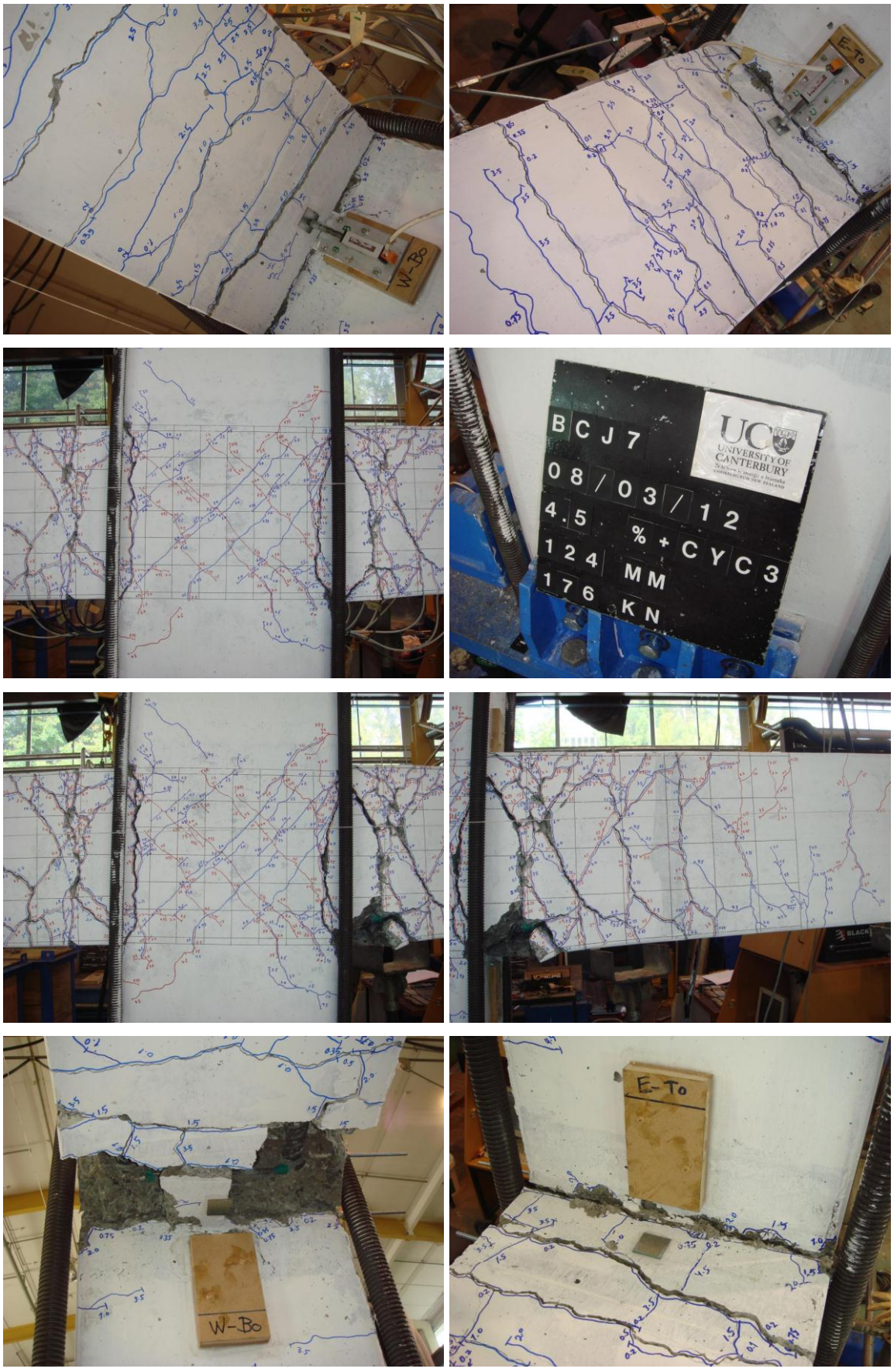

Figure E-17: Testing of BCJ7

APPENDIX F – CALCULATION OF THE CONTRIBUTION OF VARIOUS COMPONENTS TOWARDS THE OVERALL DEFORMATION OF BEAM-COLUMN SUBASSEMBLIES

DETAILS OF INSTRUMENTATION

All of the beam-column subassemblies were instrumented with load cells, potentiometers (LVDTs) and strain gauges (on the surface of reinforcements) at different locations. This appendix explains how the readings from the potentiometers were processed in order to measure the shear and flexural deformations of beam, column and joint regions. These information were later used in order to assess the contribution of each component towards the overall drift of the specimen at the top of column. Figure F-1 shows some of the pictures taken from the instrumentation of a typical specimen.

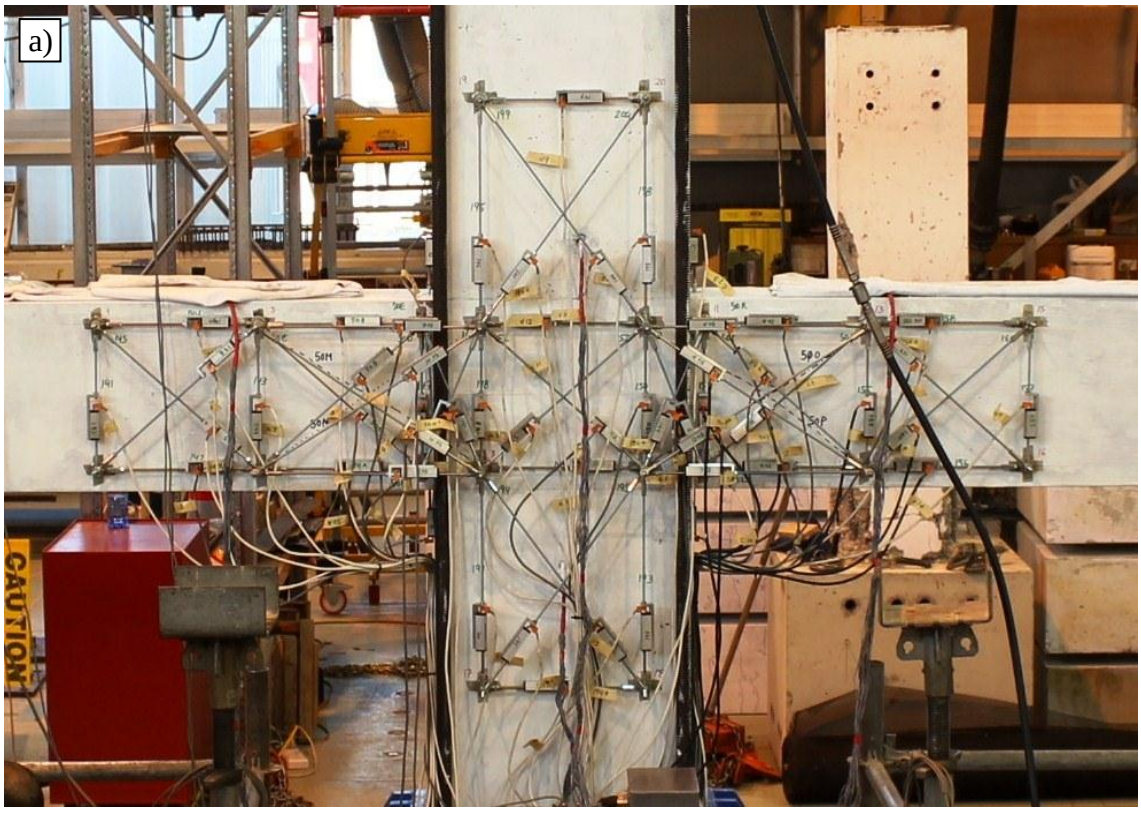

b)

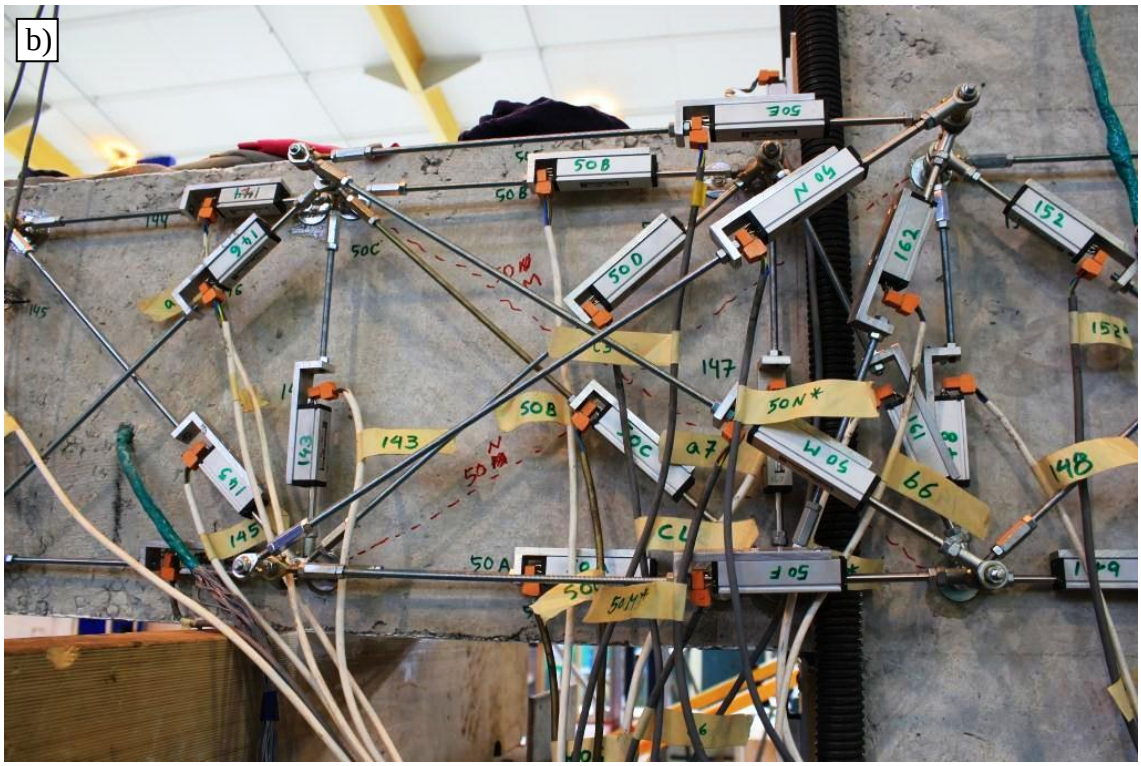
50B
50D
50C
50N*
50M*
50A
50E
147
143
145
66
48B

c)

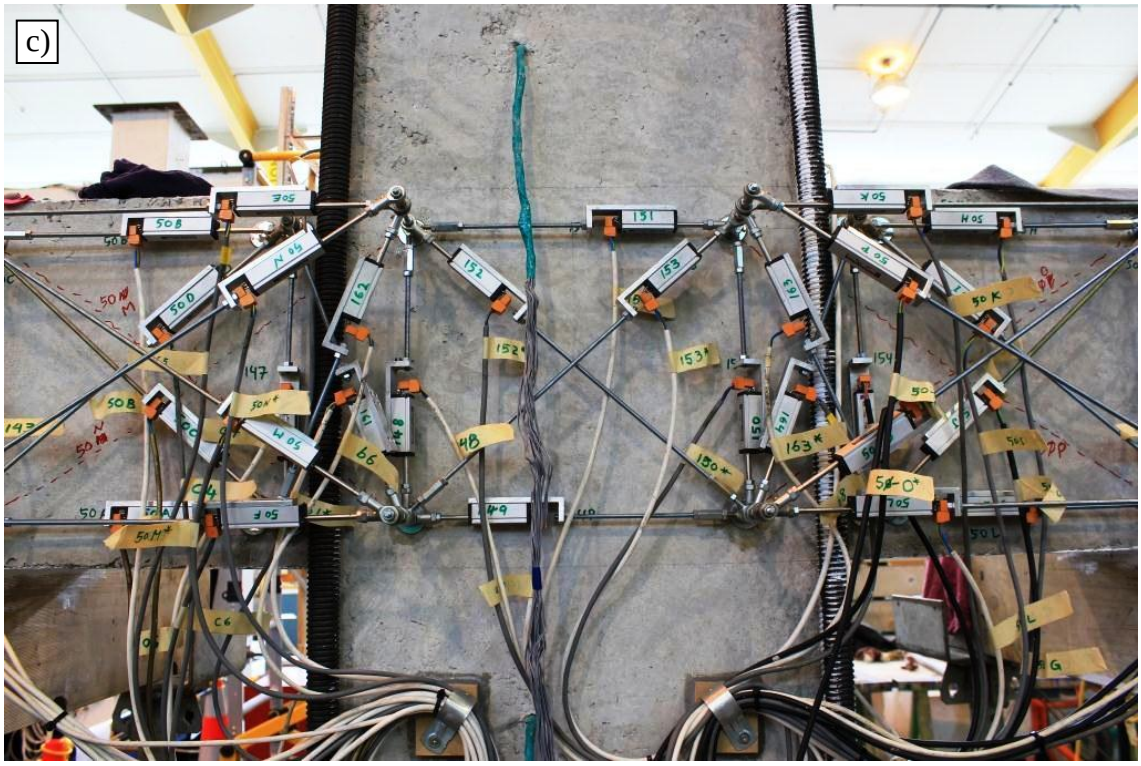
50B
50D
131
153
152
147
143
145
66
48B
50M*

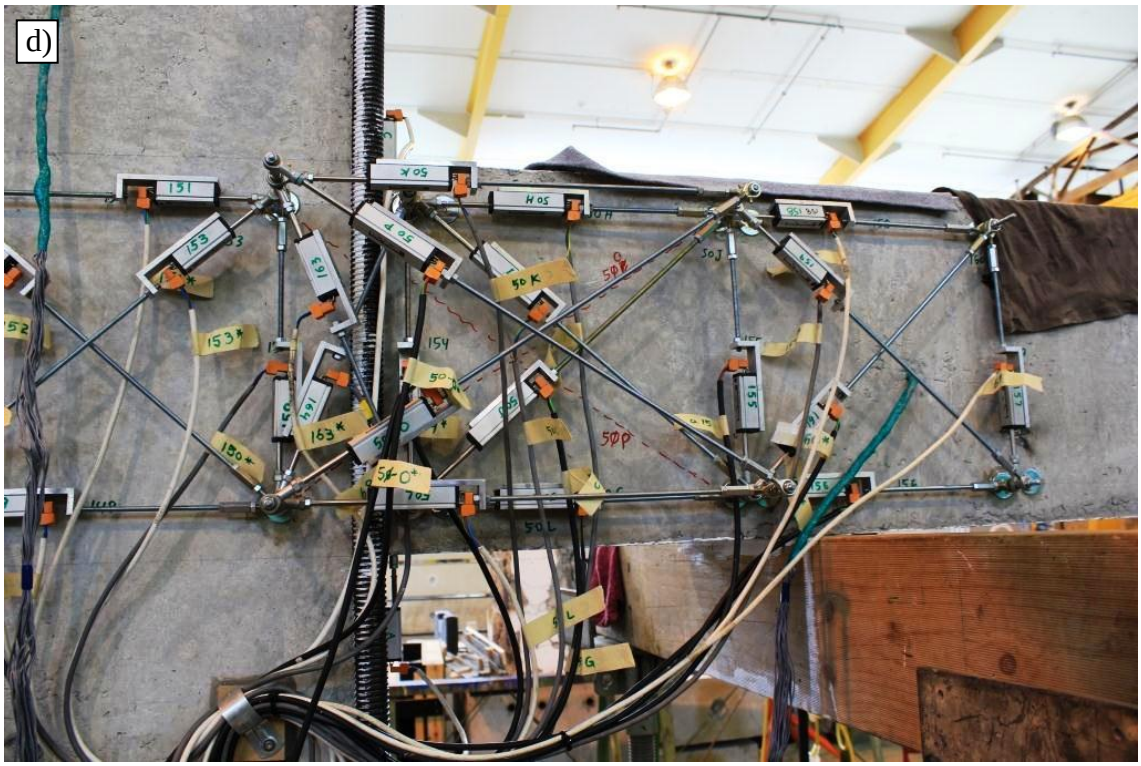

Figure F-1: Arrangements of potentiometers on BCJ-2 (a), close-up of West wing (b), close-up of joint (c), and close-up of East wing (d)

It should be noted that the position of horizontal potentiometers (gauges) was chosen in such a way that they were located at the same level of the beam bars. Therefore, the average strain of the beam bars could be calculated using the installed gauges as well as the strain gauges installed on the surface of the bars inside the concrete. Figure F-2 and Figure F-3 show in more details the layout of potentiometers. As it can be seen the gauges were placed in a grid type pattern and each grid was given an alphabetical label with its gauges numbered. Note that except for BCJ-2, in which the axial load ratio was lower than the others and column flexure needed to be monitored, none of the other specimens were equipped with potentiometers on the column face. The length between the installation points (numbered from 141 to 200 and 50A to 50P) of potentiometers was measured so that the measurements could be converted to strains later. The width and height of each gauge group was defined as 'w_x' and 'h_x', respectively; with 'x' being the gauge group letter.

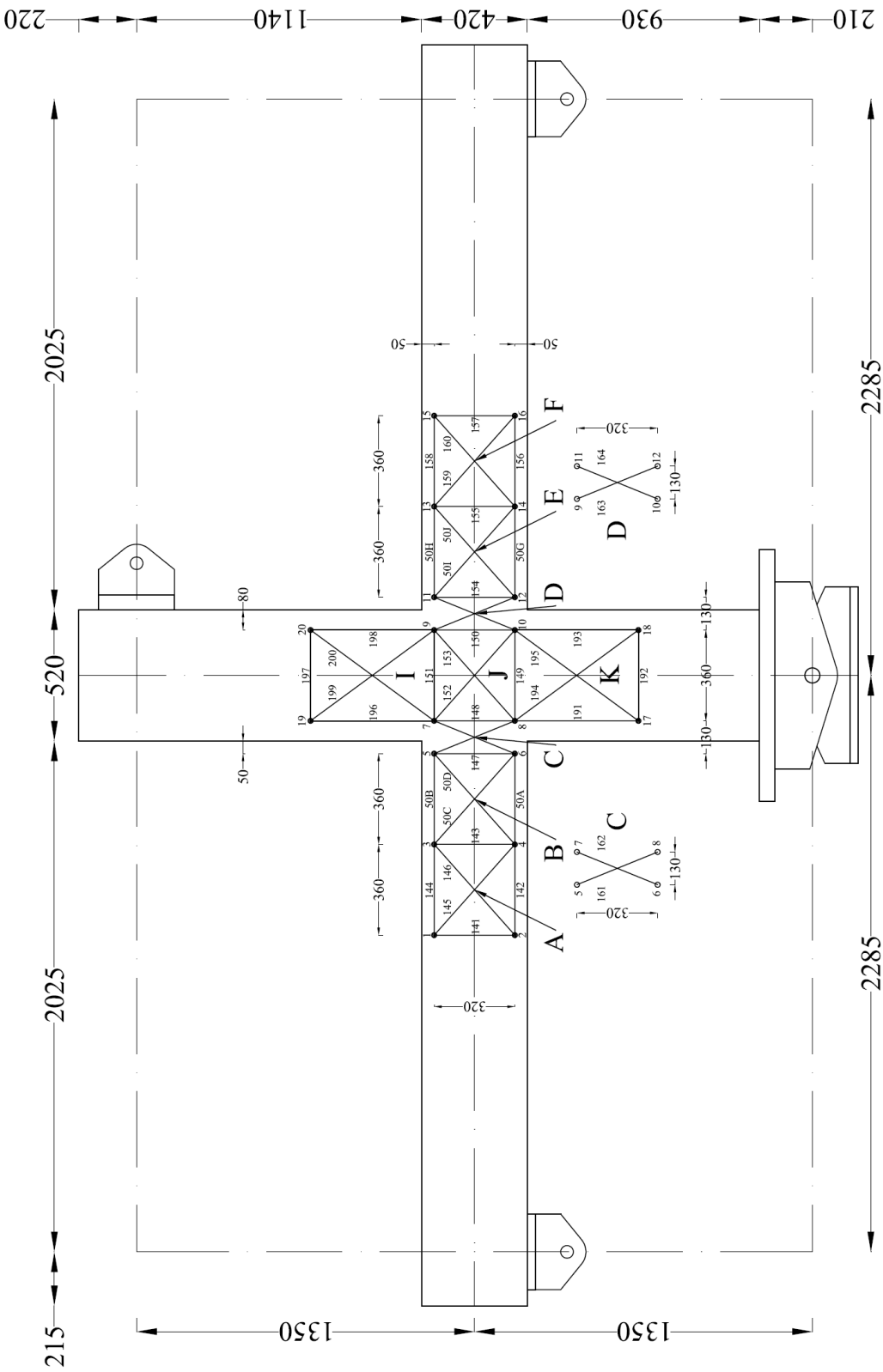

Figure F-2: Details of 1st layer of potentiometers on the surface of the specimens

Figure F-3: Details of 2nd layer of potentiometers on the surface of the specimens

CALCULATING SHEAR AND FLEXURAL DISPLACEMENT COMPONENTS

The overall deformation of the top of the column is consisted of five components; namely elastic flexure of the column, elastic flexure of the beam, rotation of the beam at the plastic hinge zone, shear deformations of the beam, and joint shear deformations. Calculation of these components is explained in the following sections; but as the effect of beam shear deformations were very small they have not been considered in the actual calculations for the specimens. In all of the calculations performed in the following sections, changes in the angles are considered to be small.

JOINT SHEAR

In calculating the effect of joint shear deformations on the overall drift of the column top, many components should be taken into consideration. Vertical and horizontal shear forces deform the joint panel which in turn translates and/or rotates the beam and column tips. It should be noted that the translational and rotational deformations occur with opposite signs (Figure F-4). For instance where the beam tip translation is downward due to the joint shear deformation, rotational displacement results in an upward displacement of the beam tip.

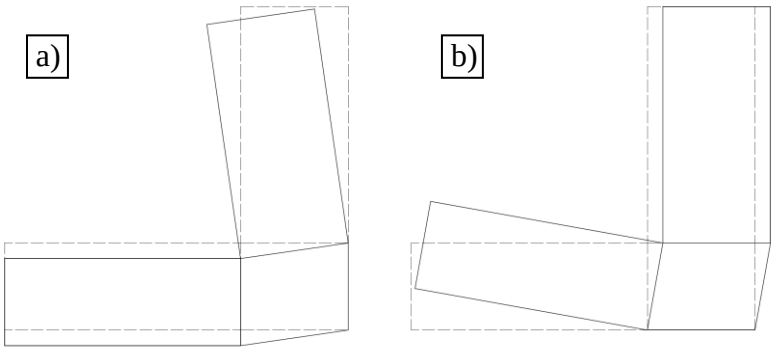

Figure F-4: Effects of vertical (a) and horizontal (b) joint shear

Assuming that the beam-column subassembly was fixed only at the centre of the joint panel, then the joint shear deformations would result both the beam and column tips to be displaced from their original position (Figure F-5). However the beam ends were prevented

from being deflected in the vertical direction. Since the deformation of the joint zone remains the same, the displacement that would have otherwise occurred at the beam tips (if they were free to move) is shifted by rigid body motion to the top of the column. The conversion of the hypothetical beam tip displacement to column top deformation is done based on the following equation.

$$\delta_{col} = \delta_{beam} \frac{L_c}{L_b} \qquad 1$$

This transformation of beam displacement to the equivalent column top deformation will be used both in this section and the following sections of this appendix for the column shear and flexural displacements.

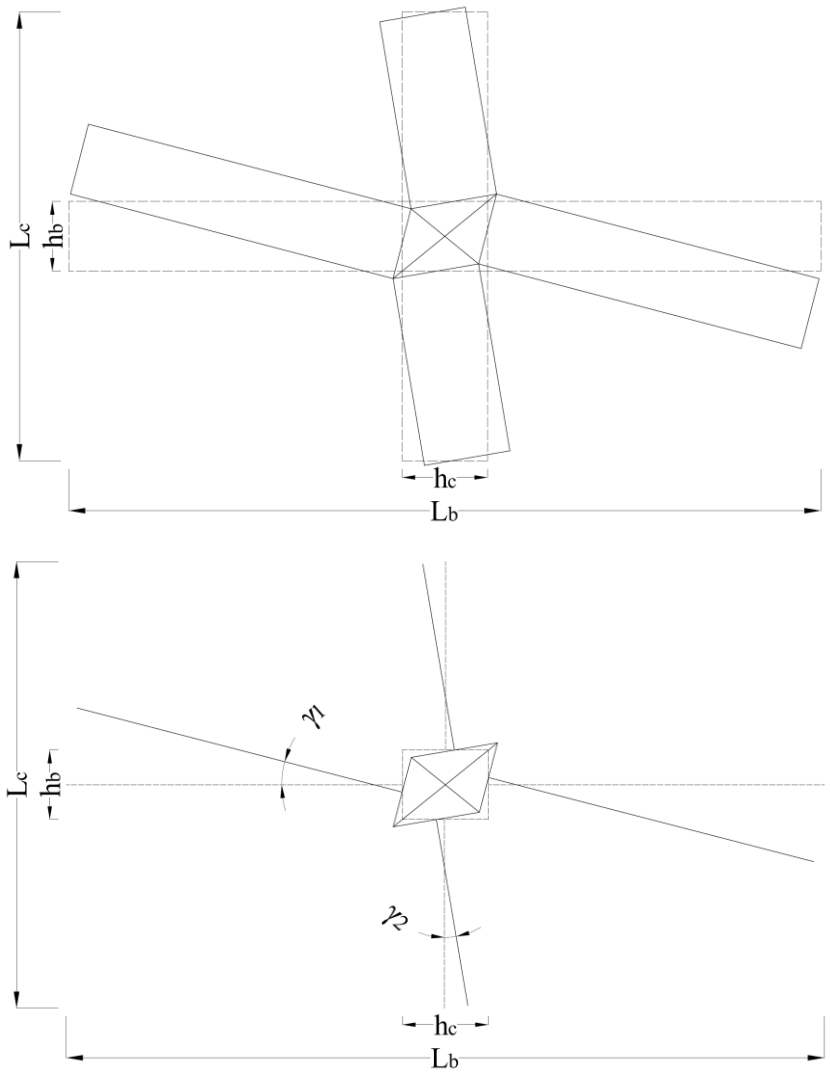

Figure F-5: Displacement of beam and column tips due to joint shear deformations

As it can be seen in Figure F-1c and Figure F-2, due to practical limitations it was not feasible to cover the whole joint panel with the gauge group installed on the joint area. Although this seems to introduce an error into the calculation of joint zone deformations, one should always consider that the actual joint panel is located in an area enclosed within the top and bottom beam bars and left and right layers of the column bars (see details in Chapter 5). Therefore the installation of potentiometers on a smaller area would not bring a substantial error into the calculations. A schematic view of the joint shear deformations is depicted in Figure F-6. Note that in Figure F-6, an extension and contraction of potentiometers are recorded with a positive and negative signs, respectively; which should be bore in mind in all of the calculations provided below.

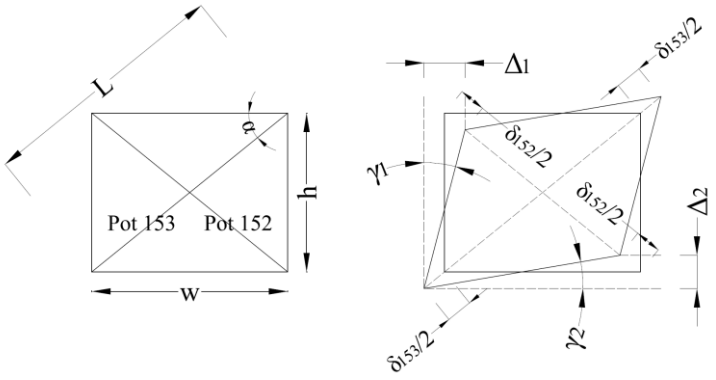

Figure F-6: Joint shear deformations and its relevant parameters

Based on the geometry in Figure F-6 it can be seen that:

$$\Delta_1 = \left(\frac{\delta_{153}}{2} - \frac{\delta_{152}}{2} \right) \times \cos(\alpha) = \left(\frac{\delta_{153} - \delta_{152}}{2} \right) \times \frac{w}{L} \qquad 2$$

$$\Delta_2 = \left(\frac{\delta_{153}}{2} - \frac{\delta_{152}}{2} \right) \times \sin(\alpha) = \left(\frac{\delta_{153} - \delta_{152}}{2} \right) \times \frac{h}{L} \qquad 3$$

Where 'δ_{153}' and 'δ_{152}' are the readings of the potentiometers installed on the joint panel (see Figure F-2). In addition considering that the joint deformations and thus the angles are small, the following equations are valid.

$$\gamma_1 = \frac{\Delta_1}{h} = \left(\frac{\delta_{153} - \delta_{152}}{2}\right) \times \frac{w}{L \times h} = \frac{\delta_{153} - \delta_{152}}{2L} \frac{1}{\tan(\alpha)} \quad 4$$

$$\gamma_2 = \frac{\Delta_2}{w} = \left(\frac{\delta_{153} - \delta_{152}}{2}\right) \times \frac{h}{L \times w} = \frac{\delta_{153} - \delta_{152}}{2L} \tan(\alpha) \quad 5$$

Referring to Figure F-4 and recalling the opposite signs of rotational and translational member displacements, the displacement of each beam and column tip is calculated as follows.

$$\delta_{beam} = \gamma_1 \left(\frac{L_b - h_c}{2}\right) - \gamma_2 \frac{h_c}{2} \quad 6$$

$$\delta_{column} = \gamma_2 \left(\frac{L_c - h_b}{2}\right) - \gamma_1 \frac{h_b}{2} \quad 7$$

Where the parameters are as defined in Figure F-5. Converting the two beam tip displacements to the equivalent column top deformation and add up to the two column displacements we get:

$$\Delta_J = \left[\gamma_1 (L_b - h_c) - \gamma_2 h_c\right] \times \frac{L_c}{L_b} + \left[\gamma_2 (L_c - h_b) - \gamma_1 h_b\right] \quad 8$$

Where 'Δ_J' is the contribution of joint shear deformation in the overall drift of the specimen at the top of the column. After expanding the above equation it can further be transformed into the following form:

$$\Delta_J = (\gamma_1 + \gamma_2) \times L_c - (\gamma_1 + \gamma_2) \times h_b - (\gamma_1 + \gamma_2) \times \frac{L_c h_c}{L_b} \quad 9$$

$$\Delta_J = (\gamma_1 + \gamma_2) \times \left(L_c - h_b - \frac{L_c h_c}{L_b}\right) \quad 10$$

$$\gamma_J = \gamma_1 + \gamma_2 = \frac{\delta_{153} - \delta_{152}}{2L}\left(\frac{1}{\tan(\alpha)} + \tan(\alpha)\right) \quad 11$$

Since all of the parameters in equations 11 and 12 are known, the contribution of joint shear deformations into the overall drift of the beam-column subassembly can easily be calculated.

BEAM AND COLUMN FLEXURAL DISPLACEMENTS

Moment area theorem can be used to derive analytical expressions to calculated the effect of the elastic flexure of the beam and column on the overall drift of the specimen; or in other words the deformation of the column top (Au, 2010). The expressions for column top deformation due to the elastic flexure of the column and beam are given in equations 12 and 14, respectively.

$$\Delta_c = \frac{F(L_c - h_b)^3}{12E_cI_c} \quad 12$$

$$E_c = 3320\sqrt{f_c'} + 6900 \quad 13$$

Δ_c = contribution of column flexure in the over drift of specimen (mm)
F = the lateral force applied at the top of the column (N)
E_c = the elastic modulus of concrete based on NZS3101 (2006) (MPa)
I_c = the effective column moment of inertial taken as 56% of the total value for the uncracked section (mm^4)

$$\Delta_{b,fl} = F\left(\frac{L_c}{L_b}\right)^2 \frac{(L_b - h_c)^3}{12E_cI_b} \quad 14$$

I_b = the effective beam moment of inertial taken as 46% of the total value for the uncracked section (mm^4)

In addition the flexural displacements of the beam and column can be approximated by calculating the angle of rotation between the inner and outer edges of each potentiometer (gauge) group and multiplying this angle by the distance between the centre of the gauge group and the centre of loading or supporting points (near the beam/column tips). Figure F-7: Definitions used to determine the rotation in a gauge group Shows a schematic view of the displacement used to determine the rotation angle (θ) over the length of the gauge group 'E'.

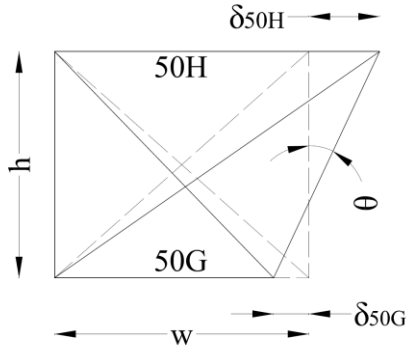

Figure F-7: Definitions used to determine the rotation in a gauge group

Note that for a beam gauge group, 'h' is the height of the group (measured vertically); whereas, for column gauge groups 'h' is the width of the gauge group (measured horizontally). Also note that extension and contraction in length are recorded with positive and negative signs, respectively. Therefore the flexural rotation within a gauge group ('E' in this case) can be determined as:

$$\theta = \frac{\delta_{50H} - \delta_{50G}}{h} \qquad 15$$

And the displacement at the end of the beam or column caused by this rotation is:

$$\Delta_{felx-x} = \theta \times D_x \qquad 16$$

$\Delta_{flex\text{-}x}$ = displacement at the end of the beam/column caused by the rotation in gauge group 'x' (mm)

D_x = distance between the centre of the gauge group and the beam or column tips at loading/support points (mm)

For the beam, the total displacement at beam tip due to beam flexure is determined by summing the flexural displacements due to each gauge group on the beam (this includes the plastic hinge rotation of the beam as well as the elastic flexure contributions). The beam displacement should also be converted to an equivalent displacement at the top of the column (Equation 17).

$$\Delta_{b,f} = \left(\Delta_{flex-A} + \Delta_{flex-B} + \Delta_{flex-C} + \Delta_{flex-D} + \Delta_{flex-E} + \Delta_{flex-F}\right) \times \frac{L_c}{L_b} \quad 17$$

The total displacement of the column top due to the flexure of the column is determined as:

$$\Delta_{c,f} = \Delta_{flex-I} + \Delta_{flex-K} \quad 18$$

BEAM AND COLUMN SHEAR DISPLACEMENTS

To determine the magnitude of shear displacements that occurred in a gauge group, it is assumed that the dimension of the gauge group parallel to the shear force does not change. As a result the two shear displacements marked '$\Delta_{shear-x}$' in Figure F-8: Definitions used to determine the shear displacement in a gauge group are equal.

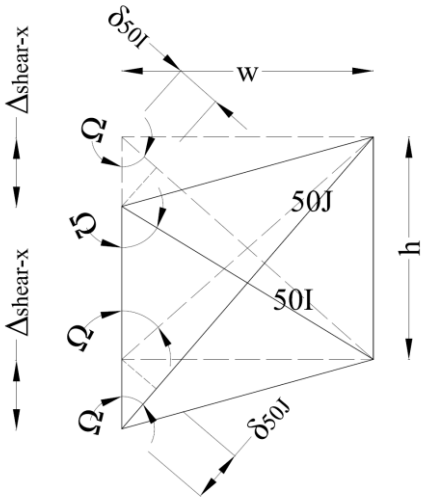

Figure F-8: Definitions used to determine the shear displacement in a gauge group

Based on the schematic view of the shear displacement (Figure F-8: Definitions used to determine the shear displacement in a gauge group) it is clear that 'δ_{50J}' is an extension (and hence a positive gauge reading) and 'δ_{50I}' is a contraction (and hence a negative gauge reading). Due to the small geometry changes of gauge blocks during testing, it is assumed that the angle 'Ω' remains constant and is given by:

$$\Omega = \tan^{-1}\left(\frac{w}{h}\right) \qquad 19$$

$$\cos(\Omega) = \frac{\delta_{50J}}{\Delta_{shear-x}} = \frac{-\delta_{50I}}{\Delta_{shear-x}} \qquad 20$$

Rearranging and summing to get an average value of '$\Delta_{shear\text{-}x}$' we have:

$$\Delta_{shear-x} = \frac{\delta_{50J} - \delta_{50I}}{2 \times \cos(\Omega)} \qquad 21$$

Apply the same concept, as explained for the total displacement of the column-top based on flexure, to the total column-top displacement due to the shear we have:

$$\Delta_{b,s} = \left(\Delta_{shear-A} + \Delta_{shear-B} + \Delta_{shear-C} + \Delta_{shear-D} + \Delta_{shear-E} + \Delta_{shear-F}\right) \times \frac{L_c}{L_b} \qquad 22$$

$$\Delta_{c,s} = \Delta_{shear-I} + \Delta_{shear-K} \quad 23$$

$\Delta_{b,s}$ = total displacement of column top due to the shear of the beam (mm)

$\Delta_{c,s}$ = total displacement of column top due to the shear of the column (mm)

REFERENCES

Au, EV 2010, The Mechanics and Design of a Non-Tearing Floor Connection Using Slotted Reinforced Concrete Beams University of Canterbury, Christchurch, New Zealand.

NZS3101 2006, 'NZS3101 Concrete structures standard Parts 1 & 2: The Desing of Concrete Structures and Commentary'. Standards New Zealand, Wellington, New Zealand, p. 698.

APPENDIX G – DIANA INPUT (*.DAT) AND ANALYSIS (*.DCF) FILES

The properties of materials (including those of the concrete and steel) used in the finite element analysis are given below. Poisson's ratios of 0.2 and 0.3 were used for concrete and steel, respectively. In the tables below the unit of the mode-I fracture energy 'GF1' is 'N/mm', modulus of elasticity 'E' is 'GPa', concrete compressive strength 'f'_c' is 'MPa', concrete tensile strength 'f_t' is 'MPa', and steel yield stress 'f_y' is 'MPa'.

	BCJ1	**BCJ2**	**BCJ3**	**BCJ4**	**BCJ5**	**BCJ6**	**BCJ7**
E_c	46.602	44.414	42.029	46.094	37.967	29.080	28.258/43.820
f'_c	124.3	112.9	101.1	121.6	82.5	48.4	45.7/109.9
f_t	7.77	7.33	6.86	7.66	6.07	4.41	4.26/7.21
GF1	0.1688	0.1631	0.1565	0.1675	0.1446	0.1147	0.1116/0.1615

BCJ1	**D25**	**D20**	**HR12**	**HR10**	**R10**	**R8**
E_s	173.61	177.82	171.38	172.95	189.30	194.98
f_y	303.64	304.65	440.80	438.11	318.73	385.50

BCJ2	**D25**	**D20**	**HR12**	**HR10**	**R10**	**R8**
E_s	185.72	185.50	180.65	194.06	192.32	199.78
f_y	307.05	530.59	430.02	461.77	318.73	413.78

BCJ3	**D25**	**D20**	**R10**	**R8**
E_s	181.46	178.78	191.99	196.08
f_y	304.35	309.46	325.43	387.24

BCJ4	**HD20**	**HD16**	**HR12**	**HR10**	**R10**	**R8**
E_s	185.50	178.18	178.41	183.93	179.97	197.79
f_y	530.59	536.97	434.26	447.02	319.50	403.73

BCJ5	**D25**	**D20**	**HR12**	**HR10**	**R10**	**R8**
E_s	177.66	169.60	193.65	187.11	183.95	198.57
f_y	341.62	305.25	447.52	453.89	321.28	448.36

BCJ6	D25	D20	HR12	HR10	R10	R8
E_s	188.07	179.68	178.45	189.19	180.07	205.85
f_y	319.71	305.25	435.67	457.19	342.69	443.60

BCJ7	D25	D20	HR12	HR10	R10	R8
E_s	181.03	176.72	183.06	188.41	189.11	194.49
f_y	315.10	302.25	449.99	443.97	297.08	449.97

After the initial FE model was generated in the FX+ environment in DIANA and the preliminary features of the material and physical properties were defined, the model was exported into the "Mesh Edit" environment. Some of the advanced material properties, constitutive models and analysis commands were defined in the "Mesh Edit" environment. Once the changes were ready and the modified model was saved, two text files were generated with extensions "*.dat" and "*.dcf" which were used as the input and analysis command files, respectively. A sample of each of these files is provided here in order to show a more detailed database for the interested reader.

DIANA INPUT DATA FILE (*.DAT)

```
Translated from FX+ for DIANA neutral file (version 1.2.0).

'DIRECTIONS'
   1  1.00000E+000  0.00000E+000  0.00000E+000
   2  0.00000E+000  1.00000E+000  0.00000E+000
   3  0.00000E+000  0.00000E+000  1.00000E+000

'COORDINATES'
   1 -2.60000E+002  1.56000E+003  0.00000E+000
   2 -2.60000E+002  1.45500E+003  0.00000E+000
   3 -2.60000E+002  1.35000E+003  0.00000E+000

Coordinate of the points continued…

'MATERI'
   1 NAME   "Linear-Conc"
     YOUNG   4.66028E+004
     POISON  2.00000E-001
   2 NAME   "Joint-Conc"
     YOUNG   4.66028E+004
     POISON  2.00000E-001
     TOTCRK  ROTATE
     COMCRV  THOREN
     CNFCRV  VECCHI
     COMSTR  124.3
     TENCRV  HORDYK
     TENSTR  7.77
     GF1     0.1688
   3 NAME   "Column-Conc"
```

```
   YOUNG   4.66028E+004
   POISON  2.00000E-001
   TOTCRK  ROTATE
   COMCRV  THOREN
   CNFCRV  VECCHI
   COMSTR  124.3
   TENCRV  HORDYK
   TENSTR  7.77
   GF1     0.1688
 4 NAME    "Beam-Conc"
   YOUNG   4.66028E+004
   POISON  2.00000E-001
   TOTCRK  ROTATE
   COMCRV  THOREN
   CNFCRV  VECCHI
   COMSTR  124.3
   TENCRV  HORDYK
   TENSTR  7.77
   GF1     0.1688
 5 NAME    "Steel_Support"
   YOUNG   2.00000E+010
   POISON  3.00000E-001
 6 NAME    D25
   YOUNG   1.73610E+005
   POISON  3.00000E-001
   YIELD   MENEGP
   YLDVAL  303.64 0.00853 19.5 18.5 0.1 0.0 0.0
 7 NAME    D20
   YOUNG   1.77820E+005
   POISON  3.00000E-001
   YIELD   MENEGP
   YLDVAL  304.65 0.00732 19.5 18.5 0.1 0.0 0.0
 8 NAME    HD20
   YOUNG   1.85500E+005
   POISON  3.00000E-001
   YIELD   MENEGP
   YLDVAL  530.59 0.00781 19.5 18.5 0.1 0.0 0.0
 9 NAME    HD16
   YOUNG   1.78180E+005
   POISON  3.00000E-001
   YIELD   MENEGP
   YLDVAL  536.97 0.00719 19.5 18.5 0.1 0.0 0.0
10 NAME    HR12
   YOUNG   1.71380E+005
   POISON  3.00000E-001
   YIELD   MENEGP
   YLDVAL  440.80 0.02537 19.5 18.5 0.1 0.0 0.0
11 NAME    HR10
   YOUNG   1.72950E+005
   POISON  3.00000E-001
   YIELD   MENEGP
   YLDVAL  438.11 0.02597 19.5 18.5 0.1 0.0 0.0
12 NAME    R10
   YOUNG   1.89300E+005
   POISON  3.00000E-001
   YIELD   MENEGP
   YLDVAL  318.73 0.00966 19.5 18.5 0.1 0.0 0.0
13 NAME    R8
   YOUNG   1.94980E+005
   POISON  3.00000E-001
   YIELD   MENEGP
```

```
      YLDVAL  385.50 0.00769 19.5 18.5 0.1 0.0 0.0
   14 NAME   "Steel_Tendon"
      YOUNG   2.00000E+010
      POISON  3.00000E-001
      NOBOND
   15 NAME   "Steel-Spring"
      YOUNG   2.00000E+010
      POISON  3.00000E-001
   16 NAME   "Steel-Spring"
      YOUNG   2.00000E+010
      POISON  3.00000E-001
      SPRING  1.75000E+004

'GEOMET'
    1 NAME   BEAM-SUPPORT
      CROSSE  7.06858E+004
    2 NAME   JOINT-CONC
      THICK   3.40000E+002
      FLAT
    3 NAME   BEAM-CONC
      THICK   3.40000E+002
      FLAT
    4 NAME   COLUMN-CONC
      THICK   3.40000E+002
      FLAT
    5 NAME   LINEAR-CONC
      THICK   3.40000E+002
      FLAT
    6 NAME   STEEL-SUPPORT
      THICK   3.40000E+002
      FLAT
    7 NAME   SPRING
      AXIS    1.00000E+000  0.00000E+000  0.00000E+000
    8 NAME   D25
      CROSSE  4.90900E+002
    9 NAME   D20
      CROSSE  3.14200E+002
   10 NAME   R8
      CROSSE  5.03000E+001
   11 NAME   R10
      CROSSE  7.85000E+001
   12 NAME   HR10
      CROSSE  7.85000E+001
   13 NAME   HR12
      CROSSE  1.13100E+002
   14 NAME   TENDON
      CROSSE  9.62100E+002

'DATA'
    1 NAME   LINEAR-CONC
    2 NAME   JOINT-CONC
      NINTEG 3 3 5
    3 NAME   COLUMN-CONC
      NINTEG 3 3 5
    4 NAME   BEAM-CONC
      NINTEG 3 3 5
    5 NAME   STEEL-SUPPORT
   22 NAME   BEAM-SUPPORT
   25 NAME   SPRING
   14 NAME   D25
   15 NAME   D20
```

```
  16 NAME   HD20
  17 NAME   HD16
  18 NAME   HR12
  19 NAME   HR10
  20 NAME   R10
  21 NAME   R8
  24 NAME   TENDON

'ELEMENTS'
CONNECT
 205 L2TRU  677 730
 206 L2TRU  685 731
   1 CQ40S  2 30 7 50 6 26 1 46
   2 CQ40S  3 34 8 51 7 30 2 47
   3 CQ40S  4 38 9 52 8 34 3 48

Element connections continued…

MATERI
/ 153-188 / 1
/ 1-16 / 2
/ 105-152 / 3
/ 17-104 / 4
/ 189-206 / 5
/ 833 / 16

DATA
/ 153-188 / 1
/ 1-16 / 2
/ 105-152 / 3
/ 17-104 / 4
/ 189-204 / 5
/ 205 206 / 22
/ 833 / 25

GEOMET
/ 205 206 / 1
/ 1-16 / 2
/ 17-104 / 3
/ 105-152 / 4
/ 153-188 / 5
/ 189-204 / 6
/ 833 / 7

'REINFORCEMENTS'
LOCATI
   1 BAR
     LINE   734 735
     LINE   736 737
     LINE   738 739
     LINE   732 733

Reinforcement locations continued…

MATERI
/ 1 / 6
/ 5 9 / 7
/ 603 / 10
/ 583 / 11
/ 343 / 12
/ 23 / 13
```

```
/ 623 / 14

GEOMET
/ 1 / 8
/ 5 9 / 9
/ 23 / 10
/ 343 / 11
/ 583 / 12
/ 603 / 13
/ 623 / 14

DATA
/ 1 / 14
/ 5 9 / 15
/ 603 / 18
/ 583 / 19
/ 343 / 20
/ 23 / 21
/ 623 / 24

'LOADS'
CASE 1
REINFO
623  PRESTR  3.89770E+002
CASE 2
DEFORM
628  TR 1  1.00000E+000

'GROUPS'
ELEMEN
1904 "Joint-Conc" / 1-16 /
1906 "Beam-Conc" / 17-104 /
1910 "Column-Conc" / 105-152 /
1914 "Linear-Conc" / 153-188 /
1924 "Steel-Plates" / 189-204 /
1947 "Beam-Support" / 205 206 /
2590 "Spring" 833
REINFO
1948 "D25-Beam(1)" 1
1956 "D20-Column(1)" 9
1952 "D20-Beam(1)" 5
1970 "R8-Beam(1)" 23
2290 "R10-Column(1)" 343
2530 "HR10-Joint(1)" 583
2550 "HR12-Joint(1)" 603
2570 "Tendon(1)" 623

'SUPPOR'
/ 704 730 731 / TR 2
/ 704 730 731 639-636(-1) 630-626(-1) / TR 3
/ 730 731 628 / TR 1

'UNITS'
FORCE N
LENGTH MM
MASS  1.00000E+003
'END'
```

DIANA ANALYSIS COMMAND FILE (*.DCF)

```
*FILOS
 INITIA
*NONLIN

 BEGIN EXECUT
   BEGIN LOAD
     LOADNR 1
     STEPS  EXPLIC  SIZES 0.1(10)
   END LOAD
   BEGIN ITERAT
     BEGIN CONVER
       ENERGY  TOLCON 0.0025
       FORCE  OFF
     END CONVER
     LINESE
     MAXITE 150
   END ITERAT
   BEGIN OUTPUT
    FXPLUS
    FILE BCJ1-R26-1-5(1)
    DISPLA  TOTAL  TRANSL  GLOBAL
    FORCE  REACTI  TRANSL  GLOBAL
    STRAIN  CRACK  GREEN
    STRAIN  PLASTI  GREEN  GLOBAL
    STRAIN  ELASTI  GREEN  GLOBAL
    STRAIN  TOTAL  GREEN  GLOBAL
    STRESS  TOTAL  CAUCHY  GLOBAL
   END OUTPUT
   TEXT "Axial"
 END EXECUT

 BEGIN EXECUT
   BEGIN LOAD
     LOADNR 2
     STEPS  EXPLIC  SIZES 1(3)   -1(6)   1(3)\
                          1(6)   -1(12)  1(6)\
                          1(10)  -1(20)  1(10)\
                          1(15)  -1(30)  1(15)\
                          1(21)  -1(42)  1(21)\
                          1(28)  -1(56)  1(28)\
                          1(41)  -1(82)  1(41)\
                          1(55)  -1(110) 1(55)\
                          1(69)  -1(138) 1(69)\
                          1(97)  -1(194) 1(97)\
                          1(124) -1(248) 1(124)
   END LOAD
   BEGIN ITERAT
     BEGIN CONVER
       DISPLA  OFF
       BEGIN ENERGY
         CONTIN
         TOLCON 0.0025
       END ENERGY
       FORCE  CONTIN
     END CONVER
```

```
     LINESE
     MAXITE 10000
     METHOD  SECANT  BROYDE
   END ITERAT
   BEGIN OUTPUT
    FXPLUS
    FILE BCJ1-R26-1-5(1)
    SELECT  STEPS 11-86 87-97(5) 101 102-112(5) 116 117-127(5) 131 132-
142(5) 146 147-167(5) 168-188(5) 189-209(5) 210-230(5)/
    DISPLA  TOTAL  TRANSL  GLOBAL
    FORCE  REACTI  TRANSL  GLOBAL
    STRAIN  CRACK  GREEN
    STRAIN  PLASTI  GREEN  GLOBAL
    STRAIN  ELASTI  GREEN  GLOBAL
    STRAIN  TOTAL  GREEN  GLOBAL
    STRESS  TOTAL  CAUCHY  GLOBAL
   END OUTPUT
   BEGIN OUTPUT
    FXPLUS
    FILE BCJ1-R26-1-5(2)
    SELECT  STEPS 231-256(5) 258 259-284(5) 286 287-312(5) 314 315-340(5)
342 343-383(5) 384-424(5) 425-465(5) 466-506(5) 507-557(5) 561 562-612(5)
616  617-667(5)  671  672-722(5)  726  727-792(5)  795  796-861(5)  864  865-
930(5) 933 934-999(5) 1002/
    DISPLA  TOTAL  TRANSL  GLOBAL
    FORCE  REACTI  TRANSL  GLOBAL
    STRAIN  CRACK  GREEN
    STRAIN  PLASTI  GREEN  GLOBAL
    STRAIN  ELASTI  GREEN  GLOBAL
    STRAIN  TOTAL  GREEN  GLOBAL
    STRESS  TOTAL  CAUCHY  GLOBAL
   END OUTPUT
   BEGIN OUTPUT
    FXPLUS
    FILE BCJ1-R26-1-5(3)
    SELECT  STEPS 1003-1098(5) 1099 1100-1195(5) 1196 1197-1292(5) 1293
1294-1389(5) 1390 1391-1511(5) 1514 1515-1635(5) 1638 1639-1759(5) 1762
1763-1883(5) 1886/
    DISPLA  TOTAL  TRANSL  GLOBAL
    FORCE  REACTI  TRANSL  GLOBAL
    STRAIN  CRACK  GREEN
    STRAIN  PLASTI  GREEN  GLOBAL
    STRAIN  ELASTI  GREEN  GLOBAL
    STRAIN  TOTAL  GREEN  GLOBAL
    STRESS  TOTAL  CAUCHY  GLOBAL
   END OUTPUT
   TEXT "Lateral"
 END EXECUT

*END
```